



# Inference of a human brain fiber bundle atlas from high angular resolution diffusion imaging

Pamela Beatriz Guevara Alvez

## ► To cite this version:

Pamela Beatriz Guevara Alvez. Inference of a human brain fiber bundle atlas from high angular resolution diffusion imaging. Other [cond-mat.other]. Université Paris Sud - Paris XI, 2011. English. NNT : 2011PA112123 . tel-00638766

**HAL Id: tel-00638766**

**<https://theses.hal.science/tel-00638766>**

Submitted on 7 Nov 2011

**HAL** is a multi-disciplinary open access archive for the deposit and dissemination of scientific research documents, whether they are published or not. The documents may come from teaching and research institutions in France or abroad, or from public or private research centers.

L'archive ouverte pluridisciplinaire **HAL**, est destinée au dépôt et à la diffusion de documents scientifiques de niveau recherche, publiés ou non, émanant des établissements d'enseignement et de recherche français ou étrangers, des laboratoires publics ou privés.

# PhD THESIS

prepared at  
**LNAO, Neurospin, CEA**

and presented at the  
**University of Paris-Sud 11**  
Graduate School of Sciences and Information Technologies,  
Telecommunications and Systems

*A dissertation submitted in partial fulfillment  
of the requirements for the degree of*

**DOCTOR OF SCIENCE**  
Specialized in Physics

## **Inference of a human brain fiber bundle atlas from high angular resolution diffusion imaging**

Pamela Beatriz GUEVARA ALVEZ

Reviewers	Dr. Nicholas Ayache	INRIA Sophia Antipolis, France
	Dr. Christian Barillot	IRISA, CNRS/INRIA, France
Examiners	Pr. Jacques Bittoun	Université Paris Sud 11, France
	Pr. Marco Catani	King's College London, United Kingdom
	Pr. Dominique Hasboun	UPMC/ CHU Pitié-Salpêtrière, France
	Dr. Cyril Poupon	LRMN, NeuroSpin, CEA, France
Adviser	Dr. Jean-François Mangin	LNAO, NeuroSpin, CEA, France



UNIVERSITÉ PARIS-SUD 11 - UFR Sciences

École Doctorale STITS

(Sciences et Technologies de l'Information  
des Télécommunications et des Systèmes)

# THÈSE

pour obtenir le titre de  
DOCTEUR EN SCIENCES  
de l'UNIVERSITÉ Paris-Sud 11

Discipline: Physique

présentée et soutenue par

Pamela Beatriz GUEVARA ALVEZ

## Inférence d'un modèle des faisceaux de fibre du cerveau humain à partir de l'imagerie de diffusion à haute résolution angulaire

*Thèse dirigée par Jean-François MANGIN*

Date prévue de soutenance: 5 octobre 2011

### Composition du jury:

<i>Rapporteurs</i>	Dr. Nicholas Ayache	INRIA Sophia Antipolis, France
	Dr. Christian Barillot	IRISA, CNRS/INRIA, France
<i>Examineurs</i>	Pr. Jacques Bittoun	Université Paris Sud 11, France
	Pr. Marco Catani	King's College London, Royaume-Uni
	Pr. Dominique Hasboun	UPMC / Pitié-Salpêtrière, France
	Dr. Cyril Poupon	LRMN, NeuroSpin, CEA, France
<i>Directeur de thèse</i>	Dr. Jean-François Mangin	LNAO, NeuroSpin, CEA, France





# Contents

<b>Contents</b>	<b>iv</b>
<b>List of Figures</b>	<b>viii</b>
<b>List of Tables</b>	<b>ix</b>
<b>List of Symbols</b>	<b>xi</b>
<b>Abstract</b>	<b>xv</b>
<b>Résumé</b>	<b>xvii</b>
<b>I Introduction</b>	<b>1</b>
<b>1 Introduction</b>	<b>3</b>
<b>II Background</b>	<b>9</b>
<b>2 Nervous Tissue and Human Brain White Matter</b>	<b>11</b>
2.1 Human Brain General Anatomy . . . . .	12
2.2 The Nervous Tissue . . . . .	17
2.3 White Matter Organization . . . . .	21
2.3.1 Association Pathways . . . . .	21
2.3.2 Commissural Pathways . . . . .	25
2.3.3 Projection Pathways . . . . .	26
2.4 Conclusion . . . . .	28
<b>3 Principles of Diffusion MRI</b>	<b>29</b>
3.1 From the diffusion phenomenon to diffusion MRI . . . . .	30
3.1.1 Diffusion Basics . . . . .	30

3.1.2	Basics on Magnetic Resonance Imaging	32
3.1.3	Diffusion-weighted MR	35
3.1.4	EPI sequence and correction of geometric distortions	38
3.2	Diffusion MRI models	40
3.2.1	Diffusion Tensor Model (DTI)	42
3.2.2	High Angular Resolution Diffusion Imaging (HARDI)	49
3.3	MR Diffusion Tractography	59
3.3.1	Streamline Deterministic Tractography	60
3.3.2	Streamline Probabilistic Tractography	64
3.3.3	Other Tractography Algorithms	66
3.4	Conclusion	69
<b>4</b>	<b>White Matter Clustering</b>	<b>71</b>
4.1	Cross-subject registration	73
4.1.1	Normalization to Talairach space	74
4.1.2	Non-linear registration methods	76
4.2	White Matter segmentation of DW images	77
4.3	ROI-based WM fiber tract segmentation	77
4.4	White Matter fiber clustering	80
4.4.1	Clustering	80
4.4.2	Fiber similarity measures	88
4.4.3	Fiber clustering methods	92
4.5	Quantitative DW measures across bundles	105
4.6	Conclusion	111
<b>III</b>	<b>Methods</b>	<b>113</b>
<b>5</b>	<b>Intra-subject fiber clustering</b>	<b>115</b>
5.1	Introduction	117
5.1.1	Previous works	117
5.1.2	Main output	118
5.1.3	Tractography dataset size	119
5.1.4	Hierarchical fiber clustering overview	120
5.2	Robust intra-subject fiber clustering	122
5.2.1	Step 1: Hierarchical decomposition	122
5.2.2	Step 2: Length-based segmentation	122
5.2.3	Step 3: Voxel-based clustering	123
5.2.4	Step 4: Extremity-based clustering	130
5.2.5	Step 5: Fascicle merge	132
5.3	Method validation and parameters tuning	135
5.3.1	Whole method evaluation using simulated datasets	136

5.3.2	Cost of scalability . . . . .	140
5.3.3	Clustering parameters setting . . . . .	143
5.4	Intra-subject fiber clustering results . . . . .	144
5.4.1	A T1-based tractography propagation mask . . . . .	144
5.4.2	Adult HARDI datasets . . . . .	148
5.4.3	Child DTI datasets . . . . .	150
5.5	Applications . . . . .	153
5.5.1	Physical phantom . . . . .	153
5.5.2	Top-down decomposition of large known WM tracts . . . . .	156
5.6	Discussion . . . . .	158
5.7	Conclusion . . . . .	159
<b>6</b>	<b>Inter-subject clustering: Inference of a multi-subject bundle atlas</b>	<b>161</b>
6.1	Two-level fiber clustering strategy . . . . .	163
6.1.1	First level: intra-subject clustering . . . . .	164
6.1.2	Second level: inter-subject clustering . . . . .	165
6.2	Inter-subject clustering validation . . . . .	169
6.3	An example of application for the analysis of U-fibers . . . . .	173
6.4	HARDI multi-subject atlas of DWM known bundles . . . . .	174
6.5	HARDI multi-subject atlas of SWM short association bundles . . . . .	178
6.6	Conclusion . . . . .	182
<b>IV</b>	<b>Application</b>	<b>185</b>
<b>7</b>	<b>Automatic segmentation of massive tractography datasets</b>	<b>187</b>
7.1	Automatic segmentation of massive tractography datasets . . . . .	189
7.2	Results . . . . .	191
7.2.1	Results for the segmentation of deep white matter bundles . . . . .	191
7.2.2	Results for the segmentation of short association bundles of SWM . . . . .	195
7.3	Conclusion . . . . .	198
<b>V</b>	<b>Conclusion</b>	<b>201</b>
<b>8</b>	<b>Conclusion</b>	<b>203</b>
<b>VI</b>	<b>Appendix</b>	<b>209</b>
<b>A</b>	<b>White Matter atlases</b>	<b>211</b>
<b>B</b>	<b>Publications of the Author Arising from this Work</b>	<b>219</b>



# List of Figures

2.1	Central nervous system . . . . .	13
2.2	Coronal slices of an human brain . . . . .	14
2.3	Human brain lobes . . . . .	16
2.4	Schematic representation of the major cellular elements of neural tissue . .	18
2.5	White matter axons main structure . . . . .	20
2.6	Anatomic relationships of several WM fiber tracts. . . . .	22
2.7	Main known white matter fiber tracts. . . . .	23
2.8	Main areas involved in language. . . . .	24
2.9	Internal face of the right hemisphere. . . . .	25
2.10	Dissection showing the course of the cerebrospinal fibers. . . . .	26
2.11	Thalamic radiations. . . . .	27
3.1	Brownian motion simulation . . . . .	31
3.2	Illustration of MRI pulse sequences . . . . .	34
3.3	Illustration of spin dephasing in <i>spin echo sequence</i> . . . . .	35
3.4	Pulse Gradient Spin Echo sequence experiment . . . . .	36
3.5	Effect of diffusion-encoding axis direction . . . . .	39
3.6	Example of a field map image. . . . .	40
3.7	Anisotropy and two-compartments model . . . . .	41
3.8	Diffusion Tensor and anitropic diffusion . . . . .	44
3.9	Mean diffusivity and Fractional anisotropy examples . . . . .	45
3.10	Example of FA as a measure of WM integrity . . . . .	46
3.11	Examples of prolate and oblate DT ellipsoids. . . . .	47
3.12	Colour encoded fiber orientation maps . . . . .	48
3.13	Partial volume effect for two fiber populations . . . . .	49
3.14	Major diffusion MRI acquisition and reconstruction methods . . . . .	50
3.15	Illustration of fODFs and dODFs for several simple WM configurations . .	52
3.16	DSI reconstruction scheme . . . . .	52
3.17	Qball reconstruction scheme . . . . .	53
3.18	Examples of spherical harmonics . . . . .	55
3.19	QBI: dODFs for the analytical and numerical solutions . . . . .	56
3.20	Spherical deconvolution illustration . . . . .	57

3.21	Sketch of the convolution/deconvolution of the dODF . . . . .	57
3.22	Sharp spherical deconvolution transform scheme . . . . .	58
3.23	Illustration of streamline tractography in DTI . . . . .	59
3.24	Example algorithms for deterministic streamline tractography in DTI . . . .	61
3.25	Example of TEND algorithm behavior . . . . .	62
3.26	Regularization of particle trajectories for HARDI . . . . .	63
3.27	Streamline deterministic and probabilistic tractography examples . . . . .	65
3.28	MFACT tractography approach . . . . .	66
3.29	Bayesian tractography probability map . . . . .	67
3.30	Example of spin-glass tractography . . . . .	67
3.31	Comparison of spin-glass and streamline tractography . . . . .	68
4.1	The Talairach atlas and normalized space . . . . .	75
4.2	Illustration of manual ROI-based WM tract segmentation . . . . .	79
4.3	Example of clustering results . . . . .	81
4.4	Matrix and graph affinity representations . . . . .	82
4.5	Hierarchical clustering example . . . . .	83
4.6	Linkage types of hierarchical clustering . . . . .	84
4.7	Example of hierarchical clustering adaptive partition . . . . .	85
4.8	Illustration of distances based on closest points . . . . .	89
4.9	Comparison of three pairwise fiber distances . . . . .	90
4.10	Illustration thresholded closest distances . . . . .	91
4.11	Examples of the product of blurred indicator functions . . . . .	93
4.12	Illustration of fiber clustering using Hierarchical Clustering . . . . .	98
4.13	Voxel-based fiber clustering results . . . . .	99
4.14	Voxel-based tractography segmentation method using HDPM model . . . .	100
4.15	Illustration of fiber segmentation method using spectral clustering . . . .	102
4.16	Illustration of WM segmentation using a mathematical framework . . . .	103
4.17	Illustration of a partition-based WM fiber clustering . . . . .	105
4.18	Example mean FA and skeleton images for TBSS method . . . . .	106
4.19	Quantitative analysis of WM tracts using distance maps . . . . .	108
4.20	Tractography-based medial representation of tracts . . . . .	109
4.21	Tract-based morphometry (TBM) . . . . .	110
4.22	Skeleton-based tract-specific statistics . . . . .	111
5.1	General scheme of the intra-subject clustering method. . . . .	121
5.2	First hierarchical decomposition of WM fibers (Step 1). . . . .	123
5.3	Examples of fiber groups of different lengths. . . . .	123
5.4	Random initial parcellation of white matter (Step 3) . . . . .	124
5.5	Illustration of WM connectivity calculation ( <i>Step 3</i> ) . . . . .	126
5.6	Example of a WM connectivity matrix histogram ( <i>Step 3</i> ) . . . . .	127
5.7	Voxel-based clustering example (Step 1) . . . . .	128

5.8	Flooding of the water analogy for Watershed transformation . . . . .	131
5.9	An example of fiber cluster and fiber fascicles extraction (Steps 3-4) . . . .	133
5.10	Fiber fascicle centroid clustering (Step 5) . . . . .	134
5.11	Example of final fiber bundles . . . . .	135
5.12	Example of simulated fiber bundle datasets. . . . .	137
5.13	Clustering results for simulated fiber bundle datasets. . . . .	139
5.14	Comparison of the method with a brute force fiber clustering . . . . .	141
5.15	Evaluation of the clustering method scalability cost. . . . .	142
5.16	Clustering parameters setting. . . . .	144
5.17	T1-based masks used for the propagation mask construction. . . . .	145
5.18	T2- and T1-based propagation masks. . . . .	146
5.19	Comparison of WM bundles for an FA- and our T1-based propagation mask. . . .	147
5.20	Final fiber bundles for an adult brain (right hemisphere). . . . .	150
5.21	A selection of long final fiber bundles for an adult brain (right hemisphere)	151
5.22	Final fiber bundles for a child brain (right hemisphere). . . . .	152
5.23	Final fiber bundles for the DTI physical phantom dataset. . . . .	154
5.24	Final fiber bundles for the six physical phantom datasets. . . . .	155
5.25	Bottom-up inference of a model of the subdivisions of the AF. . . . .	157
6.1	Addition of thalamic fiber subsets in intra-subject clustering . . . . .	165
6.2	Example of the intra-subject clustering results for one subject . . . . .	166
6.3	A general scheme of the inter-subject fiber clustering . . . . .	167
6.4	Normalized Euclidean distance used for inter-subject centroids clustering . .	168
6.5	Example of inter-subject clusters (short centroid clusters of left hemisphere)	170
6.6	Example of inter-subject clusters (long centroid clusters of left hemisphere)	171
6.7	Example of some inter-subject clusters (left hemisphere) . . . . .	172
6.8	Inter-subject clustering validation using simulated centroids . . . . .	173
6.9	Preliminary U-fiber bundle atlas from inter-subject clustering results . . . .	174
6.10	Illustration of the use of inter-subject clustering results . . . . .	175
6.11	The HARDI multi-subject atlas of known bundles . . . . .	177
6.12	Cortical regions used to label the short association bundles . . . . .	179
6.13	The HARDI multi-subject atlas of short association bundles (part 1) . . . .	180
6.14	The HARDI multi-subject atlas of short association bundles (part 2) . . . .	181
6.15	The HARDI multi-subject atlas of short association bundles . . . . .	182
7.1	Automatic fiber bundle segmentation method . . . . .	190
7.2	Automatic DWM fiber bundle segmentation results for adult brains . . . .	192
7.3	Automatic DWM fiber bundle segmentation results for child brains . . . .	193
7.4	Comparison of our DWM bundle segmentation method with a ROI-based approach . . . . .	194
7.5	Automatic SWM fiber bundle segmentation results (1) . . . . .	195
7.6	Automatic SWM fiber bundle segmentation results (2) . . . . .	196



7.7	Automatic SWM fiber bundle segmentation results (3)	197
A.1	Comparison between virtual and classical dissection results	212
A.2	Probabilistic maps of 11 white matter tracts	213
A.3	DWM and SWM atlases from manual ROI-based labeling	214
A.4	Three types of WM parcellation maps	215
A.5	Short association fibers reconstructed by the TRS automated method	217

# List of Tables

2.1	Human brain lobes localization and function . . . . .	15
4.1	Categorization of fiber clustering methods (single subject) . . . . .	94
4.2	Categorization of fiber clustering methods (multiple subjects) . . . . .	96
5.1	Pseudocode of HC adaptive partition algorithm . . . . .	130



# List of Symbols

3D	3-dimensional
AC	Anterior Commissure
ADC	Apparent Diffusion Coefficient
AF	Arcuate Fasciculus
ATR	Anterior Thalamic Radiations
CC	Corpus Callosum
CHARMED	Composite Hindered And Restricted Model of Diffusion
CG	Cingulum
CNS	Central Nervous System
CNR	Contrast to Noise Ratio
CR	Corona Radiata
CSF	Cerebrospinal fluid
CST	Corticospinal Tract
dMRI	Diffusion MRI
dODF	Diffusion Orientation Distribution Function
DOT	Diffusion Orientation Transform
DPI	Diffusion Propagator Imaging
EM	Expectation-Maximization
EPI	Echo Planar Imaging
FA	Fractional Anisotropy
FACT	Fiber Assignment by Continuous Tracking
FIFO	First In First Out
fODF	Fiber Orientation Distribution Function
FRT	Funk-Radon Transform
GFA	Generalized Fractional Anisotropy
DoF	Degrees of Freedom
DSI	Diffusion Spectrum Imaging
DT	Diffusion Tensor
DTI	Diffusion Tensor Imaging
DW	Diffusion-Weighted

DWM	Deep White Matter
ICBM	International Consortium of Brain Mapping
IFO	Inferior Fronto-Occipital Fasciculus
IL	Inferior Longitudinal Fasciculus
ITR	Inferior Thalamic Radiations
GM	Gray matter
HARDI	High Angular Resolution Diffusion Imaging
HC	Hierarchical Clustering
HDPM	Hierarchical Dirichlet Processes Mixture
LDDMM	Large Deformation Diffeomorphic Metric Mapping
MD	Mean Diffusivity
MFACT	Modified Fiber Assignment by Continuous Tracking
MI	Mutual Information
MNI	Montreal Neurological Institute
MR	Magnetic Resonance
MRI	Magnetic Resonance Imaging
NMI	Normalized Mutual Information
NMR	Nuclear Magnetic Resonance
ODF	Orientation Distribution Function
PAS	Persistent Angular Structure
PC	Posterior Commissure
PCA	Principal Component Analysis
PDF	Probability Density Function
PGSE	Pulsed Gradient Spin Echo
PNS	Peripheral Nervous System
PTR	Posterior Thalamic Radiations
QBI	Q-Ball Imaging
QSI	Q-Space Imaging
RF	Radio Frequency
ROI	Region Of Interest
SD	Spherical Deconvolution
SH	Spherical Harmonics
SNR	Signal to Noise Ratio
SPM	Statistical Parametric Mapping
STR	Superior Thalamic Radiations
SFO	Superior Fronto-Occipital Fasciculus
SS-EPI	Single-Shot Echo Planar Imaging
SWM	Superficial White Matter

TBM	Tract-Based Morphometry
TBSS	Tract-Based Spatial statistics
TE	Echo Time
TEND	Tensor Deflection
TPM	Tract Probability Map
TR	Repetition Time
UN	Uncinate Fasciculus
VBM	Voxel-Based Morphometry
VOI	Volume of Interest
WM	White Matter



# Abstract

Human brain white matter (WM) structure and organisation are not yet completely known. Diffusion-Weighted Magnetic Resonance Imaging (dMRI) offers a unique approach to study *in vivo* the structure of brain tissues, allowing the non invasive reconstruction of brain fiber bundle trajectories using tractography. Nowadays, the recent dMRI techniques with high angular resolution (HARDI) have largely improve the quality of tractography relative to standard diffusion tensor imaging. However, the resulting tractography datasets are highly complex and include millions of fibers which requires a new generation of analysis methods. Beyond the mapping of the main white matter pathways, this new technology opens the road to the study of short association bundles, which have been rarely studied before and is in the focus of this thesis. The goal is to infer an atlas of the fiber bundles of the human brain and a method mapping this atlas to any new brain.

In order to overcome the limitation induced by the size and complexity of the tractography datasets, we propose a two-level strategy, chaining intra- and inter-subject fiber clustering. The first level, an intra-subject clustering, is composed by several steps performing a robust hierarchical clustering of a fiber tractography dataset that can deal with millions of diffusion-based tracts. The end result is a set of a few thousand homogeneous bundles representing the whole structure of the tractography dataset. This simplified representation of white matter can be used further for several studies of individual bundle structure or group analyses. The robustness and the cost of the scalability of the method are checked using simulated tract datasets. The second level, an inter-subject clustering, gathers the bundles obtained in the first level for a population of subjects and performs a clustering after spatial normalization. It produces as output a model composed by a list of generic fiber bundles that can be detected in most of the population. A validation with simulated datasets is applied in order to study the behavior of the inter-subject clustering over a population of subjects aligned with affine registration. The whole method was applied to the tracts computed from HARDI data obtained for twelve adult brains. A novel HARDI multi-subject bundle atlas, representing the variability of the bundle shape and position across subjects was thus inferred. The atlas includes 36 deep WM bundles, some of these representing a few subdivisions of known WM tracts, and 94 short association bundles of superficial WM. Finally, we propose an automatic segmentation method mapping this atlas to any new subject.





# Résumé (Français)

## Chapitre 1: Introduction

La structure et l'organisation de la substance blanche n'est pas encore connue dans sa totalité. Les fibres nerveuses connectent entre-elles les neurones des différentes régions du cerveau pour former des réseaux plus ou moins complexes, à l'origine de toutes les fonctions cérébrales. Connaître la carte de la connectivité anatomique cérébrale est alors un grand défi, du plus grand intérêt pour comprendre le fonctionnement du cerveau et étudier nombreuses pathologies.

L'imagerie par résonance magnétique de diffusion (IRMd) offre une approche unique pour étudier *in vivo* la structure du tissu cérébral. Elle permet de reconstruire à travers la tractographie les trajectoires des faisceaux de fibres du cerveau de façon non-invasive.

Le modèle de diffusion le plus utilisé jusqu'à présent est le tenseur de diffusion (DTI), qui a permis le développement d'études à la fois dans le domaine clinique et dans la recherche plus fondamentale. C'est ainsi que les long faisceaux d'association de la substance blanche ont été étudiés chez le sujet sain et dans plusieurs maladies. Cependant la DTI présente quelques limitations au niveau de la représentation de la configuration des faisceaux de fibres. Avec l'émergence des IRMs plus puissantes, permettant des résolutions spatiales plus élevées, et des nouvelles techniques d'IRMd à haute résolution angulaire (HARDI), les données de tractographie sont aujourd'hui d'une meilleure qualité, mais, malgré ces progrès, ne sont pas dépourvues d'artefacts. Ces données sont plus complexes et sont très volumineuses, avec plus d'un million de fibres pour le cerveau entier.

La quantification des structures définies par la tractographie et, en particulier, l'extraction des faisceaux de fibres reste un problème non résolu. Depuis le développement de la tractographie, plusieurs méthodes ont été proposées pour segmenter les faisceaux de façon automatique. Pour l'instant, la méthode la plus fréquemment utilisée nécessite de multiples régions d'intérêt (ROI). Cette méthode est une méthode guidée, dans laquelle on effectue la tractographie des fibres en partant de graines situées dans une ROI prédéfinie, ou dans tout le cerveau, et on préserve seulement les fibres qui touchent d'autres ROI prédéfinies. D'autres approches utilisent des atlas des différentes régions du cerveau pour extraire les faisceaux connus, reposant sur la qualité du recalage entre les données de diffusion et l'atlas anatomique. D'autres méthodes cherchent à regrouper et classer

automatiquement l'ensemble de fibres généré par la tractographie en utilisant une mesure de distance entre les fibres. Une des grandes difficultés de ces approches c'est la taille des données, laquelle rend actuellement impossible un traitement suffisamment performant qui considère la totalité des données. Les approches proposées utilisent alors des échantillons des fibres ou des *a priori* qui permettent de réduire les données ou de subdiviser le problème. Ces méthodes, en général cherchent à retrouver les faisceaux les plus connus, mais il existe une grande quantité de faisceaux qui n'ont pas encore été étudiés en profondeur, et qui présentent une énorme variabilité entre les sujets, d'où la difficulté de leur étude. Quant à l'analyse inter-sujet, plusieurs méthodes d'alignement ont été proposées, ainsi que plusieurs descripteurs de forme des faisceaux, mais le problème de comparaison des faisceaux entre sujets reste encore ouvert.

Cette thèse vise à regrouper les trajectoires putatives des fibres en faisceaux cohérents. Le regroupement est réalisé dans un premier temps sujet par sujet, en utilisant une méthode robuste, capable d'analyser des jeux de données très grands, contenant plus d'un million de fibres. Elle permet d'obtenir pour chaque sujet quelques milliers de faisceaux des fibres représentant l'ensemble des données. Puis dans un second temps, les faisceaux obtenus sont comparés à travers une population de sujets afin d'inférer un modèle, qui représente une hiérarchie de la structure de la substance blanche, composée par des centaines de faisceaux des fibres, présents dans la plupart des sujets. Un atlas HARDI multi-sujet est ainsi créé, contenant la plupart des faisceaux connus de la substance blanche, ainsi qu'une centaine de faisceaux courts d'association, très peu étudiés jusqu'à maintenant.

Dans cette thèse, nous présentons d'abord le contexte général dans lequel s'inscrit notre travail. Le chapitre 1 présente les principaux concepts concernant l'anatomie du cerveau, le tissu nerveux et l'organisation de la substance blanche. Le chapitre 2 développe brièvement les principes de l'IRMd et de la tractographie. Le chapitre 3 décrit l'état de l'art des méthodes de regroupement et classification des fibres de la substance blanche. Ensuite, les méthodes développées au cours de cette thèse sont détaillées. Le chapitre 4 présente la méthode de regroupement de fibres intra-sujet, ainsi que les validations effectuées, les résultats obtenus et des exemples d'application. Le chapitre 5 décrit ensuite la méthode développée pour créer un modèle des faisceaux de fibres du cerveau humain, ainsi que l'atlas multi-sujet obtenu. Le chapitre 6 présente une méthode automatique de segmentation des faisceaux connus et des faisceaux d'association courts à partir de l'atlas multi-sujet développé. Nous finalisons par la conclusion, en discutant les contributions et les perspectives de ce travail réalisé.

## Chapitre 2: Tissu Nerveux et Matière Blanche

### Le cerveau humain

Le cerveau humain est un des organes les plus importants et complexes du corps humain. Depuis plus d'une centaine d'années, la compréhension de son organisation et de sa fonction a présenté un intérêt fondamental pour la neurologie et les neurosciences.

Le cerveau contrôle le système nerveux central (SNC) et le système nerveux périphérique et régule toutes les activités humaines. A grande échelle, le cerveau humain est composé par différents éléments comme du sang, du liquide céphalo-rachidien, de la substance blanche et de la substance grise. A cause de l'apparence du tissu cérébral, les aires riches en corps neuronaux et en cellules gliales sont appelées *substance grise*, alors que les aires contenant principalement des axones myélinisés et des cellules gliales sont appelées *substance blanche*. Ces éléments présentent aussi des contrastes différents dans une image de résonance magnétique (IRM) anatomique de contraste T1 (voir Figure 1 A).

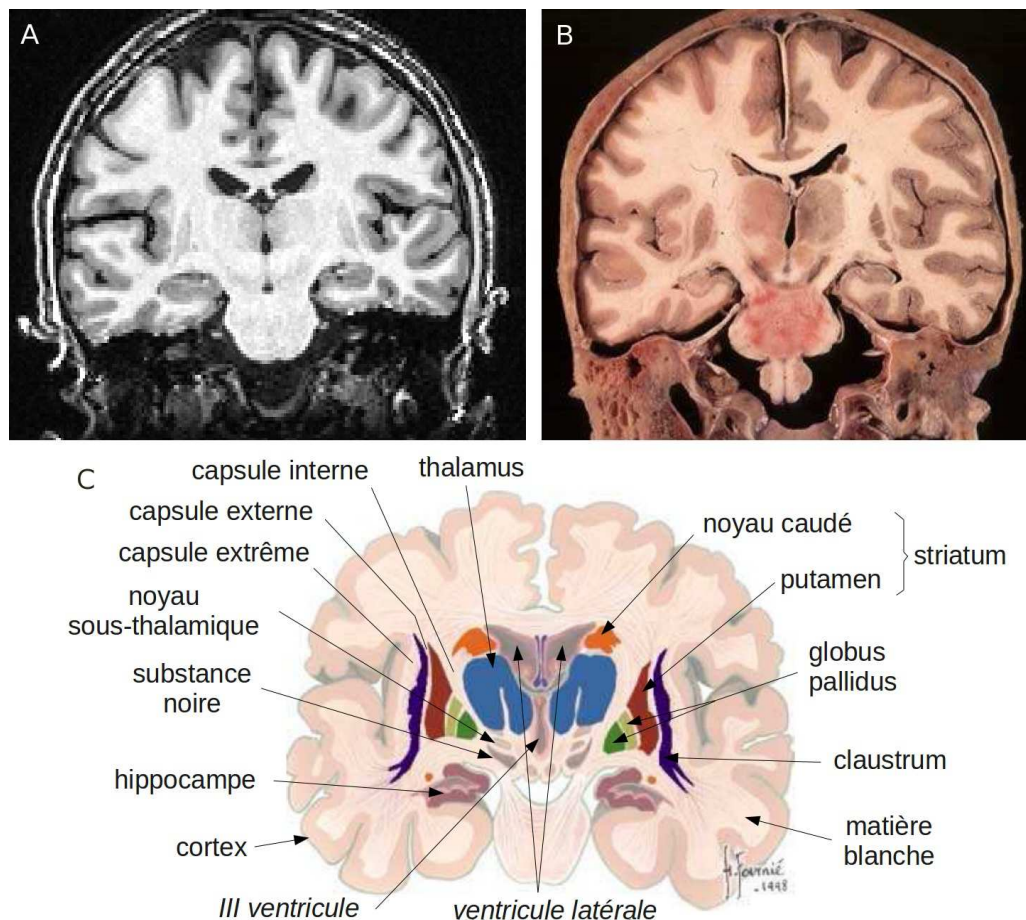


Figure 1: Coupes coronales du cerveau humain. **A** présente une coupe coronale d'une IRM anatomique T1, alors que **B** présente une coupe histologique. La substance blanche apparaît en couleur blanche à l'intérieur du cerveau. Le cortex de substance grise est la couche grise qui entoure le cerveau. **C** illustre les principales structures du cerveau dans une coupe coronale. [Figure adaptée de [Hasboun \(2007\)](#)].

Le cerveau peut être divisé en trois parties: le *télencéphale*, composé par les deux hémisphères cérébraux, le *diencéphale*, composé par des structures localisées dans le cerveau profond et le *tronc cérébral*, composé par la moëlle allongée, le pont et le mésencéphale.

Les hémisphères cérébraux contiennent le *cortex cérébral*, une couche de substance grise localisée dans la surface du cerveau. Le cortex cérébral est la structure la plus importante de la substance grise et joue un rôle majeur dans les fonctions cognitives. Les hémisphères cérébraux sont concernés premièrement par les processus sensoriels et moteurs du côté controlatéral du corps. Chaque hémisphère du cortex cérébral est divisé en cinq *lobes*: frontal, pariétal, occipital, temporal et insulaire. Chaque lobe a été associé avec différentes fonctions qui vont du raisonnement jusqu'à la perception auditive. Les lobes des deux hémisphères, bien que très similaires dans leur structure, ne sont pas complètement symétriques, et ne sont pas équivalents dans leur fonction. Les lobes présentent plusieurs sillons et convolutions, dont les plus proéminents sont très similaires entre les individus et ont des noms spécifiques.

À l'intérieur, le cerveau contient un *système ventriculaire*, constitué de quatre cavités ou ventricules contenant du liquide céphalo-rachidien, qui se continue avec le canal central et la moëlle épinière.

Les *noyaux gris centraux* (NGC) sont des noyaux de substance grise localisés dans la profondeur du cerveau, de façon symétrique, entre les deux hémisphères. Les principaux NGC sont le noyau caudé, le putamen, le globus pallidus, la substance noire et le noyau sous-thalamique. Toutes ces structures forment un système présentant des multiples connexions entre eux, et avec le cortex, le thalamus et le cervelet. Un traitement parallèle est ainsi exécuté pour permettre la planification, l'exécution et la coordination des mouvements des yeux et des membres.

Les *thalami*, localisés de façon symétrique sur le tronc cérébral, traitent et servent de point de relais de l'information sensorielle et motrice. Ils sont la porte d'entrée au cortex pour la majorité des influx provenant de l'ensemble du système nerveux. Les thalami sont fortement connectés aux différentes régions du cortex, et se connectent aussi avec l'hypothalamus, les NGC, le cervelet et la moëlle épinière.

## **Le tissu cérébral**

Les cellules du système nerveux sont principalement de deux types: les cellules nerveuses ou *neurones* et les cellules gliales ou *neuroglia*.

Les cellules gliales soutiennent, nourrissent et protègent les neurones, maintiennent leur homéostasie et les rendent plus efficaces.

Les neurones sont des éléments fondamentaux dans le système nerveux central. Ils assurent la transmission d'un signal bioélectrique appelé *influx nerveux*. Ils ont la capacité de répondre aux stimulations en les convertissant en impulsions nerveuses pour transporter l'information depuis une région à une autre du corps, en formant un réseau très complexe. Un neurone est constitué d'un corps cellulaire ou *soma*, et de deux types de prolongements, les *dendrites* et l'*axone*. Les dendrites sont des prolongements courts et très ramifiés qui

reçoivent et intègrent l'information entrante. Les axones (normalement un par neurone) présentent un diamètre relativement uniforme et peuvent avoir une longueur de entre 1 mm à plus d'un mètre. Ils distribuent les impulsions vers les autres cellules sans atténuation. Les neurones communiquent entre eux à travers des contacts spécialisés appelés synapses. Dans le SNC, l'axone est entouré par une gaine de *myéline*, formée par une prolongation d'un *oligodendrocyte*, un type particulier de cellule gliale. La myéline présente des interruptions le long de l'axone, appelées *nœuds de Ranvier*, qui aident à augmenter la vitesse de transmission de l'impulsion nerveuse (conduction saltatoire). Les axones de la substance blanche, appelés *fibres nerveuses*, sont souvent regroupés en paquets très compacts et organisés en faisceaux de fibres. Le principal enjeu de cette thèse est l'inférence d'un modèle des faisceaux de fibres de la substance blanche du cerveau humain à partir de l'imagerie de résonance magnétique de diffusion à haute résolution angulaire.

## Organisation de la substance blanche

La substance blanche est composée par les axones myélinisés qui connectent entre elles les différentes régions de substance grise du cerveau pour transmettre les impulsions nerveuses entre neurones. Dans les hémisphères, la substance blanche se retrouve entre le cortex cérébral et la substance grise sous-corticale. Elle est composée de fibres courtes superficielles, qui suivent les contours du cortex et de fibres longues, regroupées en faisceaux, localisées dans les régions plus profondes. Comme règle générale, le nombre de fibres d'un certain rang de longueurs est inversement proportionnel à leur longueur [Schüz and Braitenberg (2002)].

Les principaux faisceaux sont regroupés selon les structures qu'ils connectent: des *faisceaux commissuraux*, qui connectent entre-elles des régions des deux hémisphères, des *faisceaux d'association*, qui connectent entre-elles des régions du cortex d'un même hémisphère, et des *faisceaux de projection*, qui connectent le cortex avec les centres sous-corticaux et la moelle épinière. Une description des faisceaux de fibres les plus connus est présentée ci-dessous, fondée principalement sur les articles de Catani and Thiebaut de Schotten (2008); Aralasmak et al. (2006); Jellison et al. (2004).

## Faisceaux d'association

**Faisceau arqué:** c'est un faisceau composé de fibres associatives courtes et longues, connectant le cortex perisylvien des lobes frontal, pariétal et temporal. Pour la plupart des personnes, le faisceau arqué de l'hémisphère gauche est impliqué dans le langage, tandis que le faisceau arqué droit est souvent impliqué dans le traitement visuo-spatial et autres aspects du langage, comme la prosodie et la sémantique.

**Cingulum:** c'est un faisceau associatif médial, qui se localise le long du gyrus cingulaire, tout autour du corps calleux. Il est constitué de fibres de différentes longueurs, qui se distribuent entre le gyrus temporal antérieur et le cortex orbito-frontal. Les fibres courtes, de forme en U, connectent les lobes frontal, pariétal, occipital et temporal, et

différentes portions du cortex cingulaire. Le cingulum fait partie du système limbique et est impliqué dans l'attention, la mémoire et les émotions.

**Faisceau longitudinal inférieur:** c'est un faisceau associatif ventral composé de fibres courtes et longues, connectant les lobes occipital et temporal. Les fibres longues sont plus médiales que les courtes. Il connecte les aires visuelles avec l'amygdale et l'hippocampe et est impliqué dans la reconnaissance des visages, la perception visuelle, la lecture, la mémoire visuelle et autres fonctions reliées avec le langage.

**Faisceau unciné:** c'est un faisceau associatif ventral qui connecte le lobe temporal avec le cortex orbito-frontal médial et latéral. Ce faisceau est considéré comme une partie du système limbique, et semble être impliqué dans le traitement des émotions, de la mémoire et du langage.

**Faisceau fronto-occipital inférieur:** c'est un faisceau associatif ventral qui connecte le lobe occipital ventral avec le cortex orbito-frontal. Il est possible qu'il soit impliqué dans la lecture, l'attention et le traitement visuel. Chez les humains, il représente les seules connexions directes entre les lobes occipital et frontal.

**Fibres d'association courtes:** ce sont des fibres souvent appelées *fibres en U*, situées en dessous de la substance grise du cortex, et qui connectent des gyri adjacents. Ces fibres se localisent dans la substance blanche superficielle, entre la substance blanche profonde et le cortex. Jusqu'à présent, ces fibres n'ont pas été bien caractérisées dans la littérature. Leur localisation, nombre, trajectoires et fonctions ne sont pas suffisamment définis. Seulement deux travaux ont étudiés ces faisceaux à partir d'une analyse de groupe en utilisant une approche volumétrique, s'appuyant sur une normalisation linéaire [Oishi et al. (2008)] ou non-linéaire [Zhang et al. (2010)] du cerveau.

## Faisceaux commissuraux

**Corps calleux:** c'est le plus grand faisceau du cerveau humain, qui connecte les hémisphères cérébraux droit et gauche. Il est conventionnellement divisé en quatre sections: le *genou*, connectant les régions frontales médiales et latérales, le *rostrum*, connectant les régions orbito-frontales, le *corps*, qui passe à travers de la couronne rayonnante et qui connecte les régions frontales précentrales et les lobes pariétaux, et le *splenium*, qui connecte les lobes occipitaux. Il est impliqué dans plusieurs fonctions motrices, sensorielles et cognitives.

**Commissure antérieure:** c'est un petit faisceau qui connecte les lobes temporaux des deux hémisphères au niveau de l'amygdale. Ses fonctions sont peu connues.

**Commissure postérieure:** c'est un petit faisceau qui connecte les noyaux des nerfs crâniens, et les deux moitiés du mésencéphale et du diencephale. Il est très rarement reconstruit à partir de l'IRMd.



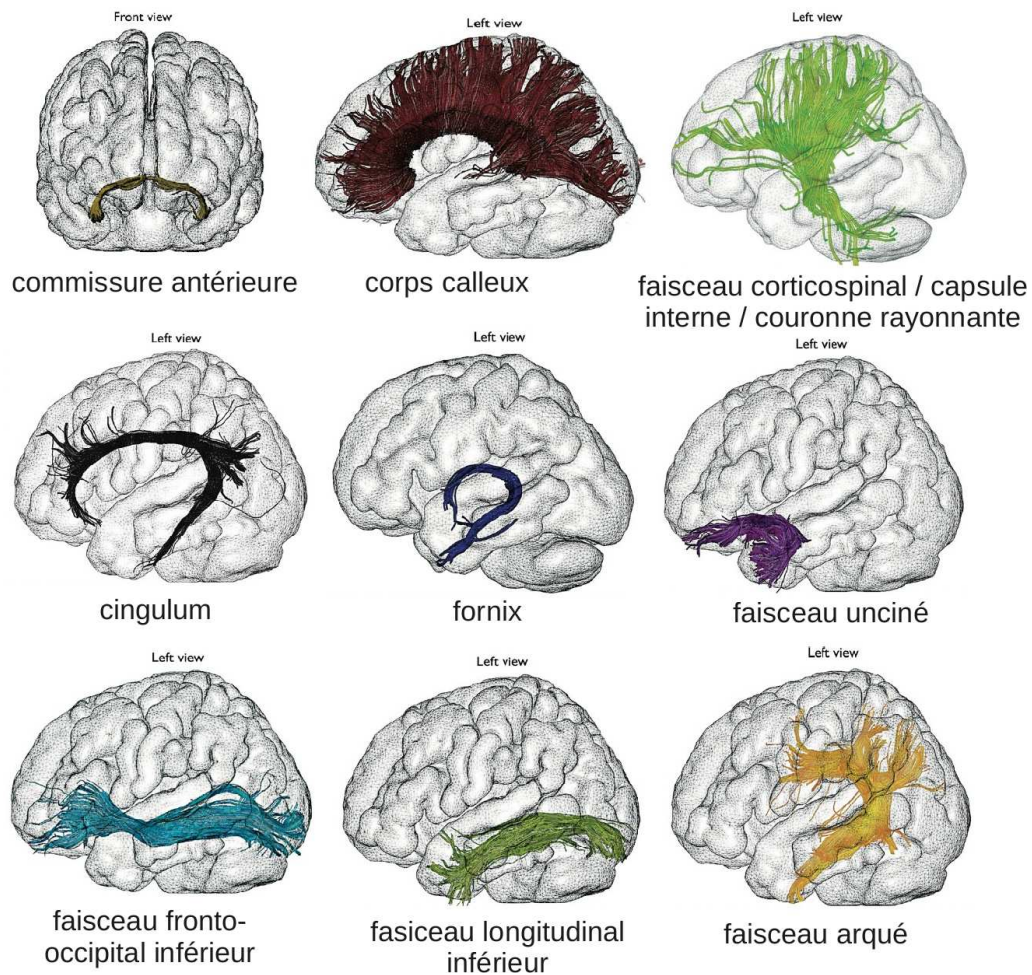


Figure 2: Les principaux faisceaux de la substance blanche décrits dans la littérature, obtenus en utilisant de la tractographie déterministe sur un champ de tenseur de diffusion. **Faisceaux commissuraux**: commissure antérieure et corps calleux. **Faisceaux de projection**: Faisceau corticospinal, capsule interne/couronne rayonnante et fornix. **Faisceaux d'association longs**: faisceau arqué, faisceau longitudinal inférieur, faisceau fronto-occipital inférieur, faisceau unciné et cingulum. [Figure adaptée de [Catani and Thiebaut de Schotten \(2008\)](#)].

### Faisceaux de projection

Ces faisceaux connectent les aires corticales avec les structures sous-corticales et la moelle épinière. Ils contiennent des fibres afférentes, qui reçoivent des informations sensorielles et des fibres efférentes, qui envoient des commandes motrices. Dans la profondeur des deux hémisphères, les fibres de projection constituent, avec les fibres thalamo-corticales, la *couronne rayonnante* et la *capsule interne*.

**Faisceau corticospinal**: ce faisceau, appelé aussi *faisceau pyramidal*, est une collection massive d'axones qui vont du cortex à la moelle épinière. Il contient principalement des axones moteurs provenant du cortex sensorimoteur primaire et du cortex prémoteur. Il passe à travers la couronne rayonnante, la capsule interne, le pédoncule cérébelleux et les régions pyramidales (moelle allongée).



**Radiations thalamiques:** elles sont composées des fibres cortico-thalamiques et thalamo-corticales qui forment un éventail plus ou moins continu. Ces fibres proviennent des noyaux thalamiques, lesquels se projettent vers une ou quelques régions corticales bien définies. Les radiations thalamiques sont souvent regroupées en quatre sous-groupes: *antérieur* (frontal), *supérieur* (pariétal), *inférieur* (temporal) et *postérieur* (occipital). Les radiations optiques se projettent vers le cortex visuel primaire tandis que les radiations acoustiques se projettent vers le lobe temporal.

**Fornix:** c'est une commissure intra- et inter-hémisphérique placée sous le corps calleux. Il relie l'hippocampe et le corps mamillaire dans chaque hémisphère. En avant, il est formé de deux colonnes (*piliers antérieurs*) qui arrivent jusqu'aux corps mamilaires. Ces piliers sont accolés vers l'arrière dans la partie moyenne, appelée le *corps* du fornix. En arrière il se divise en deux *piliers postérieurs* qui finalement longent l'hippocampe en formant un fin faisceau appelé *fimbria*. Le fornix appartient au système limbique et est impliqué dans la mémoire.

**Faisceaux cérébelleux:** connectent le cervelet aux autres régions du cerveau. Il existe trois types: pédoncules cérébelleux inférieurs, pédoncules cérébelleux moyens et pédoncules cérébelleux supérieurs.

La Figure 2 présente des reconstructions des faisceaux de fibres les plus connus à partir de l'IRMd.

## Chapitre 3: Principes de l'IRM de Diffusion

**Le phénomène de diffusion** est produit par le mouvement *brownien* des molécules d'eau [Brown (1828)]. Dans un milieu *isotrope*, *i. e.* où la diffusion est la même dans toutes les directions, chaque molécule décrit une marche aléatoire dans l'espace 3D. Pour une diffusion libre, le libre parcours moyen des molécules dépend du temps de diffusion et du *coefficient de diffusion*  $D$  [Einstein (1956)]. Pour une diffusion isotrope, le parcours moyen dépend du milieu (protéines, membranes), mais pas de la direction.

L'IRM de diffusion (IRMd) ne mesure pas directement le coefficient de diffusion, mais le déplacement moyen des molécules d'eau dans chaque voxel. La présence de membranes, inclusions et macromolécules dans les tissus entrave la marche aléatoire des molécules d'eau. Le parcours moyen mesuré est alors inférieur à celui d'un milieu libre, ce qui donne un coefficient de diffusion inférieur, appelé *coefficient de diffusion apparent* ou **ADC** [Le Bihan et al. (1986)].

Dans le tissu cérébral, la diffusion des molécules est restreinte dans l'espace intracellulaire et entravée dans l'espace extracellulaire. La diffusion est *anisotrope* si les obstacles environnants sont différents selon la direction de diffusion. C'est le cas pour la substance blanche, où les axones se regroupent de façon parallèle en faisceaux, en privilégiant la diffusion dans le sens des fibres nerveuses.

**L'IRM de diffusion** permet de mesurer indirectement la diffusion des molécules d'eau dans les tissus pour différentes directions. Elle permet ainsi d'inférer des propriétés sur la structure microscopique des tissus, comme l'ADC et l'anisotropie.

L'IRM conventionnelle repose sur les propriétés magnétiques du noyau des atomes d'hydrogène, présents dans les molécules d'eau. Chaque atome d'hydrogène ou proton, possède un moment magnétique nucléaire, appelé *spin*. Les machines d'IRM présentent un champ magnétique statique très puissant ( $B_0$ ), avec lequel les spins s'alignent, en présentant un mouvement de précession. La fréquence de précession, appelée fréquence de Larmor, est directement proportionnelle à  $B_0$ . Un signal court de radiofréquence à la fréquence de Larmor est alors appliqué pour exciter les spins et changer leur aimantation. Le retour à l'état d'équilibre des spins produit un signal de radiofréquence, mesuré par l'IRM. C'est cette mesure qui renseigne sur les propriétés des différents tissus, notamment les constantes de temps de relaxation des aimantations des spins. Une fois le signal acquis, la transformée de Fourier inverse permet de récupérer l'image.

Pour encoder l'espace, l'IRM utilise trois champs magnétiques appelés *gradients*. L'addition des gradients au champ magnétique statique  $B_0$  fait varier linéairement le champ magnétique sur tout le volume d'intérêt, dans les trois directions orthogonales de l'espace. La fréquence de Larmor devient alors dépendante de la position, ce qui permet l'encodage spatial dans l'IRM. Dans la séquence d'acquisition, les gradients sont appliqués de façon à échantillonner l'espace de fréquences (espace  $k$ ), ce qui permet d'échantillonner l'espace 3D: un gradient de *sélection de coupe* est appliqué en même temps que l'impulsion RF; un autre gradient, de *sélection de ligne*, est appliqué après l'impulsion RF et le troisième gradient est appliqué pendant la *lecture* du signal.

Les séquences d'acquisition *echo de spin* appliquent juste à mi-temps, entre la première impulsion RF et la lecture du signal, une deuxième impulsion RF. Cette impulsion de refocalisation a pour objectif de réaligner les spins déphasés à cause des inhomogénéités du champs magnétique, pour obtenir le signal le plus intense possible au moment de la lecture.

Les séquences d'IRM pondérées en diffusion utilisent deux gradients additionnels, appelés *gradients de diffusion*. Ces deux gradients successifs, courts et intenses donnent aux protons un déphasage de la précession dépendant de la position. Le premier gradient donne à la précession des protons une phase proportionnelle à leur position dans la direction du gradient. Le second gradient, exactement opposé au premier, donne aux protons un retard de phase équivalent. Les protons qui sont restés immobiles ne subissent pas de déphasage et donc pas de perte du signal. Par contre, les protons qui se sont déplacés entre l'application des deux gradients subissent un déphasage non nul proportionnel à leur déplacement le long de l'axe des gradients. Ce déphasage produit une perte de la cohérence du signal, ce qui se traduit en une réduction de l'amplitude du signal. Dans un voxel donné, plus la diffusion est importante dans une direction, plus l'image sera obscure.

La séquence *Pulse Gradient Spin Echo* (PGSE) [Stejskal and Tanner (1965)] a permis le développement de l'IRMd. Elle utilise deux gradients de diffusion de courte durée ( $\delta$ ),

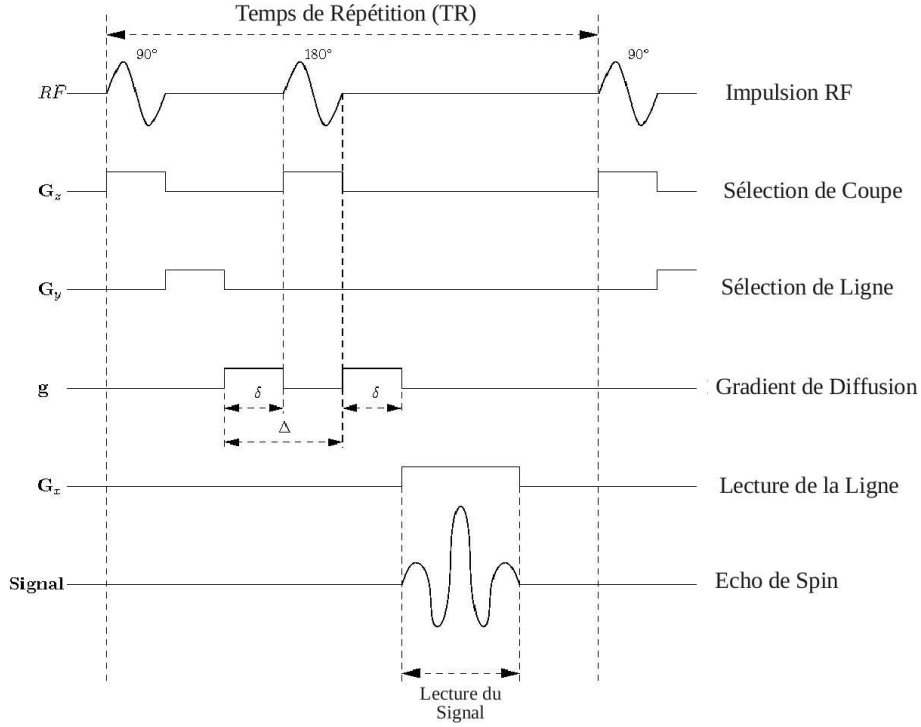


Figure 3: Séquence d'acquisition *Pulse Gradient Spin Echo* (PGSE). Deux gradients courts d'aire similaire, dans ce cas d'amplitude et durée similaire, sont utilisés. [From Descoteaux (2008)].

séparés par un intervalle de temps  $\Delta$  (voir Figure 3). Si on assume que les gradients sont infiniment courts, le signal mesuré peut s'exprimer selon l'équation:

$$f(x, y) = M_0 \left(1 - e^{-\frac{TR}{T_1}}\right) e^{-\frac{TE}{T_2}} e^{-bD}, \quad (1)$$

où  $M_0$  est la densité protonique du voxel,  $T_1$  et  $T_2$  sont les constantes de temps des relaxations dans le tissu,  $TR$  est le temps de répétition de la séquence,  $D$  est le coefficient de diffusion et le facteur  $b$  représente la sensibilité à la diffusion [Le Bihan et al. (1986)].

Les variantes de la séquence *échoplanaire* (EPI), proposée par Mansfield (1977), sont les plus utilisées actuellement car elles sont beaucoup plus rapides que la séquence PGSE. Elles produisent cependant des distorsions géométriques dans l'image à cause du train d'acquisition très long, pendant lequel toutes les erreurs d'encodage en phase s'accumulent. Ces distorsions doivent être corrigées, en fonction du type, soit par l'acquisition elle-même, soit par un post-traitement. En plus, un autre post-traitement peut être appliqué pour réduire le bruit Ricien, présent dans les données de diffusion.

## Modèles locaux de diffusion

Dans des milieux isotropes, le coefficient de diffusion est le même dans toutes les directions. Par contre, si le tissu est anisotrope, le signal change selon la direction des gradients de diffusion.

**Le Tenseur de diffusion (DTI)** permet de caractériser la diffusion en 3D [Basser et al. (1994)]. C'est un modèle simple, qui assume une distribution gaussienne des déplacements en 3D, très utilisé en clinique. Il modélise la diffusion par une matrice 3x3 symétrique et définie-positive, qui peut se représenter dans l'espace par un ellipsoïde.

Le tenseur est caractérisé par trois vecteurs propres, qui représentent les trois directions orthogonales de diffusion, qui sont aussi les trois axes principaux de l'ellipsoïde. La direction principale de diffusion sera la direction du vecteur propre associé à la valeur propre la plus élevée. Une diffusion isotrope sera représentée par une sphère, par contre, plus la diffusion est anisotrope et plus l'ellipsoïde sera allongé (voir Figure 4).

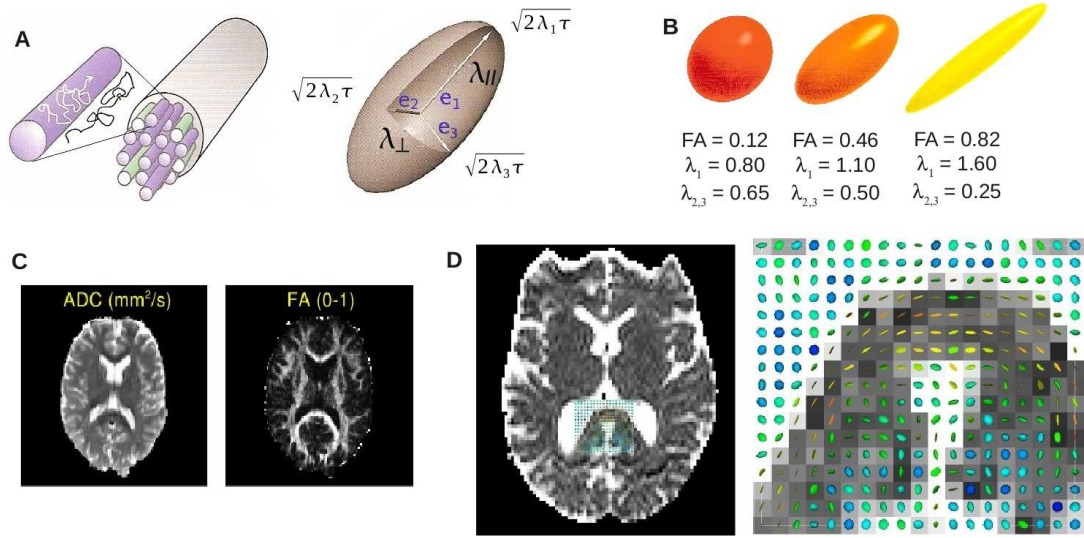


Figure 4: Imagerie du Tenseur de Diffusion (DTI). **A**: Le tenseur de diffusion peut être représenté par un ellipsoïde. Dans des tissus structurés comme les fibres nerveuses, la diffusion est anisotrope, en présentant une orientation privilégiée de diffusion, dans la direction des fibres. L'ellipsoïde représente la diffusivité parallèle ou axiale ( $\lambda_{//}$ ,  $\lambda_1$ ) et la diffusivité perpendiculaire ou radiale des fibres ( $\lambda_{\perp}$ ,  $\lambda_{2,3}$ ). [Figure adaptée de Johansen-Berg and Behrens (2009)]. **B**: Exemples d'ellipsoïdes avec une diffusivité moyenne (MD) similaire ( $0.7 \times 10^{-3} \text{ mm}^2/\text{s}$ ) et une anisotropie fractionnelle (FA) différente. **C**: Exemple d'images de diffusivité moyenne et d'anisotropie fractionnelle. **D**: A gauche, une image de MD avec la superposition des ellipsoïdes, pour une ROI. A droite, un zoom de la ROI. [Figures adaptées de Arsigny (2006)].

Des cartes de mesures scalaires peuvent être calculées à partir des tenseurs. Les valeurs les plus connues sont la diffusivité moyenne (MD), l'anisotropie fractionnelle (FA), la diffusivité parallèle  $\lambda_{//}$  et la diffusivité perpendiculaire ( $\lambda_{\perp}$ ). Ces mesures, notamment la MD et la FA, sont très utilisées dans les analyses de groupes pour caractériser les propriétés de diffusion des différentes populations.

Un minimum de 6 images pondérées en diffusion (avec différentes directions de diffusion) est nécessaire pour estimer les tenseurs, plus une image sans pondération en diffusion, appelée  $B_0$ , qui sert de référence. En pratique entre 12 et 30 images sont acquises pour augmenter la robustesse de l'estimation.

Le modèle du tenseur de diffusion est robuste et simple, mais il est fondé sur une

hypothèse très forte de diffusion libre, ne pouvant représenter qu’une population de fibres. Des configurations plus complexes, comme des croisements de plusieurs populations de fibres seront mal représentées, comme l’illustre la Figure 5. C’est ainsi que d’autres modèles plus complexes ont été proposés, nécessitant des acquisitions plus longues, avec un nombre plus élevé de directions de diffusion.

**L’Imagerie de Diffusion à Haute Résolution Angulaire (HARDI)** a été développée fortement ces dernières années, grâce à sa meilleure modélisation de la diffusion. Elle permet de distinguer les croisements de fibres à l’intérieur d’un voxel. Différentes techniques ont été proposées, avec ou sans modèle de diffusion. Elles varient aussi dans le nombre d’acquisitions requises et la puissance du gradient (facteur  $b$ ).

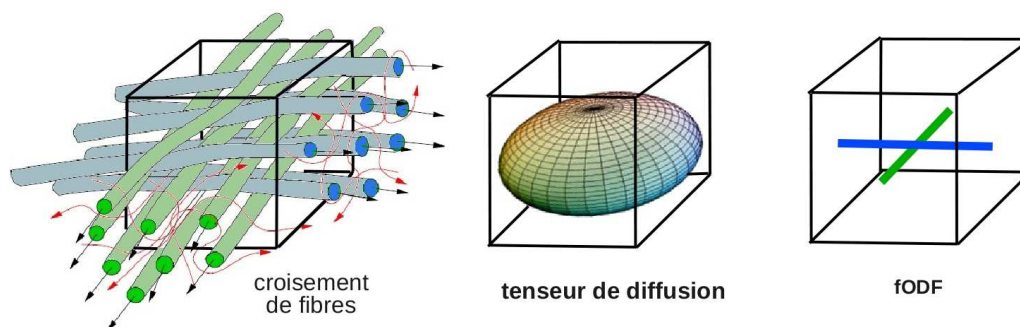


Figure 5: Illustration de l’effet de volume partiel dans un voxel, pour deux populations de fibres représentant une configuration de croisement de fibres à  $90^\circ$ . Le tenseur de diffusion aura une forme plate, avec une direction principale de diffusion indéterminée. La fonction de distribution des orientations des fibres (fODF) est composée de deux “spikes”, alignés avec les orientations des deux populations des fibres. [Adaptée de Poupon (1999b)].

Les techniques avec modèle utilisent des hypothèses sur les types de populations présentes dans chaque voxel. Les modèles les plus connus sont: le modèle *multi-tensoriel* [Tuch (2002)], le modèle “*Ball and stick*” [Behrens et al. (2003)] et le modèle *Composite hindered and restricted model of diffusion* (CHARMED).

Les techniques sans modèle cherchent à estimer la *fonction de distribution des orientations des fibres* (fODF), représentant la distribution de probabilité des orientations des fibres pour chaque voxel. Quelques techniques reconstruisent la *fonction de distribution des orientations de diffusion* (dODF), représentant la distribution de probabilité de diffusion. C’est le cas de *l’imagerie du spectre de diffusion* (DSI) [Wedeen et al. (2000)]. Cette technique fait un échantillonnage cartésien de l’espace  $q$ , pour différentes directions de diffusion et différentes valeurs de  $b$ . Elle permet alors une bonne reconstruction des croisements de fibres mais nécessite des temps d’acquisitions très longs et des gradients très puissants. D’autres techniques ont besoin d’un nombre plus raisonnable d’acquisitions. C’est le cas du *q-ball numérique* (QBI) [Tuch (2004)] et du *q-ball analytique* [Descoteaux et al. (2007)], lesquels font aussi une estimation de la dODF mais à partir d’acquisitions pour seulement une valeur de  $b$  (single-shell). D’autres méthodes, comme la *déconvolution*

sphérique [Tournier et al. (2004)] ou la *Déconvolution sphérique de l'ODF* [Descoteaux et al. (2009b)], récupèrent directement la fODF en déconvoluant le signal par la fonction réponse d'une fibre. La fODF présente une meilleure résolution angulaire que l'ODF de diffusion.

## Tractographie par l'IRM de diffusion

La tractographie utilise l'information donnée par les modèles locaux de diffusion pour inférer la connectivité anatomique du cerveau. C'est jusqu'à présent la seule technique *non-invasive* capable d'étudier chez l'homme les faisceaux de fibre de la substance blanche.

La tractographie de type "streamline" [Basser et al. (2000)] reconstruit les trajectoires des fibres à partir d'un point (ou graine), en suivant pas à pas, la ou les directions les plus probables, données par le modèle de diffusion. Chaque fibre est normalement suivie dans les deux sens, à partir de chaque graine. L'algorithme utilise différents critères d'arrêt, comme un seuil sur la courbature maximale entre deux points et un masque de tractographie, dans lequel les fibres peuvent être calculées. Deux types d'approches peuvent être utilisées: *déterministe* ou *probabiliste*. Des exemples de tractographie déterministe et probabiliste de type "streamline" sont illustrés dans la Figure 6. La tractographie déterministe suit la direction de diffusion la plus probable tandis que la tractographie probabiliste tire aléatoirement la direction dans un cône d'axe de la direction incidente [Perrin et al. (2005a)]. L'approche appelée "tractographie du cerveau entier" met des graines partout dans le cerveau en permettant la reconstruction de l'ensemble des fibres du cerveau. Ces fibres représentent les trajectoires des faisceaux de fibres de la substance blanche mais ne représentent pas de vraies fibres nerveuses. Elles sont aussi susceptibles de présenter des artefacts dus aux incertitudes des données de diffusion et aux défauts du masque de tractographie. Malgré ces inconvénients, en général, la tractographie permet de reconstruire les long faisceaux de fibres connus. En plus, en prenant un soin particulier dans toutes les étapes nécessaires à la reconstruction des fibres (correction des distorsions, débruitage, modèle HARDI, masque de tractographie à partir de l'image T1, bon recalage entre les images T1 et T2), plusieurs faisceaux d'association courts (fibres en U) peuvent aussi être reconstruits. Étant peu étudiés jusqu'à présent, ces faisceaux présentent un intérêt particulier.

## Chapitre 4: Méthodes de Classification de la Matière Blanche

### Recalage des cerveaux à travers les sujets

L'étude des structures anatomiques ou des propriétés de la diffusion dans un groupe de sujets nécessite une correspondance entre les individus. La correspondance se définit entre images ou entre régions d'intérêt, comme des sillons ou des faisceaux de la substance



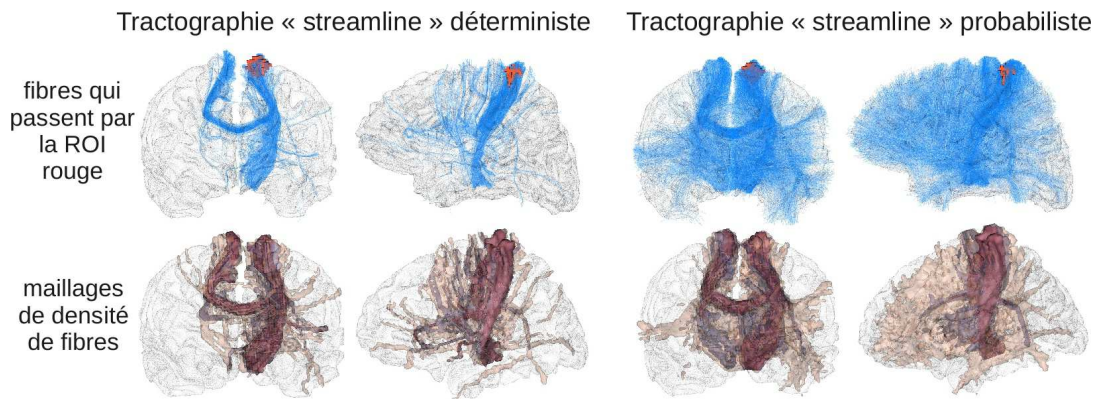


Figure 6: Exemples de tractographie déterministe et probabiliste de type "streamline", en utilisant des fODF estimées en utilisant la déconvolution sphérique des dODF à partir du QBI [Descoteaux et al. (2009b)]. La première ligne montre les fibres (en bleu), passant à travers la ROI en rouge, localisée dans le gyrus post-central. La deuxième ligne illustre les résultats avec des maillages de densités des fibres semi-transparents, pour les densités suivantes: 0.04%, 0.4% et 1.9%.

blanche. Le **recalage linéaire** est limité à des transformations globales (translations, rotations, mise à l'échelle et cisaillements). Ces transformations, avec peu de degrés de liberté, sont robustes et permettent un bon recalage entre des images d'un même sujet. Elles arrivent aussi à ajuster la position et la forme générale entre les sujets, mais des différences subsistent à petite échelle. Le **recalage non-linéaire** applique des déformations locales, avec peu de degrés de liberté, pour un recalage grossier et beaucoup de degrés de liberté pour des déformations locales plus complexes et détaillées. Le recalage avec beaucoup de degrés de liberté doit être appliqué avec précaution car les images peuvent être très déformées, jusqu'à paraître très similaires entre elles, mais sans atteindre l'homologie structurelle globale.

## L'état de l'art des méthodes de classification des faisceaux des fibres

Plusieurs stratégies ont été proposées pour segmenter un jeu de fibres issu de la tractographie. Elles sont fondées sur différentes méthodes de classification ainsi que sur des *a priori* anatomiques. Elles diffèrent aussi dans les stratégies pour trouver la correspondance entre fibres appartenant à différents sujets. La stratégie la plus simple pour segmenter les données issues de la tractographie est fondée sur des régions d'intérêt. Ces régions sont utilisées pour sélectionner ou exclure les fibres de façon plus ou moins interactive pour chaque sujet, afin de reconstruire les faisceaux connus [Wakana et al. (2007); Catani and Thiebaut de Schotten (2008)]. Cette approche a été utilisée pour créer des atlas des faisceaux de fibres à partir d'un seul sujet [Mori et al. (2005); Lawes et al. (2008)]. Une extension intéressante de cette approche consiste, en utilisant un groupe de sujets, à générer des cartes probabilistes des faisceaux de fibres dans un espace normalisé [Hua et al. (2008)]. Un groupe de ROIs peut alors être défini pour récupérer les mêmes faisceaux chez d'autres sujets. Plus récemment, des méthodes fondées sur des atlas de ROIs dans un espace normalisé ont été proposées pour extraire des faisceaux connus et plusieurs fibres d'association

courtes en utilisant des données provenant d'un groupe de sujets [Oishi et al. (2008); Zhang et al. (2010)]. Ces méthodes se sont avérées très puissantes mais elles reposent fortement sur la performance de la méthode de recalage. En plus, elles ne font pas d'analyses sur la forme des faisceaux.

D'autres méthodes définissent les faisceaux de fibres à partir d'une classification des voxels, reposant sur des mesures de similarité entre les données de diffusion locales [Bazin et al. (2009); Wassermann et al. (2008)]. Des stratégies intermédiaires regroupent les voxels de la substance blanche en fonction d'une mesure de similarité entre voxels calculée entre les fibres qui les connectent [El Kouby et al. (2005); Wang et al. (2011)]. Ces approches fondées sur les voxels, utilisent leur segmentation de la substance blanche pour extraire des groupes de fibres d'une façon qui passe à l'échelle sans difficulté. Cependant, en fonction de la complexité des données et des résultats recherchés, d'autres pré- et post- traitements peuvent être nécessaires.

Finalement, d'autres méthodes regroupent les fibres directement dans leur espace, en utilisant une mesure de similarité entre les fibres [Ding et al. (2003); Corouge et al. (2004); Gerig et al. (2004); Brun et al. (2004); O'Donnell et al. (2006); Visser et al. (2011)]. Cette stratégie peut intégrer des connaissances *a priori* sous la forme de modèles des faisceaux [Maddah et al. (2005); O'Donnell and Westin (2007)]. D'autres méthodes hybrides proposées récemment extraient les faisceaux de fibres à travers la combinaison des informations *a priori*, données par un atlas de la substance grise et blanche, et un regroupement des fibres fondé sur une mesure de similarité entre les fibres [Wassermann et al. (2010a); Li et al. (2010)].

Les méthodes de classification des fibres qui utilisent une distance (ou une similarité) entre les fibres se sont avérées être un outil puissant pour l'étude de la structure des fibres issues de la tractographie. Ces méthodes permettent de segmenter les fibres en groupes de fibres constitués de fibres présentant des formes et des positions à peu près similaires. Ces méthodes peuvent être analysées selon différents points de vues. Nous présentons ci-dessous les principaux aspects analysés: algorithme de classification, mesure de distance, données de sortie et taille des données. Les Tableaux 1 et 2 contiennent un résumé de tous les aspects analysés.

**Algorithme de classification:** différentes méthodes de classification (*clustering* en anglais) ont été utilisées. En général, les méthodes de classification non-supervisées regroupent des éléments en fonction d'une mesure de similarité sans utiliser des données étiquetées [Jain and Dubes (1988); Jain (2010)]. Elles ont besoin du calcul de la distance entre toutes les paires d'éléments, ce qui peut être très coûteux pour des grands jeux de données. Ces méthodes peuvent être de type *partitionnel* ou *hiérarchique*.

Les méthodes de type partitionnel cherchent à trouver directement une partition des éléments, en optimisant un certain critère. Le nombre de groupes est souvent un paramètre à spécifier, ce qui peut être une limitation. Les méthodes reposent sur différents principes, comme un critère des moindres carrés (e. g. les *k-moyennes* [MacQueen (1967)]), la théo-



ries des graphes (e. g. le regroupement spectral avec coupes normalisées [Shi and Malik (2000)]), la décomposition de mélange de distributions (e. g. le regroupement fondés sur des processus de Dirichlet [Blei et al. (2003)]), entre autres.

Les méthodes hiérarchiques [Johnson (1967)] sont souvent agglomératives, où chaque élément est considéré au début comme un groupe séparé, et après dans chaque pas, les groupes les plus similaires sont fusionnés, pour former finalement un arbre hiérarchique. L'arbre peut être représenté par un graphe appelé dendrogramme, qui représente toutes les fusions. Une fois l'arbre calculé, une partition plate ou adaptative peut être définie en fonction de différents critères, comme la distance entre les éléments d'un groupe ou la distance entre les groupes. Le nombre de groupes n'est pas alors une valeur à définir *a priori*.

Les groupes résultant de l'application d'une méthode de classification sont très dépendants de la méthode de classification choisie, de la mesure de similarité et de la nature des données. C'est une tâche très complexe car les groupes peuvent présenter différentes formes, tailles et densités, en plus de la présence du bruit, qui rend la détection des groupes plus difficile. Pour avoir les résultats espérés, des connaissances sur les caractéristiques et la structure des données sont nécessaires [Jain (2010)].

**Mesures de distance (ou similarité) entre les fibres:** Les mesures de distance entre fibres utilisent en général une série de points qui paramétrisent chaque fibre. Les distances les plus connues, proposées par [Corouge et al. (2004)], sont la *distance de Hausdorff* ( $d_H$ ) et la *moyenne des plus proches distances* ( $d_M$ ). Ces distances permettent d'intégrer dans une seule mesure des informations sur la forme et la position de la fibre. Une autre mesure de distance, fondée sur  $d_M$ , applique un seuil pour les distances à considérer [Zhang et al. (2008a)], ce qui permet d'éliminer des fibres très similaires. Récemment, Visser et al. (2011) utilisent la somme des distances Euclidiennes entre les points correspondants, calculée plus rapidement que les distances fondées sur les points les plus proches ( $d_H$ ,  $d_M$ ).

**Données de sortie:** La plupart des méthodes proposées se focalisent sur la segmentation directe des fibres ayant une signification anatomique (*i. e.* les long faisceaux connus de la substance blanche), en utilisant des *a priori* anatomiques donnés par des atlas de la substance grise et blanche [Wassermann et al. (2010a); Li et al. (2010)] ou des modèles des faisceaux [Maddah et al. (2005, 2007b, 2008a)]. D'autres travaux appliquent une première étape de regroupement des fibres [Zhang et al. (2008a); O'Donnell et al. (2006); Visser et al. (2011)] et puis intègrent un étiquetage manuel des groupes pour l'identification des faisceaux connus. L'avantage de la deuxième approche c'est l'indépendance des étapes de regroupement et d'identification, ce qui permet lors de la première étape, d'obtenir une information sur toute la structure des faisceaux des fibres, qui inclus des faisceaux peu connus. Nous utilisons alors cette stratégie pour étudier la substance blanche dans son ensemble et créer un modèle des faisceaux.

**Taille des données:** Avec les nouvelles techniques de diffusion à haute résolution angulaire et des machines IRM plus puissantes, les données issues de la tractographie présentent une meilleure qualité mais aussi une plus grande taille. C’est ainsi que le nombre de fibres est passé de autour de 10.000 fibres pour le cerveau entier à plus d’un million de fibres. La classification directe des fibres en utilisant une distance entre toutes les paires de fibres devient alors impossible. Différentes stratégies ont été proposées pour réduire cette surcharge, comme la prise d’un échantillon des fibres [O’Donnell et al. (2006)] ou une grande quantité d’échantillons classifiés séparément [Visser et al. (2011)]. Bien que performantes, ces méthodes présentent des inconvénients comme la définition *a priori* du nombre de groupes. Le nombre maximum de fibres analysées remonte aux alentours de 500.000 [Visser et al. (2011)]. D’autres méthodes regroupent les fibres dans l’espace des voxels, ce qui les rend beaucoup plus efficaces [El Kouby et al. (2005); Wang et al. (2011)]. Cependant, les groupes de fibres obtenus directement par une classification de ce type présentent de nombreux chevauchements qui dégradent la qualité de la classification. Des pré- et post- traitements doivent être inclus dans le cas des données complexes en fonction des résultats recherchés.

## MÉTHODES DE CLASSIFICATION DES FIBRES (UN SUJET)

MÉTHODE	IN	MESURE DE DISTANCE	MÉTHODE DE CLASSIF.	A PRIORI ANAT. / EMPIRIQUES	ANALYSE PRINCIP.	SORTIES PRINCIP.	FAISCEAUX IDENT.
Ding 2003	RG	Euclidienne (fibres)	k-NN	ROIs de graines	définit des segments correspondants / classif. des fibres	filtrage des fibres / analyse de forme	
Corouge 2004 Gerig04 2004	FS	$d_c, d_M, d_H$ (fibres)	algorithme de propagation	segmentation manuelle des faisceaux / seuil sur la distance	classif. des fibres	filtrage des fibres / analyse de forme	FCS, parties du CC
Zhang 2002 Zhang 2003	CE	$D_t$ (fibres)	CH “single-link”		culling des fibres / classif. des fibres	“streamtubes” et “streamsurfaces”	
Brun 2003 Brun 2004	CE	utilise les points extrêmes des fibres	immersion spectrale, CS Ncuts	paramètres empiriques de classification		“soft coloring” des fibres	

**Liste des abréviations (aussi valide pour le Tableau 2).**

IN (ENTRÉE): Tractographie du cerveau entier (CE), faisceau segmenté (FS) ou ROI de graines (RG).

MÉTHODE DE CLASSIF. (MÉTHODE DE CLASSIFICATION): Classification Hiérarchique (CH), Plus Proches Voisins (NN), Classification Spectrale (CS), Coupes normalisées (Ncuts).

MESURE DE DISTANCE: Distance des points les plus proches ( $d_c$ ), Moyenne des plus proches distances ( $d_M$ ), Distance de Hausdorff ( $d_H$ ), Moyenne des plus proches distances seuillées ( $D_t$ ), Plus petite moyenne des plus proches distances seuillées ( $d_{St}$ ), Plus grande moyenne des plus proches distances seuillées ( $d_{Lt}$ ), Fonction de l'indicateur flux ( $BIF$ ), Somme des distances Euclidiennes entre des points correspondants ( $d_{scp}$ ).

A PRIORI ANAT. / EMPIRIQUES (A PRIORI ANATOMIQUES / EMPIRIQUES).

FAISCEAUX IDENT. (FAISCEAUX IDENTIFIÉS): Faisceau corticospinal (FCS), Couronne rayonnante/Capsule interne (CR/CI), Faisceau longitudinal supérieur (LS), Faisceau longitudinal inférieur (LI), Faisceau fronto-occipital inférieur (FOI), Faisceau arqué (FA), Cingulum (CG), Faisceau unciné (UN), Forceps mineur (Fm), Forceps majeur (FM), Corps calleux (CC), genou du CC (GCC), splénium du CC (SCC), Radiation thalamique antérieure (RTA), Fornix (FX), Pédoncule cérébelleux moyen (PCM), Pédoncule cérébelleux supérieur (PCS), Troc cérébral (TC), Faisceau de projection dans le lobe frontal, pariétal ou occipital (FPf, FPp, FPo), CC connectant les côtés gauche et droit des lobes frontal, pariétal ou occipital (CCf, CCp, CCo).

Table 1: **Catégorisation des méthodes de classification des fibres (un sujet).**

Les méthodes ont été analysées en fonction de l'entrée principale, la méthode de classification et la mesure de distance principales, les principaux *a priori* anatomiques et empiriques utilisés pour récupérer les faisceaux, les principaux pas de l'analyse, les principales sorties et les faisceaux identifiés avec succès.

## MÉTHODES DE CLASSIFICATION DES FIBRES (PLUSIEURS SUJETS)

MÉTHODE	REC	MESURE DE DISTANCE	MÉTHODE DE CLASSIF.	A PRIORI ANATOMIQUES / EMPIRIQUES	ANALYSE PRINCIPALE	SORTIES PRINCIP.	IDENT. BUNDLES
Zhang 2005	AFF	Euclidienne (regroupe des centroïdes)	NN		correspondance entre centroïdes des groupes	correspondance entre groupes (entre 2 sujets)	
Zhang 2008	AFF	<b>US</b> : dSt, dLt (fibres) <b>MS</b> : Euclidienne (centroïdes des groupes)	<b>US</b> : CH “single-link” <b>MS</b> : NN	<b>US</b> : seuil de proximité empirique (PTh) <b>MS</b> : modèle des faisceaux (étiquetage manuel des groupes)	<b>US</b> : culling des fibres / regroupement des fibres / <b>MS</b> : correspondance entre centroïdes trouve le PTh optimale	modèle des faisceaux / identification des faisceaux (2 subjects)	<b>US</b> : FCS, CG, UN, Fm, FM, PCM, LS, LI <b>MS</b> : CG, UN, Fm, FM
ElKouby 2005	AFF	<b>US</b> : connectivité (voxels) <b>MS</b> : masque de corrélation des groupes de fibres	<b>US</b> : k-moyennes <b>MS</b> : k-moyennes	<b>US/MS</b> : nombre de groupes empirique	<b>US</b> : classification des voxels <b>MS</b> : correspondance des masques des groupes de fibres pour tous les sujets	atlas des faisceaux (11 sujets)	<b>US</b> : RTA, LI, GCC, SCC, FCS, FX <b>MS</b> : FCS, parties du CC
O'Donnell 2005 O'Donnell&Westin 2006 O'Donnell-PhD 2006	AFF	<b>US</b> : $d_M$ (fibres) <b>MS</b> : $d_M$ (fibres de tous les sujets)	CS Ncuts (méthode de Nistrom)	paramètres de classif. empiriques / étiquetage manuel des groupes	<b>US</b> : classification des fibres <b>MS</b> : classification des fibres (fibres de tous les sujets)	atlas des faisceaux embarqués (10 sujets)	<b>US/MS</b> : CC, FCS, FA, FOI, UN, LI, PCM, PCS
O'Donnell-PhD 2006 O'Donnell 2007	AFF	$d_M$ (fibres)	immersion spectrale (fibres) / NN (centroïdes)	atlas des faisceaux embarqué (fibres)	immersion des fibres / trouve NN centroïde de groupe pour chaque fibre	identification des faisceaux (5 subjects)	<b>US/MS</b> : CC, FCS, FA, FOI, UN, LI, PCM, PCS
Maddah 2005	AFF	représentation à partir de B-spline (fibres)	NN	modèle des faisceaux (fibres étiquetées)	correspondance entre fibres et fibres du modèle	identification des faisceaux	CC, CR/CI, FX, PCM
Maddah 2007 Maddah 2008b	AFF	utilise carte de distance Euclidienne pour chaque centroïde de groupe (fibres)	modèle de mélange de distrib. Gamma	une fibre par faisceau et par sujet sélectionnée manuellement	estime les paramètres de classification	affectation prob. de chaque fibre à un groupe / corresp. entre points pour chaque faisceau	CC, CR/CI, CG

... continue dans la page suivante ...

... continué de la page précédente ...

MÉTHODE	REC	MESURE DE DISTANCE	MÉTHODE DE CLASSIF.	A PRIORI ANAT. / EMPIRIQUES	ANALYSE PRINCIPALE	SORTIES PRINCIP.	FAISCEAUX IDENT.
<a href="#">Maddah 2008a</a>	AC	utilise carte de distance Euclidienne pour chaque centroïde de groupe (fibres)	modèle de mélange de distrib. Gamma (Bayesien)	atlas des faisceaux (ROIs) / définit manuellement les centres des faisceaux initiaux / seuil d'appartenance	génère faisceau à partir de ROI / utilise un atlas comme <i>a priori</i> / estime paramètres de classification	affectation prob. de chaque fibre à un groupe / corresp. entre points pour chaque faisceau	CG, UN
<a href="#">Wassermann 2010</a>	NL	dist. entre faisceaux et fibres ( <i>BIF</i> )	Classif. Hiérarchique	atlas de substance grise et blanche (ROIs)	construction de l'arbre du CH et sélection d'un groupe en utilisant information anatomique comme <i>a priori</i>	identification des faisceaux (21 sujets)	FA, CG, UN, FCS, FOI, Fm, FM
<a href="#">Li 2010</a>	NL	$pas_2$ : $d_H$ + facteur fondée sur la longueur	$pas_2$ : PCA suivie de "fuzzy c-means"	$pas_1$ : atlas de substance grise et blanche (ROIs) $pas_2$ : étiquetage manuel de 2 faisceaux pour recon. des faisceaux	$pas_1$ : utilise un atlas pour segmenter 9 faisceaux $pas_2$ : classe les fibres qui restent et identifie 2 autres faisceaux	identification des faisceaux (10 subjects)	CG, FOI, LI, UN, FA, CCf, CCp, CCo, FPf, FPp, FPo
<a href="#">Visser 2011</a>	NL	dist. entre fibres ( $d_{scp}$ )	Classif. Hiérarchique	<b>US/MS</b> : param. de classif. empiriques / étiquetage manuel des groupes	divise les données et classe chaque sous-groupe séparément (plusieurs répétitions) / garde les groupes reproductibles	identification des faisceaux	<b>US</b> : FA, CG, UN, FOI, LI <b>MS</b> : FA
<a href="#">Wang 2011</a>	NL	AC	coordonnées et orientations des points des fibres (voxels)	Modèle hiérarchique de mélange de processus de Dirichlet	parfois a besoin d'une fusion manuelle des clusters / étiquetage manuel des groupes de la base d'apprentissage	classif. des voxels, groupes de base d'apprentissage sont information <i>a priori</i>	<b>US/MS</b> : CC, FCS, FA, FOI, UN, LI, PCM, TC

**Liste des abréviations** (Les autres abréviations ont été présentées dans le Tableau 1).

REC. (MÉTHODE DE RECALAGE): affine (AFF), algorithme "congealing" (AC), non-linéaire (NL). / UN SUJET (US), PLUSIEURS SUJETS (MS)

Table 2: **Catégorisation des méthodes de classification des fibres (plusieurs sujets)**. Les méthodes ont été analysées en fonction de leur méthode de recalage, la méthode de classification et la mesure de distance principales, les principaux *a priori* anatomiques et empiriques utilisés pour récupérer les faisceaux, les principaux pas de l'analyse, les principales sorties et les faisceaux identifiés avec succès. L'entrée est une tractographie du cerveau entier pour toutes les méthodes.

## Chapitre 5: Classification des Fibres Intra-sujet

### Méthode

Comme mentionné précédemment, l'analyse des jeux de données avec plus d'un million de fibres représente un grand défi pour tout algorithme de classification. Pour surmonter la limitation sur la taille du jeu de données, nous proposons dans ce chapitre une séquence d'algorithmes effectuant une classification hiérarchique robuste des fibres d'un cerveau (intra-sujet). Cette méthode peut être considérée comme un traitement de compression des données issues de la tractographie car elle permet d'analyser plus d'un million de fibres et de les regrouper en quelques milliers de faisceaux homogènes, sans perdre d'information importante.

La méthode consiste en une décomposition hiérarchique du jeu de fibres, sous forme de plusieurs étapes appliquées de façon consécutives. Pour traiter les fibres de façon efficace, la méthode est fondée sur une étape de classification appliquée aux voxels de la substance blanche, au lieu des fibres. L'approche est fondée sur une mesure de connectivité entre les voxels de la substance blanche proposée par [El Kouby et al. \(2005\)](#). D'autres étapes ont été ajoutées, avant ou après cette étape principale, avec l'objectif d'améliorer la qualité finale des faisceaux de fibres obtenus. Toutes les étapes ont été conçues et enchaînées de façon à robustifier l'analyse entière. Le résultat final est un ensemble de quelques milliers de faisceaux de fibres, représentant la structure complète du jeu de fibres issues de la tractographie, qui peut être utilisé comme entrée d'autres analyses postérieures, comme des analyses de groupe. Un diagramme représentant une vue globale de la méthode de classification hiérarchique intra-sujet, composée de cinq pas principaux, est présenté dans la Figure 7.

Dans ce qui suit nous décrivons brièvement la méthode:

**Pas 1: Décomposition Hiérarchique.** Le jeu de fibres issu de la tractographie est divisé en quatre *sous-ensembles*: fibres de l'hémisphère droit, fibres de l'hémisphère gauche, fibres inter-hémisphériques et fibres du cervelet. Cette segmentation est réalisée en utilisant des masques des deux hémisphères et du cervelet. Elle vise à diminuer la complexité des données, en séparant des faisceaux qui se chevauchent partiellement. Les pas suivants sont appliqués séparément à chaque sous-ensemble de fibres.

**Pas 2: Segmentation fondée sur la longueur.** Les fibres sont séparées en plusieurs *groupes* de fibres de longueur similaire. De cette façon, des faisceaux de fibres qui se chevauchent partiellement sont séparés en groupes différents.

**Pas 3: Classification des voxels de substance blanche.** Une parcellisation de la substance blanche est effectuée en utilisant une classification hiérarchique des voxels en fonction d'une mesure de connectivité donnée par les fibres. Les groupes de fibres obtenus,



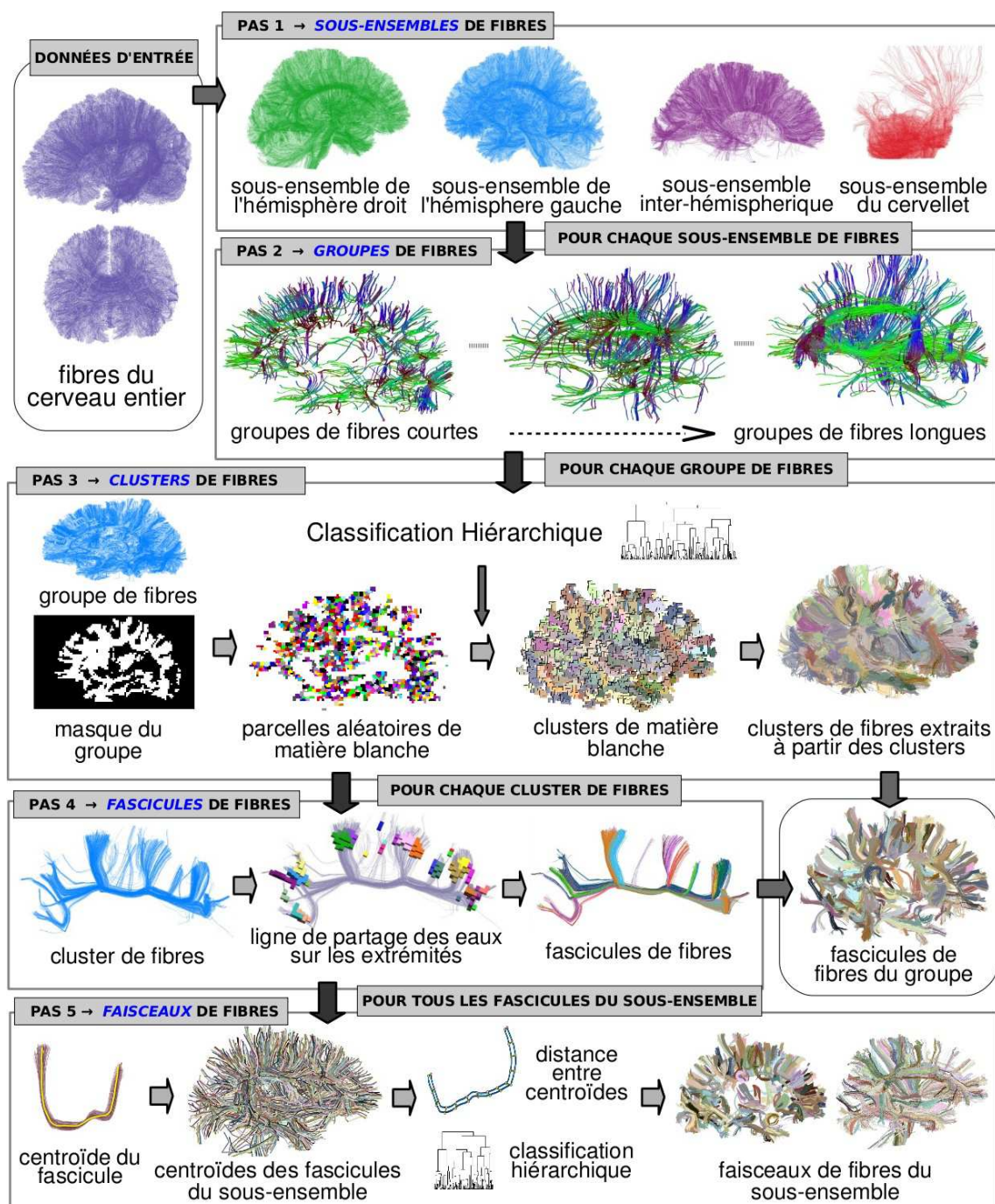


Figure 7: **Diagramme général de la méthode de classification des fibres intra-sujet:** **Pas 1: Décomposition hiérarchique:** Le jeu de données est segmenté en quatre principaux sous-ensembles de fibres. **Pas 2: Segmentation fondée sur la longueur:** Les fibres de chaque sous-ensemble sont séparées en différents groupes, constitués de fibres de longueurs similaires. **Pas 3: Classification des voxels de substance blanche:** Les fibres de chaque groupe sont classifiées à travers une segmentation des voxels de la substance blanche fondée sur la connectivité. Les clusters de fibres sont extraits à partir des clusters de voxels de la substance blanche. **Pas 4: Classification fondée sur les extrémités:** les clusters de fibres sont divisés en fascicules homogènes en se basant sur les extrémités des fibres. **Pas 5: Fusion des fascicules:** Les fascicules de fibres du sous-ensemble sont fusionnés en utilisant une distance entre paires de centroïdes des fascicules.

appelés *clusters de fibres* sont extraits à partir des groupes de voxels de la substance blanche.

La substance blanche est d’abord parcellisée aléatoirement en parcelles homogènes constituées de 3 voxels en moyenne, en utilisant un algorithme de classification k-moyennes fondé sur une distance géodésique [Flandin et al. (2002)]. Ensuite, une matrice de connectivité est calculée, contenant la connectivité entre toutes les paires de parcelles, donnée par le nombre de fibres qui les connectent, normalisée par le volume des parcelles. Une classification hiérarchique de type “average-link” est alors appliquée pour segmenter la substance blanche en groupes contenant différents faisceaux de fibres (voir la Figure 8). Pour obtenir les clusters de substance blanche, une partition adaptative de l’arbre résultant de la classification hiérarchique est effectuée, en fonction de la taille désirée des clusters. Les clusters de voxels ainsi obtenus représentent des groupes de voxels par lesquels passe un grand nombre de fibres, regroupées en plusieurs faisceaux. Les clusters de fibres sont finalement extraits à partir des clusters de voxels de substance blanche.

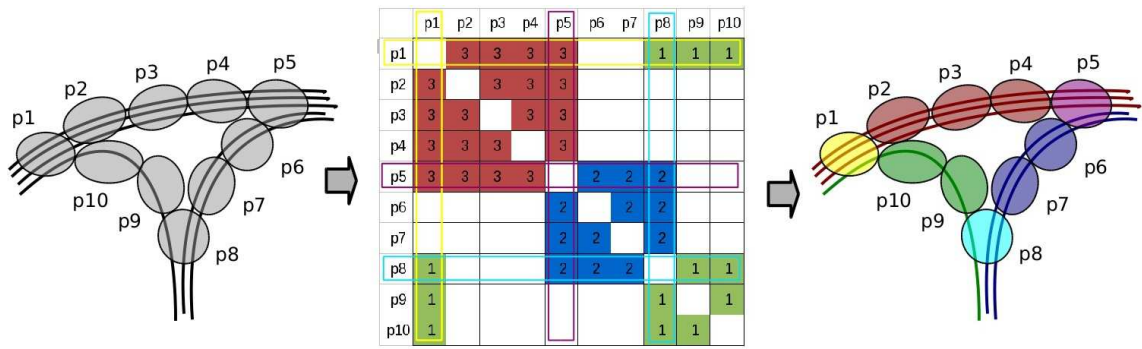


Figure 8: **Illustration de la classification de voxels de la substance blanche en fonction de la connectivité (Pas 3):** D’abord, une parcellisation aléatoire de la substance blanche est effectuée (les parcelles sont représentées en gris). Seulement les voxels traversés par les fibres sont considérés dans ce processus. Une matrice de connectivité des parcelles est alors calculée, à partir du nombre de fibres qui connectent chaque paire de parcelles. Cette valeur est normalisée par la taille des parcelles. La matrice de connectivité est alors utilisée pour regrouper les parcelles fortement connectées entre-elles. Après la classification, les parcelles en rouge ( $p_2$ - $p_4$ ), bleu ( $p_6$ - $p_7$ ) et vert ( $p_9$ - $p_{10}$ ) vont former trois clusters différents, qui donneront lieu à trois clusters de fibres. Les parcelles présentant une connectivité plus complexe, comme les parcelles en jaune ( $p_1$ ), violet ( $p_2$ ) et cyan ( $p_3$ ), sont regroupées avec le groupe de parcelles auquel elles sont le plus connectées.

**Pas 4: Classification fondée sur les extrémités.** Chaque cluster de fibres est divisé encore en plusieurs *fascicules* de fibres qui se chevauchent partiellement, à partir d’une classification fondée sur les extrémités des fibres. Un algorithme de “ligne de partage des eaux” [Vincent and Soille (1991)] est utilisé pour détecter les régions 3D présentant une haute densité d’extrémités de fibres. Chaque paire de ces régions définit alors un fascicule homogène et régulier de fibres.

**Pas 5: Fusion des fascicules.** Une dernière étape regroupe les fascicules obtenus pour tous les groupes de fibres d’un sous-ensemble. Cette classification est réalisée pour fusionner



les fascicules de fibres présentant des géométries très similaires, qui ont été sur-segmentés dans les étapes précédentes. Une fibre moyenne ou *centroïde* est calculée pour représenter chaque fascicule du sous-ensemble. Elle est calculée comme la fibre minimisant la distance moyenne vers toutes les autres fibres du fascicule. Les centroïdes sont ensuite regroupés en utilisant une classification hiérarchique de type “average-link” fondée sur une mesure de distance entre paires de centroïdes. La mesure de distance utilisée est la *distance de Hausdorff* ( $d_H$ ) [Corouge et al. (2004)]. Une distance maximale est utilisée pour définir la taille des faisceaux.

## Validation de la méthode

**Données simulées.** Pour valider notre classification hiérarchique nous avons testé d’abord la méthode avec des données simulées. Dix jeux de données simulées ont été générés, chacun fondé sur un modèle constitué de 200 faisceaux présentant différents diamètres, longueurs, formes et densités de fibres (voir la Figure 9 B). Les faisceaux ont été générés à partir de 200 fibres sélectionnées à partir d’un jeu de fibres d’un hémisphère gauche (voir la Figure 9 A). En plus, trois jeux de données de “bruit” ont été générés, constitués de fibres sélectionnées aléatoirement du même hémisphère gauche, et contenant 10%, 50% et 100% du nombre total de fibres d’un jeu de données. Ces données ont été additionnées à chaque jeu de données simulées, pour obtenir au total 30 jeux simulés de fibres (bruités). Les données ont été classifiées avec notre méthode pour valider son comportement, notamment la détection de faisceaux de fibres homogènes représentant la structure des données, constituées dans ce cas de 200 faisceaux de fibres connus. La validation a impliqué le calcul du pourcentage de récupération de tous les faisceaux des 30 jeux de données simulées. Pour cela, un centroïde a été déterminé pour chaque faisceau résultant de la classification et comparé avec les centres des faisceaux des jeux de données originaux. L’analyse des résultats confirme qu’une grande partie des faisceaux sont récupérés dans un grand pourcentage. La récupération dépend, comme la plupart des algorithmes de classification, de la densité des fibres: les faisceaux de fibres moins denses que la densité minimale de fibres inférée à partir des paramètres de la tractographie, ne sont pas détectés car ils sont considérés comme du bruit. En plus, en général, un petit pourcentage de fibres se trouvant à la périphérie des faisceaux ne sont pas récupérées car elles présentent aussi une densité très basse. Ce comportement est consistant pour tous les jeux de données.

**Évaluation du coût de l’extensibilité de la méthode.** Alors que les résultats de la validation permettent d’inférer que le coût de l’extensibilité introduit par la classification des voxels de la substance blanche (*Pas 3*) est très bas, nous avons effectué des expérimentations additionnelles pour quantifier ce coût. Premièrement, une *classification de “force brute”*, *i. e.* qui utilise une mesure de distance entre toutes les fibres du jeu de données, a été appliquée à un jeu de données simulées avec 10% de bruit ( $\sim 24.000$  fibres). La méthode utilisée est la classification hiérarchique, fondée sur la distance de Hausdorff ( $d_H$ ). Les résultats montrent que cette méthode ne récupère pas tous les faisceaux. En plus, les faisceaux récupérés sont plus bruités que ceux retrouvés par notre méthode. L’analyse

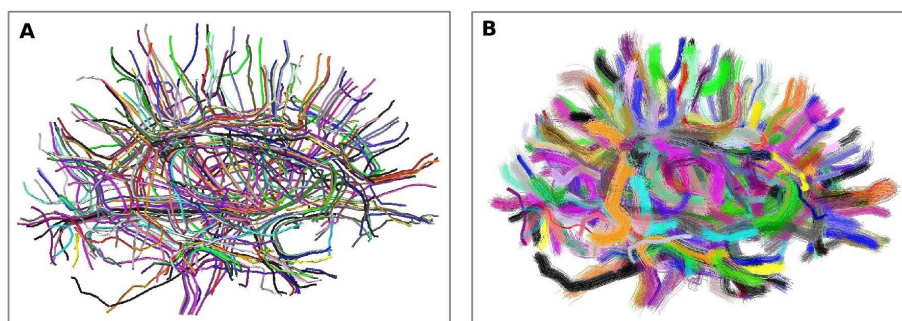


Figure 9: **Exemple d'un jeu de données simulé constitué de 200 faisceaux de fibres.** **A:** Les 200 fibres sélectionnées comme centres des faisceaux. **B:** Faisceaux générés à partir des centres en A.

des faisceaux non détectés nous conduit à deux explications: 1) dans certains cas, deux faisceaux simulés sont fusionnés à cause de fibres qui présentent des distances relativement courtes aux deux faisceaux, produites souvent par le bruit, et 2) dans d'autres cas, des fibres dues au bruit font aussi que des faisceaux de basse densité sont divisées en multiples faisceaux isolés. Ces résultats montrent que le comportement de notre méthode est acceptable et que d'autres méthodes comme la classification hiérarchique ont besoin de pre- et post- traitements pour assurer la qualité des résultats.

Un autre test a été effectué pour *évaluer l'influence de la taille des parcelles sur la qualité des résultats*: notre méthode a été appliquée à un jeu de données simulées pour une grande plage de tailles de parcelles. Les résultats n'ont pas montré une dégradation significative dans la détection des faisceaux, soutenant l'idée que notre méthode est robuste: 1) la segmentation fondée sur la longueur (*Pas 2*) permet de simplifier les données en éliminant des chevauchements des fibres, et 2) la classification fondée sur les extrémités (*Pas 4*) permet de séparer les faisceaux dès qu'ils présentent une extrémité différente.

## Résultats

La méthode de classification hiérarchique des fibres proposée a été appliquée à 12 sujets d'une base de données de cerveaux adultes [Poupon et al. (2006)]. La diffusion a été modélisée en utilisant une déconvolution sphérique de l'ODF [Descoteaux et al. (2009b)]. Les fibres du cerveau entier ont été reconstruites en utilisant un algorithme de tractographie déterministe régularisée. Les résultats sont illustrés pour l'hémisphère droit d'un sujet dans la Figure 10. Ces données contiennent un million et demi de fibres, dont 600 mille pour l'hémisphère droit, lesquelles sont réduites à un peu plus de 3000 faisceaux homogènes. La méthode a aussi été appliquée à des données de tractographie DTI de deux cerveaux d'enfants.

## Applications

Un fantôme physique [Poupon et al. (2010)] fait de fibres acryliques de petit diamètre, contenant plusieurs configurations réalistes de fibres, comme des croisements et bifurcations

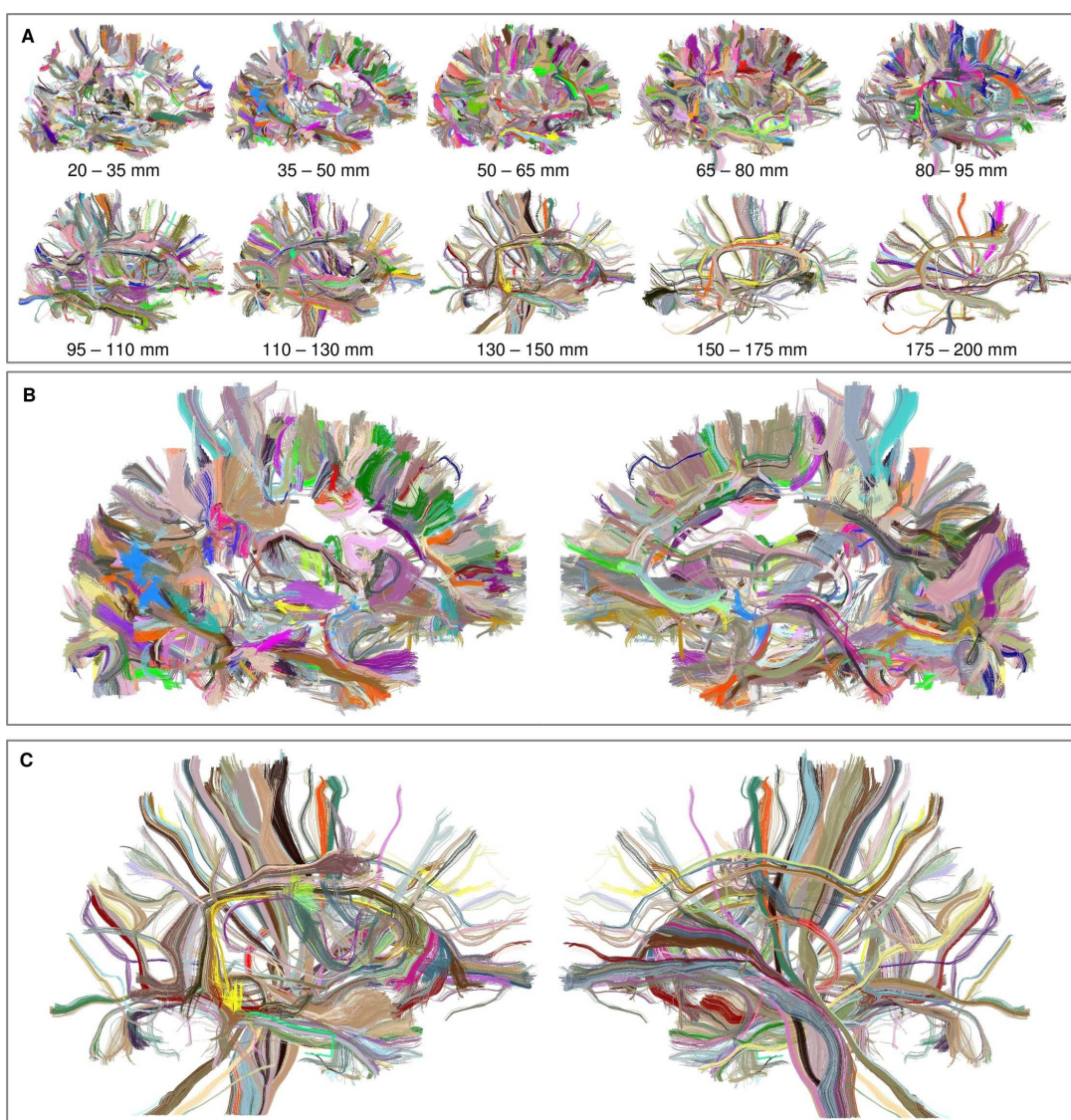


Figure 10: **Faisceaux de fibres résultants pour un cerveau adulte (hémisphère droit).** Les couleurs des faisceaux ont été sélectionnés de façon aléatoire et peuvent se répéter dans chaque groupe. **A: Vue extérieure des faisceaux.** Pour une meilleure visualisation, les faisceaux ont été séparés en 10 groupes de différentes longueurs. **B: Vues extérieure et intérieure d'une sélection de faisceaux de fibres courtes (35-50 mm).** La plupart de ces faisceaux appartiennent à des faisceaux d'association courts. **C: Vues extérieure et intérieure d'une sélection de faisceaux de fibres longues (130-150 mm).** Ces faisceaux constituent des long faisceaux de fibres connus de la substance blanche.

de fibres, a été utilisé pour montrer une application de la méthode. Six jeux de fibres ont été calculés pour ce fantôme, en utilisant trois modèles locaux de diffusion (DTI, q-ball analytique (SH q-ball) [Descoteaux et al. (2007)] et une déconvolution sphérique de l'ODF (SDT) [Descoteaux et al. (2009b)]) et deux algorithmes de tractographie (déterministe et probabiliste). Nous avons appliqué notre méthode aux six jeux de fibres, à partir du *Pas 2*. Un atlas a été créé pour retrouver les faisceaux validement reconstruits dans chaque jeu de données, c'est à dire, les faisceaux de fibres qui ont des trajectoires égales à la vérité



terrain. L’atlas, illustré dans la Figure 11 B, contient un centroïde pour chaque faisceau original du fantôme (7 au total). L’analyse des résultats a permis de comparer les différents modèles locaux de diffusion et les différentes méthodes de tractographie en retrouvant automatiquement les faisceaux validement reconstruits, montrés dans la Figure 11 C. Pour cela, nous avons calculé la proportion de leur volume par rapport au volume original, ainsi que le nombre total de fibres validement reconstruites pour chaque approche (Figure 11 D).

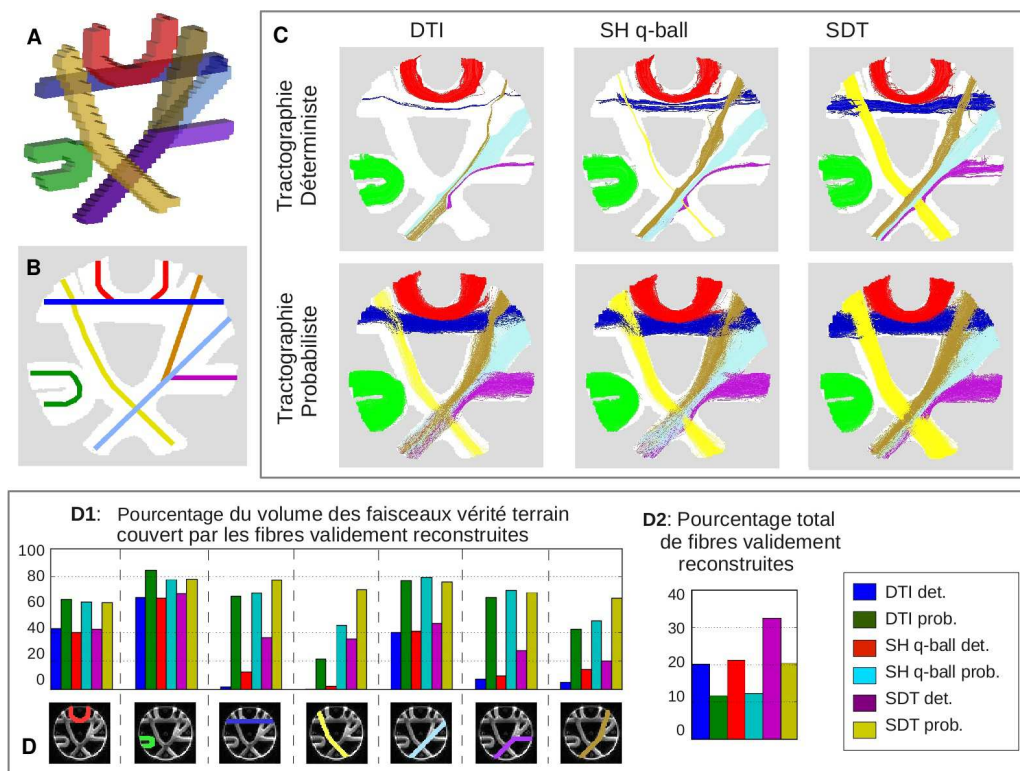


Figure 11: **Résultats pour les six jeux de données du fantôme physique. Application dans l’évaluation des modèles locaux de diffusion et les algorithmes de tractographie.** **A:** Les sept faisceaux vérité terrain (masques 3D). **B:** L’atlas des centroïdes des faisceaux vérité terrain, utilisé pour identifier automatiquement les faisceaux validement reconstruits. **C:** Faisceaux vérité terrain validement reconstruits pour chaque jeu de données: pour trois modèles locaux de diffusion (DTI, SH q-ball and SDT) et deux algorithmes de tractographie (déterministe et probabiliste). **D:** Analyse des résultats pour les six jeux de données: **D1: Pourcentage du volume des faisceaux vérité terrain couvert par les fibres validement reconstruites.** En général, la tractographie probabiliste présente une meilleure reconstruction des faisceaux. **D2: Pourcentage total de fibres validement reconstruites.** En général, comme prévu, la tractographie déterministe présente un pourcentage plus élevé de fibres validement reconstruites.

Une autre application de notre méthode a été illustrée: la décomposition “top-down” des long faisceaux de fibres connus. La tractographie permet d’envisager une analyse plus en profondeur des faisceaux connus, en les sous-divisant en plusieurs composantes [Cattani et al. (2005)]. L’approche usuelle utilise des ROIs pour décomposer les faisceaux. Nous illustrons avec le faisceaux arqué de quatre sujets, que les faisceaux résultants de notre méthode de classification peuvent être utilisés pour retrouver des décompositions

des faisceaux à travers une interface graphique (cela peut être effectué aussi de façon automatique). Dans cet exemple, le faisceau arqué a pu être divisé en six faisceaux pour les quatre sujets, dont trois faisceaux ont déjà été décrits par [Catani et al. \(2005\)](#).

### Masque de propagation de la tractographie calculé à partir de l'image pondérée en T1

Les algorithmes de tractographie ont besoin d'un masque de la substance blanche pour délimiter l'espace 3D dans lequel les fibres sont calculées. Normalement ce masque est calculé à partir d'un seuillage sur l'image de FA (seuil entre 0.1 et 0.25), mais ce masque est trop restrictif car la FA peut être très basse dans des croisements de fibres (2/3 des voxels) ou dans les régions sous-corticales à cause de l'effet de volume partiel. Nous proposons la construction d'un masque de propagation de la tractographie à partir de l'image pondérée en T1, fondée sur trois masques: un masque des deux hémisphères et du cervelet, un masque des sillons et un masque des noyaux gris centraux et des ventricules. Ce masque, contenant la substance blanche et une partie de la substance grise permet une meilleure délimitation pour la tractographie des régions sous-corticales, des structures profondes, du corps calleux, du fornix et des commissures (voir Figure 12 A). Une comparaison des faisceaux segmentés à partir des fibres reconstruites avec notre masque calculé à partir de l'image T1 et un masque fondé sur la FA est présentée dans la Figure 12 B. On peut observer une meilleure reconstruction des faisceaux surtout sur les régions sous-corticales, ce qui a un impact très important dans les fibres d'association courtes.

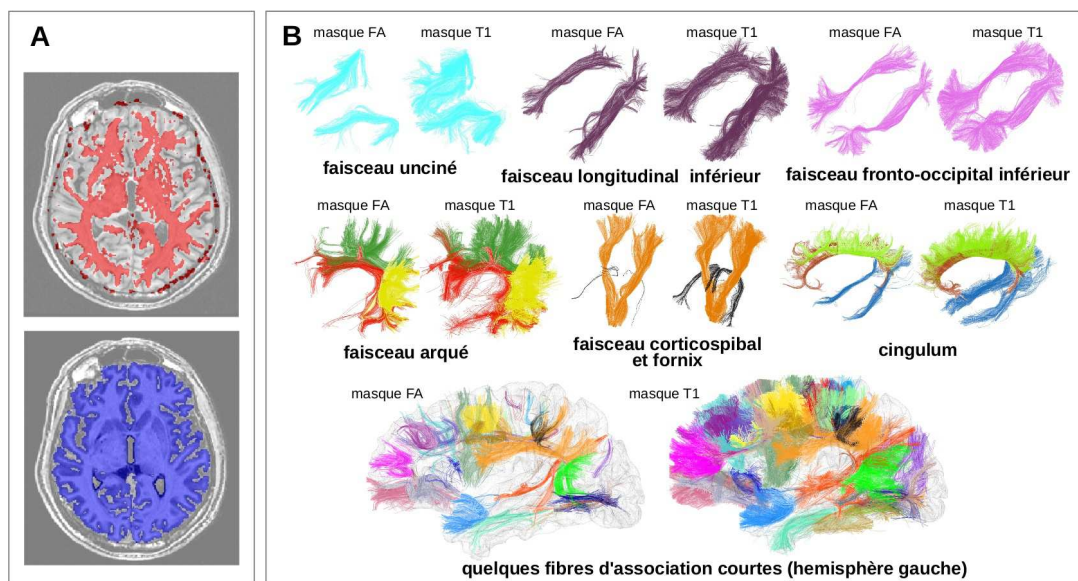


Figure 12: **Masque de propagation de la tractographie calculé à partir de l'image pondérée en T1.** A: Comparaison entre notre masque de propagation et un masque calculé à partir de la FA (seuil égal à 0.1). B: Comparaison entre des faisceaux segmentés reconstruits à partir de notre masque de propagation (*masque T1*) et un masque calculé à partir de la FA (*masque FA*), avec un seuil égal à 0.15.

## Chapitre 6: Classification des Fibres Inter-sujet: Inférence d'un atlas des faisceaux multi-sujet

Les modèles des faisceaux existants sont composés seulement par les faisceaux connus de la substance blanche profonde (DWM). Dans ces modèles, les faisceaux de la DWM sont représentés par des fibres qui ont à peu près la même forme, et ne représentent pas la variabilité de la forme et de la position des fibres à travers les sujets. Grâce aux améliorations des acquisitions, corrections et modélisation des données de diffusion, les données de tractographie actuelles présentent une grande complexité et un très grand nombre de fibres. Les faisceaux reconstruits sont alors plus complexes; quelques exemples de décomposition des faisceaux connus en fascicules ont été proposés dans la littérature [Lawes et al. (2008)]. Par exemple, le faisceau arqué a été décomposé en un segment long direct et deux segments indirects (antérieur et postérieur) [Catani et al. (2005)]. En plus, jusqu'à présent, les fibres courtes de la substance blanche superficielle ont été très rarement étudiées. La segmentation de la substance blanche reste encore un problème complexe et pas complètement résolu.

Les stratégies couramment proposées pour la reconstruction des faisceaux des fibres reposent sur deux idées complémentaires. La première approche utilise des régions d'intérêt (ROI) pour sélectionner ou exclure des fibres. Ces ROIs peuvent être définies manuellement [Catani et al. (2002); Mori et al. (2005); Wakana et al. (2007); Catani and Thiebaut de Schotten (2008)], ou en utilisant un atlas de ROIs après l'application d'une normalisation affine [Oishi et al. (2008)] ou non-linéaire [Zhang et al. (2010)]. La seconde stratégie est fondée sur un regroupement des fibres en utilisant une mesure de similarité entre paires de fibres [Corouge et al. (2004); Zhang et al. (2008a); O'Donnell et al. (2006); Visser et al. (2011)]. Cette dernière approche nécessite moins d'interaction que les approches manuelles et permet d'intégrer dans l'analyse des informations sur la forme et la position des fibres, ce qui n'est pas le cas pour la plupart des approches fondées sur les ROIs. En plus, elle permet d'intégrer de l'information *a priori* dans des modèles des faisceaux [Maddah et al. (2005); O'Donnell and Westin (2007)], ceux qui peuvent être après utilisés pour segmenter d'autres sujets. En outre, l'application d'une méthode de regroupement des fibres provenant de plusieurs sujets après une normalisation spatiale, peut aider à découvrir des nouveaux faisceaux reproductibles. Cependant, les méthodes fondées sur des regroupements présentent une limitation dans le nombre de fibres qui peuvent être analysées. Malgré deux travaux récents qui décrivent des analyses des jeux de données de tractographie très grands (jusqu'à 120.000 [Wang et al. (2011)] et 480.000 fibres [Visser et al. (2011)]), la segmentation des jeux de données massifs de fibres, présentant plus d'un million de fibres, est encore un grand défi.

L'objectif de cette thèse est l'inférence d'un modèle des faisceaux des fibres de la substance blanche du cerveau humain à partir des données de diffusion à haute résolution angulaire (HARDI). En conséquence, dans ce chapitre nous présentons une méthode qui prend comme entrée des jeux de données massifs de tractographie provenant d'une popu-

lation de sujets, et qui produit comme sortie un modèle composé d’une liste des faisceaux génériques présents dans la plupart des sujets.

### Stratégie de regroupement de deux niveaux

La méthode consiste en une stratégie de deux niveaux, enchaînant un regroupement intra-sujet, suivi d’un regroupement inter-sujet, pour traiter de très grands jeux de données issues de la tractographie.

**Premier niveau: regroupement intra-sujet.** Pour pouvoir analyser ensemble les données issues de la tractographie d’une population de sujets, nous utilisons d’abord le regroupement intra-sujet présenté dans le chapitre précédant. Ce regroupement permet d’obtenir une représentation comprimée des jeux de données individuels de fibres. Pour chaque sujet, on passe de plus d’un million de fibres à quelques milliers de faisceaux réguliers, qui peuvent être représentés par des centroïdes. Un traitement additionnel a été ajouté au *Pas 1* pour obtenir des sous-ensembles contenant les fibres qui sont connectées aux thalami: *thalamus-droit* et *thalamus-gauche*.

**Deuxième niveau: regroupement inter-sujet.** Le deuxième niveau a pour objectif de trouver une correspondance entre les faisceaux produits dans le premier niveau à travers une population de sujets. Cette analyse est effectuée séparément pour chaque sous-ensemble de fibres. La Figure 13 (A) illustre la méthode.

Premièrement, un centroïde est calculé pour chaque faisceau en utilisant la moyenne des distances les plus proches [Corouge et al. (2004); O’Donnell et al. (2006); O’Donnell and Westin (2007)]. Un centroïde représente la géométrie principale du faisceau et est localisé dans le centre du faisceau. Il est défini comme la fibre qui minimise la distance vers les autres fibres du faisceau. Une fois que tous les centroïdes provenant de tous les sujets pour le sous-ensemble analysé ont été calculés, ils sont transformés vers l’espace de Talairach en utilisant une transformation affine estimée à partir de l’image T1.

Ensuite, un **graphe d’affinités des centroïdes** est calculé en utilisant une distance entre paires de centroïdes. La distance utilisée est la distance Euclidienne maximale entre points correspondants, normalisée par la longueur de centroïde minimale ( $d_{MEN}$ ). Cette distance est plus restrictive que les distances fondées sur les points les plus proches. Pour ce calcul, les centroïdes sont échantillonnés en utilisant 21 points équidistants. La normalisation permet de rendre la distance plus restrictive pour les fibres courtes, en donnant des groupes plus compacts pour ces faisceaux. Pour construire le graphe d’affinités des centroïdes, on utilise un seuil sur la distance maximale entre centroïdes ( $M_{dn}$ ), qui varie normalement entre 10 et 15 mm.

Ce graphe d’affinités est utilisé pour effectuer un regroupement hiérarchique des centroïdes. L’arbre résultant est analysé pour extraire seulement les groupes compacts, où la distance entre tous les centroïdes est inférieure à la distance maximale  $M_{dn}$ . Les groupes qui contiennent des centroïdes provenant d’au moins la moitié des sujets sont enfin sé-



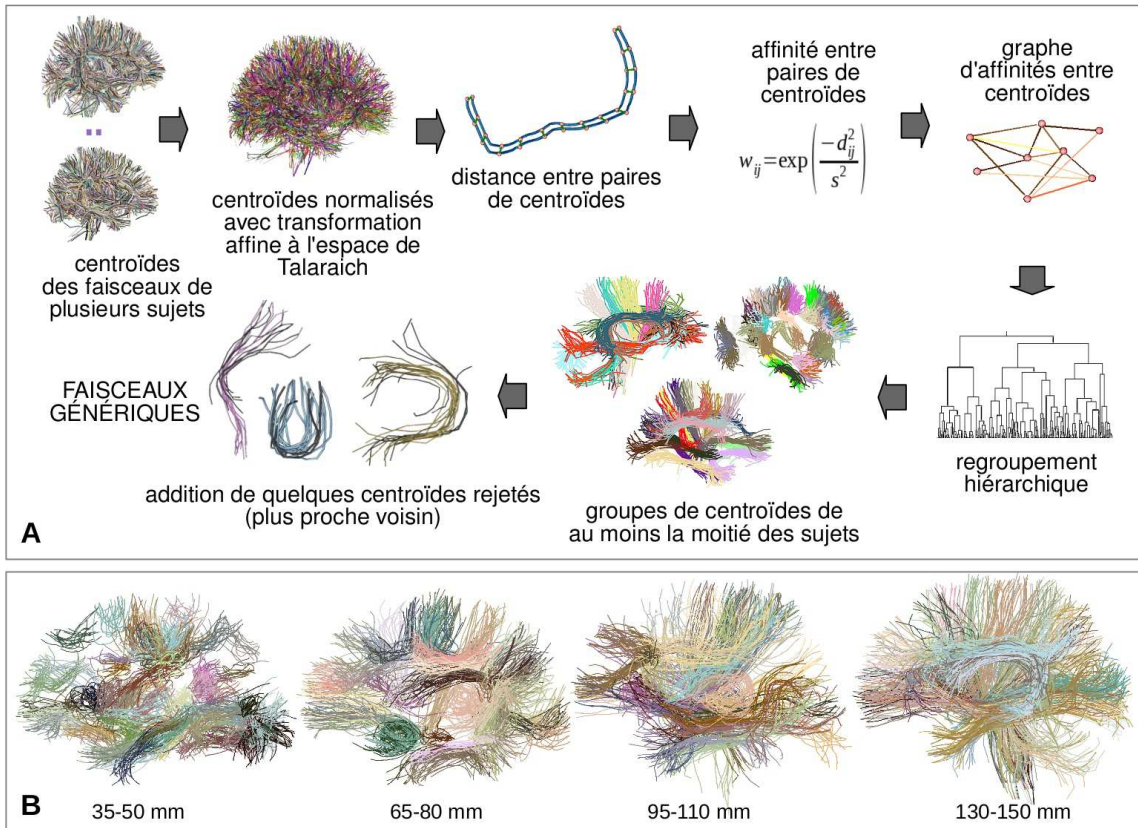


Figure 13: **Regroupement des faisceaux inter-sujet. A: Un schéma général de la méthode.** L'analyse comprend tous les faisceaux obtenus pour un sous-ensemble de fibres, provenant d'une population de sujets. Un centroïde est d'abord calculé pour chaque faisceau. Les centroïdes de la population de sujets sont alors transformés vers l'espace de Talairach. Une distance restrictive est calculée entre toutes les paires de centroïdes et convertie en affinité. Un graphe d'affinités entre centroïdes est ensuite calculé, en utilisant un seuil maximal sur la distance. Les centroïdes sont finalement regroupés en utilisant un regroupement hiérarchique. Seulement les groupes compacts, contenant des centroïdes d'au moins la moitié des sujets, sont sélectionnés comme des *faisceaux génériques*. Un pas additionnel permet d'ajouter quelques centroïdes rejetés au groupe le plus similaire. **B: Exemple de faisceaux génériques (sélection de l'hémisphère gauche).** Les faisceaux ont été calculés en utilisant une distance maximale entre fibres intra-sujet  $max\_cdist$  égale à 10 mm et une distance maximale entre centroïdes inter-sujet  $M_{dn}$  égale à 15 mm. Les faisceaux génériques sont composés des centroïdes intra-sujet obtenus dans le premier niveau de regroupement. Ils contiennent des centroïdes d'au moins six sujets différents.

lectionnés et appelés *faisceaux génériques*. Un dernier pas optionnel, relâche un peu les contraintes pour ajouter quelques centroïdes aux faisceaux génériques, qui ont été rejetés dans le regroupement. Un centroïde non attribué est inclus au faisceau générique le plus proche si sa distance au centroïde le plus proche du faisceau est inférieure à un seuil. La Figure 13 (B) montre quelques faisceaux génériques obtenus en utilisant une distance maximale entre fibres intra-sujet  $max\_cdist$  égale à 10 mm et une distance maximale entre centroïdes inter-sujet  $M_{dn}$  égale à 15 mm.

Des données simulées ont été utilisées pour évaluer le comportement de la méthode sur une population de sujets en utilisant une normalisation affine. Pour cela, 200 fibres de différentes longueur, forme et position ont été sélectionnées à partir d'un sujet pour



représenter des centroïdes intra-sujet. Ces centroïdes ont été alors transformés vers le référentiel des autres sujets en utilisant un recalage non-linéaire à partir des images T1. La méthode inter-sujet a été alors appliquée sur l'ensemble des centroïdes, transformés dans l'espace de Talairach avec une transformation affine, pour un rang de valeurs de distance  $M_{dn}$ . Les faisceaux génériques obtenus ont été comparés avec la vérité terrain, pour déterminer le nombre de faisceaux récupérés et le nombre de sujets qui les composaient. Les résultats ont montré que la normalisation affine vers un espace standard est suffisante pour retrouver les faisceaux les plus reproductibles à travers les sujets.

### **Atlas HARDI multi-sujet des faisceaux connus de la substance blanche profonde**

La stratégie de regroupement des fibres de deux niveaux a été appliquée à la base de données de 12 sujets de cerveaux adultes [Poupon et al. (2006)]. Cette analyse a été effectuée séparément pour cinq sous-ensembles de fibres: *hémisphère droit*, *hémisphère gauche*, *inter-hémisphérique*, *thalamus-droit* et *thalamus-gauche*.

Des faisceaux génériques ont été obtenus en utilisant une distance maximale entre fibres intra-sujet  $max\_cdist$  égale à 10 mm et une distance maximale entre centroïdes inter-sujet  $M_{dn}$  égale à 15 mm. Ces faisceaux ont été étiquetés manuellement pour identifier les faisceaux connus de la substance blanche profonde. Pour l'étiquetage nous avons utilisé des informations anatomiques relatives à la trajectoire et la position des faisceaux, et particulièrement à leurs extrémités, en nous appuyant sur des descriptions anatomiques [Catani and Thiebaut de Schotten (2008)]. Des segmentations des sillons et des parcellisations corticales ont été utilisées pour guider visuellement cette tâche. Un faisceau est composé alors de plusieurs groupes inter-sujet, qui tiennent compte de plusieurs sous-divisions du faisceau connu dans l'espace standard. Chaque faisceau de l'atlas est représenté par une liste de centroïdes inter-sujet calculés dans le premier niveau de la méthode. Par conséquent, l'atlas des faisceaux multi-sujet créé permet de représenter la variabilité inter-individuelle de la forme et la position des faisceaux. Cette inférence a été effectuée pour l'hémisphère gauche. Les faisceaux de l'hémisphère droit ont été calculés comme les symétriques de ceux de l'hémisphère gauche par rapport au plan inter-hémisphérique de l'espace de Talairach.

L'atlas proposé, illustré dans la Figure 14, contient un total de 36 faisceaux, composés de 11 faisceaux dans chaque hémisphère et le corps calleux. Plusieurs faisceaux connus sont divisés dans quelques fascicules.

### **Atlas HARDI multi-sujet des faisceaux d'association courts de la substance blanche superficielle**

Les faisceaux d'association courts ont été rarement étudiés; pour cette raison il n'existe pas trop d'information sur eux dans la littérature. Les études proposées jusqu'à présent utilisent des atlas de ROIs après l'application d'une normalisation affine [Oishi et al. (2008)] ou non-linéaire [Zhang et al. (2010)]. Par exemple Zhang et al. (2010) a identifié 29 faisceaux courts qui connectent des gyri adjacents. Le critère utilisé pour l'identification d'un

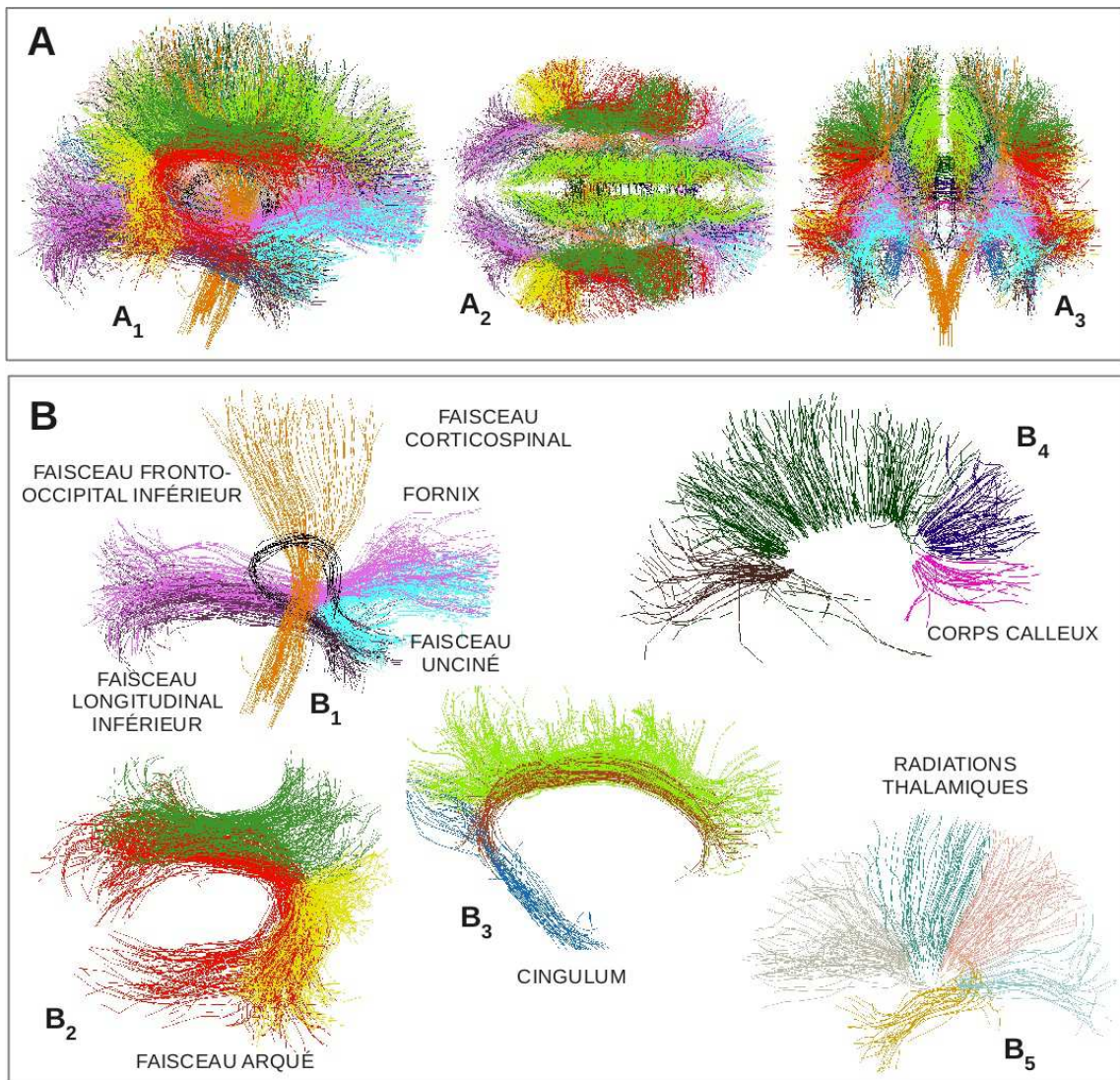


Figure 14: **Atlas HARDI multi-sujet des faisceaux connus.** **A:** Tous les faisceaux (4189 centroïdes): vues depuis la droite ( $A_1$ ), le haut ( $A_2$ ) et le front ( $A_3$ ). **B:** Vues détaillées des faisceaux.  $B_1$ : Vue intérieure du fornix (noir), faisceau unciné (cyan), faisceau fronto-occipital inférieur (violet), faisceau longitudinal inférieur (rose foncé) et faisceau corticospinal (orange) gauche.  $B_2$ : Vue extérieure des segments du faisceau arqué gauche: direct (rouge), antérieur (vert) et postérieur (jaune).  $B_3$ : Vue intérieure des fascicules du cingulum gauche: cingulaires longs (marron), cingulaires courts (vert clair) et temporaux (bleu).  $B_4$ : Vue extérieure du corps calleux: rostrum (fushia), genou (bleu foncé), corps (vert foncé) et splenium (marron foncé).  $B_5$ : Vue extérieure des radiations thalamiques gauches: antérieure (gris), supérieure motrice (sarcelle), supérieure pariétale (rose), postérieure (bleu ciel) et inférieure (ocre).

faisceau a été l'existence de fibres connectant les deux régions dans les 20 sujets étudiés. Cette méthode a démontré être puissante pour retrouver des faisceaux existant dans une population de sujets, mais elle n'inclut pas des informations fondées sur la forme et la position des fibres.

Pour inférer un modèle des faisceaux courts, nous avons appliqué alors notre méthode de regroupement des fibres de deux niveaux à la base de données de 12 sujets de cerveaux

adultes [Poupon et al. (2006)], aux sous-ensembles *hémisphère droit* et *hémisphère gauche*. Des faisceaux génériques ont été obtenus en utilisant une distance maximale entre fibres intra-sujet  $max\_cdist$  égale à 7 mm et une distance maximale entre centroïdes inter-sujet  $M_{dn}$  égale à 12 mm. Pour obtenir des faisceaux génériques compacts, le dernier pas qui ajoute des centroïdes rejetés n'a pas été appliqué.

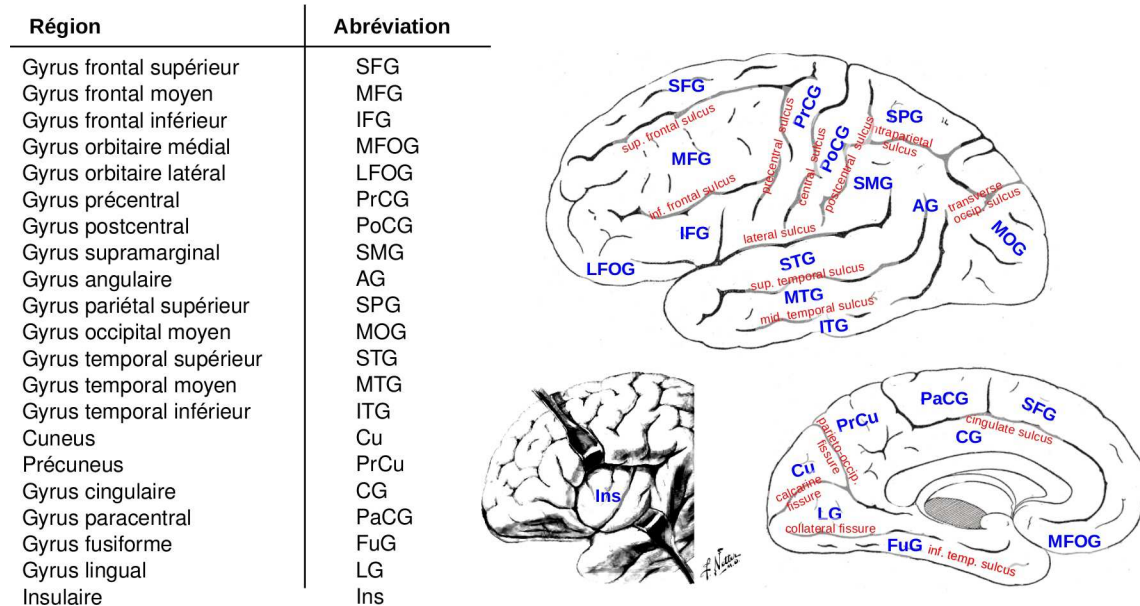


Figure 15: **Régions anatomiques de la surface corticale utilisées pour étiqueter les faisceaux d'association courts de l'atlas HARDI multi-sujet.** [Figures adaptée de <http://www.bartleby.com/107/> et <http://www.netterimages.com/>]

Ces faisceaux génériques, appartenant à la substance blanche superficielle (SWM), ont été étiquetés manuellement en utilisant des parcellisations en gyri des surfaces corticales [Cachia et al. (2003)]. L'objectif a été de donner un nom anatomique à chaque faisceau reproductible. Seulement les faisceaux présentant une forme régulière et une position non ambiguë ont été étiquetés. La Figure 15 présente les gyri qui ont été finalement utilisés dans l'étiquetage.

Cette inférence a été effectuée pour l'hémisphère gauche, en considérant les fibres entre 35 et 110 mm. Un nom a été donné à chaque faisceau de l'atlas, en suivant le critère utilisé par Zhang et al. (2010), qui proposent des noms composés par la ou les deux régions qui connectent chaque faisceau. Les faisceaux de l'hémisphère droit ont été calculés comme les symétriques de ceux de l'hémisphère gauche par rapport au plan inter-hémisphérique de l'espace de Talairach. La plupart des faisceaux étiquetés sont composés seulement par un faisceau générique. Comme dans le cas des faisceaux connus, chaque faisceau court de l'atlas est représenté par une liste de centroïdes inter-sujet calculés dans le premier niveau de la méthode, ce qui permet de représenter la variabilité inter-individuelle de la forme et la position des faisceaux. Quarante-sept faisceaux de la SWM ont été identifiés pour l'hémisphère gauche. Ils sont illustrés tous ensemble et individuellement dans la Figure 16.



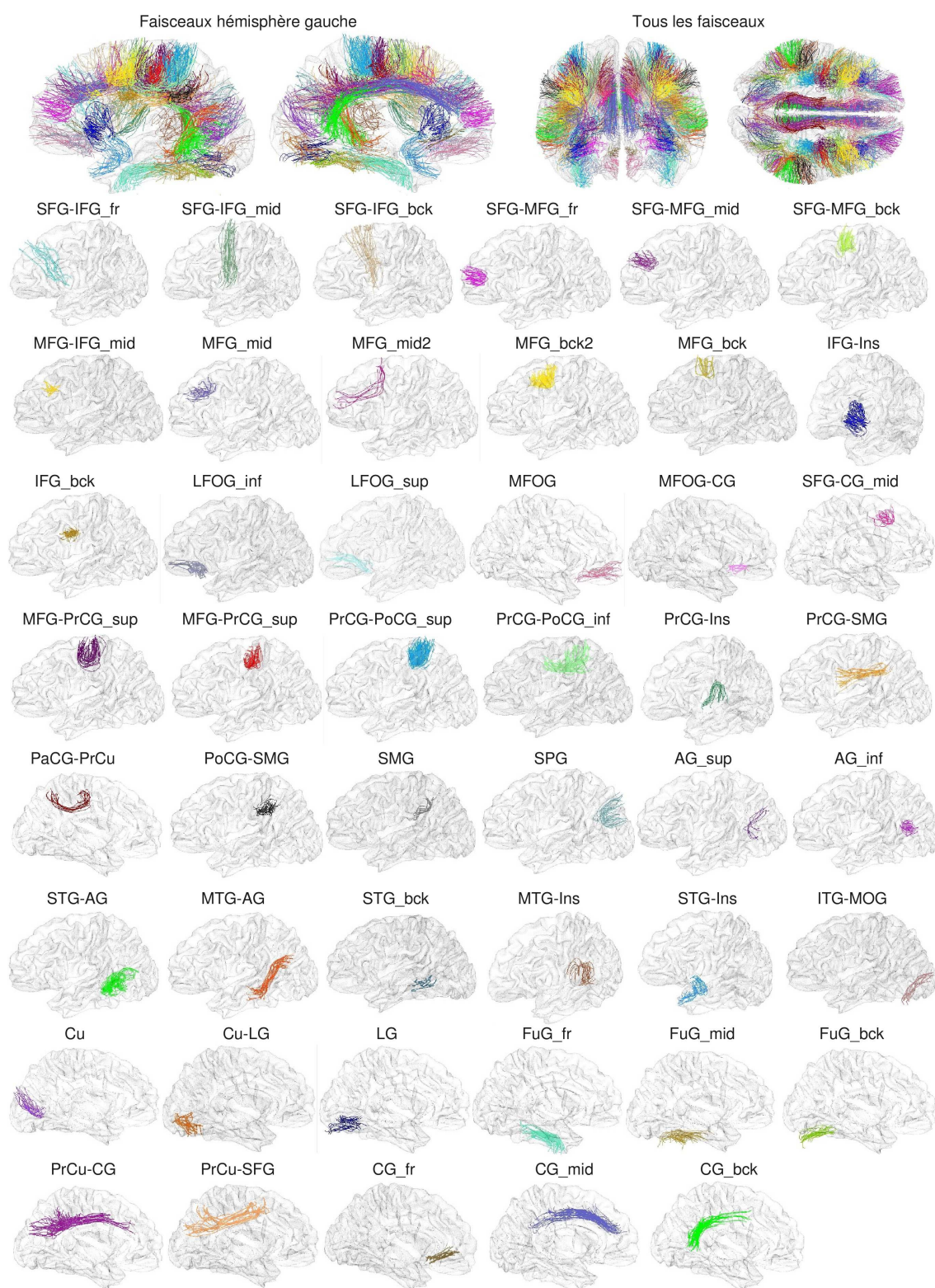


Figure 16: **Atlas HARDI multi-sujet des faisceaux d'association courts (47 faisceaux par hémisphère)**. La première ligne montre de gauche à droite: vues extérieure et intérieure des faisceaux de l'hémisphère gauche (HG), vues depuis le front et le haut de tous les faisceaux. Les lignes suivantes montrent les 47 faisceaux de l'HG. Les noms ont été attribués en fonction des régions qu'ils connectent, en suivant les noms des régions illustrés dans la Figure 15. Dans certains cas, une spécification spatiale a été ajoutée: *fr* (antérieur), *mid* (moyen), *bck* (postérieur), *sup* (supérieur) et *inf* (inférieur).

## Chapitre 7: Segmentation Automatique des Jeux de Données Massifs de Tractographie

### Méthode de segmentation automatique des faisceaux de fibres

Nous proposons une méthode simple mais puissante pour la segmentation automatique des jeux de données massifs de tractographie fondée sur l’atlas multi-sujet des faisceaux créé dans le chapitre précédant. Un schéma de la méthode est présenté dans la Figure 17.

La segmentation d’un nouveau jeu de données de fibres commence par une compression en quelques milliers de faisceaux, en utilisant le regroupement intra-sujet décrit dans le chapitre 5. Les faisceaux résultants sont alors étiquetés en employant une classification supervisée fondée sur notre atlas des faisceaux multi-sujet. Les centroïdes des faisceaux sont d’abord normalisés vers l’espace de Talairach en utilisant une transformation affine. Ensuite, des distances entre chaque centroïde du nouveau sujet et tous les centroïdes de l’atlas sont calculées.

La distance utilisée est la distance Euclidienne maximale entre points correspondants ( $d_{ME}$ ). Cette distance est restrictive et permet une bonne représentation de la similarité entre deux fibres, en prenant en compte la position et la forme des fibres. Pour ce calcul, les centroïdes de l’atlas et du nouveau sujet sont échantillonnés en 21 points équidistants. L’ensemble des distances entre centroïdes est calculé en quelques minutes.

Chaque centroïde du sujet est étiqueté par le faisceau le plus proche, à condition que la distance vers ce faisceau, c’est-à-dire la plus petite distance vers les centroïdes qui représentent le faisceau, soit inférieure à un seuil.

Pour les faisceaux de la substance blanche profonde, ce seuil est adapté à chaque faisceau en utilisant une stratégie *leave-one-out*: pour chaque faisceau, le seuil est la valeur minimale permettant l’étiquetage de tous les centroïdes de tous les sujets, en considérant un atlas fait à partir des onze sujets restants. Cette approche *leave-one-out* permet de définir un seuil spécifique pour chaque faisceau de l’atlas, comme la distance maximale des distances minimales entre un centroïde de ce faisceau chez un sujet et tous les centroïdes du même faisceau chez les autres sujets. On peut s’attendre à ce que l’augmentation de la taille de la base de données utilisée pour inférer l’atlas permettra d’améliorer l’échantillonnage de la variabilité du faisceau, ce qui diminuera les seuils utilisés pour capturer le même faisceau chez des sujets inconnus.

Pour les faisceaux d’association courts, ces seuils ont été déterminés empiriquement pour chaque faisceau de l’atlas (entre 8 et 14 mm), en considérant la longueur moyenne du faisceau et sa proximité aux autres faisceaux de l’atlas. Ce critère conduit à des seuils plus élevés pour les faisceaux longs et isolés. Une stratégie *leave-one-out* pour la détermination de ces seuils pourrait être développée dans l’avenir.

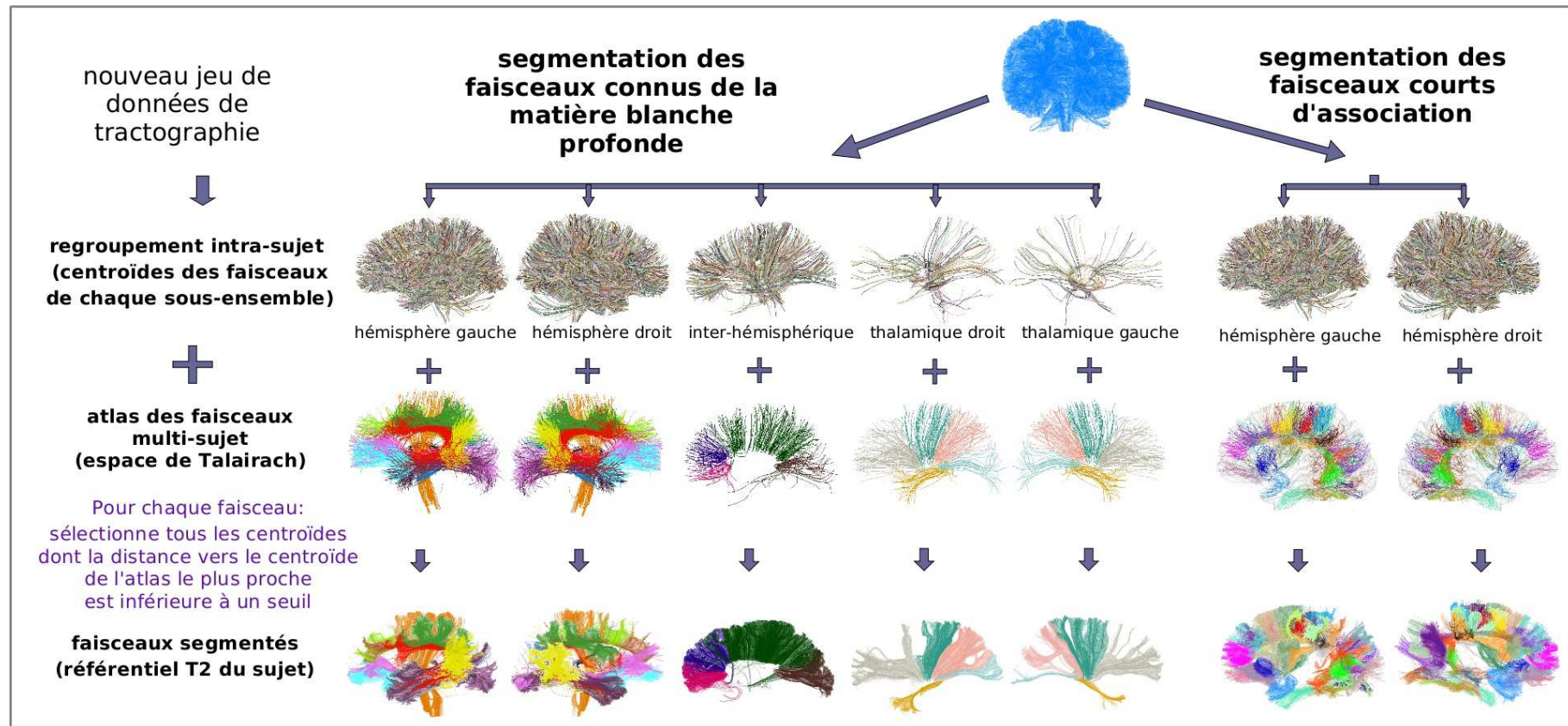


Figure 17: **Méthode de segmentation automatique des faisceaux de fibres fondée sur un atlas des faisceaux multi-sujet.** La segmentation d'un nouveau jeu de données de tractographie commence par une compression en quelques milliers de faisceaux, en utilisant le regroupement intra-sujet décrit dans le chapitre 5. Les faisceaux résultant sont alors étiquetés en employant une classification supervisée fondée sur notre atlas des faisceaux multi-sujet. Les centroïdes des faisceaux sont d'abord normalisés vers l'espace de Talairach en utilisant une transformation affine. Ensuite, des distances entre chaque centroïde du nouveau sujet et tous les centroïdes de l'atlas sont calculées. Chaque centroïde du sujet est étiqueté par le faisceau le plus proche, à condition que la distance vers ce faisceau, c'est-à-dire la plus petite distance vers les centroïdes qui représentent ce faisceau, soit inférieure à un seuil.



## Résultats

Un problème connu sur l'évaluation de la segmentation des faisceaux de la substance blanche est l'absence de vérité terrain. Cela est d'autant plus complexe pour la substance blanche superficielle, dont la cartographie est encore largement inconnue et au mieux de nos connaissances, seulement la forme de quatre faisceaux de la substance blanche superficielle a été décrite dans la littérature [Oishi et al. (2008)]. Nous évaluons notre approche à l'aide d'autres bases de données: huit adultes et quatre enfants pour la segmentation des faisceaux de substance blanche profonde, et dix adultes pour la segmentation des faisceaux d'association courts.

**Résultats pour la segmentation des faisceaux connus de la substance blanche profonde.** Huit sujets d'une base de données HARDI de sujets adultes (DB2), ont été utilisés pour tester la méthode de segmentation des faisceaux de la substance blanche profonde. Cette base de données fournit des images de haute qualité pondérées en T1 et des données DW contenant 41 directions, à partir d'une valeur  $b$  de 1000 s/mm<sup>2</sup>. La fonction des distribution des orientations de diffusion (ODF) a été reconstruite dans chaque voxel en utilisant une solution analytique du modèle q-ball [Descoteaux et al. (2007)]. La tractographie du cerveau entier a été calculée en utilisant un masque de tractographie à partir de l'image de FA, avec un seuil égal à 0.15, et un algorithme de tractographie déterministe régularisée, donnant à peu près 1.5 millions de fibres par sujet. Nous n'avons pas utilisé notre masque de propagation de la tractographie fondé sur l'image T1 afin d'éviter tout biais lors des comparaisons entre nos résultats et ceux d'autres méthodes, adaptées à un masque à partir de la FA.

Les résultats de la segmentation sont présentés dans la Figure 18 (A-E). Les faisceaux ont été coloriés en suivant les couleurs des faisceaux de l'atlas (Figure 14). Tous les faisceaux de l'atlas ont été trouvés dans tous les sujets à l'exception du fornix et du segment long (ou direct) du faisceau arqué droit. Les segmentations ont été validées par un expert. Le problème avec le fornix est généralement lié à une erreur dans le masque de tractographie normalement produite à cause du faible diamètre de ce faisceau. Le problème du faisceau arqué pourrait être lié à la symétrisation de notre atlas, qui pourrait ne pas tenir compte correctement de l'asymétrie de ce faisceau lié au langage. Cependant, en explorant l'ensemble des données de tractographie avec une méthode fondée sur des ROIs, nous n'avons pas réussi à segmenter ce tract dans les cerveaux où notre stratégie fondée sur un atlas n'as pas réussi.

Ce qui pourrait arriver, c'est que lorsque le faisceau arqué n'est pas assez large, la résolution spatiale actuelle des données de diffusion n'est pas suffisante avec une stratégie de tractographie déterministe. En effet, plusieurs études ont montré une forte asymétrie de la taille du faisceau arqué, liée à l'asymétrie du système de langage [Catani et al. (2007)]. Pour obtenir un aperçu de la qualité des résultats, les faisceaux ont été visuellement comparés à ceux obtenus avec un seuil de distance plus grand. Nous avons constaté que les seuils estimés sont proche de l'optimale pour tous les faisceaux.

Le même comportement a été observé après l'application de la méthode de segmentation à quatre enfants d'une base de données DTI.

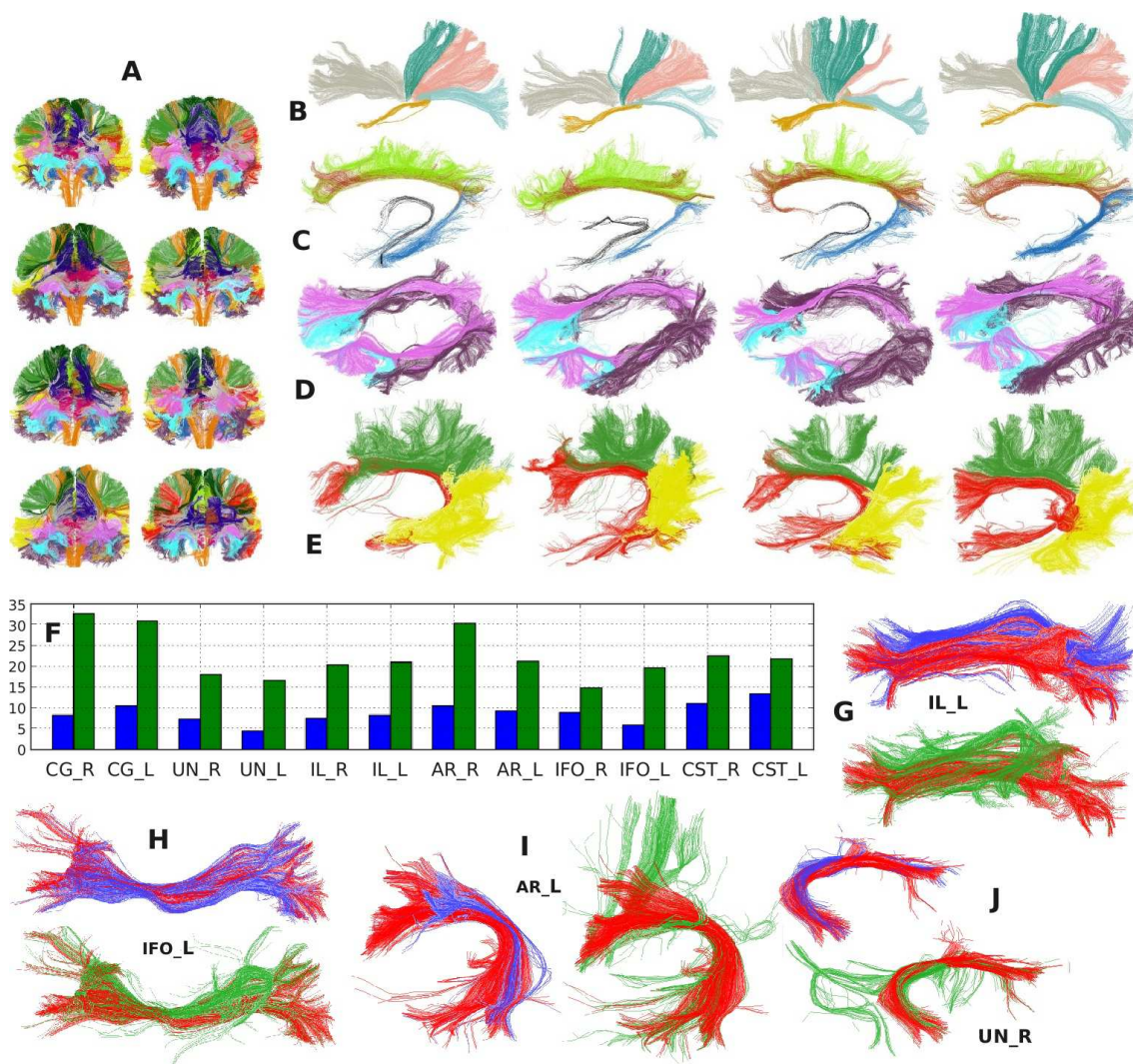


Figure 18: **A-E: Résultats pour la méthode de segmentation automatique des faisceaux de la substance blanche profonde chez l'adulte.** Les couleurs utilisées sont les mêmes que celles des faisceaux de l'atlas (Figure 14). **A**: tous les faisceaux chez les huit sujets (vue depuis le front). Les résultats qui suivent sont seulement montrés pour quatre sujets. **B**: radiations thalamiques gauches (vue depuis l'extérieur). **C**: cingulum et fornix gauches (vue depuis l'extérieur). **D**: faisceaux fronto-occipital inférieur, longitudinal inférieur et unciné droits et gauches (vue oblique depuis l'angle antérieur gauche). **E**: faisceau arqué gauche (vue depuis l'extérieur). **F-J: Une comparaison entre les résultats obtenus par notre méthode et une approche fondée sur des ROIs.** Les abréviations utilisées pour les faisceaux sont les suivantes: cingulum (CG), faisceau unciné (UN), faisceau longitudinal inférieur (IL), segment long du faisceau arqué (AR), faisceau fronto-occipital inférieur (IFO), faisceau corticospinal (CST), avec une "R" ou une "L" ajoutée, qui indique s'il s'agit du faisceau *droit* ou *gauche*, respectivement. **F**: un graphique des moyennes des distances (en mm) entre les fibres segmentées seulement par une méthode et la fibre la plus proche des fibres segmentées par les deux méthodes, pour tous les sujets. Les résultats apparaissent en bleu pour notre méthode et en vert pour la méthode fondée sur des ROIs. **G-J**: quelques exemples pour quatre faisceaux différents. Les fibres segmentées par les deux méthodes apparaissent en rouge, celles segmentées seulement par notre méthode apparaissent en bleu et celles segmentées seulement par l'approche fondée sur des ROIs apparaissent en vert.



En outre, une comparaison a été faite pour la base de données d'adultes avec une méthode très connue fondée sur des ROIs, proposée par [Zhang et al. \(2010\)](#). Pour cela, nous avons déterminé les fibres segmentées par les deux méthodes, et celles segmentées seulement par l'une des méthodes. Les fibres communes semblent être bien segmentées par les deux méthodes, suivant la définition de chaque faisceau (voir par exemple [[Catani and Thiebaut de Schotten \(2008\)](#)]). Mais, lors de l'analyse des fibres segmentées seulement par l'une des méthodes, nos résultats semblent être meilleurs pour la base de données utilisée. Pour la plupart des faisceaux, nous avons constaté que l'approche fondée sur des ROIs perd certaines fibres parfaitement adaptées à la définition et à la forme du faisceau, mais localisées dans la périphérie du faisceau. Cette faiblesse est probablement induite par un recalage non parfait. Nous avons également observé que la stratégie fondée sur des ROIs sélectionne quelques fibres présentant des trajectoire bizarres, parce que la forme des fibres n'est pas considérée dans l'analyse. Quelques exemples sont donnés pour quatre faisceaux différents dans la Figure 18 (G-J). Pour confirmer ce comportement, nous avons calculé la moyenne des distances  $d_{ME}$  entre les fibres segmentées seulement par l'une des méthodes et la fibre la plus proche segmentée par les deux méthodes, pour tous les sujets (voir la Figure 18 (F)). Cette analyse a été effectuée pour les faisceaux segmentés par les deux méthodes, présentant des définitions similaires. Toutes les distances se sont révélées plus importantes pour la méthode fondée sur des ROIs, confirmant que, en général, d'une part, notre méthode permet de détecter une quantité non négligeable de fibres qui ont une forte probabilité d'appartenir au faisceau et qui ne sont pas détectées par la méthode fondée sur des ROIs, et, d'autre part, que les fibres qui ne sont pas détectées par notre méthode sont très différentes de la forme du faisceau.

**Résultats pour la segmentation des faisceaux d'association courts** Quant à la segmentation des faisceaux d'association courts, nous avons utilisé dix sujets de la base de données DB2, mais en utilisant dans ce cas notre masque de propagation fondé sur l'image T1, qui améliore la détection de la connectivité sous-corticale.

Les résultats pour les dix sujets sont présentés dans la Figure 19. Tous les faisceaux ont été trouvés dans au moins la moitié des sujets, ce qui est cohérent avec les conditions de construction de notre atlas. Vingt-et-un faisceaux ont été trouvés dans tous les sujets, douze faisceaux ont été trouvés chez neuf sujets pour chaque hémisphère et quatorze faisceaux ont été trouvés chez entre cinq et huit sujets pour chaque hémisphère. Les segmentations ont été validées par un expert. Comme pour les faisceaux de la substance blanche profonde, les faisceaux ont été visuellement comparés à ceux obtenus à l'aide de seuils de distance plus grands. Nous avons constaté que les seuils utilisés ont été près de l'optimale pour la plupart des faisceaux. Les faisceaux longs et isolés ont été en général bien segmentés, quand ils existaient, mais certaines erreurs ont été trouvées pour les classifications des faisceaux courts localisés très près d'autres faisceaux de l'atlas.

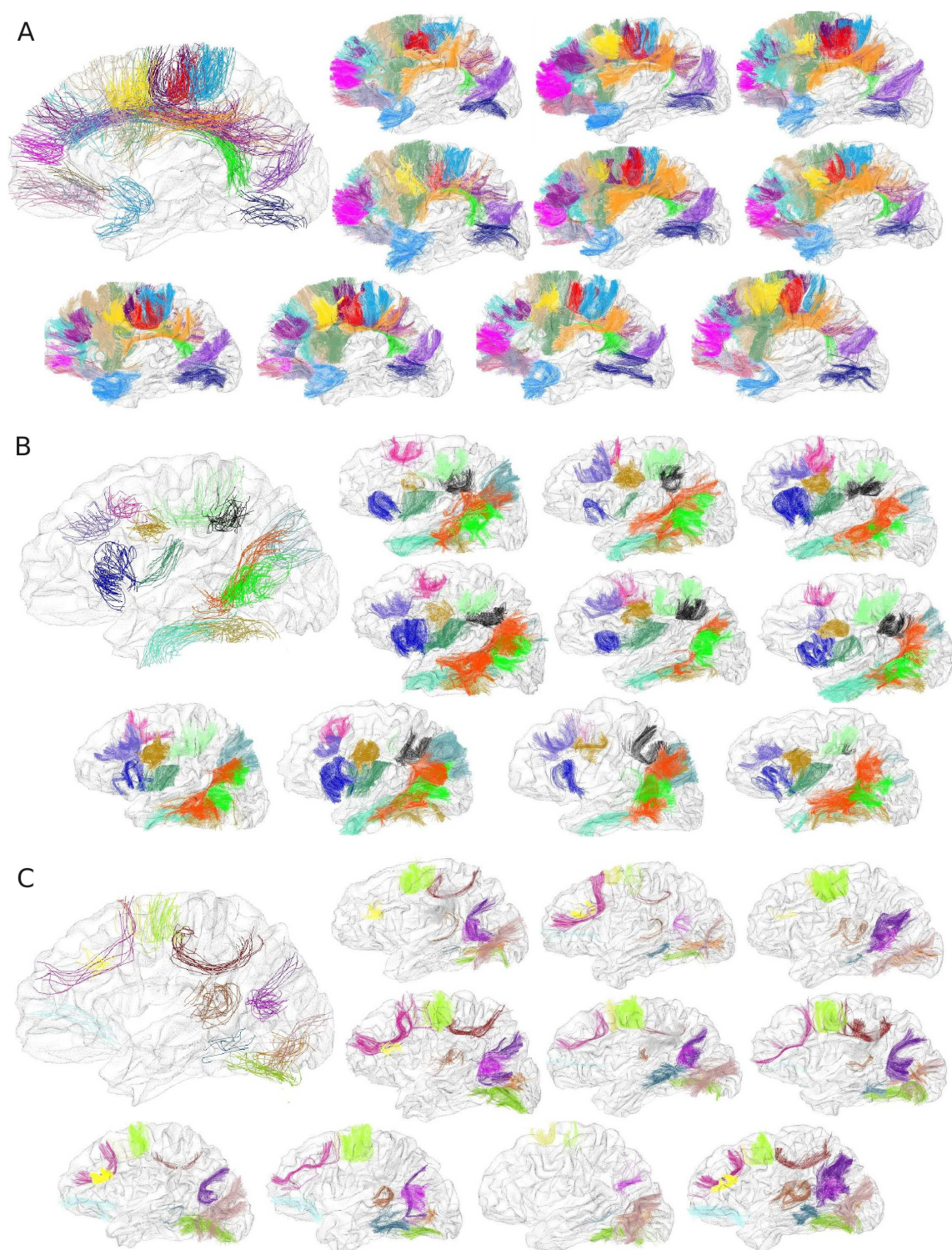


Figure 19: **Résultats pour la méthode de segmentation automatique des faisceaux courts d'association chez l'adulte.** Seulement les résultats pour l'hémisphère gauche sont montrés. Les couleurs des faisceaux sont les mêmes que celles des faisceaux de l'atlas (Figure 16). Les faisceaux ont été divisés en trois groupes, en fonction de leur reproductibilité. Les faisceaux de l'atlas sont illustrés dans le coin supérieur gauche de chaque image. **A:** Faisceaux de fibre trouvés dans tous les sujets (21 faisceaux). **B:** Faisceaux de fibre trouvés dans 9 de 10 sujets pour chaque hémisphère (12 faisceaux). **C:** Faisceaux de fibre trouvés dans 5 à 8 sujets pour chaque hémisphère (14 faisceaux).

## Conclusion

Dans cette thèse, nous avons proposé de nouvelles méthodes pour le regroupement et l'analyse des jeux de données de tractographie massifs et complexes, contenant plus d'un million de fibres. L'analyse principale se compose de deux parties: un regroupement intra-sujet et un regroupement effectué chez une population de sujets. Cette stratégie a permis l'inférence d'un modèle des faisceaux de la substance blanche du cerveau humain fondé sur l'imagerie de diffusion à haute résolution angulaire. Un atlas multi-sujet a ainsi été construit, composé de 36 faisceaux de la substance blanche profonde, et 94 faisceaux courts d'association de la substance blanche superficielle. Cet atlas est utilisé finalement pour la segmentation automatique des faisceaux connus de la substance blanche profonde et plusieurs faisceaux courts d'association chez des nouveaux sujets. Ces apports méthodologiques ont été décrits et développés dans les chapitres 4, 5 et 6 de cette thèse.

Ces contributions nécessitent certaines connaissances sur l'anatomie de la substance blanche cérébrale, les principes de l'IRM de diffusion et les méthodes de regroupement de fibres. Tous ces sujets ont été examinés et traités dans les premiers chapitres de cette thèse.

## Contributions

Tout au long de cette thèse, nous avons essayé de faire les bons choix mathématiques et algorithmiques pour résoudre les problèmes d'intérêt. Tout d'abord, nous avons utilisé une stratégie de regroupement intra-sujet hiérarchique utilisant une classification fondée sur les voxels pour une analyse efficace des jeux de données de tractographie individuels. Cette approche, composée de plusieurs étapes de traitement, garantit la robustesse et des résultats de bonne qualité. Ensuite, nous avons développé une méthode de classification inter-sujet nouvelle et efficace, capable d'analyser des jeux de données de tractographie très grands à partir d'une population de sujets et d'en déduire un modèle des faisceaux génériques présents dans la plupart des sujets. Pour faire face à la limitation de la taille des données, la méthode utilise en entrée les résultats du regroupement intra-sujet, qui consiste en quelques milliers de faisceaux représentant la structure du jeu de données de fibres dans sa totalité. Nous avons testé la robustesse et la qualité des résultats de nos méthodes en utilisant des données simulées. Le regroupement intra-sujet a été également comparé avec une autre stratégie de force-brute non-scalable. Enfin, nous avons proposé une méthode rapide, robuste et automatique de segmentation des faisceaux de la substance blanche, fondée sur l'atlas des faisceaux multi-sujet et la méthode de regroupement intra-sujet. Nous avons fait un effort spécial pour étudier et discuter l'état de l'art des méthodes de regroupement et segmentation des faisceaux pour mettre en évidence les forces et les limites des méthodes que nous avons proposées.

En résumé, les contributions importantes et originales de la thèse sont les suivantes:

### **Contributions majeures**

1. Une méthode robuste de regroupement de fibres intra-sujet pour des jeux de données massifs de tractographie.
2. Une stratégie de regroupement de fibres de deux niveaux, pour l'inférence d'un modèle des faisceaux de fibres du cerveau humain à partir des jeux de tractographie HARDI.
3. La construction d'un atlas HARDI multi-sujet des faisceaux en utilisant la stratégie de regroupement de fibres de deux niveaux.
4. Une méthode de segmentation automatique des jeux de données massifs de tractographie à partir de l'atlas multi-sujet.

### **Contributions mineures**

1. Une méthode pour la construction d'un masque de propagation de la tractographie robuste à partir des images T1.
2. Des données de tractographie simulées pour l'analyse des méthodes de regroupement de fibres intra-sujet et inter-sujet.

Nous croyons que ces contributions ont atteint l'objectif initial de cette thèse, qui a été de déduire un modèle des faisceaux de fibres de la substance blanche du cerveau humain à l'aide de l'imagerie de diffusion à haute résolution angulaire.

### **Perspectives**

Nous pensons que notre approche est une étape de l'analyse nécessaire et cruciale pour des jeux de données massifs de fibres. Ainsi, notre approche sera étendue facilement à la résolution spatiale de 1 mm qui peut maintenant être utilisé avec l'imagerie parallèle à très hauts champs. Cette résolution spatiale est censée mettre en évidence une multitude de faisceaux de fibres en U et mieux délimiter d'autres gros croisements de fibres. Par conséquent, on peut s'attendre dans un proche avenir, à voir des études plus exploratoires en vue d'améliorer notre connaissance sur la structure des faisceaux de la substance blanche, en particulier, des faisceaux d'association courts. Notre atlas est censé être raffiné dans le futur pour tenir compte de plusieurs subdivisions des faisceaux connus de la substance blanche profonde et des nouveaux faisceaux d'association courts.

En ce qui concerne les faisceaux d'association courts, chaque faisceau de fibre en U inféré dans ce travail n'a eu besoin que d'un alignement raisonnable des faisceaux provenant de la moitié des sujets, ce qui se passe dans les régions du cerveau les plus stables. Cependant, une augmentation du nombre de faisceaux de fibres en U génériques, nécessitera une amélioration de la normalisation spatiale utilisée pour comparer les faisceaux à travers les sujets. Par conséquent, l'utilisation d'une normalisation non-linéaire en s'appuyant sur

une segmentation des sillons [Auzias et al. (2011)] produira une amélioration importante sur les résultats. En outre, la poursuite des travaux va nous conduire à améliorer itérativement la normalisation spatiale à l'aide de contraintes sur les faisceaux inférés, afin de mieux aligner d'autres faisceaux [Durrleman et al. (2009)].

Néanmoins, quelle que soit l'efficacité de la stratégie de normalisation, un meilleur échantillonnage de l'ensemble de la variabilité exigera l'application de cette stratégie à une plus grande base de données HARDI. Ce sera d'un intérêt particulier pour l'étude et la représentation de la variabilité anatomique des subdivisions des voies et des faisceaux d'association courts.

En outre, une plus grande base de données est en train d'être utilisée pour la validation des résultats de la segmentation automatique des faisceaux.

Nous croyons que les principales contributions de la thèse peuvent maintenant être appliquées pour répondre à des questions plus neuroscientifiques. En fait, nos algorithmes commencent à être utilisés par les chercheurs en neurosciences, en partie parce qu'ils sont disponibles sur demande à travers le logiciel BrainVISA/Connectomist2.0<sup>1</sup>. La méthode de regroupement intra-sujet est en train d'être utilisée pour l'analyse des jeux de données de tractographie chez des enfants avec agénésie du corps calleux. De plus, des analyses des index de diffusion seront effectuées sur une grande base de données de patients atteints du syndrome bipolaire ainsi que des contrôles, en utilisant notre méthode de segmentation automatique DWM faisceaux.

Nous pensons que plusieurs applications des méthodes développées surgiront dans le futur. Les faisceaux qui résultent du regroupement intra-sujet peuvent être combinés avec des données fonctionnelles pour effectuer des études neuroscientifiques ou avec d'autres segmentations anatomiques du cerveau, comme des tumeurs, pour analyser la structure de la substance chez des cerveaux pathologiques. En outre, des méthodes pour la parcellisation de la surface corticale pourraient être développées à partir des résultats obtenus avec notre stratégie de regroupement des fibres de deux niveaux. Enfin, nous croyons que la méthode de segmentation automatique des faisceaux appartenants à la substance blanche profonde et superficielle, est un outil puissant pour le déroulement des études des données de diffusion chez des populations des sujets.

Finalement, d'un point de vue informatique, les algorithmes développés peuvent être encore optimisés par l'utilisation de la parallélisation informatique et de la codification des parties critiques du code d'une façon plus efficace, en utilisant une plate-forme comme le processeur graphique (GPU, de l'anglais Graphics Processing Unit). L'amélioration et le développement d'algorithmes capables de traiter des jeux de données de tractographie énormes sera un domaine de recherche ouvert tant que la taille des ensembles de données de tractographie continue à augmenter. C'est déjà le cas pour les jeux de données de tractographie probabiliste, qui présentent des tailles très importantes, aux alentours de 30

---

<sup>1</sup><http://brainvisa.info>

millions de fibres pour les résolutions actuelles.

## Part I

# Introduction





# Introduction

## Context

---

Human brain white matter (WM) structure and organisation are not yet completely known. Nerve fibers connect neurons of different brain regions forming more or less complex networks, which are the source of all the brain tasks. The inference of the anatomical brain connectivity mapping is therefore a great challenge, of great interest for understanding brain function and study many diseases.

Diffusion-Weighted Magnetic Resonance Imaging (DW-MRI or dMRI) offers a unique approach to study *in vivo* the structure of brain tissues. It allows the non invasive reconstruction of brain fiber bundle trajectories using tractography. The diffusion local model most used to date is the diffusion tensor (DTI) which has enabled the development of studies in both, the clinical area and the more fundamental research. In this way, white matter long association bundles have been studied in healthy subjects and for several diseases. However the DTI model has some limitations in the representation of fiber bundles complex configurations. In fact, only one population of bundles can be accurately represented by this model. With the emergence of more powerful MRI scanners that allow higher spatial resolution and new techniques of dMRI with high angular resolution (HARDI), tractography data present today a better quality, but, despite this progress, not devoid of artifacts. These tractography data present a high complexity and are very huge, containing over a million fibers for the whole brain.

How to analyse and quantify the structures defined by tractography, and in particular, how to extract the fiber bundles is therefore an unsolved problem. Since the development of tractography, several methods have been proposed to analyse WM tracts and segment them automatically. Until now, the method most frequently used requires multiple regions of interest (ROI). This approach is a guided method, in which fiber tractography is performed from seeds located in predefined ROIs, or throughout the brain, and that preserves only the fibers that pass through other predefined ROIs. Other approaches use atlases of different brain regions to extract known bundles, relying on the quality of registration between the diffusion data and the anatomical atlases.

Other approaches try to automatically cluster and classify all the fibers generated by

a whole brain tractography, using a pairwise fiber distance. These methods have shown to be very powerful as the shape and position of the fibers are considered in the analysis. One of the major limitations of these approaches is the dataset size, which currently makes impossible an efficient processing which considers all the fibers of the dataset. Thus, the proposed approaches use fiber samples, or a priori information for reducing the data or subdividing the problem.

In general, the proposed methods aim to recover the known bundles of deep white matter, which are commonly large and present a quite similar shape across subjects. But there is a big amount of bundles, in special, short association bundles of superficial white matter, that have been rarely studied, and that present a huge variability between subjects. Furthermore, deeper analyses could be performed over known bundles in order to obtain a better description, consisting in a decomposition into fascicles. Regarding inter-subject analysis, several alignment methods have been proposed, based on the whole T2 or T1 images, ROIs or on several bundle shape descriptors, but the problem of bundles comparison across subjects is still open.

In this thesis, we develop a two-level fiber clustering strategy able to analyse huge tractography datasets from a population of subjects. From this analysis, the most reproducible bundles of deep and superficial white matter can be identified. A HARDI multi-subject bundle atlas is thus inferred and also used to automatically segment bundles of new massive tractography datasets.

## Organization and Contributions of this Thesis ---

This thesis is organized in three parts. The Background part describes the white matter cerebral anatomy, the principles of DW-MRI and the existing approaches for white matter bundles clustering and segmentation. Then, the Methods part describes the methodological contributions of the thesis. Some examples of application are also described in this part. The Applications part illustrate an example of application of the developed methods.

The thesis covers two main aspects of tractography datasets analysis. First, an intra-subject clustering is proposed to deal with huge tractography datasets, without the use of strong anatomical a priori information. Then, this intra-subject clustering is used as input for an inter-subject clustering, allowing the study of white matter bundles across a population of subjects. A HARDI multi-subject model of human brain WM bundles is thus inferred. This atlas includes most of the known deep WM bundles and also a big amount of short association WM bundles. This atlas is finally used for the automatic segmentation of new massive tractography datasets.

We now give an overview of the organization and of the contributions of each chapter in turn.

## Part I: Background

**Chapter 2** presents a background on the basic aspects of brain anatomy. It details the main nervous tissues and the anatomical divisions of the brain. Since the principal interest of this thesis is anatomical connectivity, it is focused on brain white matter composition and structure, which determine how the brain is connected.

Our review starts with the macroscopic anatomical brain divisions in function of their composing tissues and main functionalities. Subsequently, the different human brain tissues and nervous tissue types are concisely described. The microscopic neuron, one of the most important nerve cells, takes a fundamental place in the description of neural tissues as gray and white matter. Finally, the organization of the human white matter is studied. Known fiber bundles are covered as well as the main parts of the brain that are connected by each fiber tract. Some fiber bundles, implicated in main high brain functions are particularly highlighted, as the case of the arcuate fasciculus and its relation with language.

**Chapter 3** This chapter presents a background on the basic principles of diffusion MRI, a technique allowing the study *in vivo* of white matter structure and its connections.

First, we introduce the concepts underlying diffusion-weighted (DW) imaging, where the diffusion of water molecules in living tissue takes a fundamental place. Next, we review the basics of Nuclear Magnetic Resonance (NMR), followed by a brief description of DW-MRI. The discussion continues with the approaches designed to locally model the diffusion signal. We start with the diffusion tensor imaging (DTI), as the most intuitive and simple mean to infer microstructure of biological tissues. This Gaussian model of diffusion allows the measurement of quantitative parameters extensively used in clinical studies. Then, more complex reconstruction algorithms, using high angular resolution diffusion data are explored. These methods overcome some limitations of the DTI model, as the impossibility to reconstruct multiple fiber distributions of water diffusion. The streamline tractography is finally introduced, a technique aiming to reconstruct three-dimensional trajectories of white matter fibers, which constitute the input dataset of this thesis.

**Chapter 4** In order to situate our work, this chapter presents a review of the main approaches used for tractographic pathways clustering and identification.

The review starts with a brief description of methods for WM segmentation based on DW-MRI images. Next, techniques based on regions of interest (ROIs) for extracting known fiber tracts are mentioned. Then, the main approaches proposed for white matter clustering and segmentation, are presented. White matter fiber clustering methods are particularly addressed. The main clustering algorithms, as well as the different fiber similarity measures described in the literature are detailed. The discussion continues with a review of the main proposed fiber clustering methods, since its beginnings until today. These methods are also summarized in a table describing, among others, the main input, outputs, clustering method, distance measure, priors, and the successfully identified bun-

dles. Finally, a brief review of the approaches proposed for the quantitative analysis of DW measures across bundles is included. The different methods for determining correspondence across bundles and for comparing WM diffusion indexes are specially addressed.

## Part II: Methods

The Methods part describes the original and most important contributions made in this thesis.

**Chapter 5** In order to overcome the tractography dataset size limitation of the standard tract-clustering strategy, we propose an intra-subject clustering method based on a voxel-based clustering approach.

First, an introduction describes the main technical aspects considered in the method design and development. Next, an overview of the method, composed by a sequence of algorithms performing a robust hierarchical clustering of a fiber tractography dataset, is presented. Then, each step of the method is detailed. The robustness and the cost of the scalability of the method are checked using simulated tract datasets. Also a comparison is performed with a brute force clustering method. The complete method is then applied to the tracts computed for twelve subjects of a HARDI adult database and for two children of a database with lower angular resolution acquisitions and a tensor model. Finally, the method is applied to the data issued from an actual phantom containing a plethora of realistic crossing, kissing, splitting and bending fiber configurations. This last experiment illustrates the interest of our compression method for comparing different diffusion local models and tractography algorithms.

Additionally, we describe the creation of a robust propagation mask stemming from T1 anatomy, which, in conjunction with tractography techniques, improves the accuracy of the anatomical connectivity of the brain by reducing false positives and increasing the detection of the subcortical connectivity.

**Chapter 6** In this chapter we present a method for the clustering of a set of tracts stemming from several subjects, after spatial normalization, with the aim to create a model of the main human brain bundles. The objective is to construct a HARDI bundle atlas, including the known bundles of deep WM, but, most interestingly, new discovered short association bundles of superficial WM.

First, the method consisting in a two-level strategy chaining intra- and inter-subject fiber clustering is described. To deal with very huge tractography datasets and reduce the complexity of the data, the method uses the intra-subject clustering presented in the previous chapter. The second level is specially detailed. It gathers the bundles obtained in the first level for a population of subjects and performs a clustering after a spatial normalization, producing as output a model composed by a list of generic fiber bundles that can be detected in most of the population. In order to study the behavior of the inter-subject clustering over a population of subjects aligned with affine registration, a validation with

simulated dataset is presented. A novel HARDI multi-subject bundle atlas, representing the variability of the bundle shape and position across subjects is finally inferred. The atlas includes 36 deep WM bundles, some of these representing a few subdivisions of known WM tracts and 94 short association bundles of superficial WM.

### **Part III: Application**

The Application part is short but illustrates the added value and the potential of the developed methods.

**Chapter 7** This chapter presents a method for the automatic segmentation of known deep white matter and some short association fiber bundles from massive dMRI tractography datasets. The method is based on the multi-subject bundle atlas derived from a two-level intra-subject and inter-subject clustering strategy, described in chapter 6.

New tractography datasets are first compressed with the intra-subject clustering. The resulting bundles are then labeled using pairwise distances to the centroids representing the multi-subject atlas bundles. The segmentation of deep white matter bundles is applied to height adults and four children while the segmentation of short association bundles is applied to ten adults. In the case of known deep WM bundles, results are compared with a ROI-based approach.

### **Appendix A**

This appendix describes the main WM atlases proposed in the literature, in particular those created or used by fiber clustering methods.

### **Appendix B**

The appendix enumerates the publications from the author arising from this thesis. We have published in a major international journal and in important conferences.

### **Software contributions**

Finally, we would like to point out that all the algorithms described in the Methods part are now available upon request as a toolbox of the BrainVISA/Connectomist2.0<sup>1</sup> software platform for analysis and visualization of tractography brain data. Part of the integration work, and all the optimization and graphical interface development has been done by Delphine Duclap (Research Engineer, Neurospin, CEA), in close collaboration with Cyril Poupon (Researcher, Neurospin, CEA) and all the BrainVISA software development team.

---

<sup>1</sup><http://brainvisa.info>



# Part II

## Background





# Nervous Tissue and Human Brain White Matter

## Contents

---

<b>2.1</b>	<b>Human Brain General Anatomy</b>	<b>12</b>
<b>2.2</b>	<b>The Nervous Tissue</b>	<b>17</b>
<b>2.3</b>	<b>White Matter Organization</b>	<b>21</b>
2.3.1	Association Pathways	21
2.3.2	Commissural Pathways	25
2.3.3	Projection Pathways	26
<b>2.4</b>	<b>Conclusion</b>	<b>28</b>

---

## Overview

---

This chapter presents a background on the basic aspects of brain anatomy. It details the main nervous tissues and the anatomical divisions of the brain. Since the principal interest of this thesis is anatomical connectivity, it is focused on brain white matter composition and structure, which determine how the brain is connected.

Our review starts with the macroscopic anatomical brain divisions in function of their composing tissues and main functionalities. Subsequently, the different human brain tissues and nervous tissue types are concisely described. The microscopic neuron, one of the most important nerve cells, takes a fundamental place in the description of neural tissues as gray and white matter. Finally, the organization of the human white matter is studied. Known fiber bundles are covered as well as the main parts of the brain that are connected by each fiber tract. Some fiber bundles, implicated in main high brain functions are particularly highlighted, as the case of the arcuate fasciculus and its relation with language. This introductory chapter is inspired from atlases, review articles and thesis chapters from [Gray (1918); Kandel and Schwartz (1985); Woolsey et al. (2008); Perrin (2006); O'Donnell (2006); Descoteaux (2008); Catani and Thiebaut de Schotten (2008); Johansen-Berg and Behrens (2009)] which are excellent sources for a general understanding of the nervous tissue, brain anatomy and white matter bundles.

**Keywords:** nervous tissue, gray matter, white matter, deep nuclei, fiber tracts, fiber bundles, projection fibers, association fibers, commissural fibers, U-fibers

### Organization of this chapter:

The chapter is organized as follows. We first give a brief overview of the human brain structure in Section 2.1. Then, the nervous tissue is described in Section 2.2. The white matter organization, including a review of deep and superficial white matter fiber tracts is finally presented in Section 2.3.

## 2.1 Human Brain General Anatomy

---

The human brain is one of the most important and complex organs in the human body. For more than one hundred years, investigating its organization and function has been of fundamental interest in neurology and neurosciences. We know very little of the complex functioning of the brain but we know quite a lot about its anatomy [Gray (1918)].

The brain controls the central nervous system (CNS), the peripheral nervous system (PNS) and regulates all human activity. Figure 2.1 shows the main divisions of the CNS. Broadly, the central nervous system is made up of the spinal cord and the brain.

At a larger scale, the human brain is made of different elements such as blood, cerebrospinal fluid (CSF), white matter (WM) and gray matter (GM). Because of the appearance of fresh brain tissue, areas rich in neurons bodies, synapses and glia are called *gray matter*, and areas containing mainly myelinated axons and glia are called *white matter*. These element classes produce also a different signal contrast under anatomical

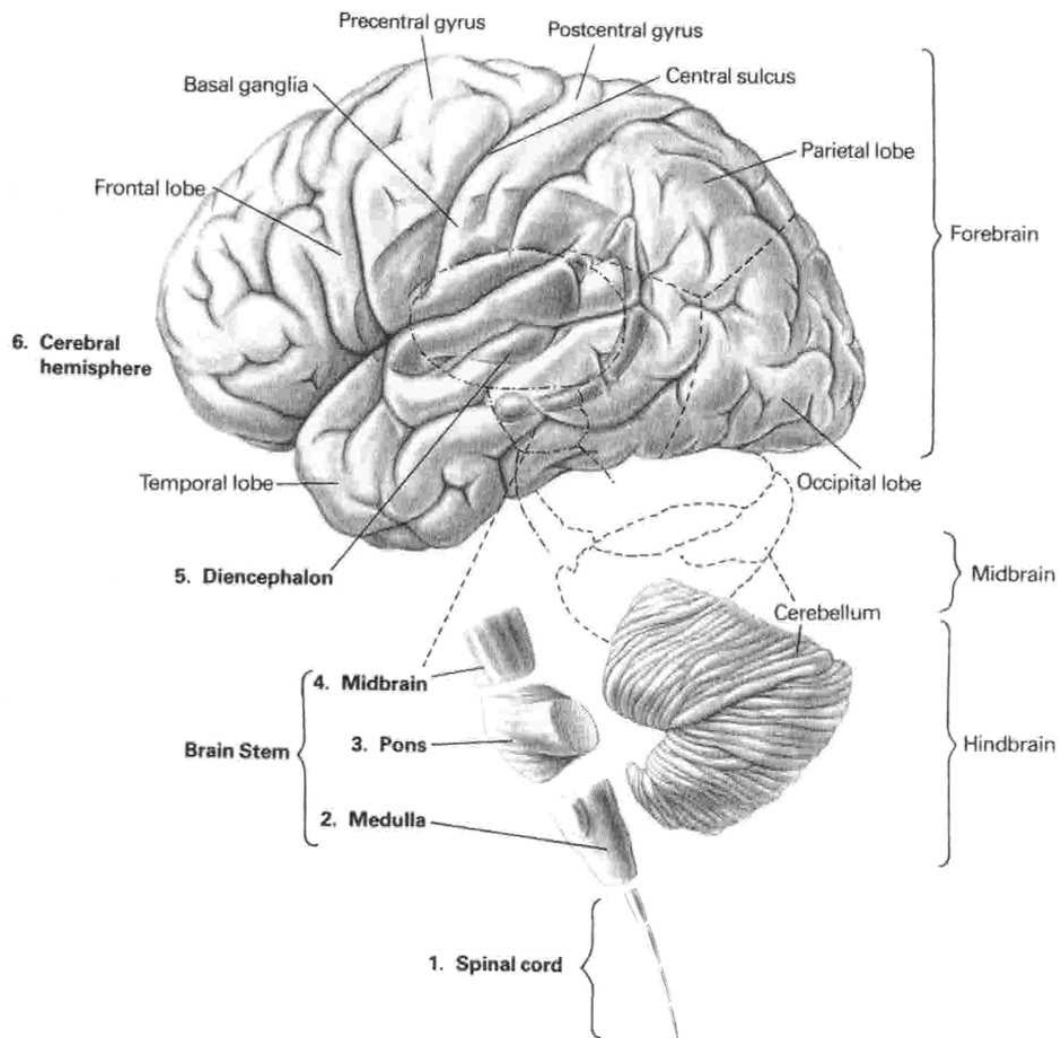


Figure 2.1: The six major divisions of the central nervous system. (1) the spinal cord; (2) medulla oblongata, (3) pons, and (4) midbrain [collectively called the brain stem]; (5) diencephalon; and (6) cerebral hemispheres. The brain is also commonly subdivided into three broader regions: the hind-brain (medulla, pons, and cerebellum), the midbrain, and the forebrain (diencephalon and cerebral hemispheres). [Adapted from [Kandel and Schwartz \(1985\)](#)].

Magnetic Resonance Imaging (MRI). Examples of brain coronal slices, for an anatomical MRI and an histological sample are illustrated in Figure 2.2. White matter appears in white color inside the brain, while the cortex of gray matter is the gray covering layer of 2–4 mm.

The brain can be divided into three main parts (cf. Figure 2.1):

- **telencephalon**, composed by the two *cerebral hemispheres* (right and left) (6)
- **diencephalon** (5), composed by a group of structures located deep within the *cerebrum*
- **brain stem**, composed by the *medulla oblongata* (2), the *pons* (3) and the *midbrain* (4)

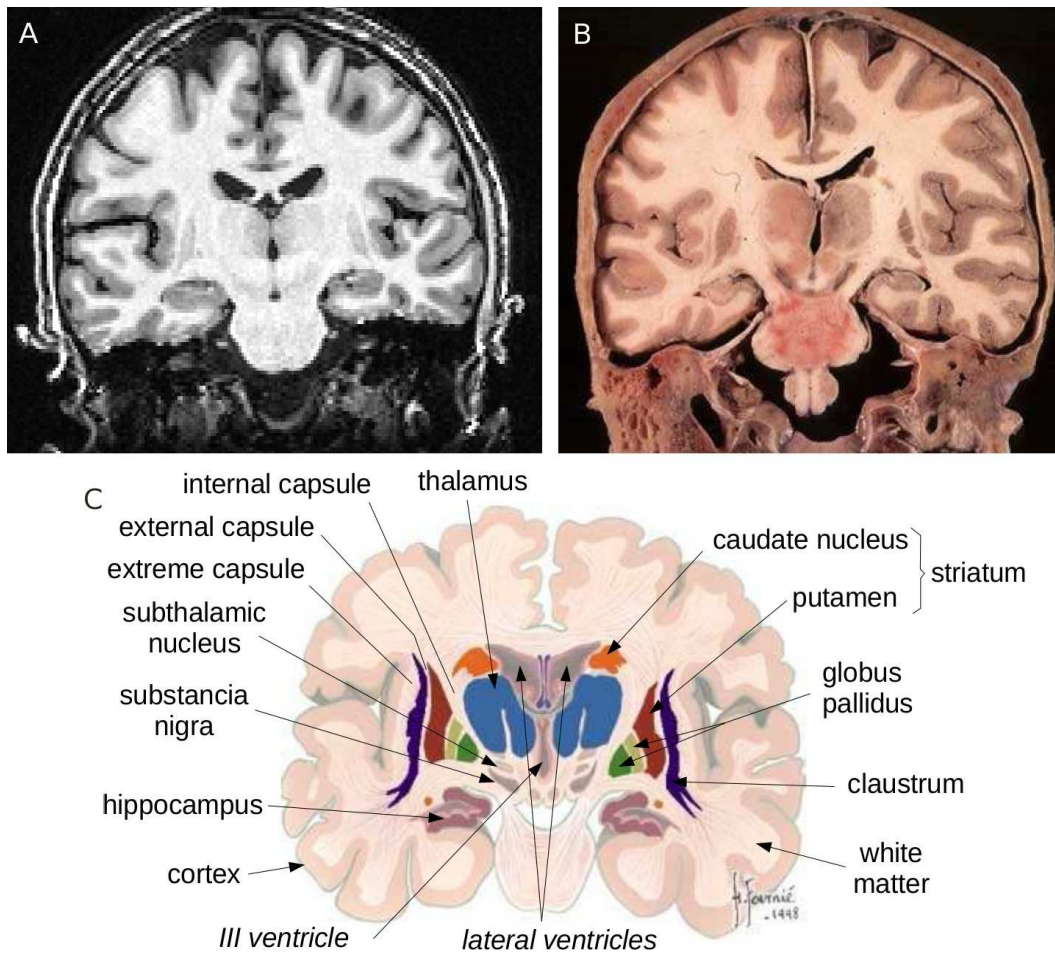


Figure 2.2: Coronal slices of human brain. A coronal slice of an anatomical MRI is presented in **A**, while **B** contains an histological slice. White matter appears in white color inside the brain, while the cortex of gray matter is the grey covering sheet. **C** illustrates the main structures present in a human brain coronal slice. Gray matter, white matter and several basal ganglia are highlighted. [Adapted from [Hasboun \(2007\)](#)].

The **hindbrain** is the structure that connects the *spinal cord* to the brain. It includes the *cerebellum*, the pons and the medulla oblongata. The structure called the **cerebrum** is composed by the diencephalon and the telencephalon.

**The Cerebral Hemispheres** contain the *cerebral cortex*, a sheet of gray matter that is outermost to the cerebrum. The cerebral cortex is the most important structure of the GM and plays a major role in cognitive functions. Cerebral hemispheres are concerned primarily with sensory and motor processes of the *contralateral* side of the body. Each hemisphere of the cerebral cortex is divided into five **lobes**: frontal lobe, parietal lobe, occipital lobe, temporal lobe and insular lobe (cf. Figure 2.3). Each one has been associated with different functions ranging from reasoning to auditory perception (see Table 2.1). Lobes from both hemispheres, although quite similar, are not completely symmetrical in

structure, nor are they equivalent in function. The lobes present several *sulci* and *gyri*. The sulci (or fissures) are the grooves and the gyri are the convolutions on the brain's surface. The more prominent gyri and sulci are very similar from one individual to another and therefore have specific names.

Lobe Name	Localization in the brain	Main Functions
Frontal	front	associated with reasoning, motor skills (primary motor, premotor and supplementary motor areas), higher level cognition (prefrontal cortex), and expressive language (Broca's area)
Parietal	middle section	associated with processing tactile sensory information (primary somatosensory cortex), language comprehension, spatial orientation and perception
Temporal	bottom section	primary auditory cortex, which is important for interpreting sounds and language (Wernicke's area), visual processing, formation of memories (hippocampus) and learning
Occipital	back section	primary visual cortex, visual association cortex
Insula	beneath parts of the parietal and temporal lobes	associated with emotion, memory and the regulation of the body's homeostasis. Influences other functions like perception, motor control, self-awareness, cognitive functioning, and interpersonal experience.

Table 2.1: Human brain lobes localization and function [Adapted from [O'Donnell \(2006\)](#)].

**The Brain Stem** is comprised of the midbrain, the pons and the medulla oblongata. The **medulla** is located directly above the spinal cord and controls many vital autonomic functions such as heart rate, breathing and blood pressure. The **pons** connects the medulla to the cerebellum and helps coordinating movement on each side of the body. Nerve impulses coming from the eyes, ears, and touch receptors are sent to the cerebellum. The pons also participates in the reflexes that regulate breathing. The brain stem contains several collections of neuron bodies (gray matter), called the *cranial nerve nuclei*. Some of these nuclei receive sensory information from the skin and muscles of the head. Other nuclei control motor output to the muscles of the face, neck and eyes. The **reticular formation** is a neural network located in the brain stem that helps controlling functions such as sleep and attention. It collects inputs from higher brain centers and passes it to motor neurons. The **midbrain** is the smallest region of the brain that acts as a sort of relay station for auditory and visual information. The midbrain controls many important functions such as the visual and auditory systems as well as eye movement. Portions of the midbrain called the *red nucleus* and the *substantia nigra* are involved in the control of body movement. The degeneration of neurons in the substantia nigra is typically associated with Parkinson's disease.



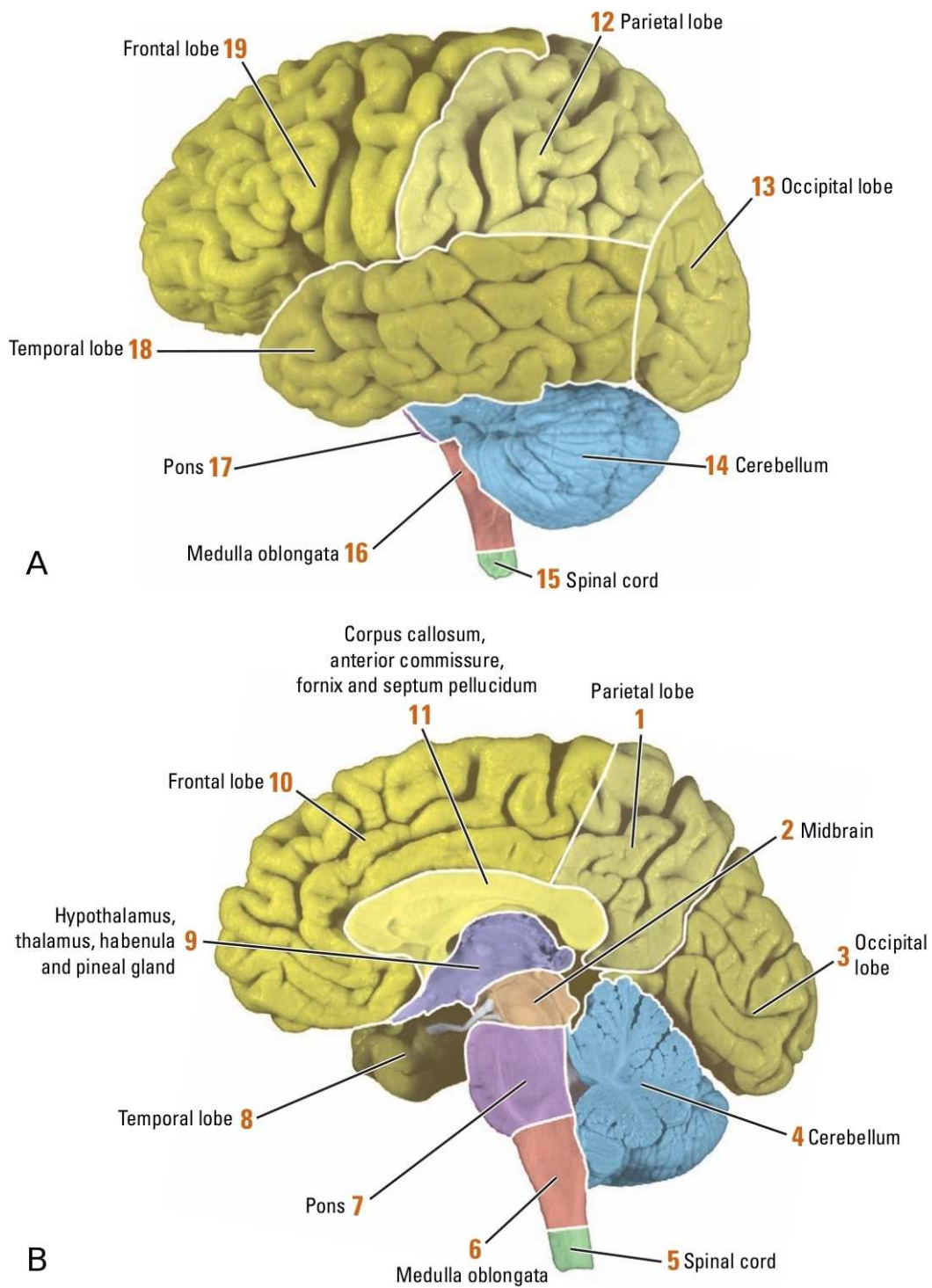


Figure 2.3: The main divisions of the brain and lobes of the cerebral cortex are colored and labeled in middle sagittal (A) and lateral (B) views of the brain. [Taken from Woolsey et al. (2008)].

**The Cerebellum** lies on top of the pons, behind the brain stem. It consists of two deeply-convoluted hemispheres. The cerebellum receives information from the balance system of the inner ear, sensory nerves, and the auditory and visual systems. Its most clearly-understood function is the coordination of motor movements, but it is also involved in basic facets of memory and learning.

**The Diencephalon** is a group of structures located deep within the cerebrum, including the *thalamus*, the *subthalamus* and the *hypothalamus*. Located above the brainstem, the **thalamus** processes and relays movement and sensory information. It is essentially a relay station, taking in sensory information and then passing it on to the cerebral cortex. The cerebral cortex also sends information to the thalamus, which then sends this information to other systems. The **hypothalamus** is a group of nuclei that lie along the base of the brain. The hypothalamus connects with many other regions of the brain and is responsible for controlling hunger, thirst, emotions, body temperature, and circadian rhythms. The hypothalamus also controls the pituitary gland by secreting hormones, which gives the hypothalamus a great deal of control over many body functions.

**The Basal ganglia** are gray matter nuclei lying deeply within each cerebral hemisphere. The main components of the basal ganglia are the *caudate nucleus*, *putamen*, *globus pallidus*, *substantia nigra*, and *subthalamic nucleus*. The caudate nucleus and the putamen form the *striatum* while the putamen and the globus pallidus comprise the structure called the *lenticular nucleus*. All these structures form a system consisting of multiple segregated pathways, involving also the entire frontal cortex, the thalamus and the cerebellum. A parallel processing is then performed to permit the planning, execution, and coordination of eye and limb movements (see Figure 2.2 C).

The **ventricular system** is a set of structures containing cerebrospinal fluid in the brain. It is continuous with the central canal of the spinal cord. The system comprises four ventricles: right and left lateral ventricles, third ventricle and fourth ventricle.

The **limbic system** is a set of brain structures including the *amygdala*, the *hippocampus*, regions of the *limbic cortex* and the anterior *thalamic nuclei*. These structures form connections between the limbic system and the hypothalamus, thalamus, and cerebral cortex. It supports a variety of functions including emotion, behavior, long term memory, and olfaction. In particular, the **hippocampus** is important in memory and learning and the amygdala has a primary role in the emotional reactions.

## 2.2 The Nervous Tissue ---

The cells of the nervous system are of two principal types: *nerve cells* or *neurons*, which are directly responsible for conveying and processing information; and *glial cells* or *neuroglia*.

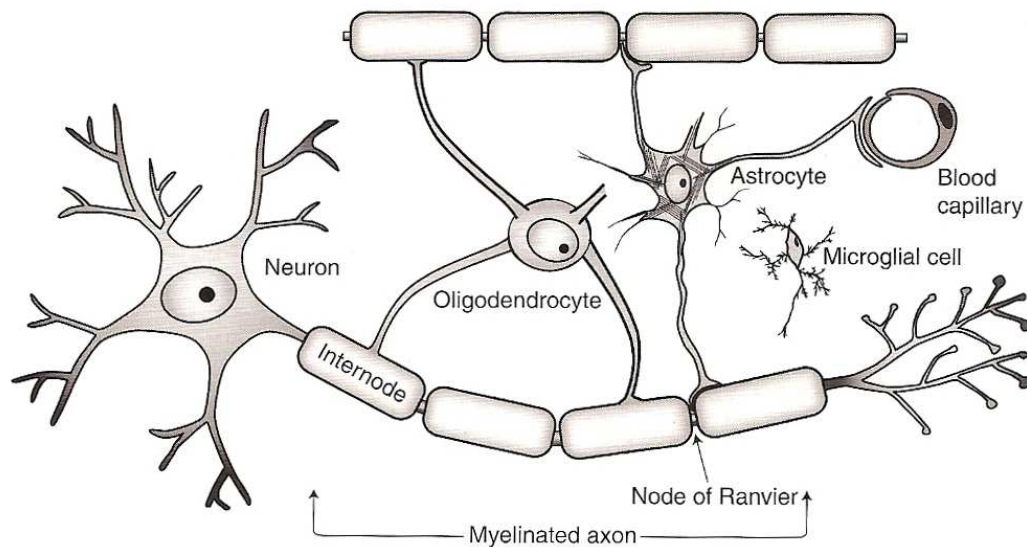


Figure 2.4: Schematic representation of the major cellular elements of neural tissue. A neural cell body in the gray matter extends several short dendritic processes and a single, long axonal process. The axon is in the white matter, surrounded by an insulating myelin sheath formed by oligodendrocytes, a glial cell. The WM also contains two other kinds of glial cells: astrocytes and microglia. [from [Johansen-Berg and Behrens \(2009\)](#)].

**Glial cells** support and protect the neurons, maintain their homeostasis and make them more efficient and effective. The three types of CNS glial cells are *astrocytes*, some star-shaped cells that help maintaining the homeostasis, *oligodendrocytes*, that form the myelin sheath surrounding the axons, and the *microglia*, that are macrophages constituting the main active immune defense of the CNS (cf. Figure 2.4).

**Nerve cells** are the fundamental elements of the central nervous system. The central nervous system is made up of about 100 billion neurons. Neurons are much like other cells of the body in their general organization and their biochemical systems. However they also possess unique features which are crucial to the functioning of the central nervous system. In essence, a given neuron may both receive and send out signals to neighboring neurons in the form of electrical pulses, conveying information or instructions from one region of the body to another, as a highly intricate network. How is this information carried through the white matter and how are the different parts of the brain connected remains unknown. About 98% of neural tissue is concentrated in the brain and spinal cord, the control centers for the nervous system. A neuron is built up of three parts: the *cell body* or *soma*, and two kind of processes, the *dendrites* and the *axon*, as shown in Figure 2.4.

The **soma** contains the nucleus of the cell and carries the biochemical transformations necessary to synthesize enzymes and other molecules necessary to the life of the neuron. It is roughly spherical or pyramidal in shape - the precise shape depending on position and function in the brain. It is typically several microns in diameter. Gray matter is composed



of unmyelinated neurons. It's gray brown color comes from the neuronal cell bodies and the capillary blood vessels. **Dendrites**, shorter processes (1 mm or less) that are tapered and branched much like limbs on a tree, receive and integrate incoming information. Most neurons have several dendrites. **Axons** (usually only one per neuron) have a relatively uniform diameter, can be highly branched, and extend for considerable distances, up to almost 2 m in tall people. Axons distribute signals to other cells (neurons, muscle cells, secretory cells, etc.) without attenuation. The principal mode of communication between neurons and from neurons to other tissues, such as muscle, is through specialized contacts called *synapses*. Typically a given neuron is connected to about ten thousand of other neurons.

The **synapses** are specific point of contact between the axon of one neuron and a dendrite. At a microscopic scale, neurons transmit signals as electrical impulses which affect their cell membrane potentials. The electrical impulse usually affects the cell membrane potential of one of the neuron's dendrites and then eventually travels along the length of this axon to transmit to other neurons. Information is transmitted across the gap by chemical secretions called *neurotransmitters*. It causes activation in the post-synaptic cell. The axon is surrounded by the *myelin* sheath, which forms a whitish, non-cellular, fatty layer around the axon. Myelin is a membranous, lipid and protein-rich structure generated by the tight wrapping of oligodendrocyte processes around the axons. A single oligodendrocyte can myelinate many axons. Myelination is a gradual developmental process that can take up to 10 or 12 years to reach completion, but the bulk of myelination occurs during the fetal and infancy stages. The myelin sheath is not continuous along the length of the axon. It is interrupted at regular distances by small unmyelinated regions called *nodes of Ranvier*. The myelinated segment between two nodes of Ranvier is termed internode. Each internode is formed by a single oligodendrocyte process (cf. Figure 2.4). At nodes of Ranvier, the axonal membrane is uninsulated and therefore capable of generating electrical activity, allowing rapid and efficient saltatory propagation of action potentials, from the soma to the axon terminus. Some axons do not attain a myelin sheath. Transverse slides of axons in the white matter are shown in Figure 2.5.

The axonal cytoskeleton consists of actin filament, microtubules, microtubule associated proteins, and neurofilaments. *Neurofilaments* provide structure and are the main determinants of axonal size (diameter). *Microtubules*, provide the tracks upon which proteins transport organelles along the axon in both directions. Both, neurofilaments and microtubules, lie parallel to the direction of the axon and appear as tube in cross-section (cf. Figure 2.5). White matter axons, also called *nerve fibers*, are often tightly packed together and highly organized in fiber bundles. White matter bundles are often called WM fiber tracts. In this thesis, we will be most interested in recovering and analyzing information about these fiber tracts from diffusion Magnetic Resonance Imaging (dMRI) images. As we will see in chapter 3, dMRI allows the study of WM integrity and the estimation of WM fiber tracts preferred orientation.

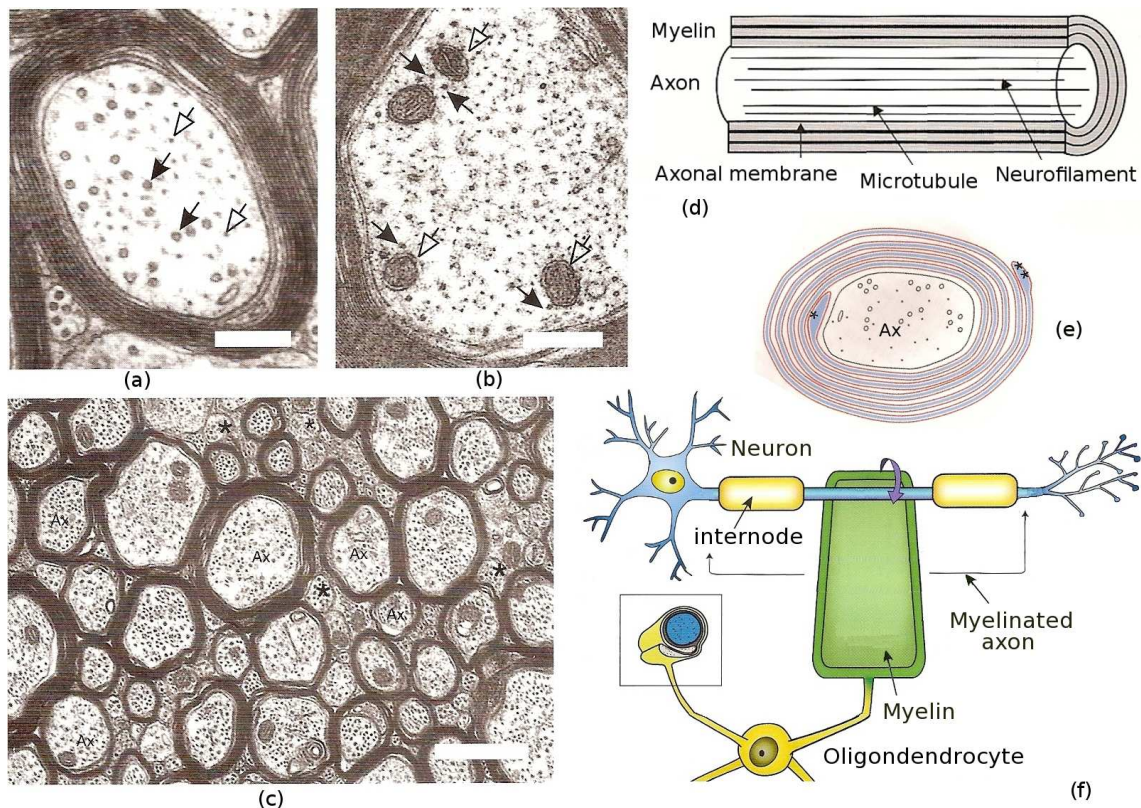


Figure 2.5: White matter axons main structure. (a, b and c) Show three electron micrographs of CNS axons. (a) Cross-section through a single myelinated axon. Neurofilaments and microtubules are elongated structures that appear as small tubes. Neurofilaments (open arrows) provide structure and are the main determinants of axonal size (diameter). Microtubules (filled arrows) provide the tracks upon which materials are transported along the axons. (b) Cross-section through a second myelinated axon. Mitochondria (open arrows) are the most frequently encountered axonal organelles. (c) Cross-section through corpus callosal axons. In the CNS, axons over  $0.2 \mu\text{m}$  in diameter are myelinated. Myelin appears as a dark band around the paler axon. Some axons (asterisks) do not attain a myelin sheath. (d) Major structural longitudinal elements of the axons. The intraaxonal space contains neurofilaments and microtubules parallel to the direction of the axon. (e) Illustration of the arrangement of the myelin sheath and the axon in cross-section. (f) Schematic of an oligodendrocyte and an associated axon. Myelin is the membranous structure generated by the tight wrapping of oligodendrocyte processes around the axons. [Adapted from [Johansen-Berg and Behrens \(2009\)](#)].

## 2.3 White Matter Organization

---

As mentioned above, white matter is composed of myelinated axons, that connect various gray matter areas of the brain to each other, and carry nerve impulses between neurons. The white matter axons can be distributed diffusely or concentrated in bundles, also called fiber tracts. In the cerebral hemispheres we can find two types of myelinated axons: short-distance (10 - 30 mm) fibers below the gray matter that follow its contours, and long distance (30 - 170 mm) fibers that are bundled into fasciculi in the deep white matter. The WM of the cerebral hemispheres surrounds the subcortical gray matter and intervenes between subcortical and cortical gray matter. There are also shorter intracortical (1 - 3 mm) unmyelinated fibers within the gray matter. The total number of long range fibers within a cerebral hemisphere is 2% of the total number of cortico-cortical fibers and is roughly the same number as those that communicate between the two hemispheres in corpus callosum. As a rough rule, the number of fibers of a certain range of lengths is inversely proportional to their length [Schüz and Braitenberg (2002)].

Three main types of neural fiber tracts are found in the WM according to their connections: *commissural tracts*, which interconnect GM areas of both cerebral hemispheres, *association tracts*, that interconnect different cortical regions of the same cerebral hemisphere, and *projection tracts*, that link the cortex with subcortical centers and with the spinal cord. The most important fiber tracts of these three pathways will be described in the following subsections based essentially on the following review articles: Catani and Thiebaut de Schotten (2008); Aralasmak et al. (2006); Jellison et al. (2004). Refer to Figure 2.6 for an illustration of the anatomic relationships of several WM fiber tracts. See also Figure 2.7 for tractography-based reconstructions of the main white matter fiber tracts described in the literature.

### 2.3.1 Association Pathways

Association pathways are tracts linking one area of the cerebral cortex to another within the same hemisphere. These tracts are arbitrarily subdivided into short and long association fibers. *Short association fibers*, linking one gyrus to its immediate neighbors, are known as subcortical U-fibers. These are located in the superficial white matter (SWM). *Long association fibers* are located in deeper parts of the WM and link cortex areas of different regions and lobes. White matter structures at the deep white matter regions (DWM) seem to share more common anatomical features across individuals, since there are many prominent axonal bundles that can be identified in all normal subjects at well-defined locations. The well known long association fibers are: the arcuate fasciculus (AF), inferior longitudinal fasciculus (ILF), inferior fronto-occipital fasciculus (IFO), uncinate fasciculus (UF), cingulum (CG) and superior fronto-occipital fasciculus (SFO).

**Arcuate fasciculus:** This tract, also called *superior longitudinal fasciculus*, is a lateral associative bundle composed of long and short fibers connecting the perisylvian cortex



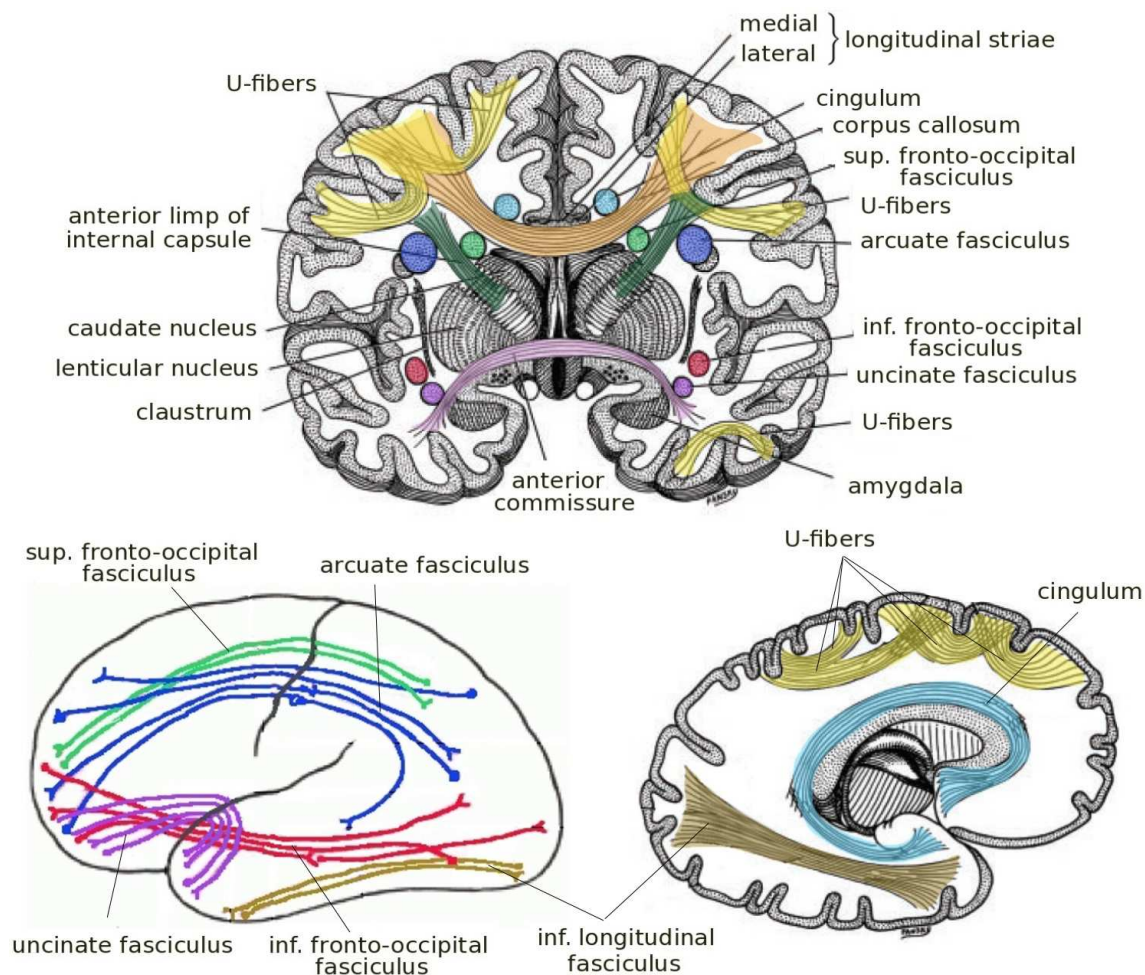


Figure 2.6: Illustration of the anatomic relationships of several WM fiber tracts. [Adapted from [Jellison et al. \(2004\)](#) and [Poupon \(1999a\)](#)]

(around the fissure of Sylvius or lateral sulcus) of the frontal, parietal, and temporal lobes. The arcuate fasciculus of the left hemisphere is commonly involved in language. The arcuate fasciculus of the right hemisphere is usually involved in visuospatial processing and some aspects of language such as prosody and semantic.

The **language function** is localized in the left hemisphere in about 90% of right-handed persons and 70% of left-handed persons. The arcuate fasciculus lies in *Broca's area* at the frontal end, which is usually associated with the production of language, or language outputs. At the other end, in the superior posterior temporal lobe, lies *Wernicke's area*, which is associated with the processing of words that we hear being spoken, or language inputs. Figure 2.8 A illustrates the arcuate fasciculus, composed by a **long direct segment** connecting this two areas. The fronto-parietal portion of the arcuate fasciculus encompasses a group of fibers with antero-posterior direction running lateral to the projection fibers of the corona radiata. At the temporo-parietal junction, the arcuate fibers arch around the lateral (Sylvian) fissure and continue downwards into the stem of the

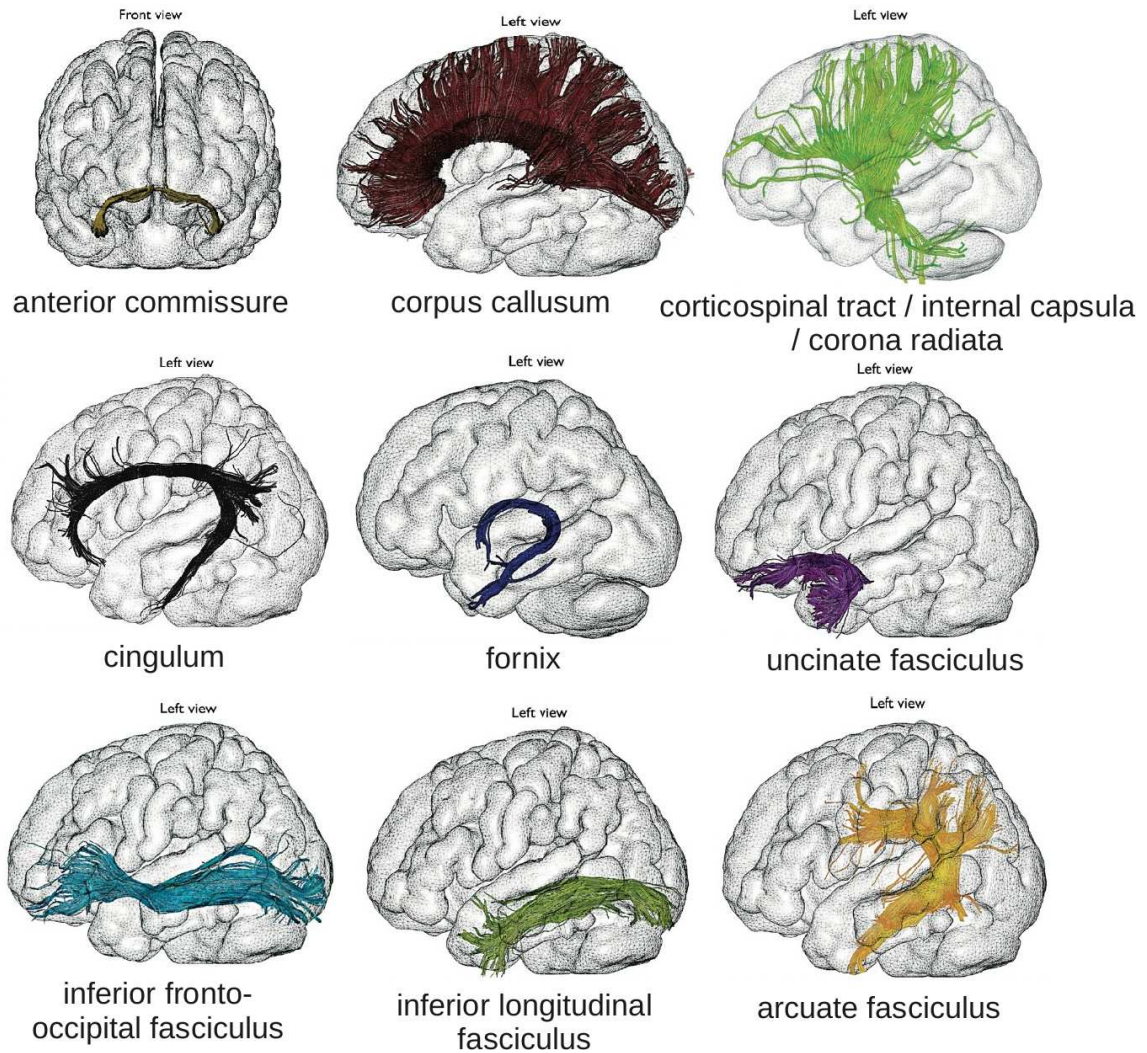


Figure 2.7: Main white matter fiber tracts described in the literature, obtained using deterministic tractography over a diffusion tensor field. **Commissural tracts:** anterior commissure and corpus callosum. **Projection tracts:** Corticospinal tract, internal capsule/corona radiata and fornix. **Long association tracts:** arcuate fasciculus, inferior longitudinal fasciculus, inferior fronto-occipital fasciculus, uncinate fasciculus and cingulum. [Adapted from [Catani and Thiebaut de Schotten \(2008\)](#)]

temporal lobe. The most lateral component of the arcuate fasciculus is composed by latero-lateral fibers approaching the perisylvian cortex. Recent tractography studies applied to the language pathways showed that the anatomy of the arcuate fasciculus contains, in addition, an indirect pathway, consisting of two segments [[Catani et al. \(2005\)](#)]. The **anterior indirect segment** links the Broca's territory with the inferior parietal lobule (Geschwind's territory) and the **posterior indirect segment** links the inferior parietal lobule with Wernicke's territory (cf. Figure 2.8 B). The Broca's area is connected also with the motor cortex, to activate the mouth and tongue for the articulation of the speech. The angular gyrus coordinates the inputs from visual, acoustic, and somatosensory cortices and relays them onward to Wernicke's area.

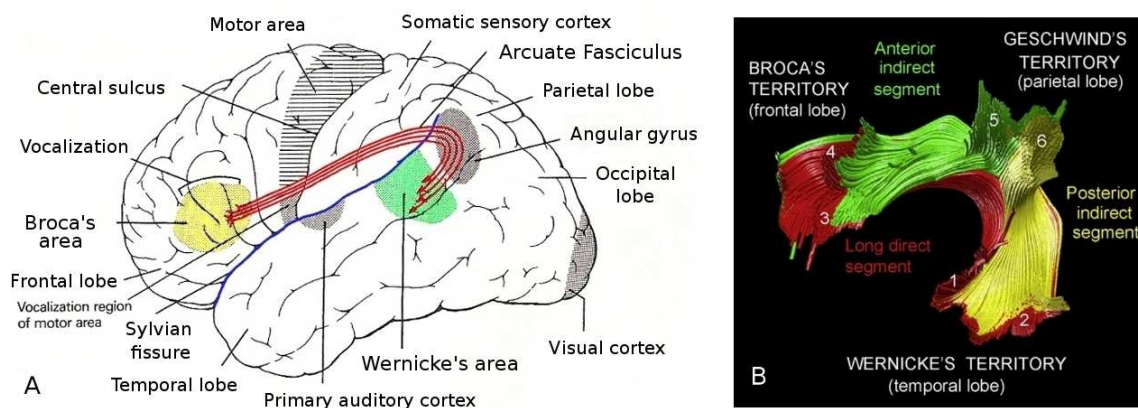


Figure 2.8: A: Main areas involved in language (lateral view of the cerebral cortex). The arcuate fasciculus (in red) connects Wernicke's area (in green) to Broca's area (in yellow). [Adapted from [Kandel and Schwartz \(1985\)](#)]. B: The parallel pathway's model of the arcuate fasciculus derived from tractography. Numbers indicate the cortical projections of the segments: 1, superior temporal lobe; 2, middle temporal lobe; 3, inferior frontal and precentral gyrus; 4, middle frontal and precentral gyrus; 5, supramarginal gyrus; 6, angular gyrus. [Adapted from [Catani and Mesulam \(2008\)](#)]

**Cingulum:** This tract is a medial associative bundle that runs within the cingulated gyrus all around the corpus callosum. It contains fibers of different length, the longest of which runs from the anterior temporal gyrus to the orbitofrontal cortex. The short U-shaped fibers connect the medial frontal, parietal, occipital, and temporal lobes and different portions of the cingulated cortex. The cingulum is part of the limbic system and is involved in attention, memory and emotions.

**Inferior longitudinal fasciculus:** This tract is a ventral associative bundle with long and short fibers connecting the occipital and temporal lobes. The long fibers are medial to the short fibers and connect visual areas to the amygdala and hippocampus. The inferior longitudinal fasciculus is involved in face recognition, visual perception, reading, visual memory and other functions related to language [[Catani and Mesulam \(2008\)](#)].

The fibers of the inferior longitudinal fasciculus lie in the central portion of the occipital and temporal lobes. Fibers present the same main orientation than the inferior fronto-occipital fasciculus.

**Uncinate fasciculus:** This tract is a ventral associative bundle that connects the anterior temporal lobe with the medial and lateral orbitofrontal cortex. This fasciculus is considered to belong to the limbic system but its functions are poorly understood. It is possible that the uncinate fasciculus is involved in emotion processing, memory and language functions [[Catani and Mesulam \(2008\)](#)].

The temporal fibers of the uncinate fasciculus are medial and anterior to the temporal fibers of the inferior longitudinal fasciculus. As the uncinate fasciculus enters the external capsule, its fibers arch forward and mix with the fibers of the inferior fronto-occipital fasciculus.



**Inferior fronto-occipital fasciculus:** This tract is a ventral associative bundle that connects the ventral occipital lobe and the orbitofrontal cortex. In his occipital course the inferior fronto-occipital fasciculus runs parallel to the inferior longitudinal fasciculus. On approaching the anterior temporal lobe, the fibers of the inferior fronto-occipital fasciculus gather together and enter the external capsule dorsally to the fibers of the uncinate fasciculus. The functions of the inferior fronto-occipital fasciculus are poorly understood, although it is possible that it participates to reading [Catani and Mesulam (2008)], attention and visual processing. In humans, it represents the only direct connections between occipital and frontal lobes. The inferior fronto-occipital fasciculus may only exist in the human brain [Catani et al. (2007)].

**Short association fibers:** These fibers, also called *U-fibers*, lie immediately beneath the gray substance of the cortex, and connect together adjacent gyri (see Figure 2.6). These fibers are located in the superficial white matter (SWM), which fills the space between the DWM and the cortex. These fiber tracts have not been well characterized in the literature. Their location, number, trajectories and fonctions are not sufficiently defined. Only four U-fiber tracts have been identified through group analysis using a voxel-based approach relying on linear brain normalization [Oishi et al. (2008)].

### 2.3.2 Commissural Pathways

Commissural pathways are connections between the two cerebral hemispheres. The *corpus callosum* (CC) is the largest link between the cerebral hemispheres, but is assisted by the *anterior commissure* (AC) and the *posterior commissure* (PC). There are also commissures within the brainstem and spinal cord.

**Corpus callosum:** This tract is the largest bundle of the human brain and connects left and right cerebral hemispheres. It is conventionally divided into four sections: the *genu*, connecting medial and lateral frontal regions, the *rostrum*, connecting orbito-frontal regions, the *body*, passing through the corona radiata and connecting precentral frontal regions and parietal lobes, and the *splenium*, connecting the occipital lobes (see Figure 2.9). The fibers of the genu and the rostrum arch

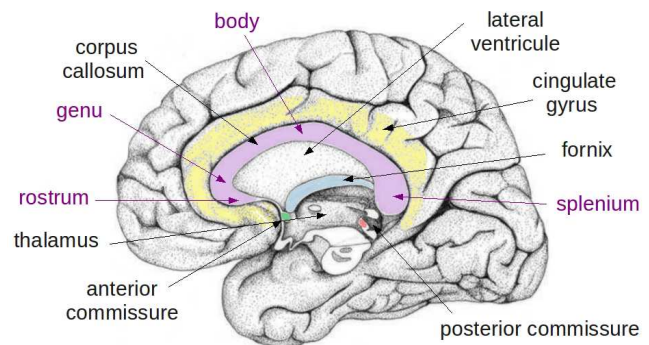


Figure 2.9: Internal face of the right hemisphere. Commissural tracts (Corpus callosum, anterior and posterior commissures) and the fornix are identified. [Adapted from Hasboun (2007)].

anteriorly to form the anterior forceps (or forceps minor), whereas those of the splenium form the posterior forceps (or forceps major). Fibers of the body and splenium constitute the *tapetum* which connects the temporal lobes. The corpus callosum allows transferring



of inputs from one hemisphere to the other and is involved in several motor, perceptual and cognitive functions. The fibers of the body of the corpus callosum are ventral to the cingulum and medial to the lateral ventricles.

**Anterior commissure:** This commissural tract connects the anterior and ventral temporal lobes (including the amygdala) of the two hemispheres. The functions of the anterior commissure are poorly understood. The fibers of the anterior commissure have a latero-lateral direction and are medial to the fibers of the external/extreme capsule, ventral to the most anterior part of the body of fornix, and anterior to the cerebral peduncles.

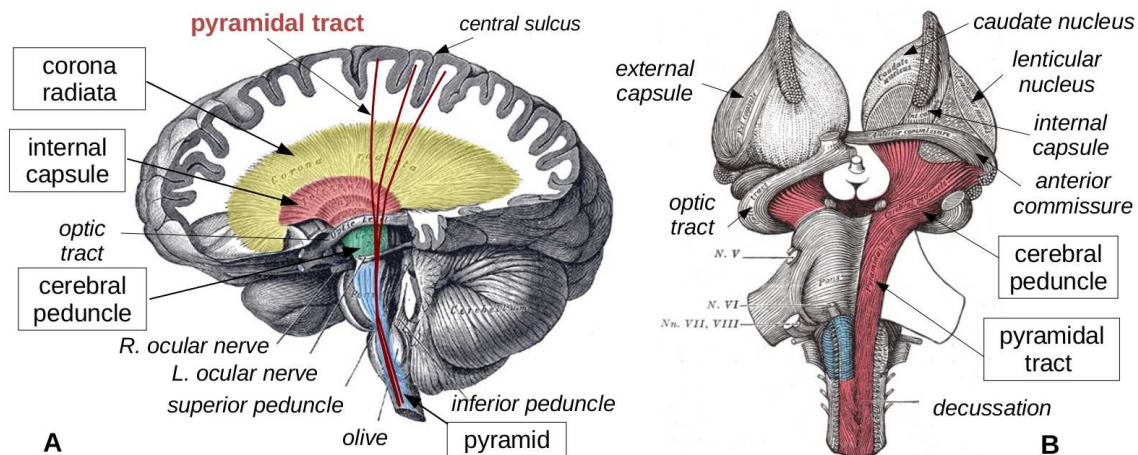


Figure 2.10: Illustration of dissection showing the course of the cerebrospinal fibers. The corticospinal tract (CST), also called pyramidal tract, connects the fronto-parietal cortex to the spinal cord. The CST pass through the Corona Radiata (CR), Internal Capsule, Cerebral Peduncle, and Pyramid (medulla oblongata) regions. The internal capsule and corona radiata contain also ascending fibers from the thalamus to the cerebral cortex. [Adapted from [Gray \(1918\)](#)]

### 2.3.3 Projection Pathways

Projection fibers are fiber tracts linking an area of cerebral cortex to a subcortical structure, such as a basal ganglion or the thalamus. The corticospinal tract (CST) and the thalamic radiations are the most known projections fibers. *Afferent tracts* carry information from different parts of the body to the cerebral cortex. The afferent projections carry optic, acoustic and somatosensory information and run upwards principally from the projection nuclei of the thalamus. *Efferent tracts* carry motor commands from the motor cortex down to the muscles and glands through the lower brain structures and the spinal cord. They reach structures like the basal ganglia, the cerebellum, the brainstem and the spinal cord. In the depths of the hemisphere, pyramidal projections constitute together, with the thalamo-cortical fibers, the *corona radiata* and the *internal capsule*.

**Corticospinal Tract:** This tract, called also *pyramidal tract*, is a massive collection of axons that travel between the cerebral cortex of the brain and the spinal cord. The CST

mostly contains the motor axons from primary sensorimotor cortex and premotor cortex. The CST is illustrated in Figure 2.10 A. It passes through the Corona Radiata, Internal Capsule, Cerebral Peduncle, and Pyramid (medulla oblongata) regions.

**Thalamic radiations:** These tracts are composed by thalamo-cortical and cortico-thalamic fibers forming a more or less continuous fan. Thalamo-cortical fibers refer to afferent fibers, projecting to almost all the regions of the cortex. These fibers come from thalamic nuclei which project to one or a few well-defined cortical areas. Cortico-thalamic projections are efferent fibers that reciprocate the thalamo-cortical ones in almost equal number and in corresponding precise order. The thalamic radiations are usually grouped into four subradiations or peduncles: anterior (frontal), superior (parietal), inferior (temporal), and posterior (occipital), as illustrated in Figure 2.11. The optic radiation, runs from the thalamus to the primary visual cortex while the acoustic tract projects to the temporal lobe.

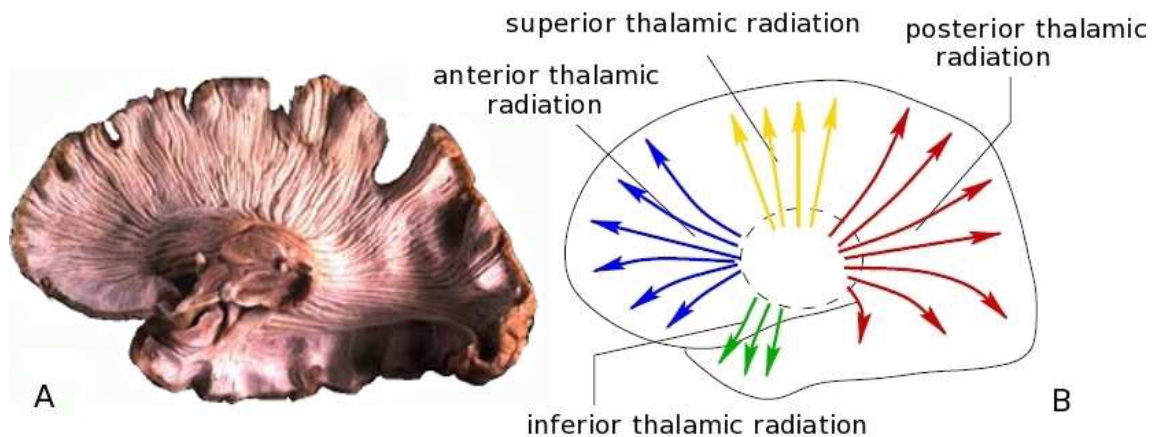


Figure 2.11: **A:** An illustration of dissection showing the course of the thalamic radiations. **B:** Thalamic radiations are usually grouped into four radiations: anterior or frontal (ATR), superior or parietal (STR), inferior or temporal (ITR), and posterior or occipital (PTR). [Adapted from Poupon (1999a)]

**The Internal capsule and corona radiata** contain ascending fibers from the thalamus to the cerebral cortex and descending fibers from the fronto-parietal cortex to sub-cortical nuclei and spinal cord. This complex projection system is the neuroanatomical backbone of perceptual and motor functions and other higher cognitive functions. The internal capsule separates the caudate nucleus and the thalamus from the lenticular nucleus. As the fibers leave the internal capsule dorsally, they fan out into the corona radiata, which is lateral to the lateral ventricles, corpus callosum, and cingulum, and medial to the arcuate fasciculus. As the fibers leave the internal capsule ventrally they continue into the cerebral peduncles, pons and pyramidal tract (cf. Figure 2.10).

**Fornix:** This tract is a projection bundle that connects the medial temporal lobe to the mammillary bodies and hypothalamus. The fornix belongs to the limbic system and is involved in memory functions.

The fibers of the body of fornix have an anterior-posterior direction and run longitudinally along the midsagittal line just below the fibers of the corpus callosum. The anterior fibers of the fornix bend downwards and cross the anterior commissure after splitting into an anterior and a posterior column for each side. The posterior fibers of the body of fornix split into a left and right branch, also known as the fimbriae of fornix. The fimbriae arch around the thalamus and continue along the medial occipito-temporal lobe to terminate in the hippocampus.

**Cerebellar tracts:** The cerebellum receives inputs from the contralateral cerebral hemisphere through the cortico-ponto-cerebellar tract via the *middle cerebellar peduncle*. It also receives peripheral inputs from the spino-cerebellar tract through the *inferior cerebellar peduncle*. The major cerebellar output is represented by the *superior cerebellar peduncle*, a flame-shaped tract posterior to the mesencephalus. The cerebellum is involved in motor learning, cognition, emotions and behavior.

## 2.4 Conclusion

---

In this brief background chapter we introduced the human brain anatomy, with special emphasis in white matter. For this, the nervous tissue was described as well as the different brain macroscopic structures. The white matter organization was particularly studied as it is of major importance for this thesis. We described the white matter global structure and the most known fiber tracts. The nomenclature of small and larger fiber bundles introduced in this chapter will be useful to identify some of our results, exposed in this thesis. Nevertheless, it must be noted that only the main fiber tracts are well described in the literature. Most of the short association fiber tracts are still unknown. Their smaller size, large number, and important inter-subject variability make their analysis a challenging and complicated task. These tracts will probably be the center of interest in the field of techniques available to infer the subcortical connectivity.

In the next chapter, we introduce the foundations of diffusion MRI. We will show that diffusion MRI constitutes a powerful non-invasive mean to investigate the architecture of the human brain white matter.

# Principles of Diffusion MRI

## Contents

---

<b>3.1 From the diffusion phenomenon to diffusion MRI . . . . .</b>	<b>30</b>
3.1.1 Diffusion Basics . . . . .	30
3.1.2 Basics on Magnetic Resonance Imaging . . . . .	32
3.1.3 Diffusion-weighted MR . . . . .	35
3.1.4 EPI sequence and correction of geometric distortions . . . . .	38
<b>3.2 Diffusion MRI models . . . . .</b>	<b>40</b>
3.2.1 Diffusion Tensor Model (DTI) . . . . .	42
3.2.2 High Angular Resolution Diffusion Imaging (HARDI) . . . . .	49
<b>3.3 MR Diffusion Tractography . . . . .</b>	<b>59</b>
3.3.1 Streamline Deterministic Tractography . . . . .	60
3.3.2 Streamline Probabilistic Tractography . . . . .	64
3.3.3 Other Tractography Algorithms . . . . .	66
<b>3.4 Conclusion . . . . .</b>	<b>69</b>

---

## Overview

---

This chapter presents a background on the basic principles of diffusion MRI, a technique allowing the study *in vivo* of white matter structure and its connections. Firstly, we introduce the concepts underlying diffusion-weighted (DW) imaging, in which the diffusion of water molecules in living tissue takes a fundamental place. Next, we review the basics of Nuclear Magnetic Resonance (NMR), followed by a brief description of DW-MRI. The discussion continues with the approaches designed to locally model the diffusion signal. We start with the diffusion tensor imaging (DTI), as the most intuitive and simple mean to infer microstructure of biological tissues. This gaussian model of diffusion allows the measurement of quantitative parameters extensively used in clinical studies. Then, more complex reconstruction algorithms, using high angular resolution diffusion data are explored. These methods overcome some limitations of the DTI model, as the impossibility to reconstruct multiple fiber distributions of water diffusion. The streamline tractography is finally introduced, a technique aiming to reconstruct three-dimensional trajectories of white matter fibers, which constitute the input dataset of this thesis. Overall, this introductory chapter is inspired from review articles and chapters from [Tuch et al. (2002); Le Bihan (2003); Campbell (2004); Jonasson et al. (2005a); Perrin (2006); Descoteaux (2008); Jones (2008); Johansen-Berg and Behrens (2009)], which are great sources for a general understanding of diffusion MRI and fiber tractography.

**Keywords:** magnetic resonance imaging (MRI), DW-MRI, diffusion tensor imaging (DTI), high angular resolution diffusion imaging (HARDI), white matter tractography, streamline tractography

### Organization of this chapter:

The chapter is organized as follows. We first review the basic principles of molecular diffusion and diffusion MRI in section 3.1. Then we focus on diffusion MRI models section 3.2, starting with diffusion tensor imaging and following with multiple fiber HARDI reconstruction algorithms. Finally, we describe white matter tractography in section 3.3.

## 3.1 From the diffusion phenomenon to diffusion MRI

### 3.1.1 Diffusion Basics

Water molecules, as all the fluid molecules, present a constant thermal agitation known as *Brownian motion* [Brown (1828)]. This phenomenon is produced by thermal chocs between molecules, which strongly modify their trajectories in such a way that they mimic a “random walk”. In an isotropic medium (i. e. the diffusion is the same in all directions), each molecule performs this random walk, leading to a random path in three-dimensional space (see Figure 3.1 A). At macroscopic scale this molecular motion yields to a *diffusion*

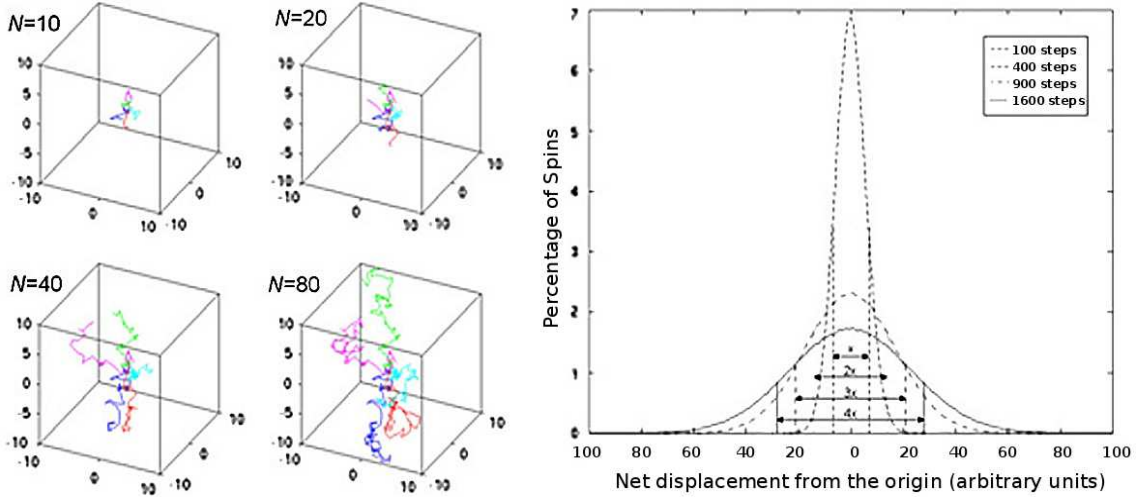


Figure 3.1: A: Simulation of trajectories of five molecules undergoing a random walk in an isotropic medium, after 10, 20, 40 and 80 steps. B: A histogram of displacement from the origin of 1 million molecules, after 100, 400, 900 and 1600 steps. The full-width at half-maximum (FWHM) scales in the ratio of 1:2:3:4, which mirrors the ratio of  $\sqrt{100}:\sqrt{400}:\sqrt{900}:\sqrt{1600}$ , demonstrating the consistency of Einstein's equation for Gaussian diffusion [From Jones (2008)].

phenomenon, a physical process essential for the normal functioning of living systems. For example, the transport of metabolites into cells is facilitated by diffusion [Jones (2008)].

Diffusion can be described by Fick's first law [Fick (1855)], which relates a diffusive flux to any concentration difference through the relationship:

$$\mathbf{J} = -D\nabla C. \quad (3.1)$$

where  $\mathbf{J}$  ( $\text{mol}/(\text{m}^2\text{s})$ ) is the net particle flux,  $\nabla C$  is the gradient of particle concentration, and  $D$  ( $\text{m}^2/\text{s}$ ) is a constant called “diffusion coefficient”. It should be noted that diffusion results solely from collisions between molecules in liquids (and also in gases). Therefore, it occurs even in thermodynamic equilibrium, i. e. even if there is no net flux, there are still diffusive fluxes nonetheless, which cancel each other.

Einstein used a probabilistic framework to describe the motion of an ensemble of particles undergoing diffusion. He introduced the concept of “displacement distribution”, representing the likelihood that a single given particle will traverse a certain distance within a particular timeframe [Einstein (1956)]. In free diffusion, the net displacement distribution is a Gaussian function whose width is determined by the diffusion coefficient and time (see Figure 3.1 B). Einstein derived an explicit relationship between the mean-squared displacement of particles,  $\langle r^2 \rangle$ , during a diffusion time  $\tau$  and the diffusion coefficient  $D$ , appearing in Fick's law (three-dimensional case):

$$\langle r^2 \rangle = 6D\tau, \quad (3.2)$$

The quantity  $r = \sqrt{6D\tau}$  is a characteristic length referred to the quadratic mean dis-

placement or diffusion distance. In the isotropic case,  $\langle r^2 \rangle$  depends on the molecule type and the medium properties but not on the direction. In DW-MRI, we do not measure the diffusion coefficient directly, but the mean displacement of water molecules within each three-dimensional volume element, or *voxel*. The voxels form the image and typically, are cube-shaped with about 2.5 x 2.5 x 2.5 mm in dimension. The presence of cell membranes, inclusions, macromolecules and so forth, present in tissue serve to hinder the pathway of the molecules undergoing their random walks. As a result, their overall displacement from their starting point in a fixed period of time is reduced compared to their mean displacement when they were in “free” condition. Thus, when we apply Einstein’s equation to compute diffusion, it will *appear* to be lower. Then, we refer to the **apparent diffusion coefficient** or **ADC** [Le Bihan et al. (1986)]. The average ADC in tissue is around  $0.7 \times 10 \text{ mm}^2/\text{s}$  at 37°C, about four times smaller than in free water.

**The Diffusion Propagator** The *diffusion propagator* formalism offers a robust descriptive framework capable of characterizing all diffusion phenomena, such as restriction and finite boundary permeability. The diffusion propagator  $P(\mathbf{r}|\mathbf{r}_0, \tau)$  gives the probability of a spin traveling from position  $\mathbf{r}_0$  to  $\mathbf{r}$  in the diffusion time  $\tau$ . In MRI, a signal is detected from a very large number of molecules present in each voxel. Therefore, the voxel averaged random displacements of water molecules can be described by a diffusion displacement probability function (PDF), called the *ensemble-average propagator* of water molecules. The diffusion average propagator is written as  $P(\mathbf{R}, \tau)$ :

$$P(\mathbf{R}, \tau) = \int_{\mathbb{R}^3} P(\mathbf{r}|\mathbf{r}_0, \tau) \rho(\mathbf{r}_0) d\mathbf{r} \quad (3.3)$$

where  $\mathbf{R} = \mathbf{r} - \mathbf{r}_0$  is the relative spin displacement and  $\rho(\mathbf{r}_0)$  is the initial spin density. To image the diffusion we must link the average-diffusion propagator to the signal measured in the MRI experiment. It is crucial to infer properties of the underlying microgeometry without the need to invoke an analytical representation of the geometry.

### 3.1.2 Basics on Magnetic Resonance Imaging

Conventional MR images reflect water properties measuring signals from hydrogen nuclei. Each hydrogen nucleus, or proton, possess a nuclear magnetic moment, called *spin*. Spins align themselves and present a precessional movement with an externally applied static magnetic field.

The Larmor equation is the most basic and fundamental equation in NMR; it states that the precessional frequency of spins in a magnetic field is directly proportional to the strength of the magnetic field  $B$ :

$$\omega = \gamma B \quad (3.4)$$

where  $\omega$  is the precessional frequency, and  $\gamma$  is the gyromagnetic ratio, a constant specific to the nucleus under examination. In water, the hydrogen nucleus (i. e. the proton) has



a gyromagnetic ratio value of approximately 42.58 MHz/Tesla.

This phenomenon is used by MRI scanners, which generate a strong *static magnetic field*, called  $B_0$ , to produce the alignment of proton spins along  $B_0$ , with a resulting net magnetization in the direction of the field. MRI scanners apply a second magnetic field of a brief duration, and oscillating at radio frequencies, called *rf pulse*. When rf pulse frequency is applied at the Larmor frequency of spins, it rotates the net magnetization away from its orientation at equilibrium, along the longitudinal axis, parallel to  $B_0$ , to create a component into the transverse plane, called the *transverse magnetization*. The longer the duration of the applied rf pulse, or the greater its field strength, the greater the tip angle that can be achieved. In the absence of externally applied RF energy, the transverse magnetization will decay exponentially to zero with a time constant T2. This decay is known as the spin-spin relaxation. Additionally, the rf-induced excitation puts all the spins in phase, i. e. on a coherent rotation (Larmor precession). After the application of the rf pulse, the component of the net magnetization along  $B_0$ , called *longitudinal magnetization* decreases exponentially with a time constant T1. This is the spin-lattice relaxation. The difference in the physical properties of the different tissue types is reflected in the relaxation times, depending on T1 and T2, which determine different MR image contrasts. For example, T1 contrast yields the typical anatomical images. In some MR acquisition schemes, the rf pulse is of 90 degree, to flip the magnetization in the transverse plane.

The rotating magnetic field generated by precessing spins induces a current in the MRI receiver coil, which is the signal used to generate MRI images. This signal, reflected in voxels brightness, depends on the coherence of the phase of the spins as they precess. Small inhomogeneities in the magnetic field create small variations in the frequencies of precessing spins, producing with time a loss of phase coherence and resulting pixel brightness. This loss of magnetization is added to the T2 decay, leading to a T2\* contrast. Typically, the phase accumulation of the spins is reversed by application of a 180 degree refocusing pulse, some time (TE/2) after the excitation rf pulse (*spin-echo sequence*). A time TE (echo time) after the excitation rf pulse, all spins are back in phase, and the magnetization is reduced only by a T2 decay (see Figure 3.3).

A third set of magnetic fields generated by MR scanners are called magnetic field *gradients*. The addition of the gradients to the static magnetic field  $B_0$  makes the magnetic field varying in a linear manner over the volume of interest, along any of three orthogonal directions. Gradient imposes a position-dependent precessional frequency, which is the basis of the spatial encoding in MRI. A *slice selection* can be performed by the application of a gradient ( $G_z$ ) simultaneously with the rf pulse, producing changes in the Larmor frequency along the direction of the gradient. Then, a given frequency corresponds to a plane perpendicular to the gradient direction, i. e. to a slice.

After spins are excited, two gradients are applied along the two in-plane directions defining the excited slice (x-y plane), to produce linear changes in precessional frequency. One gradient ( $G_y$ ) is applied after the first rf pulse and used for a *line selection*. Gradient

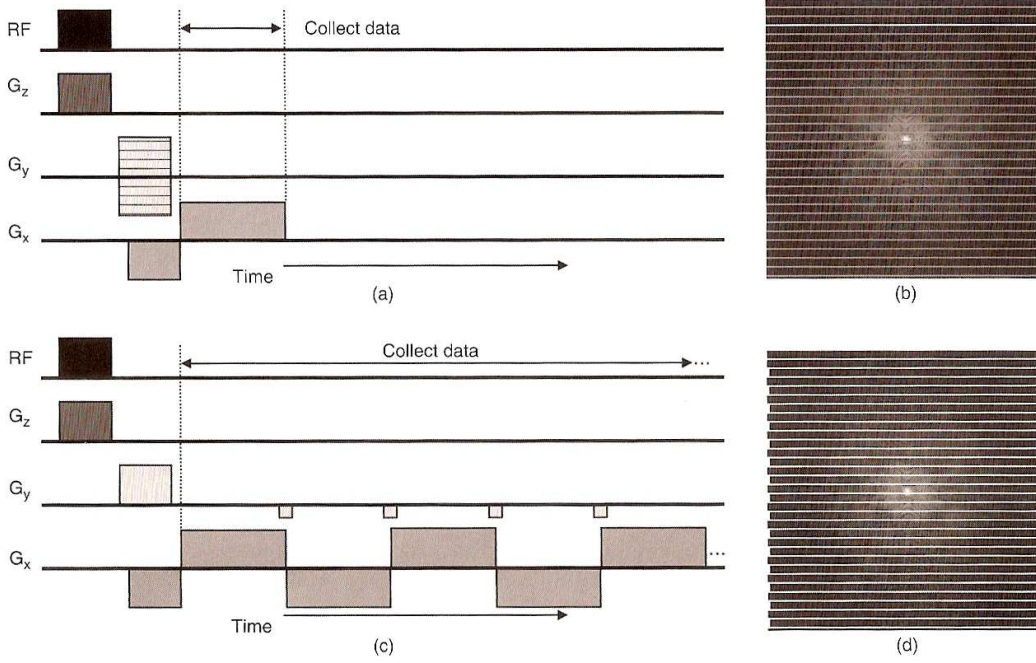


Figure 3.2: Illustration of MRI pulse sequences and their data collection trajectories. Conventional Cartesian pulse sequences (a) measure  $k$ -space (b) one line per TR (shot). White line shows one measurement trajectory, gray lines show subsequent measurement trajectories, each obtained with a Different value of  $G_y$ . Echo planar sequences (c) oscillate the frequency encoding gradient and measure multiple lines of  $k$ -space (d) per shot. [From Johansen-Berg and Behrens (2009)].

$G_y$  introduces a phase-shift in the signal dependent on the position along the y-axis. When the field gradient is removed the frequencies will return to their initial value but the phase-shifts between nuclei remain at different positions on the y-axis. Then the gradient on the x-direction,  $G_x$ , is applied and the frequencies will change again, dependent on their position along the x-axis. It is normally during the application of  $G_x$  that the signal is detected (*line readout*).

The signal measured in a receiver coil, after successively applying  $G_x$ ,  $G_y$  and  $G_z$ , can be expressed as the Fourier transform ( $F(k_x, k_y)$ ), of the transversal magnetization  $f(x, y)$ . Variables  $k_x$  and  $k_y$  are function of the area of the gradients ( $G_x$  and  $G_y$ ) and define a reciprocal spacial frequency space, known as  $k$ -space.

$$F(k_x, k_y) = \int f(x, y) e^{i2\pi[k_x x + k_y y]} dx dy \quad (3.5)$$

The MR image is then reconstructed by taking the inverse Fourier transform of  $F(K_x, K_y)$ , where a sampling of  $k$ -space is performed by the variation of space-encoding gradients ( $G_x$  and  $G_y$ ). Applying gradients  $G_x$ ,  $G_y$  and  $G_z$  in other combinations leads to different samplings of 3D  $k$ -space.

Typically the desired data is collected over several excitations (or shots), separated by a time TR (repetition time), which allows spin magnetization to recover. For spin echo

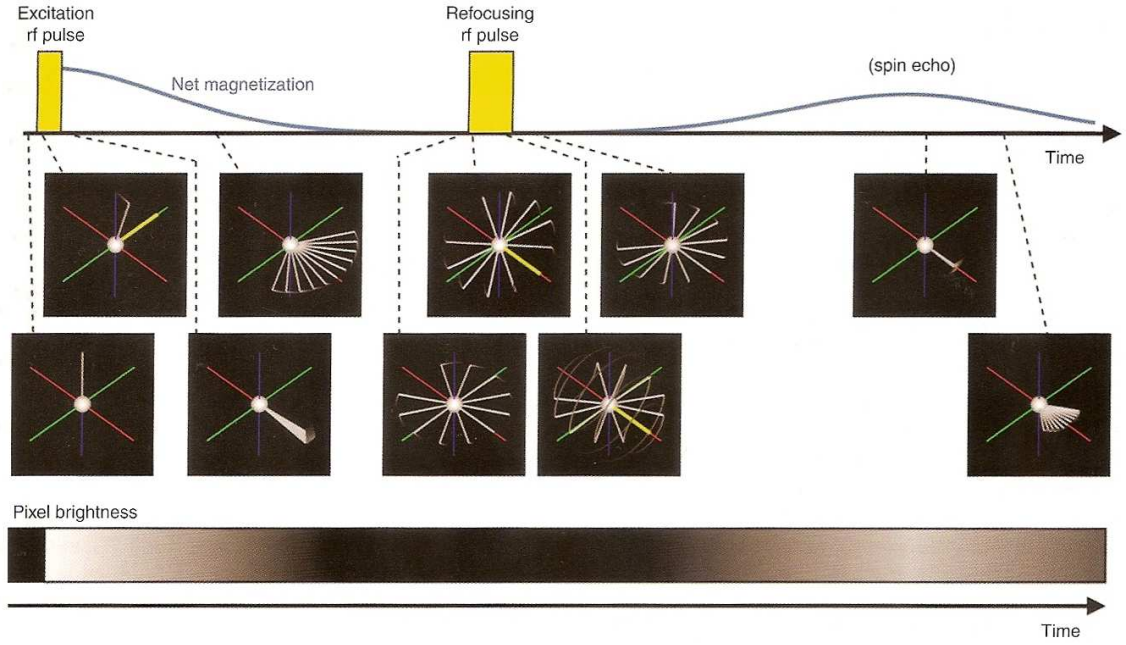


Figure 3.3: Illustration of spin dephasing in spin echo sequence. An excitation pulse (in yellow) rotates the spins into the plane perpendicular to  $B_0$ , after which they precess. Differences in precessional frequency create differences in spin phases, which increase with time, reducing the net magnetization and resulting pixel brightness. Some time ( $TE/2$ ) after the excitation rf pulse, a refocusing rf pulse flips spins about its axis, putting the more rapidly precessing spins “behind” the more slowly precessing spins. Over time the rapidly precessing spins accrue more phase than slowly ones, so that at time ( $TE$ ) after the excitation rf pulse all spins are back in phase. This is called a spin echo, and the net magnetization (and pixel brightness) reflects the total coherent magnetization of all spins, reduced only by their  $T_2$  decay after excitation. [From [Johansen-Berg and Behrens \(2009\)](#)].

sequence, the signal from each pixel in an image can be expressed as

$$f(x, y) = M_0 \left(1 - e^{-\frac{TR}{T_1}}\right) e^{-\frac{TE}{T_2}} \quad (3.6)$$

where  $M_0$  is the “spin density” in that pixel, and  $T_1$  and  $T_2$  reflect the time constants of relaxation in the tissue at that location. Figure 3.2 illustrates two different MRI pulse sequences with different data collection trajectories.

### 3.1.3 Diffusion-weighted MR

DW-MRI sequences are made sensitive to diffusion by the addition of a *diffusion-encoding gradient*. If spins remain stationary during precession, the net phase accumulation due to magnetic field inhomogeneities will be constant, and not depending on their position in the gradient (and consequently, on the precessional frequency). But, as water molecules present a permanent random walk, spins will experience changes in the strength of the magnetic field. Since the particle displacements are not coherent, a distribution of displacements is obtained and thus a *distribution of phases*. This spread of phases leads to a loss of signal coherence and therefore a reduction in signal amplitude, which in an

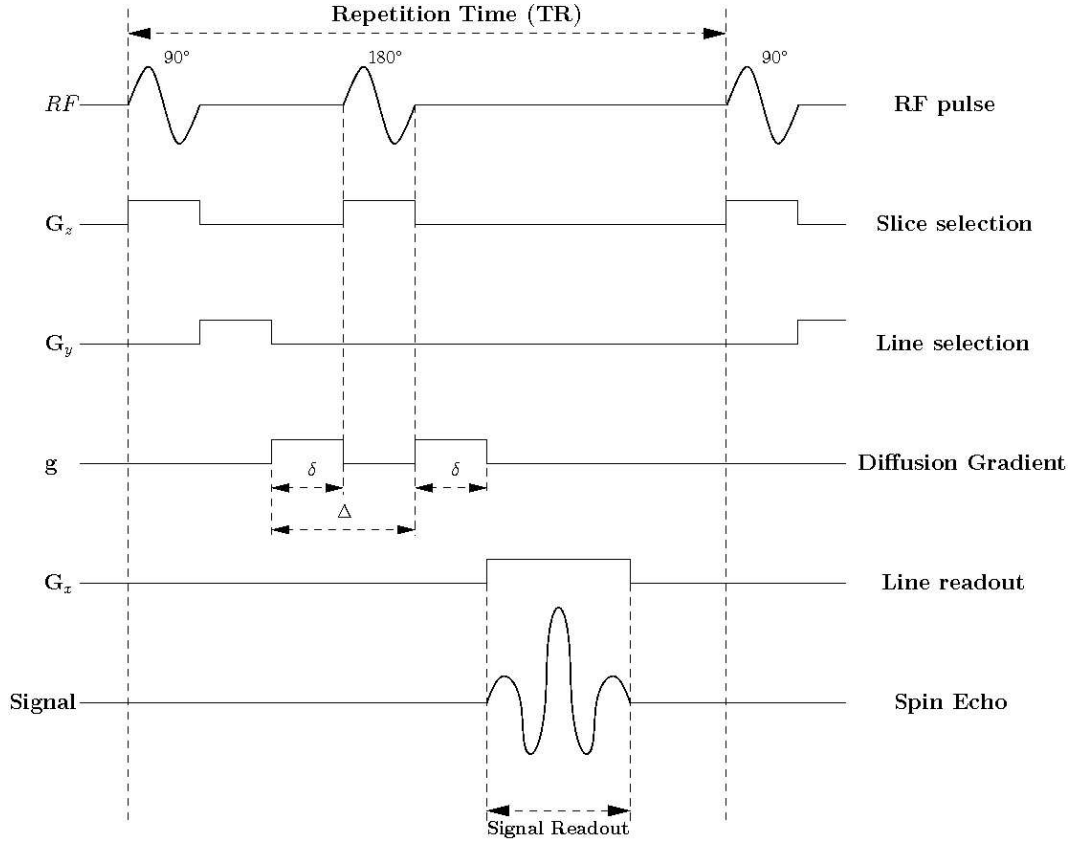


Figure 3.4: Pulse Gradient Spin Echo sequence experiment. The two gradient pulses are of equal area (in this case, they have equal magnitude and equal duration  $\delta$ ). [From Descoteaux (2008)].

image, means that the image appears darker. Diffusion-encoding gradients sensitize the MR signal to diffusion, by imposing a given phase to a molecule that is dependent on its overall displacement [Stejskal and Tanner (1965)]. The diffusion gradient is applied in one particular direction, so only the displacement of spins along the gradient direction will induce a phase-shift, which will lead to a signal representing the diffusion in the gradient direction.

The diffusion coefficient can be inferred from observations of the displacements over a given time period. The greater the spread of displacements (the higher the ADC), the greater the spread of phases – and thus the greater the loss of signal – and the voxels appears dark. Conversely, the lower the rate of diffusion, the lower the spread of phases – and thus the lower the loss of signal and the voxels appears bright.

Stejskal and Tanner (1965) introduced the *Pulsed Gradient Spin Echo* (PGSE) sequence, with two short duration gradient pulses of duration time  $\delta$ , placed on either side of the 180 degree rf pulse and separated by a time interval  $\Delta$  (see Figure 3.4). The interval between the end of the first pulse and the beginning of the second pulse,  $\Delta - \delta$  is called the “diffusion time”. By assuming the pulses to be infinitely narrow, i.e.  $\delta$  is short enough for the diffusion of the water molecule to be negligible during that time, Stejskal and Tanner (1965) provided a quantitative measurement of diffusion in a sample. If the spin displace-

ment is a result of Brownian motion, the signal of equation 3.6 is attenuated exponentially by the product of the diffusion coefficient  $D$  and a factor  $b$  which is a function of the DW-gradients and is expressed in ( $s/mm^2$ )

$$f(x, y) = M_0 \left(1 - e^{-\frac{TR}{T1}}\right) e^{-\frac{TE}{T2}} e^{-bD} \quad (3.7)$$

The factor  $b$  [Le Bihan et al. (1986)], called  $b$ -factor, represents the sensitivity to diffusion; its generalized equation is

$$b = \int_0^{TE} |k(t)|^2 dt. \quad (3.8)$$

For rectangular gradients, equation 3.8 becomes

$$b = \gamma^2 \mathbf{G}^2 \delta^2 \left( \Delta - \frac{\delta}{3} \right) \quad (3.9)$$

where  $\gamma$  is the gyromagnetic ratio,  $\mathbf{G}$  is the amplitude of the magnetic field gradient pulses,  $\delta$  is the pulse duration time and  $\Delta$  is the interval between application of the first and second pulse. The time constant  $\tau = \Delta - \frac{\delta}{3}$  defines the “effective diffusion time” where the  $\delta/3$  correction is due to the diffusion which occurs during the time in which the gradients are on.

A longer diffusion time increases the distinction between the signals in different directions. However, a longer diffusion time will lead to a lower signal-to-noise ratio (SNR) so a compromise is necessary.

The equation 3.9 is derived from the spin total phase-shift ( $\phi$ ), which is defined as

$$\phi = \gamma \int \mathbf{G}^T \mathbf{r}(t) dt = \gamma \delta \mathbf{G}^T \mathbf{R} \quad (3.10)$$

where  $\gamma$  is the nuclear gyromagnetic ratio for water protons,  $\mathbf{G}$  is the applied diffusion gradient vector and  $\mathbf{R} = \mathbf{r} - \mathbf{r}_0$  is the spin displacement during time  $\Delta$ . Therefore the measured phase-shift is proportional to the spin displacement and maps the mean diffusion within a voxel. If diffusion is not uniform in all orientations, the signal will not be the same for different gradient directions. An example is illustrated in Figure 3.5, which shows the DW signal intensity for three different diffusion-encoding directions, aligned with the three principal image axes.

The signal observed  $S$  can be expressed as a function of the baseline  $S_0$ , the signal intensity in the absence of any diffusion weighting, also called  $b = 0$  image. It is a superposition of the transverse magnetizations.

$$S = S_0 e^{-bD} \quad (3.11)$$

Both,  $S_0$  and  $S$  are weighed identically by  $M_0$ , T1 recovery and T2 decay.

To make the classical MRI experiment more intuitive, a reciprocal space, called  $q$ -space

was defined for diffusion imaging, where the *wavevector*  $\mathbf{q}$  is a vector representing a unit phase encoding step:

$$\mathbf{q} = \frac{1}{2\pi} \gamma \delta \mathbf{G}. \quad (3.12)$$

The value  $b$  can then be expressed in function of  $\mathbf{q}$  by  $b = |\mathbf{q}|^2 \tau$ .

The expression for diffusion signal presented in equation 3.11 is only valid for a Gaussian diffusion. While biological diffusion imaging studies commonly assume that the diffusion is Gaussian there is a body of experimental evidence which indicates that this assumption is not valid, principally due to diffusion restriction.

### Ensemble average diffusion propagator and $\mathbf{q}$ -space

Stejskal and Tanner showed that, if gradient pulses are Dirac pulses (narrow pulse assumption), the signal attenuation  $S(\mathbf{q}, \tau)$  can be expressed as the 3-dimensional Fourier transform  $\mathcal{F}$  of the ensemble average propagator  $P$  with respect to the spin relative displacement vector  $\mathbf{R}$ ,

$$\frac{S(\mathbf{q}, \tau)}{S_0} = \int_{\mathbb{R}^3} P(\mathbf{R}, \tau) e^{-2\pi i \mathbf{q}^T \mathbf{R}} d\mathbf{R} = \mathcal{F}[P(\mathbf{R}, \tau)], \quad (3.13)$$

where  $S_0$  is the baseline image and  $P(\mathbf{R}, \tau)$  is the average diffusion propagator of a pool of water molecules. Therefore, it is possible to obtain an average propagator from the  $S(\mathbf{q})$  data by inverting the Fourier transform in equation 3.13 with respect to the reciprocal vector  $\mathbf{q}$ . By measuring the signal for sampled points in  $q$ -space (“ $q$ -space imaging”), we can reconstruct the ensemble average diffusion propagator  $P$  in every voxel. The  $q$ -space is sampled by either varying the direction of  $\mathbf{q}$  (by the direction of  $\mathbf{G}$ ), or the magnitude of  $\mathbf{q}$  (by the magnitude of  $\mathbf{G}$  or the gradient duration  $\delta$ ). This is the idea behind  $q$ -space imaging [Callaghan (1991)]. The PDF provides a detailed description of the diffusion in the high spatial frequency regime where the Gaussian model is no longer valid. It can resolve highly complex organization of fibers such as crossings. The Gaussian function is a particular case which can be viewed as arising from either free diffusion or a low spatial frequency approximation to the restricted propagator [Tuch et al. (2002)]. More details about diffusion models are reviewed in sections 3.2.1 and 3.2.2.

#### 3.1.4 EPI sequence and correction of geometric distortions

EPI sequences use a method of collecting data much faster than PGSE experiment, called **Echo Planar Imaging** (EPI) [Mansfield (1977)]. For PSGE, the data collection trajectory is cartesian, where one line (all desired  $k_x$  locations) is read per TR (shot), with a different and increasing value of the “phase encoding” gradient ( $G_y$ ), per each line. In EPI, the trajectory is also cartesian, but the sequence oscillates the frequency encoding gradient ( $G_x$ ) and measures multiple lines of the  $k$ -space during a shot (see Figure 3.2). This sequence is used in functional MRI to measure the brain activity (BOLD signal) or in DW-MRI with added diffusion gradient pulses, to determine the brain connectivity. The



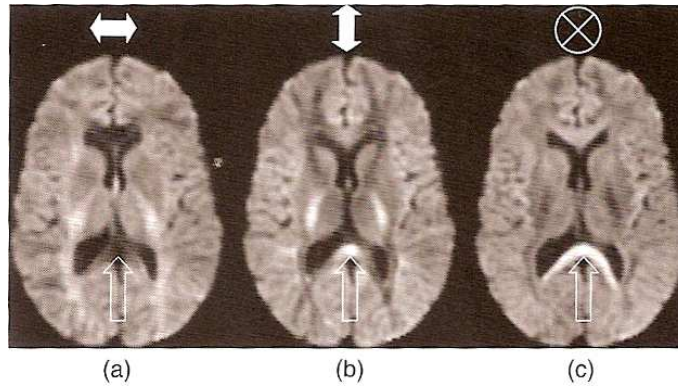


Figure 3.5: Effect of changing the axis of the diffusion-encoding gradients on the DW signal intensity. The arrows at the top of the figure show the orientation of the encoding axis. In (c), the orientation is perpendicular to the viewing plane. Dark areas have high ADC, lighter areas represent lower ADC. In the area highlighted by the lower (unfilled) arrows, which forms the midsagittal portion of the splenium of the corpus callosum, the ADC is high along the left-right axis, but low in the two orthogonal directions. [From [Johansen-Berg and Behrens \(2009\)](#)].

most common pulse sequence for DW-MRI is currently *single-shot Echo Planar Imaging* (SS-EPI), which encodes all the  $k$ -space in a single echo. This sequence allows the acquisition of a slice in less than 200 milliseconds. EPI is a very fast imaging technique but it produces several distortions in the image due to the long duration of the reading pulses. Any phase error is integrated during the echo train record. Geometric distortions, which can reach several millimeters, are a critical problem when a registration with anatomical MRI is required. In practice, these distortions are due to three main different physical phenomena: (1) spatial non-linearities of gradients, (2) gradient-induced Eddy currents, and (3) magnetic field inhomogeneities.

**Spatial non-linearities of gradients,** producing geometric warping of the image, depends only on the gradients conception and are commonly corrected by post-processings implemented in MRI systems. These algorithms do not need special subject-dependent calibrations and are executed after the acquisition.

**Eddy currents correction:** The second type of distortions is produced only in diffusion weighted EPI sequences. When strong gradients are used for the encoding of the diffusion, Eddy currents are induced in the gradients. These currents are equivalent to the addition of gradients to the spatial-encoding gradients. The encoding errors in spatial positions, resulting also in an image warping, can be modeled with an affine transformation. DW-images can be corrected, then, by their registration with an undistorted reference volume acquired without diffusion weighting. These effects can be directly compensated during the acquisition by the use of a twice refocusing spin echo technique [[Jezzard et al. \(1998\)](#); [Reese et al. \(2003\)](#)], included nowadays in most clinical MRI scanners.



**Static magnetic field inhomogeneities** are induced in regions close to the interface between two tissues with different susceptibility parameters. Local variations of magnetic field in these regions produce differences in the frequency and the phase of precession of the spins, inducing an image warping linearly dependent of the field strength. This phenomenon is specially important in EPI as TE time is long. In the human brain, these distortions appear most commonly around tissue/air boundaries, such as the frontal lobe above the sinusses. Usually, a field map (or phase map) is acquired for measuring the magnetic field inhomogeneities. The phase map is equivalent, by a multiplying factor, to a geometric distortions map  $\Delta y$ . Once the 3D distortion map has been calculated, the image can be corrected by the interpolation of the corrupted image using the deformation field  $\Delta y$ . Besides, recent parallel imaging techniques produce an important reduction of warping effect from magnetic field inhomogeneities by reducing the number of lines to read along the phase axis and consequently diminishing the echo train duration.

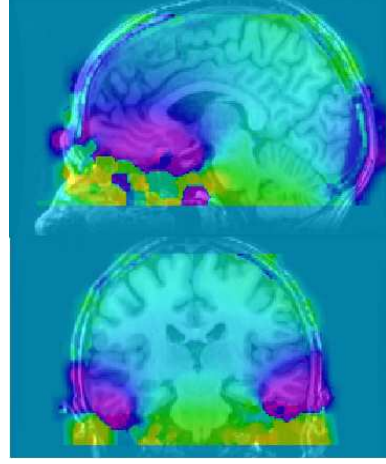


Figure 3.6: Example of a field map image.

## 3.2 Diffusion MRI models

Diffusion MRI can be used for extraction of microstructural information of neural tissue, specifically in white matter. As studied in previous section, DW-MRI can measure the mean displacement of water molecules, which is affected by tissue microstructure. Cells membranes, the axon myelin sheath, organelles and macromolecules modify the water molecules diffusion.

There are three major modes of diffusion: free diffusion, hindered and restricted [Le Bihan (1995)], those can be divided into isotropic and anisotropic. Free and hindered diffusion have been modelled by a Gaussian displacement distribution, where diffusion is represented by the  $b$ -factor. However a single exponential decay can not describe diffusion as well as would have been expected. In most cases diffusion-sensitized MRI signal attenuation in brain tissue have been very well fitted with a biexponential function corresponding to two water diffusion pools or phases in slow exchange, with a fast and a slow diffusion coefficient [Niendorf et al. (1996)]:

$$S = S_0 f_{slow} e^{-bD_{slow}} + S_0 f_{fast} e^{-bD_{fast}}, \quad (3.14)$$

where  $f$  and  $D$  are the volume fraction and the diffusion coefficient associated with the slow and fast diffusion phases, with  $f_{slow} + f_{fast} = 1$ .

The historical model distinguishes two compartements: the *extracellular* and the *intracellular* compartments, whose are separated by the semipermeable cell membranes. In

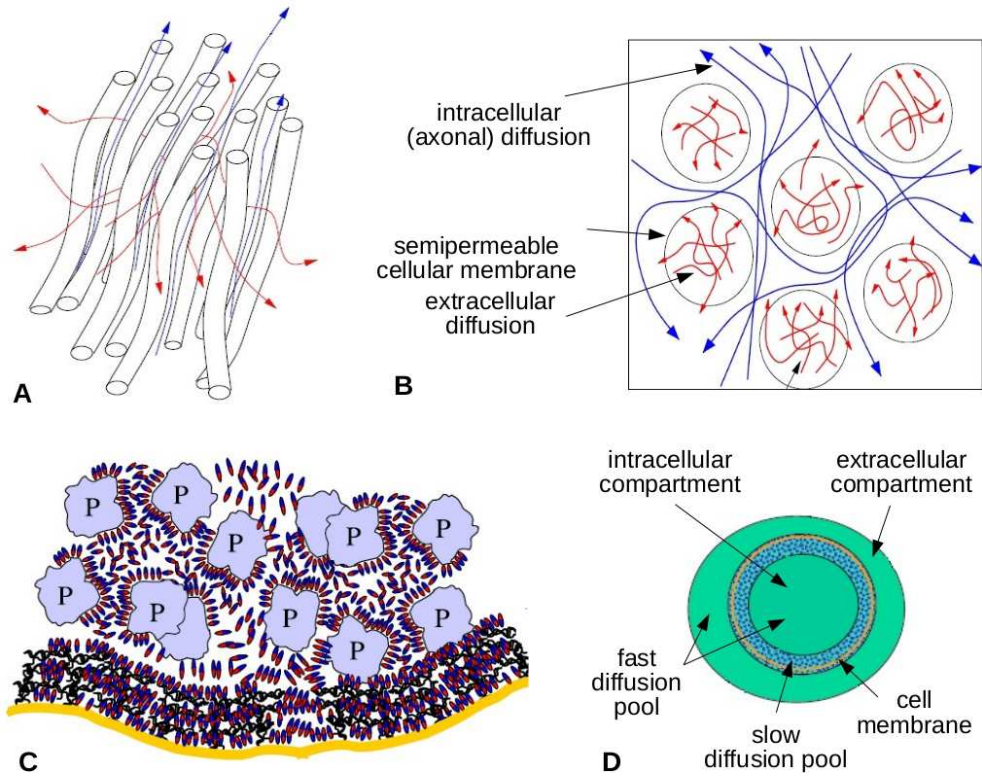


Figure 3.7: A: Illustration of the anisotropic nature of diffusion in WM, where water molecules present a preferred orientation of diffusion along WM fibers. B: Two-compartments model composed by an intracellular and an extracellular compartment. While the extracellular compartment presents a hindered diffusion, the intracellular (axonal) compartment is characterized by a restricted diffusion. [Adapted from [Poupon \(1999b\)](#)]. C: Schematic representation of the structuring effect of charged proteins (P) and membranes on water molecules. Bulk water molecules are exchanging rapidly with the water molecules in the protein hydration shells. Other water molecules are trapped in a membrane-bound layer. D: Conceptual biphasic water diffusion model. The slow diffusion pool is made of a water layer trapped by the electrostatic forces of the protein membranes and associated cytoskeleton. [Adapted from [Le Bihan \(2007\)](#)].

this model, the extracellular compartment is characterized by a hindered diffusion, determining the fast diffusion component, while the intracellular compartment presents a restricted diffusion within axons, determining the slow diffusion component. This model is controversial as the volume fractions of the two water phases obtained using the bi-exponential model do not agree with those known for the intra- and extracellular water fractions ( $F_{intra} \geq 0.80$  and  $F_{extra} \leq 0.20$ , even by taking into account differences in T2 relaxation contributions between those compartments [[Le Bihan \(2007\)](#)]). Figure 3.7 B illustrates these two components.

A more recent biphasic model defines two diffusion pools: a *fast* and a *slow* pool, delimited in function of the distance of water molecules to cell membranes. The slow pool, composed by molecules localized close to cell membranes, contain membrane-bound water. Contrarily, the fast pool is composed by bulk water and proteins-bound water [[Le Bihan \(2007\)](#)]. Figure 3.7 C-D illustrates this model.

In isotropic tissues the diffusion-weighted intensity, and therefore the ADC, is the same in all directions. However, if the signal changes when we apply different gradient encoding directions, the diffusion is anisotropic. An example of this effect is shown in Figure 3.5 where three different DW images were obtained for three orthogonal gradients. From this three images is possible to infer an ordered structure that has predominantly a left-right orientation. The highly anisotropic region indicated by arrows corresponds to fibers from the corpus callosum. The anisotropic nature of WM tissue is illustrated in Figure 3.7 A, where water molecules will present a preferred orientation of diffusion in the direction of the fibers.

For anisotropic tissue the behavior of water molecules can no longer be characterized with a single ADC. Therefore more complex models are used to characterize diffusion. The diffusion tensor model is the more simple and clinically used model; it is presented in section 3.2.1. Higher order models, have been developed to overcome some limitations of the diffusion tensor. These will be briefly reviewed in section 3.2.2.

### 3.2.1 Diffusion Tensor Model (DTI)

Stejskal employed the relation in equation 3.11 for the case of free or Gaussian diffusion. In this case the signal in DWI decays exponentially with  $b$ . This expression contains two unknowns, namely, the unattenuated echo signal  $S_0$  and the diffusion coefficient  $D$ . If the diffusion is isotropic, then  $D$  is a scalar equal to the ADC, and is easily calculated as

$$ADC = \frac{\text{Log}[S_0/S]}{b} \quad (3.15)$$

where  $b$  is the  $b$ -factor described in equation 3.9. The values of  $b$  typically used in clinical studies are inferior to  $1,500 \text{ s mm}^{-2}$ .

When the displacements are not the same in all directions, the simplest representation of the shape of diffusion in 3D is the diffusion tensor (DT) model. The diffusion tensor is a 3x3 symmetric, positive-definite matrix, originally proposed for use in diffusion MRI by Basser et al. (1994). The DW imaging modality that uses the diffusion tensor is called diffusion tensor MRI, DTI or DT-MRI. The diffusion tensor characterizes Gaussian displacements in 3D, i. e.,

$$\mathbf{D} = \begin{pmatrix} \mathbf{D}_{xx} & \mathbf{D}_{xy} & \mathbf{D}_{xz} \\ \mathbf{D}_{xy} & \mathbf{D}_{yy} & \mathbf{D}_{yz} \\ \mathbf{D}_{xz} & \mathbf{D}_{yz} & \mathbf{D}_{zz} \end{pmatrix} = \frac{1}{6\tau} \langle \mathbf{R}\mathbf{R}^T \rangle. \quad (3.16)$$

DTI approximates the diffusion PDF by a 3-variate normal distribution with zero mean. Hence,  $\mathbf{D}$  can be viewed as the covariance matrix of water molecules displacements in a given time at each imaging voxel. This diffusion tensor can be used in Einstein's and Fick's equations (eq. 3.2 and 3.1) for anisotropic diffusion. The diagonal elements of the matrix correspond to diffusivities along three orthogonal axes, while the off-diagonal elements correspond to the correlation between displacements along those orthogonal axes.

The assumption of a single-Gaussian displacement distribution is a low spatial frequency approximation of the diffusion PDF. In the diffusion tensor model, if we take the Taylor’s expansion of  $P$  about  $\mathbf{R}$  and  $\tau$  and ignore the higher order terms, equation 3.16 can be used to obtain

$$\frac{\partial P(\mathbf{R}, t)}{\partial t} = \mathbf{D} \nabla^2 P(\mathbf{R}, \tau). \quad (3.17)$$

This relation is called the diffusion equation, or heat equation [Campbell (2004)]. The solution for this equation is the Gaussian diffusion PDF. In this case, the probability  $P$  to find a molecule, initially at position  $\mathbf{r}_0$ , at  $\mathbf{r}$  after a delay  $\tau$  is then given by

$$P(\mathbf{R}, \tau) = \frac{1}{\sqrt{(4\pi\tau)^3 |\mathbf{D}|}} \exp \left( -\frac{1}{4\tau} \mathbf{R}^T \mathbf{D}^{-1} \mathbf{R} \right), \quad (3.18)$$

where  $|\mathbf{D}|$  is the determinant of the DT,  $\mathbf{D}$ , and  $\mathbf{R} = \mathbf{r} - \mathbf{r}_0$  is the molecule displacement.

For a PGSE experiment, the signal attenuation can be expressed in function of  $\mathbf{D}$

$$S(TE) = S_0 e^{-\gamma^2 \mathbf{G}^2 \delta^2 (\Delta - \frac{\delta}{3}) \hat{\mathbf{q}}^T \mathbf{D} \hat{\mathbf{q}}} = S_0 e^{-b \hat{\mathbf{q}}^T \mathbf{D} \hat{\mathbf{q}}} \quad (3.19)$$

where  $|\mathbf{D}|$  is the DT,  $\hat{\mathbf{q}}$  is the diffusion gradient orientation,  $\delta$  is the pulse duration and  $\Delta$  is the time between gradient pulses, as in equation 3.9.

In DTI, the scalar  $b$  value is replaced by a 3x3 symmetrical  $b$ -matrix,  $\mathbf{b}$ . The tensor elements are then computed by solving

$$\log \left( \frac{S}{S_0} \right) = - \sum_{i=1}^3 \sum_{j=1}^3 b_{ij} \mathbf{D}_{ij} \quad (3.20)$$

The DT can be reconstructed by the measurement of signal attenuation for six different non-coplanar and non-coplanar directions, with the addition of one non-diffusion-weighted image ( $S_0$ ). This approach uses a number of model parameters equal to the data, leading to a high sensibility to noise. Therefore, it is usual to estimate the DT from more than the minimum number of acquisitions. Several approaches have been developed for a robust estimation of the DT. These methods search a vectorial space that ensure definite-positive tensors, and define robust tensor metrics. In addition to the Euclidean space, Riemannian [Arsigny (2006); Pennec et al. (2006)] and Log-Euclidean [Arsigny et al. (2006); Fillard et al. (2007); Arsigny et al. (2007)] spaces have been defined.

The tensor isosurfaces can be thought in terms of an ellipsoid, a surface representing, the distance that a molecule will diffuse to with equal probability from the origin. To represent the ellipsoid, the DT formalism provides an “internal reference frame” called *eigensystem*. The tensor is diagonalized to calculate the eigenvalues and eigenvectors that will characterize the diffusion. The principal axes of the ellipsoid – which are mutually orthogonal – are given by the eigenvectors, scaled according to the square root of the eigenvalues. The three eigenvalues ( $\lambda_1$ ,  $\lambda_2$  and  $\lambda_3$ ), correspond to the three diffusivities

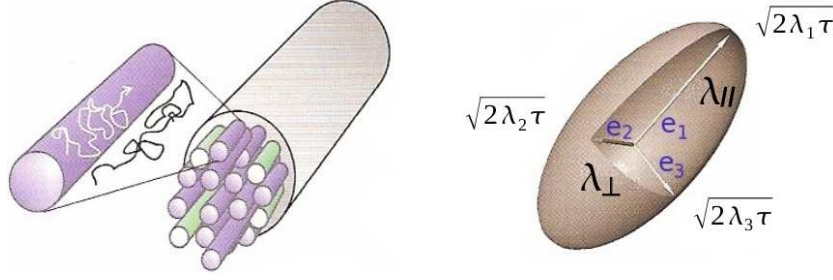


Figure 3.8: Diffusion tensor can represent anisotropic diffusion in ordered tissue as an ellipsoid reflecting parallel (i. e. axial diffusivity,  $\lambda_{//}$ ,  $\lambda_1$ ) or perpendicular (i. e. radial diffusivity,  $\lambda_{\perp}$ ,  $\lambda_{2,3}$ ) to the neural fibers. [From [Johansen-Berg and Behrens \(2009\)](#)].

along the principal axes of the diffusion tensor. The orientation of the tensor is assumed to be parallel to the principal eigenvector  $e_1$ , associated with the largest eigenvalue  $\lambda_1$ . The diffusivity of water along the length of the fibers is then represented by  $\lambda_1$  (or  $\lambda_{//}$ ), called *axial diffusivity*. The two smaller eigenvalues ( $\lambda_2$ ,  $\lambda_3$ ) are assumed to be the diffusivity perpendicular to the fibers. These two eigenvalues are often averaged to yield a single value, the *radial diffusivity* ( $\lambda_{\perp}$ ). The degree of anisotropy is calculated from differences between parallel and perpendicular diffusion. See Figure 3.8 for an example of anisotropic diffusion modeled by a DT.

### Scalar invariants for DT

An important parameter derived from DTI is the **mean diffusivity** or **MD** or **ADC**, which is the average of the three eigenvalues,

$$ADC = \frac{\lambda_1 + \lambda_2 + \lambda_3}{3} = \frac{DT_{trace}}{3} \quad (3.21)$$

and gives a measure of the bulk diffusivity. For  $b$ -value range typically used in clinical studies ( $b \leq 1,500 \text{ s mm}^{-2}$ ), the MD is fairly uniform throughout the gray and white matter ( $0.7 \times 10^{-3} \text{ mm}^2/\text{s}$ ), and higher in ventricles ( $3.2 \times 10^{-3} \text{ mm}^2/\text{s}$ ). Diffusion abnormalities, such as, acute ischemic lesions can be detected with ADC images, which are extensively used for clinical diagnosis.

The most used index for anisotropy in DTI publications is the **fractional anisotropy** or **FA** [[Basser and Pierpaoli \(1995\)](#)], expressed as

$$FA = \sqrt{\frac{3}{2}} \sqrt{\frac{(\lambda_1 - \bar{\lambda})^2 + (\lambda_2 - \bar{\lambda})^2 + (\lambda_3 - \bar{\lambda})^2}{\lambda_1^2 + \lambda_2^2 + \lambda_3^2}}. \quad (3.22)$$

This rotationally invariant parameter measures the fraction of the tensor that can be assigned to anisotropic diffusion. The FA has a range  $[0-1]$ , with 0 representing isotropic diffusion. Figure 3.9 B presents an example of ADC and FA images. The FA is low in cortical gray matter (0.2–0.4) and higher in the white matter, from  $\sim 0.45$ , in the subcor-



tical WM in the gyri, to  $\sim 0.8$  in the corpus callosum of healthy brain. In ventricles, where diffusion is more free, the FA is very low ( $\sim 0.1$ ). Figure 3.9 A illustrates examples of DT ellipsoids with same MD but different FA, ranging from nearly isotropic (lower FA) to anitropic (higher FA). Figures 3.9 C–D show examples of DT ellipsoids for an axial slice.

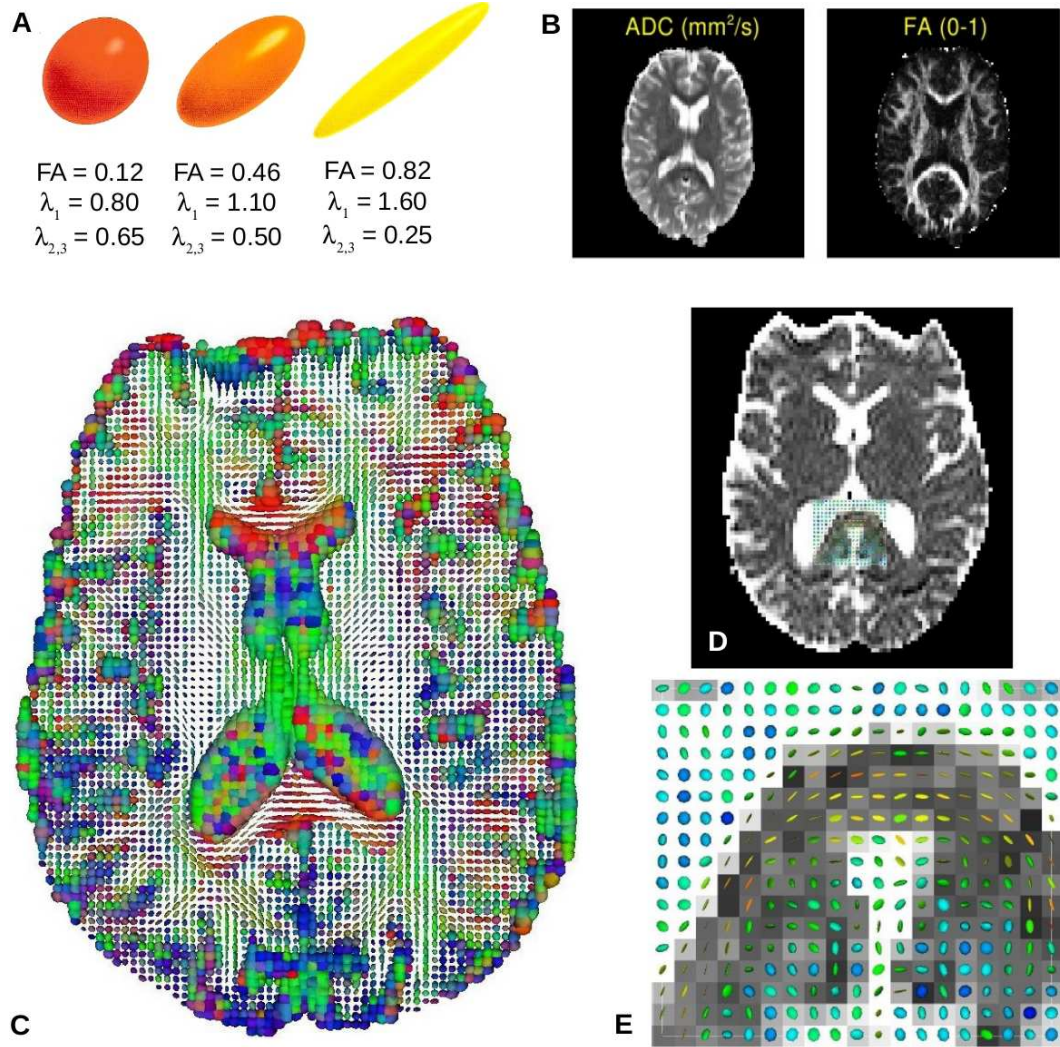


Figure 3.9: A: Examples of DT ellipsoids with same mean diffusivity ( $0.7 \times 10^{-3} \text{ mm}^2/\text{s}$ ) and different fractional anisotropy (FA), ranging from nearly isotropic (lower FA) to anitropic (higher FA) [Adated from [Johansen-Berg and Behrens \(2009\)](#)] B: Examples of MD and FA images. C: DT ellipsoids for an axial slice. Color coding according to FA. D: FA image with an overview of the position in brain for DT ellipsoids selection in E. E: Ellipsoids zoomed, color coding according to FA, background is an ADC image [Adated from [Arsigny \(2006\)](#)].

### Anisotropy as a measure of WM integrity

DTI studies determine if there are any differences in the molecular displacement of water in tissue, reflected by the DT eigenvalues, MD and FA, in specific brain regions in neurological disorders. In WM, the spacing between axons, the axon diameter, the



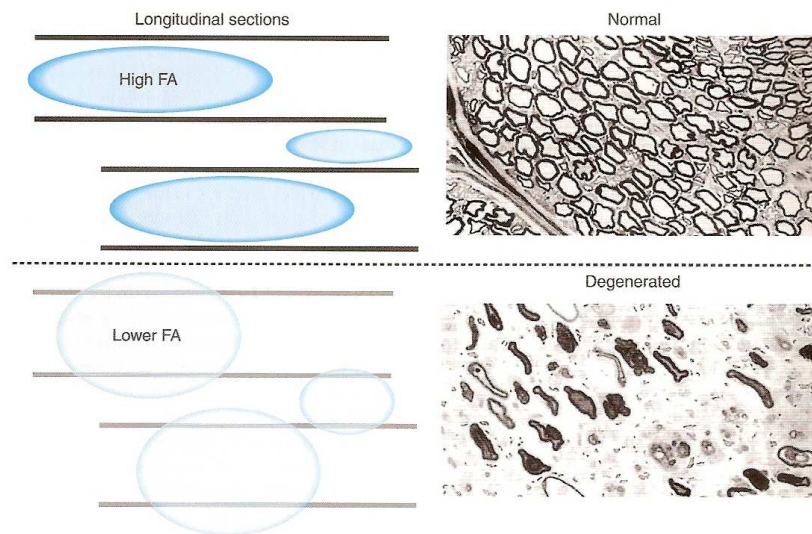


Figure 3.10: Example of FA as a measure of WM integrity. Structural damage to axons and myelin that results in a loss of directional barriers to water diffusion will reduce the degree of anisotropy. Electron micrographs are adapted from normal and degenerated frog sciatic nerve. [From [Johansen-Berg and Behrens \(2009\)](#)].

myelin thickness, etc., are variable even within the same tract, and thus, the barriers to diffusion have neither a simple, nor a regular geometry. Therefore, the measured diffusion parameters are some sort of weighted average of all the different types of water molecule behaviors within a particular voxel. Most DTI studies rely on quantitative analysis, where DT invariants of one tract in a control population are compared to the invariant values of the same tract in a patient population. These measurements expect that there had to be a consistent change throughout the voxel in order to detect a difference in diffusion.

Although, even within a tissue class such as WM, the degree of anisotropy can not be directly related with a specific structural component (number of axons, axon density, axon size, myelin thickness, packing, etc.), the degree of anisotropy is often used as a quantitative biomarker of WM “integrity”. Several experiments using non-pathological fibers without myelin have shown that anisotropy should not be considered myelin specific, as myelin is not essential in neural fibers to observe this biophysical property. Conversely, axonal membranes themselves are shown to be sufficient barriers alone to water diffusion perpendicular to the WM fibers, in comparison to diffusion along fibers. However, myelin appears to modulate the degree of anisotropy in a given fiber. A detailed bibliography about the relationship of water diffusion anisotropy and tissue microstructure is detailed in [Beaulieu \(2002\)](#) and [Johansen-Berg and Behrens \(2009\)](#), chapter 6. For an example of anisotropy as an indicator of structural damage is illustrated in Figure 3.10.

### DTI indexes and brain maturity

During brain maturation, DTI indexes as mean diffusivity and diffusion anisotropy present important changes. These changes reflect changes in brain tissue microstruc-

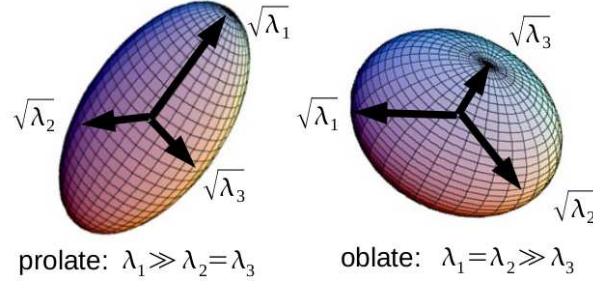


Figure 3.11: Examples of prolate and oblate DT ellipsoids [Adapted from Wikipedia].

ture. In the case of gray matter, this may reflect changes in the dendritic architecture of pyramidal cells and the presence or absence of radial glial fibers [Hüppi and Dubois (2010)].

In white matter, most fascicles seem to be organized during late intrauterine life, as fibers are to grow with the previously formed axons as guidance. Indeed, high anisotropy is already observed in poorly myelinated fascicles of premature newborns, and the patterns of fibers tracts were found already in place in infants with no differences between 5 and 17 weeks [Dubois et al. (2006)].

Two stages are assumed to be the main responsible for most diffusion changes related to WM maturation over the postnatal developmental period: the first stage of myelination, called *pre-myelination* and *myelination* [Dubois et al. (2008)]. Pre-myelination is characterized by the proliferation of oligodendrocytes lineage precursors, with a decrease in water content. As this early process is rather isotropic, it should lead to a decrease in the three diffusivity indexes ( $MD$ ,  $\lambda_{//}$  and  $\lambda_{\perp}$ ), without significant change in anisotropy. The fibers *myelination*, corresponding to the ensheathment of oligodendroglial processes around the axons, is accompanied by a further decrease in both membranes permeability and extracellular distance between membranes in the orthogonal direction to the fibers. Because of unchanged longitudinal diffusivity contrasting with decreased transverse diffusivity the anisotropy should increase while the mean diffusivity should decrease.

### Tensor shape

From FA equation (eq. 3.22), a tensor with high anitropy can present two different shapes: a *prolate* tensor, in which  $\lambda_1 \gg \lambda_2 = \lambda_3$ , or an *oblate* tensor, in which  $\lambda_1 = \lambda_2 \gg \lambda_3$  (see Figure 3.11). Since, neither the ADC nor the FA will indicate which form takes the tensor ellipsoid, two metrics have been used to characterize the DT geometry.

Prolateness can be calculated by the expression  $\delta_{1,2} = \lambda_1 - \lambda_2$ , while oblateness can be determined by  $\delta_{2,3} = \lambda_2 - \lambda_3$ .

### Colour encoded fiber orientation map

The fiber orientation can be represented using color maps, derived form DT information [Pajevic and Pierpaoli (1999)]. Each voxel can be color-encoded, following the direction

of the main tensor eigenvector, where the three cartesian directions are represented using different primary colors (red for left-right, blue for superior-inferior, and green for anterior-posterior). This yields to a cartography of the tracts positions and directions, where voxel brightness is weighted by the FA (see Figure 3.12).

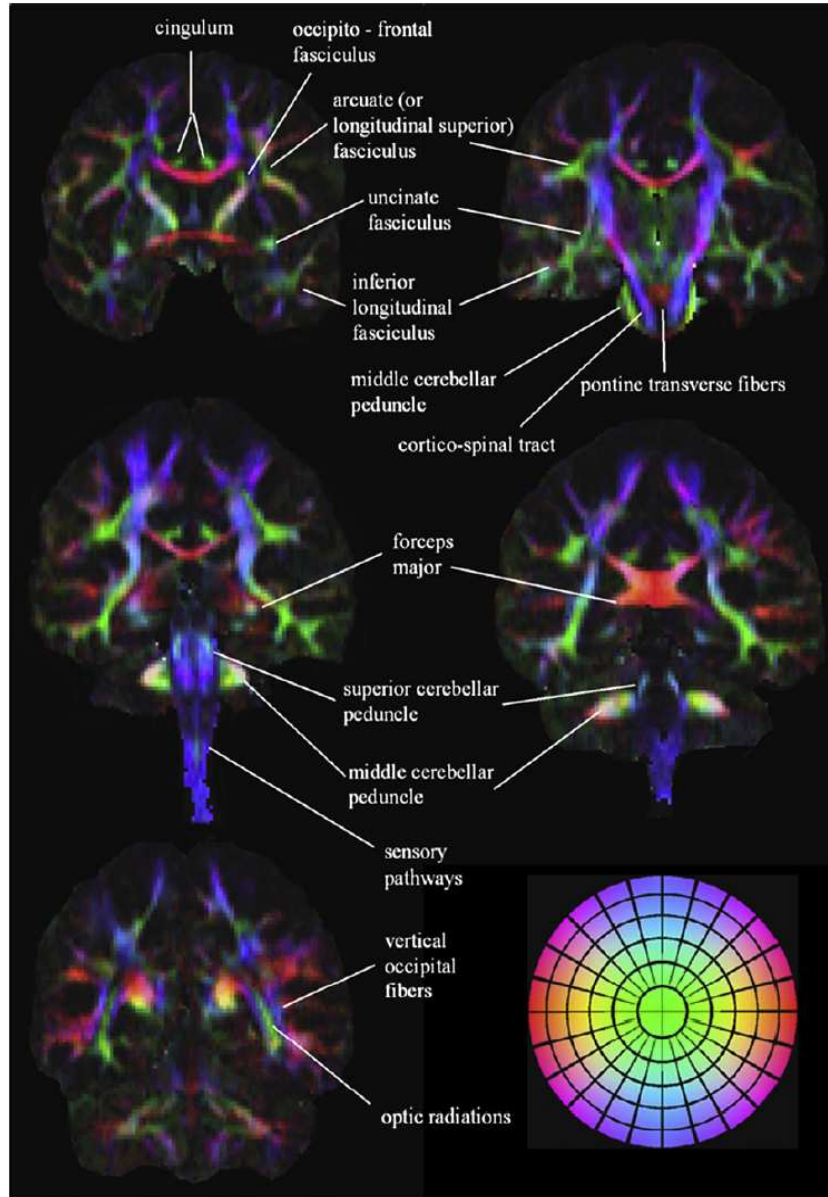


Figure 3.12: Colour encoded fiber orientation maps. Image values can be calculated with the expression  $(r, g, b) = 255FA(e_1x, e_1y, e_1z)$ , where  $e_1$  is the principal tensor eigenvector. Fibers that are predominantly oriented left-right are then shown in red, anterior-posterior fibers are shown in green and superior-inferior fibers are shown in blue (see colour wheel at lower right hand corner). [From Jones (2008)].

### 3.2.2 High Angular Resolution Diffusion Imaging (HARDI)

The signal in DWI decays exponentially with  $b$  when the diffusion is free and Gaussian. In the case where the volume-averaged diffusion PDF is non-Gaussian (e.g. when there are multiple diffusion compartments in slow exchange, or restrictive barriers), the NMR signal will no longer be mono-exponential and DTI model will be insufficient. In WM, a voxel, with size  $\sim 1\text{--}3\text{ mm}$ , contains hundreds of thousands of axon fibers, which axon radii are in the range of  $0.1\text{--}10\text{ }\mu\text{m}$ . Therefore, within a voxel a wide range of often complex configurations of fibers can exist. If more than one population of fibers are present, e. g. crossing fibers, we found a *partial volume* effect and the corresponding DT ellipsoid will be unable to represent the underlying diffusion process. About two third of white matter voxels are affected by this problem [Behrens et al. (2007)]. An example for a  $90^\circ$  fiber crossing configuration is shown in Figure 3.13. In this case, the DT is oblate, and contains none of the fiber population orientations. The *fiber orientation distribution function* (fODF) for this example has two spikes, corresponding to the two fiber populations present in the voxel. Mathematically, the fODF is a probability distribution on the sphere, where each point on the sphere corresponds to a unique orientation. In general, an ODF is usually represented by a “stretched sphere”, in which the radius is scaled by the value of the ODF. A colormap for the ODF values can also be applied to the mesh vertices. See Figure 3.16 for an example of an orientation distribution function.

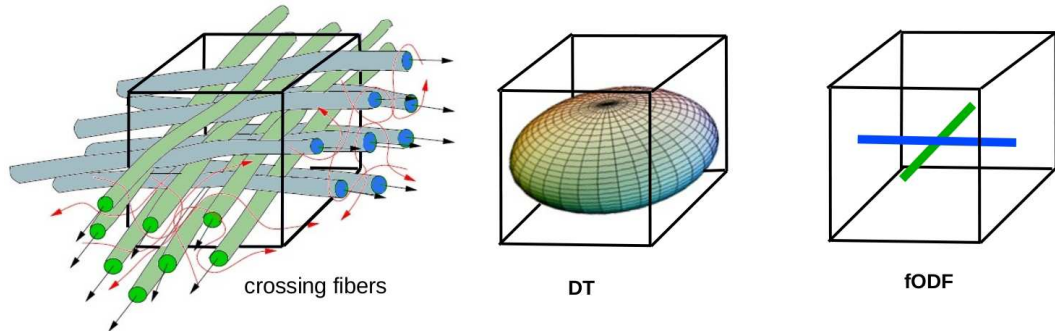


Figure 3.13: Illustration of partial volume effect within a voxel for two fiber populations representing a  $90^\circ$  fiber crossing configuration. The best fit DT will have an oblate shape, with an undefined principal direction. The fiber orientation distribution function (fODF) is composed by the two spikes, aligned with the two fiber population orientations [Adapted from Poupon (1999b)].

The limitation of DT when imaging voxels with multiple fiber populations can be overcome with **High Angular Resolution Diffusion Imaging** (HARDI), where the  $q$ -space is sampled along as many directions and magnitudes as possible for a better reconstruction of the diffusion PDF. HARDI acquisitions and reconstruction algorithms are in continuous development and improvement. We will present here a brief review of major HARDI reconstruction techniques. Some approaches are model-based while other are model-free. A schematic of the major multiple fiber HARDI reconstruction algorithms is shown in Figure 3.14.

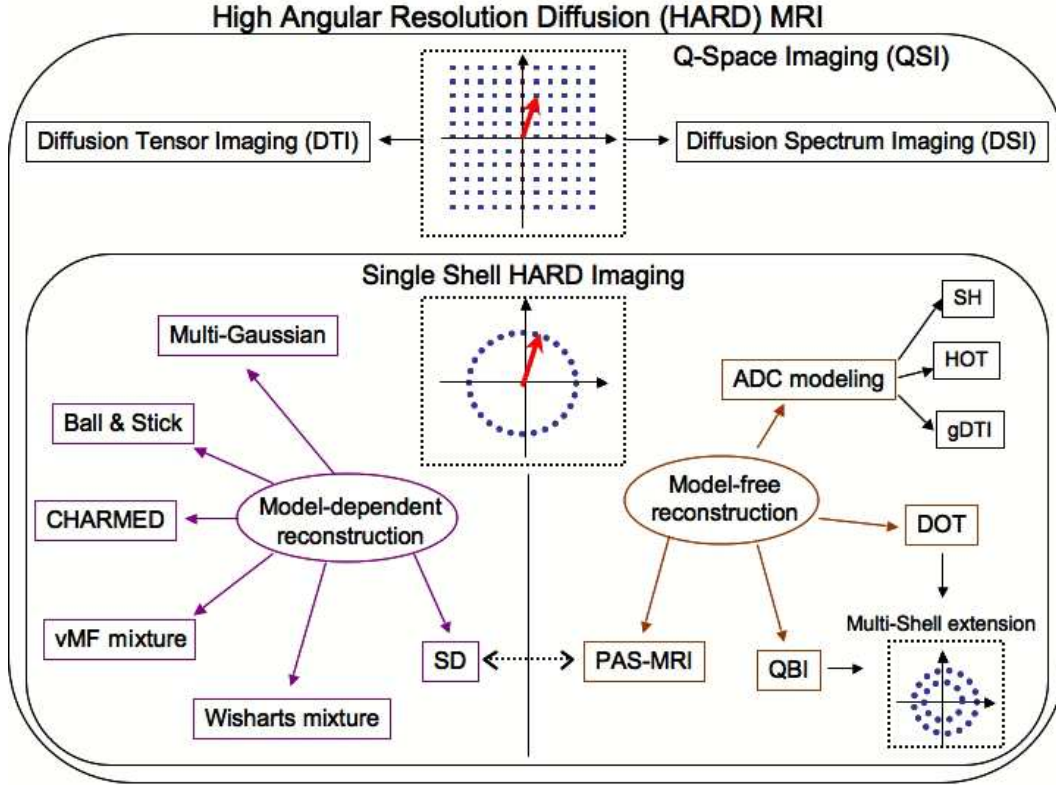


Figure 3.14: Major diffusion MRI acquisition and reconstruction methods [From Descoteaux (2008)].

HARDI reconstructions depend on the number of acquisitions and the gradient strength ( $b$ -value). Besides, the sampling of the  $q$ -space can be performed over a 3D cartesian grid or over a single shell sphere.

### Model-Based approaches

Model-based approaches resolve fiber-crossing by modeling distinct fiber population separately.

The **Multi-tensor model** or multi-Gaussian modeling is a generalization of DTI, which uses a mixture of  $n$  zero-mean Gaussians to describe the diffusion PDF. It assumes that the voxel contains  $n$  distinct populations of fibers and that there does not exist exchange within populations:

$$E(\hat{\mathbf{q}}_i) = \sum_{j=1}^n a_j e^{-b \hat{\mathbf{q}}_i^T \mathbf{D}_j \hat{\mathbf{q}}_i} \quad (3.23)$$

where  $a_j$  and  $\mathbf{D}_j$  are the volume fraction and the covariance of the  $j$ th population, and  $\hat{\mathbf{q}}_i$  is the diffusion direction encoding. The parameters of the model are estimated from a set of DW measurements. This model assumes that the number of fiber populations  $n$  is known. Most works use a maximum  $n$  of 2 because of instabilities in the non-linear optimization required for the parameter estimation. To make the numerical solution more



stable, constraints in the model can be added. For example, we can enforce the positive definiteness [Chen et al. (2004)] or fix the DT eigenvalues [Tuch (2002); Alexander et al. (2001)]. Also, a multi-Gaussian extension based on diffusion basis function of Gaussians has been used to recover multiple crossing fibers [Ramirez-Manzanares et al. (2007)].

The “**Ball and stick**” model [Behrens et al. (2003)] assumes that water molecules belong to one of two populations: a restricted population within or around fibers and a free population that does not interact with fibers. Restricted diffusion is modeled with an anisotropic Gaussian distribution with only one non-zero eigenvalue, while an isotropic Gaussian distribution is used for the free population. A mixture of restricted compartments can be used for a better representation of multiple fiber populations [Behrens et al. (2007)].

A **Composite hindered and restricted model of diffusion (CHARMED)**, [Assaf et al. (2004)] models the restricted diffusion with an analytical model for diffusion restricted to a cylinder [Neuman (1974)]. The extracellular space is modeled by a hindered diffusion using an anisotropic Gaussian model.

### Model-free approaches

Model-free approaches are *non-parametric* techniques that do not need compartment-specific information. These non-parametric techniques estimate the fODF from diffusion MRI measurements, avoiding a model selection and the definition of the number of compartments.

Some approaches reconstruct the *diffusion orientation distribution function* (dODF), which consists in an isosurface of the diffusion PDF for a certain radius  $r$ , representing the diffusion probability distribution on the sphere.

The dODF contains then the full angular information of the diffusion PDF and is defined as

$$\Psi(\mathbf{u}) = \int_0^\infty P(\alpha\mathbf{u})d\alpha, \quad (3.24)$$

where  $\mathbf{u}$  is restricted to be a unit vector. Thus, the dODF is a function on the unit sphere describing the average probability that a particle will diffuse into any given solid angle.

*Diffusion Spectrum Imaging* (DSI) and *q-ball imaging* (QBI) reconstruct the dODF. Other methods recover a function slightly different, containing the same information than the dODF. This is the case for DOT algorithm and the original PAS-MRI algorithm. Spherical deconvolution algorithms recover a more direct estimate of the fODF.

Figure 3.15 presents an illustration of fODFs and dODFs for several simple WM configurations. Both, the fODF and the dODF are probability distributions on the sphere, with the peaks in similar directions. However, while the fODF presents spikes only along the orientations of fiber populations, the dODF is a smoother function as water molecules diffusion occurs in all directions, even perpendicular to the fibers.

### Diffusion Spectrum Imaging (DSI)

Diffusion Spectrum Imaging (DSI), samples the signal on a Cartesian grid of points in



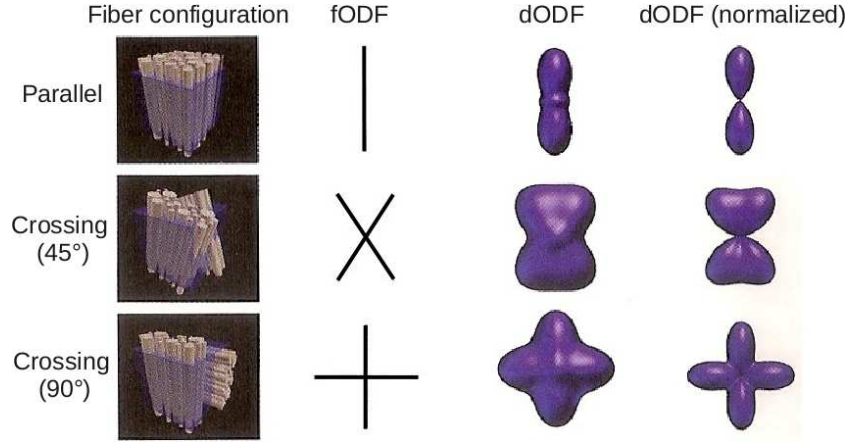


Figure 3.15: Illustration of fODFs and dODFs for several simple WM configurations. The normalized dODF is rescaled so that its minimum value become zero. This emphasizes the directional structure of the dODF without affecting peak directions [From [Johansen-Berg and Behrens \(2009\)](#)].

$q$ -space and then takes the 3D inverse Fourier transform to obtain an approximated PDF [[Wedeen et al. \(2000\)](#); [Tuch et al. \(2002\)](#); [Wedeen et al. \(2005\)](#)]. It derives from  $q$ -space imaging (QSI) [[Callaghan \(1991\)](#)]. The acquisition scheme for DSI typically samples the whole interior of a sphere in a regular grid, but some acquisitions schemes acquire only an hemisphere since the signal is supposed to be symmetric [[Gigandet \(2009\)](#)]. An example of the diffusion spectrum obtained with DSI in the case of a fiber crossing, as well as the corresponding dODF are shown in Figure 3.16.

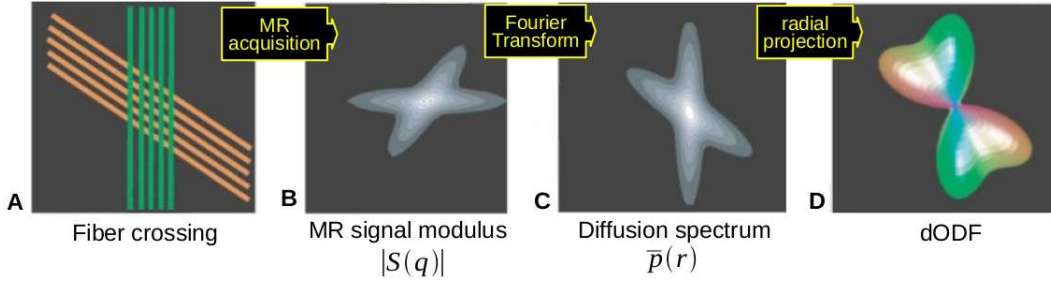


Figure 3.16: . DSI reconstruction scheme. A: tissue in a voxel with two populations of fibers that cross. B: Through the MR acquisition scheme the signal is sampled. C: In order to reconstruct the diffusion spectrum, the 3D discrete Fourier transform is taken. D: To simplify the representation of an imaging slice, the angular structure of diffusion is represented by the dODF (a polar plot of the radial projection). The color coding corresponds to the orientation of diffusion (green: vertical diffusion; red: transverse diffusion). [Adapted from [Wedeen et al. \(2005\)](#)].

The major limitations of DSI are the acquisition requirements. Firstly, the number of measurements needed for the sampling of the  $q$ -space is very high ( $\sim 500$ – $1000$ ), leading to an imaging time impracticable for very high resolution images. Another limitation is the maximum  $b$ -value needed for the acquisition ( $\sim 10000$ – $20000 \text{ s mm}^{-2}$ ). Due to relatively low maximum gradient amplitudes implemented in conventional MRI systems, high  $b$ -values require, in practice, a pulse duration  $\delta$  almost similar to the pulse spacing,  $\Delta$ . This

violates the narrow pulse assumption for Fourier relationship between the MR signal and the diffusion spectrum, which yields to slightly, but consistently underestimated diffusion displacements. The result is a considerable blurring in the PDF and consequently in the derived dODF, although, the overall distribution shape will be correct. For these reasons, i. e. long acquisitions times and a maximal diffusion gradient too high, DSI is not applicable in clinical studies. In research, DSI is only now starting to play a significant role in brain imaging as more centers are equipped with high-end magnets and multichannel head coils, and as commercially available pulse sequences are being distributed [Hagmann et al. (2010)].

### Single-shell HARDI techniques

Spherical acquisition schemes, also called *single-shell* HARDI techniques have been developed since through some assumptions they are able to overcome the “fiber-crossing problem” without having to compromise to much scan time and without major hardware requirements [Hagmann et al. (2010)]. These acquisitions have both, the diffusion time  $\tau$  and  $|\mathbf{q}|$  fixed (and then a  $b$  fixed), and only gradient direction varies among measurements. In the following sections we will review the  $q$ -ball imaging (QBI) and the *spherical deconvolution* (SD) as these techniques have presented an increasing development in the last years.

#### $q$ -ball imaging (QBI)

$q$ -ball imaging (QBI) approximates the dODF using measurements from a single-shell acquisition based upon a transformation called Funk-Radon transform (FRT),  $\mathcal{G}$  [Tuch (2002, 2004)]. This relationship establishes that the dODF (defined in equation 3.24) for a particular diffusion direction is equivalent to the circular integral about the equator perpendicular to the direction.

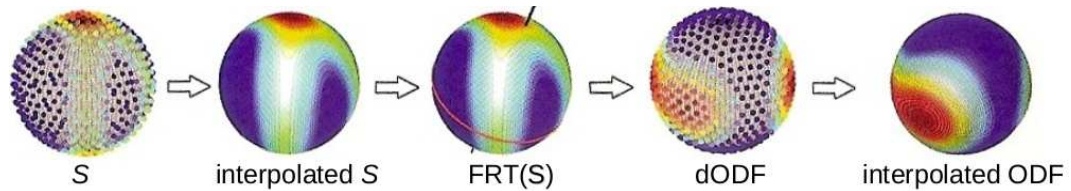


Figure 3.17: Qball reconstruction scheme. We start (left) with samples of  $S$  at fixed  $|\mathbf{q}|$  (panel 2). To sample the dODF in one direction, we sum the interpolated  $S$  around the perpendicular equator (panel 3). We repeat the procedure in various directions to obtain many samples of the dODF (panel 4). Finally, we may interpolate to approximate the continuous dODF. [From Johansen-Berg and Behrens (2009)].

The FRT can be expressed as

$$\mathcal{G}[f(\mathbf{w})](\mathbf{u}) = \int \delta(\mathbf{u}^T \mathbf{w}) f(\mathbf{w}) d\mathbf{w} \quad (3.25)$$

where  $\mathbf{u}$  and  $\mathbf{w}$  are constrained to be unit vectors. Tuch deduced the relation between the

dODF and the FRT, expressed in cylindric coordinates [(Tuch, 2004, Appendix A)]:

$$\mathcal{G}_{q'}[S(\mathbf{q})](\mathbf{u}) = 2\pi q' \int P(r, \theta, z) J_0(2\pi q' r) r dr d\theta dz \quad (3.26)$$

where  $q'$  is the radius of the acquisition shell in  $q$ -space and  $J_0$  is the zeroth-order Bessel function. For high  $\mathbf{q}$  values,  $J_0$  gets sharper and can be approximated by Dirac function  $\delta$ . This gives the  $q$ -ball expression for the dODF

$$\Psi(\mathbf{u}) = \int P(r, \theta, z) \delta(r) \delta(\theta) r dr d\theta dz. \quad (3.27)$$

See Figure 3.17 for an illustration of  $q$ -ball reconstruction. For the calculation, the discrete set of measurements must be interpolated to estimate the signal at each point of the circle. This approximation is then valid for a high value of  $b$  ( $b \geq 3,000 \text{ smm}^{-2}$ ) and an important number of measurements ( $\sim 200$ ). Anyway, due to the approximation, the calculated dODF will be smoothed, which will reduce the angular resolution and precision of peaks directions.

The original implementation [Tuch (2004)] used radial basis functions to interpolate  $S$  and has a numerical solution. Later works used analytical spherical harmonics (SH) for reconstructing the solution, which gives a more compact representation of the dODF [Anderson (2005); Hess et al. (2006); Descoteaux et al. (2007)]. These approaches avoid numerical computations, as the FRT has analytic form if  $S$  is a linear combination of SH functions, allowing a faster and more robust to noise solution.

**Spherical Harmonics Basis and numerical  $q$ -ball solution.** SH form an orthonormal set of functions with respect to the inner product. Spherical harmonics  $Y_\ell^m$  of order  $\ell$  and degree  $m$  are defined as

$$Y_\ell^m(\theta, \phi) = \sqrt{\frac{2\ell + 1}{4\pi} \frac{(\ell - m)!}{(\ell + m)!}} P_\ell^m(\cos \theta) e^{im\phi} \quad (3.28)$$

where  $\theta \in [0, \pi]$  and  $\phi \in [0, 2\pi)$ . Descoteaux et al. (2007) defined a modified basis considering only SH of even degree, in order to impose a real-valued constraint, using a single index  $j$  in terms of  $\ell$  and  $m$ :

$$Y_j = \begin{cases} \sqrt{2} \cdot \text{Re}(Y_\ell^{|m|}), & \text{if } m < 0 \\ Y_\ell^m, & \text{if } m = 0 \\ \sqrt{2} \cdot (-1)^{m+1} \text{Im}(Y_\ell^m), & \text{if } m > 0. \end{cases} \quad (3.29)$$

where  $\text{Re}(Y_\ell^m)$  and  $\text{Im}(Y_\ell^m)$  represent the real and imaginary parts of  $Y_\ell^m$  respectively,  $\ell = 0, 2, 4, \dots, L$ ,  $m = -\ell, \dots, 0, \dots, \ell$ , and  $j(\ell, m) = (\ell^2 + \ell + 2)/2 + m$ . Figure 3.18 shows some examples of modified spherical harmonics.

Thus, a truncated smooth estimation of the HARDI signal  $S_i$ , for a particular encoding

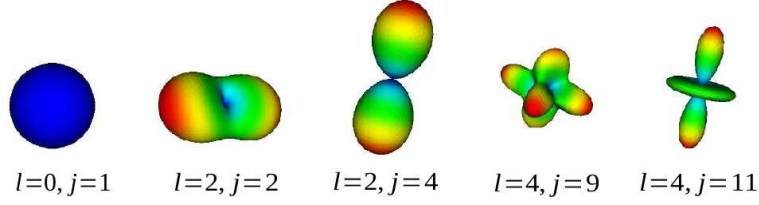


Figure 3.18: . Examples of modified spherical harmonics for orders  $\ell = 0, 2$  and  $4$  [Adapted from Descoteaux (2008)].

gradient direction  $i$  can be formulated as

$$S(\theta_i, \phi_i) = \sum_{j=1}^R c_j Y_j(\theta_i, \phi_i) \quad (3.30)$$

where  $R$  is the number of terms in the modified real and symmetric SH basis  $\mathbf{Y}$  of order  $\mathbf{L}$ , and  $c_j$  are the SH coefficients.

In order to determine the  $c_j$  coefficients for  $N$  encoding directions, we need to solve an over-determined linear system using a  $(N \times R)$  matrix  $\mathbf{B}$ , constructed with the discrete modified SH basis:

$$\mathbf{B} = \begin{pmatrix} Y_1(\theta_1, \phi_1) & Y_2(\theta_1, \phi_1) & \cdots & Y_R(\theta_1, \phi_1) \\ \vdots & \vdots & \ddots & \vdots \\ Y_1(\theta_N, \phi_N) & Y_2(\theta_N, \phi_N) & \cdots & Y_R(\theta_N, \phi_N) \end{pmatrix}. \quad (3.31)$$

Then, the least-squares solution for the  $(R \times 1)$  SH coefficient matrix  $\mathbf{C}$  is

$$\mathbf{C} = (\mathbf{B}^T \mathbf{B} + \lambda \mathbf{L})^{-1} \mathbf{B}^T \mathbf{S} \quad (3.32)$$

where  $\mathbf{S}$  is the  $(N \times 1)$  vector of input signal  $S_i$ , and  $\mathbf{L}$  is a  $(R \times R)$  Laplace-Beltrami regularization matrix with entries  $\ell(j)^2(\ell(j) + 1)^2$  along the diagonal.

**Analytical  $q$ -ball solution.** Descoteaux et al. (2007) demonstrated a new corollary of the 3D Funk-Hecke theorem for the analytical evaluation of integrals of functions on the sphere, to obtain a mathematical simplification of the Funk-Radon transform. The FRT can then be expressed in function of the SH series, in a given unit vector direction  $\mathbf{u}$ :

$$\mathcal{G}[S](\mathbf{u}) = \sum_{j=1}^R \frac{2\pi P_{\ell(j)}(0)}{S_0} c_j Y_j(\mathbf{u}) \quad (3.33)$$

where  $P_{\ell}(0)$  is the Legendre polynomial of degree  $\ell$  evaluated at 0. The SHs are then eigenfunctions of the FRT with eigenvalues depending only on the order  $\ell$  of the SH series. The ODF reconstruction in terms of SH coefficients, denoted by the  $(R \times 1)$  vector  $\mathbf{C}'$ , is

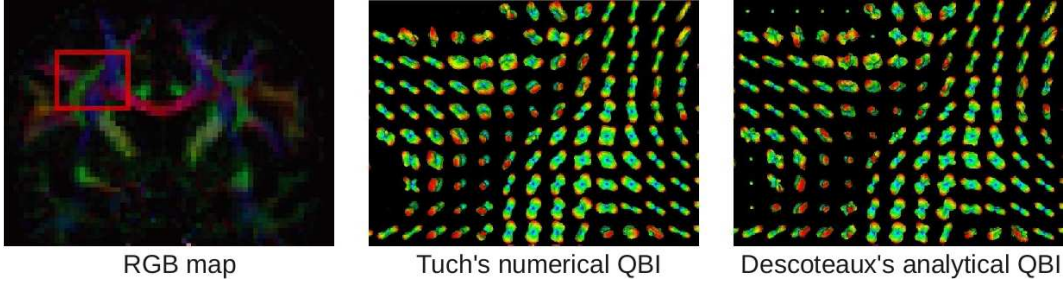


Figure 3.19: dODFs for the analytical and numerical QBI. The region of interest shows the cortical spinal tract (CST) and corpus callosum (in the plane) and the CST and longitudinal superior fibers (coming out of the plane) cross. From [Descoteaux \(2008\)](#)]

simply a diagonal linear transformation given by

$$\mathbf{C}' = \mathbf{P}\mathbf{C} \quad (3.34)$$

where  $\mathbf{P}$  is the Funk-Hecke matrix, with diagonal elements  $2\pi P_{\ell(j)}(0)/S_0$ . The final estimated ODF on the sphere can be obtained by  $\Psi = \mathbf{B}\mathbf{C}'$ . With the addition of Laplace-Beltrami regularization it is therefore possible to compute a fast and robust analytical QBI solution (see Figure 3.19).

### Generalized FA (GFA)

[Tuch \(2004\)](#) defined a generalized fractional anisotropy as an analog for  $q$ -ball of the FA in DTI. The GFA is a measure of variation of the dODF,  $\Psi$ , mathematically defined by

$$GFA = \left| \frac{\int (\Psi(\mathbf{u}) - \bar{\Psi})^2 d\mathbf{u}}{\int \Psi(\mathbf{u})^2 d\mathbf{u}} \right|^{\frac{1}{2}} \quad (3.35)$$

where  $\bar{\Psi} = (4\pi)^{-1} \int \Psi(\mathbf{u}) d\mathbf{u}$ . This definition extends to any other function of the sphere, for example, to any fODF.

### Spherical Deconvolution (SD)

Spherical Deconvolution (SD) methods recover the fODF directly from the measurements. These approaches, originally proposed by [[Tournier et al. \(2004\)](#)], consider the HARDI signal as the sum of measurements from a mixture of distributions of fiber orientations. Each measurement is viewed as a convolution of the response function produced by a single fiber ( $R$ ) with the expected true fiber distribution (fODF). Then, spherical deconvolution aims to recover an estimation of the fODF by deconvolving the measurements with  $R$ . An illustration of spherical deconvolution is shown in Figure 3.20. SD requires a model of diffusion for a fiber population in order to determine the fiber response function,  $R$ . One strategy is to model  $R$  with a Gaussian function [[Alexander \(2005\)](#)]. Other works derive  $R$  directly from real datasets calculating the average signal from most anisotropic voxels [[Tournier et al. \(2004\)](#); [Alexander and Barker \(2005\)](#)].

A major limitation of SD is its susceptibility to noise and severe instabilities for high harmonic orders, which results in spurious peaks in the recovered fODF. To reduce this effect, [Tournier et al. \(2004\)](#) used low-pass filtering, but this solution, called *filtered spherical deconvolution*, also reduces angular resolution. An improved solution, called *super-resolved constrained spherical deconvolution* was implemented in [[Tournier et al. \(2007\)](#)] by the means of a modified Tikhonov regularisation method.

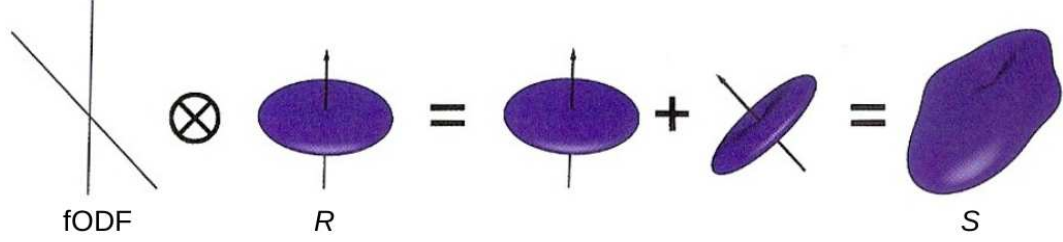


Figure 3.20: . Spherical deconvolution illustration. The response function  $R$  convolved with the fODF, gives the observed  $S$ . In the example, the convolution becomes a sum for two directions as the true fODF is zero for all others. [From [Johansen-Berg and Behrens \(2009\)](#)].

### Sharp Spherical Deconvolution of the dODF

More recently, [Descoteaux et al. \(2009b\)](#) proposed a sharp spherical deconvolution transform reconstructed from  $q$ -ball imaging with the constrained regularization described in [[Tournier et al. \(2007\)](#)]. The starting point of this deconvolution method is not the measured signal but the estimated  $q$ -ball dODF ( $\Psi_d$ ). The estimated smooth dODF is deconvolved by the dODF for a single fiber ( $R'$ ) in order to obtain a sharpened fiber ODF,  $\Psi_f$  (see Figure 3.21).

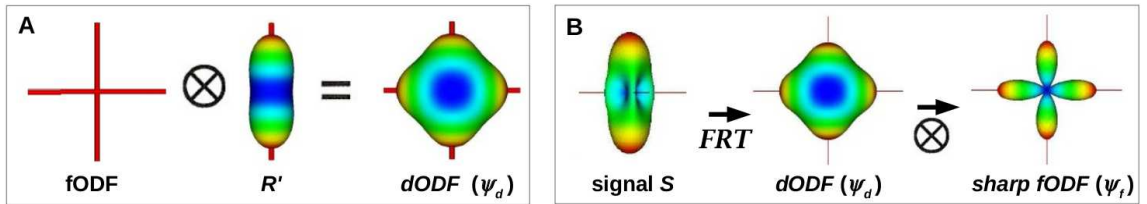


Figure 3.21: Sketch of the convolution/deconvolution of the dODF. In A, the convolution between the true fODF and the dODF kernel  $R'$  produces a smooth dODF. B shows the sketch of the deconvolution sharpening. The Funk-Radon Transform (FRT) of the HARDI signal on the sphere produces a smooth dODF. This dODF is transformed into a sharp fODF by the deconvolution with the dODF kernel of A [From [Descoteaux \(2008\)](#)].

The convolution on the sphere between the single fiber diffusion kernel  $R'$  and  $\Psi_f$  can be written as

$$\Psi_d(\mathbf{u}) = \int_{|\mathbf{w}|=1} R'(\mathbf{u} \cdot \mathbf{w}) \Psi_f(\mathbf{w}) d\mathbf{w}. \quad (3.36)$$

In order to solve this integral,  $\Psi_d$  and  $\Psi_f$  are expressed using their respective SH estimation of order  $\ell$ , given by  $\Psi = \sum_j c'_j Y_j(\mathbf{u})$  and  $\Psi_f = \sum_j f_j Y_j(\mathbf{u})$ . Then, the Funk-Hecke



theorem (equation 3.33) can be applied to solve the convolution integral between  $R'$  and the spherical harmonic  $Y_j$  over the sphere, leading to the expression

$$\Psi_f(\mathbf{u}) = \sum_{j=1}^R \frac{c'_j}{r'_j} Y_j(\mathbf{u}) \quad (3.37)$$

for any direction  $\mathbf{u}$ , where

$$r'_j = 2\pi \int_{-1}^1 P_{\ell(j)}(t) R'(t) dt. \quad (3.38)$$

The model of diffusion for a single fiber can be assumed to be an axially symmetric and prolate tensor ( $\lambda_1 \gg \lambda_2 = \lambda_3$ ) as in [Anderson (2005)]. Thus,  $R'$  can be written as

$$R'(t) = \frac{1}{8\pi b \sqrt{\lambda_2^2 \lambda_1}} \frac{1}{\sqrt{(\lambda_2/\lambda_1 - 1)t^2 + 1}}. \quad (3.39)$$

This method improves fiber detection of QBI by increasing angular resolution.

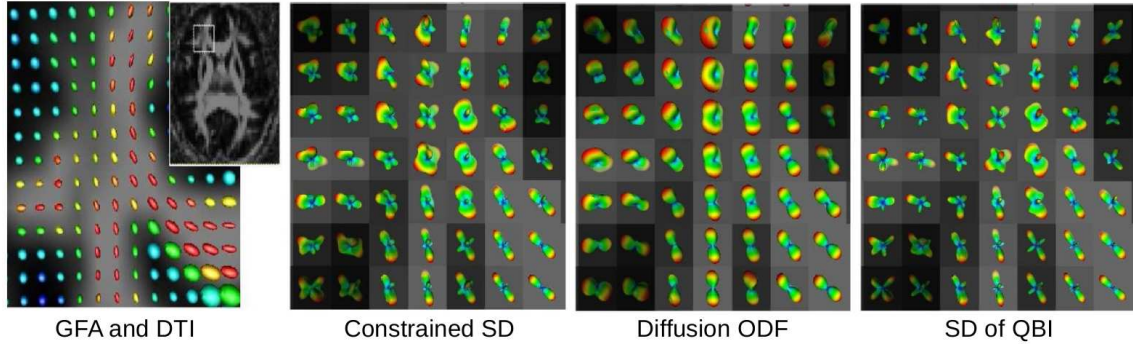


Figure 3.22: Axial slice showing intersection between the genu of the corpus callosum, the capsule fibers and the superior frontal gyrus fibers. We show the diffusion tensors, the constrained SD, the  $q$ -ball dODF and the sharp fODF overlaid on the GFA map. [From Descoteaux (2008)].

In general, spherical deconvolutions require an inferior number of measurements than QBI ( $\sim 60-80$ ), with similar requirements for  $b$ -value.

### Multiple-shell HARDI techniques

Recently, several techniques have been developed for HARDI data from multiple  $q$ -shells. These methods use acquisitions with several  $b$ -values in order to obtain a better modeling of the diffusion propagator. Multiple-shells benefit from the high signal-to-noise ratio (SNR) of the data acquired at low  $b$ -values and high angular contrast-to-noise ratio (CNR) at high  $b$ -values. For example, Aganj et al. (2010), by considering the solid angle factor, use a mathematically better definition of the ODF and resulting in a dimensionless and normalized ODF expression that can be used to estimate ODFs from single- or multiple-shell acquisitions. In another work, Descoteaux et al. (2009a) propose a diffusion propagator imaging (DPI), an analytical and linear solution of the ensemble average propagator based on a Laplace equation modeling of the diffusion signal.

### 3.3 MR Diffusion Tractography

MR diffusion tractography, also called WM tractography, uses the directional information from diffusion measurements to estimate the trajectories of white matter pathways. While invasive techniques can actively trace individual axons in animals, WM tractography is the only technique able to study human whole-brain WM tracts *non-invasively* and *in vivo*. WM tractography has major limitations related with the indirect nature and low resolution of DW data. Results contain a significant quantity of false negatives and false positives due to the inability to determine precisely the underlying fiber configuration within a voxel. Furthermore, the impossibility to differentiate efferent and afferent pathways is a fundamental limitation. However, the non-invasive nature of tractography and all the developments and improvements in DW-MRI allow the study of human brain connectivity and contribute to a better understanding of the human brain.

Tractography algorithms can be deterministic or probabilistic, local or global, model-based or model-free, and basically with two kinds of results: 3D curves or voxel-maps. In this section we will review in more detail the *streamline tractography* as its output, a set of 3D curves, is the main input of our thesis work.

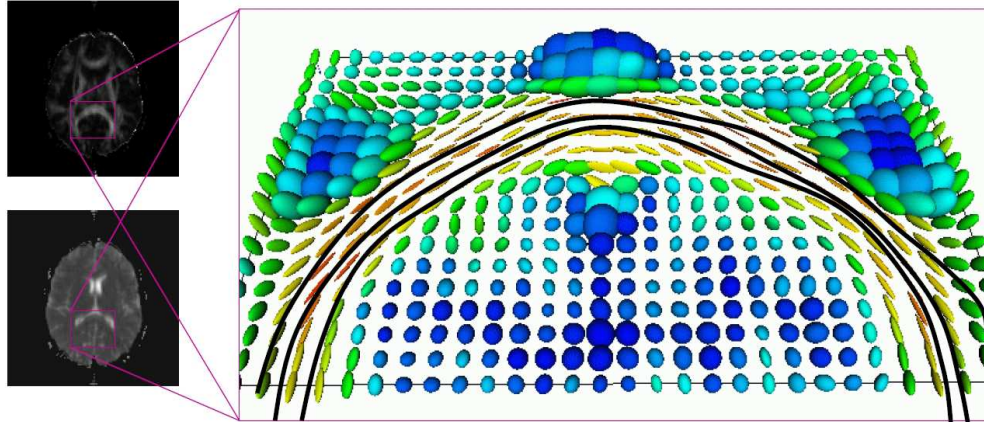


Figure 3.23: Visualization of the orientation of the principal eigenvector of one slice on a per voxel basis (projection into the axial plane), with color coding according to FA. In the slice, the traced fiber tracts reconstruct the trajectory of fibers from the splenium of the corpus callosum. From a seed point, the tractography algorithm follows the vector field determined, in DTI, by the DT principal eigenvector ( $e_1$ ).

**Streamlines** are trajectories that follow the direction of an underlying vector field. The lines can be reconstructed by starting with a “seed” and following the local vector field step-by-step. Streamline tractography defines, then, 3D space-curves that are tangent to the local fiber orientation given by the diffusion local model. These tractographic 3D curves are commonly referred to as “fibers” or “tracts”, though they do not represent individual fibers or axons. Instead, the curves represent an estimate of the trajectory of some larger white matter fiber tract. In this thesis, we will use the terms “fiber”, “tract” or “fiber tract” to refer to the trajectories obtained with tractography algorithms. Consequently, a

“fiber bundle” will be a bundle of tractographic curves and not a real anatomical bundle of neural fibers. When required, we will use the expression *white matter tract*, or *WM tract*, to address a fiber bundle representing a white matter fiber tract described by anatomists.

Mathematically, a streamline can be expressed by an equation describing the trajectory evolution [Basser et al. (2000)]:

$$\mathbf{r}'(s) = \mathbf{v}(\mathbf{r}(s)) \quad (3.40)$$

where  $\mathbf{r}(s)$  is the point  $(x, y, z)$ , located at distance  $s$  along the streamline from the starting point  $\mathbf{r}_0$ , and  $\mathbf{v}(s)$  is the local diffusion model at point  $\mathbf{r}(s)$ . The calculation of the streamline requires the resolution of this differential equation by the integration of  $\mathbf{v}$ :

$$\mathbf{r}(t) = \mathbf{r}_0 + \int_0^t \mathbf{v}(\mathbf{r}(s)) ds \quad (3.41)$$

which implies the accumulation of errors along the streamline computation. These accumulated errors are the result of integration errors, and local diffusion model estimation errors due to the uncertainty of the local diffusion and noise.

Streamline tractography requires a Region of Interest (ROI) as input; from each voxel of the ROI, a defined number of seeds are placed for trajectories generation. From each seed point, a streamline is tracked in both, retrograde and anterograde directions. The approach that uses a brain white matter mask as seed ROI is usually called a “whole-brain” or “brute-force” tractography.

In the next section (3.3.1) we will review the main streamline deterministic tractography algorithms and the concept of fiber trajectory regularization. Then, in section 3.3.2, we continue with streamline probabilistic tractography approaches, developed to better deal with fiber crossings. Finally, in section 3.3.3 we overview other important tractography techniques.

### 3.3.1 Streamline Deterministic Tractography

Streamline deterministic algorithms follow the most probable direction given by the diffusion local model [Mori et al. (1999); Conturo et al. (1999); Poupon (1999a); Basser et al. (2000); Mori et al. (2002)]. Earlier algorithms, applied to DTI, use the principal eigenvector ( $\mathbf{e}_1$ ) as the direction of local fiber orientation. Figure 3.23 shows an illustration of streamline tractography in DTI.

The FACT algorithm (Fiber Assignment by Continuous Tracking) [Mori et al. (1999)] assigns to each voxel the direction of the principal eigenvector. Thus, each trajectory follows the direction indicated by the local DT, without interpolation, as illustrated in Figure 3.24 (A1). Newer approaches require the interpolation of the diffusion local field at each trajectory point from the calculated values on the measurement grid [Conturo et al. (1999); Basser et al. (2000)] (see Figure 3.24 (A2)). These methods produce lower propagation errors than those without interpolation and are more robust to noise [Lazar and Alexander (2003)]. Tracking methods use either a constant integration step size [Con-

turo et al. (1999)] or a step size adapted to the trajectory curvature [Basser et al. (2000)]. Besides, different approaches use different numerical integration approximations, from the Euler method, which assumes a constant value during each step, to higher order integration methods, like Runge-Kutta schemes of order 2 or 4. Integration errors diminish with decreasing step size and more accurate approximations.

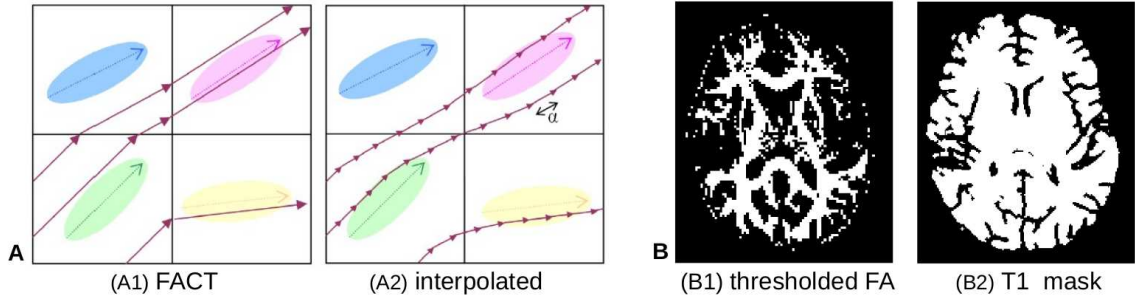


Figure 3.24: A: Example algorithms for deterministic streamline tractography in DTI. In A1, the fiber tracts are reconstructed using the FACT method [Mori et al. (1999)], where the trajectories follow the DT principal eigenvector of each voxel. In A2, the trajectories are calculated using interpolation between grid points [Conturo et al. (1999)], [From Perrin (2006)]. B: Propagation masks used as a tracking stopping criterion. In B1, the typical thresholded FA mask ( $th = 0.1$ ). In B2, a propagation mask constructed from a T1 image [Perrin et al. (2008)].

### Stopping criteria

One stopping criterion uses a **propagation mask** of white matter; if a point exits the mask, the tracking is stopped for the corresponding line. Typically the WM mask is a *thresholded mask of FA* with usual threshold values of  $\sim 0.1$ – $0.2$  (see Figure 3.24 (B1)). The tracking is then stopped if the anisotropy is too low, assuming that when FA is too small, the uncertainty of the principal diffusion direction is high. However, this criterion is rough as the FA value is not specific of a particular structural configuration and therefore constraints tracking results to region of WM with high anisotropy. In particular, FA (or GFA) can be very low in fiber crossings representing more than 2/3 of WM voxels, thus putatively discarding many valid tracts. Furthermore, because the dMRI resolution is generally coarser than standard T1-weighted MRI (on the order of 2 mm isotropic), voxels at the interface between the WM and the cortex may suffer from severe partial volume effects, artificially diminishing the FA values. Therefore, many true-positive neuronal pathways may not be revealed.

Another option is to use a *propagation mask calculated from a T1 image* [Perrin et al. (2008); Guevara et al. (2011b)]. In this case, a better definition of the WM can be achieved, as shown in Figure 3.24 (B2). This approach can be used with tracking algorithms with regularization to resolve the trajectory direction in low anisotropy locations. Besides, a good registration between T1 and T2 images is needed.

A second common stopping criterion, a **maximum curvature** threshold, aims at avoiding fast changes in the streamline direction. This criterion is based on the assumption

that real WM fibers do not present high curvatures. Therefore, if the angle between the incident trajectory and the local vector field is greater than the threshold ( $\sim 30^\circ$ – $45^\circ$ ), the tracking is stopped.

### Regularized algorithms

Alternative streamline algorithms can better resolve fibers in regions where there are crossing or fanning fibers using *trajectory regularization*. They involve the use of more information like the entire tensor information for DTI case, and the incident streamline direction.

The “Tensorlines” tracking method [Weinstein et al. (1999); Lazar et al. (2003)] estimates the local pathway direction using the tensor deflection (TEND). During the pathway calculation, the new direction ( $\mathbf{v}_{out}$ ), considers both, the local DT ( $\mathbf{D}$ ) and the incident direction ( $\mathbf{v}_{in}$ )

$$\mathbf{v}_{out} = f\mathbf{e}_1 + (1 - f)[(1 - g)\mathbf{v}_{in} + d\mathbf{D}\mathbf{v}_{in}] \quad (3.42)$$

where  $\mathbf{e}_1$  is the DT principal eigenvector. Figure 3.25 illustrates the behavior of this tracking algorithm that includes trajectory regularization. This method is less sensitive to noise and low anisotropy values than the classic approaches. However, the choice of parameter values ( $f$  and  $g$ ) is a major problem.

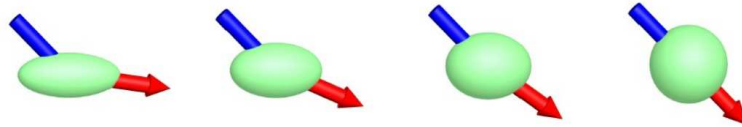


Figure 3.25: Example of TEND algorithm behavior for different shapes of local DT ellipsoids. The incident direction  $\mathbf{v}_{in}$  is in blue while the out direction  $\mathbf{v}_{out}$  is in red [From Weinstein et al. (1999)].

Another approach uses a markovian regularization of the directions field to define the fibers as a trade-off between high diffusion along fibers and low curvature constraints [Poupon et al. (2000)].

### Streamline based on HARDI

Higher diffusion models can overcome problems associated with single-tensor based methods, particularly when crossing fibers are involved. For example, an extension of the streamline based on the classical diffusion ODF reconstructed from QBI and a regularized version of the dODF was proposed [J. S. W. Campbell and Pike (2006)].

Another approach based on QBI, reconstructs regularized fiber trajectories using the shape and peak orientation of the  $q$ -ball dODFs to influence the paths of the streamlines at each step [Perrin et al. (2005b)]. This method employs a measure of anisotropy  $\alpha$  to weigh the influence of the  $q$ -ball on the particle trajectories. Even though this regularization method was proposed for QBI, it can be generalized to any HARDI diffusion local model.

Particles start from seeds with an initial direction equal to the local diffusion field. Then, if we define  $r(s)$  as the location of the particle at arc-length position  $s$ , and  $\mathbf{v}(s)$



the out direction of particle at  $r(s)$ , the next particle step is defined as

$$r(s + \delta s) = r(s) + \mathbf{v}(s)\delta s. \quad (3.43)$$

At each trajectory step, the new out direction  $\mathbf{v}(s + \delta s)$  results from a trade-off between inertia, given by the incident direction  $\mathbf{v}(s)$  and a force steeming from the diffusion local field  $\mathbf{v}_d(s)$ :

$$\mathbf{v}(s + \delta s) = \alpha \mathbf{v}_d(s) + (1 - \alpha) \mathbf{v}(s) \quad (3.44)$$

where  $\alpha$  is a parameter ranging between 0 and 1. The diffusion local model is interpolated at each location  $r(s)$  using trilinear interpolation.

For deterministic tractography, the direction  $\mathbf{v}_d(s)$  is the direction of maximum probability inside a half cone defined from the incident direction  $\mathbf{v}(s)$ . The parameter  $\alpha$  is a measure of anisotropy. For isotropic voxels,  $\alpha$  is small, and the algorithm favours the incident orientation; while for anisotropic voxels,  $\alpha$  is large, and the algorithm favours the diffusion local field direction. For QBI,  $\alpha$  was estimated as the normalized standard deviation of the interpolated  $q$ -ball. Figure 3.26 presents an illustration of this trajectory regularization algorithm for anisotropic and isotropic cases.

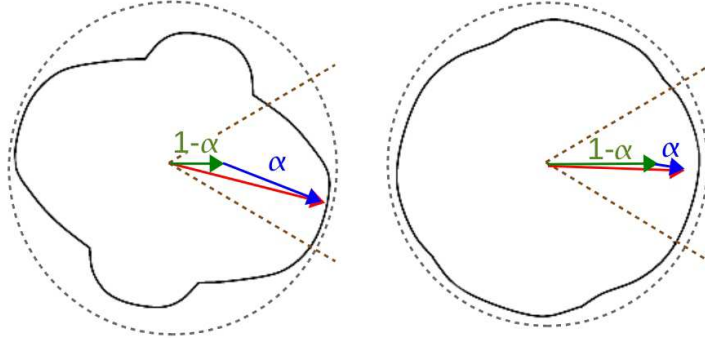


Figure 3.26: Regularization of particle trajectories for HARDI. A measure of anisotropy  $\alpha$  is used to weight the influence of the HARDI diffusion local model on the particles trajectories. For QBI, [Perrin et al. \(2005a\)](#) used the normalized standard deviation of the interpolated  $q$ -ball. [From [Perrin et al. \(2005a\)](#)].

A two-tensor fiber tractography method that estimates two tensors from the acquired MR values was also proposed [[Bergmann et al. \(2007\)](#)]. At each step of the path, the two tensors are interpolated, and the trajectory follows the tensor most aligned with the current direction. Another method using a two-tensor model was recently proposed and used to resolve fiber crossing in the corticospinal tract [[Qazi et al. \(2009\)](#)]. Although results are interesting, these methods present the difficulty of model selection in each voxel.

Streamline tracking algorithms were also proposed based on the principal direction of the dODF computed from DSI [[Tuch \(2002\)](#); [Wedeen et al. \(2008\)](#)]. Also, [Descoteaux et al. \(2009b\)](#) used an fODF estimated from a sharpening spherical deconvolution of the dODF reconstructed from QBI, for streamline deterministic fiber tracking. At each



point, the out direction  $\mathbf{v}_{out}$ , is selected as the fODF maximum that is the closest to the incoming tangent direction of the curve ( $\mathbf{v}_{in}$ ).

Deterministic algorithms are simple and fast, but are very susceptible to noise and are limited when multiple fiber populations exist within a voxel. Streamline probabilistic tractography tries to face this problem using more information about the probability distribution of the fiber orientation.

### 3.3.2 Streamline Probabilistic Tractography

Streamline probabilistic tractography algorithms use an orientation probability distribution (dODF or fODF) and Markov Chain Monte Carlo sampling to generate the streamlines. For this, a big number of seeds is randomly distributed inside each ROI voxel ( $\sim 200$ – $1,000$ ).

An example of this kind of method was proposed by Perrin et al. (2005a), which regularized deterministic streamline algorithm was described in section 3.3.1. For the probabilistic approach, each trajectory step is determined using the same expression (equation 3.44), where an anisotropy measure is used as a weighting parameter for diffusion local model direction  $\mathbf{v}_d(s)$  and incident direction  $\mathbf{v}(s)$ . The difference consists in the approach employed for determining  $\mathbf{v}_d(s)$ , which in this case is randomly chosen inside the half cone defined from the incident direction (see Figure 3.26). Then, a big number of seeds from each voxel will generate a fiber dataset representing the probability of the different connections that can exist from each voxel to the remaining GM/WM interface voxels. See Figure 3.27 for a comparison between streamline probabilistic and deterministic tractography over a field of fODF calculated with a sharpening SD of the dODF from QBI [Descoteaux et al. (2009b)]. In this example, tractography was calculated for the whole brain, using a T1 propagation mask with voxel size of  $0.9375 \times 0.9375 \times 1$  mm, and 27 seeds per voxel (see Figure 3.24 (B2)). The figure shows a selection of fibers passing through an ROI (in red) localized in the left post-central gyrus. As expected, the probabilistic method presents a higher range of probable connections.

Another streamline probabilistic tractography was proposed by Descoteaux et al. (2009b) for an fODF estimated from the sharpening SD of the dODF from QBI. The algorithm generates new seeds for streamline tracking in each fanning region, leading to a dense sample of probable directions. This method produces a set of fibers which recovers segments of WM fibers more accurately but does not reflect the continuity of the fibers or the cortical and subcortical regions they connected since they need to be cut in order to perform the splitting [Wassermann et al. (2010a)].

Finally, Chao et al. (2008) presented a streamline tractography algorithm for QBI called a *modified fiber assignment using the continuous tracking* (MFACT). This algorithm extends the FACT model to multi-fiber directions within each MR voxel. Fiber tracts initiate from the center seed point of each voxel, and spread along the directions of the local maximum diffusion, reaching the interception point on the boundary between two

voxels. Then, tracts follow the new voxel directions of the local maximum diffusion, as a region-growing method (see Figure 3.28). This tracking method seems interesting but more validations and comparisons with other methods are required.

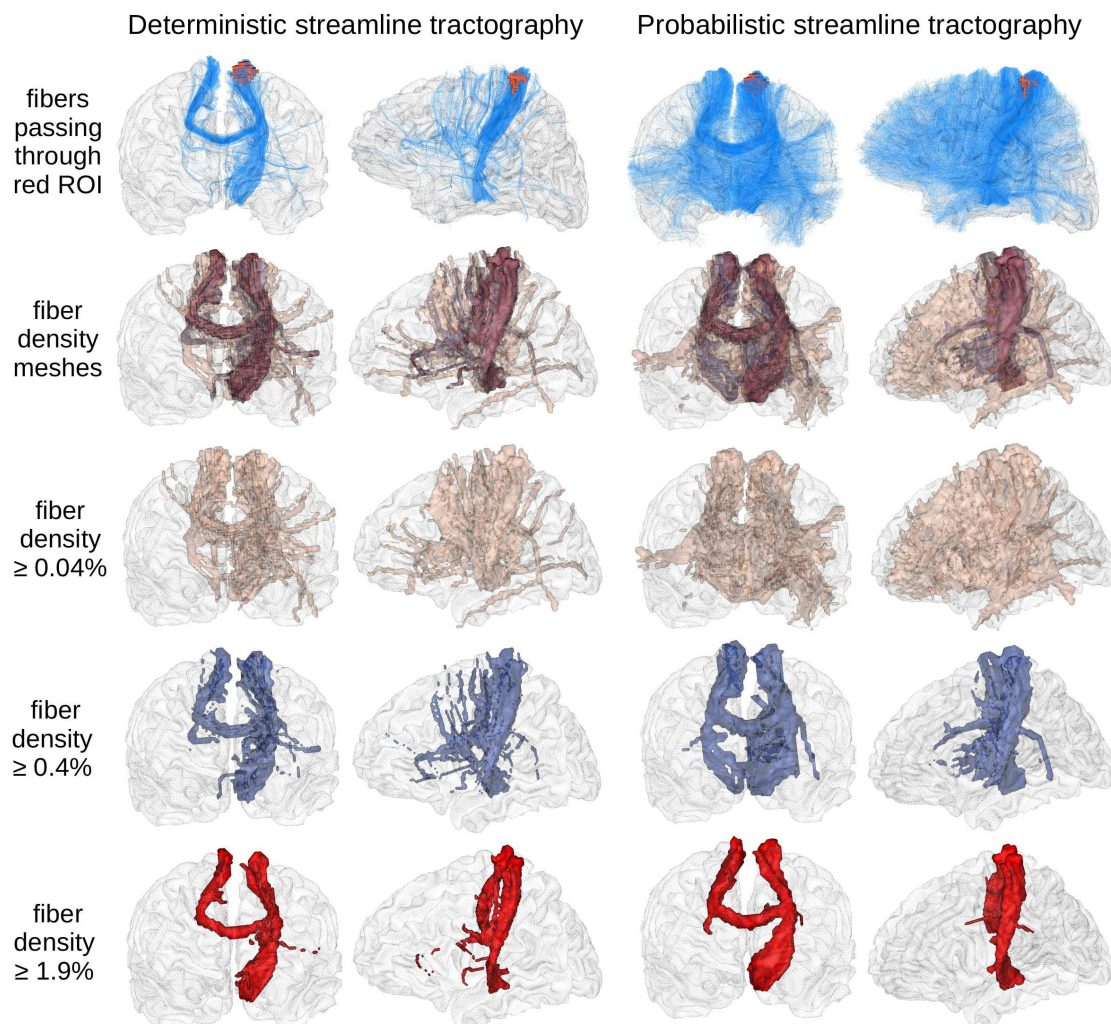


Figure 3.27: Streamline tractography examples for deterministic and probabilistic approaches, using the fODF estimated from a sharpening spherical deconvolution of the dODF from QBI [Descoteaux et al. (2009b)]. Tractography was calculated for the whole brain, using a T1 propagation mask with voxel size of  $0.9375 \times 0.9375 \times 1$  mm, and 27 seeds per voxel. The tracking algorithm is the proposed by Perrin et al. (2005a), which uses regularized particle trajectories and is implemented in *BrainVISA/Connectomist-2.0*<sup>1</sup> software. The tracking algorithm used a calculation step size of 0.46875 and a maximum curvature angle of  $30^\circ$ . Minimum and maximum allowed trajectories length were 20 and 200 mm, respectively. The first row shows the resulting fibers (in blue), passing through the red ROI, localized in the left post-central gyrus. For a better visualization and comparison of both methods, tractography results are also illustrated using fiber density meshes. Three semitransparent fiber density meshes are used, to indicate regions where fiber density is superior to 0.04% (in orange), 0.4% (in blue), and 1.9% (in red).

Probabilistic streamline tractography is robust to noise and partial volume effect. Besides, it naturally gives a probability of connection between two regions. However, the obtained tracts present a bigger number of false negatives than deterministic approaches.

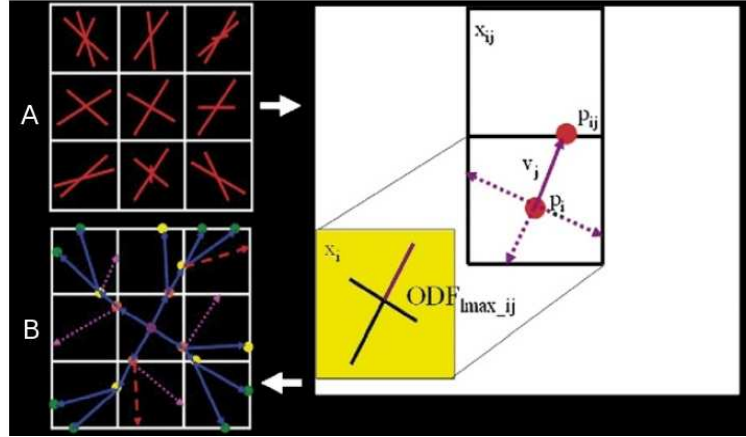


Figure 3.28: MFACT tractography approach. Fiber tracts initiate from the center seed point of each voxel, and spread along the directions of the local maximum diffusion (A). Then, tracts follow the new voxel directions of the local maximum diffusion, as a region-growing method. Tracts are stopped when the angle between two adjacent vectors is bigger than a threshold (plum dotted lines) or the length of local maximum vector is shorter than a minimum value (red dotted lines) (B). The whole process is similar to a region-growing method with hierarchical red, orange, yellow, and green points which serve as seed points for further fiber tracking. [From [Chao et al. \(2008\)](#)].

A limitation of this kind of method is the calculation time, but it can be performed in parallel. Another problem is the huge number of trajectories that is usually calculated for a whole brain, which, until now, prevents the application of “fiber clustering” algorithms to whole brain probabilistic tractography datasets.

### 3.3.3 Other Tractography Algorithms

Two other main types of tractography algorithms have been developed. The *Bayesian tractography*, which is extensively applied in brain connectivity studies, and the *global tractography*, which recent results are very promising.

#### Bayesian Tractography

A different type of probabilistic tractography approach, called *Bayesian*, estimates global connectivity, which results in a connection map indicating the confidence that each voxel is connected to the seed region [[Parker and Alexander \(2005\)](#); [Hosey et al. \(2005\)](#); [Behrens et al. \(2007\)](#); [Jbabdi et al. \(2007\)](#); [Kaden et al. \(2007\)](#); [Seunarine et al. \(2007\)](#); [Morris et al. \(2008\)](#); [Melie-García et al. \(2008\)](#)].

These methods use a model of the uncertainty of each fiber orientation represented by *posterior probability density functions* and Markov Chain Monte Carlo sampling of the streamline paths to estimate connectivity probabilities between different brain regions. The procedure runs multiple streamline tracking processes (repetitions) from each seed point so it is computationally expensive ( $\sim 1,000$ – $10,000$  streamlines per seed). The number of occasions at which each voxel  $p$  is crossed by a streamline is used to define the map of the probability  $\phi$  of connection to the start point (see Figure 3.29). These methods, in general,

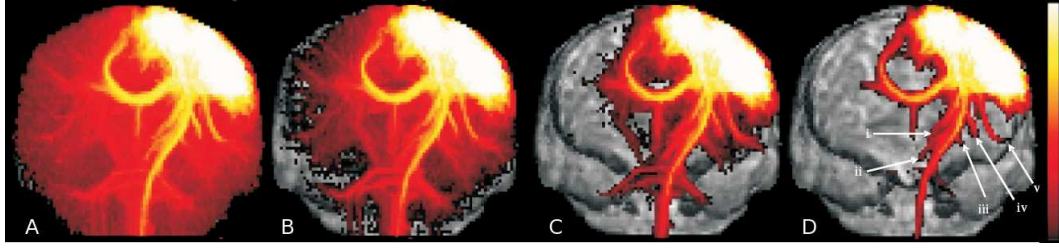


Figure 3.29: Bayesian tractography probability map ( $\phi$ ) example. Coronal projections of left motor strip connectivity at different thresholds. Logarithmic colour scale: (A)  $0.0 < \phi < 1.0$ , (B)  $0.027 < \phi < 1.0$ , (C)  $0.074 < \phi < 1.0$  and (D)  $0.20 < \phi < 1.0$ . Major apparent connections identified include: (i) thalamus, (ii) subthalamic nucleus, (iii) globus pallidus, (iv) putamen and (v) Wernicke's area [From [Parker and Alexander \(2005\)](#)].

do not produce a tractography fiber dataset, required as input for our thesis work.

### Global Tractography Algorithms

Global tractography algorithms use global properties (i. e. along the whole curve) to infer the fiber trajectories.

*Front Evolution* approaches try to find the path of least hindrance (and so, of maximum diffusivity) that connects two particular points. This is a global optimization problem that minimizes the path integral and thus, maximizes the global diffusivity [[O'Donnell et al. \(2002\)](#); [Pajevic et al. \(2002\)](#); [Jbabdi et al. \(2004\)](#); [Lenglet et al. \(2004\)](#); [Lenglet \(2006\)](#); [Jbabdi et al. \(2008\)](#)]. In practice, these methods use fast marching techniques to infer geodesic paths. These approaches are fast and less sensitive to local perturbations such as noise or partial volume effects. However, choosing a metric for which geodesics represent fiber pathway trajectories is not straightforward. Besides, geodesics have the limitation that for any pair of regions in the brain, there exists a geodesic between those regions, and it is difficult to decide if a geodesic is a fiber trajectory [[Jbabdi et al. \(2008\)](#)].

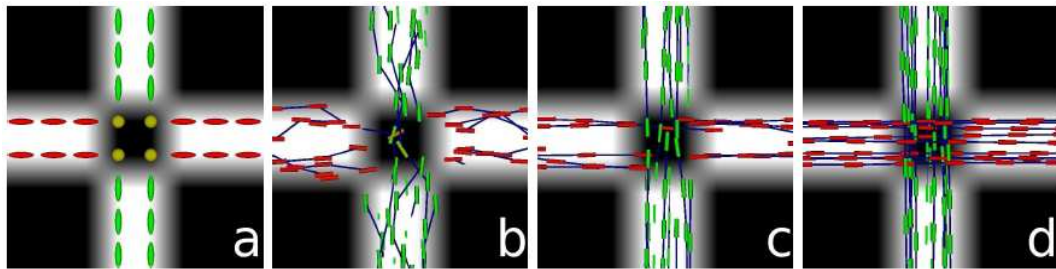


Figure 3.30: Example of spin-glass tractography of a synthetic fiber crossing over using DTI. a) The tensor field. b) The initial spin glass: spins (represented by green and red cylinders) were randomly placed and aligned with the main tensor eigenvectors. The blue links represent the spin associations. c) The minimal energetic configuration of the spin glass in b). d) After convergence: spin chains have grown and merged to reconstruct the crossing area. [From [Fillard et al. \(2009\)](#)].



Other interesting global tractography approaches use the *spin-glass* model [Poupon (1999a); Cointepas et al. (2002); Fillard et al. (2009)]. This method parameterizes the entire white matter fascicle map by pieces of fibers, represented by small line segments, called spins. Spins are encouraged to move and rotate to align with the main fiber directions, and to assemble into longer chains of low curvature. Thus, the algorithm uses the diffusion local model and the global information of spin neighbors in an iterative minimization process. Figure 3.30 shows an example of spin-glass tractography of a synthetic fiber crossing over using DTI. The algorithm only relies on the two generally admitted priors that brain fibers have a low curvature and do not end inside white matter. They do not require an estimation of the number nor directions of the fiber compartments in each voxel and can be adapted to any type of diffusion model [Fillard et al. (2009)].

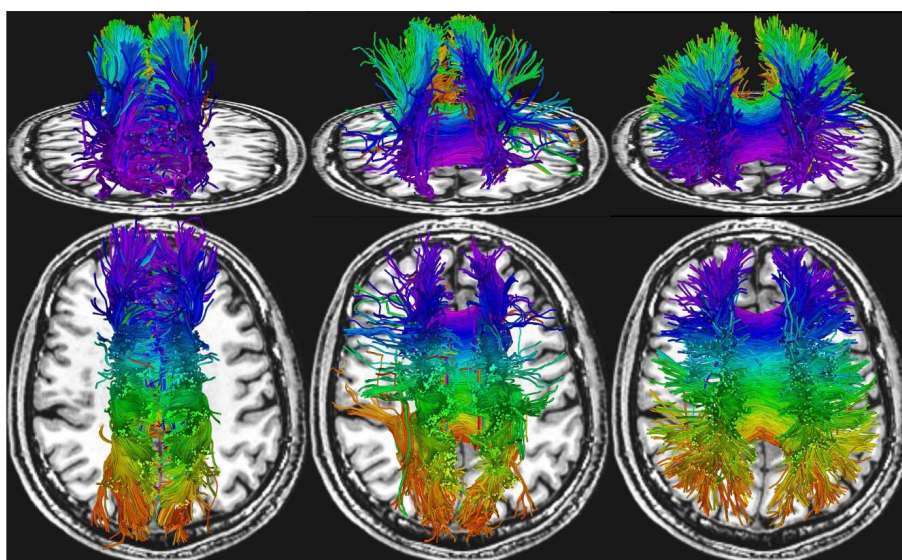


Figure 3.31: Reconstruction of callosal fibers with three methods. Left: Tensor-based streamline tractography (TBT). Middle:  $q$ -ball based streamline tractography (QBT). Right: Spin-glass tractography (SGT). All fibers of TBT are redirected vertically because of the surrounding corona radiata. QBT performed slightly better but missed a large part of the callosal fibers. SGT, by using the neighborhood to determine the most plausible pathways, was able to recover the myriad of fibers passing the corona radiata [From Fillard et al. (2009)].

Another probability-based method was introduced by Kreher et al. (2008) to extract and quantify neuronal pathways, connecting two a priori defined regions. In contrast to other approaches, this method is based on combining two independent visiting maps of different seed regions, which allows the identification of point to point connections without a priori knowledge about its course.

These global approaches are more successful than deterministic streamline based methods to recover crossing fibers (see Figure 3.31). A limitation is the requirements of computation time and memory, which are still very high.

## 3.4 Conclusion

---

In this chapter, we introduced the principles of diffusion MRI, a technique allowing the non-invasive study of human brain white matter architecture. Diffusion MRI is based on the diffusion phenomenon of water molecules within neural tissues. It measures the average displacement of water molecules along several directions, during a period of time within each voxel. Then, based on these measurements, diffusion models reconstruct a more or less direct estimation of the underlying fiber tract orientations. From models, a measure of diffusion anisotropy can also be deduced, which has been shown to be a measure of white matter integrity. Tractography methods use the estimated fiber orientation of putative fiber tracts to trace 3D trajectories representing the pathways of white matter tracts. The resulting fiber tracts strongly depend on the quality of the diffusion data as well as on the diffusion model. Noise and inherent limitations of the DW-MRI technique can not resolve the white matter configuration at microscopic scale, producing false negative and false positive curves. These issues can be partially overcome by the use of high angular resolution acquisitions (HARDI) and diffusion models capable to resolve multiple-fiber populations or fiber crossings. Anyway, WM tractography is a powerful technique able to study human whole-brain WM tracts *non-invasively* and *in vivo*. Furthermore, DW-MRI is an active research field, where techniques from MRI physics, passing through the acquisition and distortion corrections, to diffusion modelling and tractography algorithms, are in continuous improvement in order to get more accurate results. Tractographic tracts are used to study brain connectivity, and particularly, to identify white matter tracts for research and clinical studies. In the next chapter, we will review the principal methods employed to clusterize WM fiber datasets for the identification of white matter tracts.





# White Matter Clustering

## Contents

---

<b>4.1</b>	<b>Cross-subject registration . . . . .</b>	<b>73</b>
4.1.1	Normalization to Talairach space . . . . .	74
4.1.2	Non-linear registration methods . . . . .	76
<b>4.2</b>	<b>White Matter segmentation of DW images . . . . .</b>	<b>77</b>
<b>4.3</b>	<b>ROI-based WM fiber tract segmentation . . . . .</b>	<b>77</b>
<b>4.4</b>	<b>White Matter fiber clustering . . . . .</b>	<b>80</b>
4.4.1	Clustering . . . . .	80
4.4.2	Fiber similarity measures . . . . .	88
4.4.3	Fiber clustering methods . . . . .	92
<b>4.5</b>	<b>Quantitative DW measures across bundles . . . . .</b>	<b>105</b>
<b>4.6</b>	<b>Conclusion . . . . .</b>	<b>111</b>

---

## Overview

---

As we studied in previous chapter, diffusion MRI provides *in-vivo* measures that reflect the underlying tissue abnormalities. A comparison of diffusion measurements between populations can then be performed. Several methods have been proposed for diffusion parameter analysis. Some approaches directly compare diffusion indexes of white matter voxels. Other more sophisticated approaches classify white matter voxels for tract identification and posterior comparison. Instead of basing the analysis only on voxel diffusion parameters, tractographic fiber bundles can be used for a better correspondence across subjects. To achieve this, the large amount of fibers obtained from tractography algorithms require adequate processing methods for the identification of white matter tracts. Earlier techniques used regions of interest for extracting known fiber tracts. Other methods use fiber clustering to regroup fibers presenting similar shape and trajectory into fiber clusters. These methods can be used for a more automatical identification of white matter tracts. Furthermore, fiber clustering results can allow a better understanding of the structure of the fiber tracts. This thesis work is focused on this research area, by the development of a novel method for white matter fiber clustering and the inference of an atlas of WM fiber tracts.

In order to situate our work, this chapter presents a review of the main approaches used for tractographic pathways clustering and identification. Fiber clustering methods are particularly addressed, as well as the different fiber similarity measures described in the literature. Overall, this introductory chapter is inspired from review articles and chapters from [O'Donnell (2006); Moberts et al. (2005); Jain (2010); Johansen-Berg and Behrens (2009); Wassermann (2010)], which are great sources for a general understanding of white matter fiber clustering.

**Keywords:** white matter clustering, fiber tracts, WM atlas, fiber clustering, fiber distance, fiber similarity measure

### Organization of this chapter:

The chapter is organized as follows. We first describe cross-subject registration methods in section 4.1. Then, we briefly introduce methods of direct WM segmentation using DW images in section 4.2. ROI-based approaches for WM tracts segmentation are then mentioned in section 4.3. Next, we focus on WM fiber clustering methods in section 4.4, starting with a review of main clustering methods and fiber distance measures. Finally, we describe the most important approaches for WM quantitative analysis in section 4.5.

## 4.1 Cross-subject registration

---

The study of anatomical structures or diffusion (and also functional) properties across a group of subjects requires to find a correspondence between subjects. It is, to determine which location in each subject's images corresponds to the equivalent anatomical location in the other subjects. The correspondence can be found between images or between regions of interests, like sulci or WM tracts.

Registration is the spatial adjustment of one image to match another. The input image is normally of a single subject's brain, and the reference image might be a different image of the same subject, a different subject, or a "template" brain (process called *normalization*). Template images are typically created by averaging several subjects' images in some common space. Registration can be linear or non-linear [Johansen-Berg and Behrens (2009)]:

**Linear registration** limits the motions applied to the input image to global translations, rotations, scalings and shears. These low "degrees-of-freedom" (DoF) transformations tend to be robust and accurate for aligning images within subject. These transformations can also be used to align head shapes and positions between subjects, but there will be remaining smaller-scale differences.

**Non-linear registration (warping)** can apply local warps, as opposed to the simple, global transformations applied by linear registration. Non-linear registration may be constrained to only allow simple, coarse warps (low DoF), or may be allowed to apply very finely detailed, complex warps (high DoF), in order to attempt to match the input image to the reference image as perfectly as possible. Non-linear registration is normally initialized by linear registration, to get the general orientation and size matched globally.

Very high-dimensional warping must be used carefully as images can be warped so much that they look almost exactly like each other, but images may not have achieved overall structural homology, i.e. preserved how the different features relate to each other [Johansen-Berg and Behrens (2009)]. Furthermore, increasing flexibility with more DoFs comes at some cost. The most obvious penalty is that more parameter determination tends to require more computer time [Crum et al. (2004)].

Registration can be divided into geometric approaches and intensity approaches. Geometric approaches build explicit models of identifiable anatomical elements in each image. These elements typically include functionally important surfaces, curves and point landmarks that can be matched with their counterparts in the second image. These correspondences define the transformation from one image to the other [Crum et al. (2004)]. The intensity approach is done by optimisation based on an image similarity measure that quantifies the degree of similarity between intensity patterns in two images (intensity-based registration). The criterion can be the minimization of the mean squared difference [Friston et al. (1995)], the maximization of normalised cross-correlation [Studholme et al. (1995); Collins et al. (1995)], the minimization of the variance of intensity ratios [Woods

et al. (1993)] or the maximization of mutual information (MI) [Viola and Wells (1997)] or normalized mutual information (NMI) [Maes et al. (1997); Studholme (1999)]. The last three can be used for between-modality registration but MI (and NMI) is regarded as the *de-facto* standard in multimodality image registration [Gholipour et al. (2007)]. The different methods mainly differ by the regularization scheme and optimization strategy which have a crucial influence on the registration process [Hellier et al. (2003)].

Hybrid algorithms have also been proposed, combining intensity-based and model-based criteria to establish more accurate correspondences in difficult registration problems, e.g. using sulcal information to constrain intensity-based brain registration or to combine the cortical surface with a volumetric approach (see [Crum et al. (2004)]).

The transformation model defines how one image can be deformed to match another; it characterizes the type and number of possible deformations.

#### Linear transformation types:

**Rigid:** global translations and rotations. Accounts for position and orientation (6 parameters).

**Affine:** Rigid plus overall scale and shear (12 parameters).

**Piecewise linear:** A set of linear maps.

The rigid and affine transformations can be fully modeled as 4x4 matrices of translation, rotation, scale, and shear.

#### Non-linear deformation types:

**Basis functions:** Polynomial [Woods et al. (1998)] or harmonic basis functions [Ashburner et al. (1999)]. The last ones are used by the software SPM (statistical parametric mapping).

**Physical continuous models:** Viscous fluids [Christensen et al. (1996)], demons algorithms [Thirion (1998)].

**Large deformation models:** Diffeomorphisms, which define inverse consistent deformations [Ashburner (2007); Vercauteren et al. (2008, 2009)].

#### 4.1.1 Normalization to Talairach space

The Talairach atlas [Talairach and Tournoux (1988, 1993)] was generated from a single 60 year old female postmortem brain in which one half of the brain was sectioned sagittally and the other coronally (see Figure 4.1 (a) and (b)). Talairach space is defined as the standard brain space with the same dimensions as the published 1988 atlas (x=136 mm, y=172 mm, z=118 mm). The Talairach stereotaxic coordinate system is based on two relatively invariant subcortical point landmarks, the anterior commissure (AC) and the posterior commissure (PC). In this space, the principal axis corresponds to the AC-PC

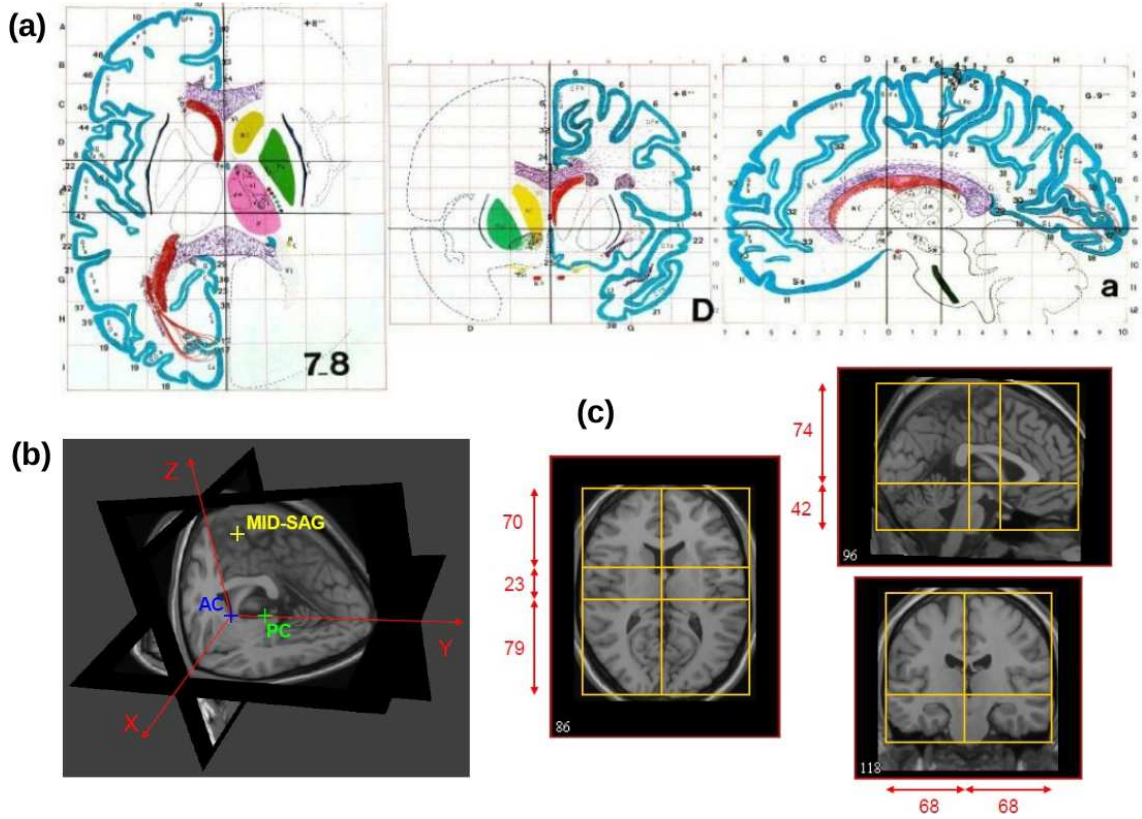


Figure 4.1: The Talairach atlas and normalized space [Talairach and Tournoux (1988)]. (a) The Talairach atlas defines 12 lobes, 55 regions, GM/WM and CSF and 71 Broadmann areas. (b) The Talairach referential can be defined by three points: AC, PC and an interhemispheric point. (c) The normalization to Talairach space defines 12 rectangular boxes using the AC, the PC and the interhemispheric plane. Each box is linearly stretched/shrunk to fit with the reference brain dimensions. [From <http://mipav.cit.nih.gov/documentation/presentations/talairach.pdf>].

line, and the origin lies at the AC. The Talairach reference frame is determined from unit vectors directed along  $+x$  and  $+y$  brain axes. The  $+y$  unit vector is parallel to the AC-PC line, arises from the AC, and is directed anteriorly. The  $+x$  unit vector is perpendicular to the interhemispheric plane and is directed to the right side of the brain. A third  $+z$  unit vector is formed as the vector cross product of the  $x$ - and  $y$ -unit vectors and is directed superiorly [Lancaster et al. (2007)].

The normalization to Talairach space is done by the definition of 3 points: AC, PC and an interhemispheric (IH) point, and the reference frame. The transformation consists in a piecewise linear registration of the brain by respect to the Talairach atlas brain. This scaling is done by centering the brain over the AC point, which will have the (0,0,0) coordinates and cutting the brain into 12 rectangular boxes. The boxes are localized in both sides of the sagittal plane (X,Z) and axial plane (X,Y), and between the two coronal planes (Y,Z) passing through AC and PC. Each box is linearly stretched/shrunk to fit with the reference brain dimensions (see Figure 4.1 (c)).

The Talairach anatomical atlas references several cerebral structures in the Talairach



referential. In this atlas, [Talairach and Tournoux \(1988\)](#) included a labelling of Brodmann areas but this map is not accurate as only anatomical landmarks were used for the localization of cytoarchitectonic areas rather than histological examination. Although a single brain cannot be a good representative of the human brain, the Talairach atlas has become the *de facto* standard in brain mapping [[Gholipour et al. \(2007\)](#)].

Other more recent and widely used templates are the Montreal Neurological Institute (MNI) templates. A first atlas, called MNI305, was created based on averaging several normal MRI brain images, registered to the Talairach coordinates [[Mazziotta et al. \(1995\)](#)]. Then, a second atlas called ICBM152, with higher spatial resolution was obtained as the average of 152 individual anatomical images, registered to the MNI305 template using affine transformations [[Mazziotta et al. \(2001\)](#)].

#### 4.1.2 Non-linear registration methods

Several non-linear registration methods have been proposed for brain normalization. These methods use different similarity measures, deformations, regularizations and optimization approaches. Some examples are ANIMAL [[Collins and Evans \(1997\)](#)], SPM2-type normalization [[Ashburner et al. \(1999\)](#)], DARTEL [[Ashburner \(2007\)](#)], AIR [[Woods et al. \(1998\)](#)], FNIRT, Diffeomorphic Demons [[Vercauteren et al. \(2009\)](#)].

An example of highly non-linear transformation is computed with the Large Deformation Diffeomorphic Metric Mapping (LDDMM) [[Huang et al. \(2008\)](#); [Miller et al. \(2005\)](#)]. The LDDMM algorithm computes a transformation,  $\varphi : \Omega \rightarrow \Omega$ , where  $\Omega \subseteq \mathbb{R}^3$  is the 3D cube on which the data are defined. The computed transformation is the end point,  $\varphi = \varphi_1$ , of a flow of vector fields,  $v_t \in V$ ,  $t \in [0, 1]$ , given by the ordinary differential equation

$$\dot{\phi}_t = v_t(\phi_t), \phi_0 = id \quad (4.1)$$

where  $\phi_0$  is the identity transformation,  $\phi_0(x) = x$ ,  $\forall x \in \Omega$ . Enforcing a sufficient amount of smoothness on the elements in the space of allowable vector fields,  $V$ , ensures that the solution to the differential equation,  $\phi_t = v_t(\phi_t)$ ,  $t \in [0, 1]$ , is in the space of diffeomorphisms. Smoothness is enforced throughout by defining the norm on the space,  $V$ , of smooth velocity vector fields through a differential operator,  $L$ , which generally represents Laplacian powers such that  $\|f\|_v^2 = \|Lf\|_2^2$ , where  $\|\cdot\|_2$  is the standard  $L^2$  norm for square integrable functions defined on  $\Omega$ .

For an evaluation of several non-linear inter-subject brain registration methods please refer to [[Klein et al. \(2009\)](#)].

## 4.2 White Matter segmentation of DW images

WM tract segmentations can be performed using DW-MRI images without the use of tractography datasets. These approaches use the information given by diffusion images and diffusion models to segment white matter tracts.

Some works proposed segmentations for DTI using front propagation methods based on some similarity measure of diffusion between voxels [Wang and Vemuri (2004, 2005); Jonasson et al. (2005a); Lenglet et al. (2006)]. For example, Jonasson et al. (2005a) use 3D geometric flow, where the 3D surface evolves with a propagation speed proportional to a measure indicating the similarity of diffusion between the tensors lying on the surface and their neighbors in the direction of propagation. More complex DT-based similarity measures such as the Kullback-Leibler divergence metric [Wang and Vemuri (2005)] and Riemannian metric [Lenglet et al. (2006)] have also been used. These DTI-based methods present the inherent limitations of the DT model and are most often blocked in regions of fiber crossings.

New methods use HARDI acquisitions to segment bundles from fields of ODFs [Hagmann et al. (2006); Jonasson et al. (2007); McGraw et al. (2006); Wassermann et al. (2008); Descoteaux and Deriche (2009)]. Hagmann et al. (2006) and Jonasson et al. (2007) use DSI data to represent diffusion as a signal mapped on a 5-dimensional space of position and orientation, defined by the location of the ODFs on the acquisition grid and their orientational information. The authors use then respectively a hidden Markov Random Field or a level set implementation in order to segment the image into homogeneous, contiguous and high diffusivity regions and to label them as a tract. Two methods were proposed using the spherical harmonics representation of the ODF described in [Descoteaux et al. (2007)]. While Wassermann et al. (2008) used ODF diffusion maps as spectral embedding method, Descoteaux and Deriche (2009) employed a region-based level set approach.

These methods can only detect gross masks or 3D surfaces of the main big WM tracts. This is because the analysis of a voxel or a group of voxels can only integrate a relatively local spatial and diffusivity information. DW-based tractography provides a more global anatomical interpretation of the diffusivity on each voxel. By tracing ensembles of axonal pathways at a sub-voxel resolution it also provides a solution to some of the problems arising from partial voluming [Wassermann et al. (2010a)].

## 4.3 ROI-based WM fiber tract segmentation

Earlier works used cortical masks to seed tractography and reconstruct known white matter tracts. This approach, called “from ROI”, generally leads to an incomplete delineation of the tracts [Mori et al. (2005)]. Other limitation is that it can not be applied successfully to pathological brains.

To overcome some limitations of streamline tractography algorithms, specially in regions with crossing fibers, a “whole-brain” or “brute-force” seeding strategy is more suitable [Mori et al. (2005); O’Donnell and Westin (2007)]. Several ROI-based methods have then

been proposed for the extraction of known WM fiber tracts from this kind of dataset, containing fiber tracts of the whole brain.

One strategy is to define the ROIs manually, which has been used in several tractography studies [Conturo et al. (1999); Basser et al. (2000); Catani et al. (2002); Mori et al. (2000); Maddah et al. (2005); Mori et al. (2005); Wakana et al. (2004, 2007)]. For example, Catani et al. (2002) presented a manual ROI approach to reconstruct white matter pathways. The method produced virtual representations of white matter tracts faithful to classical post-mortem descriptions, called *virtual dissection* of WM tracts. Using the same approach, Catani and Thiebaut de Schotten (2008) provide a template to guide the delineation of ROIs for the reconstruction of the association, projection and commissural pathways of the living human brain. The tracts can be selected using a single ROI approach (arcuate fasciculus, cingulum, corpus callosum, anterior commissure and fornix) or a two-ROIs approach (cerebellar tracts and the uncinate, inferior longitudinal and inferior fronto-occipital fasciculi). Some examples of these bundles were shown in Figure 2.7 (Chapter 2, section 2.3). In other set of works, Wakana et al. also use multiple ROIs for 11 tracts of interests, employing different types of operations, as “AND”, “OR”, and “NOT” [Wakana et al. (2004)], or “AND”, “CUT”, and “NOT” [Wakana et al. (2007)], the choice of which depends on the characteristic trajectory of each tract. See Figure 4.2 for an illustration of manual ROI-based WM tract segmentation. The main limitation of these manual approaches is that a specific protocol must be followed for the extraction of every WM tract, where an expert a priori anatomical knowledge is required to identify the course of white matter pathways and delineate ROIs. This is a very complicated task, which must be applied separately for each brain.

In a more recent work, [Zhang et al. (2008b)] proposed an automated ROI-based tract reconstruction approach. A set of reference regions of interest known to select a tract of interest was marked in a DTI atlas in MNI coordinates (ICBM-DTI-81) [Mori et al. (2008)], described in appendix A. The atlas was then linearly transformed to each subject, and the ROI set was transferred to the subject for the reconstruction of 11 well-known WM tracts.

An attractive extension of this approach consists in using a group of subjects to create probabilistic maps of the resulting WM tracts in a standard space after spatial normalization [Hua et al. (2008)]. The population-averaged statistical maps can define the standard coordinates of the reproducible regions (cores) of the tracts. Then, a set of ROIs can be defined from the probabilistic maps to catch the same WM tracts in any other subject.

Other approaches use whole brain WM/GM parcellations to extract WM tracts. For example, Oishi et al. (2008) provided a parcellation of the superficially located WM (SWM), defined as the area between the cortex and the DWM. The SWM was extracted as the WM between a WM parcellation map [Mori et al. (2008)] and the cortex, using thresholds applied to a generated probabilistic WM map. The SWM was manually parcellated into nine major structures called “blades”, which were further sub-parcellated into 23 regions based on the relationships with 24 cerebral cortical areas and the cerebellum

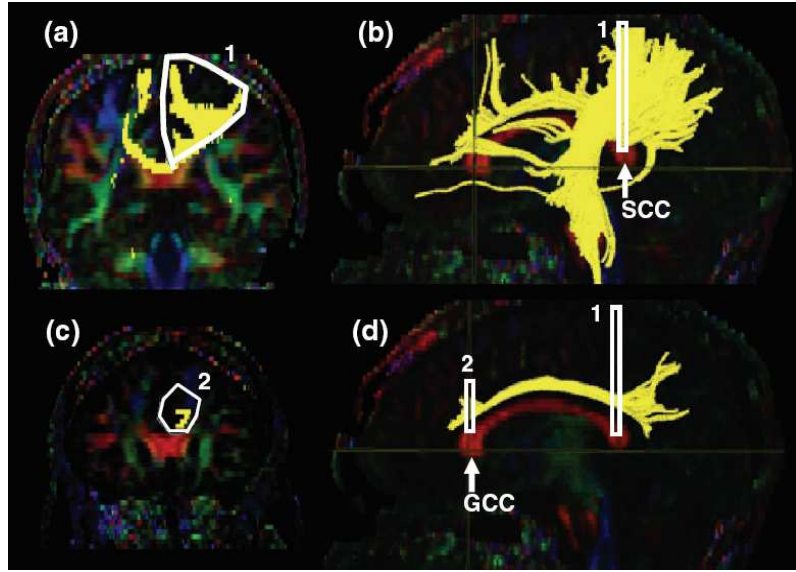


Figure 4.2: Illustration of manual ROI-based WM tract segmentation. Locations of the ROIs for the cingulum in the cingulate gyrus part (CGC) on two coronal slices (a and c) and their locations in the mid-sagittal slice (b and d). The SCC and GCC stand for the splenium of corpus callosum and the genu of corpus callosum, respectively. [From Wakana et al. (2007).]

(see appendix A). The blades were used as ROIs for tractography selections. Intra-blade fibers could not be located. Four short and one long inter-blade fibers were found. See Figure A.3 (B-D) for a 3D view of the SWM parcellation and the identified inter-blade fibers.

Oishi et al. (2009) combined single-participant white matter atlases based on DTI with highly non-linear image registration methods for automated 3D white matter segmentation. The authors created three types of WM parcellation map (WMPM) in ICBM-152 (JHU-DTI-MNI atlas) and Talairach (JHU-DTI-Talairach atlas) spaces containing pre-defined 3D anatomical regions (see appendix A). Highly non-linear dual-channel Large Deformation Diffeomorphic Metric Mapping (LDDMM) [Huang et al. (2008); Miller et al. (2005)] was used for normalization (see section 4.1).

Automated brain parcellation was achieved by warping the WMPM to normal controls and to Alzheimer’s disease patients with severe anatomical atrophy. A standard ROI set was identified by superimposing the Type III WMPM onto the LDDMM transformed images. Also JHU-DTI-MNI was non-linearly transformed to the images using SPM5 (<http://www.fil.ion.ucl.ac.uk/spm/>) to compare the registration quality with that of LDDMM.

Zhang et al. (2010) propose an automated atlas-based approach for reconstruction of WM tracts. The method uses a single-subject DTI atlas with 130 3D anatomical segmentations, called Type II WMPM [Oishi et al. (2009)], described in appendix A.

A two-step image transformation was used to warp the atlas to individual data. First, affine transformation was applied to globally adjust the brain position, rotation, and the

size. Then, the DTI atlas was warped non-linearly to individual DTI data employing dual-contrast LDDMM [Ceritoglu et al. (2009)], in which both the b0 image and the FA map were used simultaneously. Once the transformation matrix defining the reciprocal transformation was determined, the GM/WM parcellation map was transferred from the atlas to the data, for the automated segmentation of the data into 130 brain regions.

Whole-brain tractography was calculated for each subject in the subject data space, and the tract coordinates were normalized to the atlas, using the calculated (inverse) affine and LDDMM transformation. Tracts were extracted using existing anatomical knowledge about tract trajectories, called the *Template ROI Set* or TRS (the approach is so called *TRS-based* method). Thirty TRSs were established to reconstruct 30 prominent and previously well-described fiber tracts (12 corpus callosum (CC) segments, 10 thalamic projection tracts and 8 long association tracts).

The knowledge-based approach, could be applied to create TRSs for short cortico-cortical association fibers, for which the locations and trajectories are not well-known. Therefore an exhaustive search examining connections among all 24 SWM segments associated with different areas of the cortex was performed. The 56 DWM segments were all used as “NO” ROIs to remove long association fibers. From this analysis, 29 short association bundles, connecting two adjacent cortical regions, were found in all normal subjects examined (N=20), including the four U-fibers found in [Oishi et al. (2008)]. Probabilistic maps of the 59 tract trajectories were also created from the normal subjects (see Figure A.5, appendix A). A large variability was found for short association fibers, which was partly attributed to the complex axonal configuration in the SWM, but also to the limitation in precisely matching the cortical anatomy among the subjects.

## 4.4 White Matter fiber clustering ---

White matter fiber clustering regroups fibers from whole-brain tractography into clusters of fibers with similar shape and position. The aim of fiber bundling is then to partition a set of fiber pathways into different natural bundles [Ding et al. (2003)]. A fiber cluster represents a bundle containing fibers parallel to each other, and constitute a distinct structure from other fiber bundles. Therefore, the enormous amount of individual fibers provided by tractography algorithms can be reduced to a limited number of logical fiber clusters that are more manageable and understandable. Clustering can also be used to identify white matter fiber tracts and perform quantitative comparisons between subjects by unbiased measurements in anatomical structures [Moberts et al. (2005)]. In the following subsections, we will review the main clustering methods (subsection 4.4.1) and fiber similarity measures (subsection 4.4.2) proposed in the literature.

### 4.4.1 Clustering

Clustering is the process of organizing objects into groups whose members are similar in some sense. This is an unsupervised learning problem so it deals with finding a structure in

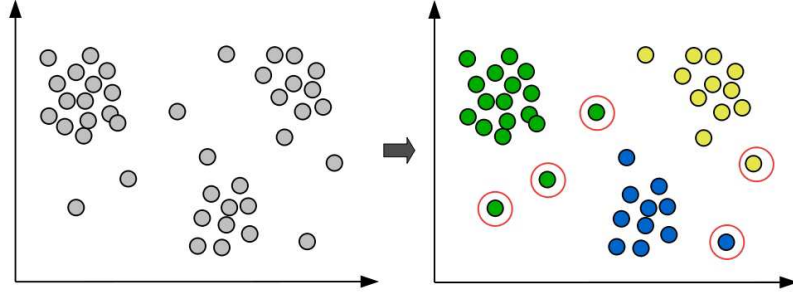


Figure 4.3: Illustration of clustering results for an example dataset. A clustering analysis could find three different clusters (in green, orange and blue). Depending on the clustering method, outliers (encircled in red) could be or not be filtered out.

a collection of unlabeled data [Jain and Dubes (1988); Jain (2010)]. The clusters must be compact and well separated, presenting a higher degree of similarity between data points belonging to the same cluster than between data points belonging to different clusters (see Figure 4.3). A wide variety of clustering methods have been proposed in the literature, each one tending to find different types of cluster structures [Jain (2010)]. Clustering methods can be roughly divided into two main classes: *hierarchical* and *partitional*. Hierarchical clustering algorithms are either agglomerative or divisive. An agglomerative hierarchical clustering method starts by putting each data point into an individual cluster, next at each stage of the algorithm the two most similar clusters are joined, forming a hierarchical forest. On the other hand, partitional algorithms, decompose directly the dataset into a set of disjoint clusters, obtaining a partition which should optimize a certain criterion.

The final clusters depend on the element similarity measure and the clustering algorithm. The definition of a cluster is a complicated task since clusters can differ in terms of their shape, size and density. Besides, the presence of noise in the data makes the detection of the clusters even more difficult. A cluster is then a subjective entity whose significance and interpretation requires domain knowledge [Jain (2010)].

An important issue in clustering is the problem of choosing the right number of clusters. The majority of partitional algorithms require this as a parameter, even though it is not possible to infer this value in advance. Several approaches have been taken to automatically infer the number of clusters. However, no method works in the general case [Wassermann (2010)]. Besides, if outliers may exist, the algorithm must be robust to them in order to find valid clusters.

**Conversion of distance to affinity.** If a distance measure is used, it must be converted to an affinity (or similarity) measure. The affinity  $a_{ij}$  between two elements  $i$  and  $j$ , can be calculated via a Gaussian kernel:

$$a_{ij} = e^{-d_{ij}/\sigma^2}, \quad (4.2)$$



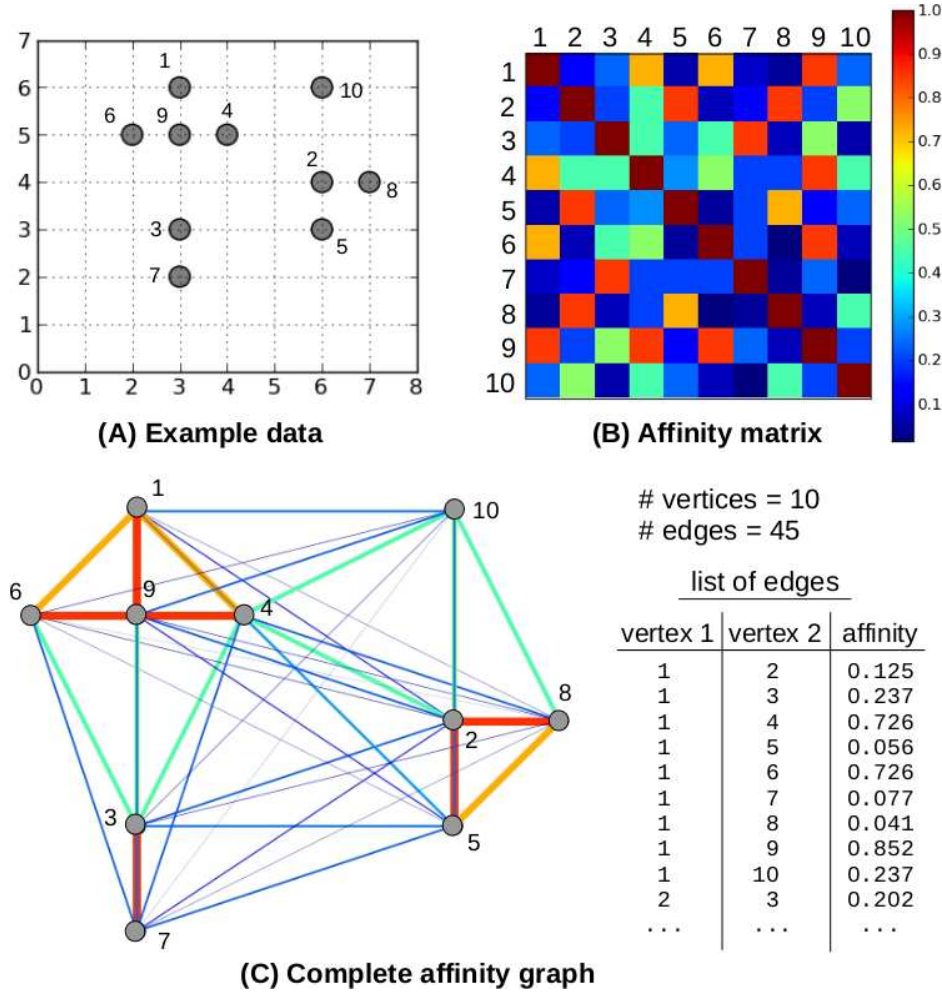


Figure 4.4: Illustration of an affinity matrix and its graph representation for an example dataset. (A) shows a set of  $N = 10$  elements to be clustered. To compute the affinity matrix, the Euclidean distance was calculated between each pair of elements. Then, distances were converted to affinity values using equation 4.2, with  $\sigma = 2.5$ . (B) shows the affinity matrix for the example data. (C) presents a complete affinity graph where vertices represent the elements and edge weights represent affinity values. The matrix and graph edges are colored using the colormap in (B). Graph information consist in a list of edges. Each edge is defined by the two vertices connected by the edge and the affinity value (weight). In the example the total number of edges is  $N(N-1)/2 = 45$ .

where  $d_{ij}$  is the distance between elements  $i$  and  $j$  and  $\sigma$  is a parameter defining the similarity scale.

**Input data.** The input for a hierarchical algorithm is an  $N \times N$  similarity (or affinity) matrix, where  $N$  is the number of objects to be clustered. On the other hand, a partitional algorithm can use either an  $N \times d$  pattern matrix, where  $N$  objects are embedded in a  $d$ -dimensional feature space, or an  $N \times N$  similarity matrix [Jain (2010)].

The similarity matrix can also be represented and stored as an undirected *weighted graph*, which vertices represent the elements and edge weights represent affinity values. A graph is a tuple  $G = (V, E)$ , where  $V = v_1, \dots, v_N$  is the set of  $N$  vertices and  $E$  are

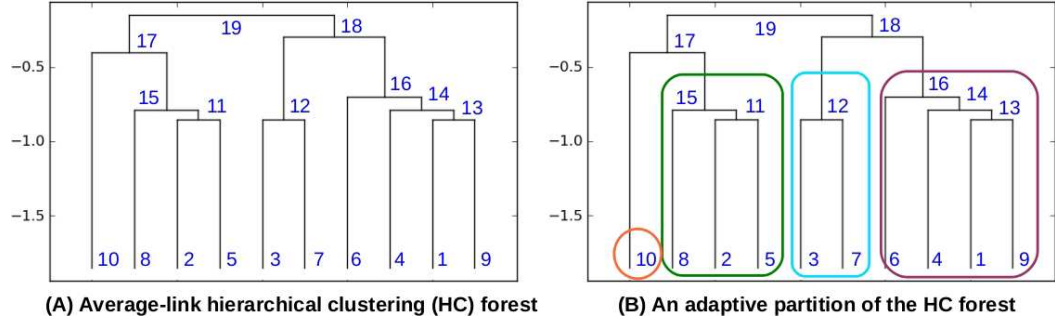


Figure 4.5: Hierarchical clustering (HC) example using average-link. (A): The dendrogram resulting from the hierarchical clustering of elements in Figure 4.4 (A), using as input the affinity graph illustrated in Figure 4.4 (C). The dendrogram contains a total number of 19 vertices ( $2N-1$ ). Elements are the leaves (1-10) and hierarchical cluster fusions are represented by non-leaf nodes (11-19). (B) Example of an adaptive partition over the HC in (A), able to reject outliers and detect clusters using a similarity threshold. Clusters are encircled in green, cyan and purple while the outlier is encircled in orange.

the edges,  $e_i = v_j, v_k$ . The degree  $d_i$  of a graph vertex  $v_i \in V$  is defined as the sum of the weights of edges attached to  $v_i$ , and the volume  $vol(A)$  of a set of vertices  $A$  is defined as the sum of the vertex degrees from all the vertices in the set. If each pair of vertices has an edge connecting them, the graph is complete and has  $N(N-1)/2$  edges. If a minimum affinity threshold is imposed, the graph complexity is reduced as edges with affinities under the threshold are not included in the graph, reducing the processing time and the disk space required to store the data. See Figure 4.4 for an example of an affinity matrix and its corresponding complete affinity graph.

## Hierarchical clustering

Most hierarchical clustering (HC) [Johnson (1967)] implementations use the agglomerative approach, where each data element is initially considered as a singleton cluster. Then, the algorithm successively merges the most similar clusters until all elements have been merged into a single remaining cluster. The result is a forest composed by one or more trees, where each tree represents a connected component of the affinity graph. The hierarchical clustering is often represented by a two dimensional diagram known as *dendrogram* which illustrates the fusions made at each successive stage of analysis. An example of such a dendrogram is illustrated in Figure 4.5 (A). A dendrogram resulting from the clustering of a complete affinity graph will contain  $2N-1$  nodes, where  $N$  is the number of elements to be clustered.

Many variants are used to defining the closest pair of clusters in function of the dissimilarity between elements  $d(\cdot, \cdot)$ . Three main techniques can be distinguished for the calculation of the dissimilarity between clusters  $D(\cdot, \cdot)$  (see Figure 4.6):

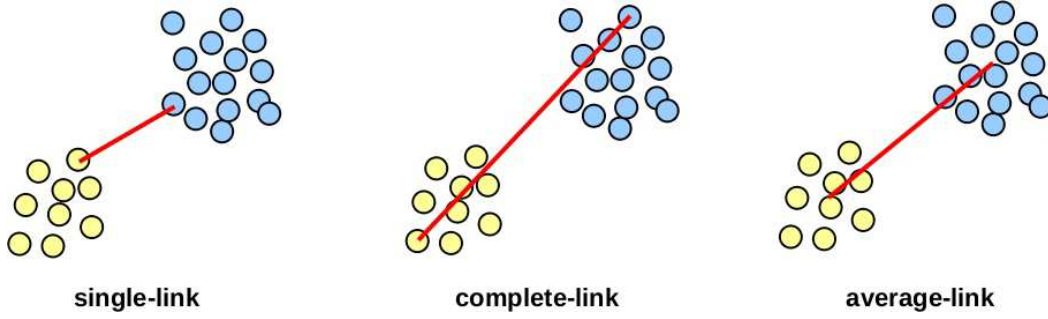


Figure 4.6: The three linkage types of hierarchical clustering: single-link, complete link and average-link.

**Single-link:** distance between clusters is defined as the distance between the closest pair of elements in the two clusters.

$$D(P, Q) = \min_{p \in P, q \in Q} d(p, q) \quad (4.3)$$

This technique is sensitive to noise and outliers and produces long, elongated clusters due to chaining effect.

**Complete-link:** distance between clusters is defined as the distance between the most distant pair of elements in the two clusters.

$$D(P, Q) = \max_{p \in P, q \in Q} d(p, q) \quad (4.4)$$

This technique makes more compact and spherical clusters and tends to produce clusters of same diameter, breaking large clusters.

**Average-link:** distance between clusters is defined as the average of pairwise distance between elements in the two clusters.

$$D(P, Q) = \frac{1}{|P||Q|} \sum_{p \in P} \sum_{q \in Q} d(p, q) \quad (4.5)$$

Is a compromise between the sensitivity of complete-link clustering to outliers and the tendency of single-link clustering to form long chains.

**Hierarchical clustering partition.** A big advantage of hierarchical clustering is that no assumptions must to be made on the number of clusters. Furthermore, the hierarchy provides much more information than a simple partition. The resulting tree can be analysed in order to find the desired partition by the application of several criteria. The simplest partition can be obtained by cutting the dendrogram at a desired level using a (dis)similarity threshold, where each resulting connected component forms a cluster. Other adaptive partitions can be performed using different criterion as cluster size, or

inter-cluster similarity, allowing also the rejection of outliers. Figure 4.5 (B) shows an adaptive partition for the toy example in Figure 4.4. In this illustration, clusters can be selected as groups with a high inter-cluster similarity and the outlier (node 10) can be detected so it is an isolated element, presenting a low similarity with the cluster which it was regrouped to (node 15). To have a perception of the results quality, the affinity matrix can be reordered so that the clustered elements are contiguous. Figure 4.7 shows the final partition and the reordered matrix.

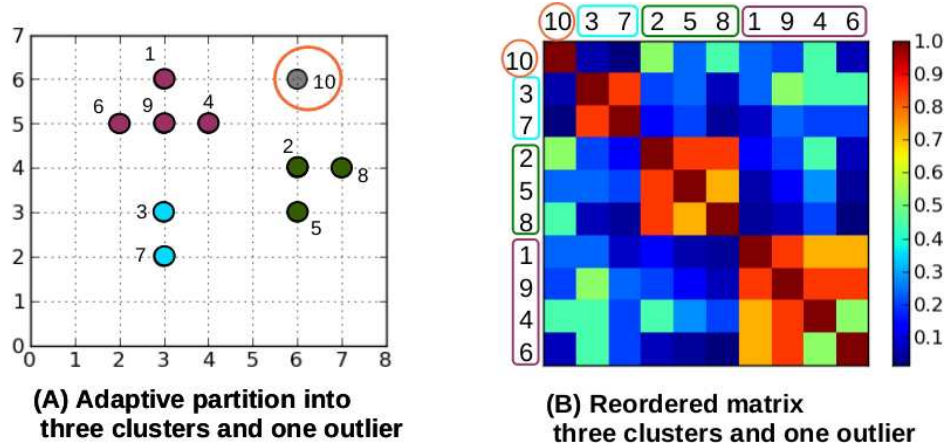


Figure 4.7: Example of hierarchical clustering adaptive partition using average-link. (A): Resulting clusters when using the partition in Figure 4.5 (A) of the hierarchical clustering tree. Clusters elements are in green, cyan and purple while the outlier is encircled in orange. (B): The reordered affinity matrix, containing clustered elements in contiguous rows. Note that the affinity between all the elements of each cluster is high while the affinity between elements of different clusters is low.

Hierarchical clustering presents the limitation to be time consuming, as its complexity is at least quadratic in the number of data points and so, not applicable for very large datasets.

### Partitional clustering

As mentioned above, partitional algorithms find directly a partition of the data and in general present the limitation to require in advance the number of clusters. These algorithms use a criterion function to be minimized with emphasis in the local structure of the data, as by assigning clusters to peaks in the probability density function, or the global structure. An optimal solution could be found with an evaluation of the criterion for all possible partitions containing  $K$  clusters, exploding the combinatorial number of search. Then, partitional algorithms usually use the optimized approach to find the solution, starting with an initial partition and moving elements so that the value of the criterion function improves. The problem is that they might converge to local minima. We briefly describe here the main families of partitional algorithms [Kaski (1997); Miranda (1999); Jain (2010); Wassermann et al. (2010a)].

**Square-error clustering methods.** The most commonly used clustering strategy is based on the square-root error criterion, defined as the sum of the Euclidean distances between each point and its cluster center.

The most known square-error clustering is the K-means algorithm [MacQueen (1967)]. Its implementation uses an iterative refinement technique, given an initial set of  $K$  cluster centroids, specified randomly or by some heuristic. The algorithm proceeds by alternating an *assignment step*, where each element is assigned to the cluster with the closest centroid and an *update step*, where new centroids are calculated for each new cluster. The algorithm is stopped when some convergence criterion is met.

The main advantages of this algorithm are its simplicity and speed which allows it to run on large datasets. One disadvantage is that it does not yield the same result with each run, since the resulting clusters depend on the initial partition. Besides, it tends to produce spherical, equal-sized clusters. Several extensions have been proposed to improve this algorithm, for example to find a better approximation to the optimal minima or generalize it to arbitrary shapes.

**Clustering by mixture decomposition.** These methods assume that the data can be represented by a mixture of several distributions. For that, a density function is modeled as a sum of parameterized functions. The clustering method estimates then the appropriate parameters for the model functions. The expectation-maximization (EM) algorithm [Dempster et al. (1977)] is commonly used for the estimation of the parameters of a mixture model, based on a maximization of the likelihood (or log-likelihood). EM is an iterative method which starts with initial parameters for the model distribution and proceeds iteratively with an expectation (E) step followed by a maximization (M) step. E step probabilistically assign points to clusters, by the computation of the expectation of the likelihood evaluated using the current estimate for the latent variables. M step computes parameters maximizing the expected likelihood found on the E step. The output of this method are the distribution parameters and a soft assignment of points to clusters.

Other approach, the Dirichlet Process clustering algorithm performs Bayesian mixture modeling [Blei et al. (2003)], where data is assumed to be samples from an infinitely parameterized probability distribution. The Dirichlet Process mixture model can be used both for flexible density estimation and for clustering when the number of clusters is a priori unknown.

**Clustering by density estimation and mode seeking.** This approach views clusters as regions of the feature space in which the elements are dense, separated by regions of low density. Then, data is seen as a density function, where the maxima, called modes, are associated to the cluster centers. Each element is assigned to the cluster with the closest center. Several algorithms have been proposed for mode-seeking

clustering. A known method, the mean-shifting algorithm [Cheng (1995)], performs for each data point in the feature space, a gradient ascent procedure on the local estimated density until convergence.

The main advantages of these methods are that there are no embedded assumptions on the shape of the distribution nor the number of modes/clusters. However, the number of patterns should be large enough to get a good estimate.

**Graph-based clustering.** Some clustering methods use graph theory to analyze the connectivity of the nodes and determine the clusters. These are based on the bi-partitioning problem, where a criterion is used to find a partition into two disjoint sets of nodes,  $A$  and its complement  $\bar{A}$ . For that, an inter-set similarity  $\sum s(A, \bar{A})$ , denoting the cost associated with  $(A, \bar{A})$ , can be defined as the total sum of weights of edges between  $A$  and  $\bar{A}$ . Thus, a *minimum-cut* (or *mincut*) criterion can be used to minimize  $\sum s(A, \bar{A})$  and found the partition. This problem can be solved efficiently, but partitioning is unbalanced as only some isolated points are separated from the main group of elements.

The *spectral graph clustering* methods solve the graph partitioning problem based on a relationship between connected components and the Laplacian of graph [Fiedler (1975)]. These algorithms map the original space to a eigen space using a matrix called Graph Laplacian, which diagonal contains the degrees  $d_i$  of the graph vertices  $V_i$ . Fiedler (1975) demonstrated that the eigenvector associated to the second smallest eigenvalue (called *Fiedler vector*) can be used to split the graph using the *mincut* criterion. Posteriorly, other criteria were defined using a particular Graph Laplacian and a different postprocessing of the eigenvector. First, Hagen and Kahng (1992) proposed the *radio-cut* that normalizes the cut with the cluster sizes (i. e. number of vertices of partition  $A$ ), leading to more balanced clusters. Then, Shi and Malik (2000) proposed the *normalized-cut*, that normalizes by the weights of the edges ( $vol(A)$ ), a method extensively used due to its better results.

Even though spectral clustering methods must solve a large eigenproblem, they can be implemented efficiently even for large datasets, but with the constraint to use a sparse similarity graph [von Luxburg (2007)], which is not the case for all the applications. Another limitation is that solutions for the eigenproblem add parameters to the algorithm which have no interpretation regarding the clustering technique but an important effect in the results [Wassermann (2010)]. Furthermore, the analysis requires data within each cluster to be uniformly sampled, which produces artifacts when this hypothesis is not met [Wassermann et al. (2008)].

More detailed reviews of clustering methods can be found in [Jain (2010); Duda et al. (2001); Wassermann (2010)].



#### 4.4.2 Fiber similarity measures

Fiber clustering methods require a similarity measure that can quantify the closeness of two fibers. Different similarity measures have been proposed in the literature. Some similarities are based on statistics over the shape of the tracts. For example, [Batchelor et al. \(2006\)](#) made use of fundamental geometric invariants, such as curvatures and torsions, or Fourier descriptors, to compare the shape of pairs of curves. In other work, [Corouge et al. \(2006\)](#) estimated a mean fiber tract shape using Procrustes analysis and characterized statistical shape deviations from this template shape along the tract. Besides, based on local curvature and torsion, [Leemans et al. \(2006\)](#) defined a fiber similarity measure used for fiber datasets coregistration. These measures does not take into account partial overlapping of fibers as a similarity feature and are unsuited for automatic classification of fibers in the brain [[Wassermann \(2010\)](#)].

One approach, presented by [Jonasson et al. \(2005b\)](#) uses voxels to perform a pairwise comparison of distance and shape between fibers. The similarity measure was evaluated as the number of intersections between fibers, represented by the number of times that two fibers share the same voxel. This metric is a simple attempt for considering partial overlapping of fibers.

Other set of works use different similarity measures based on the sequence of points parameterizing each fiber tract [[Ding et al. \(2003\)](#); [Corouge et al. \(2004\)](#); [Gerig et al. \(2004\)](#); [O'Donnell and Westin \(2007\)](#); [Maddah et al. \(2008b\)](#)]. In an early work, [Ding et al. \(2003\)](#) determined corresponding curve segments and used Euclidean distance to define a piece-wise similarity measure. This approach is not adapted for whole-brain tractography datasets as it requires a particular 2D region for the seeding of fiber tracts.

In [[Corouge et al. \(2004\)](#)], the authors performed a clustering using similarity of adjacent curves and an iterative processing scheme for grouping sets of curves to bundles and rejecting the outliers. They proposed three fiber pairwise distances, where a fiber  $F_i$ , is represented by a set of 3D points,  $\mathbf{p}_k$ ,  $\mathcal{F} = \{F_i, F_i = \{\mathbf{p}_k\}\}$ :

**Closest point distance**,  $d_c$ , defined as the closest distance between pairs of curves  $F_i$  and  $F_j$ :

$$d_c(F_i, F_j) = \min_{\mathbf{p}_k \in F_i, \mathbf{p}_l \in F_j} \|\mathbf{p}_k - \mathbf{p}_l\|, \quad (4.6)$$

where  $\|\cdot\|$  is the euclidean norm.

**Mean of closest distances**,  $d_M$ , defined as the mean of the closest distances for every point of curve  $F_i$  to curve  $F_j$ :

$$d_M(F_i, F_j) = \text{mean}(d_m(F_i, F_j), d_m(F_j, F_i)), \quad (4.7)$$

with  $d_m(F_i, F_j) = \text{mean}_{\mathbf{p}_l \in F_i} \min_{\mathbf{p}_k \in F_j} \|\mathbf{p}_k - \mathbf{p}_l\|$ .

**Hausdorff distance**,  $d_H$ , as the maximum of the closest distances for every point of

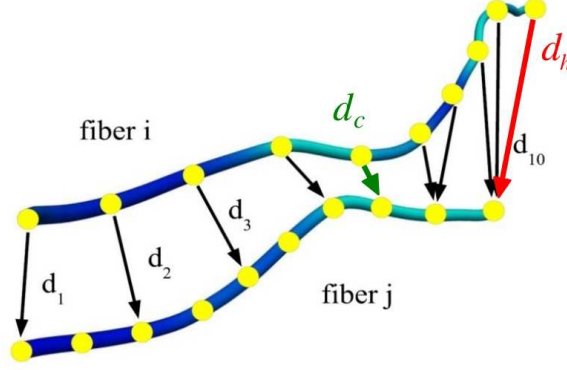


Figure 4.8: Illustration of distances based on closest points. The directed closest points distances (only from fiber  $i$  to  $j$ ) are represented with arrows ( $d_1, d_2, \dots, d_{10}$ ). The closest point distance  $d_c$  is represented by the green arrow (see equation 4.6). The directed maximum closest distance ( $d_h$ ) is represented by the red arrow. The Hausdorff distance ( $d_H$ ) will be the maximum of the two directed distances  $d_h$  (see equation 4.8). The directed mean of closest distances ( $d_m$ ) will be the mean of the distances ( $d_1, \dots, d_{10}$ ). The mean of closest distances ( $d_M$ ) will be the mean of the two  $d_m$  distances (see equation 4.7) [Adapted from O'Donnell and Westin (2007)].

curve  $F_i$  to curve  $F_j$ :

$$d_H(F_i, F_j) = \max(d_h(F_i, F_j), d_h(F_j, F_i)), \quad (4.8)$$

$$\text{with } d_h(F_i, F_j) = \max_{\mathbf{p}_k \in F_i} \min_{\mathbf{p}_l \in F_j} \|\mathbf{p}_k - \mathbf{p}_l\|.$$

See Figure 4.8 for an illustration of the closest distances between two fibers. The distance  $d_c$  can not discriminate different fiber shapes since it encodes only very coarse information about fiber similarity and closeness. On the contrary,  $d_M$  provides a global similarity measure integrated along the whole curve [Corouge et al. (2004)]. The Hausdorff distance  $d_H$  is a worst-case distance.

Figure 4.9 shows an example of these three fiber similarity measures for four fibers. The distances between the red fiber and the other fibers (cyan, green and blue) were calculated. In this example, we can see that the blue and green fibers have a similar  $d_c$  distance, even though the green fiber is more similar to the red fiber. Even worst, the cyan fiber, which presents a shape quite different, has a very small  $d_c$  distance. Distance  $d_M$  is more suitable for a better representation of the average resemblance between fibers but distance  $d_H$  appears more accurate if a stringent similarity measure is required. These distances can deal with a variable degree of partial overlapping and have been used successfully for a whole-brain white matter fiber clustering [O'Donnell and Westin (2007)].

In [O'Donnell and Westin (2005); O'Donnell et al. (2006); O'Donnell (2006)] the authors used the mean of closest point distance (equation 4.7). They also proposed another symmetrized fiber similarity measure, defined as the minimum of the directed closest dis-

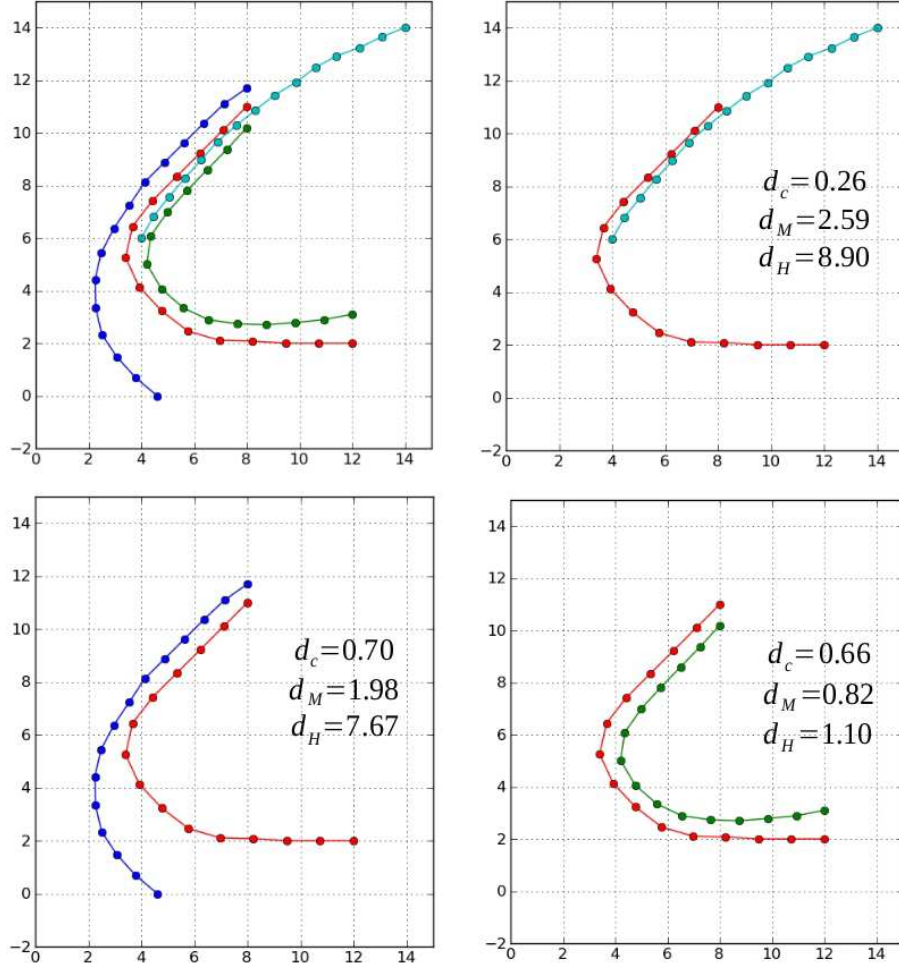


Figure 4.9: Comparison of three pairwise fiber distances: Closest point distance ( $d_c$ ), mean of closest distances ( $d_M$ ) and Hausdorff distance ( $d_H$ ). The distances between the red fiber and other three fibers (cyan, green and blue) were calculated. Distance  $d_c$  is the less discriminant distance, while distance  $d_M$  is more suitable for a good representation of the average resemblance between fibers. On the other side, distance  $d_H$  appears more accurate if a stringent similarity measure is required.

tances,  $d_m$  (equation 4.7).

$$d_{Min}(F_i, F_j) = \min(d_m(F_i, F_j), d_m(F_j, F_i)). \quad (4.9)$$

In these works, fibers were subsampled using 15 equidistant points to reduce calculation times, while keeping a good precision in cluster results.

Zhang et al. defined a distance between two fibers as the average distance from any point on the shorter fiber to the closest point on the longer fiber. In order to emphasize important differences between a pair of trajectories, the average only considered distances above a threshold  $t$  [Zhang and Laidlaw (2002); Zhang et al. (2003)]. The distance, called

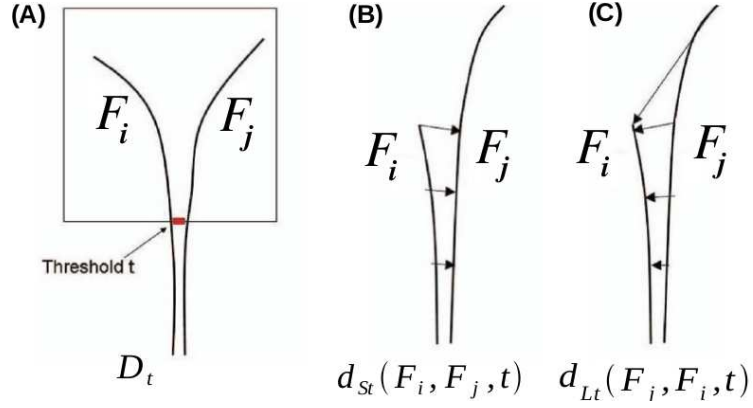


Figure 4.10: Illustration of thresholded closest distances. (A) Distance measure  $D_t$  proposed to emphasize important differences between a pair of fibers, defined in equation 4.10 [Zhang and Laidlaw (2002); Zhang et al. (2003)].  $Q$  and  $R$  are considered different if they branch for a portion of their lengths. Without the threshold, the mean of closest distances between  $Q$  and  $R$  is low if they stay close for a large part of their lengths. (B) and (C) are two symmetric distances based on the mean of closest distances, where only distances above a threshold are considered in the calculation of the mean (see equation 4.11). (B) illustrates the shorter mean of thresholded closest distance  $d_{St}$  while (C) illustrates the longer mean of thresholded closest distance  $d_{Lt}$  [From Zhang et al. (2008a)].

mean of thresholded closest distances, was then defined as

$$D_t = \frac{\int_{s_0}^{s_1} \max(\text{dist}(s) - t, 0) ds}{\int_{s_0}^{s_1} \max\left(\frac{\text{dist}(s) - t}{|\text{dist}(s) - t|}, 0\right) ds}, \quad (4.10)$$

where  $s$  parameterizes the arc length of the shorter trajectory,  $s_0$  and  $s_1$  are the starting and end points of  $s$ , and  $\text{dist}(s)$  is the shortest distance from location  $s$  on the shorter trajectory to the longer trajectory (see Figure 4.10 (A)).

Two symmetric distances were later proposed in [Zhang et al. (2008a)]. First, the distance  $d_t$  was defined by using a threshold on the minimum contributing distance for the mean of closest distances between curves, as

$$d_t(F_i, F_j, t) = \frac{\text{mean}}{\mathbf{p}_k \in F_i, (\min_{\mathbf{p}_l \in F_j} \|\mathbf{p}_k - \mathbf{p}_l\|) > t} \min_{\mathbf{p}_l \in F_j} \|\mathbf{p}_k - \mathbf{p}_l\|, \quad (4.11)$$

where  $t$  is the minimum threshold. Then, the **shorter mean of thresholded closest distances** was defined as

$$d_{St} = \min(d_t(F_i, F_j, t), d_t(F_j, F_i, t)), \quad (4.12)$$

and the **longer mean of thresholded closest distances** was defined as

$$d_{Lt} = \max(d_t(F_i, F_j, t), d_t(F_j, F_i, t)). \quad (4.13)$$

The distance  $d_{St}$  is a discrete approximation of  $D_t$ . Usually, distance  $d_{St}$  is smaller than  $d_{Lt}$  as the unmatched part of the longer curve only counts in  $d_{Lt}$  (see Figure 4.10).

Wassermann et al. (2010a) defined a similarity measure between bundles (or fibers) using a mathematical framework for performing statistical analysis of fiber tracts and bundles. The model includes diffusion information and relates each bundle (or fiber) with a ROI in the volume, mapping every voxel to a degree of membership to the bundle, the bundle's *blurred indicator function* (BIF). Each fiber  $\mathcal{F}$  is then modeled as a BIF,  $\mathcal{Y}_{\mathcal{F}} : \mathbf{p} \in \mathbb{R}^3 \rightarrow \mathbb{R}$ , presenting a maximal level set that corresponds to  $\mathcal{F}$ . The  $\mathcal{Y}_{\mathcal{F}}$  is blurred according to the DT field, along the direction of the fiber.

The BIF is then modeled by a Gaussian Process (GP)

$$\mathcal{Y}_{\mathcal{F}}(\mathbf{p}) \sim GP(\mathcal{Y}_{\mathcal{F}}^*(\mathbf{p}), \mathcal{C}_{\mathcal{F}}(\mathbf{p}, \mathbf{p}')) , \quad (4.14)$$

where the mean function  $\mathcal{Y}_{\mathcal{F}}^*(\mathbf{p})$  and covariance function  $\mathcal{C}_{\mathcal{F}}(\mathbf{p}, \mathbf{p}')$  are the parameters of this stochastic process. A similarity measure between bundles was defined to quantify the overlapping of bundles. For that, the inner product between two bundles,  $\mathcal{F}$  and  $\mathcal{F}'$ , is defined as

$$\langle \mathcal{F}, \mathcal{F}' \rangle := \int_{\mathbb{R}^3} \mathcal{Y}_{\mathcal{F}}^*(\mathbf{p}) \mathcal{Y}_{\mathcal{F}'}^*(\mathbf{p}) d\mathbf{p}, \quad (4.15)$$

with its induced norm  $\|\mathcal{F}\|^2 := \langle \mathcal{F}, \mathcal{F} \rangle$ .

The similarity measure is then normalized in order to get values between 0 and 1

$$\langle \mathcal{F}, \mathcal{F}' \rangle_{norm} := \frac{\langle \mathcal{F}, \mathcal{F}' \rangle}{\|\mathcal{F}\| \|\mathcal{F}'\|}. \quad (4.16)$$

This metric serves then as a probabilistic measure of inclusion of two fibers (or bundles). Figure 4.11 illustrates some examples of this similarity measure.

In a recent work, Visser et al. (2011) proposed a fiber similarity measure, that can be called the *sum of the Euclidean distances between corresponding points*. This measure defines the distance between two tracts as:

$$d_{scp}(A, B) = \min \left( \sum_{i=1}^{N_p} \|a_i - b_i\|, \sum_{i=1}^{N_p} \|a_i - b_{N_p-i+1}\| \right), \quad (4.17)$$

where  $a_i$  and  $b_i$  are the position vectors of the points of the tracts  $A$  and  $B$  respectively. A resampling of the tracts must be performed to use this distance measure as the same number of points ( $N_p$ ) is required in all the fibers (25 points were used by the authors). This distance measure presents the advantage to be computationally more efficient than other distances based on the minimum distance between points.

#### 4.4.3 Fiber clustering methods

Several fiber clustering methods have been proposed in the literature. The different approaches use different similarity measures and clustering algorithms. A priori requirements also vary from one method to another as well as the characteristics of the input

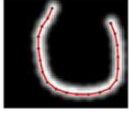
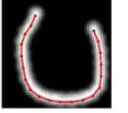
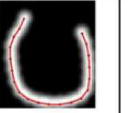
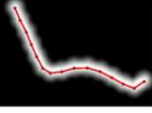

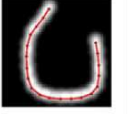
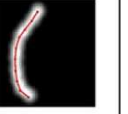
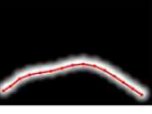



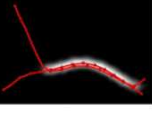
	FF & UNC	FF & FF	FF & FF	CgC & CgC
$y_{\mathcal{F}}^*(\mathbf{p})$				
$y_{\mathcal{F}'}^*(\mathbf{p})$				
$y_{\mathcal{F}}^*(\mathbf{p})y_{\mathcal{F}'}^*(\mathbf{p})$				
$\langle \mathcal{F}, \mathcal{F}' \rangle$	4.26	115.61	48.03	2089.
$\frac{\langle \mathcal{F}, \mathcal{F}' \rangle}{\ \mathcal{F}\  \ \mathcal{F}'\ }$	0.093	0.800	0.474	0.600

Figure 4.11: Examples of the product of blurred indicator functions (BIF) for different fiber pairs, the value of the inner product operation  $\langle \mathcal{F}, \mathcal{F}' \rangle$ , and the inner product normalized by its natural norm  $\|\mathcal{F}\|$ . Inner product quantifies the overlapping of BIFs. A larger inner product means that fibers are more similar and relates to the volume of the overlapping. The normalized inner product quantifies similarity ranging from 0 when overlapping is null to 1 when the two fibers are identical. The compared fibers have been extracted from different anatomical tracts of a dMRI image, the frontal forceps (FF), the uncinate fasciculus (UNC), and the cingulate cortex section of the cingulum (CgC) [From Wassermann et al. (2010a)].

fiber datasets, which complexity increases as diffusion acquisitions and diffusion models are improved. We reviewed the main works proposed in the literature and separated them into two main groups: *single subject* and *multiple subject* fiber clustering methods.

Single subject methods are the first attempts to cluster fiber datasets. These works propose important fiber similarity measures and test different clustering methods. We present in table 4.1 a categorization of single subject fiber clustering methods. Methods were analyzed in function of the main input, the main clustering method and the distance measure, the main anatomical or empirical priors used to recover WM tracts, the main analysis steps, the main outputs and the successfully identified bundles.

Multiple subject fiber clustering methods have been developed from several years with the main objective of identifying well known WM tracts. Several methods propose both, single subject (SS) and multiple subject (MS) approaches, sometimes with different outputs for each case. These approaches require a registration between subjects or to a template, where non-linear strategies become more and more popular. We present in table 4.2 a categorization of multiple subject fiber clustering methods. Methods were analyzed in function of the registration method, the main clustering method and the distance measure, the main anatomical or empirical priors used to recover WM tracts, the main analysis steps, the main outputs and the successfully identified bundles. All the reviewed methods use as input a whole-brain tractography datasets.

Above is presented a more detailed review of the most important works in the domain.



FIBER CLUSTERING METHODS (SINGLE SUBJECT)

METHOD	IN	DISTANCE MEASURE	CLUSTERING METHOD	MAIN ANATOMICAL / EMPIRICAL PRIORS	MAIN ANALYSIS	MAIN OUTPUTS	IDENT. BUNDLES
Ding 2003	RS	Euclidean (fibers)	k-NN	seed ROIs	define corresponding segments / fiber clustering	filtered tract / shape analysis	
Corouge 2004 Gerig04 2004	ST	$d_c, d_M, d_H$ (fibers)	propagation algorithm	manual segmentation of tracts / distance threshold	fiber clustering	filtered tract / shape analysis	CST, part of CC
Zhang 2002 Zhang 2003	WB	$D_t$ (fibers)	single-link HC		fiber culling / fiber clustering	streamtubes & streamsurfaces	
Brun 2003 Brun 2004	WB	use fiber end points	spectral embedding, Ncuts SC	empirical clustering parameters		soft coloring of fiber tracts	

**List of abbreviations (also valid for Table 4.2).**

IN (INPUT): whole-brain tractography (WB), segmented tract (ST) or ROI-seeding (RS).

CLUSTERING METHOD: Hierarchical clustering (HC), Nearest Neighbor (NN), Spectral Clustering (SC).

DISTANCE MEASURE: Closest point distance ( $d_c$ ), Mean of closest distances ( $d_M$ ), Hausdorff distance ( $d_H$ ), Mean of thresholded closest distances ( $D_t$ ), Shorter mean of thresholded closest distances ( $d_{St}$ ), Longer mean of thresholded closest distances ( $d_{Lt}$ ), Blurred indicator function ( $BIF$ ), Sum of the Euclidean distances between corresponding points ( $d_{scp}$ ).

IDENT. BUNDLES (IDENTIFIED BUNDLES): Corticospinal tract (CST), Corona radiata/Internal capsule (CR/IC), Superior longitudinal fasciculus (SL), Inferior longitudinal fasciculus (IF), Inferior fronto-occipital (IFO), Arcuate fasciculus (AF), Cingulum (CG), Uncinate fasciculus (UN), Forceps minor (Fm), Forceps major (FM), Corpus callosum (CC), genu of CC (GCC), splenium of CC (SCC), Anterior thalamic radiation (ATR), Fornix (FX), Middle cerebellar peduncle (MCP), Superior cerebellar peduncle (SCP), Brainstem (BS) Projection tract penetrating frontal, parietal or occipital lobe (PTf, PTp, PTo), CC connecting left&right frontal, parietal or occipital lobes (CCf, CCp, CCo).

Table 4.1: **Categorization of fiber clustering methods (single subject).**

Methods were analyzed in function of the main input, the main clustering method and the distance measure, the main anatomical or empirical priors used to recover WM tracts, the main analysis steps, the main outputs and the successfully identified bundles.

## FIBER CLUSTERING METHODS (MULTIPLE SUBJECTS)

METHOD	REG	DISTANCE MEASURE	CLUSTERING METHOD	ANATOMICAL / EMPIRICAL PRIORS	MAIN ANALYSIS	MAIN OUTPUTS	IDENT. BUNDLES
Zhang 2005	AFF	Euclidean (cluster centroids)	NN		match cluster centroids	cluster correspondance between 2 subjects	
Zhang 2008	AFF	<b>SS</b> : $d_{St}$ , $dLt$ (fibers) <b>MS</b> : Euclidean (cluster centroids)	<b>SS</b> : single-link HC <b>MS</b> : NN	<b>SS</b> : empirical proximity threshold (PTh) <b>MS</b> : bundle template (manual cluster labeling)	<b>SS</b> : fiber culling / fiber clustering / <b>MS</b> : match cluster centroids / search optimal PTh	bundle template / bundle indentification (2 subjects)	<b>SS</b> : CST, CG, UN, Fm, FM, MCP, SL, IL <b>MS</b> : CG, UN, Fm, FM
ElKouby 2005	AFF	<b>SS</b> : connectivity (voxels) <b>MS</b> : fiber cluster mask correlation	<b>SS</b> : k-means <b>MS</b> : k-means	<b>SS/MS</b> : empirical number of clusters	<b>SS</b> : voxel-based clustering <b>MS</b> : clustering for matching fiber cluster masks from all subjects	bundle atlas from 11 subjects	<b>SS</b> : ATR, IL, GCC, SCC, CST, FX <b>MS</b> : CST, parts of CC
O'Donnell 2005 O'Donnell&Westin 2006 O'Donnell-PhD 2006	AFF	<b>SS</b> : $d_M$ (fibers) <b>MS</b> : $d_M$ (fibers from all subjects)	Ncuts SC (Nistrom method)	empirical clustering parameters / manual cluster labeling	<b>SS</b> : fiber clustering <b>MS</b> : fiber clustering (fibers from all subjects)	embedded bundle atlas from 10 subjects	<b>SS/MS</b> : CC, CST, AF, IFO, UN, IL, MCP, SCP
O'Donnell-PhD 2006 O'Donnell 2007	AFF	$d_M$ (fibers)	spectral embedding (fibers) / NN (centroids)	embedded bundle atlas (fibers)	fiber embedding / search nearest cluster centroid for each fiber	bundle identification (5 subjects)	<b>SS/MS</b> : CC, CST, AF, IFO, UN, IL, MCP, SCP
Maddah 2005	AFF	based on B-spline representation (fibers)	NN	bundle template (labeled fibers)	match fibers with template fibers	bundle identification	CC, CR/IC, FX, MCP
Maddah 2007 Maddah 2008b	AFF	use Euclidean distance map from each cluster center (fibers)	Gamma mixture model	one manually selected fiber per bundle and per subject	estimate clustering parameters	probabilistic assignment of each fiber to cluster / point correspondence within each bundle	CC, CR/IC, CG

... continued on next page ...

... continued from previous page...

METHOD	REG	DISTANCE MEASURE	CLUSTERING METHOD	ANATOMICAL / EMPIRICAL PRIORS	MAIN ANALYSIS	MAIN OUTPUTS	IDENT. BUNDLES
Maddah 2008a	CA	use Euclidean distance map from each cluster center (fibers)	Gamma mixture model (Bayesian)	bundle atlas (ROIs) / manually define initial bundle centers / membership threshold	tract bundle from ROI / use atlas as prior / estimate cluster parameters	probabilistic assignment of each fiber to cluster / point correspondence within each bundle	CG, UN
Wassermann 2010	NL	dist. between bundles (and fibers) using <i>BIF</i>	Hierarchical clustering	WM/GM atlas (ROIs)	construction of HC tree and cluster selection using anatomical info.	bundle identification (21 subjects)	AF, CG, UN, CST, IFO, Fm, FM
Li 2010	NL	<i>step2</i> : $d_H$ + fiber length mismatch factor	<i>step2</i> : PCA followed by fuzzy c-means	<i>step1</i> : WM/GM atlas (ROIs) <i>step2</i> : manually label 2 fiber tracts for fiber cluster recognition	<i>step1</i> : use atlas to segment 9 bundles <i>step2</i> : cluster remaining fibers and identify 2 other bundles	bundle identification (10 subjects)	CG, IFO, IL, UN, AF, CCf, CCp, CCo, PTf, PTp, PTo
Visser 2011	NL	dist. between fibers ( $d_{scp}$ )	Hierarchical clustering	<b>SS/MS</b> : empirical clustering parameters / manual labelling of clusters	divide the data and cluster each subset separately (several repetitions) / keep reproducible clusters across repetitions	bundle identification	<b>SS</b> : AF, CG, UN, IFO, IL <b>MS</b> : AF
Wang 2011	CA	fiber point coordinates and orientations (voxels)	Hierarchical Dirichlet processes mixture model	sometimes requires a manual merge of clusters / manual labelling of clusters for training data	voxel-based clustering, use clusters from training data as prior information	tractography segmentation and classification	<b>SS/MS</b> : CC, CST, AF, IFO, UN, IL, MCP, BS

**List of abbreviations** (Remaining abbreviations presented in Table 4.1).

REG. (REGISTRATION METHOD): affine (AFF), congealing algorithm (CA), non-linear (NL).

SINGLE SUBJECT (SS), MULTIPLE SUBJECTS (MS)

Table 4.2: **Categorization of fiber clustering methods (multiple subjects)**. Methods were analyzed in function of the registration method, the main clustering method and the distance measure, the main anatomical or empirical priors used to recover WM tracts, the main analysis steps, the main outputs and the successfully identified bundles. The input is whole-brain tractography for all the methods.

**Fiber clustering for priorly segmented tracts.** Corouge et al. (2004) in their early work developed an iterative algorithm to reject outliers and to cluster curves to fiber bundles based on pairwise distance metrics measuring position and shape similarity of pairs of fibers, described in section 4.4.2. In this work, the inputs were fiber tracts already extracted from another method and the clustering was used to reject outliers. The method uses a distance threshold  $t$ , and a propagation algorithm so that, for each fiber  $F_i$  within a class  $\mathcal{C}$ , at least one fiber  $F_j$ ,  $j \neq i$  in  $\mathcal{C}$  is such that  $d(F_i, F_j) < t$ . This is similar to the algorithms employed by Gerig et al. (2004) and Ding et al. (2003). However, Ding et al. (2003) use seeding ROIs to construct fiber tracts and determine corresponding curve segments to cluster fibers.

**Fiber clustering for whole-brain tractography datasets.** These approaches aim to reduce the complexity of the data and identify the main white matter fiber tracts.

Zhang et al. applied single-link hierarchical clustering based on the distance described in equation 4.10 for fiber dataset visualization and analysis [Zhang and Laidlaw (2002); Zhang et al. (2003)]. In order to remove redundant fibers, the shorter member of any two pairs of curves that exceeded a prespecified threshold was culled, resulting in a sparse fiber dataset. They used two kinds of 3D objects to represent the fibers: “streamtubes” and “streamsurfaces”. Streamtubes, presenting a shape similar to streamlines, were displayed in regions with high anisotropy. Streamsurfaces were surfaces representing regions with planar anisotropy.

In [Zhang and Laidlaw (2005)], clusters were matched across two subjects. Datasets were first roughly registered by matching a bounding box surrounding the whole brain WM. For each path cluster, the centroids of the starting points, middle points, and end points were calculated and concatenated to form a nine-valued feature vector. Fiber clusters from the two subjects were then matched up according to the Euclidean distance between their feature vectors (see Figure 4.12 (A)).

In Zhang et al. (2008a), the authors presented an improved version of their previous works [Zhang et al. (2003); Zhang and Laidlaw (2005)]. First, the distance  $d_{St}$  (equation 4.12) was used for fiber culling, in order to remove “broken short fibers” along a longer neighbor. Then, fibers were clustered using a single-linkage hierarchical clustering based on the distance  $d_{Lt}$  (equation 4.13), which captures any difference between fibers. The number of clusters was defined using a proximity threshold, which was varied between 0.1 and 10 mm.

An expert rater interactively selected a proximity threshold to achieve visually optimal clusters, i.e. a solution that appeared to be the most accurate global representation of known white-matter anatomy. The identified clusters from four subjects were aligned using an affine registration to build a WM bundle template. This template was used to automatically identify bundles from two new subjects. The subjects were first clustered and then, the resulting clusters were registered to the template and matched with labelled

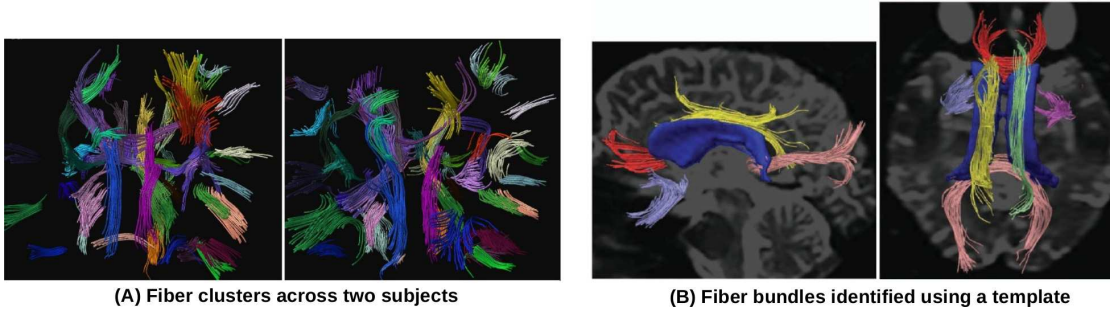


Figure 4.12: Illustration of fiber clustering using Hierarchical Clustering. (A) Fiber clusters across two subjects. Clusters were obtained for each subject using single-link HC and the distance  $D_t$ , described in equation 4.10 [Zhang et al. (2003)]. Clusters were then matched up according to a distance between their feature vectors [From Zhang and Laidlaw (2005)]. (B) Fiber clusters were identified for one subject, using the method in [Zhang et al. (2008a)]. Clusters were first obtained for each subject using single-link HC and the distance  $d_{Lt}$  (equation 4.13), and then were identified using a bundle template [From Zhang et al. (2008a)].

template clusters using a distance between cluster centroids. The algorithm searched for a proximity threshold on each new subject that maximized the matching (see Figure 4.12 (B)).

The limitation of this work was the assumption that there exists a threshold that can segregate a set of trajectories into discrete clusters that are anatomically significant. Long thick coherent white-matter tracts or those whose geometry is distinct from their neighbors were identified with high confidence in the fiber bundle models. In contrast, shorter thinner white-matter tracts like the anterior commissure were almost completely missing [Zhang et al. (2008a)]. More proximal fiber bundles were not included in the model, for example, the inferior longitudinal fasciculus with the fronto-occipital fasciculus, which present close trajectories in the brain. Furthermore, the accuracy of the labeling results was also likely to be affected by the anatomical variation of a fiber bundle type across the subjects and the registration errors.

In [El Kouby et al. (2005)], a two-stage inference strategy was proposed, composed by a first intra-subject clustering and then a matching of bundles across subjects. The intra-subject clustering was based on white matter voxel connectivity instead of a direct similarity measure between fiber tracts. First, the subject WM mask was aligned to Talairach space and parcellated into a grid of cubic ROIs of 5 mm. Then, a connectivity matrix was created, containing for each pair of ROIs the number of fiber tracts crossing them, and posteriorly binarized. A k-means clustering was performed based on the Euclidean distance between matrix rows. Final bundles were extracted from WM clusters, as the fibers included at least a 60% in the cluster. The inter-subject clustering used smoothed 3D masks to represent bundles. A similarity measure was computed as the correlation coefficient between bundle representations. Then, a k-means was applied to match bundles across subjects. The method was applied to eleven subjects, where some

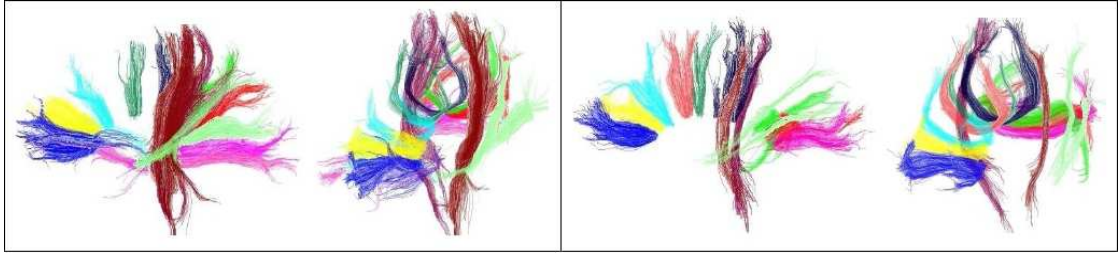


Figure 4.13: Voxel-based fiber clustering results across subjects, described in [El Kouby et al. (2005)]. The figure shows the results of the clustering for two of the eleven subjects. For each subject two views are presented. Each color denotes a cluster that gathers bundle across most of the subjects.

known anatomical bundles were identified across most of the subjects (see Figure 4.13). The analysis of fiber tracts in the voxel domain is an interesting idea but the proposed implementation required several postprocessings in order to clean-up the results and get the final bundles.

A recent work proposed by Wang et al. (2011) also clusters voxels instead of fibers. This work uses fiber point coordinates and orientation to determine the similarity between voxels. The clustering of the voxels is performed using a hierarchical Dirichlet processes mixture (HDPM) model. The number of clusters is automatically learned driven by data with a Dirichlet process prior. The bundle models are learned from training data without supervision. These models can then be used as priors to cluster (or classify) fibers of new subjects, with the possibility to create new clusters for structures not observed in the training data. As in [El Kouby et al. (2005)], the dMRI WM voxels are uniformly parcellated in order to create the *voxels* (or parcels) to be clustered. The size of the parcels is a parameter used to define the scale of the analysis, e. g. the size of the bundles (see Figure 4.14 B). The approach used to extract the fiber bundles from the voxel clusters is not explained. As the method proposed by El Kouby et al. (2005), this work is based on similarity measures between voxels, instead of computing pairwise distances between fibers, allowing the analysis of huge tractography datasets. The largest dataset used had 120,000 fibers. The method is compared with the method proposed by O'Donnell and Westin (2007), over DTI data. Results obtained by Wang et al. (2011) method shown better completeness and correctness, for the number of clusters determined automatically by the HDPM approach, even though in some test datasets the authors performed a manual merge of some clusters in order to segment the anatomical structures. See examples of segmentations in Figure 4.14 A-B.

This approach is very interesting but some limitations may exist when only using a voxel-based strategy, without any pre- or post-processing steps. As we will explain in next chapter, we also use this kind of strategy to cluster fibers, but with the addition of several pre- and post-processing steps that make the method more robust. We think that the use of voxel-based clustering alone can decrease the quality of the results when



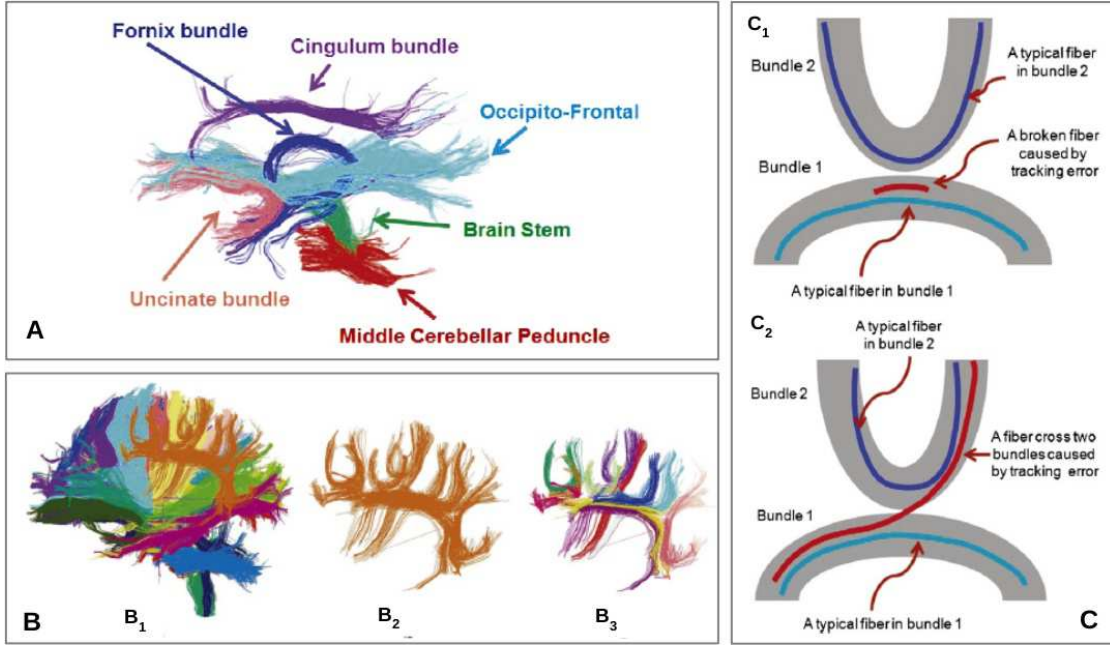


Figure 4.14: A voxel-based tractography segmentation method using hierarchical Dirichlet processes mixture (HDPM) model [Wang et al. (2011)]. **A**: Anatomical labels of some fiber bundles generated by the method. **B**: An example of multiscale clustering. The spatial range of the whole brain is 240 mm x 240 mm x 240 mm. ( $B_1$ ): The clustering result when the space is quantized into voxels of size 12.5 mm x 12.5 mm x 12.5 mm. The bundles correspond to structures at a large scale. ( $B_2$ ): One bundle from ( $B_1$ ). ( $B_3$ ): The space is quantized into voxels of size 3.5 mm x 3.5 mm x 3.5 mm and the bundle in ( $B_2$ ) is further clustered into smaller bundles corresponding to structures at a finer scale. **C**: Tractography errors which generate short broken fibers in ( $C_1$ ) and fibers crossing two bundles in ( $C_2$ ).

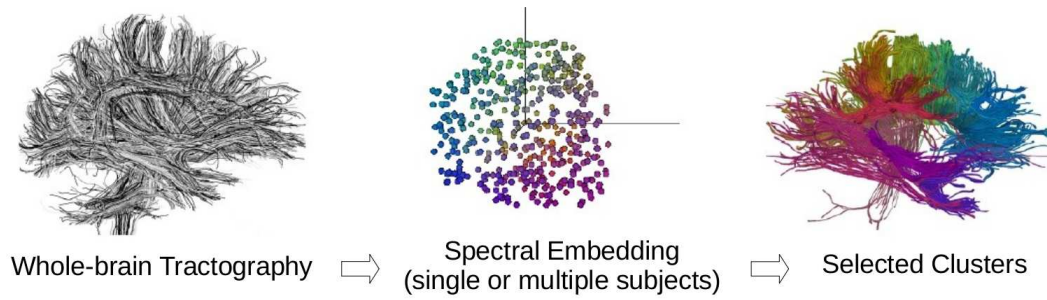
overlapping bundles exist, i. e. sharing an important amount of voxels (see section 5.3.2). In general, methods that only use a voxel-based strategy assume that fiber bundles are not overlapped (see Figure 4.14) which may lead in a loss of fibers and bundles. For example, in Figure 4.14 C, the method consider errors a short bundle overlapped with a longer bundle or a bundle overlapped with two other bundles. In these specific examples, these configuration are probably errors, but other overlapping configurations may be valid, as several bundle fascicles sharing the central part of a long bundle, or short association fibers partially overlapped with long deep WM bundles. This issue may be negligible in the case of DTI tractography datasets using a FA-based propagation mask, for the study of long association bundles. But in the case of complex tractography datasets, as those we use in this thesis, this issue is more important. We calculate HARDI tractography datasets using a T1-based propagation mask (see section 5.4.1) that allows a better reconstruction of fiber bundles, specially in the subcortical regions, which is in particular relevant for short association bundles. Fibers of different shape and length present then a higher overlapping and the study of short association bundles requires a more robust approach. In next chapter we describe how we overcome this problem.

Brun et al. (2003) presented the idea of pseudo-coloring (soft clustering) fiber tracts to enhance the visualization of human white matter fiber datasets. A spectral embedding was used to map each data point to a low-dimensional Euclidean space, using a distance that only considered the endpoints for a pair of fiber tracts. In [Brun et al. (2004)], the authors performed a clustering of fiber tracts using Normalized Cuts.

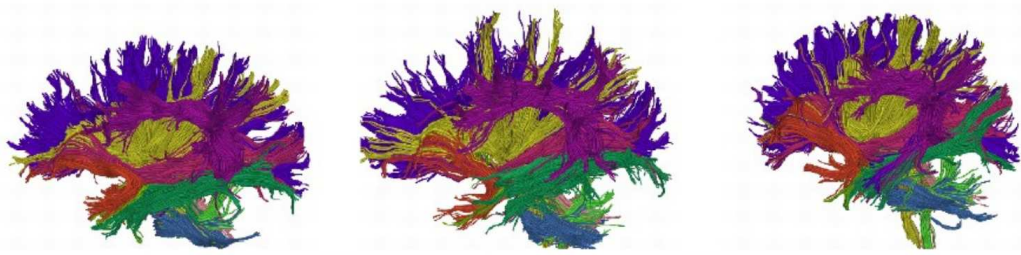
O'Donnell et al. also used spectral clustering to regroup fiber tracts, and find correspondence between subjects [O'Donnell and Westin (2005); O'Donnell et al. (2006); O'Donnell (2006)]. To determine the embedding space, the authors used the Normalized Cut with the Nistrom method [Fowlkes et al. (2004)]. Then, instead of computing the entire affinity matrix directly, a random sample of paths ( $\sim 1500$ ) was used to calculate the affinity matrix and determine the eigenvectors. The affinity was calculated from a symmetrized version of the mean closest point distance [Corouge et al. (2004)] between fibers, described in section 4.4.2. Figure 4.15 (A) illustrates the spectral embedding of the paths. To find matching clusters in all subjects, multiple subjects (spatially aligned) were simultaneously embedded and used to give a segmentation of the input tractography. In many cases, an anatomical structure was subdivided into many clusters. Clusters were manually associated with anatomical labels in order to create a “high-dimensional” white matter atlas containing a representation of the known anatomical deep WM tracts in the embedded space [O'Donnell and Westin (2006, 2007)]. The atlas was constructed based on ten different subjects and was then used to automatic segment the most known fiber bundles from other five subjects. Figure 4.15 (B) shows an example of the results, where several well known white matter tracts were identified.

Maddah et al. (2005) used hand-selected ROIs in white matter to construct a bundle template to which curves from a new subject can be registered. B-spline representation of the fiber tracts was used for pairwise comparison of the fiber tracts extracted from the subject to those from the atlas. This supervised clustering compared first the projected tracts with the major bundles in the atlas and then with the smaller ones.

Maddah et al. presented a statistical model of fiber bundles, calculated as the mean and standard deviation of a parametric representation of the fibers [Maddah et al. (2007a, 2008a)]. Using this model representation, expectation-maximization (EM) was performed to cluster the fibers in a Gamma mixture model framework. Point-by-point correspondence of the fibers within a bundle was obtained by building distance maps from each cluster center at every iteration of the EM algorithm. The similarity of each trajectory to the center was done by computing the Mahalanobis distance. A penalty term was added to the distance for each missing point in order to handle partial overlapping. The distance was also normalized by the fiber length. Besides, a threshold on the membership likelihoods was used to identify outliers. The method was only applied to some big fiber bundles. The result of clustering was the probabilistic assignment of the fiber trajectories to each cluster, an estimate of the cluster parameters, and point correspondences. This approach required user initialization, by manually selecting a fiber which is known to be in each



**(A) Spectral embedding of fiber tracts from whole-brain tractography**



**(B) Results of automatic segmentation**

Figure 4.15: Illustration of fiber segmentation method using spectral clustering [O'Donnell and Westin (2005); O'Donnell et al. (2006)]. (A) represents the embedding and clustering process. The input is whole-brain tractography (left). Spectral embedding (center) is performed using the Normalized Cuts method. This produces a representation of each path from tractography (of a single subject or multiple subjects) as a point in the embedding space. Finally, a clustering solution is found in the embedding space, and used to give a segmentation of the input tractography (right). Then embedding vectors are an actual sample of 500 fibers from the whole population, with the first 3 dimensions displayed. The colors of the clusters (right) are assigned according to the embedding coordinates. In many cases, an anatomical structure will be subdivided into many clusters. (B) shows the results of automatic segmentation for three subjects, using the WM atlas proposed in [O'Donnell and Westin (2006, 2007)]. To construct the atlas, clusters forming the anatomical WM tracts were manually labelled [From O'Donnell (2006).]

desired bundle.

Maddah et al. (2008b) proposed a Bayesian approach to incorporate anatomical information in the clustering of fiber trajectories. An expectation-maximization (EM) algorithm is used to cluster the trajectories, in which an atlas serves as the prior on the labels. The authors employed the atlas described in [Wakana et al. (2004)], (see appendix A), which contains labeled regions of the major anatomical fiber bundles. Fibers were first projected to the MNI atlas space and the atlas ROIs were used for the calculation of the initial membership probability of each trajectory. This anatomical prior gave more robustness to the algorithm but it was still needed to define initial bundle centers.

Wassermann et al. (2010a) used an anatomical atlas in conjunction with a fiber similarity metric to cluster and classify WM fibers. They proposed a Gaussian process framework that facilitates mathematical operations between tracts by the definition of an inner product space (see section 4.4.2). The model includes diffusion information and relates each

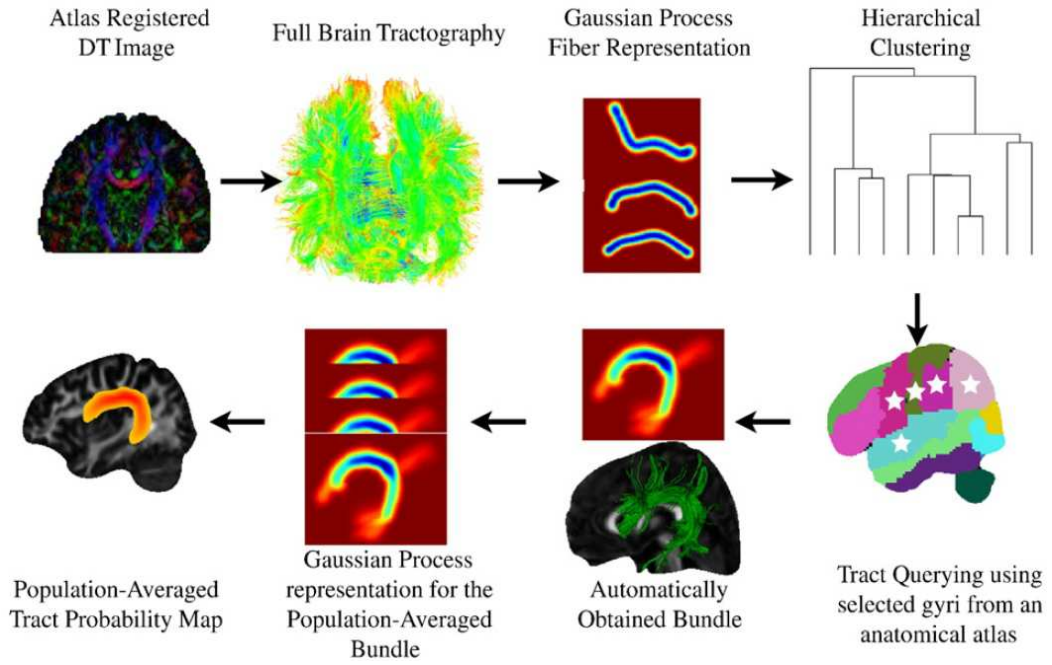


Figure 4.16: Illustration of WM segmentation using the mathematical framework described in [Wassermann et al. (2010a)]. The procedure clusters WM fibers into anatomical bundles and produces a tract probability map for each bundle. First, diffusion tensor MR images are registered using a deformable registration of DT and whole-brain tractography is then calculated to obtain around 10,000 fibers per brain. The Gaussian process representation for each fiber is subsequently produced. Well-known anatomical WM tracts were identified from the datasets of 21 healthy subjects, by applying a clustering and a tract-querying algorithm to each subject individually. Finally a population-averaged tract probability map can be generated for each bundle [From Wassermann et al. (2010a)].

bundle (or fiber) with an ROI in the volume, mapping every voxel to a degree of membership to the bundle, the bundle’s *blurred indicator function*. The similarity measure was defined for fiber bundles and fiber tracts, which are considered as single-fiber bundles.

The method first registers diffusion tensor MR images using a deformable registration of diffusion tensor [Yang et al. (2008)]. Then, whole-brain tractography is calculated to obtain around 10,000 fibers per brain. Subsequently, the Gaussian process representation is produced for each fiber. A hierarchical agglomerative clustering is then applied to each subject individually in order to obtain a dendrogram. Clusters are automatically selected by the use of a publicly available atlas that has a parcellation of the brain gyri on the gray and white matter [Wakana et al. (2004)] as anatomical volumetric information. For the identification of each WM tract, this step employs a “tract query”, which defines a set of gray and white matter regions that the tract must traverse. Well-known anatomical WM tracts like the arcuate or the uncinate fasciculus were identified for datasets of 21 healthy subjects. Finally, the authors created population-averaged tract probability maps for each identified bundle (see Figure 4.16).

Li et al. (2010) proposed an hybrid top-down and bottom-up approach for automatic clustering and labeling of WM fibers, which utilizes both brain parcellation results and similarities between WM fibers. The top-down step is first applied to the fiber dataset. This is an anatomy guided clustering, aiming to group WM fibers based on the brain regions they penetrate or pass. The MNI atlas was used to parcel the subject's DTI images and label WM/GM structures. This ROI-based step extracts 9 major WM bundles from tractography data, following an specified order for the extraction of each bundle. First, corpus callosum fibers connecting frontal, parietal and occipital lobes are extracted, followed by fibers forming the projection tracts penetrating the frontal, parietal and occipital lobes. Finally, the cingulum, the inferior fronto-occipital and the inferior longitudinal fasciculus consecutively obtained.

The second step, based on a similarity-based clustering aims to separate and identify two other bundles (superior longitudinal and uncinate fasciculus). First, a nonlinear method of kernel principal component analysis (PCA) is used to project the remaining fibers onto a principal component space. Then, a fuzzy c-mean clustering algorithm is applied to automatically group the fibers in the feature space. The Hausdorff distance [Corouge et al. (2004)] is used as the fiber similarity metric, with the addition of a fiber length mismatch factor. Once the clusters were obtained, a feature-based recognition algorithm is applied based on a manual fiber bundle extraction method [Wakana et al. (2007)] and the construction of a histogram of fiber endpoint GM regions.

In a recent work, Visser et al. (2011) proposed a clustering method of WM fibers that can be applied to large tractography datasets. The input tracts are first randomly partitioned into subsets of  $N_s = 10,000$  tracts. Each subset is then clustered separately, based on the assumption that the clusters found in these subsets are, to some degree, similar to those that could be found when clustering the entire original dataset at once. A hierarchical clustering with complete linkage is performed to cluster the fiber tracts of each subset using the *sum of the Euclidean distances between corresponding points* fiber similarity measure (see section 4.4.2). An arbitrary number of clusters ( $N_c$ ) is then defined and used to get the final partition, large enough to avoid merging major anatomical tracts.

The procedure of creating subsets and clustering is repeated a defined number of times ( $N_r$ ), called repetitions; in practice  $N_r$  was set to 100. Results from all repetitions are then combined, using a cluster matching procedure across realisations, in order to find coherent clusters in the original dataset with good reproducibility. A pruning procedure is finally performed to remove fibers with low reproducibility scores. Results are presented for a single subject, where 4 known long WM tracts and one U-fiber bundle were identified using  $N_c$  equal to 500. The method was also applied to a dataset containing data from 15 subjects in order to find corresponding bundles across subjects. For this analysis, another number of clusters was used, equal to 350. Results are only shown for the arcuate fasciculus (see Figure 4.17).



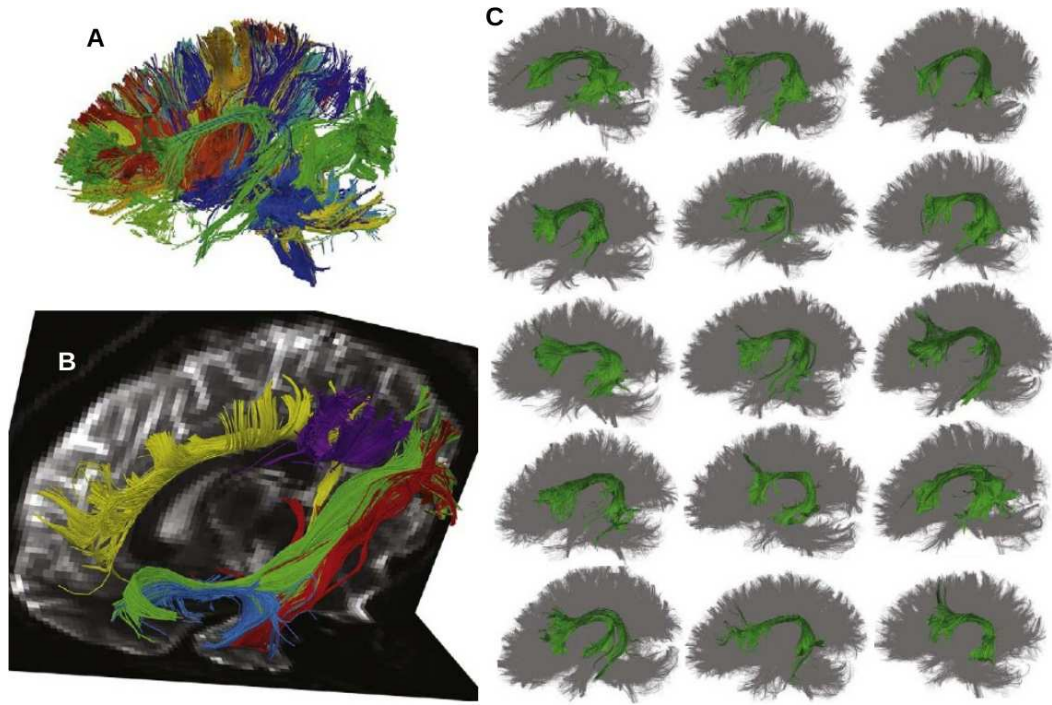


Figure 4.17: Illustration of the partition-based WM fiber clustering described in [Visser et al. (2011)]. **A:** Some clusters (1/9 of the 500 clusters) obtained by clustering streamlines in a single subject. **B:** Clusters corresponding to cingulum (yellow, three clusters), inferior fronto-occipital fasciculus (green), inferior longitudinal fasciculus (red) and uncinate fasciculus (blue). A cluster of U-fibers is shown in purple. **C:** Long segment of left arcuate fasciculus across 15 subjects. Spurious tracts were pruned by applying a threshold of 50, i.e. half the number of repetitions, to the number of assignments to the final cluster [From Visser et al. (2011)].

## 4.5 Quantitative DW measures across bundles

As we mentioned in previous chapter, diffusion MRI provides *in-vivo* measures reflecting the underlying tissue properties. A comparison of diffusion measurements between populations can then be performed in order to study, for example, the brain development or neurological disorders. Furthermore, this analysis can help on the identification of potential brain targets for new therapeutic interventions and the evaluation of the efficacy of new treatments [Johansen-Berg and Behrens (2009)]. Two main types of approaches have been proposed: *voxel-based* and *tract-based* quantification of diffusion indexes.

**Voxel-based DW quantitative analyzes** perform the calculation of diffusion invariant statistics over the WM voxels. Early works measured mean FA or other scalars in ROIs within tracts. For example Kubicki et al. (2003) studied mean FA, trace of DT, and mean area of a segmented part of the cingulum for schizophrenia patients compared with normal subjects.

Other approaches quantify average diffusion measures for each tract [Jones et al. (2006); Hua et al. (2008)]. Hua et al. (2008), for example, used probabilistic maps of some WM tracts to perform automated tract-specific quantification of FA and MD, by



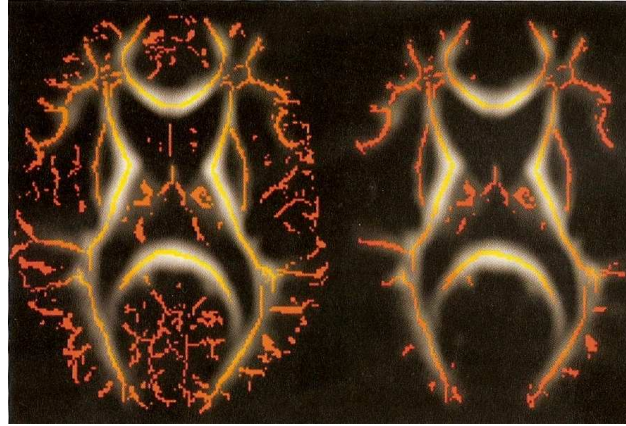


Figure 4.18: Example mean FA image (grayscale) underneath the unthresholded (left) and thresholded (at  $FA = 0.2$ ) (right) skeleton calculated by *Tract-Based spatial statistics* method (TBSS) [Smith et al. (2006)]. In each subject, locally high FA values are then aligned (or projected) to the group FA skeleton to then perform voxelwise statistics across subjects [From Johansen-Berg and Behrens (2009)].

the calculation of weighted average of these quantitative parameters. This probabilistic approach was proposed for MRI datasets without tractography data.

Wassermann et al. (2010a) also used population-averaged tract probability maps for a set of known WM bundles, identified using an atlas-based clustering method (see section 4.4). For each bundle, extracted from each subject, the authors quantified its similarity with respect to the corresponding population-averaged bundle using a normalized similarity metric, that quantifies the overlapping of two bundles using an inner product operation (see section 4.4.2).

Other voxel-based methods quantify diffusion along tracts that are approximately perpendicular to some image plane. These approaches can use anatomical landmarks for registration and image slices for quantification. For example, Wakana et al. (2007) projected manually extracted 3D tracts to one anatomical axis, for calculating tracts size (in voxels), FA and T2 values. For inter-subject analysis, tract-specific profiles of FA and T2 were determined along the tracts. The tract length was normalized using anatomical landmarks along its course for alignment purposes. For example, the CST was segmented into the midbrain, internal capsule, and corona radiata regions. The length of these separate regions from each subject was then linearly adjusted before group profile comparison.

Using a more sophisticated approach, Smith et al. (2006), proposed a “skeletonization” of white matter, called TBSS, *Tract-based spatial statistics*. This approach uses spatial skeletons to define locations likely to correspond to central parts of fiber bundles in order to perform statistical analysis of DTI. First, a mean FA image is calculated using non-linear registration. Then, a skeletonized mean FA is calculated using thinning and then applying an above threshold (see Figure 4.18).

In each subject, locally high FA values are then aligned (or projected) to the group FA skeleton. For that, at each point in the skeleton, the subject’s FA image is searched in the perpendicular tract direction to find the maximum FA value and assign it to the skeleton voxel. Finally, voxelwise statistics across subjects are performed (voxel-based morphometry, VBM [Ashburner and Friston (2000)]). A disadvantage is that by working in a voxel coordinate system the method could mix information from nearby but differently oriented tracts [O’Donnell et al. (2009)]. The advantage is that it is automatical, solve alignment and smoothing problems and allows the investigation of the whole brain [Johansen-Berg and Behrens (2009)].

An approach closer to TBSS was proposed by [Kindlmann et al. (2007)], using “anisotropy creases”. The method extends to tensor fields the notion from classical computer vision of ridges and valleys, calculated using differential geometry applied to DT data. Anisotropy creases are used to extract a surface skeleton of the major WM pathways, in that ridges of anisotropy coincide with interiors of fiber tracts, and valleys of anisotropy coincide with the interfaces between adjacent but distinctly oriented tracts. Compared to TBSS, this analysis leads to a potentially more accurate modeling of FA structure [Johansen-Berg and Behrens (2009)].

**Tract-based DW quantitative analyzes** use 3D tracts extracted from tractography datasets to perform the statistical analysis of diffusion properties along tracts.

These approaches commonly use generated coordinate systems based on fibers, in order to handle different fiber tract shapes and find fiber paths correspondences along the length of the fibers.

A statistical bundle model with point correspondences along fibers was constructed using an unified method for fiber clustering and measurement [Maddah et al. (2008a)], described in section 4.4. The method employs an EM algorithm to cluster the trajectories in a Gamma mixture model. A distance map and a labeling map are used to obtain the correspondence between fiber points and a cluster center. The mean and standard deviation of cluster shape and FA values along the normalized arc length of the cluster centers were calculated for five bundles (see Figure 4.19). This method is based on bundle centerlines so it is well-suited for tubular structures, but larger sheet-like structures like the corpus callosum have to be divided into several tubular bundles.

In other work, Corouge et al. (2006) proposed a method for within-subject parameterization of fiber tracts by arc length. The method requires the manual specification of a cutting plane defining common start points on all fibers used to determine corresponding points. Coordinates are assigned to each fiber based on the (positive or negative) distance along the fiber from the cutting plane. Distance along fibers were determined using spline

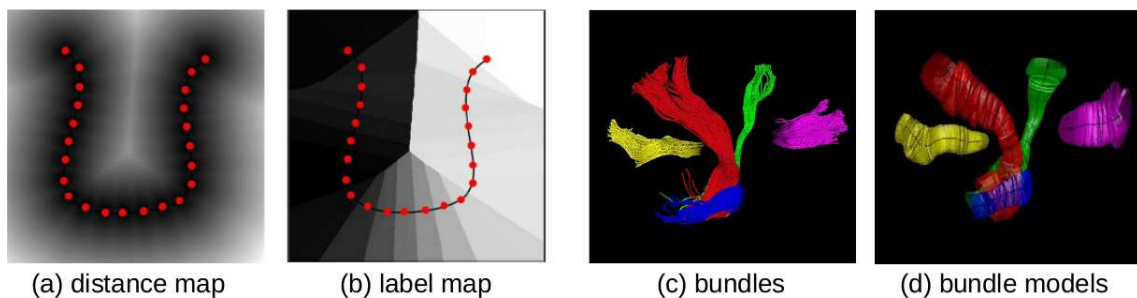


Figure 4.19: Quantitative analysis of WM tracts using distance maps for point correspondences along fibers, proposed by [Maddah et al. \(2008a\)](#). (a) Distance map from sample points on a cluster center and (b) the point correspondence label map with the center overlaid. Each region in the label map, displayed by a different color, consists of all the points in the space that have the minimum distance to a specific point on the cluster center. Therefore, projecting any curve onto this label map determines the point correspondence of each of its samples to the center based on which region that sample is located. (c) Trajectories of 5 different clusters used for quantitative analysis: splenium (yellow), corticospinal (red), corticobulbar (green), middle cerebellar peduncle (blue), and genu (magenta). (d) A model representation of the bundles as the mean trajectory and the isosurfaces corresponding to spatial variation of the clusters [From [Maddah et al. \(2008a\)](#)].

representation of the fibers and Procrustes analysis. A mean fiber was obtained to model the fiber tract shape and parameterize DT along the fibers. DT were averaged across corresponding longitudinal positions to create mean tensor values along the mean fiber. Profiles of FA, MD and eigenvalues were constructed for several single-subject fiber tracts.

[Yushkevich et al. \(2008\)](#) employed a method to project white matter information to a medial representation of pre-defined sheet-like white matter tracts. First, average tensor images from all subjects are created in standard space. Tractography is then performed over the average DT images and the major WM tracts are manually segmented [[Wakana et al. \(2004\)](#)]. Segmented tracts are subsequently fitted with deformable geometric medial models. Then, tensor-derived quantities lying on the interior of a fasciculus are projected onto its medial manifold along the direction orthogonal to the boundary of the fasciculus (called *spoke direction*). Two strategies are used to perform this dimensionality reduction. The first one, for each point on the surface, finds the location of the *highest FA* and assigns its diffusion features to the point. The second strategy averages tensor-based features along the spoke direction. The method establishes a canonical two-dimensional coordinate space for the fasciculi where the results from different white matter studies can be compared. This parametric representation allows then statistical mapping of individual fasciculi and provides an easy and attractive way to visualize and interpret statistical differences. This method seems to be more robust than TBSS, where the skeletonization is applied to the set of all voxels with above-threshold FA, resulting in a skeleton consisting of hundreds or thousands of branches, some of which may be spurious and sensitive to noise [[Yushkevich et al. \(2008\)](#)]. However, this framework is inappropriate for non sheet-like tracts, such as the cingulum and the fornix.

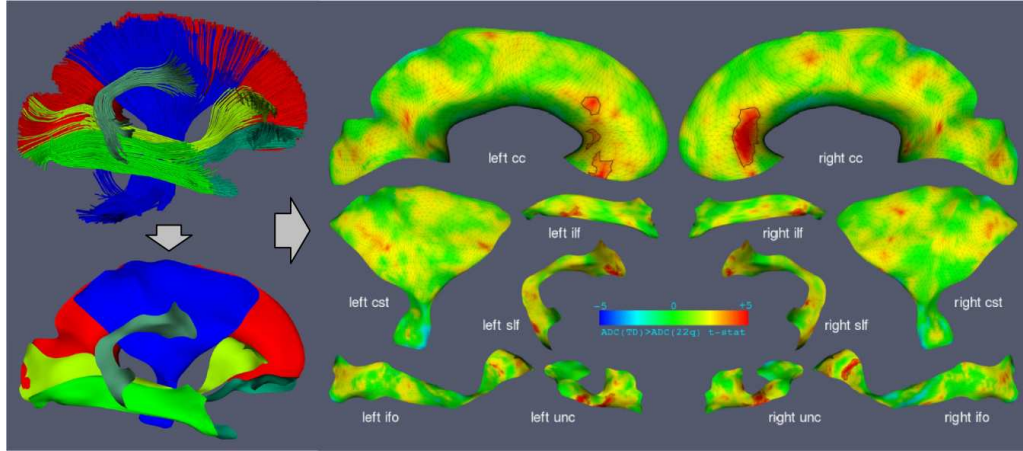


Figure 4.20: Tractography-based medial (skeletonized) representation of tract structure [Yushkevich et al. (2008)]. Top left: Fiber tracking results for the six selected fasciculi. Bottom left: Skeletons of the models fitted to the six fasciculi. Right: The result of projecting tract-center MD values onto the medial surfaces, and then testing statistically across subjects. T-statistic maps on the medial surfaces show where MD is significantly different in patients with pediatric chromosome 22q11.2 deletion syndrome, compared with controls [Adapted from Yushkevich et al. (2008) and Johansen-Berg and Behrens (2009)].

In Zhang et al. (2009), the authors proposed a tract-specific framework for WM morphometry combining macroscopic and microscopic tract features. The method uses the skeleton-based modeling of sheet-like WM fasciculi using continuous medial representation, described by Yushkevich et al. (2008). This medial representation allows the creation of a thickness map for each tract of each subject, providing a macroscopic characterization of WM tracts. Diffusion features are also projected onto the same skeleton surface of each subject, using *highest FA* strategy [Yushkevich et al. (2008)], for the characterization of microstructural WM features. The framework allows nonparametric statistical mappings of group differences on thickness and diffusion properties. Also, a multivariate analysis can be performed, to directly exploit the relationship between thickness and diffusion properties. The framework was used to quantify WM atrophy in Amyotrophic Lateral Sclerosis.

In Goodlett et al. (2009) the authors propose a framework for statistical comparison of fiber bundle diffusion properties between populations of diffusion tensor images. First, unbiased diffeomorphic atlas building for DTI is used to compute a normalized coordinate system for populations of diffusion images. Diffeomorphic transformations between each subject and the atlas provide spatial normalization which is used to parametrize tract oriented measures across a population. Diffusion properties, such as fractional anisotropy (FA) and tensor norm, along fiber tracts are modeled as multivariate functions of arc length and are statistically compared in order to find significant differences between populations. The method was tested on two clinical studies of neurodevelopment for some tubular bundles as the splenium and the genu of the corpus callosum and the corticospinal tract.

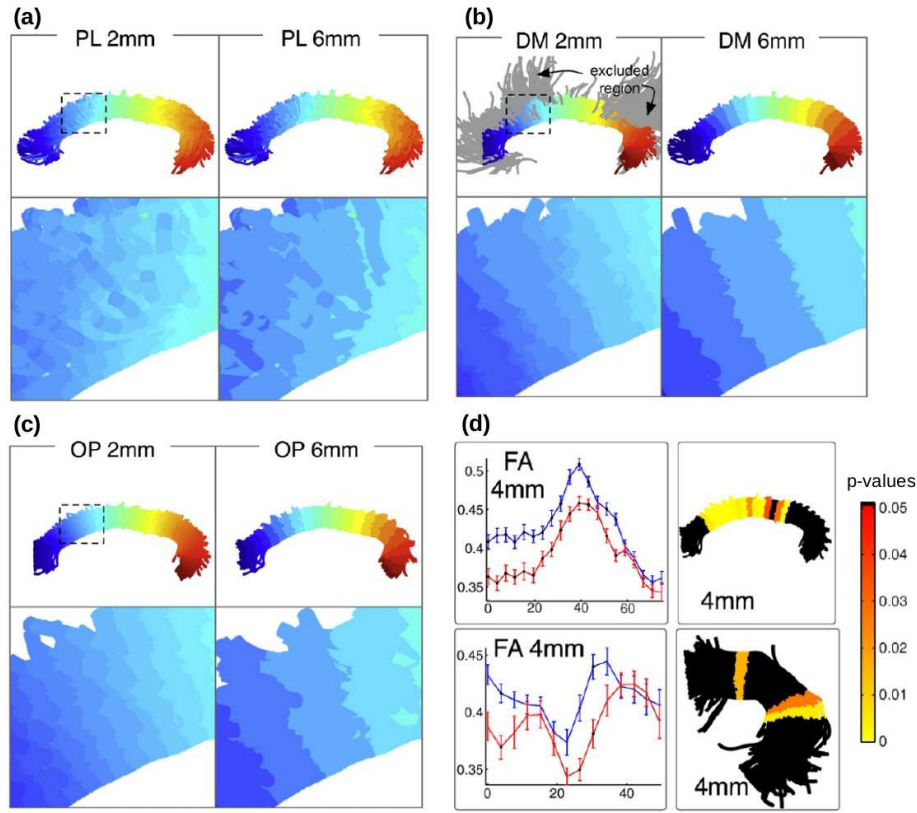


Figure 4.21: Tract-based morphometry (TBM) method [O'Donnell et al. (2009)]. (a), (b) and (c) figures show arc length parameterizations in color, for the entire bundle and in a zoomed region (dashed square), for three different fiber coordinate systems: cutting plane (PL), distance map (DM) and optimal point match method (OP). In gray, the leftmost DM image gives an example of regions that were excluded during matching. Note that PL is less spatially consistent, and DM is adversely affected by prototype curvature at lower size scales. As fibers leave the structure and before they are truncated, OP is more likely to increment the arc length than DM, leading to subtle differences at 6 mm. (d) Interhemispheric FA analysis for 4 mm scale in cingulum (top) and arcuate fasciculus (bottom). For each arc length coordinate, each subject's mean FA was computed for the left and right bundles. The (group) mean and standard error of these per-subject means is shown vs. arc length in mm (left column). The multiple comparison corrected p-value for significant difference is overlaid on a sample of fibers from the group (right column) [From O'Donnell et al. (2009)].

In a recent work, O'Donnell et al. (2009) proposed an approach called *tract-based morphometry* (TBM), first presented in [O'Donnell et al. (2007)], for WM fiber tracts group analysis using subject-specific tractography bundle segmentations. The method generates an arc length parameterization of the bundle with point correspondences across all fibers and all subjects. The authors present a quantitative comparison of fiber coordinate systems from the literature: *cutting plane* (PL) [Corouge et al. (2006)], *distance map* (DM) [Maddah et al. (2008a)] and a new *optimal point match* method (OP). The OP method was found to reduce spatial distortion and to improve intra- and inter-subject variability of FA measurements. The method also allows the generation of arc length correspondences across hemispheres, enabling, for example, a TBM study of



interhemispheric diffusion (FA, MD, eigenvalues) asymmetries in the arcuate fasciculus and the cingulum bundle (see Figure 4.21).

In Wassermann et al. (2010b), the authors presented a *skeleton-based tract-specific* statistical analysis on WM tracts. This method models each tract by the skeleton of its tract probability map (TPM), obtained by the clustering method presented in Wassermann et al. (2010a) (see section 4.4). The skeleton is obtained using an adapted version of the thinning algorithm of [Smith et al. (2006)]. Once the skeleton has been created, all the voxels within the thresholded TPM are projected to the closest point on the skeleton (see Figure 4.22). For that, the scalar diffusivity measure is calculated at every selected voxel and projected to the skeleton by following the direction perpendicular to the skeleton at the voxel, until the skeleton is reached. These diffusivity values are averaged according to their probability of being in the bundle (given by the TPM). Finally, for each voxel in the skeleton, a voxel-based analysis is performed in order to find voxels presenting differences among patients and controls. The method was applied to find the differences between 34 schizophrenia patients and 24 healthy controls. The advantage of this method is that it is not bound to a sheet- or tube-representation.

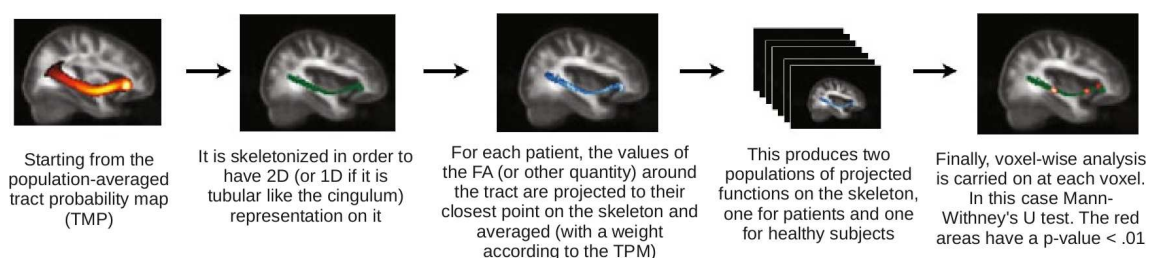


Figure 4.22: Skeleton-based tract-specific statistical analysis on a WM tract [Adapted from Wassermann et al. (2010b)].

## 4.6 Conclusion

In this chapter we presented a review of the more relevant WM fiber clustering and fiber bundle identification approaches. These methods require the use of clustering algorithms for fiber tracts regrouping, and fiber distance measures for the evaluation of fiber closeness. For the identification of known anatomical WM tracts, the addition of anatomical information is also needed, being it most of the time in the form of GM/WM atlases or labeled cluster centroids.

The clustering and identification of WM tracts is a complicated task for several reasons. First, anatomical WM tracts present different shapes and sizes and several bundles overlap over a non-negligible portion of their trajectory. Second, even though the relative localization of WM tracts remains the same across subjects, inter-subject variability is very important. Shape and size of white matter tracts change across subjects, requiring the use of sophisticated methods for WM tracts alignment and identification. Furthermore, the



analysis is highly dependent on the quality of DW images (i. e. spatial and angular resolution), as well as on the diffusion local model and tractography algorithm. All these aspects impose a challenging robustness to the analysis that is rarely satisfied. Besides, new high resolution DW-images allow the computation of huge tractography datasets, wich can not be analyzed with state-of-the art fiber clustering methods.

Most proposed approaches are focused on the clustering and identification of known DWM tracts. Until now, short association SWM tracts, have been poorly studied, and their identification is still an opened research area.

Therefore, we have focused our work in the development of a fiber clustering algorithm able to deal with very big tractography datasets for the identification of DWM and SWM tracts. Next chapter will describe the strategy we adopted to cluster intra-subject fiber datasets, allowing an important dimensionality reduction for further analyses.

# **Part III**

## **Methods**



# Intra-subject fiber clustering

## Contents

---

<b>5.1</b>	<b>Introduction</b>	<b>117</b>
5.1.1	Previous works	117
5.1.2	Main output	118
5.1.3	Tractography dataset size	119
5.1.4	Hierarchical fiber clustering overview	120
<b>5.2</b>	<b>Robust intra-subject fiber clustering</b>	<b>122</b>
5.2.1	Step 1: Hierarchical decomposition	122
5.2.2	Step 2: Length-based segmentation	122
5.2.3	Step 3: Voxel-based clustering	123
5.2.4	Step 4: Extremity-based clustering	130
5.2.5	Step 5: Fascicle merge	132
<b>5.3</b>	<b>Method validation and parameters tuning</b>	<b>135</b>
5.3.1	Whole method evaluation using simulated datasets	136
5.3.2	Cost of scalability	140
5.3.3	Clustering parameters setting	143
<b>5.4</b>	<b>Intra-subject fiber clustering results</b>	<b>144</b>
5.4.1	A T1-based tractography propagation mask	144
5.4.2	Adult HARDI datasets	148
5.4.3	Child DTI datasets	150
<b>5.5</b>	<b>Applications</b>	<b>153</b>
5.5.1	Physical phantom	153
5.5.2	Top-down decomposition of large known WM tracts	156
<b>5.6</b>	<b>Discussion</b>	<b>158</b>
<b>5.7</b>	<b>Conclusion</b>	<b>159</b>

---

## Overview

---

Diffusion Magnetic Resonance Imaging allows noninvasive study of brain white matter structure through the measurement of the diffusion of water molecules. The local fiber orientation distribution can be inferred from this data and fiber trajectories can be reconstructed using tractography algorithms. A wide variety of acquisition schemes, diffusion models and tractography algorithms have been proposed in the literature. There is no consensus yet on the best choices. An interesting way to compare the alternative approaches lies in the further exploitation of the large sets of generated tracts for performing fiber bundle segmentations.

As discussed in the previous chapter, various strategies have been proposed for the segmentation of a set of diffusion-based tracts. Within the most recent approaches, methods based on tract clustering using a pairwise distance between fibers have shown to be a powerful tool for the study of diffusion-based tract structure. The main problem of the standard tract-clustering strategy is the computational load related to the manipulation of the pairwise distances.

In order to overcome this limitation, in this chapter we develop a sequence of algorithms performing a robust intra-subject hierarchical clustering that can deal with millions of diffusion-based tracts. The end result is a set of a few thousand homogeneous bundles. The method only relies on the tract geometry. This simplified representation of white matter can be used further for group analyses. The bundles can also be labelled using ROI-based strategies in order to perform bundle oriented morphometry. A large amount of the final bundles are putative U-fiber tracts connecting cortical areas separated by a few folds.

The robustness of the method is checked first using simulated tract datasets. The complete method is then applied to the tracts computed from HARDI data obtained for twelve adult brains. The method is also tested with the tracts obtained from two children using lower angular resolution acquisitions and a tensor model. Finally, the method is applied to the data issued from an actual phantom containing a plethora of realistic crossing, kissing, splitting and bending fiber configurations. This last experiment illustrates the interest of our compression method for comparing different tractography algorithms.

Additionally, we describe the creation of a robust propagation mask stemming from T1 anatomy, which, in conjunction with tractography techniques, improves the accuracy of the anatomical connectivity of the brain by reducing false positives and increasing the detection of the subcortical connectivity.

**Keywords:** white matter clustering, fiber tracts, fiber clustering, fiber distance, fiber similarity measure, voxel-based clustering, hierarchical clustering, extremity-based clustering

### Organization of this chapter:

The chapter is organized as follows. We first give a brief overview of previous works and the proposed method in Section 5.1. Then, we detail our hierarchical intra-subject fiber clustering method in Section 5.2. Method validation and parameters tuning issue are subsequently addressed in Section 5.3. Results are then presented in Section 5.4. Two applications are described in Section 5.5.

## 5.1 Introduction

---

The analysis of white matter organization from the results of tractography methods is a delicate task. The “spaghetti plate” made up by the tracts resulting from the current methods, indeed, is far from being a perfect representation of white matter structure. The poor spatial resolution of diffusion acquisitions puts strong limitations on the diameter of the bundles that can be mapped. Moreover, the difficulties raised by the numerous fiber crossings and white matter bottlenecks result in many spurious bundles. Furthermore, the arise of high angular resolution diffusion imaging (HARDI), in combination with more complex diffusion local models and tractography algorithms generates each time more complex and bigger tractography datasets. The analysis of diffusion-based tracts is then far from being a simple and solved problem and new methods are continuously developed in order to deal with the increasing complexity of the data.

Various strategies have been proposed for the segmentation of a set of diffusion-based tracts. In this introductory section we resume the different approaches used until now, which were described in more details in the previous chapter. The main motivations that pushed us to develop our clustering strategy are subsequently described. Finally, we present a brief overview of our hierarchical fiber clustering.

### 5.1.1 Previous works

The simplest approach proposed for the segmentation of a tractography dataset is based on regions of interest (ROI) used to select or exclude tracts [Wakana et al. (2007); Catani and Thiebaut de Schotten (2008)]. A specific set of ROIs can be defined more or less interactively for each subject in order to highlight a well-known anatomical WM tract. This approach has been employed to create single-subject white matter tract atlases [Mori et al. (2005); Lawes et al. (2008)]. An attractive extension of this approach consists in using a group of subjects to create probabilistic maps of the resulting WM tracts in a standard space after spatial normalization [Hua et al. (2008)]. Then, a set of ROIs can be defined from the probabilistic maps to catch the same WM tracts in any other subject. Alternative methods define WM tracts from a voxel-based clustering relying on similarity measures between the local diffusion data [Bazin et al. (2009); Wassermann et al. (2008)]. Intermediate strategies consists in clustering white matter voxels according to similarity measures based on the tracts that cross them [El Kouby et al. (2005); Wang



et al. (2011)]. These voxel-based approaches can use their segmentation of white matter to split the set of tracts into pieces. Finally, a number of methods propose to infer the tract clustering from pairwise similarity measures defined in the tract space [Ding et al. (2003); Corouge et al. (2004); Gerig et al. (2004); Brun et al. (2004); O'Donnell et al. (2006); Visser et al. (2011)]. This last strategy can embed a priori knowledge represented by WM tract templates [Maddah et al. (2005); O'Donnell and Westin (2007)]. Other recent hybrid approaches extract the most known WM tracts by the combination of a priori information given by a GM/WM atlas and a fiber clustering based on a similarity measure [Wassermann et al. (2010a); Li et al. (2010)]. For more details on these fiber segmentation methods, see chapter 4.

Within the proposed methods for white matter segmentation and analysis, approaches based on tract clustering using a pairwise distance between fibers have shown to be a powerful tool for the study of diffusion-based tract structure. These methods allow the segmentation of tractography datasets into fiber clusters containing fibers of more or less similar shape and position.

### 5.1.2 Main output

Most of the proposed methods are focused in finding directly clusters with anatomical meaning, where a priori anatomical knowledge is given by a GM/WM atlas [Wassermann et al. (2010a); Li et al. (2010)] or a bundle template [Maddah et al. (2005, 2007b, 2008a)] and Wang et al. (2011)?? Other works apply a first step of fiber clustering [Zhang et al. (2008a); O'Donnell et al. (2006); Visser et al. (2011)] and then a second step that embeds a manual labelling of the clusters for the identification of known WM tracts.

In our thesis work we preferred the second approach, since a first intra-subject fiber clustering can be considered as a first-level processing stage consisting in a compression operation that enables the posterior analysis and segmentation of WM structure. We propose then an intra-subject clustering method that only relies on the tract geometry and does not use any strong anatomical a priori knowledge. The motivation for developing this kind of method is the further exploitation of the resulting fiber clusters, in order to, not only identify known WM tracts, but, more interestingly, allow a deeper study of known WM tracts structure and the identification of new WM fiber tracts.

The hierarchical decomposition provided by our method aims, then, at providing the possibility to develop a bottom-up strategy for the study and decomposition of large WM pathways. An example is provided in section 5.5 for the arcuate fasciculus. Furthermore, an interesting research topic is the analysis of the large amount of putative U-fiber tracts, connecting cortical areas separated by a few folds, obtained for each subject.

In next chapter, we will show that the simplified representation of white matter given by our intra-subject clustering can be used for group analysis and the inference of a brain fiber bundle model [Guevara et al. (2010)].

### 5.1.3 Tractography dataset size

The main problem of the standard tract-clustering strategy is the computational load related to the manipulation of the pairwise distances. Some clustering methods need the computation and storage of the full matrix of pairwise distances. For dataset size over a few tens of thousands fibers, this requirement becomes prohibitive. Other clustering algorithms reduce the disk space requirements by storing the matrix using a more compressed representation, like a sparse matrix or a weighed graph. However, the computation of all the pairwise distances is still required.

To overcome in part this limitation, [O'Donnell et al. \(2006\)](#) proposed a method that determines features from a single random subset of a multiple subject whole brain set of streamlines. These features are then used to assign the remaining streamlines. The limitation of this two-step approach is that the results are heavily influenced by any errors or bias introduced by the particularities of the initial random subset [[Visser et al. \(2011\)](#)].

[Visser et al. \(2011\)](#) overcome the problem of needing to store a full matrix of pairwise distances by randomly partitioning all the tracts in the dataset and clustering the smaller resulting subsets. The method expects that the clusters found in these subsets are, to some degree, similar to those that could theoretically be found when clustering the entire original dataset at once. By repeating the procedure and combining the results from all repetitions, the method can find coherent clusters in the original dataset with good reproducibility. In this approach, the processor time scales linearly with the number of streamlines. A limitation is that the method requires the pruning of the final clusters. This process in some cases could filter out fibers that could be interesting for more detailed analyses like a decomposition of known bundles.

Besides, a disadvantage of the two mentioned methods is the initial definition of the number of clusters, from which final results are highly dependent. Our method, does not require the number of clusters as a priori parameter. Other parameters are of course needed, but most of these are set in function of tractography data itself. In section 5.3 we will address in more detail the parameters tuning issue.

An efficient solution consists in basing the fiber clustering method on a clustering performed in the space of white matter voxels, as proposed by [El Kouby et al. \(2005\)](#) and [Wang et al. \(2011\)](#) (see section 4.4). During this clustering, white matter voxels are merged when they are connected by several tracts, leading to reconstruct gross masks of the underlying bundles. Each mask is then used to obtain a small set of related fibers representing individual fiber clusters. This strategy scales up well when a detailed sampling of the white matter structure is required by the application. However, the individual clusters directly obtained by this method contain a big number of overlapping bundles, a phenomenon that reduces the quality of the final individual clusters and group analysis results.

#### 5.1.4 Hierarchical fiber clustering overview

As described earlier, dealing with millions of tracts presents a challenge to any clustering algorithm. In order to overcome the limitation of tractography dataset size without the loss of meaningful information, in this chapter we develop a sequence of algorithms performing a robust intra-subject hierarchical clustering that can deal with millions of diffusion-based tracts. The method uses a hierarchical decomposition of the fiber set, based on several consecutive steps.

The strategy adopted to efficiently deal with tractography dataset size limitation is the inclusion of a step using a voxelwise segmentation of white matter. This approach is based on the measure of connectivity between white matter voxels, proposed by [El Kouby et al. \(2005\)](#). Other steps are added before and after this main step in order to increase the quality of the voxel-wise clustering. All the processing steps are conceived and chained in a way that gives robustness to the whole analysis. The end result is a set of a few thousand homogeneous bundles, representing the whole diffusion-based tracts structure, that can be used in subsequent processing stages, in order to perform group analyses.

Here is a sketch of the complete hierarchical decomposition resulting from this tuning, made up of five main steps (see [Figure 5.1](#)):

**Step 1: Hierarchical decomposition.** The complete tract set is segmented into right hemisphere, left hemisphere, inter-hemispheric and cerebellum tracts. This segmentation is achieved using hemisphere and cerebellum masks. The following steps are applied separately to each subset.

**Step 2: Length-based segmentation.** Tracts are split into different groups of similar length. Partially overlapping bundles of different length are then separated into different groups.

**Step 3: Voxel-based clustering.** A connectivity-based parcellation of white matter is performed using an average-link hierarchical clustering. Fiber clusters are then extracted from white matter clusters.

**Step 4: Extremity-based clustering.** Each fiber cluster is split further into partially overlapping homogeneous fascicles, from a clustering applied to the extremities of the tracts. A watershed approach is used to detect 3D regions with high tract extremity density. Each pair of such regions is defining a homogeneous fascicle.

**Step 5: Fascicle merge.** A final clustering is performed to merge fascicles with very similar geometries that could be over-segmented in the preceding steps. A centroid tract is computed as a representative for each significant fascicle. These centroids are clustered using an average-link hierarchical clustering and a pairwise distance between centroids.

The whole method is detailed in the following section.

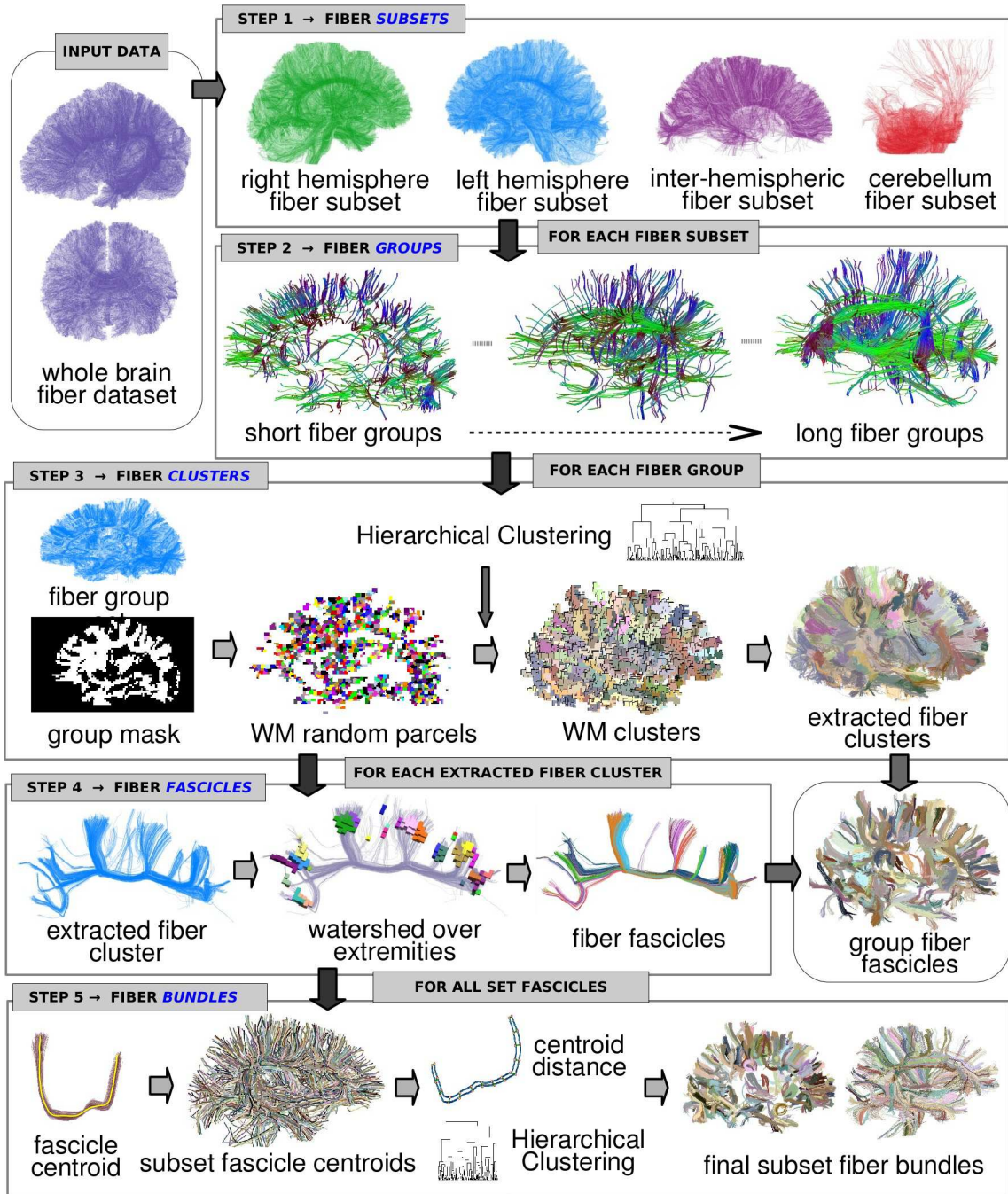


Figure 5.1: **A general scheme of the fiber segmentation method:** **STEP 1: Hierarchical decomposition:** The complete tract set is segmented into four main fiber subsets. **STEP 2: Length-based segmentation:** Fibers from each subset are separated into different groups, containing fibers of similar length. **STEP 3: Voxel-based clustering:** Fibers from each length group are clustered through a white matter connectivity-based parcellation. Fiber clusters are extracted from the resulting white matter cluster masks. **STEP 4: Extremity-based clustering:** extracted fiber clusters are divided into fascicles using fiber extremities. **STEP 5: Fascicle merge:** Fiber fascicles are clustered together across subsets using a pairwise distance between fascicle centroids.

## 5.2 Robust intra-subject fiber clustering

As described in the introduction, the proposed method is an intra-subject hierarchical fiber clustering made up of five main steps (cf. Figure 5.1). The processing steps are conceived and chained in a way that give robustness to the whole analysis. A crucial step (*Step 3: Voxel-based clustering*) performs a clustering in the space of white matter voxels. This strategy enables the whole method to deal with huge fiber datasets. Other preliminary steps of the decomposition (*Step 1: Hierarchical decomposition*) and (*Step 2: Length-based segmentation*) are used to split the tracts before the voxel-wise clustering in order to reduce the amount of overlapping bundles and improve the quality of the results. A post-processing step (*Step 4: Extremity-based clustering*) was included in order to improve the final clusters and add robustness to the whole method. Finally, a last step (*Step 5: Fascicle merge*) was added in order to agglomerate fiber fascicles that were over-segmented in preceding steps. In the following sections we detail each step of our intra-subject clustering method.

### 5.2.1 Step 1: Hierarchical decomposition

The complete fiber set is first segmented into four parts, called *subsets* (see Figure 5.2). The segmentation is performed using a mask of hemispheres and cerebellum provided by BrainVISA<sup>1</sup> [Mangin et al. (1996)]:

1. Fibers included in left hemisphere;
2. Fibers included in right hemisphere;
3. Fibers partly included in each hemisphere;
4. Fibers passing mostly through the cerebellum.

The split and merge strategy performed during the following steps is applied separately to each of the four subsets.

This segmentation step was implemented based on the observation that most analysed WM tracts are completely comprised in only one hemisphere, then a segmentation of fibers into the two hemispheres is suitable. Furthermore, WM tracts partly included in each hemisphere share an important part of their trajectories with WM tracts included only in one hemisphere. Therefore, the separation of these subsets importantly reduces the amount of overlap between the underlying bundles. The same observation can be applied for WM tracts passing mostly through the cerebellum.

Figure 5.2 shows the used WM mask and an example of segmented fibers.

### 5.2.2 Step 2: Length-based segmentation

Each fiber subset is split into different *fiber groups* containing fibers of similar lengths. This step is a key contributor to the robustness of the whole process, because overlapping

---

<sup>1</sup><http://brainvisa.info>



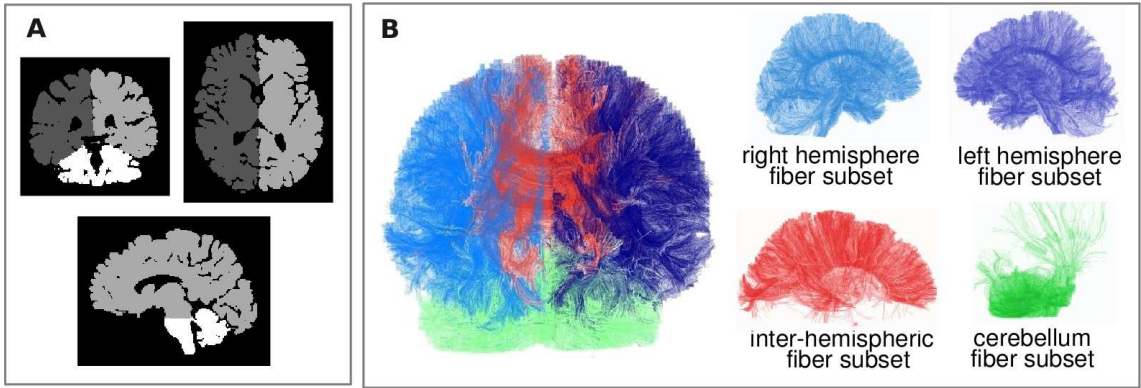


Figure 5.2: **Hierarchical decomposition of WM fibers (Step 1)**. The complete tract set is segmented into four main fiber subsets: *left hemisphere*, *right hemisphere*, *inter-hemispheric* and *cerebellum*. **A**: The mask of hemispheres and cerebellum, provided by BrainVISA. **B**: An example of decomposition.

bundles are rarely attributed to the same group. Less overlap results in easier clustering tasks for the following steps. Indeed, two bundles sharing a white matter bottleneck are difficult to split during voxel-based white matter segmentation. Note that the last processing step (*Step 5*) aims at overcoming oversplitting that may occur during *Step 2* when a fiber bundle length is too close to one of the arbitrary thresholds defining the groups. Note also that the length-based segmentation yields an ideal way to process the data in parallel in order to get important speed-up. The default number of fiber length groups was set to ten, with the following fiber lengths: 20-35 mm, 35-50 mm, 50-65 mm, 65-80 mm, 80-95 mm, 95-110 mm, 110-130 mm, 130-150 mm, 150-175 mm and 175-200 mm. If a tractography dataset contains longer fibers, other groups with a maximum range of 25 mm are added. Short fiber groups were defined with smaller length ranges since a length difference is more significant for short fibers. Additionally, short fibers are commonly superior in number than long fibers.

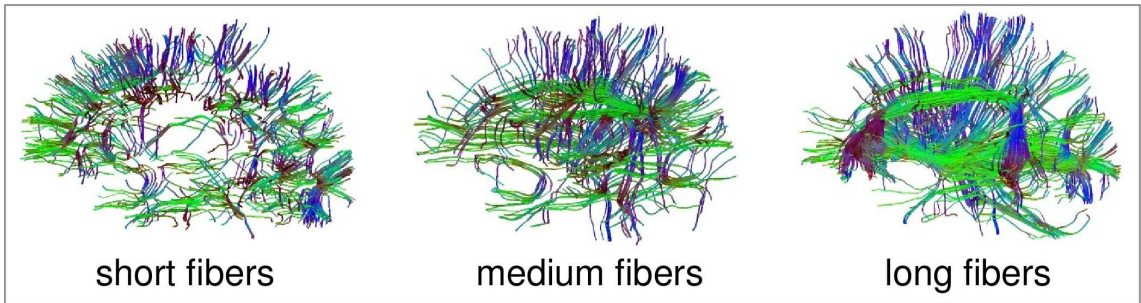


Figure 5.3: **Examples of fiber groups of different lengths (Step 2)**.

### 5.2.3 Step 3: Voxel-based clustering

Each fiber group obtained in the previous step is divided using a connectivity-based parcellation of white matter voxels. For the sake of computational efficiency, the clustering is



not performed directly on the voxels but on parcels whose volume is about three times the diffusion voxel size. A fiber group specific T2-based mask (called *fiber group mask*) is made up from the voxels crossed by more than a minimum number of tracts (*th\_tracts*). The other voxels are not used during the clustering as these are voxels with low fiber density, usually located in the periphery of the WM bundles (see Figure 5.4 A-B). This WM group mask is first randomly parcellated using an algorithm based on the K-means clustering using geodesic distances proposed by Flandin et al. (2002). The aim of the algorithm is to regroup voxels into “homogeneous” and connected parcels in order to get an uniform and random parcellation of WM volume. The inputs are the volume of interest (VOI), which is in our case defined by the fiber group mask and parcellation resolution, given by the *average parcel size* (*parcel\_size*). For an average parcel size of 3 voxels, it creates about 12,000 random parcels per fiber group (see Figure 5.4 C). Some details of the WM parcellation are described below.

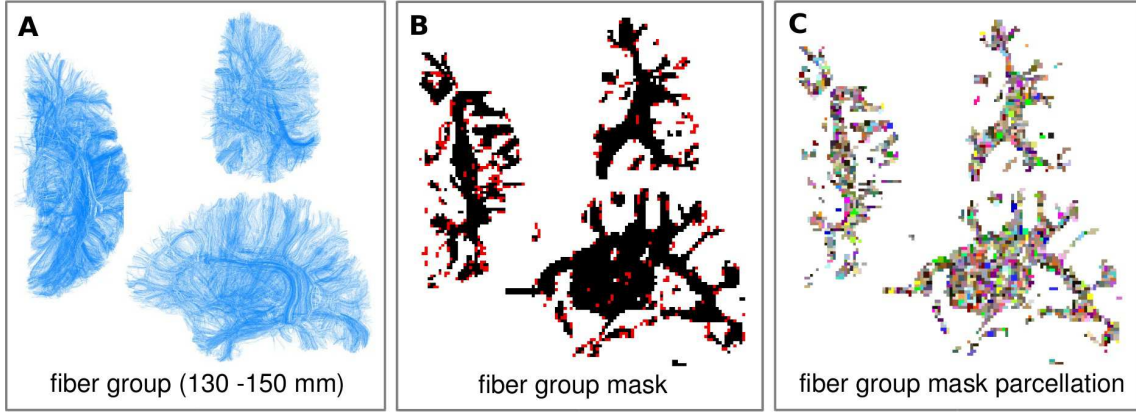


Figure 5.4: **Random initial parcellation of white matter (Step 3).** **A:** Example of a fiber group of an adult subject (left hemisphere, 130 - 150 mm). **B:** The T2-based *fiber group mask* corresponding to the fibers in **A**. The mask is made up from the voxels crossed by more than a minimum number of tracts, *th\_tracts*, in this case equal to 4. Voxels belonging to the mask are shown in black. Discarded voxels, shown in red, are low fiber density voxels, usually located in the periphery of the WM bundles. **C:** A random parcellation of the group mask in **C**, with an average parcel size of 3 voxels.

### Random parcellation of WM

The WM parcellation uses a K-means algorithm based on geodesic distance between the mask voxels. The volume of interest, defined by the fiber group mask, is described by a set of  $N$  3D coordinates  $x_i$ , where  $N$  is the number of voxels in the VOI. Parcels are defined as connected clusters of anatomical voxels, represented by their centers of mass  $\bar{x}_j$ . The problem is then to find simultaneously a partition of the voxels  $x_i$  into  $k = \text{int}(N/\text{parcel\_size})$  classes  $C_j$  and the cell positions  $\bar{x}_j$  minimizing the intra-class variance:

$$I_{\text{intra}} = \sum_{j=1}^k \sum_{i \in C_j} d^2(x_i, \bar{x}_j) \quad (5.1)$$

This optimization problem is solved using the K-means algorithm in the classification context of [Flandin et al. \(2002\)](#). After an initialization step that randomly selects  $k$  distinct voxels in the volume of interest as the initial cell positions, the criterion is solved using an alternate minimization of  $I_{intra}$  over:

1. **The partition of the data** (given cell positions): each voxel  $x_i$  is assigned to the class  $C_j$  that minimizes the distance to  $\bar{x}_j$ . Due to the non-convexity of the domain, a geodesic 3D distance (the shortest path within the volume of interest) is used, implemented by a 3D discrete Voronoï diagram with geodesic distances.
2. **The cell positions** (given a data partition): the position  $\bar{x}_j$  is chosen to minimize the variance of the  $x_i$ 's assigned to this class. It consists in computing the “center of mass” of each cell. In practice, as the used average parcel size is very small (3 voxels), most of the cells are still convex and the standard Euclidean center of mass is a good approximation.
3. **Elimination of small parcels**: this step was added in order to remove very small parcels. Once data is partitioned, centroids of very small parcels (less than 1/3 of the desired average parcel size) are removed. Voxels are then reassigned to neighbor parcels.

Finally, the K-means clustering algorithm consists in repeating these estimations until convergence, reached when voxels assignments to the cells are the same at two consecutive steps. As observed by [Flandin et al.](#) the algorithm always converges in a small number of iterations (typically a few dozen).

The elimination of small parcels, representing 5% of the total number of parcels, is a simple step that improves the parcellation statistics. For the default average parcel size used, equal to 3 voxels, final parcellation leads to a mean parcel size of about 3.16 voxels, with a standard deviation of about 1 voxel for all fiber groups.

### Connectivity-based segmentation of WM

Once the initial random WM parcellation is calculated, white matter parcels are clustered based on the connectivity between the parcels in order to perform a WM segmentation. The segmentation is achieved using an average-link hierarchical clustering applied to the parcels.

**Connectivity measure.** First, a parcel connectivity matrix is computed from the number of tracts passing through each pair of parcels. This number is normalized by the parcel size. The connectivity  $C$  between parcels  $i$  and  $j$  is then defined as:

$$C(P_i, P_j) = \frac{nf(i, j)}{V_i + V_j}, \quad (5.2)$$

where  $nf(i, j)$  is the number of fibers passing through parcels  $i$  and  $j$  and  $V$  is the parcel size in voxels. See Figure 5.5 for a scheme explaining the white matter connectivity calculation.

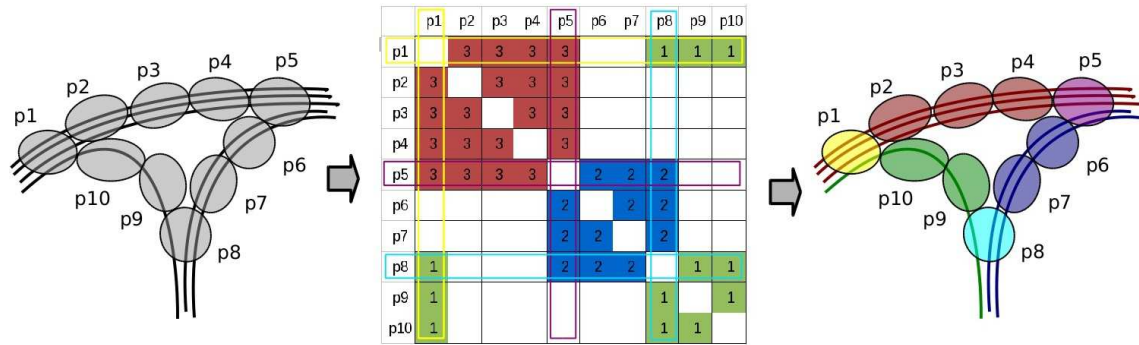


Figure 5.5: **Scheme illustrating the white matter connectivity calculation:** First, a random parcelization of the white matter is performed (parcels are represented in gray). Only voxels crossed by fibers are considered in this process. Then, a parcel connectivity matrix is computed, from the number of tracts passing through each pair of parcels. This number is normalized by the parcels size (not done in the example). The connectivity matrix is clustered in order to regroup parcels strongly connected. After the clustering, in the last figure, parcels in red ( $p_2$ - $p_4$ ), blue ( $p_6$ - $p_7$ ) and green ( $p_9$ - $p_{10}$ ) will form three different clusters, corresponding to three different fiber clusters. Parcels presenting a more complex connectivity, like parcels in yellow ( $p_1$ ), purple, ( $p_2$ ) and cyan ( $p_3$ ), are clustered with the most connected parcels.

The matrix is thresholded at one percent of the maximum connectivity. This threshold (called *min\_pconn*) is a very low threshold, but it allows the elimination of a big amount of weak connectivity values, speeding-up the clustering process.

To illustrate this phenomenon, we took an example fiber group of the left hemisphere of an adult subject (cf. section 5.4.2), with fiber lengths between 110 and 130 mm. The group mask contains 11,040 parcels with an average parcel size of 3.2 voxels at T2 resolution and a standard deviation of 1.0. The maximum connectivity value is 13.0 while the minimum not null connectivity value is equal to 0.06. The matrix presents a total number of 5,591,700 not null connectivities, representing 4.6% of the total number of pairwise connectivity values.

Figure 5.6 presents the histogram of the not null connectivities for this example dataset. Frequencies are represented using 100 equidistant ranges of connectivity. Using the normal scale (Figure 5.6 (A)), it can be noted that most of the not null connectivity values present a very low magnitude. In fact, using the threshold *min\_pconn* at 1% (0.13), all the connectivities represented by the first bar of the histogram are discarded. The number of these weak connectivities is 4,847,316, equivalent to the 86.7% of the not null connectivity values. For a better visualization, Figure 5.6 (B) shows the histogram on a logarithmic scale. After thresholding the matrix, only contains 744,384 not null connectivities, which represent 0.6% of the total number of pairwise connectivity values.

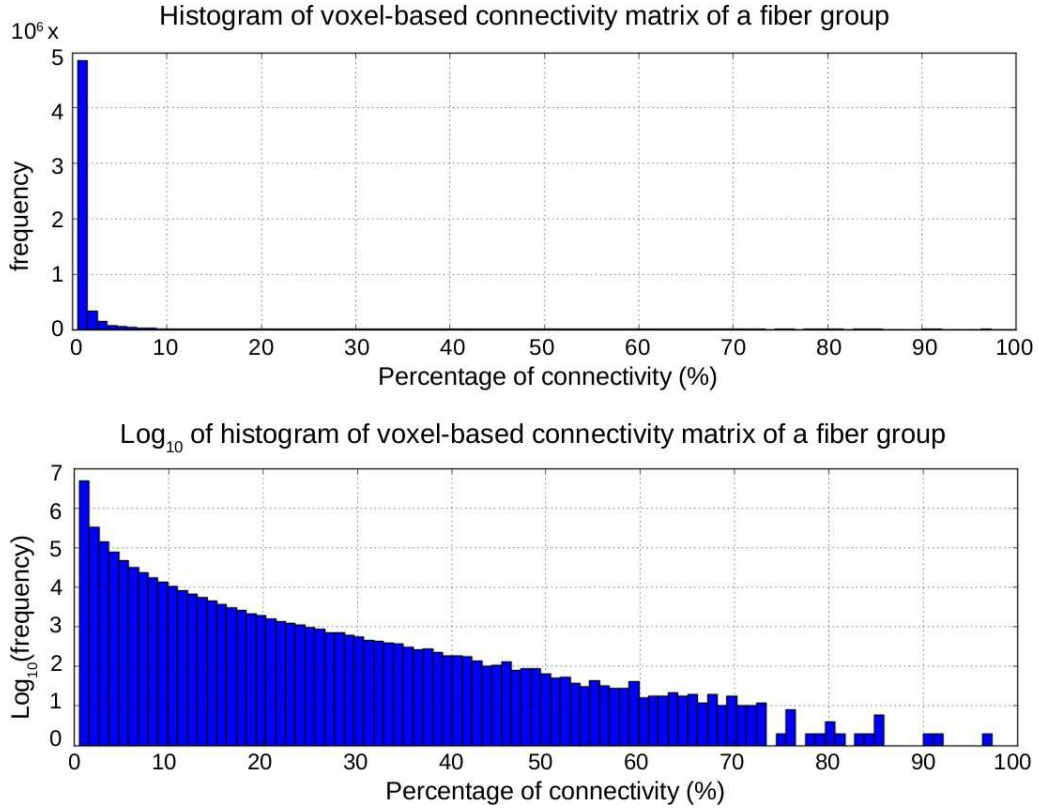


Figure 5.6: **Example of a WM connectivity matrix histogram (fiber group: 110-130 mm).** Only not null connectivities are considered in the histogram. Frequencies are represented using 100 equidistant ranges of connectivity (in percentage). Using the threshold *min\_pconn* at 1%, all the connectivities represented by the first bar (86.6%) of the histogram are discarded. **A:** Histogram without scaling. **B:** Histogram using logarithmic scale.

**Hierarchical clustering.** For clustering the WM parcels, we used a hierarchical clustering (HC) [Johnson (1967)] agglomerative approach, where each data element is initially considered as a singleton cluster (see previous chapter, section 4.4.1). Typically, a  $N \times N$  similarity (or affinity) matrix is used as input, where  $N$  is the number of objects to be clustered. We used the implementation of the *nipy*<sup>2</sup> library, which receives as input an undirected *weighted graph*,  $G = (V, E)$ . The vertices  $V = v_1, \dots, v_N$  of this graph represent the elements and edge weights,  $e_i = v_j, v_k$ , represent affinity values, obtained from the affinity matrix. As mentioned in the previous chapter, the advantage of using an affinity graph is that the disk space required to store the data is reasonable. Furthermore, if a minimum affinity threshold is imposed, the graph complexity is reduced, decreasing even more the required disk space and the processing time.

The HC algorithm successively merges the most similar clusters until all elements have been merged into a single last cluster. The result is a forest composed by one or more trees, where each tree represents a connected component of the input affinity graph.

We used the *average-link* variant (cf. equation 4.5) to define the closest pair of clusters

<sup>2</sup><http://nipy.sourceforge.net/nipy/stable/index.html>

in function of the dissimilarity between elements. The distance between clusters is then defined as the average of the pairwise distance between elements in the two clusters. It is a compromise between the sensitivity of complete-link clustering to outliers and the tendency of single-link clustering to form long chains.

**Hierarchical clustering adaptive partition.** A big advantage of hierarchical clustering over partitional algorithms is that no assumption is required relative to the number of clusters. In addition, the hierarchy provides much more information than a simple partition, and can be analyzed further in order to find the desired partition according to additional a priori knowledge. To perform the voxel-based clustering, we implemented an algorithm performing an adaptive partition of the tree resulting from the HC.

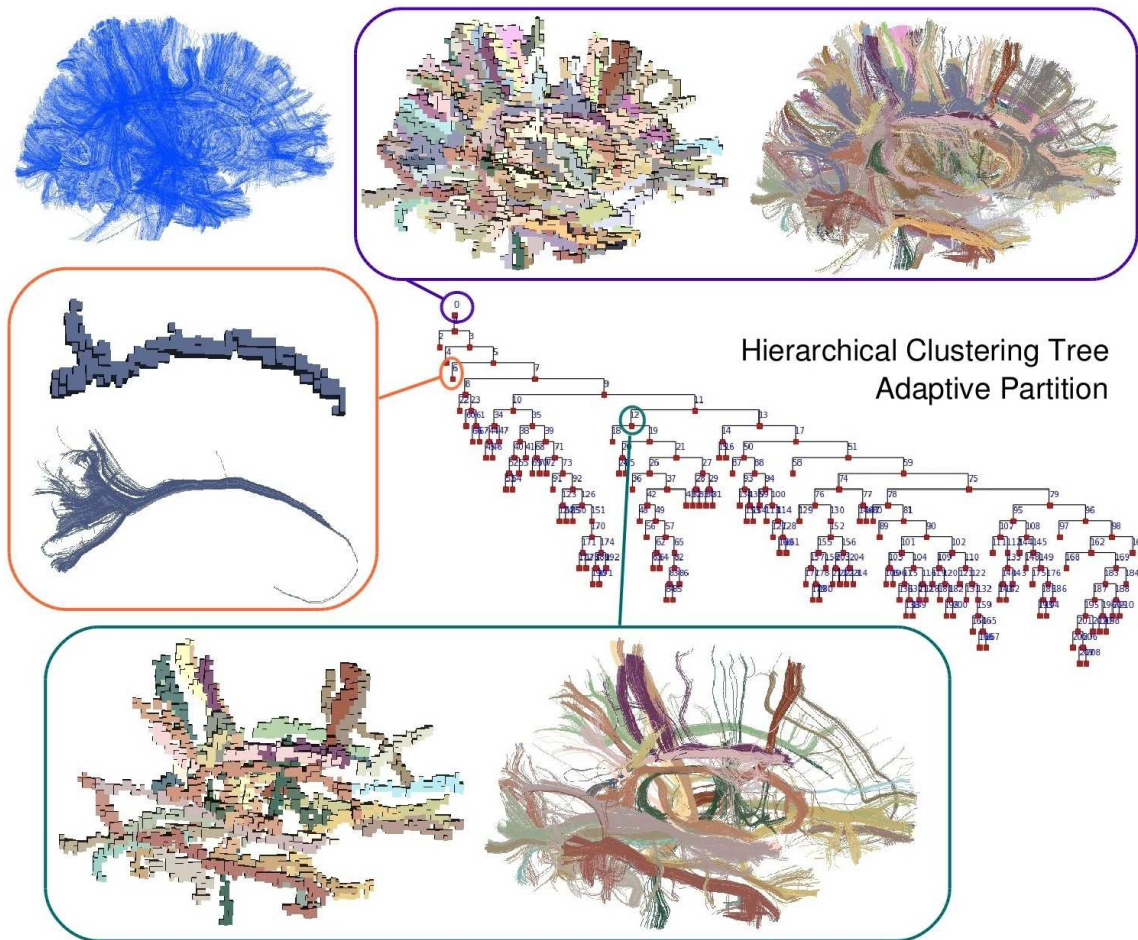


Figure 5.7: **An example of a voxel-based clustering (right hemisphere, group length: 95-110 mm):** The upper left figure shows all the group fibers (in blue). The graph represents the hierarchical clustering (HC) adaptive partition resulting from the whole HC tree analysis. Nodes represent original tree nodes that were preserved during the analysis. Leaves represent final WM clusters. Three examples of voxel clusters and their respective extracted fiber clusters are presented: (1) the whole set of clusters, encircled in blue, corresponding to the root node, (2) a single cluster, encircled in orange, and (3) an intermediate node containing several clusters, encircled in green. The resulting tree does not have a special interpretation, just the leaves (final clusters) are used in the posterior steps.



The algorithm analyzes and recursively splits each HC tree (more than one tree can be obtained if there are unconnected components in the data). This aims to find an adaptive partition where each cluster contains ideally only one putative fiber bundle, but more usually a white matter tract is made up of a set of different bundles sharing a bottleneck. The tree analysis discards the small isolated clusters, using a maximum cluster size threshold, called (*small\_size*). At the same time, the algorithm splits the large clusters until reaching sizes compatible with the largest actual white matter tracts. Once this threshold on size (*th\_clust1*) has been reached, the splitting process is pushed further as long as the two resulting pieces are of similar sizes and bigger than a low threshold (*th\_clust2*).

This heuristics stems from the observation that this part of the tree corresponds to the splitting of a thick bundle into almost parallel fascicles, events that we want to accept. The low threshold aims at preventing a fascicle to be cut in the middle. Note that the goal of this step is not to reach the thinnest segmentation as possible, but to prepare small fiber sets in order to get high sensitivity during *Step 4*. Hence these two thresholds can be varied in a large range without important modifications of the end result of the whole process. Increasing the thresholds is just pushing more segmentation work toward *Step 4*. Since the *Step 4*, based on fiber extremities, is also scaling well with the number of fibers, the main role of *Step 3* is to reduce as much as possible overlaps between fiber extremities, in order to optimize sensitivity. See Figure 5.7 for an example of a voxel-based fiber group adaptive partition.

**HC adaptive partition implementation.** The algorithm uses a queue **Q** to stock the nodes to be analyzed. It starts from the top nodes of the HC trees and recursively analyzes the hierarchical structure to decide which nodes will determine the final clusters. Table 5.1 presents the pseudocode of the algorithm.

**Fiber cluster extraction.** Once the partition into putative bundles has been computed, each cluster mask is used to extract corresponding diffusion-based *fiber clusters*. Tracts are selected when they are included at least a minimum percentage (*extr\_percent*) inside the cluster mask. Bundles containing less than a minimum number of tracts (*th\_tracts2*) are discarded before the following step. Figure 5.7 and Figure 5.9 (A) show some examples of voxel clusters and their respective extracted fiber clusters.

The number of resulting extracted fiber clusters depends on the fiber group: short fiber groups present a bigger number of fiber clusters, but in average an adult brain contains about one hundred clusters per fiber group.



---

```

add HC top nodes to Q
while Q is not empty:
    n := next node in Q
    if n.size < small_size:
        discard node
    else if n.size > th_clust1:
        split node (add children to queue)
    else:
        if n.ch1.size > th_clust2
           and n.ch2.size > th_clust2
           and dabsn(n.ch1.size, n.chil1.size) < 0.2
            split node (add children to queue)

```

---

Table 5.1: **Pseudocode of HC adaptive partition algorithm.**

The algorithm uses a queue **Q** to stock the nodes to be analyzed. It starts from the top nodes of the HC trees and recursively analyzes the hierarchical structure to decide which nodes will determine the final clusters. Variable **n.size** is the total size of the parcels within a node **n** (in voxels), composed by all the node descendants, **n.ch1.size** and **n.ch2.size** are the size of the parcels within the two direct children nodes of **n**, and *dabs<sub>n</sub>*( $\cdot, \cdot$ ) is the absolute value of the normalized difference between parcel sizes of two nodes.

In practice, threshold *th\_tracts* is set automatically according to the voxel size of the tracking propagation mask and the number of seeds per voxel. Thresholds *th\_clust1* and *th\_clust2* are set automatically depending on the parcel size and fiber length.

A good range for the minimum percentage of fiber cluster extraction (*extr\_percent*) was empirically found to be 40-60%. Values within this range ensure that a big percentage of fibers is extracted and that fiber clusters have a good quality. A value too big will discard too much fibers and a very small value will lead to too noisy clusters, decreasing sometimes the quality of the final results. Section 5.3.3 describes default parameters setting.

Anyway, all the fibers discarded during every step of the method are carefully stored. These fibers can be analysed and, for example, be used as input of a second clustering iteration.

#### 5.2.4 Step 4: Extremity-based clustering

A fiber cluster is made up of smaller fiber bundles presenting an important overlap inside deep white matter. An analysis performed over each fiber cluster is then crucial to divide the fiber clusters into these different fiber bundles. Focusing on their extremities is the only way to distinguish them (see Figure 5.9 (A-B)). Thus, this step aims at dividing the extracted fiber clusters into more regular bundles, called *fascicles*, based on their extremity configurations.

In order to get a set of 3D regions representing the different fascicle extremities, a *density image* of fiber extremities is created for each extracted fiber cluster at the scale of diffusion data (T2 image). In the ideal case, the fiber bundles that compose a fiber cluster will present distinct regions in the density image. The cluster division could then

be easily performed by selecting the fibers connecting each pair of extremity regions. In practice, this rarely occurs as fiber extremities of different bundles are commonly fused forming connected components in the 3D image.

A solution is to segment the density image in order to identify the different extremity regions, presenting a distinguishable peak of density. An adequate image segmentation algorithm for this problem is the 3D watershed transformation, described below.

**Watershed algorithm.** The watershed transformation, initially introduced by [Beucher and Lantuéjoul \(1979\)](#), is a region-growing method that segments an image following a geophysical model of rain falling on a terrain. In 2D, a gray-scale image is seen as a topographic relief, where the set of points on the surface that lead to the same minimum is known as a *catchment basin* and borders between catchment basins are *watershed lines*. The image is segmented into several regions, represented by the different basins (see Figure 5.8 A).

In 3D, the objective is the same, to associate each voxel with the corresponding closest local minimum. For segmenting our density image of fiber extremities we use an adapted version for 3D images and graphs of the watershed method. This algorithm was proposed by [Vincent and Soille \(1991\)](#) and is implemented in the *nipy* library. The method is based on an *immersion process analogy*, where each gray-level minimum represents a catchment basin. In 2D, the water starts filling all the catchment basins from the bottom. As the water level increase, dams are built at the places where the water coming from two different minima would merge. When everything has been filled, the dams represent the watershed lines (see Figure 5.8 B).

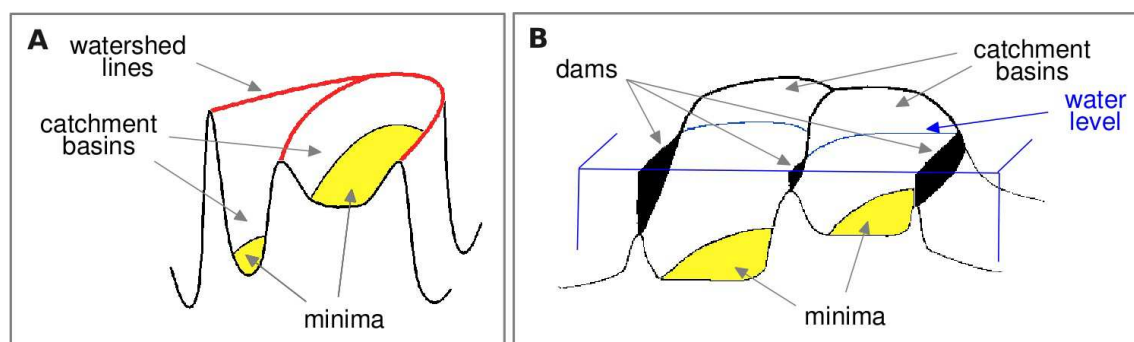


Figure 5.8: **Flooding of the water analogy for Watershed transformation.** **A:** Each gray-level minimum represents a *catchment basin* and borders between catchment basins are *watershed lines*. [Adapted from <http://www.esiee.fr/~info/tw/a2si04c.ppt>] **B:** The water starts filling all the catchment basins from the bottom. The algorithm builds dams at the places where the water coming from two different minima would merge. When everything has been filled, the dams represent the watershed lines [Adapted from [Vincent and Soille \(1991\)](#)].

The algorithm efficiently simulates the flooding of the water in the image. It is based on *sorting* the pixels in increasing order of their gray-levels followed by a *flooding* step using the sorted pixels. For each gray level  $h$ , pixels having value  $h$  are directly accessed

and analysed in order to evaluate their potential membership to a catchment basin. A FIFO (*first in first out*) queue is used to process the pixels.

The algorithm implements morphological region-growing on the graph and analyses the *geodesic influence zone* of the catchments. It uses data structures allowing a direct access to the neighbors of a given vertex (18-connectivity is used).

Image segmentation based on the use of watershed transformation has proved to be an efficient method provided that the main drawback of this technique is suppressed. This drawback consists in the over-segmentation produced by the watershed transformation if applied directly on the images to be segmented [Beucher (1994)]. Several approaches have been proposed for eliminating the over-segmentation problem. The simplest solution is to apply some pre-processings, like smoothing to remove small local minima. Anyway, over-segmentation of bundles is overcome during next step. Another solution is the use of an a priori collection of markers, introduced in the watershed algorithm allowing the segmentation of the selected regions exclusively [Beucher and Meyer (1992)]. Another approach is the merging of the catchment basins of watershed belonging to almost homogeneous regions [Beucher (1994)]. This merging can be based on edge strength or on valley depth, resulting in an elimination of superfluous watershed lines (pruning).

After the analysis of the density and segmented images, obtained by the watershed algorithm, we conclude that there is no need to apply any pre- or post- processing to the images. We use directly the density image of fiber extremities as input for the watershed, and the output image is used to divide clusters into several fascicles without any pruning. This is due to the characteristics of the density images of fiber extremities, which present a natural smooth shape, with a reduced number of local minima.

**Fiber cluster division.** The 3D regions obtained by the watershed segmentation are used to divide the extracted fiber clusters into several fascicles. Each fascicle is composed by the fibers whose extremities pass through two particular regions. An example of fiber cluster subdivision into fascicles is shown in Figure 5.9 (B-C). Typically, a fiber cluster is divided into 3-12 homogeneous fascicles.

**Optional fascicle denoising.** An optional post-processing step is applied to filter out outliers, *i. e.* fibers that present a path slightly different than most of the fascicle fibers. This processing is applied separately to each fascicle. A bundle density image is created and automatically thresholded with a value *th\_out1* depending on the number of tracking seeds per voxel. The resulting mask will contain a region with the fascicle 3D shape. Fibers whose path is more than 20% out of this region will be considered outliers. This step is not essential but brings a cleaner image of a group of fiber fascicles.

### 5.2.5 Step 5: Fascicle merge

This step considers all the fascicles from all the fiber length groups of a subset. It consists in a second clustering, aiming at agglomerating fiber fascicles that were over-segmented

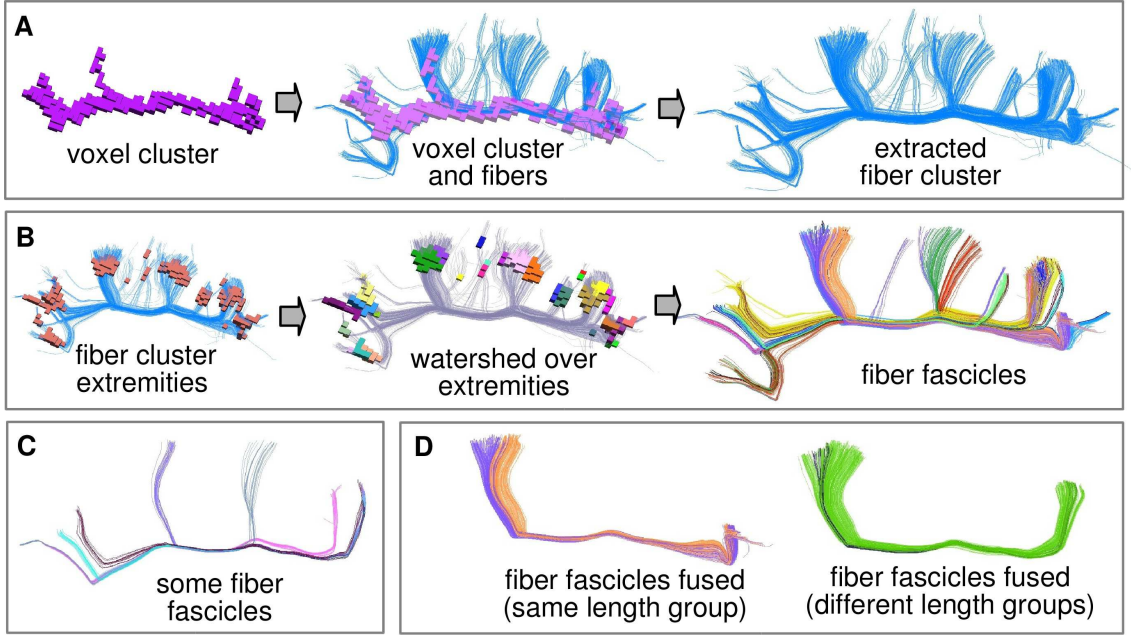


Figure 5.9: **An example of fiber cluster and fiber fascicles extraction (right hemisphere). A: Fiber cluster extraction from a cluster mask (Step 3).** Group length: 95-110 mm. The cluster mask is shown in purple. Fibers included at least 60% in the mask were extracted (in blue) to form the fiber cluster. **B: Extremity-based clustering (Step 3).** 3D regions representing the different fascicle extremities (in red) were first determined. The regions were then segmented by a 3D watershed into high density peaks. The obtained regions (in different random colors) were used to divide the extracted fiber cluster into several fascicles. Fascicles were randomly colored. **C: An example of some obtained fascicles.** Fascicles present different shapes and extremities. **D: Two examples of fiber fascicles fused after the centroid clustering (Step 5).** In purple and orange, the fusion of two fascicles that were subdivided after Step 4. In green and black, the fusion of two fascicles belonging to different length groups, 95-110 mm and 80-95 mm, respectively.

in the length-based segmentation step (*Step 2*) or in the fiber cluster extremity-based subdivision step (*Step 4*), whenever catchment bassins are oversegmented. For this, a *centroid tract* is computed as a representative for each fascicle. Then an average-link hierarchical clustering is applied based on a pairwise distance between centroids from all fascicles in the subset.

**Fascicle centroid calculation.** A fascicle centroid, representing the main fascicle geometry, is localized in the center of the fascicle and is determined as the tract minimizing a distance to the rest of the fascicle fibers. The distance measure employed is a symmetrized version of the mean closest point distance [Corouge et al. (2004); O'Donnell et al. (2006); O'Donnell and Westin (2007)]. This distance is described in section 4.4.2 of previous chapter, where the different fiber distance measures proposed in the literature are detailed. For completeness, we present below the distance measures used by our method.

The direct mean closest point distance,  $d_m$ , is defined as the mean of the distances

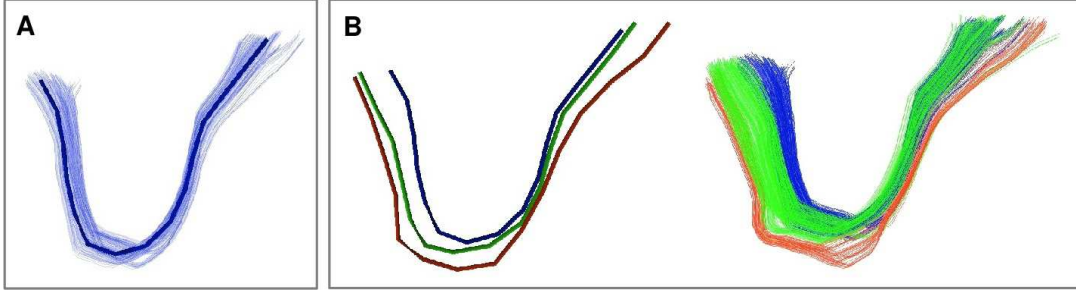


Figure 5.10: **Fiber fascicle centroid clustering.** **A: An example of fascicle centroid.** A fascicle centroid is determined as the tract minimizing the mean closest point distance to the rest of the fascicle fibers. **B: Fascicle centroid cluster example.** The fascicle centroids (in the left) are fused, as they satisfy the clustering criteria, based on the Hausdorff distance. The fascicles (in the right) come from two different fiber length groups: 50-65 mm (blue and green) and 65-80 mm (red).

between pairs of closest points on two fibers:

$$d_m(F_i, F_j) = \text{mean}_{p_k \in F_i} d_k(p_k, F_j), \quad (5.3)$$

where  $d_k$  is the distance between point  $k$  on fiber  $i$  and the closest point on fiber  $j$ :

$$d_k(p_k, F_j) = \min_{p_l \in F_j} \|p_k - p_l\|, \quad (5.4)$$

where  $\|\cdot\|$  is the Euclidean norm.

The symmetrized mean closest point distance,  $d_M$ , is defined as the mean of the two directed distances between fibers  $i$  and  $j$ :

$$d_M(F_i, F_j) = \text{mean}(d_m(F_i, F_j), d_m(F_j, F_i)), \quad (5.5)$$

See Figure 4.8 for an illustration of the closest point distances between two fibers. This distance provides a global similarity measure integrated along the whole curve and is, therefore, adequated for the centroid calculation. Before the distance calculation, the fascicle centroids are sampled using 15 equidistant points, as proposed by O'Donnell et al. (2006). An example of fascicle centroid is shown in Figure 5.10 (A).

**Fascicle centroid clustering.** Centroids are first determined for all the fascicles belonging to a fiber subset. Then, these are clustered based on another pairwise distance, the Hausdorff distance [Corouge et al. (2004)], which is more stringent than the mean closest point distance. This aims at regrouping only fascicles that have a very similar shape and position.

The Hausdorff distance  $d_H$  is defined as the maximum of the distances between pairs of closest points on two fibers:

$$d_H(F_i, F_j) = \max \left( \max_{p_k \in F_i} d_k(p_k, F_j), \max_{p_k \in F_j} d_k(p_k, F_i) \right) \quad (5.6)$$

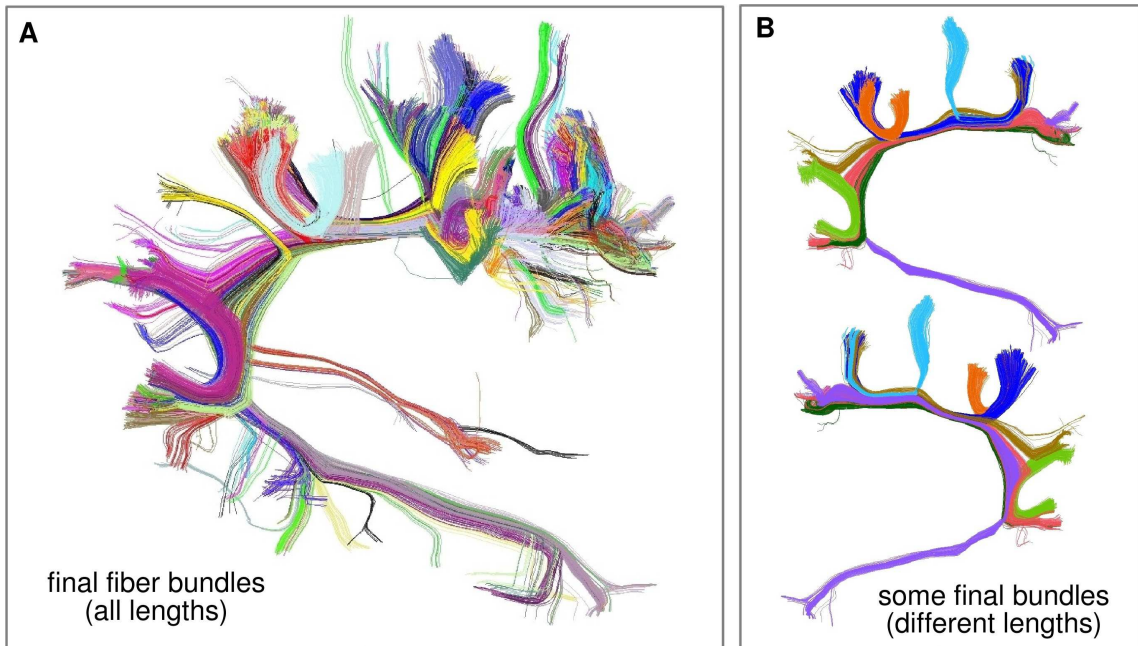


Figure 5.11: **An example of final fiber bundles (right hemisphere, arcuate fasciculus). A: A selection of final bundles from the subset (all lengths).** Fiber bundles were selected using the cluster mask used in Figure 5.9 A. Bundles were randomly colored. **B: Exterior and interior view of a selection of fiber bundles in E.** Fiber bundles selected had more than 100 tracts and presented different lengths: 150-175 mm (purple), 130-150 mm (pink), 110-130 mm (dark green), 95-110 mm (ochre), 80-95 mm (blue), 65-80 mm (cyan), 50-65 mm (light green), 30-50 mm (orange).

A maximal distance between fibers ( $max\_cdist$ ) is used to define the clusters, with usual values between 5 and 12 mm. To perform the clustering, the pairwise distance is converted to a pairwise fiber affinity [O'Donnell and Westin (2007)] (cf. equation 4.2). When constructing the affinity graph, only edges with affinities superior to the maximal distance are stored in the graph. The graph is then used to perform an average-link hierarchical clustering over the centroids for merging fascicles. An example of the fusion of fascicles from different fiber length groups and their respective centroids can be seen in Figure 5.10 (B). Figure 5.11 shows another example of the final fiber bundles obtained after the fascicle centroid clustering. This step reduces the number of final fiber bundles in between a 40% to a %70 of the fiber fascicles, depending on the maximal distance value.

## 5.3 Method validation and parameters tuning

We tested first our hierarchical clustering with simulated datasets. The goal here is to validate that the behavior of the method corresponds to the objective, namely detecting the homogeneous bundles of tracts embedded in the “spaghetti plate”.

For that, we generated ten simulated datasets, each one based on a model containing 200 bundles presenting different length, diameter, shape, and tract density. Then, three noise fiber sets were added to each simulated dataset, to get a total of 30 simulated fiber datasets. The simulated datasets were clustered with our intra-subject clustering



algorithm. Results were analysed in order to evaluate and validate the proposed method.

Furthermore, one simulated dataset was employed to evaluate the cost of scalability of our approach. First, the proposed method was compared with a non-scalable brute force clustering of the fibers. Then, we evaluated the impact in the quality of the results of the average parcel size used in the voxel-based clustering (*Step 3*). To accomplish that, we analysed the results for different parcel size values, when applying the whole clustering method and only the voxel-based clustering step.

### 5.3.1 Whole method evaluation using simulated datasets

**Simulated datasets.** We generated ten simulated datasets, each based on a model containing 200 bundles with various length, diameter, shape, and tract density. These 200 bundles were defined from the right hemisphere tract set of one of the adult subjects (cf. section 5.4.2). These tracts were randomly selected from a precalculated subset of tracts where a minimum pairwise distance was imposed. The distance measure used was the Hausdorff distance  $d_H$  (cf. equation 5.6), and the minimum distance was set to 4 mm. See Figure 5.12 (A) for an example of the selected tracts for a simulated fiber dataset.

Selected tracts were considered as the simulated bundle centroids. A variable number of tracts were added around each centroid, each resulting from a different translation of this centroid. The components of the translation vector were randomly determined following a normal distribution with a mean  $\mu = 0$  and a standard deviation,  $\sigma$ , varying between 1.0 and 2.0 mm. The number of bundle tracts was randomly sampled from a normal distribution with  $\mu = 100$  and  $\sigma = 80$ , and a minimum threshold set to 10 tracts, leading to an average of 22,000 tracts per dataset. Four simulated bundles with different number of fibers and sigma are shown in Figure 5.12 (C-F). The resulting fiber bundles for a simulated dataset can be seen in Figure 5.12 (B).

**Noise addition.** Once a bundle model was created, additional tracts were added in the dataset, simulating spurious tracts produced by the tractography algorithm. These tracts were selected from the same adult brain. A minimum distance  $d_H$  was imposed between each pair of such spurious tracts (cf. equation 5.6). We have performed experiments with three different amounts of such noise, defined as a percentage of the total number of tracts in the model dataset. The percentages used were 10% (minimum distance of 0.7 mm), 50% (minimum distance of 0.25 mm) and 100% (minimum distance of 0.2 mm). See Figure 5.12 (G-I) for an example of the spurious tract datasets.

Each of the ten model datasets was combined independently with the three different noise datasets, producing a final number of 30 noisy fiber datasets. Examples of noisy datasets with 10%, 50% and 100% of noise are shown in Figure 5.12 (J-L). In these figures, spurious tracts and bundle tracts are in different colors. It should be noted that since the fiber bundle centroids for datasets generation and the noise fibers were selected from the same brain, some fibers from noise datasets and from generated bundles presented a very similar shape. In those cases, it was not possible to differentiate them.

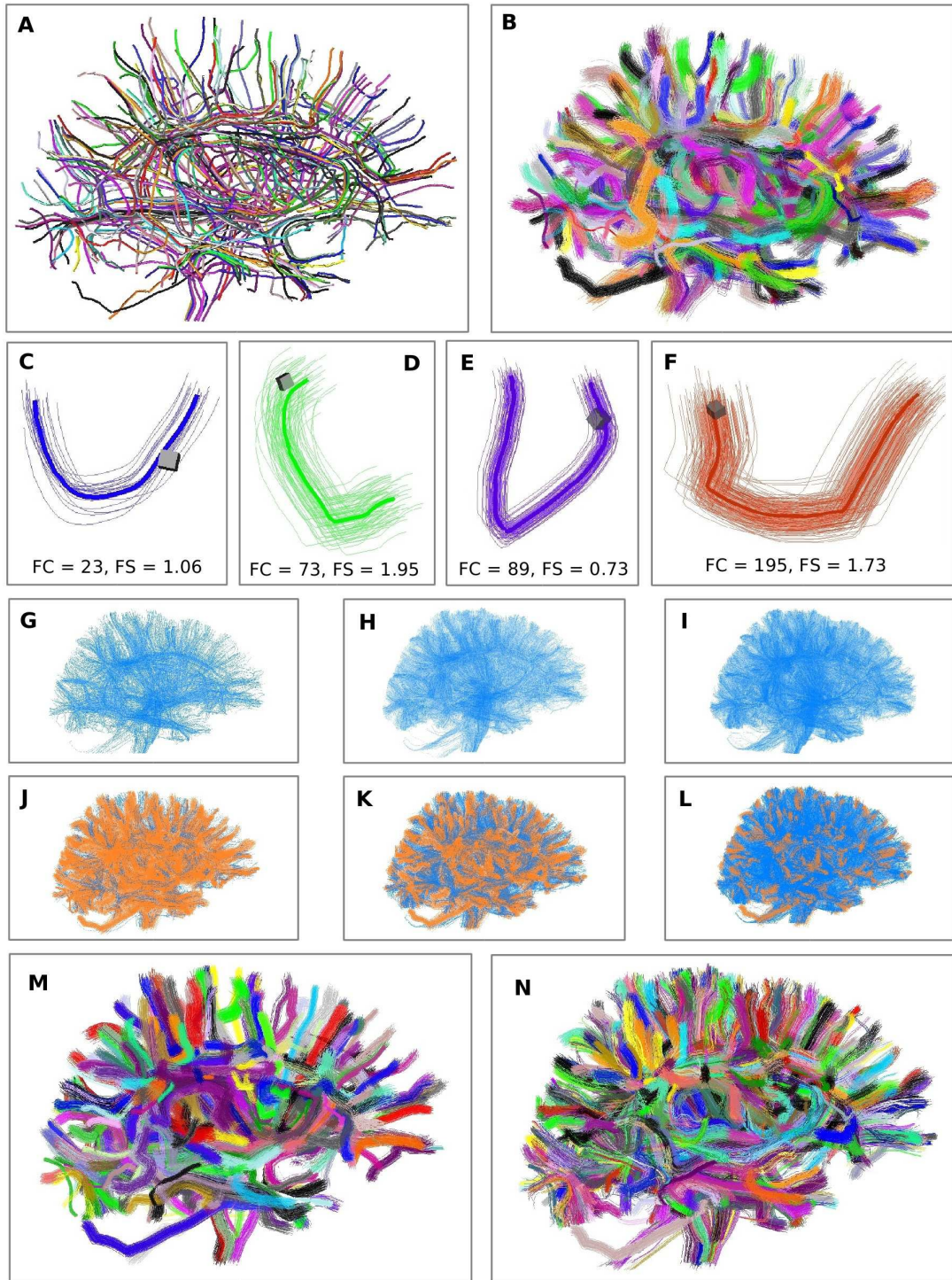


Figure 5.12: **Example of simulated fiber bundle datasets.** **A:** Lateral view of the two hundred fibers selected as bundle centroids. Centroids were randomly colored. **B:** Bundles generated from the centroids in **A**. **C-F:** Examples of four generated bundles with different number of fibers (FC), and sigma (FS) in mm. For a better perception of bundle length and density, a reference voxel (in gray) was added to each bundle. **G-I:** Noise fiber datasets with a percentage of 10%, 50% and 100% of the total fiber number in **B** (corresponding to 2,200, 11,000 and 22,000 fibers respectively). **J-L:** Generated noisy fiber datasets, for 10% , 50% and 100% of noise, resulting from the combination of a fiber dataset (in **B**) and a noise dataset (in **G-I**). **M,N:** Resulting fiber bundles after the method application for 10% and 100% of noise.

**Simulated fiber datasets clustering.** The developed method was applied to each generated noisy dataset. Since only one fiber subset was represented in the generated fiber datasets (right hemisphere), the method was applied from *Step 2* (section 5.2). We set the T2 voxel size and seed density equal to the original brain, leading to a minimal fiber density of 10 fibers per voxel (*th\_tracts*).

**Simulation results and method evaluation.** Resulting fiber bundles for the example fiber dataset with 10% and 100% of noise are shown in Figure 5.12 (M, N). Note that the results for the 100% of added noise brought a more noisy image as some noise fibers were added to fiber bundles. Also, some bundles containing only a small number of noise fibers of similar shapes were additionally detected.

To evaluate the results, we searched a correspondence between detected fiber bundles of each simulated dataset and the final bundles of the model. For accomplishing this task, we calculated a bundle centroid for each final bundle and determined the closest bundle centroid within the model. We used the Hausdorff distance  $d_H$  (cf. equation 5.6) with a very strict threshold. In some cases, some thick bundles were separated into two final bundles; that is not an error since our analysis allows the splitting of big bundles.

Figure 5.13 (A-J) shows the clustering results for the example fiber dataset, with 10% of noise (Figure 5.12 (J)). The central scatter plot (Figure 5.13 (E)) represents all the bundles in function of their sigma and number of fibers. The color codes the percentage of recovered fibers in each bundle. Recovered fibers, corresponding to the majority of the cases, take colors between blue and red, in function of the recovery percentage. A small number of bundles, not recovered, are shown in black, while some bundles, presenting more fibers than the simulated bundles (more than 100% recovery) are in dark red. Surrounding figures show different cases of bundle recovery.

Simulation results show that recovery percentage is bigger as the fiber number is bigger and fiber sigma is lower. This denotes the normal dependency of our method and other clustering methods on the fiber density. Bundles with a very low density, as the example in figure H, were not detected because the number of fibers per voxel was even lower than the number of seeds per voxel. Figures (C, F, G, I and J) represent the most usual fiber bundle results, where more than 90% of the fibers were recovered (red color). Nevertheless the most interesting result is the fact that the detection was all the time right in the center of the bundle, where density is high, while missing fibers were located in the periphery of the bundle, where density is low. Figures A, B and D show typical cases where the percentage of recovery was low. Figure G shows a special case where 100% of the fibers were recovered: this case corresponds to a very dense fiber bundle. It should be noted that fiber bundles manually selected from a brain, for example those in [Catani and Thiebaut de Schotten \(2008\)](#), present mostly an uniform fiber distribution, rather than a normal one, which would lead to a very satisfying recovery percentage.

Figure 5.13 (K) presents three scatter plots containing the results for the ten generated datasets, with 10%, 50% and 100% of noise. From the results, we can verify that



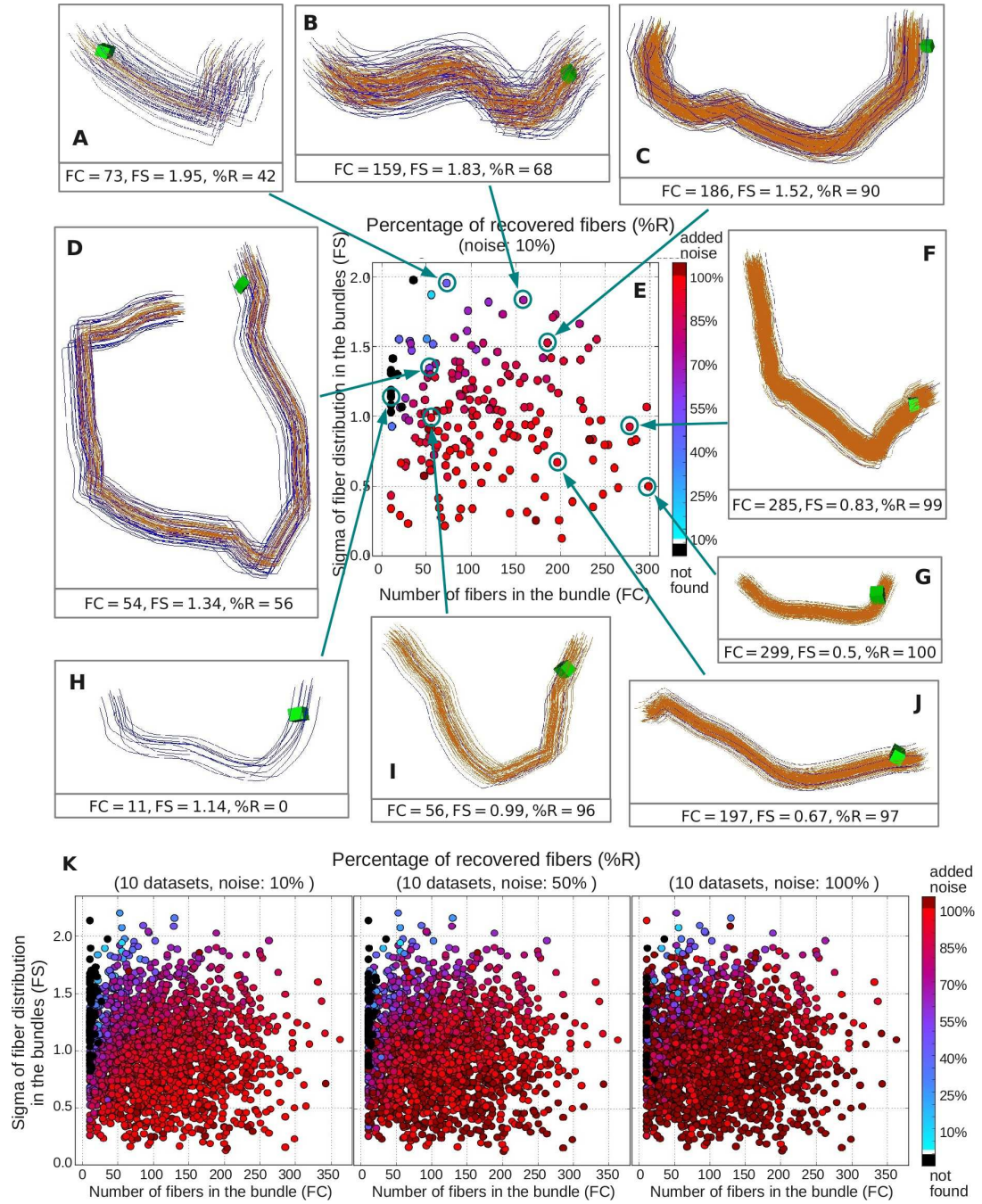


Figure 5.13: **Clustering results for simulated fiber bundle datasets.** **A-J:** Example of clustering results for one fiber dataset with 10% of noise. The central scatter plot (**E**) represents all the bundles in function of their sigma (FS) and number of fibers (FC). The color codes the percentage of recovered fibers (%R). The percentage varies from blue, for poorly recovered bundles, to red for bundles totally recovered. Bundles not found are in black, while bundles with a percentage higher than 100% of recovery are in dark red. Surrounding figures show different cases of bundle recovery. Recovered fibers are in orange while not recovered fibers are in blue. For a better perception of bundle length and density, a reference voxel (in green) was added to each bundle. **K:** Three scatter plots containing the results for the ten generated datasets, with 10%, 50% and 100% of noise.

the behavior of the method was preserved throughout all the simulated datasets: a big percentage of fibers was recovered, depending on the local fiber density. In other words, fibers presenting more than the minimum expected local bundle density were successfully recovered. Also, note that when the added noise was higher, the percentage of recovery also increased, and more bundles presented a recovery percentage greater than 100% (in dark red). That is not surprising if we consider that noise fibers were generated from the same dataset than simulated datasets centroids. Therefore, due to the big number of noise fibers, some were very similar to fibers from the generated bundles and were clustered together. This caused also a decrease in the number of not recovered bundles (in black).

### 5.3.2 Cost of scalability

While the results of the validation tend to show that the cost of the scalability introduced by the white matter parcel clustering (*Step 3*) is very low, we performed additional experiments in order to quantify this cost. We first applied a brute force clustering of the fibers to one of the simulated datasets. Results were analysed in order to compare this non scalable approach with the proposed method. Secondly, we applied our clustering method to one of the simulated datasets for a range of parcel sizes and evaluated the impact of the parcel size in the quality of the final clusters.

**Comparison with a brute force clustering method.** We performed a brute force clustering of the fibers of one of the simulated datasets with 10% of noise (24,623 fibers). For this purpose, we applied average-link hierarchical clustering using the same fiber-to-fiber distance as in the bundle centroid clustering of our method (*Step 5*), *i. e.* the Hausdorff distance (cf. equation 5.6). We performed iterative agglomeration of the fibers using a threshold on the fiber distance equal to 10 mm, a value slightly superior to the maximum intra-bundle distance between fibers within the dataset. Computational time was beyond 6 hours versus 15 minutes for our approach. Figure 5.14 presents the clustering results.

Figure 5.14 (E) shows an scatter plot representing the recovery rate of the simulated bundles in function of their geometry for the brute force HC. It can be observed that with these settings, the brute force approach did not recover all the simulated bundles. Figure 5.14 (A) shows the resulting fibers clusters for brute force HC. These are more noisy than the clusters found by our method (compare with Figure 5.12 (M)). This phenomenon can be observed in Figure 5.14 (B), which shows a comparison of brute force HC and our method results for one cluster. Our method recovered a cluster (in red) similar to the original (in blue), while brute force HC added noise to the cluster (in green).

A detailed analysis of the missed bundles led to two explanations:

1. In some few situations, two simulated bundles get merged because at least one short distance exists between the fibers generated by the simulation process, or because a short distance path made up of noise fibers can be found. An example of two fused clusters is illustrated in Figure 5.14 (C).

2. In some other situations occurring with low density bundles, noise fibers create a drift of the hierarchical clustering leading to split a bundle in several clusters.

Both of these difficulties are classical weaknesses of the hierarchical clustering strategy. A dedicated heuristic could probably improve the situation, but in our opinion, performing the hierarchical clustering in the space of fibers would require the same kind of additional steps as proposed in our method to reach robustness: for instance, an extremity-based clustering (like in *Step 4*) could overcome the first kind of failures, while a merge step would overcome the second kind of failures (like in *Step 5*).

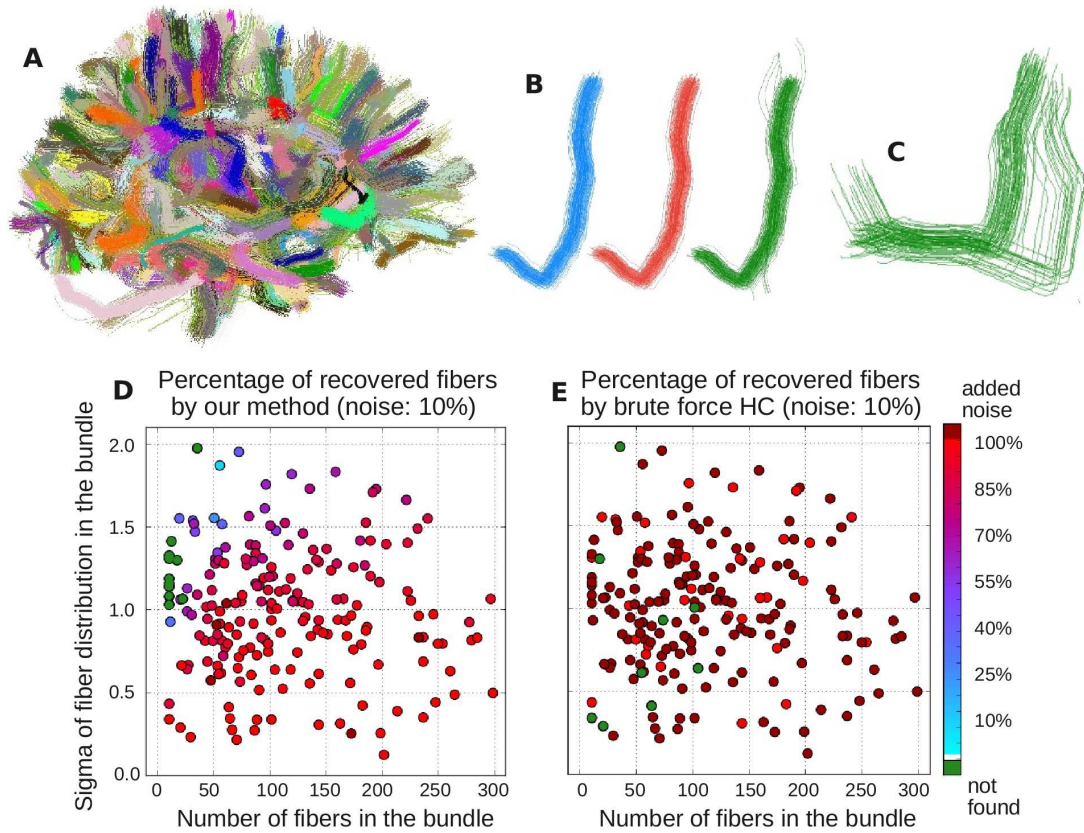


Figure 5.14: **Comparison of the method with a brute force fiber clustering.** A simulated fiber dataset with 10% of noise (24,623 fibers) was used to compare the results with a brute force hierarchical clustering (HC) of the fibers. **A:** Resulting fiber bundles after the application of a brute force HC using the same fiber-to-fiber distance as in the bundle centroid clustering of our method (*Step 5*) and a threshold on the fiber distance equal to 10 mm. **B:** Comparison of brute force HC and our method results for one cluster: original bundle (in blue), our method (in red) and brute force HC (in green) resulting clusters. **C:** Example of two fused clusters in brute force HC. **D:** Scatter plot representing recovery rate of the simulated bundles in function of their geometry (duplicated from Figure 5.13). The color codes the percentage of recovered fibers. **E:** Same scatter plot for the brute force HC, which recovers a larger percentage of fibers but also adds more noise fibers to the clusters. In addition, some clusters are not recovered.

Anyway, it should be noted that our method recovers most of the simulated bundles with some failures occurring only with low density bundles, which is a reasonable behavior. Hence, we do think that performing some of the clustering operations in the space of



white matter voxels has no straightforward negative effect on the clustering performances. Nevertheless, in order to understand the influence of the size of the white matter parcels on the behavior of our method, we have applied the clustering for a range of parcel sizes.

**Evaluation of the influence of the parcel size in the quality of the results.** A simulated fiber dataset with 10% of noise (24,623 fibers) was used to test the impact of the parcel resolution on the clustering results. We first have applied our complete clustering method for a range of parcel sizes, from 1 to 25 voxels per parcel.

Figure 5.15 (E) presents the number of recovered bundles in function of the average parcel size (in T2 voxels) for our whole clustering method. No spurious merge of original bundles was observed but some thick original bundles could be split into smaller parallel bundles, behavior that we accept in this chart. Therefore we did not observe significant modifications relative to the detection of the simulated bundles using the complete intra-subject clustering method.

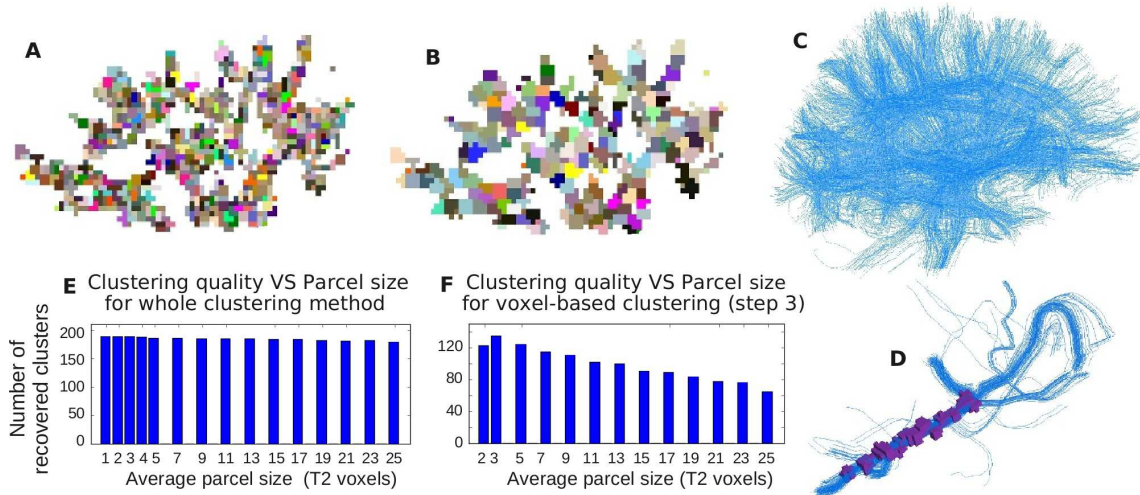


Figure 5.15: **Evaluation of the clustering method scalability cost.** A simulated fiber dataset with 10% of noise (24,623 fibers) was used to test the influence of the parcel resolution on the clustering results. **A:** WM parcellation for an average parcel size of 3 voxels. **B:** WM parcellation for an average parcel size of 15 voxels. **C:** Discarded fibers (3,152 fibers) for the whole clustering method using an average parcel size of 3 voxels. The method discards a big amount of noise fibers (91%) (note the similarity with Figure 5.12 G), as well as low density bundles (5% of simulated fibers). **D:** An example of fused bundles of different lengths (in blue) extracted from a WM cluster (in purple) of voxel-based clustering. This figure illustrates the utility of the length-based parcellation, which separates overlapping bundles before the voxel-based clustering. **E:** Number of recovered bundles in function of the average parcel size (in T2 voxels) for our whole clustering method. No spurious merge of original bundles was observed but some thick original bundles could be split into smaller parallel bundles, behavior that we accept in this chart. **F:** Same chart as in C) using only the voxel-based clustering (Step 3). Without length-based and extremity-based clustering, clustering quality drops when parcel size increases. Furthermore, a lot of bundles are not recovered even with the smallest parcel resolution.

This supports the claim that our hierarchical approach provides robustness to the method:

1. A lot of ambiguities are overcome by the initial length-based parcellation (*Step 2*): several bundles overlapping in white matter are usually attributed to different length sets. Hence, the clustering of white matter parcels yields relatively simple structures embedding only a few bundles. Figure 5.15 (D) shows an example of fused bundles of different lengths extracted from a WM cluster.
2. The watershed-based clustering of the fiber extremities (*Step 4*) usually manages to separate these bundles because the split works as soon as one of the two extremity sets are not overlapping.

Increasing the size of the white matter parcels increases the number of bundles to be separated during *Step 4*, without leading to major difficulty except for very large parcels.

Figure 5.15 (C) shows the discarded fibers (3,152 fibers) for the whole clustering method using an average parcel size of 3 voxels. The method discards a big amount of noise fibers. After comparing the discarded fibers with the original dataset, it was found that a 91% of discarded fibers correspond to noise fibers. Note the similarity of these discarded fibers with Figure 5.12 (G), where the noise fibers are shown. Low density bundles, representing a 5% of simulated fibers are also discarded.

In order to provide more insight into this behavior, we performed a second study where we did not apply the initial length-based split (*Step 2*) and the final extremity-based clustering (*Step 4*). Results are shown in Figure 5.15 (F). In this case, clustering quality drops when parcel size increases. Furthermore, a lot of bundles are not recovered even with the smallest parcel resolution. The resulting clustering method is then much less robust and the results are impacted by the parcel size.

### 5.3.3 Clustering parameters setting

Most of the clustering parameters are set automatically according to a simple heuristic taking the fiber tracking parameters as input. A few other parameters are set empirically. Figure 5.16 contains an exhaustive list of all parameters with a description of recommended ranges and default values.

A. Tractography parameters		
Name	Description	
<i>seeds_pv</i>	number of seeds per T2 voxel of the tracking propagation mask	
<i>voxel_size</i>	average T2 voxel size of the tracking propagation mask (in mm)	
<i>FLF</i>	fiber length factor (value ranging from 0, for the min. fiber length to 1, for the max. fiber length)	

B. Clustering parameters		
Name	Description [step]	Recommended values [min ... max, default]
<i>length_num</i>	number of fiber length groups [2]	[ 8 ... 12, <b>10</b> ] using an increasing length range with fiber length
<i>th_tracts</i>	min. number of tracts for T2 fiber mask construction [3]	$seeds\_pv * [ 0.5 \dots 2, \mathbf{1} ] / voxel\_size$
<i>th_tracts2</i>	minimum number of fibers in extracted clusters [3]	$seeds\_per\_voxel * [ 0.5 \dots 2, \mathbf{1} ]$
<i>parcel_size</i>	average WM parcel size (in T2 voxels) [3]	[ 3 ... 5, <b>3</b> ]
<i>min_psize</i>	minimum parcel size for WM parcellation [3]	$parcel\_size / [ 3 \dots 5, \mathbf{3} ]$
<i>size_factor</i>	calculated: WM parcels size factor	$parcel\_size / voxel\_size * 4$
<i>min_pconn</i>	min. WM parcel connectivity percentage [3]	[ 1 ... 3, <b>1</b> ] %
<i>small_size</i>	maximum size of outliers (in T2 voxels) [3]	$parcel\_size * [ 3 \dots 5, \mathbf{4} ]$
<i>tclust_1</i>	maximum cluster size (in T2 voxels) [3]	$(1 + FLF * 0.5) * size\_factor * [100 \dots 250, \mathbf{150}]$
<i>tclust_2</i>	minimum cluster size (in T2 voxels) [3]	$(1 + FLF * 0.5) * size\_factor * [ 15 \dots 40, \mathbf{25} ]$
<i>extr_p</i>	percentage of fibers extraction from WM clusters [3]	[ 40 ... 60, <b>60</b> ] %
<i>th_out1</i>	minimum number of tracts for extremity masks [4]	$seeds\_pv * [ 0.5 \dots 2, \mathbf{0.5} ]$
<i>max_cdist</i>	maximal distance between fiber centroids (in mm) [5]	[3 ... 15, <b>5</b> ] mm

Figure 5.16: **Clustering parameters setting.** **A:** Tractography parameters used for clustering parameters setting. **B:** Recommended ranges and default values for clustering parameters.

## 5.4 Intra-subject fiber clustering results

The complete method was applied to the tracts computed from HARDI data obtained for twelve adult brains. The method was also tested with the tracts obtained from two children using lower angular resolution acquisitions and a tensor model.

### 5.4.1 A T1-based tractography propagation mask

Diffusion MRI tractography needs to be constrained by a white matter mask defining the 3D space within which fibers are tracked. Most techniques usually threshold the fractional anisotropy (FA) maps (typical threshold between 0.1-0.2) assuming that when FA is too small, the uncertainty of the principal diffusion direction is high. However, this criterion is rough as the FA value is not specific of a particular structural configuration and therefore constrains tracking results to region of WM with high anisotropy. In particular, FA (or GFA) can be very low in fiber crossings representing more than 2/3 of WM voxels, thus putatively discarding many valid tracts. Furthermore, because the diffusion-weighted MRI resolution is generally coarser than standard T1-weighted MRI (on the order of 2 mm isotropic), voxels at the interface between the WM and the cortex may suffer from severe partial volume effects, artificially diminishing the FA values. Therefore, many true-positive neuronal pathways may not be revealed.

To overcome these problems, we propose the use of a propagation mask stemming from T1 anatomy. Existing anatomical pipelines suffer from several limitations. First,

the partial volume effect will fail at delineating some small structures like the fornix, the posterior (PC) and anterior commissures (AC). In addition, deep brain structures, commonly crossed by efferent and afferent fibers, would not be systematically well included due to their low contrast in the conventional T1-weighted data. Finally, the conventional millimeter resolution of T1-weighted data at 1.5T or 3.0T can cause partial volume effects in cortical regions that lead to spurious connections between neighboring gyri.

We propose the creation of a robust propagation mask stemming from T1 anatomy [Duclap (2010); Guevara et al. (2011a)], based on three T1-based masks. This is an improved version of a T1-based propagation mask originally proposed by [Perrin et al. (2008)].

Two masks are obtained with the T1-MRI pipeline of BrainVISA software:

- A mask of both hemispheres and the cerebellum, called the *brain mask*
- A mask of the sulci skeleton, called the *sulci mask*, calculated through a homotopic multiscale erosion of a brain mask (see Figure 5.17).

A first processing subtracts the dilated sulci mask to the brain mask in order to prevent any connection between different gyri and to ensure that the fibers are stopped in the GM/WM interface. An intermediate propagation mask is thus obtained.

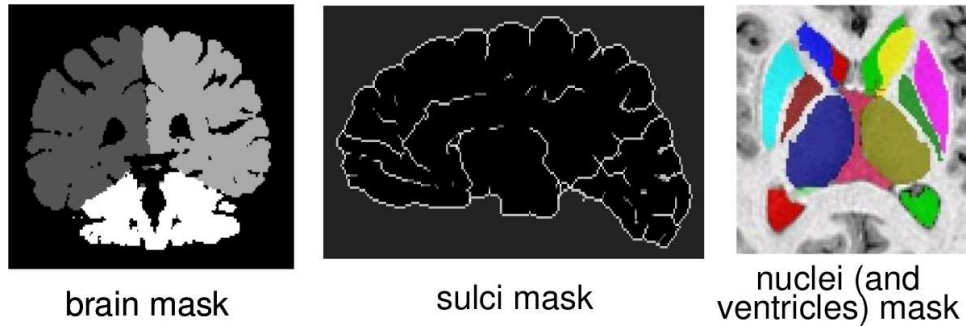


Figure 5.17: T1-based masks used for the propagation mask construction.

In order to ensure a good delineation of deep structures, of the corpus callosum (CC), of the fornix, and of AC/PC, a mask of deep nuclei and ventricles, called the *nuclei mask* is employed (see Figure 5.17). The deep nuclei segmentation is obtained using a deformable model constrained with a probabilistic atlas [Marrakchi-Kacem et al. (2010c)]. The ventricles segmentation is calculated using a robust histogram analysis of the T1 data guided by a probabilistic atlas of the ventricles, as described in [Marrakchi-Kacem et al. (2010b)]. The nuclei mask is dilated and added to the intermediate propagation mask in order to fill all the deep brain regions. The ventricles are subsequently subtracted from this mask to obtain the final robust propagation mask. Last, the cerebellum can be optionally included in the final mask.

This mask allows a better tracking of fibers until the GM/WM interface, which is of particular interest for the study of short association U-fibers. Contrary to usual FA-based

masks failing at including low FA regions such as AC/PC, the fornix or crossings, this technique provides an accurate mask of the brain WM+GM independent of the DW data quality (see Figure 5.18). Note, that a good registration between T1 and T2 images is needed, which implies a good correction of the susceptibility induced geometrical distortions of T2 images.

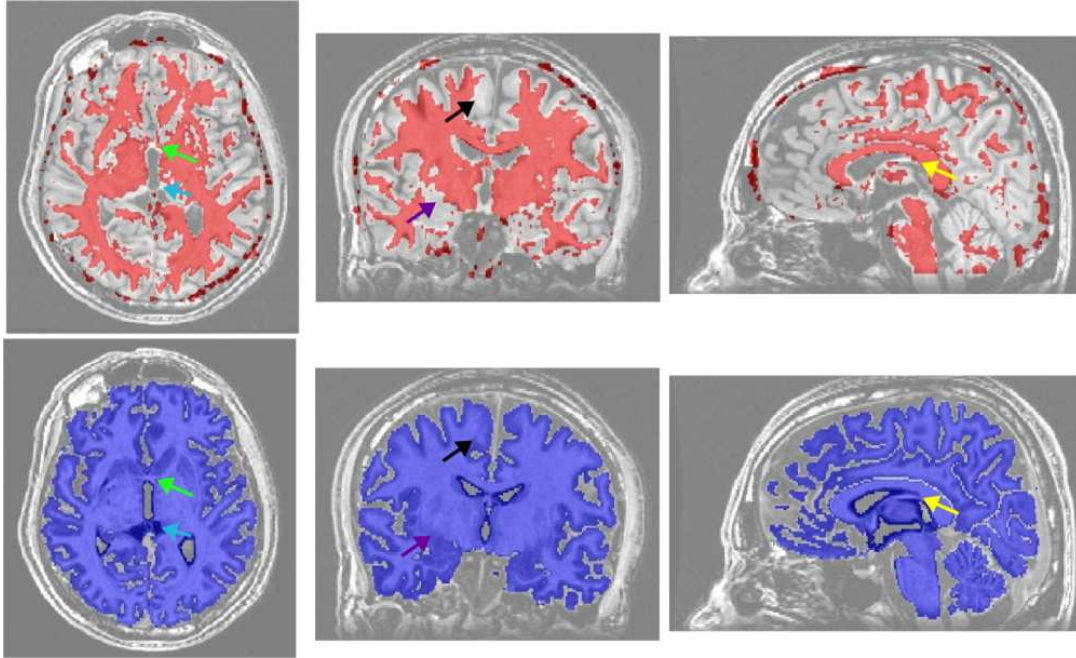


Figure 5.18: **Axial, coronal and sagittal views of the propagation masks.** **red:** FA mask ( $th = 0.1$ ). **blue:** our propagation mask. Note the good delineation in our mask of the AC (green arrows), the PC (cyan arrows), the subcortical WM (black arrows), the deep nuclei (violet arrows) and the fornix (yellow arrows).

In order to compare the tractography data obtained with both masks (our T1-based and a FA-based mask), we segmented the bundles for two tractography datasets of the same subject, using both, a FA-based mask ( $th = 0.15$ ) and our T1-based mask. Tractography datasets were calculated using regularized deterministic tractography based on orientation distribution functions, calculated from the analytical q-ball model [Descoteaux et al. (2007)] (spherical harmonics order = 6 and regularization factor = 0.006), and the same tracking parameters (7 seeds/voxel at T2 resolution, aperture angle = 30, tracking step = 0.5).

First, known WM bundles were determined using an automatic bundle segmentation method based on a multi-subject bundle atlas, described in chapter 7. The results are shown in Figure 5.19 (A). We can see that our T1-based mask leads to thicker fiber bundles, containing more fibers in the subcortical regions. Also, some short association bundles were determined using the same bundle segmentation method based on a multi-subject bundle atlas of short association bundles (see Figure 5.19 (B)). We can see that our T1-based mask allows a better reconstruction of most short association bundles. In



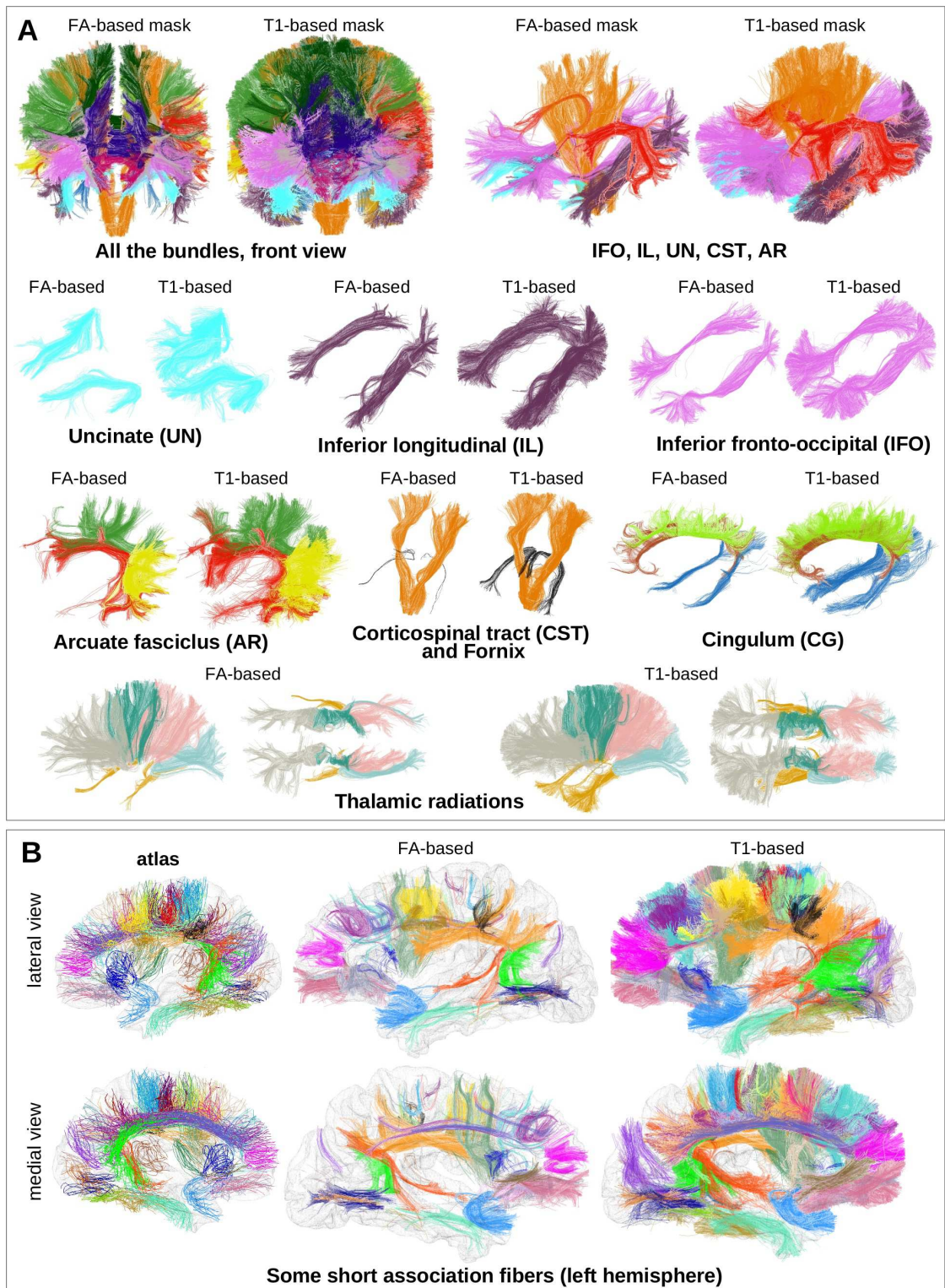


Figure 5.19: A comparison of known (A) and short (B) WM bundles segmented using an automatic bundle segmentation method based on a multi-subject bundle atlas, for two tractography datasets of the same subject, using both, a FA-based mask ( $th = 0.15$ ) and our T1-based mask. DW data was acquired using a Siemens 3.0 T Tim Trio system with a  $b$ -value=1000 and 41 DW orientations.



average, the bundles reconstructed with the FA-based mask presented only 18% of the number of fibers reconstructed with our T1-based method. In some cases, bundles that were successfully reconstructed by our mask were not reconstructed at all by the FA-based mask (20%). In other important number of cases, the FA-based mask led to bundle reconstruction with less than 5% of the fibers obtained with our T1-based mask (25%).

We can note that the use of the proposed T1-based propagation mask in conjunction with tractography techniques improves the accuracy of the anatomical connectivity of the brain by reducing false positives and increasing the detection of the subcortical connectivity. This mask was used in recent connectivity studies, as those described in [Roca et al. (2009, 2010); Marrakchi-Kacem et al. (2010a)].

**Fiber datasets.** All the fiber tract datasets were reconstructed using a streamline deterministic tractography algorithm and the described T1-based propagation mask, both provided by *BrainVISA/Connectomist-2.0* software. The tracts were calculated as the trajectories of particles with inertia, leading to regularized curvature [Perrin et al. (2005a)]. This method has been validated using a crossing phantom made up of sheets of parallel haemodialysis fibers and through the successful tracking of the primary auditory tract in the human brain.

#### 5.4.2 Adult HARDI datasets

**Adult HARDI datasets.** The analysis was performed for twelve subjects of the NMR public database <sup>3</sup> [Poupon et al. (2006)]. This database provides high quality T1-weighted images and diffusion data acquired with a GE Healthcare Signa 1.5 Tesla Excite II scanner. The diffusion data presents a high angular resolution (HARDI) based on 200 directions and a b-value of 3,000 s/mm<sup>2</sup> (voxel size of 1.875 x 1.875 x 2 mm). DW-weighted data were acquired using a twice refocusing spin echo technique [Reese et al. (2003)] compensating Eddy currents to the first order. Geometrical distortions linked to susceptibility artifacts were corrected using a phase map acquisition. T1 and DW-weighted data were optimally aligned using a rigid 3D transform estimated by an automatic registration algorithm based on mutual information. Registration was performed between the average of 5 diffusion-free T2-weighted images and the high resolution T1-weighted image.

**Adult HARDI datasets diffusion models.** Raw high angular resolution diffusion imaging (HARDI) data was first denoised with a Non-Local Means filter adapted to Rician noise (NLMr), described in Descoteaux et al. (2008). The diffusion Orientation Distribution Function (ODF) was then reconstructed in each voxel using a spherical deconvolution of fiber Orientation Distribution Function (fODF). It is a spherical deconvolution transform (SDT) reconstructed from q-ball imaging [Descoteaux et al. (2009b)] with a constrained regularization [Tournier et al. (2007)], using a maximum spherical harmonic (SH) order 8 and a Laplace-Beltrami regularization factor  $\lambda = 0.006$ .

---

<sup>3</sup>Thanks to Dr. Cyril Poupon for providing this HARDI database

**Adult HARDI datasets tractography.** Streamline deterministic tractography was initiated from two seeds in each voxel of the T1-based propagation mask (voxel size of  $0.9375 \times 0.9375 \times 1.2$  mm), in both retrograde and anterograde directions, according to the maximal direction of the underlying ODF. Retrograde and anterograde tracking were merge into one single tract. Tracking was stopped either when the particle exited the propagation mask, or when the angle between the two last moves exceeded  $30^\circ$ , or when the tract length exceeded 200 mm. Finally, tracts shorter than 20 mm were filtered out, leading to a set of about 1.5 millions tracts per subject.

**Results for adult HARDI datasets.** The twelve datasets were separated into the ten default length groups, described in *Step 2* (section 5.2). The remaining parameters were also set automatically, in function of the number of seeds per voxel and fiber length. Results are shown for the right hemisphere (RH) of one subject (cf. Figure 5.20). This RH subset contained a total number of 598,953 fibers, from a total of 1,573,894 fibers for the whole brain. A total of 3,159 final fiber bundles were obtained for the subset.

Due to the big number of fiber bundles it was not possible to perceive the clustering results in one image. For a better visualization, the fiber bundles were displayed in separated groups, with different fiber lengths (see Figure 5.20 (A)). Figure 5.20 (B) presents the exterior and interior view of a group of short fiber bundles (35-50 mm). Most of these bundles belong to short association fiber tracts, like U fibers. An exterior and interior view of a group of long fiber bundles (130-150 mm) is shown in Figure 5.20 (C). These bundles are part of known deep white matter tracts, like the cortico-spinal tract and the arcuate fasciculus. Note that anatomical WM tracts are composed by several resulting bundles, presenting different shapes and lengths. Different views of a selection of long final fiber bundles for the same adult brain are also shown in Figure 5.21.

Another example of the fiber bundles generated by our method can be seen in Figure 5.11 (A), which shows all the bundles passing through a voxel ROI. A selection of these bundles, with different lengths, is presented in Figure 5.11 (B). This example reveals the complexity achieved by the method results, where a very heterogeneous group of bundles sharing the same white matter paths were successfully clustered.

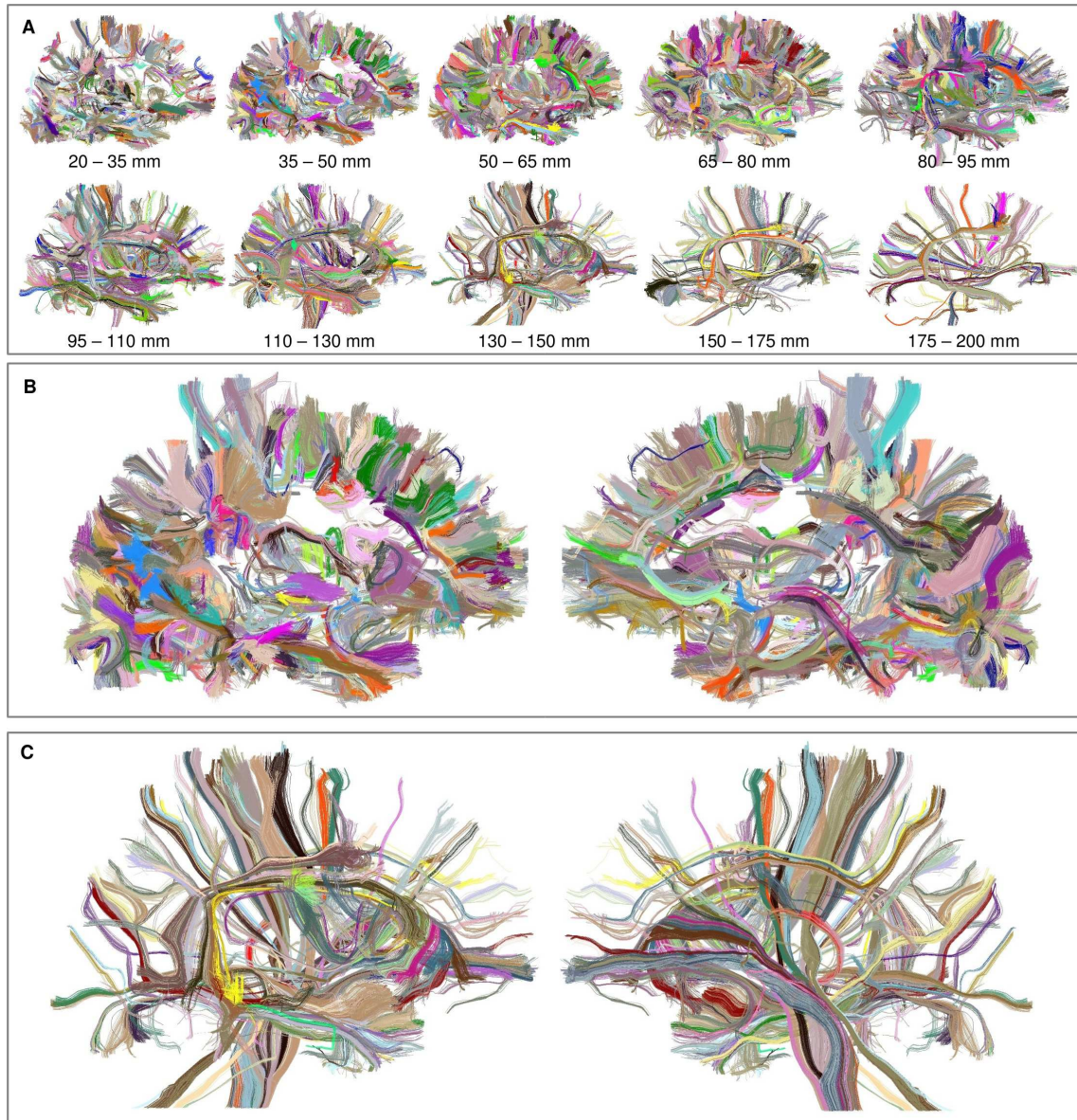


Figure 5.20: **Final fiber bundles for an adult brain (right hemisphere).** Bundle colors were randomly assigned and could be repeated within a group. **A: Exterior view of the whole subset results.** For a better visualization, fiber bundles were separated into ten length groups. **B: Exterior and interior view of a group of short fiber bundles (35-50 mm).** Most of these bundles belong to association fiber tracts. **C: Exterior and interior view of a group of long fiber bundles (130-150 mm).** These bundles are part of known deep white matter fiber tracts.

### 5.4.3 Child DTI datasets

**Child DTI datasets.** The method was applied to two normal children between 9 and 11 years old. This database<sup>4</sup> provides high quality T1-weighted images and diffusion data acquired with a Siemens 3.0T Tim Trio system equipped with a whole body coil (40 mT/m, 200 T/m/s) and a 12-channel head antenna. The diffusion sensitization used

<sup>4</sup>Thanks to Dr. Ghislaine Dehaene-Lambertz for providing the child brain datasets



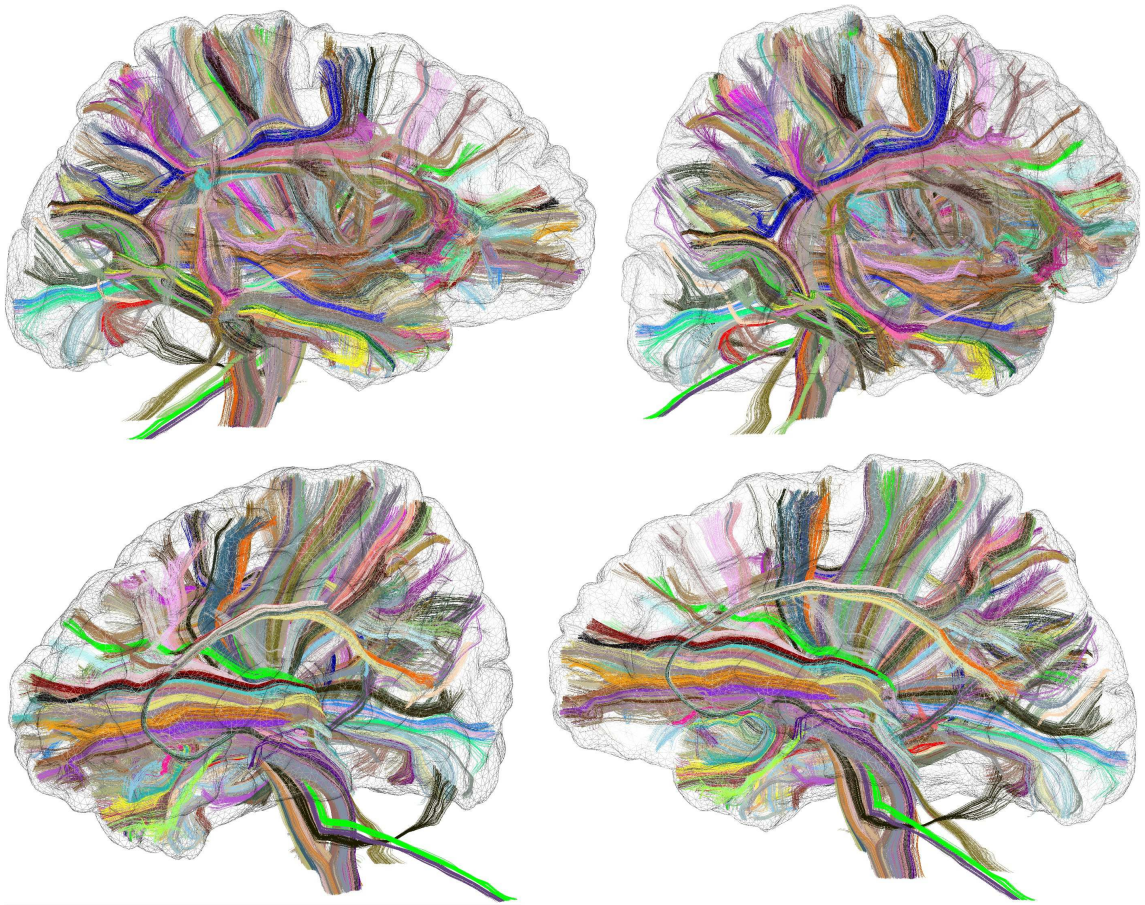


Figure 5.21: **Different views of a selection of long final fiber bundles for an adult brain (right hemisphere).**

30 uniformly distributed gradient directions with a b-value of  $1,000 \text{ s/mm}^2$  (voxel size of  $1.875 \times 1.875 \times 3 \text{ mm}$ ). The T1-weighted image and the DW-weighted dataset were optimally aligned with the same method as for the adult datasets.

**Child DTI datasets diffusion models.** Raw diffusion data was also denoised with the NLMr filter [Descoteaux et al. (2008)]. Then, a Diffusion Tensor Field (DTI) was calculated in each voxel using *BrainVISA/Connectomist-2.0* software.

**Child DTI datasets tractography.** Fiber tracts were calculated using streamline deterministic tractography, from two seeds in each voxel of the T1-based propagation mask (voxel size of  $1 \times 1 \times 1 \text{ mm}$ ), in both retrograde and anterograde directions, according to the first eigenvector of the tensor. Stopping criteria were the same as for the adult datasets.

**Results for child DTI datasets.** As for adult datasets, each fiber subset was separated into the ten default length groups, and all the parameters were automatically determined. Figure 5.22 presents the resulting final bundles (2,078 in total) for the right hemisphere of one brain. This subset had 283,446 fibers, from a total of 723,460 fibers for the whole

brain. For a better visualization, fiber bundles were also separated into ten length groups (cf. Figure 5.22 (A)). Figure 5.22 (B) presents the exterior and interior view of a group of short fiber bundles (35-50 mm). An exterior and interior view of a group of long fiber bundles (130-150 mm) is shown in Figure 5.22 (C).

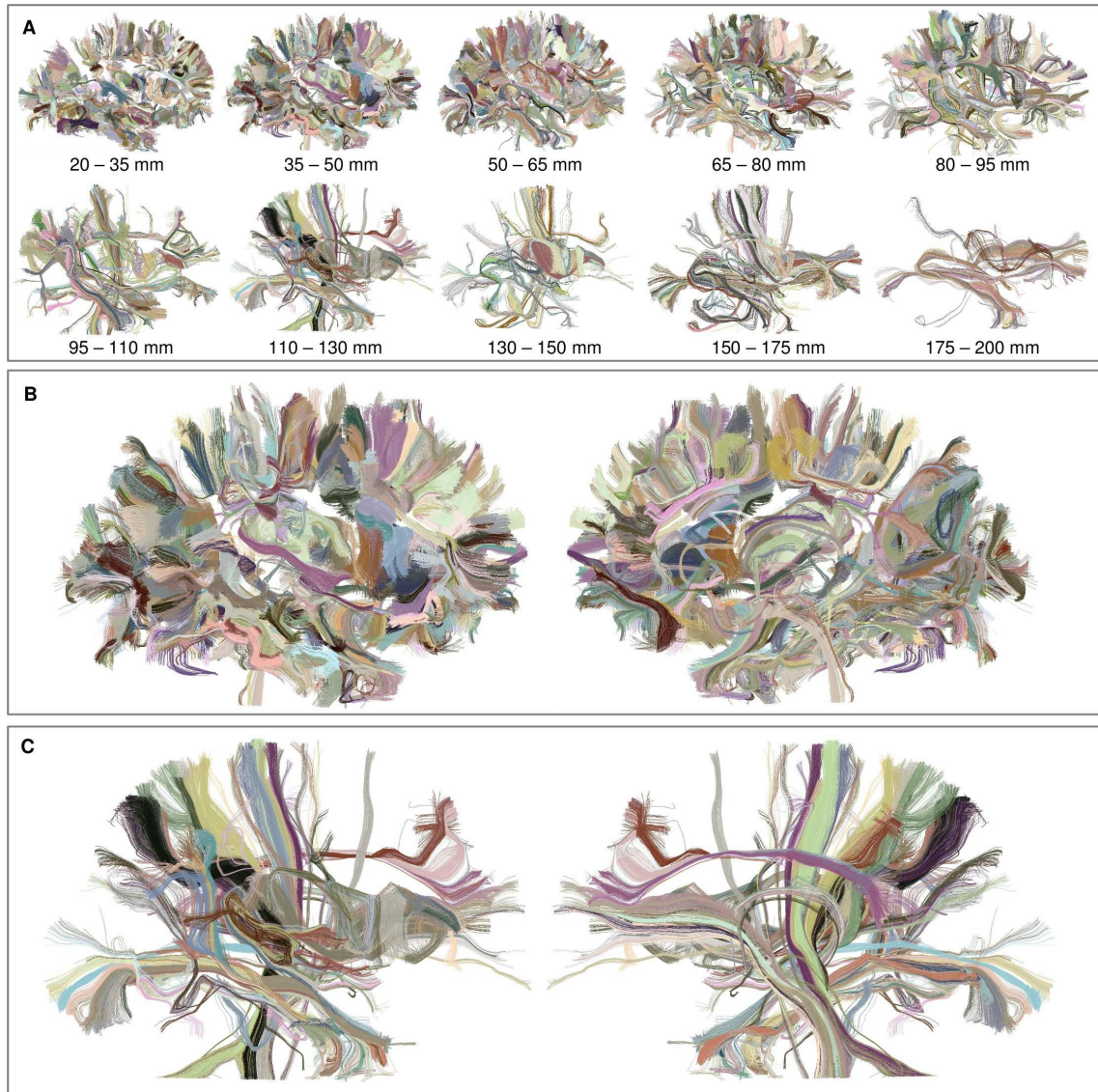


Figure 5.22: **Final fiber bundles for a child brain (right hemisphere).** Bundle colors were randomly assigned and could be repeated within a group. **A: Exterior view of the whole subset results.** For a better visualization, fiber bundles were separated into ten length groups. **B: Exterior and interior view of a group of short fiber bundles (35-50 mm).** Most of these bundles belong to association fiber tracts. **C: Exterior and interior view of a group of long fiber bundles (110-130 mm).** These bundles are part of known deep white matter fiber tracts.



## 5.5 Applications

The method was applied to the data issued from an actual phantom containing a plethora of realistic crossing, kissing, splitting and bending fiber configurations [Poupon et al. (2010)]. This last experiment illustrates the interest of our compression method for comparing different tractography algorithms.

The utility of our intra-subject clustering method is also illustrated with two examples. First, the hierarchical decomposition provided by our method is used as a bottom-up strategy for a preliminary study and decomposition of the arcuate fasciculus. Secondly, an example for U-fiber tracts, connecting cortical areas separated by a few folds, illustrates the use of our clustering results for population analysis and the inference of a brain fiber bundle model [Guevara et al. (2010)]. This research topic is addressed in details in next chapter.

### 5.5.1 Physical phantom

**Phantom datasets.** The MR phantom [Poupon et al. (2010)], created for the *MICCAI 2009 Workshop on Diffusion Modelling and the Fibre Cup*<sup>5</sup>, is made of small-diameter acrylic fibers, chosen for their high hydrophobicity and flexibility that ensure good control of the phantom geometry [Poupon et al. (2008)]. It contains a plethora of realistic crossing, kissing, splitting and bending fibre configurations created as a ground truth dataset for the validation of high angular resolution diffusion imaging (HARDI) and tractography algorithms. Diffusion data was acquired on a Siemens 3.0 T Tim Trio system equipped with a whole body coil (40 mT/m, 200 T/m/s) and a 12-channel head antenna. The analyzed dataset has a resolution of 3 x 3 x 3 mm (image size: 64 x 64 x 3) and a b-value of 1,500 s/mm<sup>2</sup>. It is composed by two repetitions of 65 directions each, corresponding to one baseline and 64 diffusion gradients.

**Phantom datasets diffusion models.** Three different diffusion models were calculated for the phantom dataset:

1. Diffusion Tensor Field (DTI).
2. An analytical solution for q-ball imaging (QBI) using spherical harmonic (SH q-ball) basis [Descoteaux et al. (2007)]. A maximum SH order of 8 and a Laplace-Beltrami regularization factor  $\lambda = 0.006$  were used.
3. The spherical deconvolution of fiber Orientation Distribution Function (fODF) described in Descoteaux et al. (2009b), using a maximum SH order of 8 and a Laplace-Beltrami regularization factor  $\lambda = 0.006$ .

**Phantom datasets tractography.** Two kinds of tractography for each diffusion model were calculated: streamline deterministic and probabilistic. A phantom propagation mask

<sup>5</sup><http://www.lnao.fr/spip.php?article106>



was created in a super-resolution of three times the T2 resolution (voxel size equal to  $1 \times 1 \times 1$  mm). This resolution allowed a better definition of the phantom borders. The voxels of this mask were also used to define fiber seeds, from which fibers were tracked in both retrograde and orthograde directions. Deterministic tractography was initiated from one seed per voxel, according to the maximal direction of the underlying ODF. Probabilistic tractography was initiated from eight seeds per voxel according to a probability distribution defined from the underlying ODF. Stopping criteria were the same as above, with the exception of the maximum fiber length, set to 180 cm.

**Results for phantom datasets.** The six fiber datasets of the MR phantom were clustered. No big change was needed for applying the method to these datasets (section 5.2). Just the first rough fiber segmentation (*Step 1*) was skipped and each fiber dataset was processed as one subset from *Step 2*. The obtained results are presented in Figures 5.23 and 5.24.

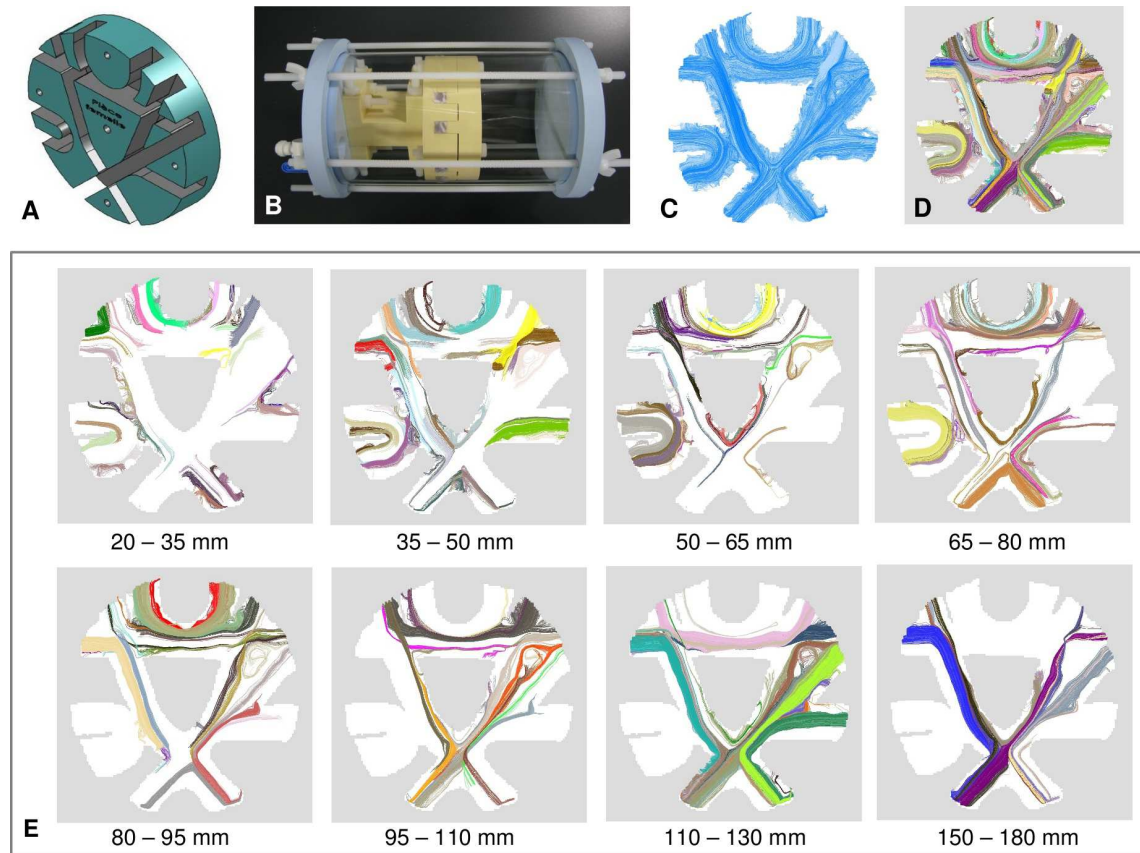


Figure 5.23: **Final fiber bundles for the DTI physical phantom dataset.** **A:** 3D illustration of the phantom design. The female container piece. **B:** The phantom container. **C:** DTI deterministic fiber dataset. The dataset had 46,362 fibers between 20 and 180 mm. **D:** The whole set of final bundles for DTI deterministic dataset (in C). Bundle colors were randomly assigned and could be repeated within a group. **E:** A selection of final bundles for DTI deterministic dataset (in C). Bundle colors are the same as in D. Bundles were separated into nine length groups. Eight groups are shown.

The whole resulting fiber bundles set is shown only for one dataset: DTI deterministic fiber dataset. The original dataset had 46,362 fibers between 20 and 180 mm (cf. Figure 5.23 (C)). Clustering results were composed by 296 fiber bundles, shown in Figure 5.23 (D). In order to improve the visualization, the set of final bundles for this dataset was separated into nine length groups (eight groups are shown in Figure 5.23 (E)). Clustering results for all the tested datasets presented a very large number of fiber bundles, of different lengths and shapes. Most of these did not correspond to the seven phantom ground truth (GT) bundles, illustrated by the means of 3D masks in Figure 5.24 (A). The complexity of the results was higher in the case of streamline probabilistic datasets.

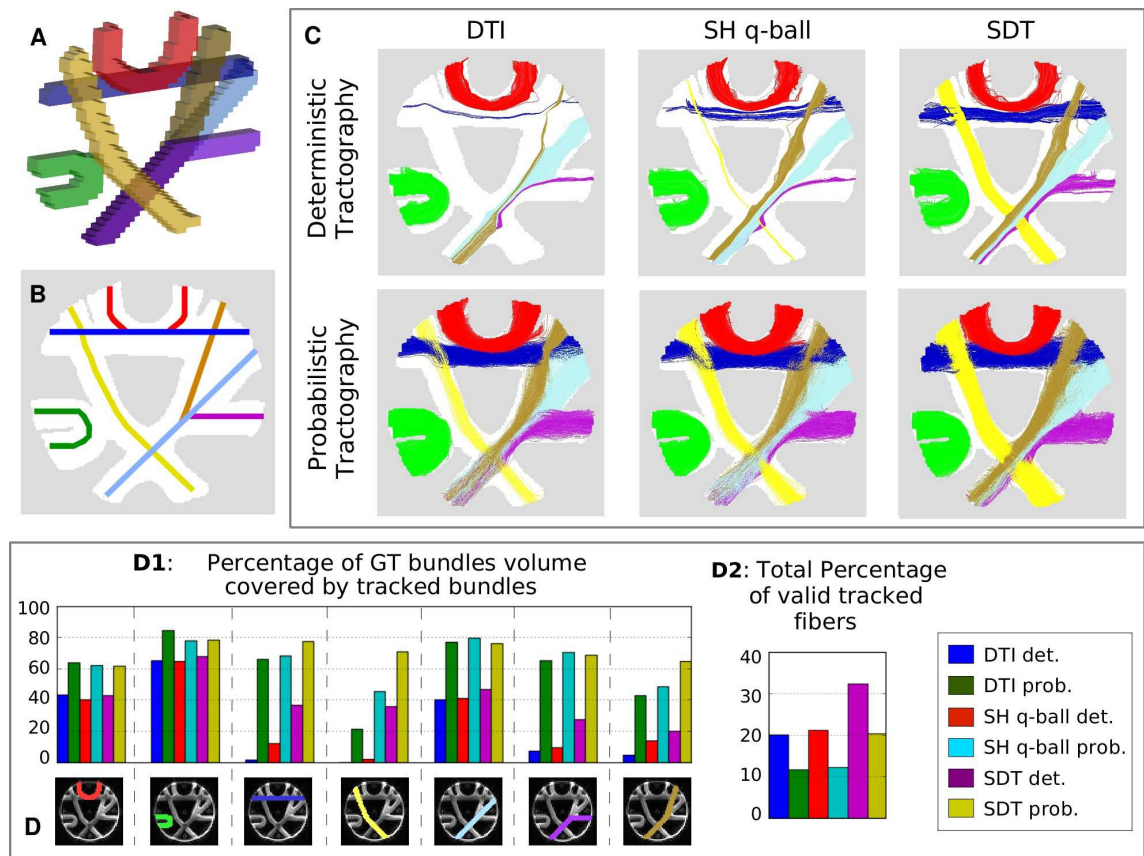


Figure 5.24: **Final fiber bundles for the six physical phantom datasets. Application to diffusion local models and tractography algorithms evaluation.** **A:** The seven ground truth (GT) bundles (3D masks). The bundle masks, in different colors, were manually constructed. **B:** Centroids of ground truth bundles. Bundle centroids were manually generated and used to automatically identify ground truth bundles in clustered datasets. To classify, a maximum pairwise distance was used between ground truth bundle centroids and the clustered bundle centroids of each dataset. **C:** Ground truth bundles automatically identified in the six clustered datasets. Results for three diffusion local models (DTI, SH q-ball and SDT) and two tractography algorithms (deterministic and probabilistic). Bundles were colored as in A. **D:** Analysis of the six datasets. **D1: Percentage of ground truth bundles volume covered by valid bundles.** In general, probabilistic tractography algorithms presented a better coverage of GT bundles. **D2: Total percentage of valid tracked fibers.** In general, as expected, deterministic tractography algorithms presented a higher percentage of valid fibers.

Resulting fiber bundles of the six phantom fiber datasets were analyzed to evaluate the used diffusion local models and tractography algorithms. For this, we developed a method to automatically identify ground truth bundles in the clustered datasets. The analysis was based on bundle centroid representations, and on a pairwise distance  $d_H$  between centroids (cf. equation 5.6). Ground truth bundle centroids were manually generated and used as an atlas of known bundles (see Figure 5.24 (B)). The pairwise distance was used to compare GT bundle centroids and clustered bundle centroids of each dataset. Clustered bundles presenting a distance inferior to a threshold were selected. Ground truth bundles, automatically identified for the six clustered datasets, are shown in Figure 5.24 (C). Results are presented for the three diffusion local models (DTI, SH q-ball and SDT) and the two tractography algorithms (deterministic and probabilistic). Bundles follow the colors used for ground truth bundle 3D masks. Note that only identified bundles are shown, but a significant part of the tracked bundles did not correspond to GT bundles and were filtered out by the classification process. To analyze the results, we calculated the total percentage of valid tracked fibers, i. e. forming the GT bundles, plotted in Figure 5.24 (D2). We can note that in any case, the total number of valid fibers was inferior to 35%. In general, as expected, deterministic tractography presented a higher percentage of valid fibers.

Besides, we compared the volume of the tracked bundles with the volume of the corresponding ground truth bundles. Ground truth bundle volumes were calculated in voxels, using the 3D masks shown in Figure 5.24 (A). Figure 5.24 (D1) contains a bar plot illustrating the percentage of ground truth bundle volumes covered by the tracked bundles. From the results, we can note that, in general, streamline probabilistic tractography algorithms presented a better coverage of GT bundles. The performance of local diffusion models depended on the complexity of the fiber bundles configuration. For example, from Figure 5.24 (D1), we can see that the green U fiber, which is isolated from the other bundles, was successfully tracked by all the models. In the opposite side, more complex bundles (ochre, yellow), presenting crossing or splitting configurations, were differently tracked by each method. In these cases, DTI model, as expected, presented a lower performance than higher order models (SH q-ball, SDT). From the whole phantom datasets analysis, it is possible to infer that SDT approach presented most of the time the best tracking results.

### 5.5.2 Top-down decomposition of large known WM tracts

Our intra-subject method can deal with the complexity of white matter structures, where several fiber bundles can share the same paths. We do think that the fiber clustering provided by our method is a prerequisite to address one of the emerging applications of tractography: the inference of the subdivisions of the main white matter pathways [Catani et al. (2005)].

The usual approach for the decomposition of large pathways consists in designing sets of ROI selecting the embedded bundles. This top-down strategy can rely on a priori knowledge about the underlying architecture. The hierarchical decomposition provided by our method aims at providing the possibility to develop a complementary bottom-up



strategy. Once all the fibers belonging to a large pathway have been selected, using for instance a probabilistic map in a reference space, our decomposition allows 3D visualization of each of the embedded fascicles with a different color. A dedicated interface allows the selection of specific fascicles according to their trajectory and the localization of their extremities in order to build a model of the pathway reproducible across individuals.

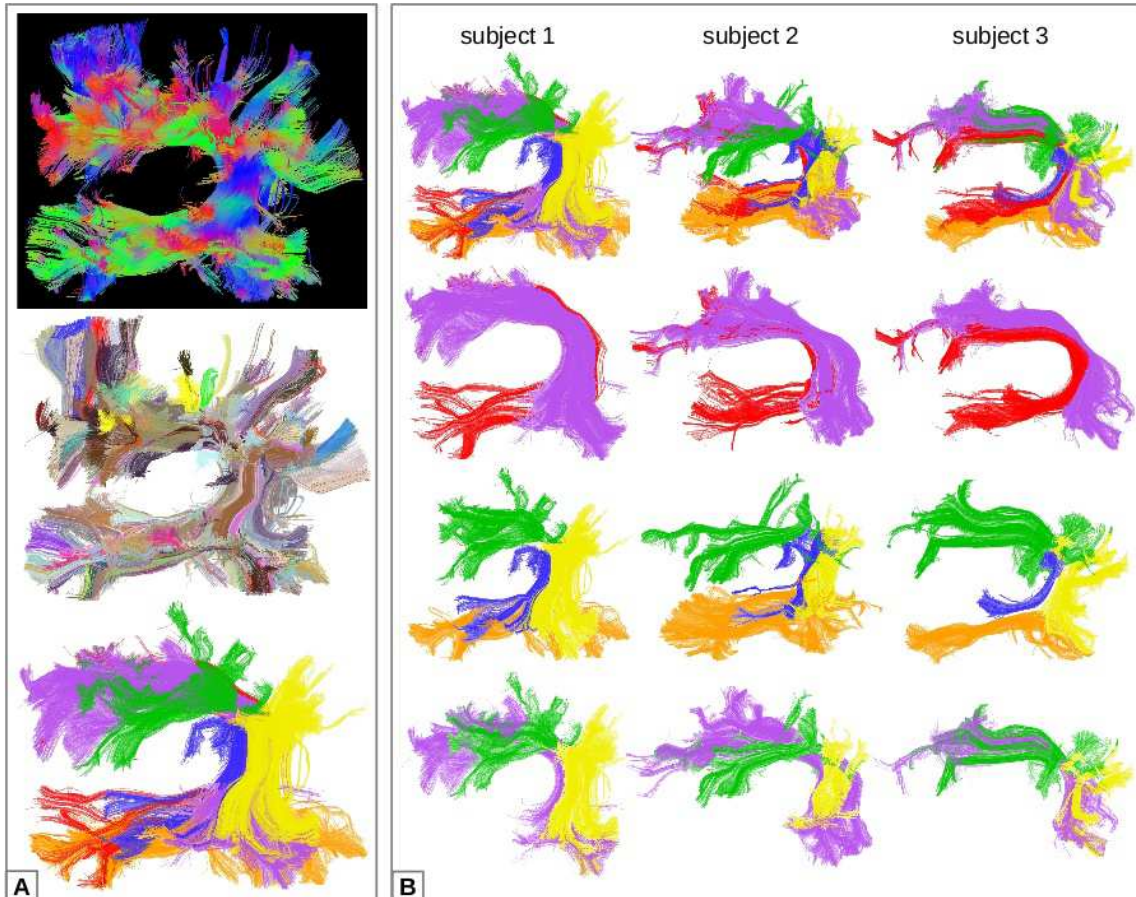


Figure 5.25: **An example of application of the fiber clustering: bottom-up inference of a model of the subdivisions of the arcuate fasciculus.** **A:** Illustration of cluster selection for one subject. **(top:)** About 35,000 fibers forming the arcuate fasciculus were extracted for analysis using a ROI. Without the clustering information, fibers can only be visualized using for instance a color coding for orientation. Hence, the inner structure of the pathway is difficult to catch. **(middle:)** The clustering of this fiber set provided about 100 consistent fascicles. Each fascicle can be coded by a color. Then the user can select specific fascicles using a dedicated interface in order to build a model of the subdivisions of the pathway. **(bottom:)** Here most of the fascicles were merged into six subdivisions that look reproducible across 3 subjects. **B: The subdivision model inferred from the three individuals.** **First row:** The six subdivisions identified in the three different subjects. For visualization purposes, these subdivisions are split into two long (**second row**) and four short (**third row**) fascicle sets. Three of these subdivisions seem to match the three bundles described by Catani et al. (2005) (**last row**).

We have performed such an inference from three individuals for the arcuate fasciculus. We could reproduce the decomposition of Catani into three subdivisions (see Figure 5.25). We have also pushed the model inference further in order to illustrate the potential of the method. We could highlight six reproducible subdivisions of the pathway. This result

however should be confirmed with a larger dataset. In the future, automatic inference of this kind of model could be performed by a clustering applied to the centroids of the bundles at the population level. Note that comparing the models inferred from two different populations could be performed at several levels. One may discover the absence of a specific subdivision in one of the populations, or morphometric differences of one subdivision matched across the two populations relative to diameter, length or diffusion-based parameters like FA.

## 5.6 Discussion

---

As for any fiber clustering method, our results depend strongly on the quality of the tractography results. First, of course, our method can not detect bundles that are not tracked. Fibers are filtered out when they do not belong to a bundle with high fiber density. This is an efficient way to clean up a fiber dataset. Some fibers belonging to actual bundles may be discarded but such fibers can not be distinguished from noise without accurate a priori knowledge about the actual white matter structure. Some of the bundles surviving the filtering process may also be spurious. Considering that the current a priori knowledge about white matter structure is very sparse, we do think that the main road to address this problem is statistical analysis across a large group of subjects [Guevara et al. (2010)]. However, this is a complex issue because similar configurations of bundle crossing across subjects could lead to similar spurious bundles. Besides, spurious final bundles can be found due to errors in the propagation mask. Since this mask defines where fibers are tracked, bundles can be erroneously cut or fused. Nevertheless, independently of the tracking results, our method is a powerful tool to extract the main bundles that constitute the dataset.

Our method is able to cluster huge fiber datasets that are summarized into a reasonable number of fiber bundles. Hence, our approach will scale up easily to the 1 mm spatial resolution that can now be achieved with highly parallel imaging or very high fields. This spatial resolution is bound to highlight a myriad of U-fiber bundles and to better delineate bundle crossing and inner structure of large pathways.

The method is made up of several processing steps, conceived and chained in a way that give robustness to the whole analysis. A consequence of this is a good behavior using the default settings for the four different fiber datasets: adult brain with SDT diffusion model and deterministic tractography, child brain with DTI and deterministic tractography, simulated fiber bundles with added noise, and finally, the phantom datasets, composed by three diffusion local models (DTI, SH q-ball and SDT) and two tractography algorithms (streamline deterministic and probabilistic).

The multiplication of the number of processing steps leads to a multiplication of the number of parameters that had to be tuned to reach robustness. While this may appear at first glance as a difficult problem, most of these parameters were set without real tuning. Indeed, the hierarchical decomposition has mainly been designed to achieve robustness to parameter tuning. The experiments described above relative to dependence on white

matter parcel size illustrate this point. Tuning this parameter within reasonable ranges changes the hierarchical levels at which bundle separations occur, but the final result is stable. We do think that the parameters driving the length-based decomposition, the parcel generation or the heuristics driving the hierarchical clustering of white matter parcels have the same behavior. Changing these parameters will change the path of hierarchical decompositions without large qualitative consequences on the end result.

In our opinion, the parameter driving the centroid merge is the only parameter with qualitative influence on the final results. It has to be set by the user according to the needs. This key parameter is the threshold on centroid distance used to merge the fine-scale fascicles. In the examples shown above, this threshold was set in order to overcome spurious splits induced by the length-based segmentation (*Step 2*), but this threshold can be increased whenever the user is interested in bundles with larger diameters.

It should be noted that our method has been designed to be biased towards agglomerating fascicles into tubes. This is directly resulting from the chosen clustering algorithm. Indeed, we do think that the frequent sheet-like geometry of fiber pathways [Jones et al. (2006); Smith et al. (2006)] corresponds to the organization of the deep white matter, while each sheet splits into tubular pieces when reaching the cortical targets. For instance, at the level of corpus callosum, white matter has a sheet like organization, but following fibers until the cortical gyri allows the split of this sheet into tubular pieces. When the sheet is corresponding to a gyrus geometry we hope that variations of the fiber density along the gyrus allows the clustering to split the sheet into meaningful tubular pieces. For instance, we hope that the motor gyrus corticospinal tracts can be split into tubular bundles following some kind of homunculus-based organization. This hypothesis will have to be tested relative to functional data.

## 5.7 Conclusion

---

In this chapter we proposed a novel robust clustering of WM fibers calculated from tractography. The analysis is mainly based on geometrical fiber properties and no strong anatomical a priori are used. The output consists in some thousands of homogeneous fiber bundles. The compressed representation obtained can be used as input to more sophisticated analysis algorithms that can not deal with millions of fibers. We do think that our approach is a necessary and crucial processing step for the analysis of huge fiber datasets. Additional anatomical information can be used to extract and analyze particular white matter tracts. An example was detailed with the phantom analysis. It was shown that our clustering method, applied to a hardware phantom gives a robust and powerful way to evaluate HARDI local models and tractography algorithms. But the most important application is the inference of a brain fiber bundle model from an inter-subject analysis.

In the next chapter, we present a clustering algorithm that can be applied to the bundles obtained from the intra-subject clustering analysis of a population of subjects in order to infer a fiber bundle atlas of the human brain.





# Inter-subject clustering: Inference of a multi-subject bundle atlas

## Contents

---

<b>6.1</b>	<b>Two-level fiber clustering strategy . . . . .</b>	<b>163</b>
6.1.1	First level: intra-subject clustering . . . . .	164
6.1.2	Second level: inter-subject clustering . . . . .	165
<b>6.2</b>	<b>Inter-subject clustering validation . . . . .</b>	<b>169</b>
<b>6.3</b>	<b>An example of application for the analysis of U-fibers . . . . .</b>	<b>173</b>
<b>6.4</b>	<b>HARDI multi-subject atlas of DWM known bundles . . . . .</b>	<b>174</b>
<b>6.5</b>	<b>HARDI multi-subject atlas of SWM short association bundles</b>	<b>178</b>
<b>6.6</b>	<b>Conclusion . . . . .</b>	<b>182</b>

---

## Overview

---

The continuous improvement of DW-MRI acquisition schemes, diffusion models and tractography algorithms leads to increasingly complex and large tractography datasets. Current tractography datasets reconstruct known WM tracts represented by thousands of fibers, composed by various fiber fascicles of different shapes and lengths. Also, a big amount of short association bundles can be reconstructed in each subject.

Current bundle models contain only well-known fiber bundles of deep white matter (DWM). In these models, known DWM tracts are represented by fibers with the same shape, and do not represent the variability of shape and position of fiber bundles across subjects. Furthermore, until now, short fibers of superficial white matter (SWM) have been rarely studied.

The usual strategies proposed for the reconstruction of fiber bundles follow two complementary ideas. The first approach is based on regions of interest (ROI) used to select or exclude tracts. The second strategy is based on tract clustering using pairwise similarity measures. This last approach requires less interaction than manual approaches and integrates fiber shape and position information in the analysis, which is not the case of most ROI-based segmentation approaches. Furthermore, the clustering of a set of tracts stemming from several subjects, after spatial normalization, can help to discover new reproducible bundles. However, the clustering-based methods commonly present a limitation on the number of fibers that can be analyzed.

Hence, this chapter presents a method taking as input the sets of massive tractography datasets of a population of subjects and producing as output a model composed by a list of generic fiber bundles that can be detected in most of the population. The method consists in a two-level strategy chaining intra- and inter-subject fiber clustering. To deal with very huge tractography datasets and reduce the complexity of the data, the method uses the intra-subject clustering presented in the previous chapter. A novel HARDI multi-subject bundle atlas consisting in 36 DWM bundles and 94 short association bundles, 47 per hemisphere, is thus inferred.

**Keywords:** WM clustering, WM atlas, fiber clustering, fiber similarity measure, fiber bundle model, U-fibers, short association bundles

### Organization of this chapter:

The chapter is organized as follows. We first describe the two-level clustering strategy in Section 6.1. Then, we present a validation of the method using simulated data in Section 6.2. The resulting atlas for long known bundles is presented in section 6.4. Finally, the inferred atlas for short association bundles is presented in section 6.5.

## 6.1 Two-level fiber clustering strategy

The continuous improvement of DW-MRI acquisition schemes, diffusion models and tractography algorithms leads to increasingly complex and large tractography datasets. Unlike a simplistic bundle model, where known white matter (WM) tracts are represented by a relatively small number of fibers with the same shape, current tractography datasets reconstruct WM tracts represented by thousands of fibers, composed by various fiber fascicles of different shapes and lengths. Literature presents several examples of decomposition of major WM tracts [Lawes et al. (2008)]. For instance, the arcuate fasciculus is decomposed in a direct and an indirect WM pathway. The direct connection runs medially between Broca's and Wernicke's area. The indirect pathway runs laterally and is composed by an anterior segment connecting the inferior parietal cortex (Geschwind's area) and Broca's area and a posterior segment connecting Geschwind's and Wernicke's area [Catani et al. (2005)]. Also, a big amount of short association bundles, that until now have been rarely studied, can be tracked in each subject. The segmentation of WM fiber bundles is therefore a complex and not completely solved problem.

The segmentation of anatomical bundles requires the inclusion of anatomical information in some way, in a more or less interactive manner, depending on the used approach. The usual strategies proposed for the reconstruction of fiber bundles follow two complementary ideas. The first approach is based on regions of interest (ROI) used to select or exclude tracts. For the segmentation of new tractography data, the ROIs can be defined manually [Catani et al. (2002); Mori et al. (2005); Wakana et al. (2007); Catani and Thiebaut de Schotten (2008)], or using an ROI atlas after the application of affine [Oishi et al. (2008)] or non-linear [Zhang et al. (2010)] normalization. These automatic ROI-based approaches have shown to be very powerful but present a big dependence on the normalization quality. Furthermore, these methods do not use fiber shape and position information to detect the bundles. The second strategy is based on tract clustering using pairwise similarity measures [Zhang et al. (2008a); O'Donnell et al. (2006); Visser et al. (2011)]. This last approach is potentially less intensive in terms of user interaction and can also embed predefined knowledge represented by a bundle template [Maddah et al. (2005); O'Donnell and Westin (2007)]. For example, O'Donnell and Westin (2007) created a "high-dimensional" WM atlas containing a representation of the known anatomical deep WM 3D tracts from ten different subjects, in an embedded space (see section 4.4). The atlas was then used to automatically segment the most known 3D fiber bundles from five other subjects. The anatomical information embedded in manually labelled clusters can also be used as prior data for the clustering/classification of new tractography datasets [Wang et al. (2011)]. Other recent hybrid approaches extract the most known WM tracts by the combination of a priori information given by a GM/WM atlas and a fiber clustering based on a similarity measure [Wassermann et al. (2010a); Li et al. (2010)].

The fiber clustering approach has been successfully used to map the well-known fiber bundles of deep white matter (DWM). However, the clustering-based methods commonly present a limitation on the number of fibers that can be analyzed. The studies across a

population of subjects are then limited in the number of tracts and the number of subjects that can be analyzed together. In spite of two recent works that describe the analysis of huge datasets (120,000 [Wang et al. (2011)] and 480,000 fibers [Visser et al. (2011)]), the segmentation of huge tractography datasets, presenting more than one million tracts, is still a challenge.

Furthermore, it would be very interesting to apply a clustering using tract pairwise similarity measures to complex massive tractography datasets stemming from several subjects. This strategy could help to discover new reproducible bundles, in particular short association bundles. The limitation on the tractography dataset size can be one of the reasons why until now short fibers of superficial white matter (SWM) have been rarely considered. Other issues than can also make more difficult this kind of study are the big inter-subject variability of these tracts as well as their important number.

Our goal is to infer a model of the brain white matter organisation from HARDI tractography results computed for a group of subjects. For that, we use a fiber clustering approach able to overcome the limitation on the tractography size and additionally allows considering the shape of the fibers in the analysis. We propose a two-level strategy chaining intra and inter-subject fiber clustering. The first level, the multiresolution intra-subject clustering presented in the previous chapter, can be viewed as a compression procedure reducing a huge set of fibers to a few thousand bundles. The second level is an inter-subject clustering of the resulting fiber bundles. This group analysis relies on a pairwise distance between bundles computed after affine spatial normalization. A simulation is performed in next section to prove that affine normalization is sufficient to detect consistent clusters in the bundle space.

### 6.1.1 First level: intra-subject clustering

This step is developed following a multiresolution paradigm including five steps, described in the previous chapter (chapter 5). See section 5.2 for an overview of the whole method, which is illustrated in Figure 5.1.

A key point in this clustering is the use of a voxel-based parcellation of the white matter, allowing the analysis of any number of fibers. This parcellation produces small fiber clusters that can be split further using additional clustering performed in the space of fiber extremities. The resulting output is a set of a few thousand of thin and regular bundles, composed by fibers presenting similar length and shape. In addition, during the analysis most of noise fibers are discarded, leading to a cleaner fiber dataset. Due to its regular shape, each resulting fiber bundle can be represented by a single fiber, called a bundle centroid. This compressed representation of a tractography dataset allows the application of further processing steps that could not be applied to the whole fiber dataset.

In order to get a good representation of the thalamic radiations in the model, a processing is added to the *Step 1*, a hierarchical decomposition of the tractography dataset that originally uses a mask of both brain hemispheres and the cerebellum. The analysis

uses a mask of the thalami, described in [Marrakchi-Kacem et al. (2010c)], for cutting and extracting the fibers passing through these structures. The fibers passing through each thalamus form two additional fiber subsets: *left-thalamus* and *right-thalamus*, that are processed separately from the *Step 2*, as the other subsets. Figure 6.1 shows a scheme of the *Step 1* of the intra-subject clustering including these new subsets. Figure 6.2 (A) shows all the resulting bundles for a subject, composed by the six fiber subsets: *right hemisphere*, *left hemisphere*, *interhemispheric*, *cerebellum*, *right thalamic* and *left thalamic* fibers.

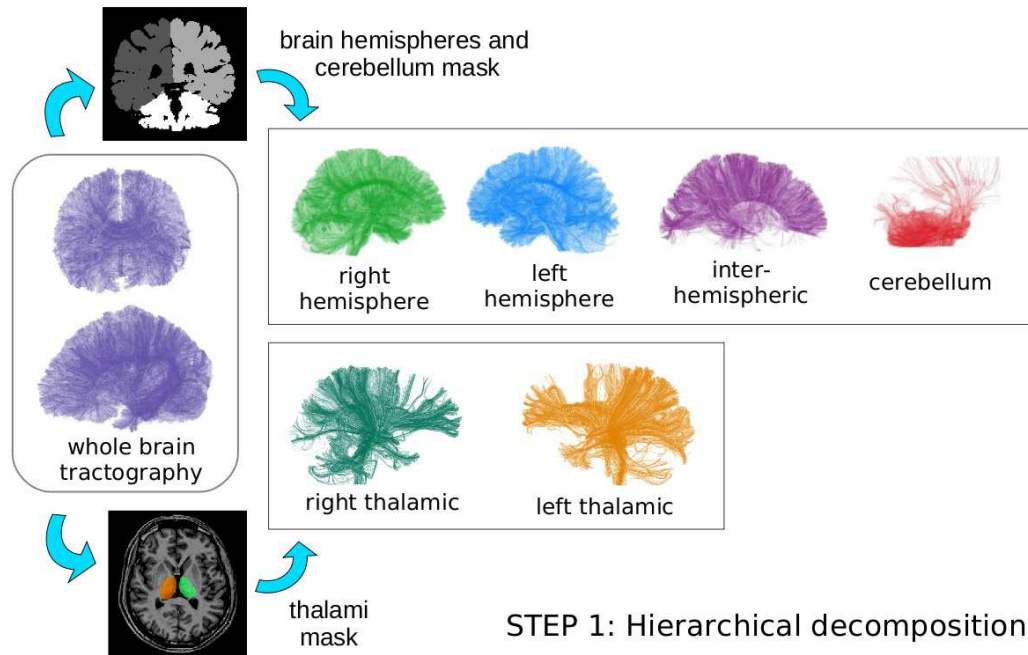


Figure 6.1: **Addition of thalamic fiber subsets in hierarchical decomposition (Step 1) of intra-subject clustering.** A thalami mask, described in [Marrakchi-Kacem et al. (2010c)] is used to cut and extract the fibers passing through these structures.

### 6.1.2 Second level: inter-subject clustering

The second clustering level aims at matching the putative bundles produced by the previous level across a population of subjects. This step is very similar to the clustering performed in section 5.2.5 (*Step 5*), where the subject fascicle centroids are clustered using a pairwise distance. But here the calculation considers the bundles obtained from all the subjects for a fiber subset. Figure 6.3 illustrates the main steps of the clustering.

A centroid is first calculated for each bundle using the mean of the two mean closest point distances [Corouge et al. (2004); O'Donnell et al. (2006); O'Donnell and Westin (2007)] (see equation 5.5). A bundle centroid, representing the main geometry of the bundle, is localized in the center of the bundle and is determined as the tract minimizing the distance to the rest of the fascicle fibers. In order to make this processing more efficient, a random sample of one hundred fibers is used to perform the calculation of each



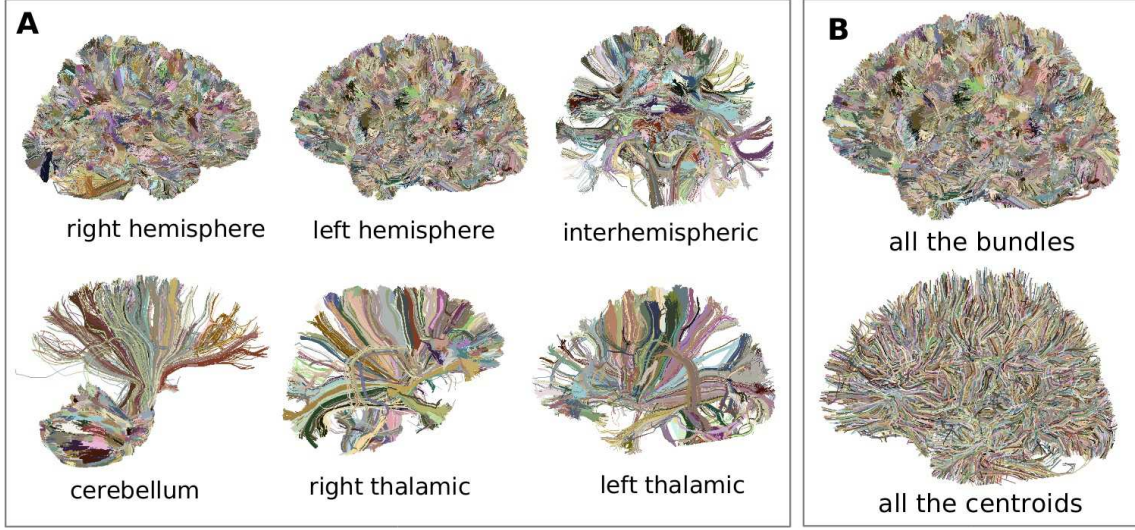


Figure 6.2: **Example of the intra-subject clustering results for one subject.** **A:** All the subject resulting bundles. Bundles are separated into six subsets: *right hemisphere*, *left hemisphere*, *interhemispheric*, *cerebellum*, *right thalamic* and *left thalamic* fibers. **B:** All the bundles and the corresponding centroids obtained for the left hemisphere subset.

bundle centroid. This simplification is possible as fibers belonging to a bundle present very similar shapes, lengths and positions. Figure 6.2 (B) shows the resulting centroids for all the bundles obtained for the left hemisphere of a subject.

Once all the centroids from all the subjects for the analyzed subset are computed, they are transformed to the Talairach space (TS) using an affine transformation estimated from the T1-weighted image. Then, a bundle centroid affinity graph is computed using a pairwise distance between fibers.

**Centroids pairwise distance.** The distance measure used is the maximum of the Euclidean distances between corresponding points, normalized by the minimum centroid length, called ( $d_{ME}$ ).

The maximum of the Euclidean distances between corresponding points ( $d_{ME}$ ) is defined, for two fibers A and B as

$$d_{ME}(A, B) = \min \left( \max_i \| \mathbf{a}_i - \mathbf{b}_i \|, \max_i \| \mathbf{a}_i - \mathbf{b}_{N_p-i} \| \right), \quad (6.1)$$

where  $\mathbf{a}_i$  and  $\mathbf{b}_i$  are the position of the points of fibers A and B respectively, for  $i = 0..N_p - 1$ . This stringent measure puts a focus on matching bundles with similar shapes and positions in Talairach space. It is more restrictive than distances based on the closest points [Corouge et al. (2004); O'Donnell et al. (2006)]. For the calculation, the centroids are resampled using 21 equally distributed points.

To take into account the length of the centroids, we normalize this distance by the

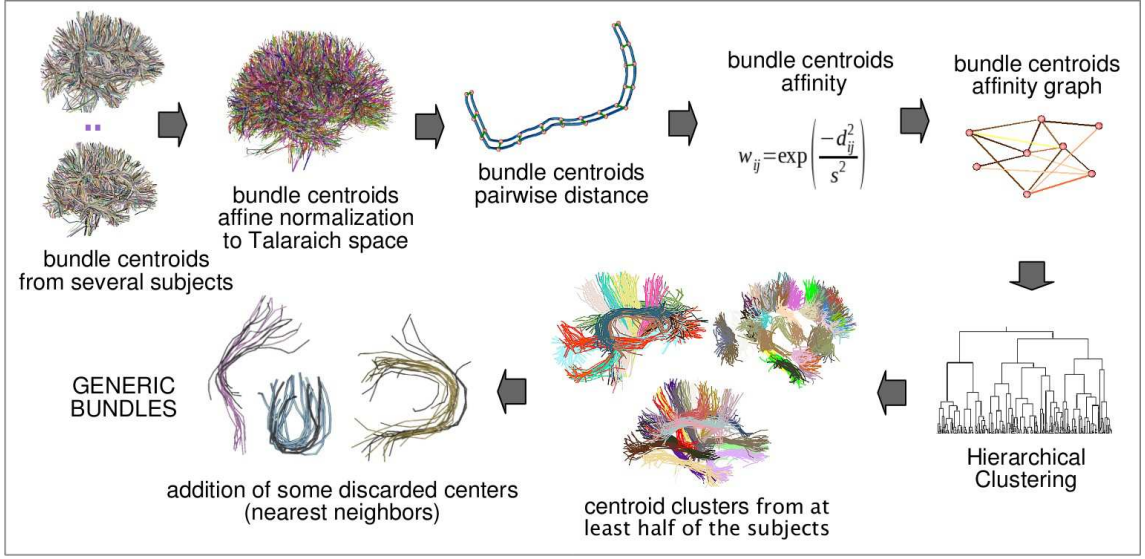


Figure 6.3: **A general scheme of the inter-subject fiber clustering.** This analysis considers all the bundles obtained for a subset with the intra-subject clustering from a population of subjects. First, a bundle centroid is calculated for each subset bundle. Then, all the bundle centroids from all the subjects are transformed to the Talairach space. A restrictive distance is calculated between all the pairs of centroids and converted to an affinity value. A bundle centroids affinity graph is then calculated, using a maximum distance threshold. The centroids are clustered using a Hierarchical Clustering and tight clusters containing centroids from at least half of the subjects are selected as generic bundles. An optional final step adds discarded close centroids to the tight clusters.

minimum centroid length ( $l$ ):

$$d_{ME_n}(A, B) = \begin{cases} d_{ME}(A, B) - \frac{nf \cdot (l - \min L)}{(\max L - \min L)}, & \text{if } l < \frac{d_{ME}(A, B) \cdot (\max L - \min L)}{nf} + \min L; \\ 0, & \text{otherwise.} \end{cases} \quad (6.2)$$

where  $l$  is the minimum centroid length,  $\max L$  and  $\min L$  are the maximum and minimum fiber lengths in the tractography dataset and  $nf$  is the normalization factor.

Then, the distance  $d_{ME_n}(A, B)$  will be equal to the non-normalized distance  $d_{ME}(A, B)$  for a pair of centroids  $A$  and  $B$ , with a minimum centroid length equal to  $\min L$ . As the minimum centroid length increases, the distance  $d_{ME_n}(A, B)$  decreases linearly until reaching a distance equal to  $d_{ME}(A, B) - nf$ , for a minimum centroid length equal to  $\max L$ . Typically, we used  $\min L = 20$  mm,  $\max L = 250$  mm and  $nf = 10.0$ . Figure 6.4 (A) presents a plot of  $d_{ME_n}(A, B)$  in function of the minimum centroid length ( $l$ ) for three different values of  $d_{ME}$  (5, 10 and 15 mm). This normalization makes more restrictive the distance for short centroids, which will lead to very tight clusters for short association fibers, avoiding the inclusion of outliers.

**Centroids affinity graph.** For the construction of the affinity graph, a maximum distance threshold ( $M_{dn}$ ) is used to define the maximum normalized distance  $d_{ME_n}$  between centroids. Then, for a fixed threshold  $M_{dn}$ , the non-normalized Euclidean distance between

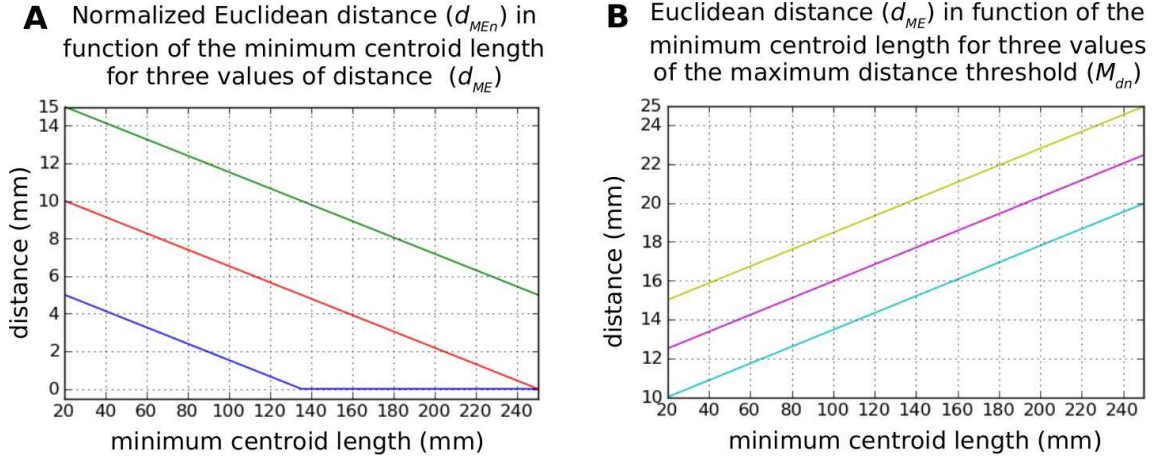


Figure 6.4: **Normalized Euclidean distance used for inter-subject centroids clustering.** The distance used is the maximum of the Euclidean distances between corresponding points ( $d_{ME}$ ), normalized by the minimum centroid length ( $l$ ), called  $d_{ME_n}$ . The maximum and minimum fiber lengths in the tractography dataset are  $minL = 20$  mm and  $maxL = 250$  mm, and the normalization factor is  $nf = 10.0$ . **A:** A plot of  $d_{ME_n}$  (see equation 6.2) in function of the minimum centroid length ( $l$ ) for three different values of  $d_{ME}$ : 5 mm (blue), 10 mm (red) and 15 mm (green). The normalized distance decreases linearly with the minimum centroid length ( $l$ ). **B:** A plot representing the non-normalized distance  $d_{ME}$  in function of the minimum centroid length ( $l$ ), for three different values of maximum normalized distance threshold  $M_{dn}$ . Three different values of maximum normalized distance threshold  $M_{dn}$  are illustrated: 10 mm (cyan), 12.5 mm (magenta) and 15 mm (ocre). The normalized distance is then less restrictive for long centroids, which present in general bigger shape variations than short association fibers.

corresponding points ( $d_{ME}$ ) will be close to  $M_{dn}$  for a pair of short centroids and will be higher for a pair of long centroids. Figure 6.4 (B) presents a plot of the maximum distance threshold  $M_{dn}$  in function of the minimum centroid length ( $l$ ) for three different values of  $d_{ME}$  (10, 12.5 and 15 mm). For the construction of the affinity graph, the distances are converted to affinities using the equation 4.2.

**Centroids clustering.** The affinity graph is used to compute an average-link hierarchical clustering. The resulting tree is analyzed in order to extract only very tight clusters, where the distance between all the fibers within a cluster is inferior to the maximum distance threshold ( $M_{dn}$ ). The resulting clusters, called *generic bundles*, are discarded if they do not contain at least half of the subjects.

**Addition of discarded close centroids to the tight clusters.** An optional final procedure aims at relaxing the constraints in order to recover some instances of the generic bundles that were missed during the stringent clustering analysis. The goal is to be less demanding on the match between centroids, which is specially important for the subjects that present a deficient normalization in Talairach space. For each non attributed centroid, we compute the distance to each of the centroids of the tight clusters. When the distance to the nearest neighbor is below a threshold  $M_{dNN}$ , the non attributed centroid is added to the final generic bundle representation. The distance measure used is the normalized

Euclidean distance  $d_{ME_n}$  (see equation 6.2). We use the same distance as for the centroids clustering as it takes into account the centroids length. At the same time, the already calculated affinity graph is employed, avoiding the recalculation of the distances. The threshold is calculated as  $M_{dNN} = M_{dn} * 0.75$ . Most of the added centroids belong to long fiber bundles.

Figures 6.5 and 6.6 show an example of the clusters obtained for a maximal intra-subject distance between fibers *max\_cdist* equal to 10 mm and a maximum inter-subject centroid distance  $M_{dn}$  equal to 15 mm. For a better visualization of the results, a sample of some clusters are shown in Figure 6.7.

## 6.2 Inter-subject clustering validation

In order to study the behavior of the inter-subject clustering over a population of subjects aligned with affine registration, we created a simulated dataset of fiber bundle centroids. First, one subject of the adult NMR HARDI database (cf. section 5.4.2) was selected to generate a set of 200 simulated bundle centroids. The bundle centroids were fibers selected from the right hemisphere of the subject with a minimum pairwise distance across the set. The distance used was the maximum Euclidean distance between corresponding points  $d_{ME}$  (cf. equation 6.1). The minimum distance was set to 12 mm (see Figure 6.8 A). The obtained bundle centroids set was transformed to the space of each one of the eleven remaining subjects of the database, using a non-rigid transform, calculated between T1-weighted images. To normalize the images we applied non-rigid Diffeomorphic Demons [Vercauteren et al. (2009)] after an affine normalization using MedINRIA software <sup>1</sup>.

Hence, we obtained a set of 200 ground truth clusters, each one containing a centroid in each subject (see Figures 6.8 B and D). In addition, 500 fibers from each subject were selected to simulate noise. These fibers were pairwise separated by a minimum distance equal to 11 mm (see. Figure 6.8 C). For each subject, we got a fiber dataset of 700 fibers, 200 centroids and 500 added noise fibers, leading to a total number of 8,400 fibers for the twelve subjects.

We applied the inter-subject clustering to the fibers dataset, with the maximum distance within clusters ( $M_{dn}$ ) varying from 5 to 25 mm, with a length normalization factor ( $nf$ ) equal to 0. Resulting clusters were analyzed and compared with the ground truth. First, only clusters containing centroids from a minimum of seven different subjects were selected. Then, a cluster was counted as *recovered* only if all its centroids belonged to the same simulated cluster, otherwise, it was counted as a *missed* cluster. Fig. 6.8 E presents the simulation results as a function of the distance  $M_{dn}$ . From the analysis, we note, as expected, that the number of recovered clusters (color bars) increases with  $M_{dn}$ , as well as the number of subjects in the clusters (from 7 to 12, indicated by different colors in the color bars). For distances  $M_{dn}$  superior to 11 mm, a large number of clusters was recovered, but for distances between 11 and 15 mm, most of the clusters miss some centroids.

<sup>1</sup><http://www-sop.inria.fr/asclepios/software/MedINRIA>



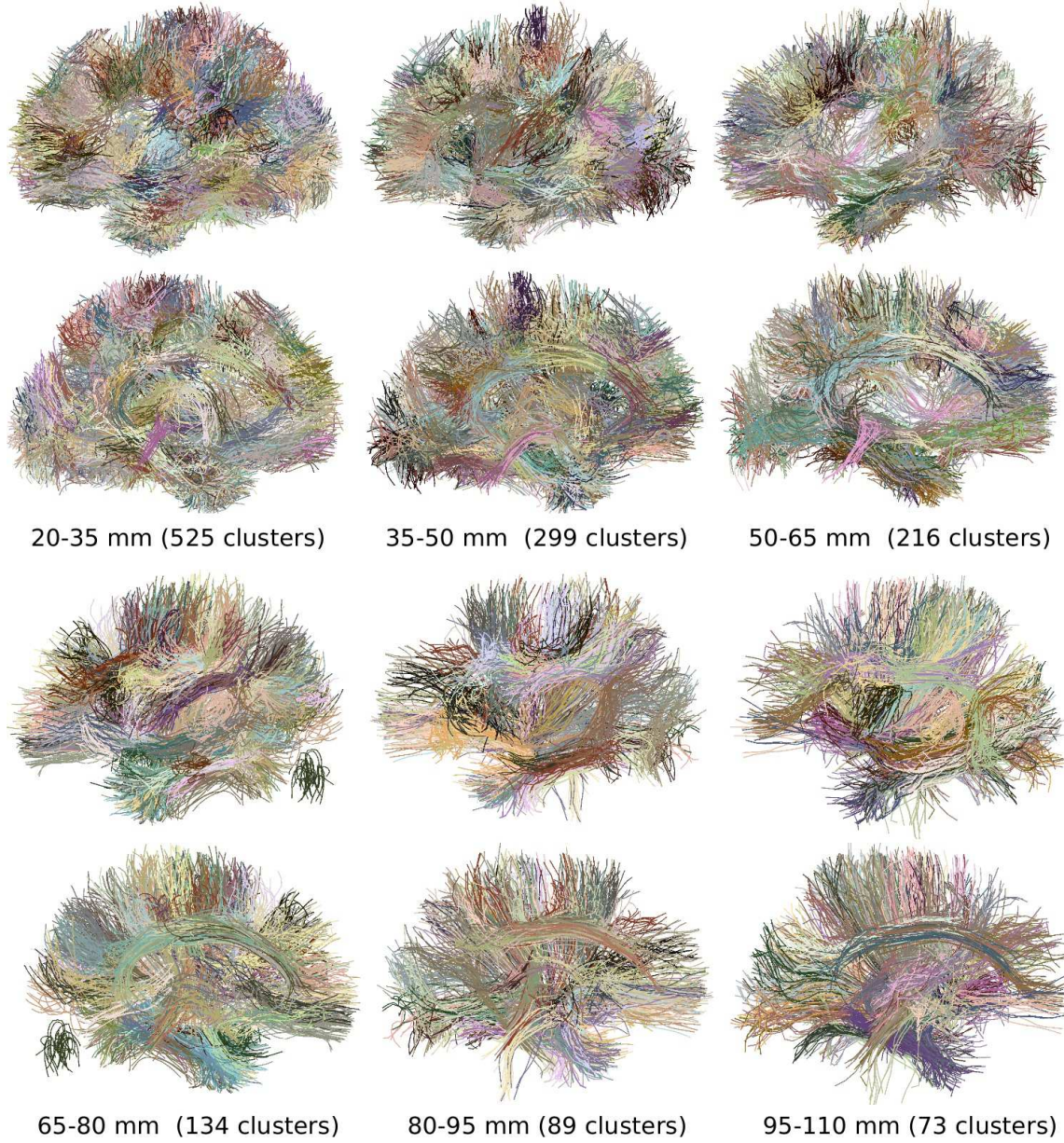


Figure 6.5: **Example of inter-subject clusters (short centroid clusters of left hemisphere).** Example of the short clusters obtained for a maximal intra-subject distance between fibers  $max\_cdist$  equal to 10 mm and a maximum inter-subject centroid distance  $M_{dn}$  equal to 15 mm. Clusters are composed by the intra-subject centroids obtained in the first level clustering. They are composed by centroids from a minimum of 6 different subjects. Clusters are separated into groups of different centroid length. This figure shows clusters between 20 and 110 mm. See long clusters in Figure 6.6. Colors may be repeated in different clusters.

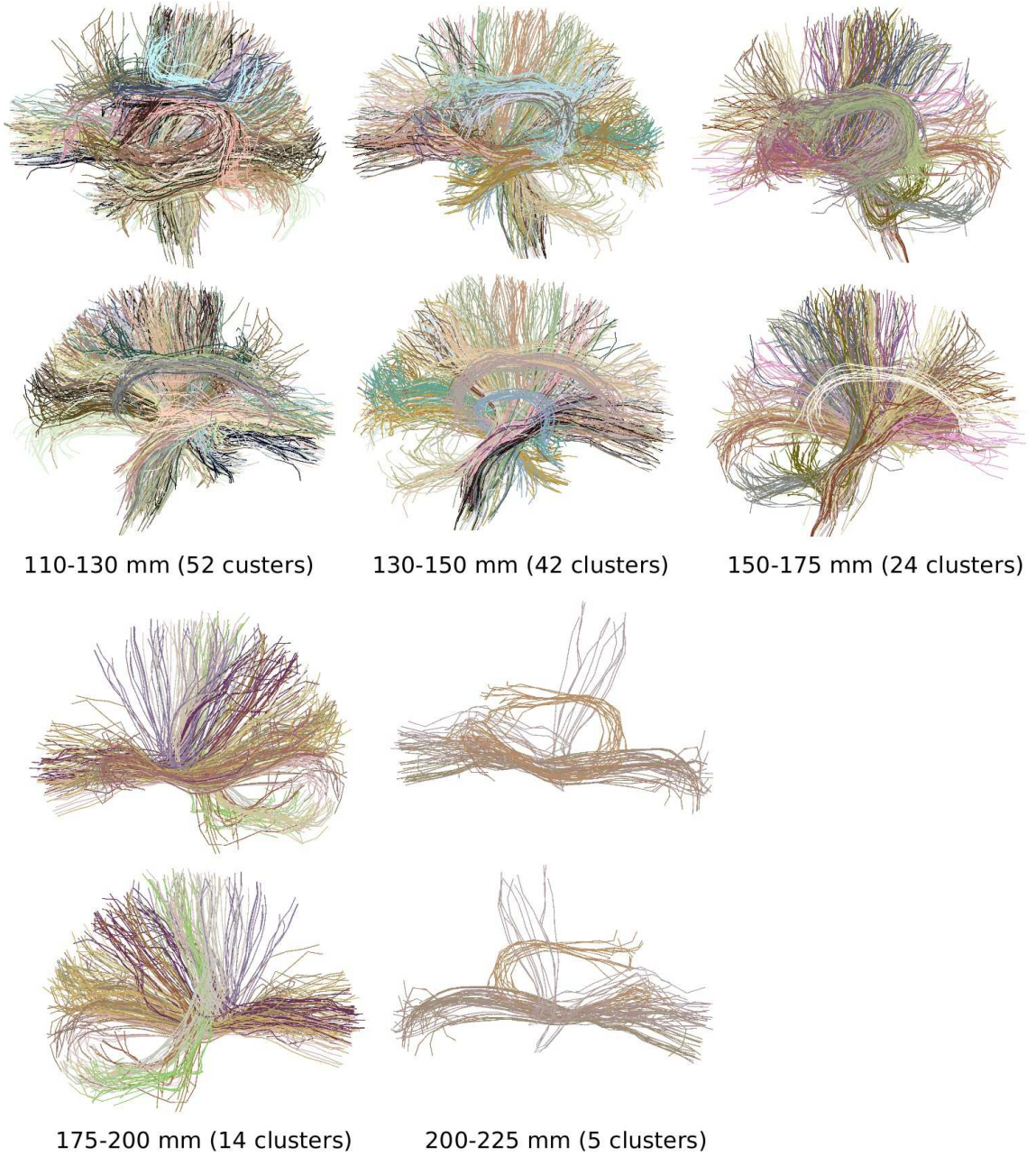


Figure 6.6: **Example of inter-subject clusters (long centroid clusters of left hemisphere).** Example of the long clusters obtained for a maximal intra-subject distance between fibers  $max\_cdist$  equal to 10 mm and a maximum inter-subject centroid distance  $M_{dn}$  equal to 15 mm. Clusters are composed by the intra-subject centroids obtained in the first level clustering. They are composed by centroids from a minimum of 6 different subjects. Clusters are separated into groups of different centroid length. This figure shows clusters between 110 and 225 mm. No cluster was found between 225 and 250 mm. See short clusters in Figure 6.5. Colors may be repeated in different clusters.





Figure 6.7: **Example of some inter-subject clusters (left hemisphere).** These clusters are a sample of the clusters obtained for a maximal intra-subject distance between fibers  $max\_cdist$  equal to 10 mm and a maximum inter-subject centroid distance  $M_{dn}$  equal to 15 mm, shown in Figures 6.5 and 6.6. Clusters are composed by centroids from a minimum of 6 different subjects.

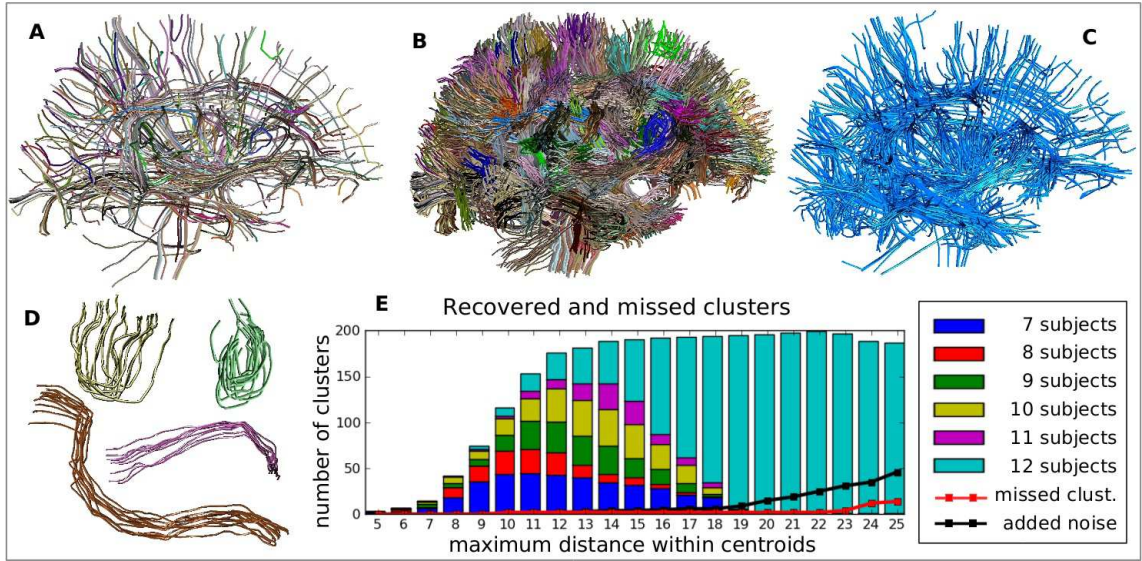


Figure 6.8: **Inter-subject clustering validation using simulated centroids.** **A:** The original 200 fibers selected from the right hemisphere of a subject, used as simulated bundle centroids. **B:** The 200 simulated bundles for the 12 subjects in Talairach space. Each bundle contains one centroid from each subject. **C:** Noise fibers set of one subject. A noise set is determined for each subject, composed by 500 fibers. **D:** A selection of bundles from B. Note that, in spite of the inter-subject variability of the bundles, the fibers of a bundle present a close shape. **E:** Inter-subject clustering simulation results. Recovered clusters are presented using color bars, missed clusters are indicated with a red line and clusters with added noise with a black line.

This behavior is accepted by the method, which adds a cluster to the model as soon as it includes at least half of the subjects. The red line indicates the number of missed clusters, which is very low. These are most of the time fused with other clusters. The black line shows the number of recovered clusters that contain also added noise fibers. Finally, a large number of clusters made up of only noise fibers was found but discarded by the method because none of these clusters had fibers from more than six different subjects.

## 6.3 An example of application for the analysis of U-fibers

Most of the fiber clustering and bundle automatic segmentation methods have targeted the large WM tracts described in anatomy books. In return, the cartography of the U-fiber bundles of superficial white matter (SWM) is a complex and largely unachieved task for the human brain. Oishi et al. performed a study of the structure of SWM using a voxel-based group analysis relying on linear normalization [Oishi et al. (2008)]. They could identify only four U-fiber bundles because of the blurring resulting from the linear normalization process. In a recent work, Zhang et al. (2010) improved the results, finding 29 short association fibers connecting different brain regions. This kind of ROI-based approaches have shown to be very powerful but present a big dependence on the normalization quality. Furthermore, no analysis is performed on the fibers shape.

Hence, tract clustering into putative bundles performed for each subject followed by

bundle clustering performed across subjects, described in section 6.1, is an attractive alternative. Indeed similarities defined in the space of tracts overcome some of the ambiguities occurring at a voxel-based similarity level. A preliminary attempt to infer a U-fiber bundle atlas from such a strategy coupled with linear normalization led to about 30 putative U-fiber bundles matched across a group of 12 subjects [Guevara et al. (2009, 2010)]. For this atlas, a maximal intra-subject distance between fibers  $max\_cdist$  equal to 5 mm, a maximum inter-subject centroid distance  $M_{dn}$  equal to 10 mm and a length normalization factor ( $nf$ ) equal to 10.0 were used. Each U-fiber bundle is a short generic bundle, i. e., an inter-subject cluster composed by the individual centroids from the intra-subject clustering (see Figure 6.9).

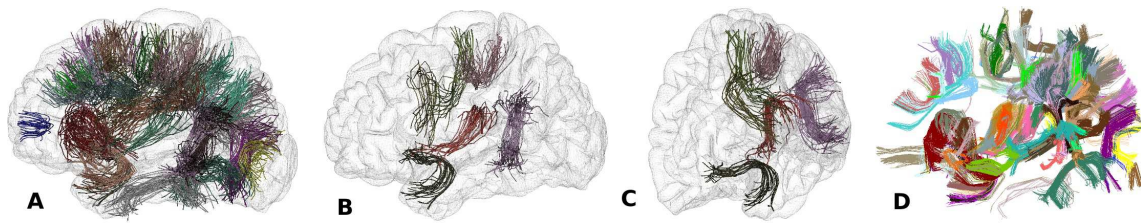


Figure 6.9: **Preliminary U-fiber bundle atlas from inter-subject clustering results.** A preliminary attempt to infer automatically an U-fiber bundle atlas using the inter-subject clustering was presented in Guevara et al. (2009, 2010). This strategy, coupled with linear normalization led to about 30 putative U-fiber bundles matched across a group of 12 subjects. **A:** The U-fiber bundle atlas (left size), containing about 30 short generic bundles. Each bundle is an inter-subject cluster, composed by the individual centroids from the intra-subject clustering. **B-C:** Two views for a selection of the U-fibers from the bundle atlas in A. **D:** The short generic bundles corresponding to a one subject.

A selection of the most reproducible U-fibers of this preliminary atlas are illustrated in Figure 6.10. This illustration shows nine U-bundles present in four subjects. The main sulci of these regions are shown in order to verify the correspondence of the fibers between subjects. Analyzing the links between the folding patterns and U-bundles will help to discard spurious match across fiber bundles and to improve our understanding of the folding variability.

## 6.4 HARDI multi-subject atlas of DWM known bundles

The two-level clustering was performed using the method described above, applied on the twelve subjects of the adult NMR HARDI database (cf. section 5.4.2). First, intra-subject clustering, briefly described in section 6.1, and detailed in previous chapter, was applied to each dataset. This intra-subject clustering reduces the tractography dataset information from more than one million of tracts to a few thousand fiber bundles. The analysis was performed for the following segments: *right hemisphere*, *left hemisphere*, *interhemispheric*, *right thalamic* and *left thalamic* fibers. The *cerebellum* segment could not be analyzed as the dMRI data of this database does not include systematically this structure.

The intra-subject bundle centroids were calculated for each subset for all the subjects, using a maximal intra-subject distance between fibers  $max\_cdist$  equal to 10 mm. Then, the



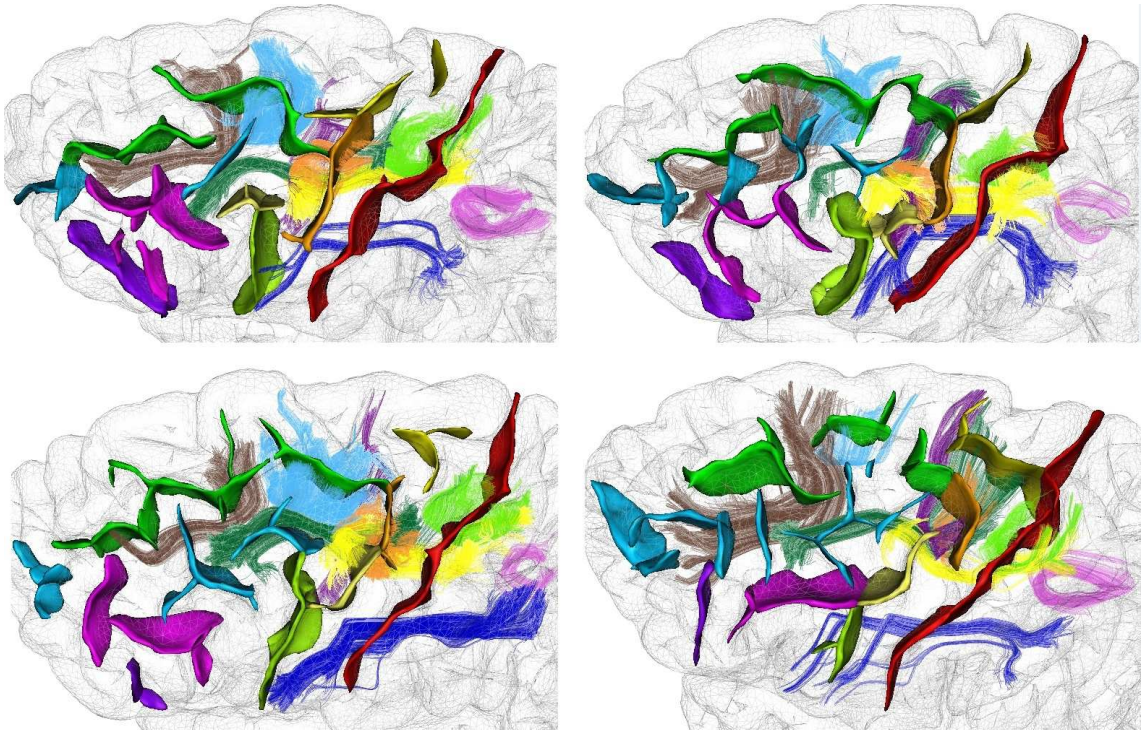


Figure 6.10: **Illustration of the use of inter-subject clustering results for U-fibers analysis.** The figure presents a selection of the most reproducible U-fibers of the preliminary atlas, illustrated in Figure 6.9, located in the fronto-parietal cortex. Nine U-bundles are presented in four subjects. For visual guidance, the main sulci of these regions are shown: central sulcus (red), several subdivisions of the precentral sulcus (orange, yellow), superior frontal sulcus (green), intermediate frontal sulcus (light blue), inferior frontal sulcus (purple).

inter-subject clustering was performed across subjects, separately for each subset, in order to infer a list of generic bundles with consistent shape and localization in the normalized space. The maximum inter-subject centroid distance  $M_{dn}$  was set to 15 mm and the length normalization factor ( $nf$ ) was set to 10.0. In order to get population representative clusters, only clusters composed by centroids from at least half of the subjects were selected. The resulting clusters are those shown in Figures 6.5 and 6.6.

The inter-subject clusters computed from the database of 12 brains were manually labeled in order to identify known WM tracts. Each atlas bundle is then represented by the complete set of individual centroids belonging to the underlying intra-subject clusters. For labelling, our criteria included various anatomical informations related to the bundle path and localization, and especially to the cortical morphology around bundle extremities. We used anatomical definitions of each bundle, as those described in Catani and Thiebaut de Schotten (2008). Sulci segmentations and cortical surface parcellations into gyri were used as visual guidance. A last visual inspection led to discard a few artefactual centroids clearly including spurious parts like loops.

An atlas bundle corresponds then to several inter-subject clusters to account for subdivisions of the underlying pathway often presenting large variability across subjects. Each

atlas bundle is further represented by the list of the centroids of the first level clusters from all the subjects to get a better sampling of the shape and localization variability.

The resulting multi-subject representation provides a good sampling of the inter-subject variability of the bundle trajectory after affine normalization. The atlas inference was done for the bundles of the left hemisphere (LH) and the corpus callosum. The bundles of the right hemisphere were obtained using the symmetric of those of the LH with respect to Talairach inter-hemispheric plane. The goal is to get a symmetric atlas for the validation described in this thesis. Ongoing work aims at performing the same inference for the right hemisphere in order to remove any bias.

The proposed atlas includes a total of 36 bundles, composed by 11 WM tracts in each hemisphere and the corpus callosum. Several tracts are divided into a few fascicles:

- Arcuate fasciculus (left and right)
  - Direct segment
  - Anterior segment
  - Posterior segment
- Inferior longitudinal fasciculus (left and right)
- Inferior fronto-occipital fasciculus (left and right)
- Uncinate fasciculus (left and right)
- Cingulum (left and right)
  - Cingulate long fibers
  - Cingulate short fibers
  - Temporal fibers
- Corticospinal tract (left and right)
- Fornix (left and right)
- Thalamic radiations (left and right)
  - Anterior radiations
  - Superior motor radiations
  - Superior parietal radiations
  - Posterior radiations
- Corpus callosum
  - Rostrum
  - Genu
  - Body
  - Splenium

Figure 6.11 shows the HARDI multi-subject atlas of known bundles, composed by a total of 4189 centroids.



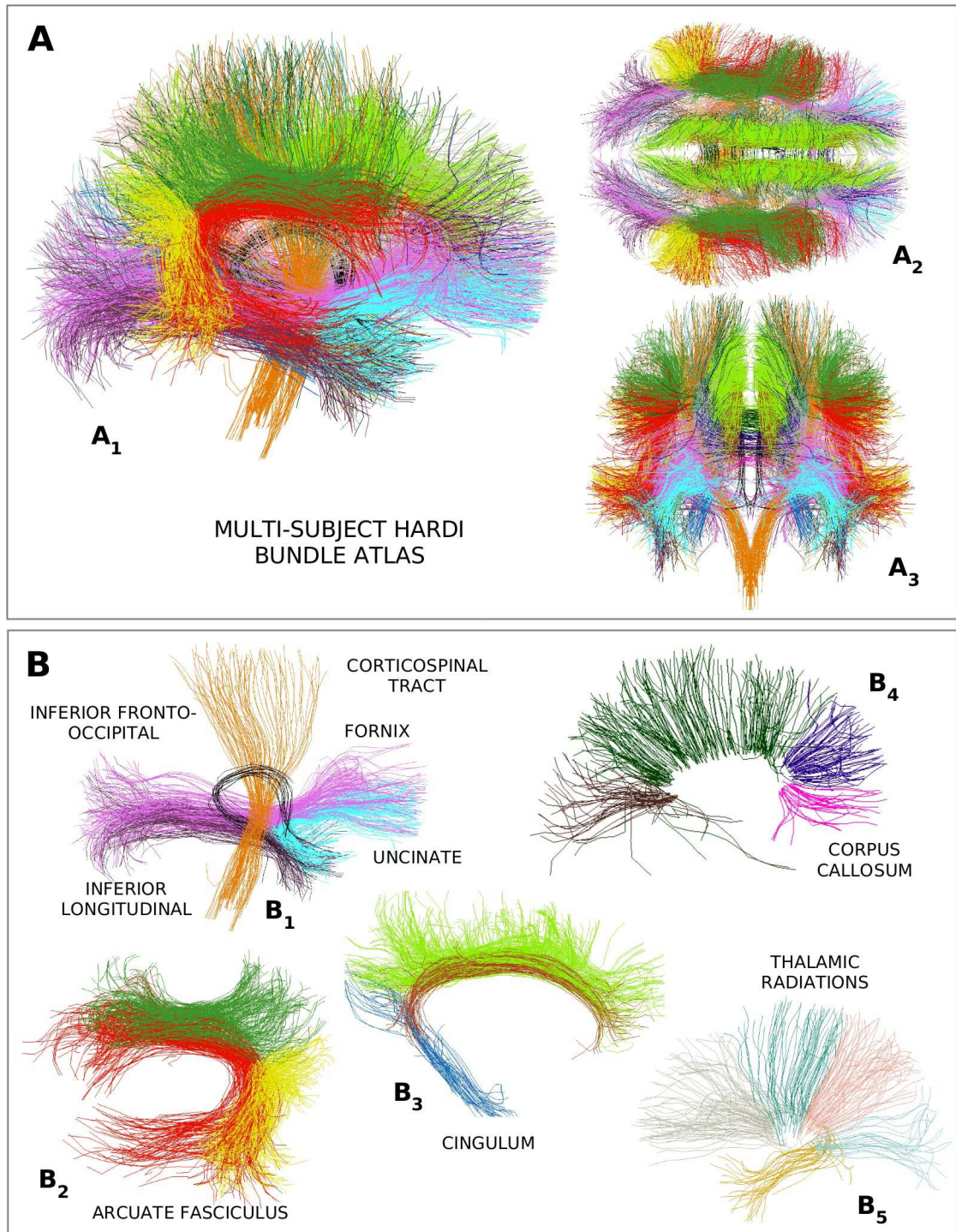


Figure 6.11: **The HARDI multi-subject atlas of known bundles.** **A:** All the bundles (4189 centroids): right ( $A_1$ ), top ( $A_2$ ) and front ( $A_3$ ) views. **B:** A detailed view of the bundles.  $B_1$ : Interior view of left fornix (black), uncinate (cyan), inferior fronto-occipital (violet), inferior longitudinal (purple) and corticospinal (orange) tracts.  $B_2$ : Exterior view of the left arcuate fasciculus segments: direct (red), anterior (green) and posterior (yellow).  $B_3$ : Interior view of the left cingulum fascicles: long cingulate (brown), shorts cingulate (light green) and temporal (blue).  $B_4$ : Exterior view of the corpus callosum tracts: rostrum (fuchsia), genu (dark blue), body (dark green) and splenium (dark brown).  $B_5$ : Exterior view of the left thalamic radiations: anterior (gray), superior motor (teal), superior parietal (pink), posterior (light blue) and inferior (ocre).



## 6.5 HARDI multi-subject atlas of SWM short association bundles

---

Short bundles have been rarely studied, therefore there does not exist detailed anatomical description in the literature. As mentioned above, only ROI-based approaches [Oishi et al. (2008); Zhang et al. (2010)] have been used to study the structure of superficial white matter (SWM). For example, Zhang et al. (2010) used an atlas-based brain GM/WM segmentation, relying on non-linear normalization, to identify short association bundles reproducible across subjects (see Section 4.3). All the pair of adjacent cortical regions were analyzed in order to find those that were connected by fibers in a population of 20 subjects. Twenty-nine short association bundles, connecting two adjacent cortical regions, were found in all the subjects. Even though this kind of approach has shown to be very powerful, it presents a big dependence on the normalization quality. Furthermore, no analysis was performed on the fibers shape. The only condition used was the existence of fibers connecting both cortical regions (and not passing through deeper regions), which may lead to irregular and different bundles across subjects.

In order to study the short association bundles and construct a HARDI multi-subject atlas of these bundles, we applied our two-level fiber clustering strategy (section 6.1). The intra-subject bundle centroids were calculated for the *left hemisphere* and *right hemisphere* subsets for all the subjects, using a maximal intra-subject distance between fibers *max\_cdist* equal to 7 mm. Then, the inter-subject clustering was performed across subjects separately for each subset, in order to infer a list of generic bundles with consistent shape and localization in the normalized space. The maximum inter-subject centroid distance  $M_{dn}$  was set to 12 mm, and the length normalization factor (*nf*) was set to 10.0. In order to get population representative clusters, only clusters composed by centroids from at least half of the subjects (six subjects) were selected. The final addition of closest centroids described was not performed in order to keep very tight clusters.

The inter-subject clusters belonging to SWM were manually labeled using a gyral parcellation of the cortical surfaces [Cachia et al. (2003)], in order to give an anatomical name to each reproducible bundle. Only clusters that presented a regular shape and an unambiguous localization were selected and labeled. Figure 6.12 shows the gyri that were finally used to label the short association bundles.

The atlas inference was done for the bundles of the left hemisphere, with a length between 35 and 110 mm. A name was given for each bundle, following the criterion used by Zhang et al. (2010), who proposed bundle names composed by the two regions (or only one region in some cases) connecting each bundle (see Figure A.5). Most of the labeled bundles are composed by only one generic bundle (or inter-subject cluster), but some bundles are composed by a few clusters.

In some cases, we could differentiate subdivisions of some bundles, connecting two different gyri. In that cases, we added a string to the name in order to specify the bundle position: *sup* (superior), *mid* (middle), *inf* (inferior) for superior-inferior axis differentiation, and *fr* (frontal), *mid* (middle), *bck* (back) for anterior-posterior axis differentiation.

Region	Abbreviation
Superior frontal gyrus	SFG
Middle frontal gyrus	MFG
Inferior frontal gyrus	IFG
Medial fronto-orbital gyrus	MFOG
Lateral fronto-orbital gyrus	LFOG
Precentral gyrus	PrCG
Postcentral gyrus	PoCG
Supramarginal gyrus	SMG
Angular gyrus	AG
Superior parietal gyrus	SPG
Middle occipital gyrus	MOG
Superior temporal gyrus	STG
Middle temporal gyrus	MTG
Inferior temporal gyrus	ITG
Cuneus	Cu
Pre-cuneus	PrCu
Cingulate gyrus	CG
Paracentral gyrus	PaCG
Fusiform gyrus	FuG
Lingual gyrus	LG
Insular	Ins

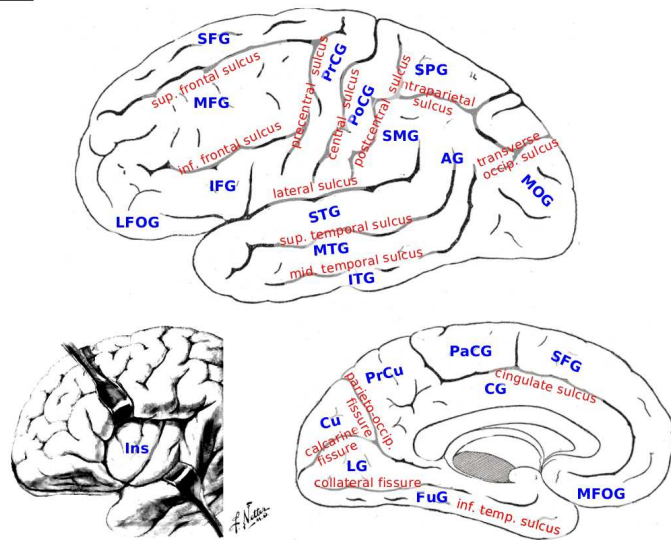


Figure 6.12: **Anatomical regions of the cortical surface used to label the short association bundles of the HARDI multi-subject atlas.** [Images were adapted from <http://www.bartleby.com/107/> and <http://www.netterimages.com/>]

Sometimes a number was added when more than one bundle was found within the same location. Most of the labeled bundles are composed by only one generic bundle. Forty seven SWM bundles were identified for the left hemisphere; these bundles are individually illustrated in Figures 6.13 and 6.14.

The bundles of the right hemisphere were obtained using the symmetric of those of the left hemisphere with respect to Talairach inter-hemispheric plane. The same inference can be performed for the right hemisphere in order to remove any bias. Figure 6.15 shows different views of the SWM bundle atlas.

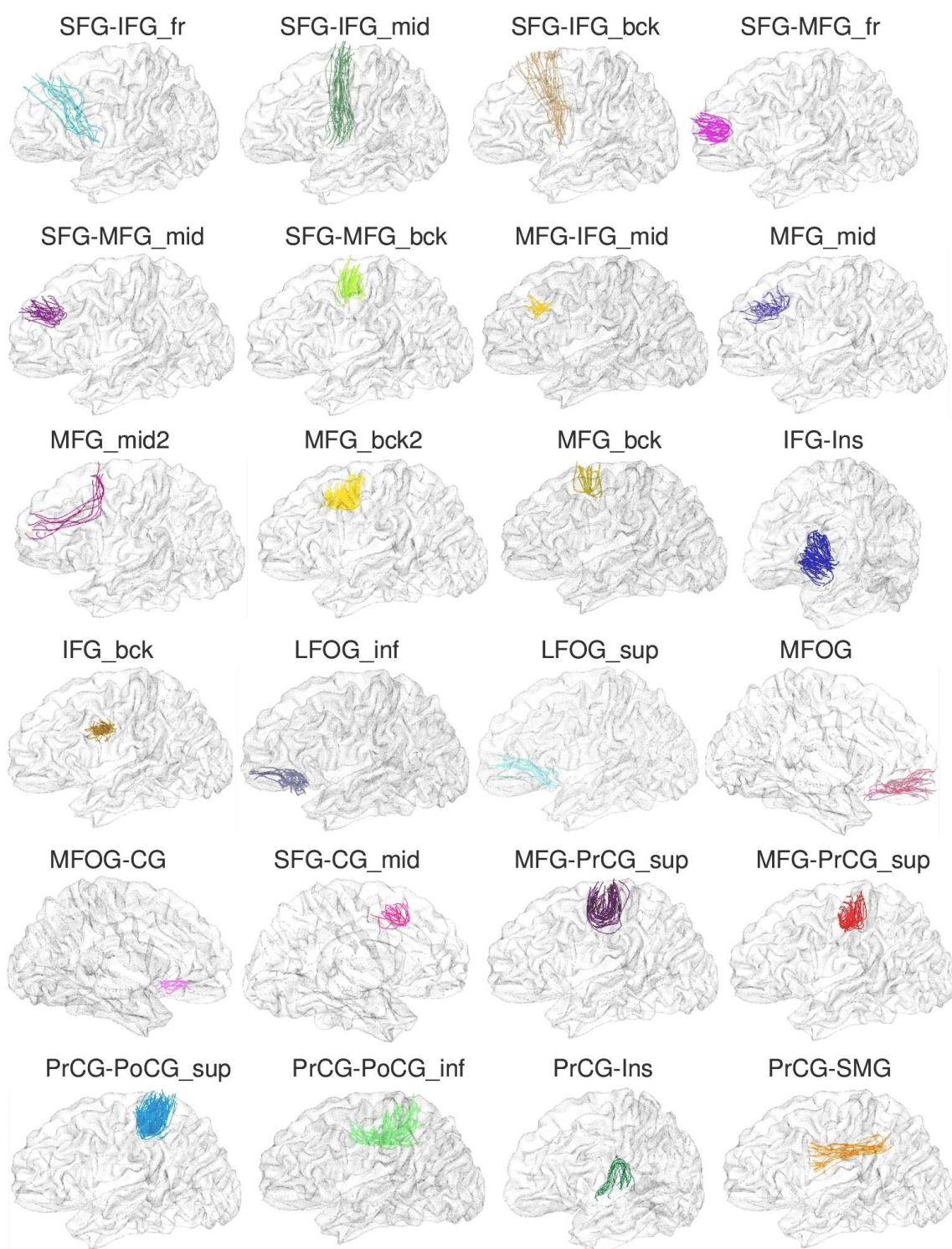


Figure 6.13: **The HARDI multi-subject atlas of short association bundles: Part 1 (24 bundles).** The whole atlas includes a total of 47 bundles per hemisphere. The second group of bundles is shown in Figure 6.14. Bundle names were assigned in function of the regions that the bundles connect, following the region names illustrated in Figure 6.12. In some cases, an additional spatial specification was added: *fr* (frontal), *mid* (middle), *bck* (back), *sup* (superior) and *inf* (inferior).



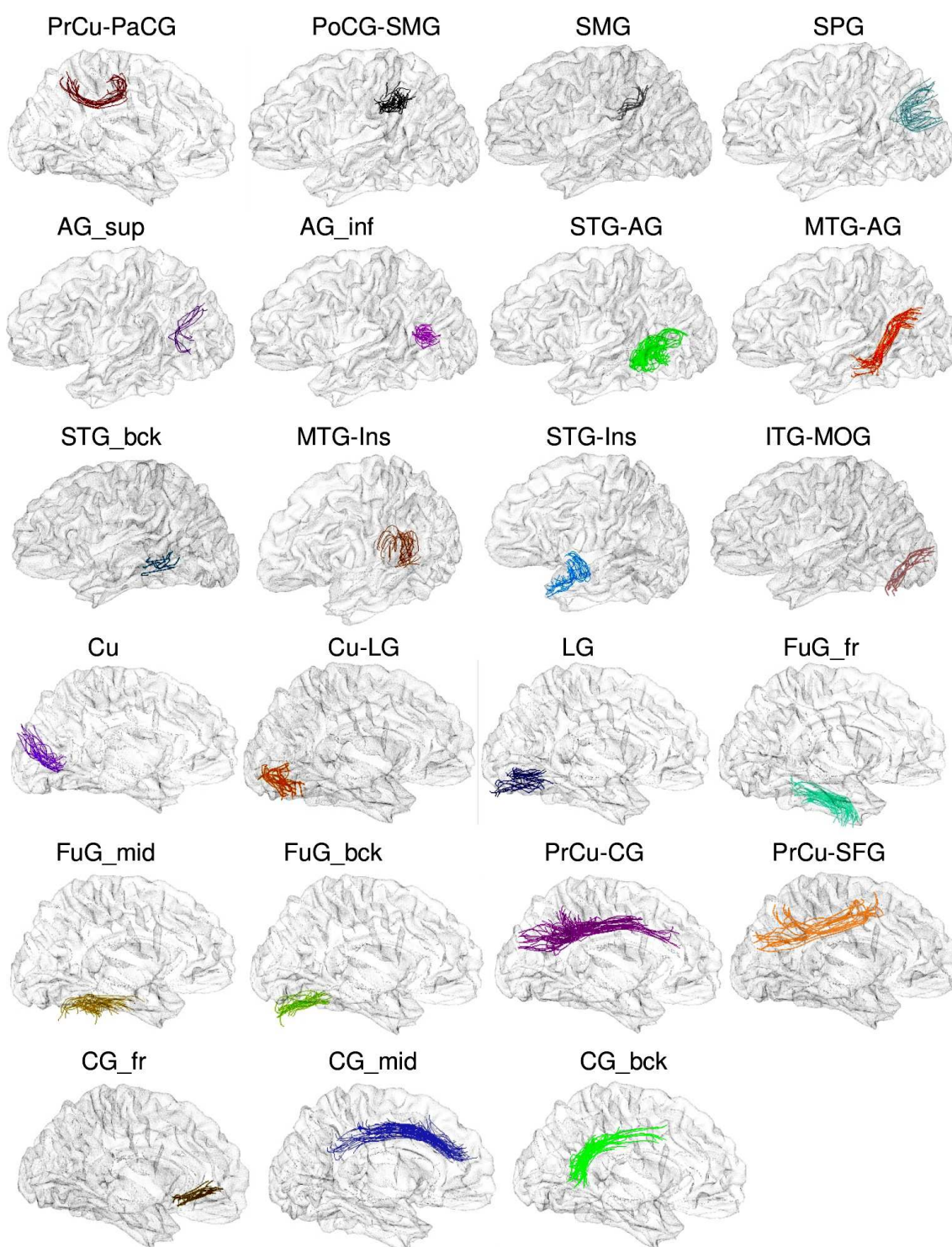


Figure 6.14: **The HARDI multi-subject atlas of short association bundles: Part 2 (23 bundles).** The whole atlas includes a total of 47 bundles per hemisphere. The first group of bundles is shown in Figure 6.13. Bundle names were assigned in function of the regions that the bundles connect, following the bundle names illustrated in Figure 6.12. In some cases, an additional spatial specification was added: *fr* (frontal), *mid* (middle), *bck* (back), *sup* (superior) and *inf* (inferior).

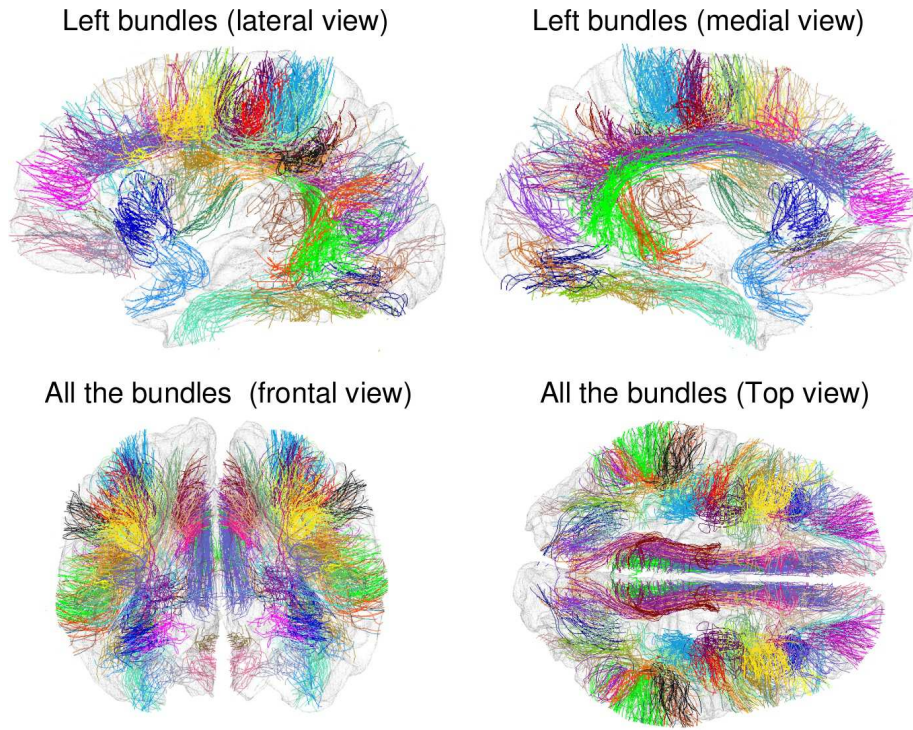


Figure 6.15: **The HARDI multi-subject atlas of short association bundles.** The whole atlas includes a total of 47 bundles per hemisphere. The inference was done from a two-level fiber clustering strategy for the left hemisphere. The bundles of the right hemisphere were obtained using the symmetric of those of the left hemisphere with respect to Talairach inter-hemispheric plane.

## 6.6 Conclusion

In this chapter we presented a method inferring a model of the brain white matter organisation from HARDI tractography results computed for a group of subjects.

As for any fiber tracts analysis method, our results depend strongly on the quality of the tractography results. Our method can not detect bundles that are not tracked in individuals. Also, spurious bundles can not be differentiated from real bundles if they are reproducible across subjects. Besides, anomalous final bundles can be found due to errors in the propagation mask. Since this mask defines where fibers are tracked, bundles can be erroneously cut or fused. Nevertheless, independently of the tracking results, our method is a powerful tool to extract the main generic bundles that are present in most of the subjects.

Our method is able to analyze huge fiber datasets and infer a model of the generic bundles present in a population. The first level, composed by an intra-subject clustering, can be seen as a compression of information and a filtering, where bundles representing the individual whole white matter structure are identified. The second level, an inter-subject clustering, deals with a reasonable number of bundle centroids from a population of subjects and is capable to extract generic bundles present in most of the subjects. Long known bundles were identified, but the result of major significance is the capability to

identify generic short association bundles, which cartography is a complex and unachieved task for the human brain. Hence, our approach will scale up easily to the 1 mm spatial resolution that can now be achieved with highly parallel imaging or very high fields. This spatial resolution is bound to highlight a myriad of U-fiber bundles and better delineate other bigger bundles crossing.

The multi-subject representation of our model, embedding the shape and localization variability of the bundles is a powerful tool for further analyses. It has been shown recently to be more efficient than the usual single template approach for brain structure recognition because of weaknesses of the spatial normalization paradigm [Lyu et al. (2010)]. An example is given in the next chapter for the automatic segmentation of new tractography datasets.

As fiber shape and position information is used for its inference, the proposed HARDI multi-subject atlas allows a better decomposition of the known DWM bundles, which can be of great interest to neuroanatomists and neuroscientists. For instance, the cingulum is a bundle composed by fibers of different lengths, including a big number of short U-shaped fibers [Catani and Thiebaut de Schotten (2008)]. Our atlas contains a separated representation of the long and the short fibers which can allow a systematic identification of both kind of bundles. The same principle was applied to the arcuate fasciculus, which was divided into one long and two short segments, as described by Catani et al. (2005). Our atlas is bound to be refined with more of such subdivisions of the known DWM tracts in the near future. This capability to represent subdivisions of fiber bundles is also true for SWM bundles. Several examples were included in the proposed HARDI multi-subject atlas of short association bundles, for instance the fibers connecting the superior and inferior frontal gyri, were divided into three bundles: an anterior, a middle and a posterior bundle.

We have shown that the affine registration to standard space is sufficient to align reasonably the deep tracts across all the subjects. Furthermore, it allows the inference of a model of the most reproducible short association bundles in a population of subjects. Each U-fiber bundle inferred in this work did require a reasonable alignment of the bundles of only half of the subjects, which happens in the most stable brain regions. However, increasing the number of generic U-fiber bundles, will require an improvement of the spatial normalisation used to compare bundles across subjects. Therefore, the use of non-linear normalization relying on sulci segmentation [Auzias et al. (2011)] will have an important improvement on the results. Moreover, further work will lead us to improve iteratively the spatial normalization using the inferred bundles as constraints in order to better align other bundles [Durrleman et al. (2009)].

Nevertheless, whatever the efficiency of the normalization strategy, a better sampling of the bundle variability will require the application of this strategy to a bigger HARDI database. This will be of special interest for the study and representation of the anatomical variability of tract subdivisions and short association bundles.





**Part IV**

**Application**



# Automatic segmentation of massive tractography datasets

## Contents

---

<b>7.1</b>	<b>Automatic segmentation of massive tractography datasets . . .</b>	<b>189</b>
<b>7.2</b>	<b>Results . . . . .</b>	<b>191</b>
7.2.1	Results for the segmentation of deep white matter bundles . . .	191
7.2.2	Results for the segmentation of short association bundles of SWM	195
<b>7.3</b>	<b>Conclusion . . . . .</b>	<b>198</b>

---

## Overview

---

As described in previous chapters, there are two usual strategies proposed for the segmentation of fiber bundles. The first approach is based on regions of interest (ROI) used to select or exclude tracts. The second strategy is based on tract clustering using pairwise similarity measures. This last approach requires less interaction than manual approaches and integrates fiber shape and position information in the analysis, which is not the case of most ROI-based segmentation approaches. However, the clustering-based methods commonly present a limitation on the number of fibers that can be analyzed. In spite of two recent works that describe the analysis of huge datasets the segmentation of huge tractography datasets, presenting more than one million tracts, is still a challenge.

Hence, in this chapter we present a direct application of the methods developed in this thesis, for the automatic segmentation of fiber bundles from massive tractography datasets. The method uses a priori information embedded in the multi-subject (MS) fiber bundle atlas developed in previous chapter. This atlas represents the shape and localization variability of 36 deep white matter bundles and 94 short association bundles of superficial white matter. Some atlas bundles are hierarchically subdivided into several fascicles to take into account subdivisions of the WM tracts described in the literature. This multi-subject strategy, has been shown recently to be more efficient than the usual single template approach for brain structure recognition because of weaknesses of the spatial normalization paradigm [Lyu et al. (2010)].

The method builds upon the multiresolution intra-subject clustering that can compress millions of tracts into a few thousand consistent bundles, described in chapter 5. New tractography datasets are first compressed with the intra-subject clustering. The resulting bundles are then labeled using a pairwise distance to the centroids representing the multi-subject atlas bundles. The segmentation of deep white matter bundles is applied to eight adults and four children while the segmentation of short association bundles is applied to ten adults.

**Keywords:** WM clustering, WM atlas, fiber clustering, U-fibers, WM bundle segmentation, tractography segmentation

### Organization of this chapter:

The chapter is organized as follows. We first describe automatic bundle segmentation method in Section 7.1. Then, we present the results in Section 7.2. These are shown separately for known deep white matter tracts and short association bundles of superficial white matter.



## 7.1 Automatic segmentation of massive tractography datasets

---

We propose a simple but powerful method for the segmentation of new massive tractography datasets using the multi-subject atlas described in chapter 6. This bundle atlas was constructed from twelve subjects of a HARDI adult database. Each atlas bundle is represented by the multi-subject list of the centroids of intra-subject clusters in order to get a good sampling of the shape and localization variability of the bundle trajectory after affine normalization. The atlas includes 36 deep white matter bundles, some of these representing a few subdivisions of known WM tracts and 94 short association bundles of superficial white matter.

A scheme of the automatic segmentation method is shown in Figure 7.1. The segmentation of a new tractography dataset begins with a compression into a few thousand bundles, using the intra-subject clustering described in chapter 5. Then, the resulting bundles are labeled using a supervised classification based on the fiber bundle atlas. The bundle centroids are normalized to the Talairach Space using an affine transformation. Then pairwise distances are computed between each centroid of the new subject and all the centroids of the atlas.

The distance measure used is the maximum of the Euclidean distances between corresponding points ( $d_{ME}$ ), defined in equation 6.1. As mentioned before, this restrictive distance is a good representation of the similarity between two fibers, as it takes into account the fiber positions and shapes. For the calculation, the atlas fibers and the individual centroids are resampled using 21 equally distributed points. The whole set of pairwise distances is obtained in a few minutes.

Each individual centroid is labeled by the closest atlas bundle, provided that the distance to this bundle, namely the smallest pairwise distance to the centroids representing this bundle, is lower than a threshold.

For known deep white matter bundles, this threshold is adapted to each atlas bundle using a leave-one-out strategy: for each atlas bundle, the threshold is the minimum value allowing the labeling of all the centroids of each subject considering the atlas made up by the eleven other subjects. This leave-one-out point of view leads to define each atlas bundle specific threshold as the maximum of the minimum distance from one centroid of this bundle to all the centroids of the same bundle belonging to the other subjects. One may expect that increasing the size of the database used to infer the atlas will improve the sampling of the bundle variability, which will decrease the thresholds used to catch the same bundle in unknown subjects.

For short association bundles, this threshold was empirically adapted to each atlas bundle (between 8–14 mm) taking into account the bundle mean fiber length and the proximity to other atlas bundles, leading to higher thresholds for long and isolated bundles. A leave-one-out strategy for the determination of the thresholds could be implemented in the future.

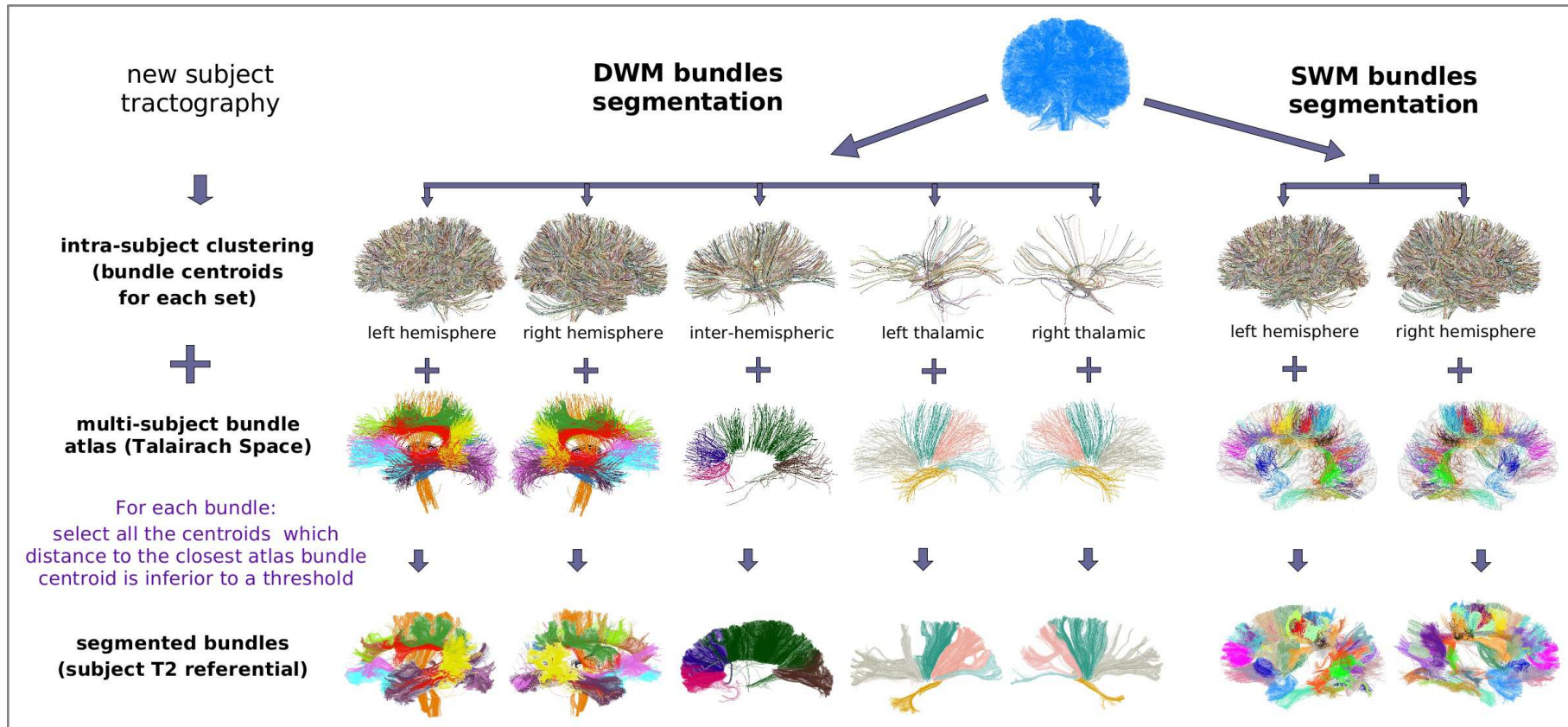


Figure 7.1: **Automatic fiber bundle segmentation method based on the multi-subject bundle atlas.** The segmentation of a new tractography dataset begins with a compression into a few thousand bundles, using the intra-subject clustering described in chapter 5. Then, the resulting bundles are labeled using a supervised classification based on the fiber bundle atlas. The bundle centroids are first normalized to the Talairach Space using an affine transformation. Then, pairwise distances are computed between each centroid of the new subject and all the centroids of the atlas. Each individual centroid is labeled by the closest atlas bundle, provided that the distance to this bundle, namely the smallest pairwise distance to the centroids representing this bundle, is lower than a threshold.

## 7.2 Results

---

A general problem for evaluating white matter bundle segmentation is the lack of gold standard. This is even more complex for superficial white matter, which cartography is still largely unknown and to the best of our knowledge, only the shape of four SWM bundles has been described in the literature [Oishi et al. (2008)]. We evaluate our approach using other databases: eight adults and four children for the segmentation of deep white matter bundles, and ten adults for the segmentation of short association bundles.

### 7.2.1 Results for the segmentation of deep white matter bundles

**Adult HARDI test database.** Eight subjects of another adult HARDI database<sup>1</sup> (DB2), were used to test the segmentation method of known deep white matter bundles. This database provides high quality T1-weighted images and DW data acquired with a Siemens 3.0 T Tim Trio system. The DW data is based on 41 directions and a b-value of  $1000 \text{ s/mm}^2$  (voxel size of  $2 \times 2 \times 2 \text{ mm}$ ). DW data were acquired using a twice refocusing spin echo technique compensating Eddy currents to the first order. Geometrical distortions linked to susceptibility artifacts were corrected using a phase map acquisition. T1 and DW data were automatically realigned using a rigid 3D transform. The diffusion Orientation Distribution Function (ODF) was reconstructed in each voxel using an analytical solution of the q-ball model [Descoteaux et al. (2007)], with a maximum spherical harmonic order  $SH_{max} = 6$  and a Laplace-Beltrami regularization factor  $\lambda_{LB} = 0.006$ . Whole-brain tractography was performed using an FA-based tractography mask, with a threshold equal to 0.15, and a regularized deterministic tractography algorithm [Perrin et al. (2005a)]. We do not used our T1-based tractography propagation mask in order to avoid any bias when performing comparisons between our results and other methods, adapted to a FA-based mask. Tractography was initiated from seven seeds in each voxel of the mask, in both retrograde and anterograde directions, according to the maximal direction of the underlying ODF. Tracking parameters included a maximum curvature angle of  $30^\circ$  and a minimum and maximum fiber length of 20 mm and 250 mm, respectively, leading to a set of about 1.5 millions tracts per subject.

**The segmentation results** are presented in Figure 7.2. Bundles are colored following the colors of the known DWM atlas (Figure 6.11). All the atlas bundles were found in all the subjects with the exception of the fornix and the longest subdivision of the right arcuate fasciculus. The segmentations were validated by an expert. The problem with the fornix was usually related to a common error in the tractography mask induced by the small diameter of this tract. The right arcuate fasciculus problem could be related to the symmetrization of our atlas that can not correctly account for asymmetry of this tract related to language. However, exploring the tractography dataset further with a ROI-based strategy to select fiber tracts, we did not manage to segment this tract in the

---

<sup>1</sup>Thanks to Drs. Marion Leboyer and Josselin Houenou for providing this HARDI brain datasets



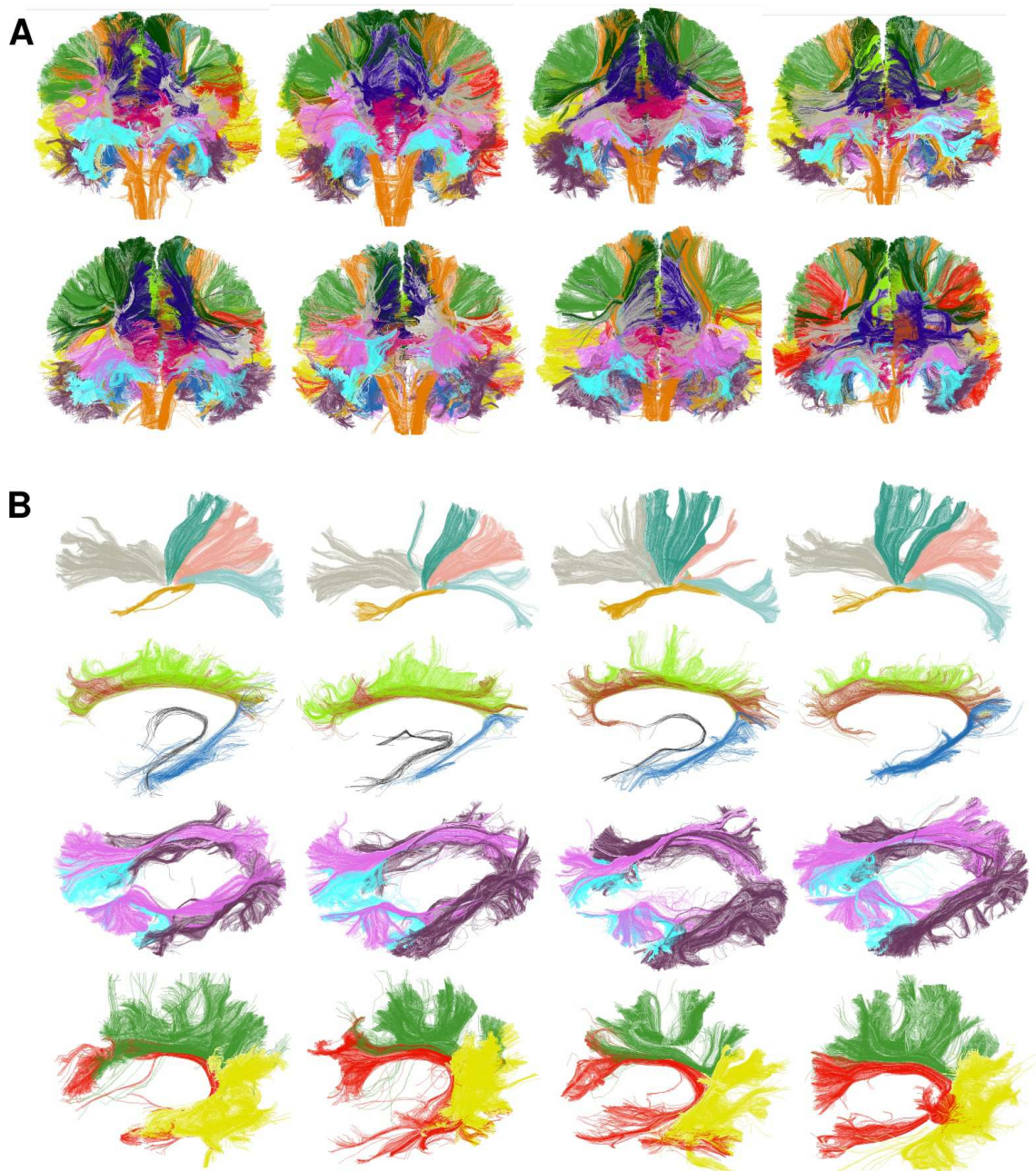


Figure 7.2: **Automatic DWM fiber bundle segmentation results for adult brains.** Colors are the same as for the bundle atlas (Fig. 6.11). **A:** all the bundles for the eight subjects (front view). **B:** some bundles segmented, for four subjects: **First row:** left thalamic radiations (exterior view). **Second row:** left cingulum and fornix (exterior view). **Third row:** left and right inferior fronto-occipital, inferior longitudinal and uncinate (oblique view from left anterior angle). **Fourth row:** left arcuate fasciculus (exterior view).

brains where our atlas-based strategy failed. What could happen is that when the right arcuate fasciculus is not large enough, the current spatial resolution of diffusion data is not sufficient with a deterministic tracking strategy. Indeed several studies have shown large asymmetry of the size of the arcuate fasciculus related to asymmetry of the language

system [Catani et al. (2007)]. To get an insight of the quality of the results, the bundles were visually compared with those obtained using larger distance thresholds. It was found that the estimated thresholds were close to optimal for all the bundles.

The same behaviour was found after the application of the segmentation method to four children of the Child DTI database, described in section 5.4.3. Results are shown in Figure 7.3.



Figure 7.3: **Automatic DWM fiber bundle segmentation results for child brains.** Colors are the same as for the bundle atlas (Fig. 6.11). **First row:** corpus callosum bundles (left exterior view). **Second row:** left arcuate fasciculus (exterior view). **Third row:** left thalamic radiations (exterior view). **Fourth row:** left inferior fronto-occipital, inferior longitudinal, uncinate and corticospinal tract (exterior view). **Fifth row:** left cingulum and fornix (exterior view).

**Comparison with a ROI-based approach.** A comparison was also done for the adult database with a well known method, proposed by Zhang et al. (2010). For that, we determined the fibers segmented by both methods, and those segmented only by one of the methods. The common fibers seem to be well segmented by both methods, following the definition of each bundle (see for example [Catani and Thiebaut de Schotten (2008)]). But, when analyzing the fibers segmented only by one of the methods, our results seem to be better for the tested database. For most bundles, we noted that the ROI-based approach is



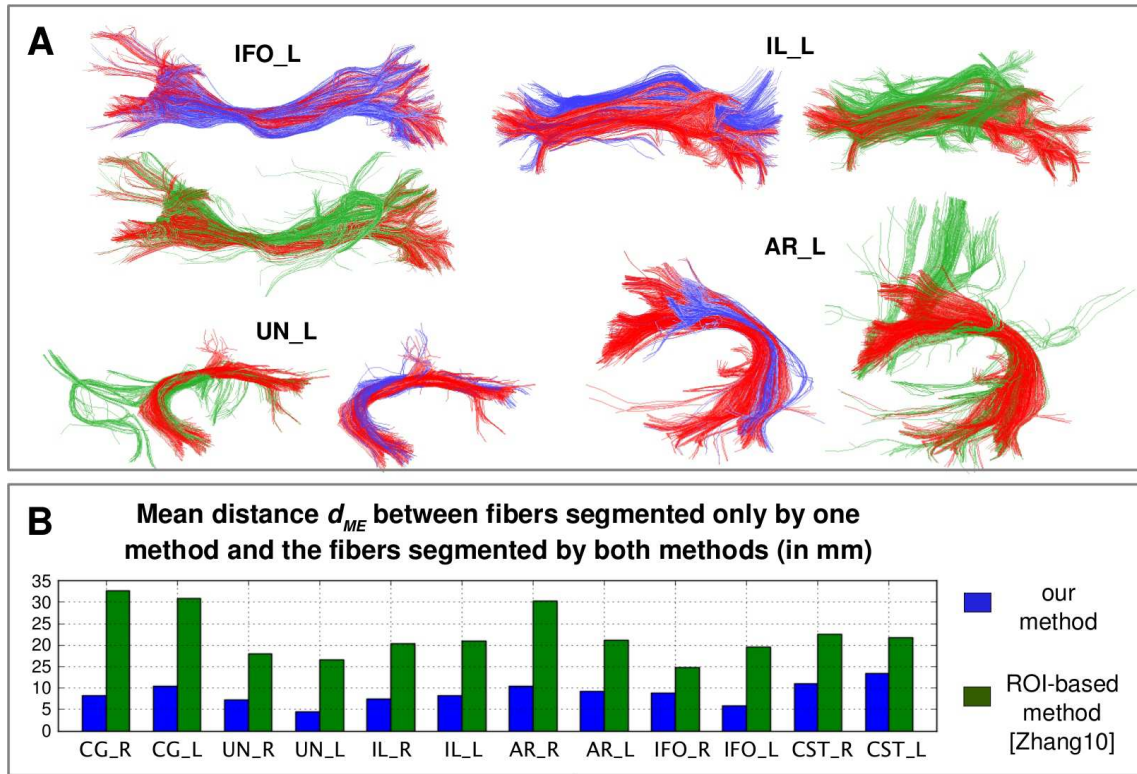


Figure 7.4: **Comparison of our DWM bundle segmentation method with a ROI-based approach [Zhang et al. (2010)].** Bundle abbreviations are the following: cingulum (CG), uncinate (UN), inferior longitudinal (IL), long segment of the arcuate fasciculus (AR), inferior fronto-occipital (IFO), corticospinal tract (CST), with an added "R" or "L", indicating the *right* or *left* bundles, respectively. **A:** Examples for some individual bundles. Bundles segmented by both methods are colored in red, bundles segmented only by our method are colored in blue, and bundles segmented only by the ROI-based approach are colored in green. **B:** Plot of the mean distances  $d_{ME}$  (in mm) between the fibers segmented by each method and the closest fiber segmented by both methods, for all the subjects.

missing some tracts perfectly fitting the definition and the shape of the bundle, but located at the bundle periphery. This weakness is probably induced by non perfect registration. We also noted that the ROI-based strategy selects spurious fibers with weird trajectory because fiber shape is not considered. Some examples are given for four different bundles in Figure 7.4 (A). To confirm this behaviour, we calculated the mean distance  $d_{ME}$  (see equation 6.1) between the fibers segmented by each method and the closest fiber segmented by both methods, for all the subjects (see Figure 7.4 (B)). This analysis was performed for the fiber bundles segmented by both methods and which presented similar definitions. All the distances were found to be bigger for the ROI-based method, confirming that, in general, our method detects a non negligible amount of fibers with a strong probability to belong to the bundle that are missed by the ROI-based method, and that the fibers not detected by our method are quite different from the bundle shape.

## 7.2.2 Results for the segmentation of short association bundles of SWM

For the segmentation of short association bundles, we used ten subjects of the database DB2 (described above), but using in this case our T1-based propagation mask, that improves the detection of this subcortical connectivity (see section 5.4.1).

The results for the ten subjects are presented in Figures 7.5, 7.6 and 7.7. All the bundles were found in at least half of the subjects, which is consistent with our atlas construction requirements. Twenty-one bundles were found in all the subjects (see Figure 7.5), twelve bundles were found in nine subjects (see Figure 7.6) and fourteen bundles were found in between five and eight subjects (see Figure 7.7). The segmentations were validated by an expert. As for deep WM bundles, the bundles were visually compared with those obtained using larger distance thresholds. It was found that the chosen thresholds were close to optimal for most of the bundles. Long and isolated bundles were in general well segmented, when these existed, but some classifications errors were found in short bundles localized very close to other atlas bundles.

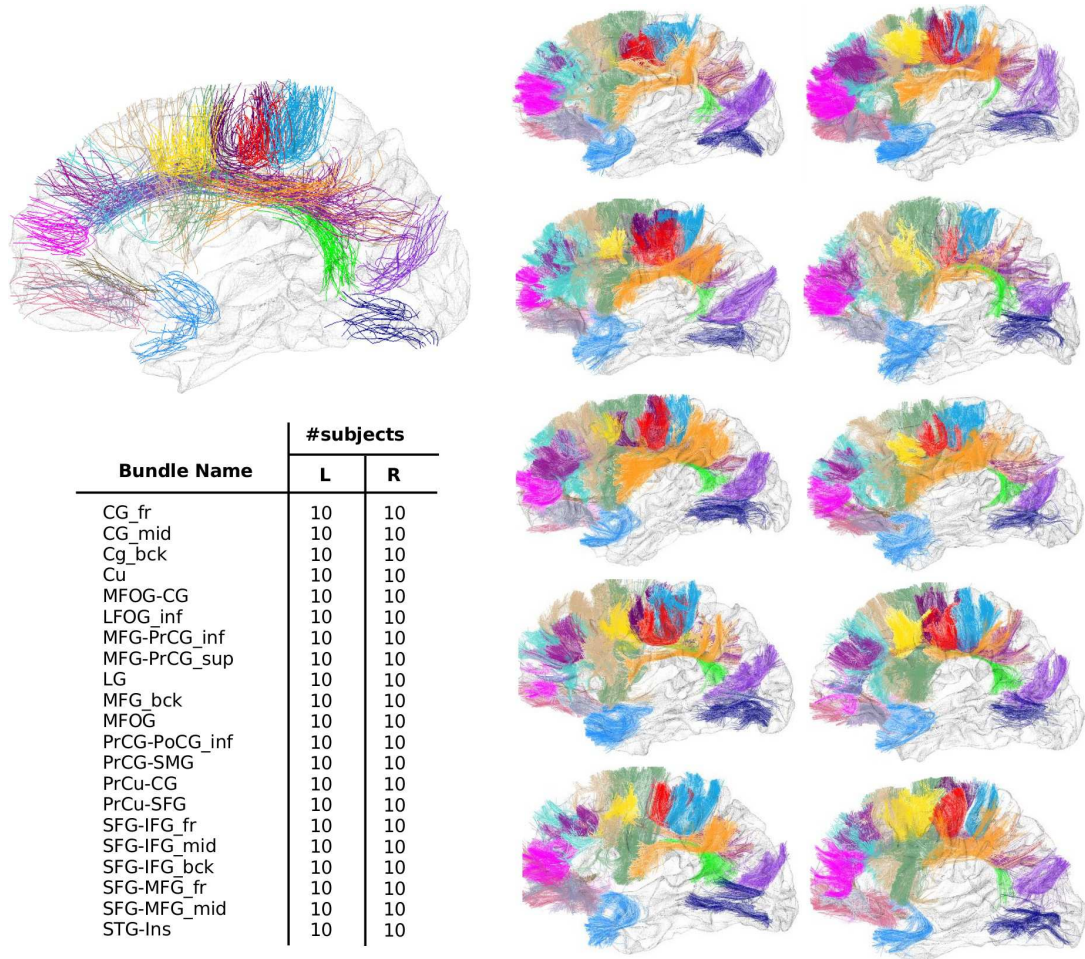


Figure 7.5: **Automatic SWM fiber bundle segmentation results (1)**. Colors and names are the same as for the bundle atlas (Fig. 6.15). The figure shows the 21 short association bundles found in both hemispheres (left (L) and right (R)), of all the subjects (10 subjects).

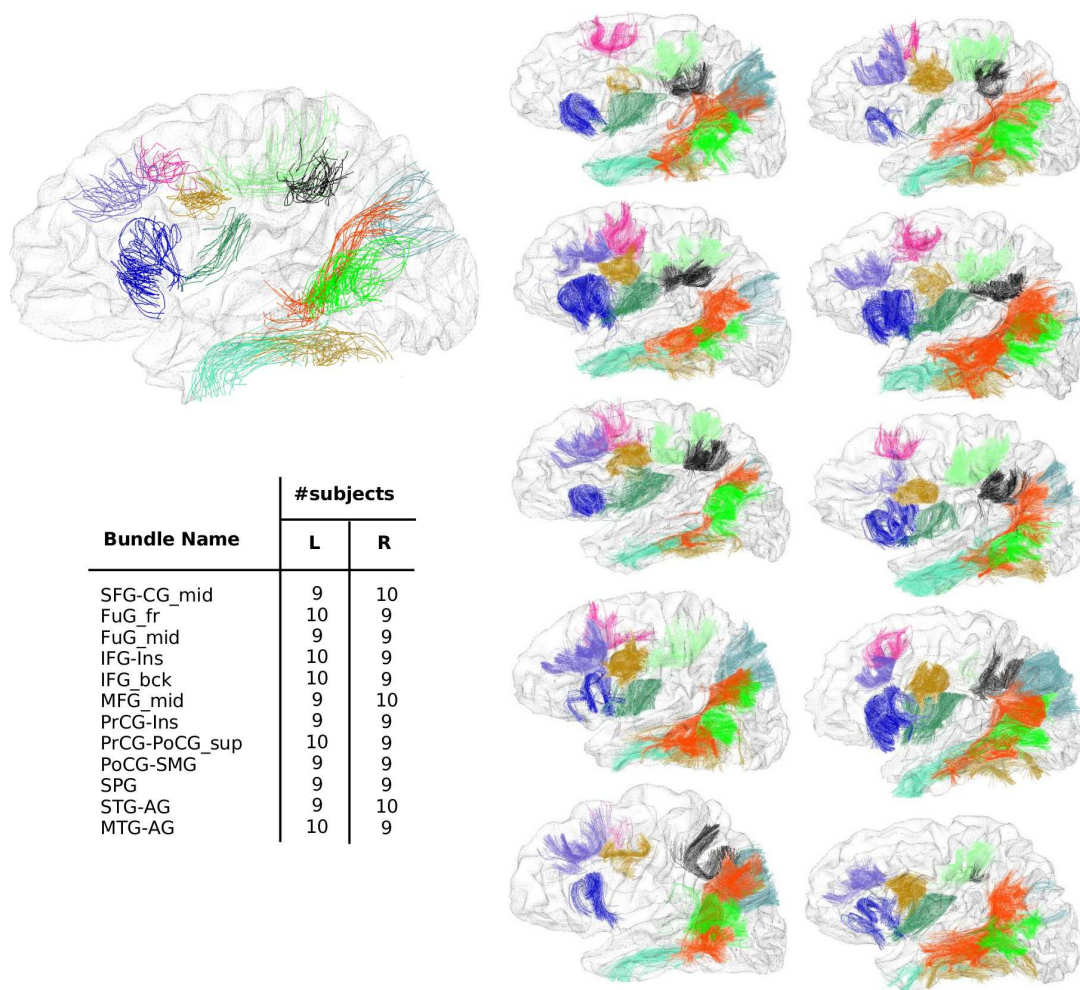


Figure 7.6: **Automatic SWM fiber bundle segmentation results (2)**. Colors and names are the same as for the bundle atlas (Fig. 6.15). The figure shows the 12 short association bundles found in 9 of the 10 hemispheres (left (L) and right (R)) of the ten subjects.



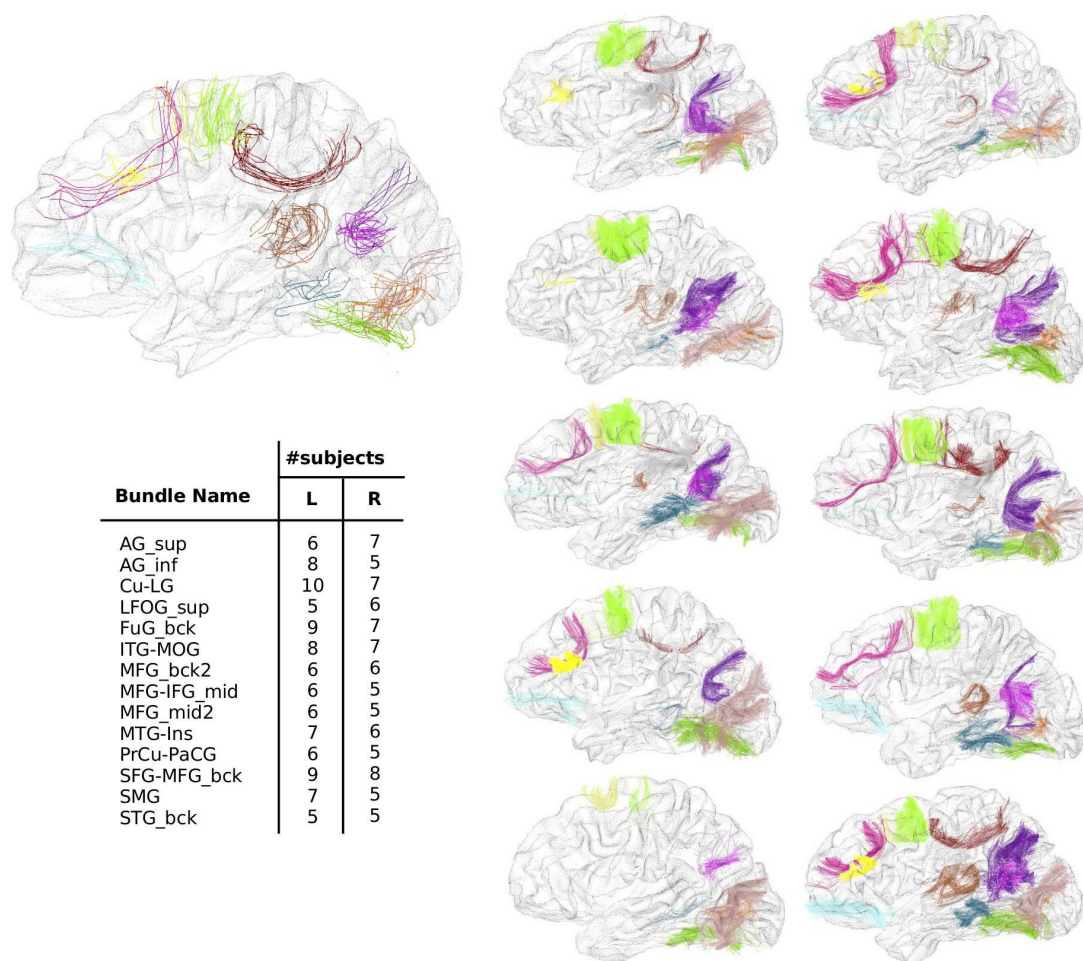


Figure 7.7: **Automatic SWM fiber bundle segmentation results (3)**. Colors and names are the same as for the bundle atlas (Fig. 6.15). The figure shows the 14 short association bundles found in 5 to 8 hemispheres (left (L) and right (R)) of the ten subjects.

## 7.3 Conclusion

---

Our results depend strongly on the quality of the tractography results: bundles that are not tracked in individuals can not be segmented. Therefore, a future research program could be the use of the deep white matter atlas to add a priori knowledge in the tractography algorithm.

Nevertheless, the current method is already successful for the major tracts of deep WM. Thanks to the use of a novel multi-subject representation of bundles and shape information, the bundles are cleaner than when using a ROI-based strategy, which may improve the sensitivity of morphometric studies.

Furthermore, this new atlas and the possibility to manipulate massive tractography datasets allow fine decompositions of the bundles, for instance the arcuate fasciculus and the cingulum. The cingulum is a good example of what a clustering-based method using a restrictive distance measure and a bundle atlas can do. This bundle is composed by fibers of different lengths, including a big number of short U-shaped fibers [Catani and Thiebaut de Schotten (2008)]. Some methods extract only the long fibers [Wang et al. (2011)], other methods extract the long and the short fibers together [Zhang et al. (2010); Visser et al. (2011)]. Our method is the first to extract separately the long and the short fibers. The same principle was applied to the arcuate fasciculus, which was divided into one long and two short segments, as described by Catani et al. (2005).

Regarding short association bundles, the proposed method shows that it is possible to segment the most reproducible superficial white matter bundles using our clustering-based approach in a population of subjects. Furthermore, this new atlas and the possibility to manipulate massive tractography datasets allow also finer decompositions of the SWM bundles, for instance, we proposed two subdivisions of the bundle connecting the pre- and post-central gyri. Our atlas is bound to be refined with more of such subdivisions for both, deep and superficial WM, in the near future.

The results presented in this chapter show that our multi-subject representation of the variability of bundles, combined with a robust affine normalization is sufficient to get systematic recognition of the large known bundles of deep white matter. In our opinion, our approach including parsimony relative to atlas registration is more robust than approaches requiring risky non-linear normalization. Nevertheless, the inclusion of better normalization could allow a better sampling of the bundle variability with a smaller number of brains. However, the anatomical variability of tract subdivisions could impose a minimum number of brains whatever the efficiency of the normalization strategy.

In the case of short association bundles, the proposed method has more limitations. This is due in part to the high inter-subject variability of short association bundles of SWM and the current limitations of dMRI techniques. As mentioned above, our results depend strongly on the quality of the tractography results, and some bundles are not systematically tracked, a problem that particularly affects SWM due to the partial volume



effect. We think that an important improvement can be obtained by the use of non-linear normalization relying on anatomical segmentations [Auzias et al. (2011)]. First, the atlas construction can be performed using this kind of normalization, leading to a better multi-subject representation of the variability of the atlas bundles. Furthermore, the recognition of the bundles should be also improved if non-linear normalization is used between the subjects and the atlas, reducing the classification errors produced in bundles presenting very similar shapes and close positions.



**Part V**

**Conclusion**



# Conclusion

In this thesis, we have proposed new methods for the clustering and analysis of massive and complex tractography datasets, containing more than a million of fibers per subject and presenting complex fiber configurations. The main analysis is composed by two parts: an intra-subject clustering and a clustering performed across a population of subjects. This strategy allowed the inference of a human brain white matter (WM) bundle model based on high angular resolution diffusion imaging. A multi-subject atlas was thus inferred, composed by 36 deep WM bundles, some of these representing a few subdivisions of known white matter tracts and 94 short association bundles of superficial white matter. Finally, this atlas is used for the automatic segmentation of known deep WM and some short association fiber bundles from massive dMRI tractography datasets.

These methodological contributions were described and developed in the Methods part of the thesis and the bundle segmentation application was shown in a separate Application part.

These contributions required some background knowledge on cerebral white matter anatomy, diffusion MRI principles and fiber clustering methods. All these topics were reviewed and covered in the Background part of the thesis.

All along this thesis, we have tried to make the good mathematical and algorithmic choices to solve the problems of interest. First, we used an intra-subject hierarchical clustering strategy based on a voxel-based clustering for an efficient analysis and compression of individual tractography datasets. This approach, composed by several processing steps, ensures robustness and good results quality to the whole method. Then, we developed a new and efficient inter-subject clustering method, able to analyse huge tractography datasets from a population of subjects and infer a model of generic bundles present in most of the subjects. To deal with the limitation of dataset size, the method uses as input the intra-subject clustering results, consisting in a few thousand bundles representing the whole fiber dataset structure. Overall, we have tested the robustness and the results quality of our methods using simulated datasets. The intra-subject clustering was also compared with another brute-force non-scalable strategy. Finally, we proposed a fast, robust and automatic bundle segmentation method, based on the created multi-subject bundle atlas and the intra-subject clustering method. We have made a special effort to study and discuss many existing state-of-the-art methods in the literature to highlight the



strengths and limitations of the proposed methods.

As for any fiber tracts analysis method, our results depend strongly on the quality of the tractography results. Our method can not detect bundles that are not tracked in individuals. Besides, anomalous final bundles can be found due to errors in the propagation mask. Since this mask defines where fibers are tracked, bundles can be erroneously cut or fused. Nevertheless, independently of the tracking results, the developed methods are a powerful tool for the analysis of tractography datasets structure, the extraction of the main generic bundles that are present in a population of subjects and the segmentation of massive tractography-based datasets.

## Contributions

Throughout the thesis, we have enumerated our major and minor contributions. In summary, the important and original contributions of the thesis are:

### Major contributions.

**A robust intra-subject fiber clustering method of massive diffusion-based datasets.** This novel robust clustering of white matter fibers can deal with millions of diffusion-based tracts. It is made by a sequence of algorithms in a way that give robustness and good results quality. The analysis is mainly based on geometrical fiber properties and no strong anatomical a priori are used. The output consists in a few thousands of homogeneous fiber bundles, where each one can be represented by a bundle centroid. This compressed representation can be used as input to more sophisticated analysis algorithms that can not deal with millions of fibers. In addition, during the analysis most of noise fibers are discarded, leading to a cleaner fiber dataset. An example of application was detailed with the phantom analysis. It was shown that our clustering method, applied to a hardware phantom gives a robust and powerful way to evaluate local diffusion models and tractography algorithms.

**A two-level fiber clustering strategy for the inference of a WM bundle model from HARDI tractography datasets.** We presented a method inferring a model of the brain white matter organisation from HARDI tractography results computed for a group of subjects. Our method is able to analyze huge fiber datasets and infer a model of the generic bundles present in a population. The first level uses the developed intra-subject clustering, that can be seen as a compression of information and a filtering, where bundles representing the individual whole white matter structure are identified. The second level, an inter-subject clustering, deals with a reasonable number of bundle centroids from a population of subjects and is capable to extract generic bundles present in most of the subjects. Long known bundles were identified, but the result of major significance is the

capability to identify generic short association bundles, which cartography is a complex and unachieved task for the human brain.

Using simulated datasets we shown that the affine registration to standard space is sufficient to align reasonably the deep tracts across all the subjects and the most reproducible short association bundles in a population of subjects.

**The construction of a HARDI multi-subject bundle atlas using the two-level fiber strategy.** The generic bundles obtained with the developed two-level fiber clustering strategy were manually labelled in order to create a HARDI multi-subject bundle atlas in the Talairach space. For labelling, our criteria included various anatomical information related to the bundle path and localization, and especially to the cortical morphology around bundle extremities. We used sulci segmentations and cortical surface parcellations as visual guidance.

In the case of known deep white matter bundles, we used the anatomical definitions proposed in the literature. The created atlas includes a total of 36 bundles, composed by 11 white matter tracts in each hemisphere and the corpus callosum, with several tracts divided into a few fascicles. Regarding short association bundles of superficial white matter, which have been rarely studied until now, our labelling was based on the name of the cortical regions that are connected by each bundle. A total of 47 SWM bundles were thus identified for each hemisphere.

As fiber shape and position information is used for its inference, the proposed HARDI multi-subject atlas allows a better decomposition of the known DWM bundles and short association bundles of SWM, which can be of great interest to neuroanatomists and neuroscientists. This multi-subject representation of our atlas, embedding the shape and localization variability of the bundles is a powerful tool for further analyses.

### **An automatic method for the segmentation of massive tractography datasets.**

We developed a method for the automatic segmentation of massive tractography datasets based on the multi-subject bundle atlas. The method allows a fast and robust segmentation of the bundles of DWM and SWM represented in the atlas and successfully tracked in the dataset. The method builds upon the multiresolution intra-subject clustering, that can compress millions of tracts into a few thousand consistent bundles. New tractography datasets are first compressed with this intra-subject clustering and the resulting bundles are then labeled using a pairwise distance to the centroids representing the multi-subject atlas bundles.

The results show that our multi-subject representation of the variability of bundles, combined with a robust affine normalization is sufficient to get systematic recognition of the large known bundles of DWM. In our opinion, our approach including parsimony relative to atlas registration is more robust than approaches requiring risky non-linear normalization. Nevertheless, the inclusion of better normalization could allow a better sampling of the bundle variability with a smaller number of brains. However, the

anatomical variability of tract subdivisions could impose a minimum number of brains whatever the efficiency of the normalization strategy. In the case of short association bundles, the proposed method has more limitations, due in part to the high inter-subject variability of short association bundles of SWM and the current limitations of dMRI techniques.

### **Minor contributions.**

**A method for the construction of a robust T1-based tractography propagation mask.** To overcome the limitations of the FA-based propagation mask, we propose the use of a robust propagation mask stemming from T1 anatomy. The mask is constructed using three anatomical segmentations obtained with the T1 image, allowing a better delimitation of the cortical regions and the inclusion of the deep nuclei and other small brain structures.

This mask, in conjunction with tractography techniques, improves the accuracy of the anatomical connectivity of the brain by reducing false positives and increasing the detection of deep nuclei and subcortical connectivity. It was already used in cortico-cortical and striato-thalamo-cortical connectivity studies. Furthermore, this mask allowed us to study the organization of superficial WM and infer a model of short association bundles.

**Simulated tractography datasets for the analysis of intra-subject and inter-subject fiber clustering.** We developed a total of 30 tractography datasets, corresponding to ten different tractography data combined with three different noise datasets, for the analysis of intra-subject clustering methods. We also developed a set of tractography datasets for the evaluation of inter-subject clustering methods, consisting in 200 bundle centroids per subject, for a database of twelve subjects.

We believe that these contributions meet the initial goal of this thesis that was to infer a model of human brain white matter bundles using high angular resolution diffusion imaging.

### **Perspectives**

We do think that our approach is a necessary and crucial processing step for the analysis of huge fiber datasets. Hence, our approach will scale up easily to the 1 mm spatial resolution that can now be achieved with highly parallel imaging at very high fields. This spatial resolution is bound to highlight a myriad of U-fiber bundles and better delineate other bigger bundles crossing. Therefore, we can expect in the near future, to see more exploratory studies in order to improve the knowledge of WM bundles structure, in special,

of short association bundles. Our atlas is bound to be refined with more subdivisions of the known DWM tracts and more short association bundles in the near future.

Regarding short association bundles, each U-fiber bundle inferred in this work did require a reasonable alignment of the bundles from only half of the subjects, which happens in the most stable brain regions. However, increasing the number of generic U-fiber bundles, will require an improvement of the spatial normalisation used to compare bundles across subjects. Therefore, the use of non-linear normalization relying on sulci segmentation [Auzias et al. (2011)] will have an important improvement on the results. Moreover, further work will lead us to improve iteratively the spatial normalization using the inferred bundles as constraints in order to better align other bundles [Durrleman et al. (2009)].

Nevertheless, whatever the efficiency of the normalization strategy, a better sampling of the bundle variability will require the application of this strategy to a bigger HARDI database. This will be of special interest for the study and representation of the anatomical variability of tract subdivisions and short association bundles.

Furthermore, a bigger database is been used for the validation of the automatic bundle segmentation results.

We believe that the main contributions from the thesis can now be applied to answer more neuroscientific questions. In fact, our algorithms are starting to be used by neuroscientists, in part because they are available on demand through the Brain-VISA/Connectomist2.0 software<sup>1</sup>. The intra-subject clustering method is been used for the analysis of tractography datasets from children with corpus callosum agenesis, allowing a better understanding of the bundle structure for this pathology, which is very different than normal brains. Furthermore, diffusion analyses will be performed over a big database of patients with bipolar syndrome and controls using our automatic DWM bundles segmentation method.

We think that several applications of the developed methods will arise in the future. The resulting fiber bundles of the individual fiber clustering can be combined with functional data for neuroscientific studies or with other brain segmentations like tumors, for the analysis of WM structure in pathological brains. Furthermore, cortical surface parcellation methods could be developed based on the results obtained with our two-level fiber clustering strategy. Fiber clusters present in most of the population may be processed in order to find diffusion-based reproducible cortical brain regions across a population of subjects. Finally, we believe that the automatic segmentation method of known DWM bundles and also several SWM bundles will be a powerful tool for tract based diffusion studies.

From a computer sciences point of view, the developed algorithms can be optimized by the use of computer parallelization and the codification of time-consuming parts using a more efficient platform as the Graphics Processing Unit (GPU). The improvement and

---

<sup>1</sup><http://brainvisa.info>

development of algorithms able to deal with huge tractography datasets will be a continuous research area as tractography datasets size will continue to increase. These datasets are already extremely huge in the case of streamline probabilistic tractography, which are composed by about 30 millions of fibers for the current spatial resolutions.



**Part VI**

**Appendix**



# White Matter atlases

WM atlases are commonly used as input, intermediate step or output of fiber segmentation and identification methods. Some of these atlases are images with gray matter and/or white matter labeled regions. Other consist of labeled tractographic fibers in some normalized space. In this section we briefly describe the most known WM atlases, some of these already cited in previous chapters.

As described in section 4.3, [Wakana et al. \(2004\)](#) generated two- and three-dimensional WM atlases created on the basis of high-spatial-resolution DT-MRI and 3D tract reconstruction of 17 prominent WM tracts. The WM tracts were selected using a manual ROI-based approach, over a whole-brain tractography. Then, 3D tracts were superimposed on coregistered anatomic MR images to parcel the white matter and generate the 3D atlas. These parcellation maps were also compared with coregistered DTI color maps to provide a 2D color map atlas with structural assignments.

[Maddah et al. \(2005\)](#) also created a bundle template using hand-selected ROIs in white matter. This atlas was then used to identify fiber tracts from a new subject (see section 4.4.3).

As mentioned in section 4.3, [Catani and Thiebaut de Schotten \(2008\)](#) proposed another method to reconstruct WM pathways using an ROI approach. The authors provided a template to guide the delineation of ROIs for the reconstruction of the association, projection and commissural pathways. An average dataset was used for the DT template, calculated from the DT-MRI of 12 subjects spatially normalized. Then, the average color and FA diffusion tensor images were combined to create a split-half template with delineated ROIs. An atlas of the 3D reconstructions of the single tracts was generated from two subjects and was provided as anatomical reference in the Montreal Neurological Institute (MNI) space.

[O'Donnell and Westin \(2006, 2007\)](#) created a “high-dimensional” WM atlas containing a representation of the known anatomical deep WM 3D tracts in an embedded space (see section 4.4). The atlas was constructed using tractography datasets from ten different subjects using a spectral clustering approach [[O'Donnell et al. \(2006\)](#)] and an expert

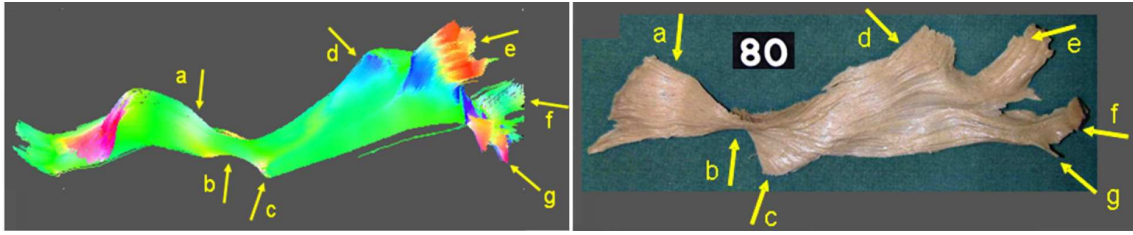


Figure A.1: Example of comparison performed by [Lawes et al. (2008)] between fiber tracts from tractography with tracts isolated with classical post-mortem dissection. Illustration for the left inferior fronto-occipital fasciculus. (left) Track representation of the whole fasciculus from the mean DTI. (right) The dissected inferior fronto-occipital fasciculus [From Lawes et al. (2008).]

labeling of WM clusters. The atlas was then used to automatically segment the most known 3D fiber bundles from five other subjects O'Donnell and Westin (2007).

Lawes et al. (2008) presented a method for constructing a white matter atlas from DT tractography by making use of the locations of the anatomical terminations of individual streamlines that pass through white matter. The method provides a manually labeled preliminary map of WM regions close to gray matter (juxtacortical white matter), used to map pathways termination voxels. For that, a mean normalized DTI created from 15 healthy subjects was used to perform a whole-brain tractography. Every seed voxel that gave rise to a streamline was assigned a "combined label", made as a combination of the numbers corresponding to the areas connected by the track termination points. A normalized whole-brain map of seed points (voxel centers) was then created, where each seed voxel was labelled by its membership to a specific track. Tracks were then reconstructed for each subject by initiating tractography from the center of seed points bearing the same anatomical label. The anatomical labels, initially defined by a priori knowledge of brain anatomy, were subsequently modified by the morphology of the fiber tracks. Inter-subject track variability maps were determined for the major tracks studied. Finally, the tracks produced by this technique were compared to tracts dissected in postmortem brains, showing a close correspondence of the fiber tracts from tractography with tracts isolated with classical dissection (see Figure A.1). This work is a common reference in the literature due to this comparison.

Hua et al. (2008) created a white matter parcellation atlas based on probabilistic maps of 11 major white matter tracts derived from the DTI data of 28 normal subjects (see Figure A.2). White matter tracts were manually extracted using the protocol for the delineation of ROIs proposed by [Wakana et al. (2004)]. Subjects were registered into a common template in the DTI-JHU space ([lbam.med.jhmi.edu](http://lbam.med.jhmi.edu)) [Wakana et al. (2004)] and the MNI-ICBM152 space ([www.loni.ucla.edu/ICBM](http://www.loni.ucla.edu/ICBM)) [Mazziotta et al. (2001)]. For each subject, an affine transformation was calculated to register the DTI images to the template and then used to transform subject's fiber tracts to this common space. The

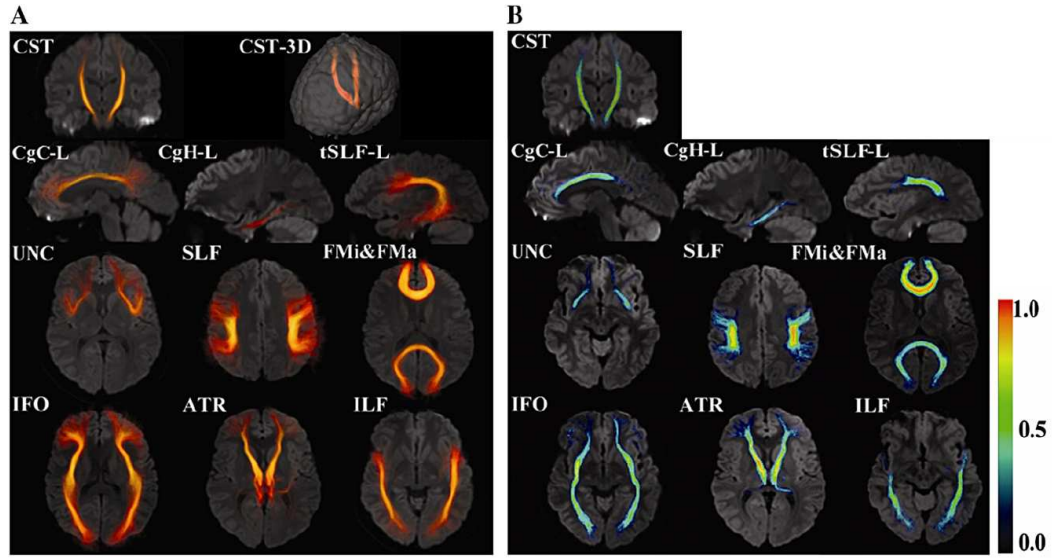


Figure A.2: Probabilistic maps of 11 white matter tracts, proposed by [Hua et al. \(2008\)](#). Results are superimposed on a single-subject JHU template. The 3D volume rendering of the averaged tract (A) and color-scaled probabilistic maps (B) are superimposed on 2D slices. Maximum intensity projection is used for the color intensity in (A). The color in (B) represents probability, as shown in the color bar. [From [Hua et al. \(2008\)](#).]

tract binarized masks in the standard coordinates were averaged over the 28 subjects to generate probabilistic maps, in which each pixel contains information about the probability. In this approach, pixels that belong to core regions of tracts, which are reproducible in the normal population, have larger weighting while the less reproducible regions are mostly at peripheral regions close to the cortex. The probabilistic approach diminishes contributions of random errors through the group-averaging process. Nonetheless, the probabilistic maps can contain erroneous white matter regions [[Hua et al. \(2008\)](#)].

[Mori et al. \(2005\)](#) provided a book containing annotated 3D WM tracts images and crosssectional maps derived from DTI data. 3D WM tracts were manually extracted from fiber tractography using the method described in [[Wakana et al. \(2004\)](#)]. The 2D atlas is arranged in a series of axial, coronal, and sagittal images. Color maps are presented at multiple slice levels and the three orientations, and WM structures are identified, assigned and annotated by comparison with their reconstructed 3D trajectories.

[Mori et al. \(2008\)](#) introduced a stereotaxic population-averaged WM atlas, called ICBM-DTI-81, in which DTI-based white matter information was fused with an existing anatomical template (ICBM-152) [[Mazziotta et al. \(2001\)](#)]. DWI images from 81 normal subjects were normalized to the template using an affine transformation. Population-averaged data was obtained by simple scalar averaging of tensor elements. From the averaged tensor field, the FA and color-coded (RGB) maps were recalculated. Twenty height deep WM (DWM) structures were manually segmented using RGB maps, into various anatomical regions, to obtain a WM parcellation map (WMPM) (See Figure A.3 (A)).



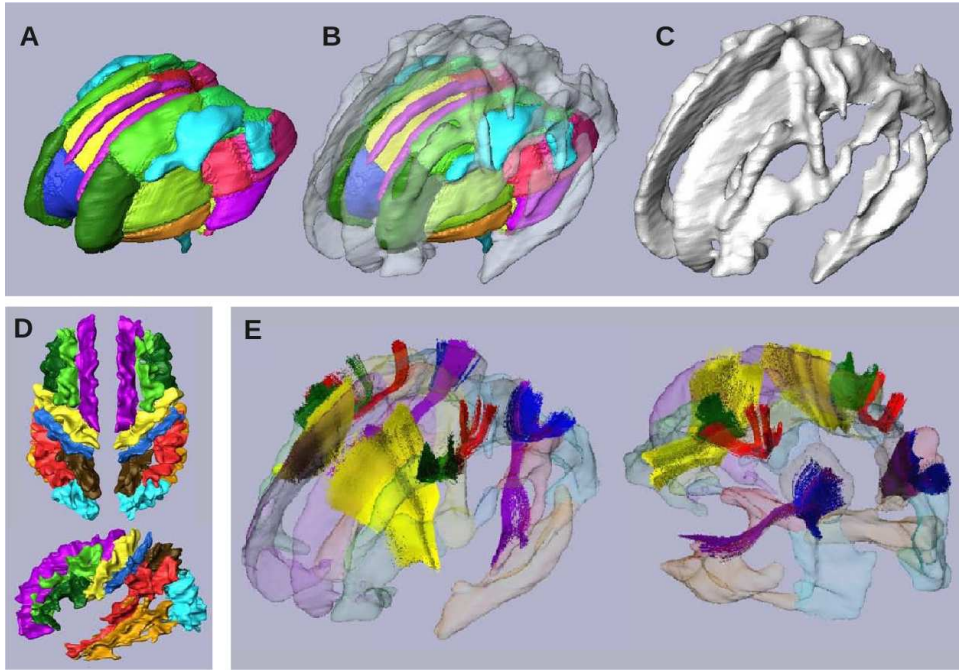


Figure A.3: DWM and SWM atlases from manual ROI-based labeling [Oishi et al. (2008)]. **A** A 3D view of the ICBM-DTI-81 atlas, hand-segmented deep WM parcellation map (WMPM) [Mori et al. (2008)]. **B-C** The SWM obtained in [Oishi et al. (2008)], defined by 0.6 WM probability, with (B) and without (C) the DWM. **D** Results of the nine blades of SWM manually identified for one individual brain. **E** The four identified short association fibers: frontal (yellow), fronto-central (green), central (red), and parietal (blue). The parieto-temporal long association fiber is shown in purple [From Oishi et al. (2008)].

Oishi et al. (2008) provided a parcellation of the superficially located WM (SWM), defined as the area between the cortex and the DWM. First, a “probabilistic” WM map was generated from WM binarized FA maps of the 81 subjects used for the construction of the WMPM [Mori et al. (2008)]. The SWM was extracted as the WM between the WMPM and the cortex, using thresholds applied to the probabilistic WM map. The SWM was then manually parcellated into nine major structures called “blades”. The 9 blades were further sub-parcellated into 23 regions based on the relationships with 24 cerebral cortical areas and the cerebellum. The blades were used as ROIs for tractography selections. Intra-blade fibers could not be located.

Four short and one long inter-blade fibers were found. The four short association fibers were designated as follows: frontal (connecting the superior frontal and the inferior frontal blades); fronto-central (connecting the middle frontal and the pre-central blades); central (connecting the pre- and post-central blades); parietal (connecting the superior parietal and the parieto-temporal blades). A parieto-temporal long association fiber bundle (connecting the superior parietal and the parieto-temporal blades) was also described. See Figure A.3 (B-E) for a 3D view of the SWM parcellation and the identified inter-blade fibers.

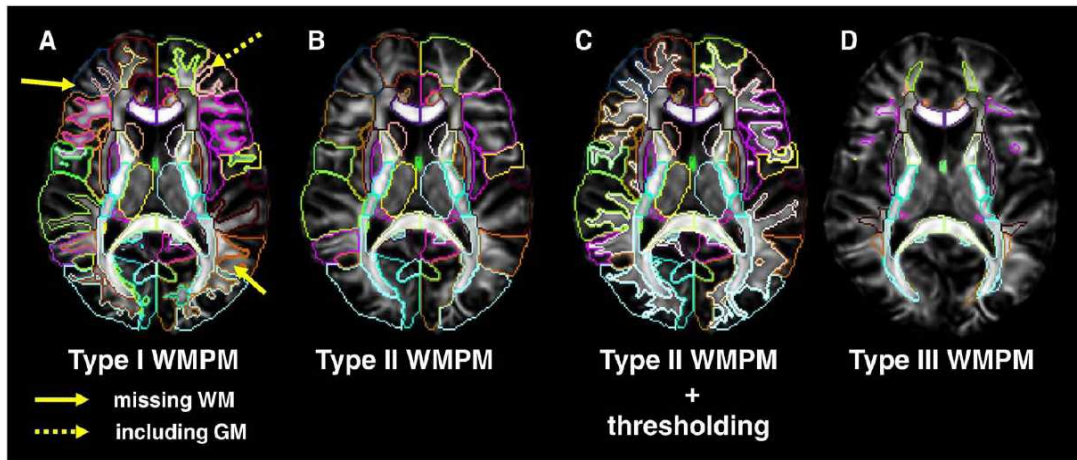


Figure A.4: Normalized FA map overlaid with Type I-III WM parcellation maps (WMPMs) [Oishi et al. (2009)]. (A) Type I WMPM cannot accurately delineate the boundary of the SWM because of excessive anatomical differences between the atlas and the participant. Yellow solid arrows indicate the WM areas, which were misclassified as “cortex” based on Type I WMPM. A yellow dotted arrow indicates the cortex, which was misclassified as “WM” based on Type I WMPM. (B) Type II WMPM parcellates the cortex and associated SWM together. (C) After the type II parcellation, SWM structures can be individually parcellated using the FA threshold of 0.25. (D) Type III WMPM can label the core part of SWM, defined by the white matter probability (90% in the presented case) [From Oishi et al. (2009)].

Oishi et al. (2009) generated single-participant WM atlases based on DTI. High-quality DTI data from a single-participant were B0-distortion-corrected and transformed to the ICBM-152 atlas (JHU-DTI-MNI atlas) or to Talairach coordinates (JHU-DTI-Talairach atlas). The atlas was generated based on the anatomical labeling in the ICBM-DTI-81 atlas. First, the DWM structures were manually segmented into 28 regions [Mori et al. (2008)]. Then, the SWM areas beneath the cortex were defined, based on a population-averaged WM probability map and manually parcellated into 23 regions [Oishi et al. (2008)]. The parcellation map, containing more than 100 regions, was called WM parcellation map (WMPM).

Three different WMPM were defined (see Figure A.4). WMPM *Type I* contains manual parcellation of 176 structures (56 DWM, 46 SWM, 10 subcortical GM, 52 gyri, 10 others). WMPM *Type II* contains manual parcellation of 130 structures, where 22 SWM of Type I WMPM are included in the corresponding gyri (56 DWM, 10 subcortical GM, 52 gyri, 10 others). WMPM *Type III* contains manual parcellation of SWM and the DWM areas (56 DWM, 46 SWM). The outline of the SWM is based on 90% white matter probability, so these are not clear anatomical boundaries. In this WMPM, structures in the cerebellum and the cingulum white matter are not included.

To create the “probabilistic” WM map, data from 21 normal participants were used first to define individual WM binary masks using a FA threshold of 0.25. Then, a dual-channel Large Deformation Diffeomorphic Metric Mapping (LDDMM) [Ceritoglu et al. (2009)] was performed to register each participant’s data to the JHU-DTI-MNI template,

using FA and b0 images. Finally, the normalized binarized WM masks were averaged to obtain the probabilistic WM map in each pixel in the ICBM152 coordinates. A 90% WM probability was used to define the boundary of the SWM in Type III WMPM.

The atlas was used to perform automated brain segmentation by warping the WMPM to normal controls and Alzheimer’s disease patients with severe atrophy.

[Zhang et al. \(2010\)](#) used the Type II WMPM [[Oishi et al. \(2009\)](#)], to perform an atlas-based tract segmentation of 30 well-known DWM and 29 SWM tracts. The approach defined a *Template Roi Set* (TRS) for the extraction of each bundle (see more details in section [4.3](#)).

Probabilistic maps of the 59 tract trajectories were created from twenty normal subjects. For that, the normalized fiber streamlines of each tract were converted to binary images, which were averaged across the subjects (see Figure [A.5](#)). The atlas and the fiber probability maps were incorporated into RoiEditor software ([www.mristudio.org](http://www.mristudio.org)).

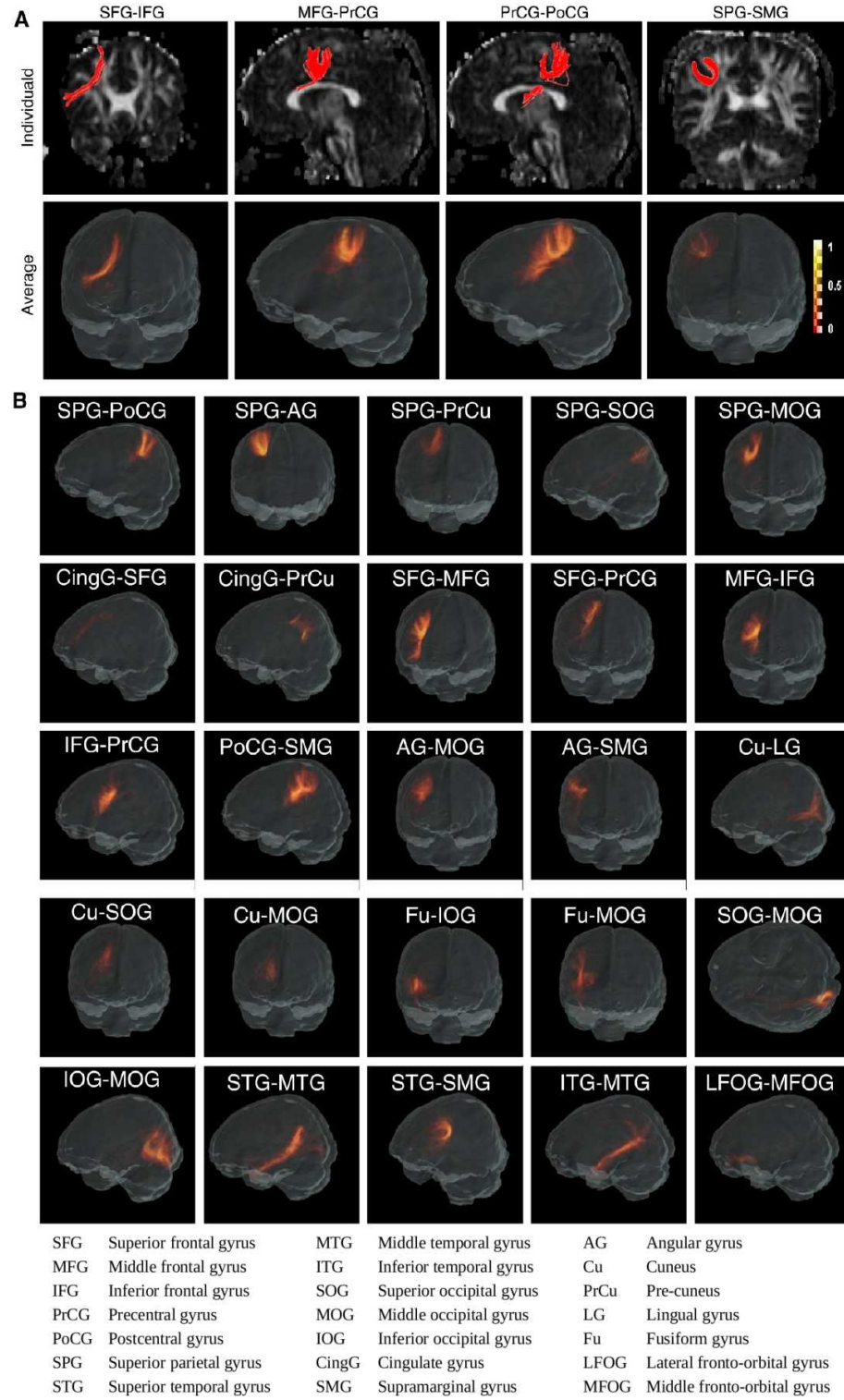


Figure A.5: Short association fibers (short AF) reconstructed by the TRS automated method [Zhang et al. (2010)]. (A) The individual cases and the probabilistic maps of four U-fibers connecting the following cortical region pairs: SFG-IFG (frontal short AF); MFG-PrCG (fronto-central short AF); PrCG-PoCG (central short AF); and SFG-SMG (parietal short AF). (B) The probabilistic maps of the other 25 short AF connecting the cortical region pairs as indicated in the figure. The color scale bar is the same for figures (A) and (B). [From Zhang et al. (2010)].





## Publications of the Author Arising from this Work

### Journal papers

1. Pamela Guevara, Cyril Poupon, Denis Rivière, Yann Cointepas, Maxime Descoteaux, Bertrand Thirion and Jean-François Mangin. *Robust clustering of massive tractography datasets*. Neuroimage, Volume 54, Issue 3, Pages 1975-1993, 2011.

### Conference papers

1. Pamela Guevara, Delphine Duclap, Cyril Poupon, Linda Marrakchi-Kacem, Josselin Houenou, Marion Leboyer and Jean-François Mangin. *Automatic fiber bundle segmentation in massive tractography datasets using a multi-subject bundle atlas*. In MICCAI 2011 Workshop on Computational Diffusion MRI (CDMRI'11), Toronto, Canada, September 2011.
2. Pamela Guevara, Delphine Duclap, Cyril Poupon, Linda Marrakchi-Kacem, Josselin Houenou, Marion Leboyer and Jean-François Mangin. *Segmentation of short association bundles in massive tractography datasets using a multi-subject bundle atlas*. III Chilean Workshop on Pattern Recognition (CWPR 2011), Pucón, Chile, November 2011.
3. Pamela Guevara, Cyril Poupon, Denis Rivière, Yann Cointepas, Linda Marrakchi, Maxime Descoteaux, Pierre Fillard, Bertrand Thirion and Jean-François Mangin. *Inference of a HARDI fiber bundle atlas using a two-level clustering strategy*. Medical Image Computing and Computer Assisted Intervention (MICCAI) 2010, Beijing, China, September 2010.
4. Linda Marrakchi-Kacem, Christine Delmaire, Alan Tucholka, Pauline Roca, Pamela Guevara, Fabrice Poupon, Jérôme Yelnik, Alexandra Durr, Jean-François Mangin, Stéphane Lehericy and Cyril Poupon. *Analysis of the striato-thalamo-cortical connectivity on the cortical surface to infer biomarkers of Huntington's disease*. Medical Image Computing and Computer Assisted Intervention (MICCAI) 2010, Beijing, China, September 2010.

5. Pauline Roca, Alan Tucholka, Denis Rivière, Pamela Guevara, Cyril Poupon and Jean-François Mangin. *Inter-subject Connectivity-based Parcellation of a Patch of Cerebral Cortex*. Medical Image Computing and Computer Assisted Intervention (MICCAI) 2010, Beijing, China, September 2010.
6. Pauline Roca, Denis Rivière, Pamela Guevara, Cyril Poupon and Jean-François Mangin. *Tractography-Based Parcellation of the Cortex using a Spatially-Informed Dimension Reduction of the Connectivity Matrix*. Medical Image Computing and Computer Assisted Intervention (MICCAI) 2009, London, UK, September 2009.
7. Pamela Guevara, Yann Cointepas, Denis Rivière, Cyril Poupon, Bertrand Thirion and Jean-François Mangin. *Inference of a fiber bundle atlas using a two-level clustering strategy*. In MICCAI 2009 Workshop on Diffusion Modelling, London, UK, September 2009.
8. Pamela Guevara, Muriel Perrin, Pascal Cathier, Yann Cointepas, Denis Rivière, Cyril Poupon and Jean-François Mangin. *Connectivity-based parcellation of the cortical surface using Q-ball imaging*. 5th IEEE International Symposium on Biomedical Imaging: From Nano to Macro (ISBI'08), Paris, France, May 2008.

#### Conference abstracts

1. Pamela Guevara, Delphine Duclap, Linda Marrakchi-Kacem, Denis Rivière, Yann Cointepas, Cyril Poupon, and Jean-François Mangin. *Accurate tractography propagation mask using T1-weighted data rather than FA*. Annual Meeting of ISMRM, Montréal, Canada, May 2011.
2. Linda Marrakchi-Kacem, Christine Delmaire, Alan Tucholka, Pauline Roca, Pamela Guevara, Sophie Lecomte, Fabrice Poupon, Jérôme Yelnik, Alexandra Durr, Jean-François Mangin, Stéphane Lehericy and Cyril Poupon. *Using surface connectivity atlases to measure striato-cortical "disconnection rate" in Huntington disease*. Annual Meeting of ISMRM, Montréal, Canada, May 2011.
3. Linda Marrakchi-Kacem, Christine Delmaire, Alan Tucholka, Pauline Roca, Pamela Guevara, Sophie Lecomte, Fabrice Poupon, Jérôme Yelnik, Alexandra Durr, Jean-François Mangin, Stéphane Lehericy and Cyril Poupon. *Distribution of the functional atrophy in the striatum territory of Huntington's patients*. Annual Meeting of ISMRM, Montréal, Canada, May 2011.
4. Pamela Guevara, Cyril Poupon, Denis Rivière, Yann Cointepas, Maxime Descoteaux, Laurent Larivière, Grégory Tournier, Pierre Fillard, Bertrand Thirion and Jean-François Mangin. *Evaluation of HARDI local diffusion models and tractography algorithms using fiber clustering*. 16th annual meeting of the Organization for Human Brain Mapping (HBM), Barcelona, Spain, June 2010.

5. Pauline Roca, Alan Tucholka, Denis Rivière, Pamela Guevara, Cyril Poupon and Jean-François Mangin. *Inter-subject Connectivity-based Parcellation of the Human Post-central Gyrus*. 16th annual meeting of the Organization for Human Brain Mapping (HBM), Barcelona, Spain, June 2010.
6. Pamela Guevara, Yann Cointepas, Denis Rivière, Cyril Poupon, Bertrand Thirion and Jean-François Mangin. *A framework for a hierarchical fiber bundle model inference using high angular resolution diffusion imaging*. 15th annual meeting of the Organization for Human Brain Mapping (HBM), San Francisco, USA, June 2009.
7. Pauline Roca, Denis Rivière, Pamela Guevara, Cyril Poupon and Jean-François Mangin. *DWI-based parcellation of the human cortex with a new dimension reduction of the connectivity matrix*. 15th annual meeting of the Organization for Human Brain Mapping (HBM), San Francisco, USA, June 2009.
8. Pamela Guevara, Muriel Perrin, Pascal Cathier, Yann Cointepas, Denis Rivière, Cyril Poupon and Jean-François Mangin. *Connectivity-based parcellation of the cortical surface using q-ball diffusion imaging*. 14th annual meeting of the Organization for Human Brain Mapping (HBM), Melbourne, Australia, June 2008.



# Bibliography

- Aganj, I., C. Lenglet, G. Sapiro, E. Yacoub, K. Ugurbil, and N. Harel: 2010, ‘Reconstruction of the orientation distribution function in single- and multiple-shell q-ball imaging within constant solid angle’. *Magn Reson Med* **64**(2), 554–566. [58]
- Alexander, A. L., K. M. Hasan, M. Lazar, J. S. Tsuruda, and D. L. Parker: 2001, ‘Analysis of partial volume effects in diffusion-tensor MRI’. *Magn Reson Med* **45**(4), 770–780. [51]
- Alexander, D. C.: 2005, ‘Maximum Entropy Spherical Deconvolution for Diffusion MRI’. In: *Image Processing in Medical Imaging*, Vol. LNCS 3565. pp. 76–87. [56]
- Alexander, D. C. and G. J. Barker: 2005, ‘Optimal imaging parameters for fiber-orientation estimation in diffusion MRI’. *Neuroimage* **27**(2), 357–367. [56]
- Anderson, A.: 2005, ‘Measurements of Fiber Orientation Distributions Using High Angular Resolution Diffusion Imaging’. *Magnetic Resonance in Medicine* **54**, 1194–1206. [54, 58]
- Aralasmak, A., J. L. Ulmer, M. Kocak, C. V. Salvan, A. E. Hillis, and D. M. Yousem: 2006, ‘Association, commissural, and projection pathways and their functional deficit reported in literature’. *J Comput Assist Tomogr* **30**(5), 695–715. [xxi, 21]
- Arsigny, V.: 2006, ‘Processing Data in Lie Groups: An Algebraic Approach. Application to Non-Linear Registration and Diffusion Tensor MRI’. Thèse de sciences (phd thesis), École Polytechnique. [xxvii, 43, 45]
- Arsigny, V., P. Fillard, X. Pennec, and N. Ayache: 2006, ‘Log-Euclidean Metrics for Fast and Simple Calculus on Diffusion Tensors’. *Magnetic Resonance in Medicine* **56**(2), 411–421. [43]
- Arsigny, V., P. Fillard, X. Pennec, and N. Ayache: 2007, ‘Geometric Means in a Novel Vector Space Structure on Symmetric Positive-Definite Matrices’. *SIAM Journal on Matrix Analysis and Applications* **29**(1), 328–347. [43]
- Ashburner, J.: 2007, ‘A fast diffeomorphic image registration algorithm’. *Neuroimage* **38**(1), 95–113. [74, 76]
- Ashburner, J., J. L. Andersson, and K. J. Friston: 1999, ‘High-dimensional image registration using symmetric priors’. *Neuroimage* **9**(6 Pt 1), 619–628. [74, 76]
- Ashburner, J. and K. J. Friston: 2000, ‘Voxel-based morphometry—the methods’. *Neuroimage* **11**(6 Pt 1), 805–821. [107]



- Assaf, Y., R. Z. Freidlin, G. K. Rohde, and P. J. Basser: 2004, ‘New Modeling and Experimental Framework to Characterize Hindered and Restrcted Water Diffusion in Brain White Matter’. *Magnetic Resonance in Medicine* **52**, 965–978. [51]
- Auzias, G., O. Colliot, J. Glaunes, M. Perrot, J.-F. Mangin, A. Trouve, and S. Baillet: 2011, ‘Diffeomorphic Brain Registration Under Exhaustive Sulcal Constraints’. *IEEE Transactions on Medical Imaging* **30**(6), 1214–1227. [lx, 183, 199, 207]
- Basser, P. J., J. Mattiello, and D. Le Bihan: 1994, ‘Estimation of the effective self-diffusion tensor from the NMR spin echo’. *J Magn Reson B* **103**(3), 247–254. [xxvii, 42]
- Basser, P. J., S. Pajevic, C. Pierpaoli, J. Duda, and A. Aldroubi: 2000, ‘In vivo fiber tractography using DT-MRI data’. *Magn Reson Med* **44**(4), 625–632. [xxix, 60, 61, 78]
- Basser, P. J. and C. Pierpaoli: 1995, ‘Inferring microstructural features and the physiological state of tissues from diffusion-weighted images’. *NMR Biomed* **8**(7-8), 333–344. [44]
- Batchelor, P. G., F. Calamante, J.-D. Tournier, D. Atkinson, D. L. G. Hill, and A. Connelly: 2006, ‘Quantification of the shape of fiber tracts’. *Magn Reson Med* **55**(4), 894–903. [88]
- Bazin, P.-L., J. Bogovic, D. Reich, J. L. Prince, and D. L. Pham: 2009, ‘Belief Propagation Based Segmentation of White Matter Tracts in DTI’. In: *MICCAI 2009, LNCS 5762, Springer-Verlag*. [xxxi, 117]
- Beaulieu, C.: 2002, ‘The basis of anisotropic water diffusion in the nervous system - a technical review’. *NMR in Biomedicine* **15**, 435–455. [46]
- Behrens, T. E., H. J. Berg, S. Jbabdi, M. F. Rushworth, and M. W. Woolrich: 2007, ‘Probabilistic diffusion tractography with multiple fibre orientations: What can we gain?’. *Neuroimage* **34**(1), 144–155. [49, 51, 66]
- Behrens, T. E. J., M. W. Woolrich, M. Jenkinson, H. Johansen-Berg, R. G. Nunes, S. Clare, P. M. Matthews, J. M. Brady, and S. M. Smith: 2003, ‘Characterization and propagation of uncertainty in diffusion-weighted MR imaging’. *Magn Reson Med* **50**(5), 1077–1088. [xxviii, 51]
- Bergmann, Ø., G. Kindlmann, S. Peled, and C.-F. Westin: 2007, ‘TWO-TENSOR FIBER TRACTOGRAPHY’. In: *4th International Symposium on Biomedical Imaging*. Arlington, Virginia, USA, pp. 796–799. [63]
- Beucher, S.: 1994, ‘Watershed, hierarchical segmentation and waterfall algorithm’. In: J. Serra and P. Soille (eds.): *Proc. Mathematical Morphology and its Applications to Image Processing*. Fontainebleau, pp. 69–76, Kluwer Ac. Publ. [132]
- Beucher, S. and C. Lantuéjoul.: 1979, ‘Use of watersheds in contour detection’. In: *Int. Workshop on Image Processing*. Rennes, France. [131]
- Beucher, S. and F. Meyer: 1992, *Mathematical Morphology in Image Processing*, Chapt. The Morphological approach of segmentation: the watershed transformation, pp. 433–481. Marcel Dekker. [132]
- Blei, D. M., A. Y. Ng, M. I. Jordan, and J. Lafferty: 2003, ‘Latent Dirichlet allocation’. *Journal of Machine Learning Research* **3**, 993–1022. [xxxii, 86]

- Brown, R.: 1828, ‘A brief account of microscopical observations made in the months of June, July and August, 1827, on the particles contained in the pollen of plants; and on the general existence of active molecules in organic and inorganic bodies’. *Phil. Mag.* **4**, 161–173. [xxiv, 30]
- Brun, A., H. jeong Park, H. Knutsson, and C. fredrik Westin: 2003, ‘Coloring of DT-MRI fiber traces using Laplacian eigenmaps’. In: *In EUROCAST*. pp. 564–572. [xxxiv, 94, 101]
- Brun, A., H. Knutsson, H. jeong Park, M. E. Shenton, and C. fredrik Westin: 2004, ‘Clustering fiber traces using normalized cuts’. In: *MICCAI 2004, LNCS 5762, Springer-Verlag*. pp. 368–375. [xxxi, xxxiv, 94, 101, 118]
- Cachia, A., J.-F. Mangin, D. Rivière, et al.: 2003, ‘A generic framework for parcellation of the cortical surface into gyri using geodesic Voronoï diagrams’. *Med. Image Anal.* **7**(4), 403–416. [1, 178]
- Callaghan, P. T.: 1991, *Principles of nuclear magnetic resonance microscopy*. Oxford: Oxford University Press. [38, 52]
- Campbell, J.: 2004, ‘Diffusion Imaging of White Matter Fibre Tracts’. Ph.D. thesis, McGill University, Montreal, Canada. [30, 43]
- Catani, M., M. P. G. Allin, M. Husain, L. Pugliese, M. M. Mesulam, R. M. Murray, and D. K. Jones: 2007, ‘Symmetries in human brain language pathways correlate with verbal recall’. *Proc Natl Acad Sci U S A* **104**(43), 17163–17168. [liv, 25, 193]
- Catani, M., R. J. Howard, S. Pajevic, and D. K. Jones: 2002, ‘Virtual in vivo interactive dissection of white matter fasciculi in the human brain’. *Neuroimage* **17**(1), 77–94. [xlv, 78, 163]
- Catani, M., D. K. Jones, and D. H. ffytche: 2005, ‘Perisylvian language networks of the human brain’. *Ann Neurol* **57**(1), 8–16. [xlili, xlv, 23, 156, 157, 163, 183, 198]
- Catani, M. and M. Mesulam: 2008, ‘The arcuate fasciculus and the disconnection theme in language and aphasia: history and current state’. *Cortex* **44**(8), 953–961. [24, 25]
- Catani, M. and M. Thiebaut de Schotten: 2008, ‘A diffusion tensor imaging tractography atlas for virtual in vivo dissections’. *Cortex* **44**(8), 1105–1132. [xxi, xxiii, xxx, xlv, xlviii, lvi, 12, 21, 23, 78, 117, 138, 163, 175, 183, 193, 198, 211]
- Ceritoglu, C., K. Oishi, X. Li, M.-C. Chou, L. Younes, M. Albert, C. Lyketsos, P. C. van Zijl, M. I. Miller, and S. Mori: 2009, ‘Multi-contrast large deformation diffeomorphic metric mapping for diffusion tensor imaging’. *NeuroImage* **47**(2), 618 – 627. [80, 215]
- Chao, Y.-P., J.-H. Chen, K.-H. Cho, C.-H. Yeh, K.-H. Chou, and C.-P. Lin: 2008, ‘A multiple streamline approach to high angular resolution diffusion tractography’. *Med Eng Phys* **30**(8), 989–996. [64, 66]
- Chen, Y., W. Guo, Q. Zeng, X. Yan, F. Huang, H. Zhang, G. He, B. Vemuri, and Y. Liu: 2004, ‘Estimation, Smoothing, and Characterization of Apparent Diffusion Coefficient Profiles From High Angular Resolution DWI’. In: *Computer Vision and Pattern Recognition*, Vol. 1. pp. 588–593. [51]
- Cheng, Y.: 1995, ‘Mean shift, mode seeking, and clustering’. *IEEE Trans. on Pattern Analysis and Machine Intelligence* **17**(8), 790–799. [87]

- Christensen, G. E., R. D. Rabbitt, and M. I. Miller: 1996, ‘Deformable templates using large deformation kinematics’. *IEEE Trans Image Process* **5**(10), 1435–1447. [74]
- Cointepas, Y., C. Poupon, and J.-F. Mangin: 2002, ‘A spin glass based framework to reconstruct brain fiber bundles from images of the water diffusion process’. *Information Processes* **2**(1), 30–36. [68]
- Collins, D. L. and A. C. Evans: 1997, ‘Animal: Validation and Applications of Nonlinear Registration-Based Segmentation’. *IJPRAI* **11**(8), 1271–1294. [76]
- Collins, L. D., C. J. Holmes, T. M. Peters, and A. C. Evans: 1995, ‘Automatic 3-D model-based neuroanatomical segmentation’. *Hum Brain Mapp* **3**(3), 190–208. [73]
- Conturo, T. E., N. F. Lori, T. S. Cull, E. Akbudak, A. Z. Snyder, J. S. Shimony, R. C. McKinstry, H. Burton, and M. E. Raichle: 1999, ‘Tracking neuronal fiber pathways in the living human brain’. *Proc Natl Acad Sci U S A* **96**(18), 10422–10427. [60, 61, 78]
- Corouge, I., P. Fletcher, S. Joshi, S. Gouttard, and G. Gerig: 2006, ‘Fiber tract-oriented statistics for quantitative diffusion tensor MRI analysis’. *Medical Image Analysis* **10**, 786–798. [88, 107, 110]
- Corouge, I., S. Gouttard, and G. Gerig: 2004, ‘Towards a shape model of white matter fiber bundles using diffusion tensor MRI’. In: *ISBI 2004*. [xxxi, xxxii, xxxiv, xl, xlv, xlvi, 88, 89, 94, 97, 101, 104, 118, 133, 134, 165, 166]
- Crum, W. R., T. Hartkens, and D. L. G. Hill: 2004, ‘Non-rigid image registration: theory and practice’. *Br J Radiol* **77 Spec No 2**, S140–S153. [73, 74]
- Dempster, A. P., N. M. Laird, and D. B. Rubin: 1977, ‘Maximum Likelihood from Incomplete Data via the EM Algorithm’. *Journal of the Royal Statistical Society* **39**, 1–38. [86]
- Descoteaux, M.: 2008, ‘High Angular Resolution Diffusion MRI: From Local Estimation to Segmentation and Tractography’. Ph.D. thesis, Universite de Nice - Sophia Antipoli. [xxvi, 12, 30, 36, 50, 55, 56, 57, 58]
- Descoteaux, M., E. Angelino, S. Fitzgibbons, and R. Deriche: 2007, ‘Regularized, Fast and Robust Analytical Q-Ball Imaging’. *Magn. Reson. Med.* **58**, 497–510. [xxviii, xlii, liv, 54, 55, 77, 146, 153, 191]
- Descoteaux, M. and R. Deriche: 2009, ‘High Angular Resolution Diffusion MRI Segmentation Using Region-Based Statistical Surface Evolution’. *Journal of Mathematical Imaging and Vision* **33**(2), 239–252. [77]
- Descoteaux, M., R. Deriche, D. L. Bihan, J.-F. Mangin, and C. Poupon: 2009a, ‘Diffusion propagator imaging: using Laplace’s equation and multiple shell acquisitions to reconstruct the diffusion propagator’. *Inf Process Med Imaging* **21**, 1–13. [58]
- Descoteaux, M., R. Deriche, T. R. Knösche, and A. Anwender: 2009b, ‘Deterministic and Probabilistic Tractography Based on Complex Fibre Orientation Distributions’. *IEEE Transactions in Medical Imaging* **28**(2), 269–286. [xxix, xxx, xli, xlii, 57, 63, 64, 65, 148, 153]

- Descoteaux, M., N. Wiest-Daesslé, S. Prima, C. Barillot, and R. Deriche: 2008, ‘Impact of Rician Adapted Non-Local Means Filtering on HARDI’. In: *MICCAI 2008, LNCS 5762, Springer-Verlag*. Springer-Verlag. [148, 151]
- Ding, Z., J. Gore, and A. Anderson: 2003, ‘Classification and Quantification of Neuronal Fiber Pathways Using Diffusion Tensor MRI’. *Magnetic Resonance in Medicine* **49**, 716–721. [xxxi, xxxiv, 80, 88, 94, 97, 118]
- Dubois, J., G. Dehaene-Lambertz, M. Perrin, J.-F. Mangin, Y. Cointepas, E. Duchesnay, D. Le Bihan, and L. Hertz-Pannier: 2008, ‘Asynchrony of the early maturation of white matter bundles in healthy infants: quantitative landmarks revealed noninvasively by diffusion tensor imaging’. *Hum. Brain Mapp.* **29**(1), 14–27. [47]
- Dubois, J., L. Hertz-Pannier, G. Dehaene-Lambertz, Y. Cointepas, and D. L. Bihan: 2006, ‘Assessment of the early organization and maturation of infants’ cerebral white matter fiber bundles: a feasibility study using quantitative diffusion tensor imaging and tractography’. *Neuroimage* **30**(4), 1121–1132. [47]
- Duclap, D.: 2010, ‘Optimisation et création de l’interface graphique de la classification multi-résolution de fibres calculées à partir d’IRM de diffusion à haute résolution angulaire’. Master’s thesis, Institut Supérieur des BioSciences de Paris. [145]
- Duda, R., P. Hart, and D. Stork: 2001, *Pattern classification*. Wiley-Interscience. [87]
- Durrleman, S., P. Fillard, X. Pennec, A. Trounev, and N. Ayache: 2009, ‘A Statistical Model of White Matter Fiber Bundles based on Currents’. In: *Proc. 21th IPMI*. Williamsburg, VA, pp. 114–125, Springer. [lx, 183, 207]
- Einstein, A.: 1956, *Investigations on the Theory of the Brownian Movement*. Dover Pubns. [xxiv, 31]
- El Kouby, V., Y. Cointepas, C. Poupon, D. Rivière, N. Golestani, J. B. Poline, D. Le Bihan, and J.-F. Mangin: 2005, ‘MR diffusion-based inference of a fiber bundle model from a population of subjects’. In: *MICCAI 2005, LNCS 5762, Springer-Verlag*, Vol. 8. pp. 196–204. [xxxi, xxxiii, xxxv, xxxvii, 95, 98, 99, 117, 119, 120]
- Fick, A.: 1855, ‘On liquid diffusion’. *Philos. Mag. J. Sci.* **10**, 31–39. [31]
- Fiedler, M.: 1975, ‘A property of eigenvectors of nonnegative symmetric matrices and its application to graph theory’. *Czechoslovak Mathematical Journal* **25**, 619–633. [87]
- Fillard, P., X. Pennec, V. Arsigny, and N. Ayache: 2007, ‘Clinical DT-MRI Estimation, Smoothing and Fiber Tracking with Log-Euclidean Metrics’. *IEEE Transactions on Medical Imaging* **26**(11), 1472–1482. PMID: 18041263. [43]
- Fillard, P., C. Poupon, and J.-F. Mangin: 2009, ‘A Novel Global Tractography Framework based on an Adaptive Spin Glass Model’. In: *MICCAI 2009, LNCS 5762, Springer-Verlag*. [67, 68]
- Flandin, G., F. Kherif, X. Pennec, G. Malandain, N. Ayache, and J.-B. Poline: 2002, ‘Improved detection sensitivity of functional MRI data using a brain parcellation technique’. In: *Proc. 5th MICCAI*. Tokyo, Japan, pp. 467–474, Springer Verlag. [xxxix, 124, 125]

- Fowlkes, C., S. Belongie, F. Chung, and J. Malik: 2004, ‘Spectral grouping using the Nystrom method’. *IEEE Trans. Pattern Anal. Mach. Intell.* **26**(2), 214–225. [101]
- Friston, K. J., J. Ashburner, C. D. Frith, J.-B. Poline, J. D. Heather, and R. S. J. Frackowiak: 1995, ‘Spatial registration and normalization of images’. *Hum. Brain Mapp.* **3**(3), 165–189. [73]
- Gerig, G., S. Gouttard, and I. Corouge: 2004, ‘Analysis of Brain White Matter via Fiber Tract Modeling’. In: *IEEE EMBS 2004*. [xxxi, xxxiv, 88, 94, 97, 118]
- Gholipour, A., N. Kehtarnavaz, R. Briggs, M. Devous, and K. Gopinath: 2007, ‘Brain functional localization: a survey of image registration techniques’. *IEEE Trans Med Imaging* **26**(4), 427–451. [74, 76]
- Gigandet, X.: 2009, ‘Global Brain Connectivity Analysis by Diffusion MR Tractography: Algorithms, Validation and Applications’. Ph.D. thesis, Ecole Polytechnique Fédérale de Lausanne, Laussane, Switzerland. [52]
- Goodlett, C. B., P. T. Fletcher, J. H. Gilmore, and G. Gerig: 2009, ‘Group analysis of DTI fiber tract statistics with application to neurodevelopment’. *Neuroimage* **45**(1 Suppl), S133–S142. [109]
- Gray, H.: 1918, *Anatomy of the human body*. Philadelphia: Lea & Febiger, 1918. NEW YORK: BARTLEBY.COM, 2000. [12, 26]
- Guevara, P., Y. Cointepas, D. Rivière, C. Poupon, B. Thirion, and J.-F. Mangin: 2009, ‘Inference of a fiber bundle atlas using a two-level clustering strategy’. In: *Proceedings of DMFC Workshop at MICCAI*. [174]
- Guevara, P., D. Duclap, L. Marrakchi-Kacem, D. Rivière, Y. Cointepas, C. Poupon, and J.-F. Mangin: 2011a, ‘Accurate tractography propagation mask using T1-weighted data rather than FA’. In: *ISMRM conference*. [145]
- Guevara, P., C. Poupon, D. Rivière, Y. Cointepas, M. Descoteaux, B. Thirion, and J.-F. Mangin: 2011b, ‘Robust clustering of massive tractography datasets’. *NeuroImage* **54**(3), 1975–1993. [61]
- Guevara, P., C. Poupon, D. Rivière, Y. Cointepas, L. Marrakchi, M. Descoteaux, P. Fillard, B. Thirion, and J.-F. Mangin: 2010, ‘Inference of a HARDI Fiber Bundle Atlas Using a Two-Level Clustering Strategy’. In: *MICCAI 2010*, Vol. LNCS 6361. pp. 550–557, Springer-Verlag. [118, 153, 158, 174]
- Hagen, L. and A. B. Kahng: 1992, ‘New spectral methods for ratio cut partitioning and clustering’. *IEEE Trans. Computer-Aided Design* **11**(9), 1074–1085. [87]
- Hagmann, P., L. Cammoun, X. Gigandet, S. Gerhard, P. E. Grant, V. Wedeen, R. Meuli, J.-P. Thiran, C. J. Honey, and O. Sporns: 2010, ‘MR connectomics: Principles and challenges’. *J Neurosci Methods* **194**(1), 34–45. [53]
- Hagmann, P., L. Jonasson, T. Deffieux, R. Meuli, J.-P. Thiran, and V. J. Wedeen: 2006, ‘Fibertract segmentation in position orientation space from high angular resolution diffusion MRI’. *Neuroimage* **32**(2), 665–675. [77]
- Hasboun, D.: 2007, ‘Cours de Neuroanatomie Fonctionnelle’. Faculté de Médecine Pitié Salpêtrière, Université Pierre et Marie Curie. [xix, 14, 25]

- Hellier, P., C. Barillot, I. Corouge, B. Gibaud, G. L. Goualher, D. L. Collins, A. Evans, G. Ma-landain, N. Ayache, G. E. Christensen, and H. J. Johnson: 2003, ‘Retrospective evaluation of intersubject brain registration’. *IEEE Trans Med Imaging* **22**(9), 1120–1130. [74]
- Hess, C., P. Mukherjee, E. Han, D. Xu, and D. Vigneron: 2006, ‘Q-Ball Reconstruction of Multi-modal Fiber Orientations Using The Spherical Harmonic Basis’. *Magnetic Resonance in Medicine* **56**, 104–117. [54]
- Hosey, T., G. Williams, and R. Ansorge: 2005, ‘Inference of Multiple Fiber Orientation in High Angular Resolution Diffusion Imaging’. *Magnetic Resonance in Medicine* **54**, 1480–1489. [66]
- Hua, K., J. Zhang, S. Wakana, H. Jiang, X. Li, D. Reich, P. Calabresi, J. Pekar, P. van Zijl, and S. Mori: 2008, ‘Tract probability maps in stereotaxic spaces: Analyses of white matter anatomy and tract-specific quantification’. *NeuroImage* **39**, 336–347. [xxx, 78, 105, 117, 212, 213]
- Huang, H., C. Ceritoglu, X. Li, A. Qiu, M. I. Miller, P. C. M. van Zijl, and S. Mori: 2008, ‘Correction of B0 susceptibility induced distortion in diffusion-weighted images using large-deformation diffeomorphic metric mapping’. *Magn Reson Imaging* **26**(9), 1294–1302. [76, 79]
- Hüppi, P. S. and J. Dubois: 2010, ‘Diffusion tensor imaging of brain development’. *Seminars in Fetal and Neonatal Medicine* **11**, 489–497. [47]
- J. S. W. Campbell, P. Savadjiev, K. S. and G. Pike: 2006, ‘Validation and Regularization in Diffusion MRI Tractography’. In: *ISBI 2006*. pp. 351–354. [62]
- Jain, A. K.: 2010, ‘Data clustering: 50 years beyond K-means’. *Pattern Recognition Letters* **31**(8), 651–666. [xxxi, xxxii, 72, 81, 82, 85, 87]
- Jain, A. K. and R. C. Dubes: 1988, *Algorithms for Clustering Data*. Prentice Hall College Div. [xxxi, 81]
- Jbabdi, S., P. Bellec, G. Marrelec, V. Perlberg, and H. Benali.: 2004, ‘A level set method for building anatomical connectivity paths between brain areas using DTI.’. In: *ISBI 2004*. pp. 1024–1027. [67]
- Jbabdi, S., P. Bellec, R. Toro, J. Daunizeau, M. Pèlègrini-Issac, and H. Benali: 2008, ‘Accurate anisotropic fast marching for diffusion-based geodesic tractography’. *Journal of Biomedical Imaging* **2008**. [67]
- Jbabdi, S., M. W. Woolrich, J. L. R. Andersson, and T. E. J. Behrens: 2007, ‘A Bayesian framework for global tractography’. *Neuroimage* **37**(1), 116–129. [66]
- Jellison, B. J., A. S. Field, J. Medow, M. Lazar, M. S. Salamat, and A. L. Alexander: 2004, ‘Diffusion tensor imaging of cerebral white matter: a pictorial review of physics, fiber tract anatomy, and tumor imaging patterns’. *AJNR Am J Neuroradiol* **25**(3), 356–369. [xxi, 21, 22]
- Jezzard, P., A. S. Barnett, and C. Pierpaoli: 1998, ‘Characterization of and correction for eddy current artifacts in echo planar diffusion imaging’. *Magn Reson Med* **5**, 801–812. [39]
- Johansen-Berg, H. and T. E. Behrens: 2009, *Diffusion MRI: From Quantitative Measurement to In-vivo Neuroanatomy*. Academic Press. [xxvii, 12, 18, 20, 30, 34, 35, 39, 44, 45, 46, 52, 53, 57, 72, 73, 105, 106, 107, 109]



- Johnson, S. C.: 1967, ‘Hierarchical clustering schemes’. *Psychometrika* **32**, 241–254. [xxxii, 83, 127]
- Jonasson, L., X. Bresson, P. Hagmann, O. Cuisenaire, R. Meuli, and J.-P. Thiran: 2005a, ‘White matter fiber tract segmentation in DT-MRI using geometric flows’. *Medical Image Analysis* **9**, 223–236. [30, 77]
- Jonasson, L., X. Bresson, J.-P. Thiran, V. J. Wedeen, and P. Hagmann: 2007, ‘Representing diffusion MRI in 5-D simplifies regularization and segmentation of white matter tracts’. *IEEE Trans Med Imaging* **26**(11), 1547–1554. [77]
- Jonasson, L., P. Hagmann, J. Thiran, and V. Wedeen: 2005b, ‘Fiber tracts of high angular resolution diffusion MRI are easily segmented with spectral clustering.’. In: *13th Annual Meeting ISMRM, Miami*. [88]
- Jones, D. K.: 2008, ‘Studying connections in the living human brain with diffusion MRI’. *Cortex* **44**(8), 936–952. [30, 31, 48]
- Jones, D. K., M. Catani, C. Pierpaoli, S. J. C. Reeves, S. S. Shergill, M. O’Sullivan, P. Golesworthy, P. McGuire, M. A. Horsfield, A. Simmons, S. C. R. Williams, and R. J. Howard: 2006, ‘Age effects on diffusion tensor magnetic resonance imaging tractography measures of frontal cortex connections in schizophrenia’. *Hum Brain Mapp* **27**(3), 230–238. [105, 159]
- Kaden, E., T. R. Knosche, and A. Anwander: 2007, ‘Parametric spherical deconvolution: Inferring anatomical connectivity using diffusion MR imaging’. *NeuroImage* **37**, 474–488. [66]
- Kandel, E. R. and J. H. Schwartz: 1985, *Principles of neural science*. Elsevier Science Publishing Co., Inc., second edition. [12, 13, 24]
- Kaski, S.: 1997, ‘Data exploration using self-organizing maps’. Ph.D. thesis, Helsinki University of Technology. [85]
- Kindlmann, G., X. Tricoche, and C.-F. Westin: 2007, ‘Delineating white matter structure in diffusion tensor MRI with anisotropy creases’. *Med Image Anal* **11**(5), 492–502. [107]
- Klein, A., J. Andersson, B. A. Ardekani, J. Ashburner, B. Avants, M.-C. Chiang, G. E. Christensen, D. L. Collins, J. Gee, P. Hellier, J. H. Song, M. Jenkinson, C. Lepage, D. Rueckert, P. Thompson, T. Vercauteren, R. P. Woods, J. J. Mann, and R. V. Parsey: 2009, ‘Evaluation of 14 nonlinear deformation algorithms applied to human brain MRI registration’. *Neuroimage* **46**(3), 786–802. [76]
- Kreher, B. W., S. Schnell, I. Mader, K. A. Il’yasov, J. Hennig, V. G. Kiselev, and D. Saur: 2008, ‘Connecting and merging fibres: pathway extraction by combining probability maps’. *Neuroimage* **43**(1), 81–89. [68]
- Kubicki, M., C.-F. Westin, P. G. Nestor, C. G. Wible, M. Frumin, S. E. Maier, R. Kikinis, F. A. Jolesz, R. W. McCarley, and M. E. Shenton: 2003, ‘Cingulate fasciculus integrity disruption in schizophrenia: a magnetic resonance diffusion tensor imaging study’. *Biol Psychiatry* **54**(11), 1171–1180. [105]
- Lancaster, J. L., D. Tordesillas-Gutiérrez, M. Martínez, F. Salinas, A. Evans, K. Zilles, J. C. Mazziotta, and P. T. Fox: 2007, ‘Bias between MNI and Talairach coordinates analyzed using the ICBM-152 brain template’. *Hum Brain Mapp* **28**(11), 1194–1205. [75]

- Lawes, I. N. C., T. R. Barrick, V. Murugam, N. Spierings, D. R. Evans, M. Song, and C. A. Clark: 2008, ‘Atlas-based segmentation of white matter tracts of the human brain using diffusion tensor tractography and comparison with classical dissection’. *Neuroimage* **39**(1), 62–79. [xxx, xlv, 117, 163, 212]
- Lazar, M. and A. L. Alexander: 2003, ‘An error analysis of white matter tractography methods: synthetic diffusion tensor field simulations.’. *Neuroimage* **20**(2), 1140–1153. [60]
- Lazar, M., D. Weinstein, J. Tsuruda, K. Hasan, K. Arfanakis, M. Meyerand, B. Badie, H. Rowley, V. Haughton, A. Field, and A. Alexander: 2003, ‘White Matter Tractography Using Diffusion Tensor Deflection’. In: *Human Brain Mapping*, Vol. 18. pp. 306–321. [62]
- Le Bihan, D.: 1995, *Diffusion and Perfusion Magnetic Resonance Imaging: Applications to Functional MRI*. Raven Press. [40]
- Le Bihan, D.: 2003, ‘Looking into the functional architecture of the brain with diffusion MRI’. *Nat Rev Neurosci* **4**(6), 469–480. [30]
- Le Bihan, D.: 2007, ‘The ‘wet mind’: water and functional neuroimaging’. *Phys Med Biol* **52**(7), R57–R90. [41]
- Le Bihan, D., E. Breton, D. Lallemand, et al.: 1986, ‘MR imaging of intravoxel incoherent motions: application to diffusion and perfusion in neurologic disorders’. *Radiology* **161**(2), 401–407. [xxiv, xxvi, 32, 37]
- Leemans, A., J. Sijbers, S. D. Backer, E. Vandervliet, and P. Parizel: 2006, ‘Multiscale white matter fiber tract coregistration: a new feature-based approach to align diffusion tensor data’. *Magn Reson Med* **55**(6), 1414–1423. [88]
- Lenglet, C.: 2006, ‘Geometric and Variational Methods for Diffusion Tensor MRI Processing’. Ph.D. thesis, Université de Nice-Sophia Antipolis. [67]
- Lenglet, C., R. Deriche, and O. Faugeras: 2004, ‘Inferring white matter geometry from diffusion tensor MRI: Application to connectivity mapping’. In: *ECCV 2004, PT 4, Proceedings of*. pp. 127–140, SpringerVerlag. [67]
- Lenglet, C., M. Rousson, and R. Deriche: 2006, ‘DTI segmentation by statistical surface evolution’. *IEEE Trans. Medical Imaging* **25**(6), 685–700. [77]
- Li, H., Z. Xue, L. Guo, T. Liu, J. Hunter, and S. T. C. Wong: 2010, ‘A hybrid approach to automatic clustering of white matter fibers’. *Neuroimage* **49**(2), 1249–1258. [xxxi, xxxii, xxxvi, 96, 104, 118, 163]
- Lyu, I., J.-K. Seong, S. Y. Shin, K. Im, J. H. Roh, M.-J. Kim, G. H. Kim, J. H. Kim, A. C. Evans, D. L. Na, and J.-M. Lee: 2010, ‘Spectral-based automatic labeling and refining of human cortical sulcal curves using expert-provided examples’. *Neuroimage* **52**(1), 142–157. [183, 188]
- MacQueen, J. B.: 1967, ‘Some Methods for Classification and Analysis of Multivariate Observations’. In: *Proceedings of 5th Berkeley Symposium on Mathematical Statistics and Probability*. pp. 281–297. [xxxi, 86]

- Maddah, M., A.U.Mewes, S. Haker, W. Grimson, and S. Warfield: 2005, ‘Automated Atlas-Based Clustering of White Matter Fiber Tracts from DTMRI’. In: *MICCAI 2005, LNCS 5762*, Springer-Verlag. [xxxi, xxxii, xxxv, xlv, 78, 95, 101, 118, 163, 211]
- Maddah, M., W. Grimson, S. Warfield, and W. Wells: 2008a, ‘A Unified Framework for Clustering and Quantitative Analysis of White Matter Fiber Tracts’. *Medical Image Analysis* **12**(2), 191–202. [xxxii, xxxvi, 96, 101, 107, 108, 110, 118]
- Maddah, M., W. Wells, S. Warfield, C.-F. Westin, and W. Grimson: 2007a, ‘Probabilistic Clustering and Quantitative Analysis of White Matter Fiber Tracts’. In: *IPMI 2007*. [xxxv, 95, 101]
- Maddah, M., W. Wells, S. Warfield, C.-F. Westin, and W. Grimson: 2007b, ‘A Spatial Model of White Matter Fiber Tracts’. In: *ISRMN 2007*. [xxxii, 118]
- Maddah, M., L. Zollei, W. Grimson, C.-F. Westin, and W. Wells: 2008b, ‘A Mathematical Framework for Incorporating Anatomical Knowledge in DT-MRI Analysis’. In: *ISBI 2008*. [xxxv, 88, 95, 102]
- Maes, F., A. Collignon, D. Vandermeulen, G. Marchal, and P. Suetens: 1997, ‘Multimodality image registration by maximization of mutual information’. *IEEE Trans Med Imaging* **16**(2), 187–198. [74]
- Mangin, J.-F., J. Regis, and V. Frouin: 1996, ‘Shape Bottlenecks and Conservative Flow Systems’. In: *IEEE Workshop on Mathematical Methods in Biomedical Image Analysis (MMBIA ’96)*. San Francisco, CA, USA, pp. 319–328, IEEE Computer Society. [122]
- Mansfield, P.: 1977, ‘Multi-Planar Image Formation using NMR Spin Echoes’. *Journal of Physics C* **10**, 55–58. [xxvi, 38]
- Marrakchi-Kacem, L., C. Delmaire, A. Tucholka, P. Roca, P. Guevara, F. Poupon, J. Yelnik, A. Durr, J.-F. Mangin, S. Lehericy, and C. Poupon: 2010a, ‘Analysis of the Striato-Thalamo-Cortical Connectivity on the Cortical Surface to Infer Biomarkers of Huntington’s Disease’. In: *MICCAI 2010*, Vol. LNCS 6362. pp. 217–224, Springer-Verlag. [148]
- Marrakchi-Kacem, L., C. Poupon, E. Jouvent, I. Rekik, J.-F. Mangin, and F. Poupon: 2010b, ‘Robust Automatic Segmentation of Ventricles : Application to a Genetic Small Vessel Disease, CADASIL’. In: *HBM 2010*. Barcelona, Spain. [145]
- Marrakchi-Kacem, L., C. Poupon, J.-F. Mangin, and F. Poupon: 2010c, ‘Multi-contrast deep nuclei segmentation using a probabilistic atlas’. In: *Proc. IEEE Int Biomedical Imaging: From Nano to Macro Symp*. pp. 61–64. [145, 165]
- Mazziotta, J., A. Toga, A. Evans, P. Fox, J. Lancaster, K. Zilles, R. Woods, T. Paus, G. Simpson, B. Pike, C. Holmes, L. Collins, P. Thompson, D. MacDonald, M. Iacoboni, T. Schormann, K. Amunts, N. Palomero-Gallagher, S. Geyer, L. Parsons, K. Narr, N. Kabani, G. L. Gualther, D. Boomsma, T. Cannon, R. Kawashima, and B. Mazoyer: 2001, ‘A probabilistic atlas and reference system for the human brain: International Consortium for Brain Mapping (ICBM)’. *Philos Trans R Soc Lond B Biol Sci* **356**(1412), 1293–1322. [76, 212, 213]
- Mazziotta, J. C., A. W. Toga, A. Evans, P. Fox, and J. Lancaster: 1995, ‘A probabilistic atlas of the human brain: theory and rationale for its development. The International Consortium for Brain Mapping (ICBM)’. *Neuroimage* **2**(2), 89–101. [76]

- McGraw, T., B. Vemuri, R. Yezierski, and T. Mareci: 2006, 'Segmentation of High Angular Resolution Diffusion MRI Modeled as a Field of von Mises-Fisher Mixtures'. In: *European Conference on Computer Vision (ECCV)*, Vol. 3953. pp. 463–475. [77]
- Melie-García, L., E. J. Canales-Rodríguez, Y. Alemán-Gómez, C.-P. Lin, Y. Iturria-Medina, and P. A. Valdés-Hernández: 2008, 'A Bayesian framework to identify principal intravoxel diffusion profiles based on diffusion-weighted MR imaging'. *Neuroimage* **42**(2), 750–770. [66]
- Miller, M. I., M. F. Beg, C. Ceritoglu, and C. Stark: 2005, 'Increasing the power of functional maps of the medial temporal lobe by using large deformation diffeomorphic metric mapping'. *Proc Natl Acad Sci U S A* **102**(27), 9685–9690. [76, 79]
- Miranda, M. I.: 1999, 'Clustering Methods and Algorithms'. [85]
- Moberts, B., A. Vilanova, and J. J. van Wijk: 2005, 'Evaluation of fiber clustering methods for diffusion tensor imaging'. In: *Proc. IEEE Visualization VIS 05*. pp. 65–72. [72, 80]
- Mori, S., B. J. Crain, V. P. Chacko, and P. C. van Zijl: 1999, 'Three-dimensional tracking of axonal projections in the brain by magnetic resonance imaging'. *Ann Neurol* **45**(2), 265–269. [60, 61]
- Mori, S., W. E. Kaufmann, C. Davatzikos, B. Stieltjes, L. Amodi, K. Fredericksen, G. D. Pearlson, E. R. Melhem, M. Solaiyappan, G. V. Raymond, H. W. Moser, and P. C. M. van Zijl: 2002, 'Imaging cortical association tracts in the human brain using diffusion-tensor-based axonal tracking'. *Magn Reson Med* **47**(2), 215–223. [60]
- Mori, S., W. E. Kaufmann, G. D. Pearlson, B. J. Crain, B. Stieltjes, M. Solaiyappan, and P. C. van Zijl: 2000, 'In vivo visualization of human neural pathways by magnetic resonance imaging'. *Ann Neurol* **47**(3), 412–414. [78]
- Mori, S., K. Oishi, H. Jiang, L. Jiang, X. Li, K. Akhter, K. Hua, A. V. Faria, A. Mahmood, R. Woods, A. W. Toga, G. B. Pike, P. R. Neto, A. Evans, J. Zhang, H. Huang, M. I. Miller, P. van Zijl, and J. Mazziotta: 2008, 'Stereotaxic white matter atlas based on diffusion tensor imaging in an ICBM template'. *Neuroimage* **40**(2), 570–582. [78, 213, 214, 215]
- Mori, S., S. Wakana, P. C. M. van Zijl, and L. M. Nagae-Poetscher: 2005, *MRI Atlas of Human White Matter, First Edition*. Elsevier Science. [xxx, xlv, 77, 78, 117, 163, 213]
- Morris, D. M., K. V. Embleton, and G. J. M. Parker: 2008, 'Probabilistic fibre tracking: differentiation of connections from chance events'. *Neuroimage* **42**(4), 1329–1339. [66]
- Neuman, C. H.: 1974, 'Spin echo of spins diffusing in a bounded medium'. *Journal of Chemical Physics* **60**(11), 4508–4511. [51]
- Niendorf, T., R. M. Dijkhuizen, D. G. Norris, M. van Lookeren Campagne, and K. Nicolay: 1996, 'Biexponential diffusion attenuation in various states of brain tissue: implications for diffusion-weighted imaging'. *Magn Reson Med* **36**(6), 847–857. [40]
- O'Donnell, L.: 2006, 'Cerebral White Matter Analysis Using Diffusion Imaging'. Ph.D. thesis, Harvard-MIT Division of Health Sciences and Technology, France. [xxxv, 12, 15, 72, 89, 95, 101, 102]

- O'Donnell, L., S. Haker, and C.-F. Westin: 2002, 'New Approaches to Estimation of White Matter Connectivity in Diffusion Tensor MRI: Elliptic PDEs and Geodesics in a Tensor-Warped Space'. In: *MICCAI 2002, LNCS 5762, Springer-Verlag*. Tokyo, Japan, pp. 459–466. [67]
- O'Donnell, L. and C.-F. Westin: 2005, 'White Matter Tract Clustering and Correspondence in Populations'. In: *MICCAI 2005, LNCS 5762, Springer-Verlag*. Palm Springs, CA, USA, pp. 140–147. [xxxv, 89, 95, 101, 102]
- O'Donnell, L. and C.-F. Westin: 2006, 'High-Dimensional White Matter Atlas Generation and Group Analysis'. In: *MICCAI 2006, LNCS 5762, Springer-Verlag*. Copenhagen, Denmark, pp. 243–251. [xxxv, 95, 101, 102, 211]
- O'Donnell, L. and C.-F. Westin: 2007, 'Automatic Tractography Segmentation Using a High-Dimensional White Matter Atlas'. *IEEE Transactions on Medical Imaging* **26**(11), 1562–1575. [xxxi, xxxv, xlv, xlvi, 77, 88, 89, 95, 99, 101, 102, 118, 133, 135, 163, 165, 211, 212]
- O'Donnell, L. J., M. Kubicki, M. E. Shenton, M. H. Dreusicke, W. E. L. Grimson, and C. F. Westin: 2006, 'A method for clustering white matter fiber tracts'. *AJNR Am J Neuroradiol* **27**(5), 1032–1036. [xxxi, xxxii, xxxiii, xlv, xlvi, 89, 101, 102, 118, 119, 133, 134, 163, 165, 166, 211]
- O'Donnell, L. J., C.-F. Westin, and A. J. Golby: 2007, 'Tract-Based Morphometry'. In: *MICCAI 2007, LNCS 5762, Springer-Verlag*. pp. 161–168. [110]
- O'Donnell, L. J., C.-F. Westin, and A. J. Golby: 2009, 'Tract-based morphometry for white matter group analysis'. *Neuroimage* **45**(3), 832–844. [107, 110]
- Oishi, K., A. Faria, H. Jiang, X. Li, K. Akhter, J. Zhang, J. T. Hsu, M. I. Miller, P. C. M. van Zijl, M. Albert, C. G. Lyketsos, R. Woods, A. W. Toga, G. B. Pike, P. Rosa-Neto, A. Evans, J. Mazziotta, and S. Mori: 2009, 'Atlas-based whole brain white matter analysis using large deformation diffeomorphic metric mapping: application to normal elderly and Alzheimer's disease participants'. *Neuroimage* **46**(2), 486–499. [79, 215, 216]
- Oishi, K., K. Zilles, K. Amunts, A. Faria, H. Jiang, X. Li, K. Akhter, K. Hua, R. Woods, A. W. Toga, G. B. Pike, P. Rosa-Neto, A. Evans, J. Zhang, H. Huang, M. I. Miller, P. C. M. van Zijl, J. Mazziotta, and S. Mori: 2008, 'Human brain white matter atlas: Identification and assignment of common anatomical structures in superficial white matter'. *Neuroimage* **43**(3), 447–457. [xxii, xxxi, xlv, xlviii, liv, 25, 78, 80, 163, 173, 178, 191, 214, 215]
- Pajevic, S., A. Aldroubi, and P. J. Basser: 2002, 'A continuous tensor field approximation of discrete DT-MRI data for extracting microstructural and architectural features of tissue'. *J Magn Reson* **154**(1), 85–100. [67]
- Pajevic, S. and C. Pierpaoli: 1999, 'Color schemes to represent the orientation of anisotropic tissues from diffusion tensor data: Application to white matter fiber tract mapping in the human brain'. *Magnetic Resonance in Medicine* **42**(3), 526–540. [47]
- Parker, G. and D. Alexander: 2005, 'Probabilistic anatomical connectivity derived from the microscopic persistent angular structure of cerebral tissue'. *Phil. Trans. R. Soc. B* **360**, 893–902. [66, 67]

- Pennec, X., P. Fillard, and N. Ayache: 2006, 'A Riemannian Framework for Tensor Computing'. *International Journal of Computer Vision* **66**, 41–66. [43]
- Perrin, M.: 2006, 'Imagerie de diffusion à haute résolution angulaire : étude du modèle q-ball par couplage simulations — fantômes et applications au suivi de fibres et à la parcellisation du cortex'. Ph.D. thesis, Université Paris XI, France. [12, 30, 61]
- Perrin, M., Y. Cointepas, A. Cachia, C. Poupon, B. Thirion, D. Rivière, P. Cathier, V. El Kouby, A. Constantinesco, D. Le Bihan, and J.-F. Mangin: 2008, 'Connectivity-Based Parcellation of the Cortical Mantle Using q-Ball Diffusion Imaging'. *Int J Biomed Imaging* **2008**, 368–406. [61, 145]
- Perrin, M., C. Poupon, Y. Cointepas, B. Rieul, N. Golestani, C. Pallier, D. Rivière, A. Constantinesco, D. Le Bihan, and J.-F. Mangin: 2005a, 'Fiber tracking in q-ball fields using regularized particle trajectories'. *Inf Process Med Imaging* **19**, 52–63. [xxix, 63, 64, 65, 148, 191]
- Perrin, M., C. Poupon, R. Rieul, P. Leroux, A. Constantinesco, J.-F. Mangin, and D. Le Bihan: 2005b, 'Validation of q-ball imaging with a diffusion fibre-crossing phantom on a clinical scanner'. *Philos Trans R Soc Lond B Biol Sci* **360**(1457), 881–891. [62]
- Poupon, C.: 1999a, 'Anatomie cérébrale et imagerie médicale'. Internal Report, SHFJ/CEA. [22, 27, 60, 68]
- Poupon, C.: 1999b, 'Détection des faisceaux de fibres de la substance blanche pour l'étude de la connectivité anatomique cérébrale'. PhD thesis, Ecole Nationale Supérieure des Télécommunications, Paris, France. [xxviii, 41, 49]
- Poupon, C., C. Clark, V. Frouin, et al.: 2000, 'Regularization of diffusion-based direction maps for the tracking of brain white matter fascicles'. *NeuroImage* **12**(2), 184–195. [62]
- Poupon, C., L. Laribiere, G. Tournier, J. Bernard, D. Fournier, P. Fillard, M. Descoteaux, and J.-F. Mangin: 2010, 'A diffusion hardware phantom looking like a coronal brain slice'. In: *Joint ISMRM/ESMRMB conference*. [xli, 153]
- Poupon, C., F. Poupon, L. Alliol, et al.: 2006, 'NMR: a free database dedicated to the anatomofunctional study of the human brain connectivity'. In: *HBM*. Florence, Italy. [xli, xlviii, 1, 148]
- Poupon, C., B. Rieul, I. Kezele, M. Perrin, F. Poupon, and J.-F. Mangin: 2008, 'New diffusion phantoms dedicated to the study and validation of high-angular-resolution diffusion imaging (HARDI) models'. *Magn Reson Med* **60**(6), 1276–1283. [153]
- Qazi, A. A., A. Radmanesh, L. O'Donnell, G. Kindlmann, S. Peled, S. Whalen, C.-F. Westin, and A. J. Golby: 2009, 'Resolving crossings in the corticospinal tract by two-tensor streamline tractography: Method and clinical assessment using fMRI'. *Neuroimage* **47 Suppl 2**, T98–106. [63]
- Ramirez-Manzanares, A., M. Rivera, B. C. Vemuri, P. Carney, and T. Mareci: 2007, 'Diffusion Basis Functions Decomposition for Estimating White Matter Intravoxel Fiber Geometry'. *IEEE Transactions in Medical Imaging* **26**(8), 1091–1102. [51]



- Reese, T. G., O. Heid, R. M. Weisskoff, and V. J. Wedeen: 2003, ‘Reduction of eddy-current-induced distortion in diffusion MRI using a twice-refocused spin echo’. *Magn Reson Med* **49**(1), 177–182. [39, 148]
- Roca, P., D. Rivière, P. Guevara, C. Poupon, and J.-F. Mangin: 2009, ‘Tractography-Based Parcellation of the Cortex using a Spatially-Informed Dimension Reduction of the Connectivity Matrix’. In: *MICCAI 2009, LNCS 5762, Springer-Verlag*. [148]
- Roca, P., A. Tucholka, D. Rivière, P. Guevara, C. Poupon, and J.-F. Mangin: 2010, ‘Inter-subject Connectivity-Based Parcellation of a Patch of Cerebral Cortex’. In: *MICCAI 2010*, Vol. LNCS 6362. pp. 347–354, Springer-Verlag. [148]
- Schüz, A. and V. Braitenberg: 2002, *Cortical Areas: Unity and Diversity*, Chapt. The human cortical white matter: Quantitative aspects of corticocortical long-range connectivity, pp. 377–386, Conceptual Advances in Brain Research. London, UK: Taylor & Francis. [xxi, 21]
- Seunarine, K. K., P. A. Cook, M. G. Hall, K. V. Embleton, G. J. M. Parker, and D. C. Alexander: 2007, ‘Exploiting peak anisotropy for tracking through complex structures’. In: *Mathematical Methods in Biomedical Image Analysis (MMBIA 2007)*. [66]
- Shi, J. and J. Malik: 2000, ‘Normalized cuts and image segmentation’. *IEEE Trans. on Pattern Analysis and Machine Intelligence* **22**(8), 888–905. [xxxii, 87]
- Smith, S. M., M. Jenkinson, H. Johansen-Berg, D. Rueckert, T. E. Nichols, C. E. Mackay, K. E. Watkins, O. Ciccarelli, M. Z. Cader, P. M. Matthews, and T. E. J. Behrens: 2006, ‘Tract-based spatial statistics: voxelwise analysis of multi-subject diffusion data’. *Neuroimage* **31**(4), 1487–1505. [106, 111, 159]
- Stejskal, E. and J. Tanner: 1965, ‘Spin diffusion measurements: Spin echoes in the presence of a time-dependent field gradient’. *J. Chem. Phys.* **42**(1), 288–292. [xxv, 36]
- Studholme, C.: 1999, ‘An overlap invariant entropy measure of 3D medical image alignment’. *Pattern Recognition* **32**(1), 71–86. [74]
- Studholme, C., D. L. G. Hill, and D. J. Hawkes: 1995, ‘Multiresolution Voxel Similarity Measures for MR-PET Registration’. In: Y. Bizais, C. Barillot, and R. Di Paola (eds.): *Proceedings of Information Processing in Medical Imaging*, Vol. 3. Ile de Berder, France, pp. 287–298. [73]
- Talairach, J. and P. Tournoux: 1988, *Co-Planar Stereotaxic Atlas of the Human Brain. 3-Dimensional Proportional System : An Approach to Cerebral Imaging*. Thieme Medical Publishers, Inc., Georg Thieme Verlag, Stuttgart, New York. [74, 75, 76]
- Talairach, J. and P. Tournoux: 1993, *Referentially oriented cerebral MRI anatomy. Atlas of stereotaxic anatomical correlations for gray and white matter*. Thieme Medical Publishers, Inc., Georg Thieme Verlag, Stuttgart, New York, 1 edition. [74]
- Thirion, J. P.: 1998, ‘Image matching as a diffusion process: an analogy with Maxwell’s demons’. *Med Image Anal* **2**(3), 243–260. [74]
- Tournier, J.-D., F. Calamante, and A. Connelly: 2007, ‘Robust determination of the fibre orientation distribution in diffusion MRI: non-negativity constrained super-resolved spherical deconvolution’. *Neuroimage* **35**(4), 1459–1472. [57, 148]

- Tournier, J.-D., F. Calamante, D. G. Gadian, and A. Connelly: 2004, ‘Direct estimation of the fiber orientation density function from diffusion-weighted MRI data using spherical deconvolution’. *NeuroImage* **23**(3), 1176–1185. [xxix, 56, 57]
- Tuch, D.: 2002, ‘Diffusion MRI of Complex Tissue Structure’. Ph.D. thesis, Massachusetts Institute of Technology. [xxviii, 51, 53, 63]
- Tuch, D. S.: 2004, ‘Q-ball imaging’. *Magn. Reson. Med.* **52**(6), 1358–1372. [xxviii, 53, 54, 56]
- Tuch, D. S., T. G. Reese, M. R. Wiegell, N. Makris, J. W. Belliveau, and V. J. Wedeen: 2002, ‘High angular resolution diffusion imaging reveals intravoxel white matter fiber heterogeneity’. *Magn Reson Med* **48**(4), 577–582. [30, 38, 52]
- Vercauteren, T., X. Pennec, A. Perchant, and N. Ayache: 2008, ‘Symmetric log-domain diffeomorphic Registration: a demons-based approach’. *MICCAI 2008* **11**(Pt 1), 754–761. [74]
- Vercauteren, T., X. Pennec, A. Perchant, and N. Ayache: 2009, ‘Diffeomorphic demons: efficient non-parametric image registration’. *Neuroimage* **45**(1 Suppl), S61–S72. [74, 76, 169]
- Vincent, L. and P. Soille: 1991, ‘Watersheds in digital spaces: an efficient algorithm based on immersion simulations’. *IEEE Trans. Pattern Anal. Mach. Intell.* **13**(6), 583–598. [xxxix, 131]
- Viola, P. and W. M. Wells, III: 1997, ‘Alignment by Maximization of Mutual Information’. *Int. J. Comput. Vision* **24**, 137–154. [74]
- Visser, E., E. H. J. Nijhuis, J. K. Buitelaar, and M. P. Zwiers: 2011, ‘Partition-based mass clustering of tractography streamlines’. *Neuroimage* **54**(1), 303–312. [xxxi, xxxii, xxxiii, xxxvi, xlv, 92, 96, 104, 105, 118, 119, 163, 164, 198]
- von Luxburg, U.: 2007, ‘A Tutorial on Spectral Clustering’. *Statistics and Computing* **17**(4), 395–416. [87]
- Wakana, S., A. Caprihan, M. M. Panzenboeck, J. H. Fallon, M. Perry, R. L. Gollub, K. Hua, J. Zhang, H. Jiang, P. Dubey, A. Blitz, P. van Zijl, and S. Mori: 2007, ‘Reproducibility of quantitative tractography methods applied to cerebral white matter’. *Neuroimage* **36**(3), 630–644. [xxx, xlv, 78, 79, 104, 106, 117, 163]
- Wakana, S., H. Jiang, L. M. Nagae-Poetscher, P. C. M. van Zijl, and S. Mori: 2004, ‘Fiber tract-based atlas of human white matter anatomy’. *Radiology* **230**(1), 77–87. [78, 102, 103, 108, 211, 212, 213]
- Wang, X., W. E. L. Grimson, and C.-F. Westin: 2011, ‘Tractography segmentation using a hierarchical Dirichlet processes mixture model’. *Neuroimage* **54**(1), 290–302. [xxxi, xxxiii, xxxvi, xlv, 96, 99, 100, 117, 118, 119, 163, 164, 198]
- Wang, Z. and B. Vemuri: 2004, ‘Tensor Field Segmentation Using Region Based Active Contour Model’. In: Springer (ed.): *European Conference on Computer Vision (ECCV)*, Vol. LNCS 3024. pp. 304–315. [77]
- Wang, Z. and B. C. Vemuri: 2005, ‘DTI Segmentation Using an Information Theoretic Tensor Dissimilarity Measure’. *IEEE Transactions in Medical Imaging* **24**(10), 1267–1277. [77]

- Wassermann, D.: 2010, ‘Automated in vivo dissection of white matter structures from Diffusion Magnetic Resonance Imaging’. Ph.D. thesis, University of Nice-Sophia Antipolis. [72, 81, 87, 88]
- Wassermann, D., L. Bloy, E. Kanterakis, R. Verma, and R. Deriche: 2010a, ‘Unsupervised white matter fiber clustering and tract probability map generation: Applications of a Gaussian process framework for white matter fibers’. *Neuroimage* **51**, 228–241. [xxxi, xxxii, xxxvi, 64, 77, 85, 91, 93, 96, 102, 103, 106, 111, 118, 163]
- Wassermann, D., M. Descoteaux, and R. Deriche: 2008, ‘Diffusion maps clustering for magnetic resonance q-ball imaging segmentation’. *Int J Biomed Imaging* **2008**, 526–906. [xxxi, 77, 87, 117]
- Wassermann, D., E. Kanterakis, R. C. Gur, R. Deriche, and R. Verma: 2010b, ‘Diffusion-Based Population Statistics Using Tract Probability Maps’. In: *MICCAI 2010*, Vol. LNCS 6361. pp. 631–639, Springer-Verlag. [111]
- Wedeen, V., T. Reese, D. Tuch, M. Wiegell, J.-G. Dou, R. Weiskoff, and D. Chessler: 2000, ‘Mapping fiber orientation spectra in cerebral white matter with Fourier-transform diffusion MRI’. In: *Proceedings of the International Society of Magnetic Resonance in Medicine*. p. 82. [xxviii, 52]
- Wedeen, V. J., P. Hagmann, W.-Y. I. Tseng, T. G. Reese, and R. M. Weisskoff: 2005, ‘Mapping complex tissue architecture with diffusion spectrum magnetic resonance imaging’. *Magn Reson Med* **54**(6), 1377–1386. [52]
- Wedeen, V. J., R. P. Wang, J. D. Schmahmann, T. Benner, W. Y. I. Tseng, G. Dai, D. N. Pandya, P. Hagmann, H. D’Arceuil, and A. J. de Crespigny: 2008, ‘Diffusion spectrum magnetic resonance imaging (DSI) tractography of crossing fibers’. *Neuroimage* **41**(4), 1267–1277. [63]
- Weinstein, D., G. Kindlmann, and E. Lundberg: 1999, ‘Tensorlines: Advection-Diffusion based Propagation Through Tensor Fields’. In: *IEEE Proceedings Visualization*. pp. 249–253. [62]
- Woods, R. P., S. T. Grafton, J. D. Watson, N. L. Sicotte, and J. C. Mazziotta: 1998, ‘Automated image registration: II. Intersubject validation of linear and nonlinear models’. *J Comput Assist Tomogr* **22**(1), 153–165. [74, 76]
- Woods, R. P., J. C. Mazziotta, and S. R. Cherry: 1993, ‘MRI-PET registration with automated algorithm’. *J Comput Assist Tomogr* **17**(4), 536–546. [73]
- Woolsey, T. A., J. Hanaway, and M. H. Gado: 2008, *The Brain Atlas: A Visual Guide to the Human Central Nervous System*. John Wiley & Sons Inc. [12, 16]
- Yang, J., D. Shen, C. Davatzikos, and R. Verma: 2008, ‘Diffusion tensor image registration using tensor geometry and orientation features’. *MICCAI 2008* **11**(Pt 2), 905–913. [103]
- Yushkevich, P. A., H. Zhang, T. J. Simon, and J. C. Gee: 2008, ‘Structure-specific statistical mapping of white matter tracts’. *Neuroimage* **41**(2), 448–461. [108, 109]
- Zhang, H., S. P. Awate, S. R. Das, J. H. Woo, E. R. Melhem, J. C. Gee, and P. A. Yushkevich: 2009, ‘A Tract-Specific Framework for White Matter Morphometry Combining Macroscopic and Microscopic Tract Features’. In: *MICCAI 2009*, Vol. LNCS 5762. pp. 141–149, Springer-Verlag. [109]

- Zhang, S., S. Correia, and D. H. Laidlaw: 2008a, ‘Identifying White-Matter Fiber Bundles in DTI Data Using an Automated Proximity-Based Fiber-Clustering Method’. *IEEE Transactions on Visualization and Computer Graphics* **14**(5), 1044–1053. [xxxii, xxxv, xlv, 91, 95, 97, 98, 118, 163]
- Zhang, S., C. Demiralp, and D. H. Laidlaw: 2003, ‘Visualizing diffusion tensor MR images using streamtubes and streamsurfaces’. *IEEE Transactions on Visualization and Computer Graphics* **9**(4), 454–462. [xxxiv, 90, 91, 94, 97, 98]
- Zhang, S. and D. H. Laidlaw: 2002, ‘Hierarchical Clustering of Streamtubes’. Technical Report CS-02-18, Brown University Computer Science Department. [xxxiv, 90, 91, 94, 97]
- Zhang, S. and D. H. Laidlaw: 2005, ‘DTI Fiber Clustering and Cross-subject Cluster Analysis’. In: *Proceedings International Society for Magnetic Resonance in Medicine (ISMRM)*. Miami, FL. [xxxv, 95, 97, 98]
- Zhang, W., A. Olivi, S. J. Hertig, P. van Zijl, and S. Mori: 2008b, ‘Automated fiber tracking of human brain white matter using diffusion tensor imaging’. *Neuroimage* **42**(2), 771–777. [78]
- Zhang, Y., J. Zhang, K. Oishi, A. V. Faria, H. Jiang, X. Li, K. Akhter, P. Rosa-Neto, G. B. Pike, A. Evans, A. W. Toga, R. Woods, J. C. Mazziotta, M. I. Miller, P. C. van Zijl, and S. Mori: 2010, ‘Atlas-guided tract reconstruction for automated and comprehensive examination of the white matter anatomy’. *NeuroImage* **52**(4), 1289 – 1301. [xxii, xxxi, xlv, xlviii, l, lvi, 79, 163, 173, 178, 193, 194, 198, 216, 217]